frontiers | Research Topics

Beyond borders: exploring diverse roles of heterocyclic compounds in combatting infections and cancer

Edited by
Afzal Basha Shaik, Richie Bhandare, Mukhlesur Rahman and Kamal Dua

Published in
Frontiers in Chemistry

ISSN 1664-8714
ISBN 978-2-8325-6138-6
DOI 10.3389/978-2-8325-6138-6

About Frontiers

Frontiers is more than just an open access publisher of scholarly articles: it is a pioneering approach to the world of academia, radically improving the way scholarly research is managed. The grand vision of Frontiers is a world where all people have an equal opportunity to seek, share and generate knowledge. Frontiers provides immediate and permanent online open access to all its publications, but this alone is not enough to realize our grand goals.

Frontiers journal series

The Frontiers journal series is a multi-tier and interdisciplinary set of open-access, online journals, promising a paradigm shift from the current review, selection and dissemination processes in academic publishing. All Frontiers journals are driven by researchers for researchers; therefore, they constitute a service to the scholarly community. At the same time, the *Frontiers journal series* operates on a revolutionary invention, the tiered publishing system, initially addressing specific communities of scholars, and gradually climbing up to broader public understanding, thus serving the interests of the lay society, too.

Dedication to quality

Each Frontiers article is a landmark of the highest quality, thanks to genuinely collaborative interactions between authors and review editors, who include some of the world's best academicians. Research must be certified by peers before entering a stream of knowledge that may eventually reach the public - and shape society; therefore, Frontiers only applies the most rigorous and unbiased reviews. Frontiers revolutionizes research publishing by freely delivering the most outstanding research, evaluated with no bias from both the academic and social point of view. By applying the most advanced information technologies, Frontiers is catapulting scholarly publishing into a new generation.

What are Frontiers Research Topics?

Frontiers Research Topics are very popular trademarks of the *Frontiers journals series*: they are collections of at least ten articles, all centered on a particular subject. With their unique mix of varied contributions from Original Research to Review Articles, Frontiers Research Topics unify the most influential researchers, the latest key findings and historical advances in a hot research area.

Find out more on how to host your own Frontiers Research Topic or contribute to one as an author by contacting the Frontiers editorial office: frontiersin.org/about/contact

Beyond borders: exploring diverse roles of heterocyclic compounds in combatting infections and cancer

Topic editors
Afzal Basha Shaik — Vignan's Foundation for Science, Technology and Research (VFSTR), India
Richie Bhandare — Ajman University, United Arab Emirates
Mukhlesur Rahman — University of East London, United Kingdom
Kamal Dua — University of Technology Sydney, Australia

Citation
Shaik, A. B., Bhandare, R., Rahman, M., Dua, K., eds. (2025). *Beyond borders: exploring diverse roles of heterocyclic compounds in combatting infections and cancer*. Lausanne: Frontiers Media SA. doi: 10.3389/978-2-8325-6138-6

Table of contents

frontiers | Frontiers in Chemistry

TYPE Editorial
PUBLISHED 04 March 2025
DOI 10.3389/fchem.2025.1578852

OPEN ACCESS

EDITED AND REVIEWED BY
Michael Kassiou,
The University of Sydney, Australia

*CORRESPONDENCE
Afzal B. Shaik,
bashafoye@gmail.com

RECEIVED 18 February 2025
ACCEPTED 21 February 2025
PUBLISHED 04 March 2025

CITATION
Shaik AB, Bhandare RR, Rahman MM and Dua K (2025) Editorial: Beyond borders: exploring diverse roles of heterocyclic compounds in combatting infections and cancer.
Front. Chem. 13:1578852.
doi: 10.3389/fchem.2025.1578852

Editorial: Beyond borders: exploring diverse roles of heterocyclic compounds in combatting infections and cancer

Afzal B. Shaik[1,2]*, Richie R. Bhandare[3,4], M. Mukhlesur Rahman[5] and Kamal Dua[6,7]

[1]Department of Pharmaceutical Sciences, School of Biotechnology and Pharmaceutical Sciences, Vignan's Foundation for Science, Technology and Research, Guntur, India, [2]Center for Global Health Research, Saveetha Medical College, Saveetha Institute of Medical and Technical Sciences, Chennai, Tamil Nadu, India, [3]College of Pharmacy & Health Sciences, Ajman University, Ajman, United Arab Emirates, [4]Center of Medical and Bio-Allied Health Sciences Research, Ajman University, Ajman, United Arab Emirates, [5]The Medicines Research Group, School of Health, Sports and Bioscience, University of East London, London, United Kingdom, [6]Faculty of Health, Australian Research Centre in Complementary and Integrative Medicine, University of Technology Sydney, Ultimo, NSW, Australia, [7]Discipline of Pharmacy, Graduate School of Health, University of Technology Sydney, Ultimo, NSW, Australia

KEYWORDS

bioactive heterocyclic compounds, medicinal chemistry, anti-infective agents, anticancer agents, natural product chemistry, computational chemistry, synthesis and semisynthesis, drug design

Editorial on the Research Topic
Beyond borders: exploring diverse roles of heterocyclic compounds in combatting infections and cancer

This Research Topic aimed to explore the advancements and applications of heterocyclic compounds, highlighting their importance in contemporary medicinal chemistry. The objective was to examine their diverse roles in tackling two major health concerns: infectious diseases and cancer. Currently, cancer and infectious diseases are among the most prevalent and challenging health conditions, significantly affecting the overall wellbeing of the population. According to the World Health Organization (WHO), approximately 20 million new cancer cases were diagnosed globally in 2022, with 9.7 million deaths attributed to the disease. Projections suggest that by 2050, the number of cancer cases could rise to 35 million (Seigel et al., 2023). Antimicrobial resistance (AMR) is recognized as one of the top ten global health threats, posing significant risks not only to human health but also to environmental wellbeing. It is classified as a quintessential One Health challenge. The most concerning pathogens, characterized by multidrug resistance (MDR), extended-drug resistance, and even pan-drug resistance phenotypes, are collectively referred to by the acronym ESCAPE, encompassing *Enterococcus faecium*, *Staphylococcus aureus*, *Clostridium difficile*, *Acinetobacter baumannii*, *Pseudomonas aeruginosa*, and *Enterobacteriaceae* (De Oliveira et al., 2020). Recent developments in this area have shown the potential of heterocyclic compounds to offer more targeted and effective treatments with fewer side effects. Therefore, this Research Topic invited papers that showcased recent progress in medicinal and natural product chemistry, including the isolation and characterization,

design, synthesis, and application of heterocyclic compounds as promising anti-infective and anticancer agents.

This Research Topic covers a total of fourteen original research articles investigating ligands spanning broad therapeutic areas like breast/prostate cancer, inflammatory bowel disease, antitubercular ligands, antimicrobials, anticholinergic and antidiabetic. Seven papers focused on exploring heterocyclic compounds from natural products using various techniques such as molecular dynamics, nanoparticles, *in silico* and GC-MS profiling and quantum analysis while the remaining papers emphasised the use of heterocyclic fragments for various therapeutics activities.

Mashud et al. investigated the potential inhibitory effects of specific compounds present in leaf extract from *Mangifera indica* on the growth of drug-resistant breast cancer protease. The chemical compounds present in the plant were analysed using molecular modelling techniques, such as molecular docking, molecular dynamics (MD) simulations, quantum mechanics (QM) calculations, and the Absorption, Distribution, Metabolism, Excretion, and Toxicity (ADMET) method, in order to examine three key chemical constituents: quercetin, catechin, and ellagic acid. The ligands underwent extensive testing to determine their effectiveness against the 3w32-overexpressing breast cancer protein. This study used molecular docking tools and molecular dynamic studies identified ligands with strong binding affinity for the breast cancer protein that overexpressed 3w32. The study identified three ligands that not only surpassed the efficacy of the FDA-approved treatment, but also fulfilled the requirements for a possible new inhibitor of breast cancer.

Barik et al. explored the potential use of silver nanoparticles (AgNPs) for treating periodontal infections, synthesized using leaf extract from *Azadirachta indica*. The eco-friendly green synthesis process utilizes the plant as a natural stabilizer and reducer, facilitating the formation of silver nanoparticles. Various analytical techniques, including transmission electron microscopy (TEM), Fourier-transform infrared spectroscopy (FTIR), Zeta potential analysis, and ultraviolet-visible spectroscopy (UV-Vis), were employed to characterize the AgNPs. The antimicrobial and antioxidant properties of AgNPs were tested to evaluate their effectiveness against periodontal infections. The results demonstrate significant antibacterial and antioxidant activity, inhibiting biofilm formation and bacterial viability. The study has suggested that AgNPs derived from *A. indica* may serve as a safe, effective, and environmentally friendly alternative to traditional therapies for treating periodontal infections.

Mallela et al. investigated the anticancer effects of methanolic extracts from Lotus seeds (MELS) on cell proliferation inhibition, apoptosis induction, and cell cycle arrest in ovarian cancer cell lines. They also reported the phytochemical composition of MELS using gas chromatography-mass spectrometry (GC-MS) analysis. Additionally, molecular docking studies were conducted to support the *in vitro* anticancer effects by examining the inhibitory potential of MELS on human survivin protein. The *in-vitro* findings demonstrated significant inhibition of SKOV3, A2780, SKOV3-CisR, and A2780-CisR cells by MELS, in comparison to acetone, petroleum ether, n-hexane extracts, and the standard drug, cisplatin. They employed GC-MS to analyse and characterize 14 potential phytocompounds present in MELS. Molecular docking results showed that oleic acid, stigmast-5-en-3-ol, phytol, and glyceryl linolenate exhibited strong binding affinities to survivin. These findings suggest that the phytochemicals identified in MELS may have therapeutic potential for the management of ovarian cancer.

Kirboga et al. reported the binding affinities and interaction profiles of selected cannabinoids and stilbenoids on eight proteins through molecular docking and molecular dynamics simulations. They identified ligands with the highest binding affinities, and their pharmacokinetic properties were assessed using ADMET analysis. The results revealed that GMP synthase showed the strongest binding affinity with Cannabistilbene I, indicating hydrophobic interactions and multiple hydrogen bonds. Similarly, Chitin Synthase 2 also demonstrated significant binding with Cannabistilbene I. In contrast, ligands like Cannabinolic acid and 8-hydroxycannabinolic acid exhibited moderate binding affinities, highlighting the variability in interaction strengths across different proteins. Experimental validation is essential to confirm their therapeutic potential. This study is pivotal for future research, emphasizing the importance of evaluating binding affinities, pharmacokinetic profiles, and multi-target interactions to identify promising antifungal agents.

Belal et al. focused on the antiviral properties of natural indoles, Gardflorine A–C, extracted from *Gardneria multiflora* Makino. Utilizing molecular docking, ADMET analysis, and computational approaches—including Frontier molecular orbital (FMO) analysis, natural bond orbital (NBO) analysis, and density functional theory (DFT)—the authors evaluate these compounds' potential as multi-target antiviral ligands against HIV and HCV proteins.

Edis et al. highlighted the potential of clove extract-mediated nanoparticle synthesis as an effective approach for integrating medications with metals at the nanoscale. These nanoparticles exhibited a synergistic effect with the heterocyclic antibiotic clarithromycin, enhancing its therapeutic efficacy, reducing side effects, and improving antimicrobial activity. The authors synthesized silver nanoparticles using clove extract, resulting in AgNPC and AgNPCA (A = clarithromycin). Various instrumental techniques, including SEM, EDS, DLS, UV-Vis, FTIR, and XRD, were used to analyze the compounds. When tested against different microbes, the nanoparticles demonstrated antibacterial properties ranging from intermediate to strong. The study underscores the potential of clove extract-mediated AgNP synthesis, both alone and in combination with clarithromycin.

Altin et al. described the therapeutic potential of *Laurus nobilis* leaves, emphasizing their rich phenolic content and bioactive properties, including antioxidant, antidiabetic, and anticholinergic effects. The phenolic compounds in the ethanolic extracts were analysed using LC-MS/MS, while antioxidant activity was assessed through ferric thiocyanate, DPPH, ABTS assays, and metal reduction potential tests. Anticholinergic and antidiabetic properties were evaluated via inhibition studies on acetylcholinesterase (AChE), butyrylcholinesterase (BChE), and α-glucosidase (α-GLY) enzymes, complemented by *in silico* analysis to investigate binding mechanisms. Vanillic acid and catechin hydrate were identified as the most abundant phenolics, with the extract demonstrating superior lipid peroxidation inhibition compared to Trolox and α-tocopherol. Moderate radical scavenging activity and metal reduction potential further

supported its bioactivity. In silico results revealed a strong binding affinity of phenolics to target enzymes, reinforcing their therapeutic potential. This study has highlighted the promising antioxidant, antidiabetic, and anticholinergic properties of *L. nobilis* extracts for potential medicinal applications.

Thakur et al. designed novel analogues of Cabozantinib (CBZ) using a bioisosteric approach to develop compounds with reduced toxicity, improved safety, and enhanced potency against multi-drug-resistant cancers. The physicochemical, medicinal, and ADMET properties were assessed using ADMETLab 3.0. Additionally, the authors evaluated the drug-likeness and drug scores of the analogues. Molecular docking studies were conducted using AutoDock Vina, with BIOVIA Discovery Studio employed for visualizing key interactions. The docking scores for the ligands ranged from −8.0 to −6.4 kcal/mol against the target protein. Molecular dynamics (MD) simulations of selected compounds, performed using the Schrödinger suite, demonstrated that the complexes remained stable throughout the simulation period. This study has highlighted the potential of two promising ligands as candidates for the development of novel anticancer agents for treating various cancers.

Al-Wahaibi et al. described total synthesis of a series of disalicylic acid methylene/Schiff base hybrids designed to function as antibacterial agents by targeting DNA gyrase and DHFR. Their study identified several compounds with potent antibacterial activity against both Gram-positive and Gram-negative bacteria, demonstrating inhibition zones (IZ) comparable to or exceeding those of the reference drug Ciprofloxacin.

Shahi et al. focused on developing dihydropyrimidinone and dihydropyridine derivatives of thymol and evaluating their antimicrobial properties. The synthesized compounds showed broad spectrum *in-vitro* antibacterial activity against *P. aeruginosa* and methicillin-resistant *S. aureus* (MRSA). Among the derivatives, they identified a promising compound with the most potent antibacterial activity against both *P. aeruginosa* and MRSA. Furthermore, the most potent compound exhibited synergistic effects when combined with vancomycin, enhancing its antibacterial efficacy. In silico analysis of its physicochemical properties confirmed compliance with all drug-likeness criteria. Lastly, molecular docking studies revealed that the promising compound had a stronger binding affinity to the target protein than thymol, providing valuable insights into its potential mechanism of action.

Gupta et al. computationally designed novel analogues of Apalutamide with the aim of enhancing pharmacokinetic properties and minimizing toxicity. Drug-likeness (DL) and drug score (DS) were also assessed. Molecular docking and molecular dynamics (MD) simulations were performed to evaluate the binding affinities of the designed analogues and compare their binding orientations with those of the ligands in the original crystal structure. The findings indicate that two analogues exhibit potential as antiandrogen ligands for the treatment of prostate cancer.

Sabt et al. synthesized a series of novel compounds by conjugating 4-carboxyquinoline with triazole motifs. These compounds were evaluated for their antimicrobial efficacy against various *Mycobacterium* strains, including *M. bovis* BCG, *M. tuberculosis*, and *M. abscessus*. Additionally, their inhibitory potential against the InhA enzyme was assessed. Several molecules demonstrated significant activity against *M. tuberculosis*. Molecular docking analysis revealed key interactions between these compounds and the target enzyme, while molecular dynamics (MD) simulations confirmed the stability of the quinoline-triazole conjugate complexes with InhA. Furthermore, the most potent compound underwent *in silico* ADME analysis to predict its pharmacokinetic properties. This study provides valuable insights into the development of novel, safe, and effective small-molecule therapeutics for tuberculosis treatment.

Arif et al. reported the development of a novel isatin derivative capable of degrading estrogen receptor alpha (ERα) in estrogen-dependent breast cancer cells. A series of hydrazide derivatives were synthesized and evaluated *in vitro* for their antiproliferative activity against the MCF-7 (ER+) cell line. The effect of the most potent compound on ERα expression was further analyzed using Western blot analysis. Additionally, *in silico* pharmacokinetic predictions were conducted using various computational tools, including pkCSM, to assess the activity profiles of the synthesized compounds.

Zhao et al. identified novel chrysin derivatives with promising therapeutic potential for inflammatory bowel disease (IBD). Among them, a potent compound exhibited significant inhibitory activity against TNF-α-induced monocyte adhesion to the colonic epithelium. Mechanistic studies revealed that this compound suppresses reactive oxygen species (ROS) production and downregulates the expression of ICAM-1 and MCP-1, key mediators of monocyte-epithelial adhesion, as well as the transcriptional activity of NF-κB. *In vivo* experiments further demonstrated its efficacy in mitigating colitis in animal models. These findings highlight the compound's potential as a promising candidate for IBD management.

In summary, the fourteen original articles featured in this Research Topic have presented recent advancements in the application of heterocyclic scaffolds across various therapeutic areas, including breast cancer, inflammatory bowel disease, and tuberculosis. The collective findings of these studies offer valuable insights for researchers in organic and medicinal chemistry, particularly those focused on chemotherapy. This Research Topic has also emphasized the challenge of antimicrobial resistance and underscores the significance of heterocycles as privileged structures in drug design, making it highly relevant to Frontiers readers in this field. The heterocyclic ring systems discussed herein may be of particular interest to medicinal chemists for the synthesis of bioactive compounds and the development of novel analogues, thereby contributing to chemotherapy drug discovery efforts and addressing the global issue of resistance.

Author contributions

AS: Writing–original draft. RB: Writing–original draft. MR: Writing–review and editing. KD: Writing–review and editing.

Funding

The author(s) declare that no financial support was received for the research, authorship, and/or publication of this article.

Conflict of interest

The authors declare that the research was conducted in the absence of any commercial or financial relationships that could be construed as a potential conflict of interest.

The author(s) declared that they were an editorial board member of Frontiers, at the time of submission. This had no impact on the peer review process and the final decision.

Generative AI statement

The author(s) declare that no Generative AI was used in the creation of this manuscript.

Publisher's note

All claims expressed in this article are solely those of the authors and do not necessarily represent those of their affiliated organizations, or those of the publisher, the editors and the reviewers. Any product that may be evaluated in this article, or claim that may be made by its manufacturer, is not guaranteed or endorsed by the publisher.

References

De Oliveira, D. M., Forde, B. M., Kidd, T. J., Harris, P. N., Schembri, M. A., Beatson, S. A., et al. (2020). Antimicrobial resistance in ESKAPE pathogens. *Clin. Microbiol. Rev.* 33(3), 10–128. doi:10.1128/cmr.00181-19

Siegel, R. L., Miller, K. D., Wagle, N. S., and Jemal, A. (2023). Cancer statistics, 2023. *CA a cancer J. Clin.* 73(1), 17–48. doi:10.3322/caac.21763

frontiers | Frontiers in Chemistry

TYPE Original Research
PUBLISHED 27 May 2024
DOI 10.3389/fchem.2024.1406051

OPEN ACCESS

EDITED BY
Ahmed A. Al-Karmalawy,
Ahram Canadian University, Egypt

REVIEWED BY
Haytham O. Tawfik,
Tanta University, Egypt
Hazem Elkady,
Al-Azhar University, Egypt

*CORRESPONDENCE
Funeng Geng,
haoyishenggfn@126.com
Qi Liao,
kamper1@163.com

RECEIVED 24 March 2024
ACCEPTED 07 May 2024
PUBLISHED 27 May 2024

CITATION
Zhao P, Hou Y, Yan T, Kang J, Tian Y, Li J, Zeng C, Geng F and Liao Q (2024), Synthesis and biological evaluation of chrysin derivatives containing α-lipoic acid for the treatment of inflammatory bowel disease.
Front. Chem. 12:1406051.
doi: 10.3389/fchem.2024.1406051

Synthesis and biological evaluation of chrysin derivatives containing α-lipoic acid for the treatment of inflammatory bowel disease

Pengyu Zhao[1], Yusen Hou[2,3], Tingting Yan[4], Jie Kang[5], Ye Tian[6], Jiaxin Li[7], Chenjuan Zeng[6], Funeng Geng[2,4]* and Qi Liao[4]*

[1]School of Clinical Medicine, Chengdu University of Traditional Chinese Medicine, Chengdu, China, [2]School of Pharmacy, Chengdu University of Traditional Chinese Medicine, Chengdu, China, [3]State Key Laboratory of Southwestern Chinese Medicine Resources, College of Pharmacy, Chengdu University of Traditional Chinese Medicine, Chengdu, China, [4]Sichuan Key Laboratory of Medical American Cockroach, Chengdu, China, [5]Yunnan Shengke Pharmaceutical Co., Ltd., Kunming, China, [6]Guizhou Yunfeng Pharmaceutical Co., Ltd., Xingyi, China, [7]Sichuan Engineering Research Center for Medicinal Animals, Chengdu, China

This study introduces newly discovered chrysin derivatives that show potential as candidate molecules for treating inflammatory bowel disease (IBD). Compound **4b**, among the synthesized compounds, displayed significant inhibitory effects on monocyte adhesion to colon epithelium induced by TNF-α, with an IC_{50} value of 4.71 μM. Further mechanistic studies demonstrated that **4b** inhibits the production of reactive oxygen species (ROS) and downregulates the expression of ICAM-1 and MCP-1, key molecules involved in monocyte-epithelial adhesion, as well as the transcriptional activity of NF-κB. *In vivo* experiments have shown that compound **4b** exhibits a dose-dependent inhibition of 2, 4, 6-trinitrobenzenesulfonic acid (TNBS)-induced colitis in rats, thereby validating its effectiveness as a colitis inhibitor in animal models. These results indicate that **4b** shows considerable promise as a therapeutic agent for managing IBD.

KEYWORDS

inflammatory bowel disease, chrysin derivatives, small molecules, anti-inflammatory activity, TNF-α

1 Introduction

The pathogenesis of inflammatory bowel disease (IBD) is a multifaceted process that encompasses the interplay of genetic predisposition, environmental triggers, and immune dysregulation within the gastrointestinal system (Seyedian S et al., 2019). The etiology of the disease involves alterations in the innate immune response of the body. TNF-α functions to induce inflammation by stimulating the synthesis of additional pro-inflammatory cytokines and adhesion

Abbreviations: α-LA, α-lipoic acid; CCK-8, cell-counting kit-8; H&E, hematoxylin and eosin; IBD, inflammatory bowel disease; ICAM, intercellular adhesion molecule; IFNγ, interferon gamma; iNOS, inducible nitric oxide synthase; LPS, lipopolysaccharide; MCP-1, monocyte chemotactic protein-1; NF-κB, nuclear factor-kappaB; NMR, nuclear magnetic resonance; NO, nitric oxide; ROS, reactive oxygen species; TMS, tetramethylsilane; TNBS, 2,4,6-trinitro-benzenesulfonic acid; SD, Sprague-Dawley.

molecules, facilitating the attachment and transmigration of white blood cells across the intestinal epithelium (Jang D et al., 2021). The critical phase in the development of inflammation and tissue damage seen in IBD entails the influx of additional inflammatory cells into the compromised intestinal epithelium (Saez A et al., 2021; Wang J. et al., 2023). To date, TNF-α inhibitors have demonstrated significant efficacy in managing chronic inflammatory conditions, such as IBD, through their ability to suppress the expression of pro-inflammatory cytokines and adhesion molecules (Peng J et al., 2014; Willrich et al., 2015). Currently, the most effective therapeutic approach for individuals diagnosed with IBD involves the use of anti-tumor necrosis factor-α (anti-TNF-α) antibodies, such as infliximab. However, the known toxicities of the antibody likely hamper its clinical deployment, encompassing infections, immunosuppression, and malignancies (Hemperly and Vande Casteele, 2018; Parigi et al., 2021). Hence, the advancement of more potent and secure medications is imperative for the treatment of IBD.

Natural products are considered to be valuable resources for the initiation of drug discovery (Li et al., 2016; Atanasov et al., 2021). Chrysin, a naturally occurring flavonoid, exhibits a diverse range of biological activities including antibacterial, anti-tumor, antioxidant, anti-allergic, and anti-inflammatory properties (Naz et al., 2019; Oršolić et al., 2022). Extensive evidence supports the notion that chrysin exerts a wide array of anti-inflammatory effects by targeting multiple molecular pathways and their associated targets (Zeinali et al., 2017). Specifically, chrysin possesses anti-inflammatory effects by reducing the production of pro-inflammatory cytokines TNF, IL-1, and IL-6 (Ahad et al., 2014; Faheem et al., 2023). However, the therapeutic effectiveness of chrysin has been hindered by its inadequate aqueous solubility and low bioavailability (Li Y et al., 2019; Bhowmik et al., 2022). Consequently, numerous chrysin derivatives have been synthesized with the aim of augmenting their bioactivities under physiological circumstances (Wang Q et al., 2014; Ghorab et al., 2023). Especially, Chen *et al.* conducted the preparation of various chrysin derivatives incorporating aromatic substituents or long-chain aliphatic hydrocarbons (Chen et al., 2020). Likewise, Li *et al.* prepared a collection of chrysin derivatives featuring diverse amino acid species. In comparison to the parent molecule, these derivatives exhibited enhanced *in vitro* bioactivities (Li Y et al., 2021). These studies have illuminated the importance of chrysin derivatization as a promising method in the development of more effective treatment strategies.

α-Lipoic acid (α-LA) is a ubiquitous biological antioxidant that traverses the blood-brain barrier and serves as a cofactor for enzymes crucial to cellular metabolism (Salehi et al., 2019). Its remarkable ability to neutralize free radicals and uphold cellular oxidoreductive equilibrium has garnered significant attention, particularly in relation to its potential therapeutic efficacy in various ailments, including IBD (Wang Z et al., 2022). In particular, α-LA derivatives bearing the indoles scaffold demonstrate notable anti-inflammatory efficacy by inhibiting the production of pro-inflammatory factors such as nitric oxide (NO) and inducible nitric oxide synthase (iNOS) in lipopolysaccharide (LPS) and interferon gamma (IFNγ)-stimulated RAW 264.7 macrophages (Prieto-Hontoria et al., 2016). Additionally, the *in vivo* studies provided evidence that α-LA effectively attenuated the concentrations of TNF-α. Therefore, considering the functional specificity of α-LA, the incorporation of this compound into chrysin holds the potential to enhance both the bioactivities and physicochemical properties.

In this study, a series of chrysin derivatives were prepared through introducing α-LA functional group. Next, all synthesized compounds were subjected to initial *in vitro* screening to assess their potential anti-inflammatory effects on the adhesion of monocytes to colon epithelial cells induced by TNF-α. Among them, **4b** was identified as a promising candidate molecule. *In vitro* and *in vivo* experiments have shown that **4b** exhibits notable inhibitory effects on TNF-α-induced adhesion of monocytic-colonic epithelial cells. The aforementioned findings collectively indicate that **4b** possesses the potential to serve as a lead molecule in the therapeutic intervention of IBD.

2 Results and discussion

2.1 Design and synthesis

To date, several studies have demonstrated that the introduction of suitable substituents on the hydroxyl group at seven-position of chrysin could improve bioactivities. As demonstrated in Figure 1, this study involved the identification of a series of chrysin derivatives that integrate α-LA through a pharmacophore fusion strategy, which entailed the incorporation of α-LA into chrysin using diverse linker groups. Compounds **4a–d** can be prepared using the general procedure shown in Scheme 1. Specifically, chrysin **one** underwent a substitution reaction in the presence of K_2CO_3, potassium iodide, and compounds **2a–d** containing bromine atom and Boc-protected amino group to attach the intermediate. The deprotection of the compound was conducted utilizing trifluoroacetic acid in dichloromethane, followed by the coupling with 2-chloroethanesulfonyl chloride to yield compounds **3a–d**. Finally, compounds **4a–d** were synthesized by amide condensation reaction of **3a–d** and α-LA.

2.2 Biological evaluation

2.2.1 Structure-activity relationship of synthesized molecules

TNF-α, a prominent cytokine, serves as a key mediator in the inflammatory response by facilitating the recruitment of white blood cells to the mucosa (Zhang L et al., 2019). Its pivotal role in initiating intestinal inflammation, a hallmark of IBD, underscores its significance in the pathogenesis of this condition (Larabi A et al., 2020). During the *in vitro* screening process aimed at identifying potential compounds with the ability to reduce intestinal inflammation, we assessed the inhibitory effects of all synthesized compounds (**4a–d**) on the adhesion of monocytes to HT-29 human colonic epithelial cells induced by TNF-α. Moreover, chrysin and α-LA were employed as standard reference compounds in the assay. As indicated in Table 1, the synthesized compounds **4a–d** exhibited significantly higher inhibitory activities in comparison to positive control molecules, with IC_{50} values falling within the low micromolar range. Furthermore, in comparison to compound **4a** containing a polyethylene glycol linker group, compounds **4b–d** incorporating rigid (cycloaliphatic) linker groups demonstrated increased effectiveness in reducing the TNF-α-induced adhesion of monocytic cells to colonic epithelial cells. This effect is likely attributed to the incorporation of a rigid linker group, which enhances the equilibrium between *in vitro* potency and physicochemical properties, thereby promoting cellular penetration. Among the synthesized molecules analyzed, compound **4b**, which contains a piperazine group, demonstrated the most potent inhibitory activity, as indicated by its IC_{50} value of 4.71 μM. Thus, This could potentially serve as

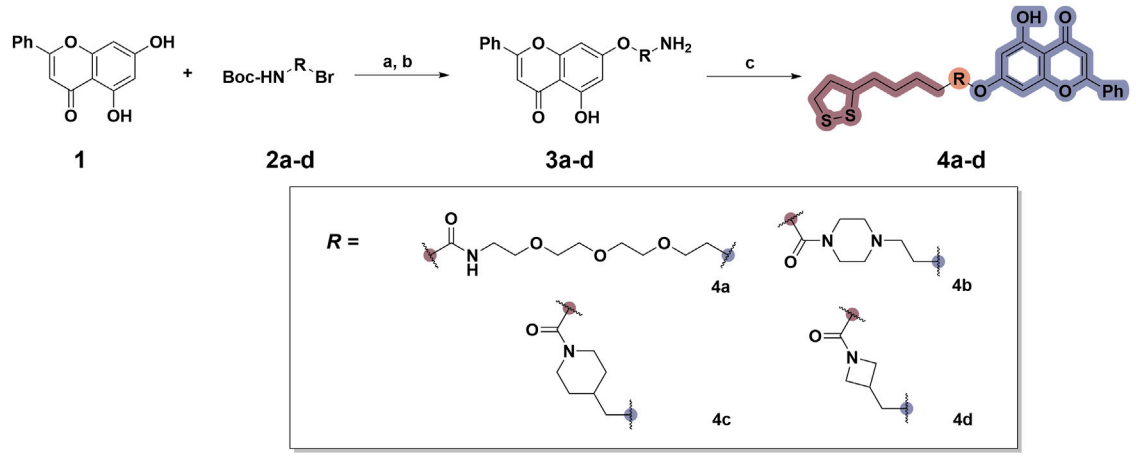

SCHEME 1
Synthetic routes for the synthesis of chrysin derivatives **4a–d** utilizing α-lipoic acid as a precursor. Regents and conditions: (a) K_2CO_3, KI, acetone, 65°C; (b) CF_3COOH, DCM, r. t.; (c) HATU, DIPEA, DMF, α-LA, r. t.

TABLE 1 *In vitro* inhibitory potency of compounds 4a–d against TNF-α-induced adhesion of monocytes to colon epithelial cells HT-29.

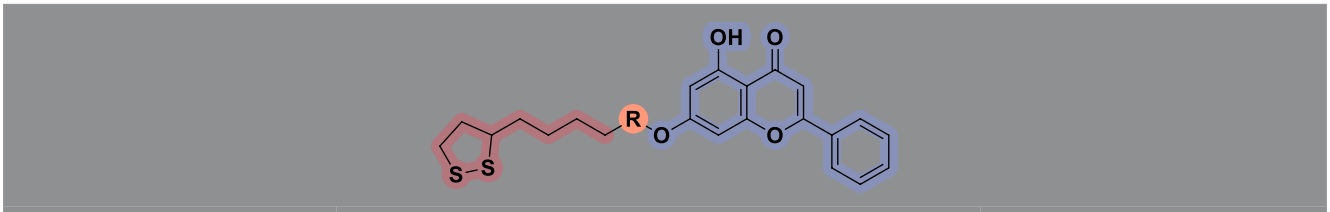

Compd	R	IC_{50}[a] (μM)
4a	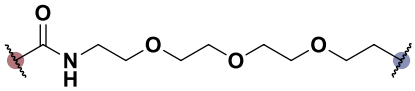	9.47 ± 0.48
4b	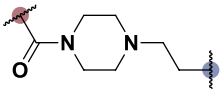	4.71 ± 0.16
4c	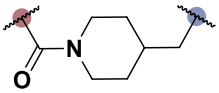	6.73 ± 0.94
4days	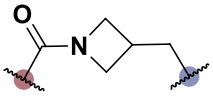	5.61 ± 0.32
Chrysin	–	>30
α-LA	–	12.7 ± 0.6

[a]The results represent the mean ± standard deviation (SD) of three independent experiments conducted in triplicate.

a valuable initial step in the process of identifying a chrysin-based molecule that could be efficacious in the treatment of IBD.

2.2.2 Compound 4b suppresses the adhesion induced by TNF-α in HT-29 cells by downregulating the expression of chemokine molecules and inhibiting the associated signaling pathways

As demonstrated in Figure 2A, compound 4b exhibited significant inhibitory activity against the adhesion of monocytes to HT-29 cells induced by TNF-α, with an IC_{50} value of 4.71 μM. Subsequently, this study investigated the potential mechanism of action of 4b by evaluating its influence on TNF-α-stimulated monocyte-epithelial adhesion in HT-29 cells, with a particular focus on determining if the inhibitory effect of 4b is due to the reduction of adhesion molecule expression. Figure 2B demonstrates that 4b effectively suppressed TNF-α-induced intercellular adhesion molecule (ICAM)-1 expression in a manner that was dependent on concentration. Numerous studies have demonstrated that TNF-α stimulates the expression of monocyte chemotactic protein-1 (MCP-

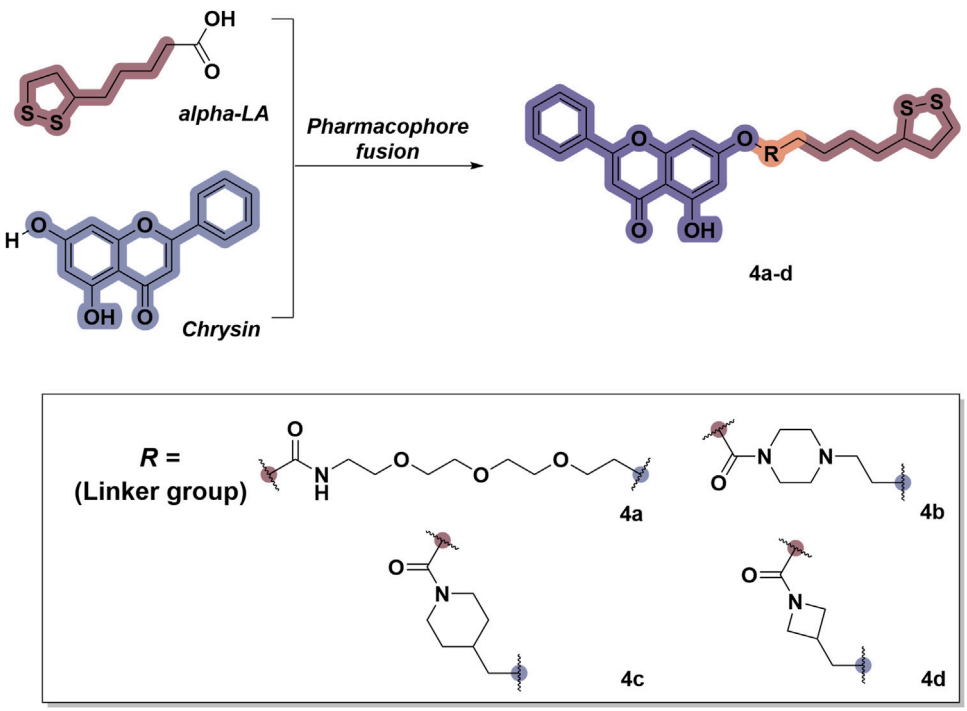

FIGURE 1
Design and synthesis of novel chrysin derivatives containing α-LA.

1), a chemokine that plays a crucial role in directing the migration of leukocytes to sites of inflammation (Radaei Z et al., 2020; Navaei-Alipour N et al., 2021). Furthermore, **4b** significantly suppressed the expression of MCP-1 in a concentration-dependent manner.

Upon interaction with its receptors, TNF-α triggers a cascade of signaling pathways that ultimately culminate in the activation of nuclear factor-kappaB (NF-κB), a pivotal transcription factor involved in the regulation of genes associated with inflammatory processes (Wang Y. et al., 2023). In order to investigate the potential relationship between the inhibitory effect of **4b** on ICAM-1 and MCP-1 expression, as well as its impact on NF-κB transcriptional activity, the inhibitory potency of **4b** on NF-κB transcription was determined. The observed inhibition of NF-κB activity in HT-29 cells by **4b** exhibited a dose-dependent effect, as illustrated in Figure 2C.

2.2.3 ROS production induced by TNF-α is effectively inhibited by compound 4b

The activation of NF-κB in the downstream signaling of TNF-α is dependent on reactive oxygen species (ROS), which are regulated by redox-sensitive transcription factors (Thoma and Lightfoot, 2018). This study further examined the ability of compound **4b** to inhibit the production of ROS induced by TNF-α. Firstly, the ROS assay kit was utilized to identify ROS, and TNF-α-induced HT-29 cells were exposed to varying concentrations of test compounds for a duration of 48 h. Subsequently, the cells were treated in accordance with the manufacturer's instructions of the kit, and the levels of ROS were quantified using fluorescence microscopy. As illustrated in Figure 3, compound **4b** demonstrated a notable inhibitory effect on the generation of ROS induced by TNF-α in a dose-dependent fashion. These findings are congruent with the outcomes obtained through flow cytometry analysis.

2.2.4 The advantageous effects of compound 4b in mitigating TNBS-induced colitis in rat models

The efficacy of **4b** in treating IBD was assessed in a rat model of colitis induced by 2, 4, 6-trinitro-benzenesulfonic acid (TNBS). Next, the rats received oral administration of **4b** at dosages of either 30 or 60 mg/kg. Rats subjected to TNBS colitis displayed manifestations of inflammation, hematochezia, weight loss, and decreased mobility relative to the control group. Additionally, TNBS-treated rats exhibited a substantial decline in body weight, stunted growth, and a notable increase in colon tissue weight attributed to congested edema (Figure 4A). The TNBS-induced colitis was effectively mitigated in a dose-dependent manner following oral administration of **4b**. Significantly, notable improvements were observed in terms of both body weight loss and inflammation in the colon tissue. The administration of 60 mg/kg **4b** demonstrated the most significant efficacy in the treatment of TNBS-induced colitis (Figure 5). Furthermore, in order to investigate the impact of 4b on the reversal of mucosal inflammation and damage, histological examination using hematoxylin and eosin (H&E) staining was conducted on colonic tissue sections from various experimental groups. The results depicted in Figure 6 demonstrate that treatment with 4b significantly reduced colonic inflammation and crypt damage induced by TNBS in mice.

The secretion of pro-inflammatory mediators is a characteristic feature of colitis induced by TNBS. Our findings in Figure 4B indicate a significant increase in the levels of IL-1β, IL-6, and

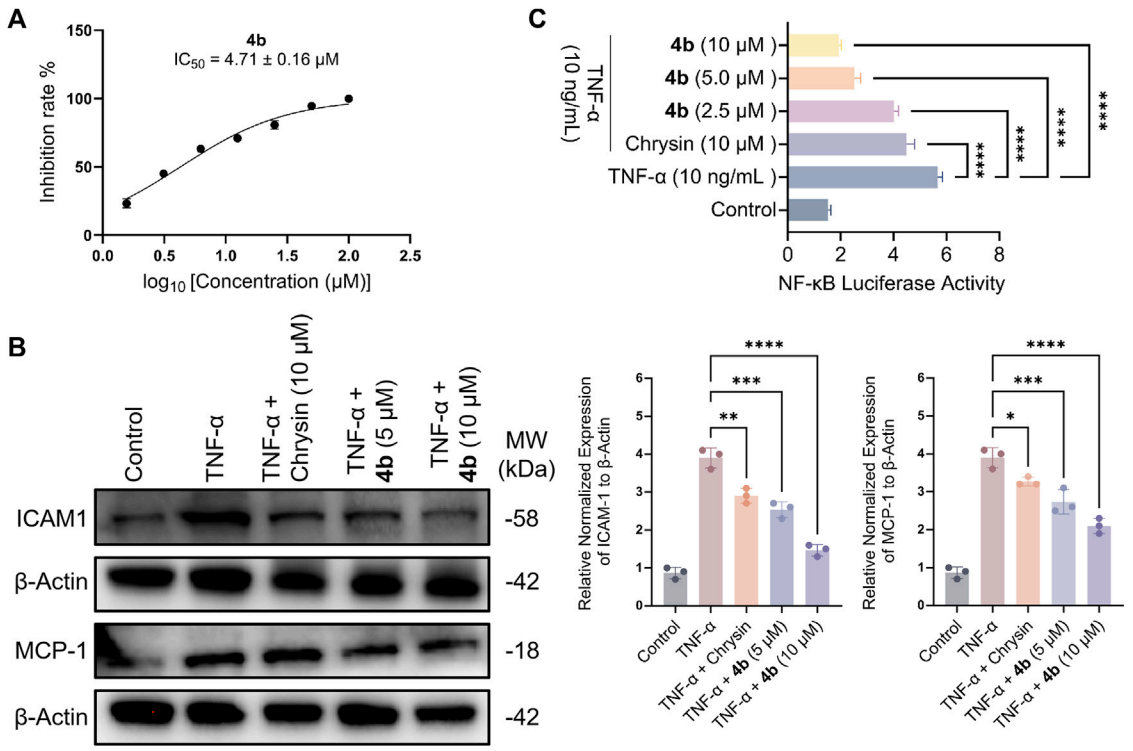

FIGURE 2
Compound **4b** demonstrates an *in vitro* anti-inflammatory effect. **(A)** The impact of **4b** on the adherence of monocytes to HT-29 cells stimulated by TNF-α was evaluated. Cell viability was assessed through the utilization of the cell-counting kit-8 (CCK-8) assay, which quantifies cell numbers. **(B)** Western blotting assay. The study examined the inhibitory impact of chrysin and **4b** on the expression of ICAM-1 and MCP-1 in TNF-α-stimulated HT-29 cells. β-Actin was utilized as a reference protein for the purpose of normalization. **(C)** The test compounds demonstrated inhibition of NF-κB transcriptional activity induced by TNF-α. The error bar displayed the SD, $*p < 0.05$, $**p < 0.01$, $***p < 0.001$ and $****p < 0.0001$, compared with the control groups.

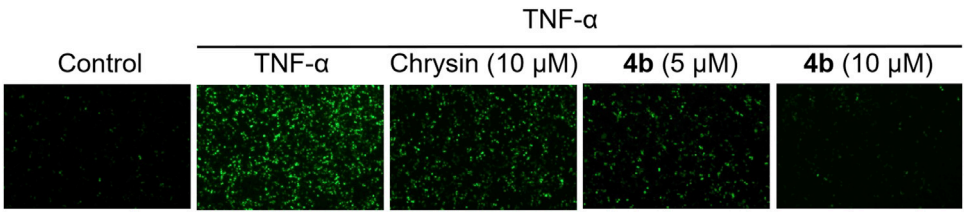

FIGURE 3
Inhibition of ROS production induced by TNF-α through the application of **4b**. The HT-29 cells were subjected to pretreatment with test compounds for a duration of 1 h before being exposed to TNF-α (10 ng/mL) for a period of 30 min. The cells were subjected to treatment as outlined in the ROS assay kit protocol. Fluorescence microscopy was employed to observe intracellular ROS.

TNF-α in the serum following TNBS challenge. Importantly, **4b** demonstrated a dose-dependent inhibition of the production of these pro-inflammatory cytokines. Furthermore, the JAK/STAT signaling pathway plays a significant role in inflammatory processes, as evidenced by numerous studies indicating that cytokine signaling is initiated through activation of the JAK and STAT family of kinases. In order to clarify the precise mechanism underlying the therapeutic effects of **4b** *in vivo*, we conducted an analysis of various inflammation-related markers through Western blotting assay, including the pro-inflammatory cytokine IL-6, phosphorylated JAK2 (p-JAK2), total JAK2, phosphorylated STAT3 (p-STAT3), and total STAT3. The data presented in Figure 7 indicates a significant increase in the levels of IL-6, p-JAK2, and p-STAT3 in the colonic tissues of mice with TNBS-induced colitis. Furthermore, in comparison to the TNBS-induced group, **4b** demonstrated the ability to inhibit the expression of IL-6, p-JAK2, and p-STAT3 in a dose-dependent manner. Notably, the findings demonstrate that **4b** did not alter the overall levels of JAK2 and STAT3 in colonic tissues across all concentrations tested, indicating that the inhibition of p-JAK2 and p-STAT3 was not

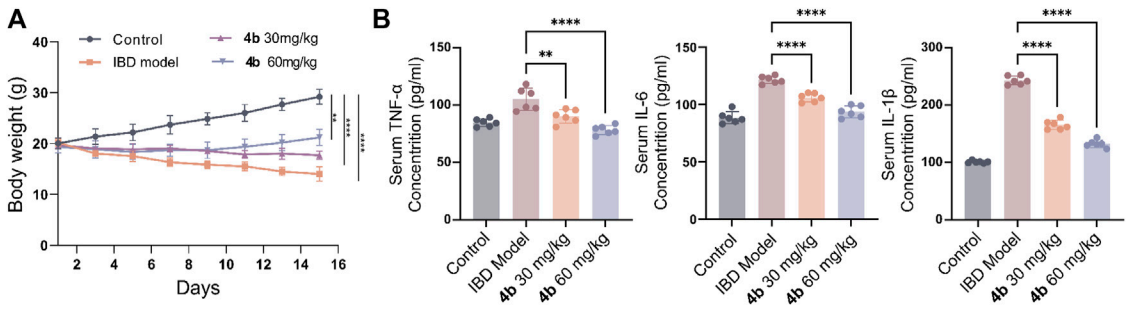

FIGURE 4
The advantageous effects of compound **4b** in mitigating TNBS-induced colitis in rat models. **(A)** Changes in body weight in rats with colitis induced by TNBS after treatment with the experimental compound. **(B)** The levels of pro-inflammatory cytokines, specifically TNF-α, IL-1β, and IL-6, in serum were measured *via* ELISA to assess the suppressive impact of **4b** on their production. The error bar indicated the SD, $^{**}p < 0.01$ and $^{***}p < 0.001$ compared with the control groups.

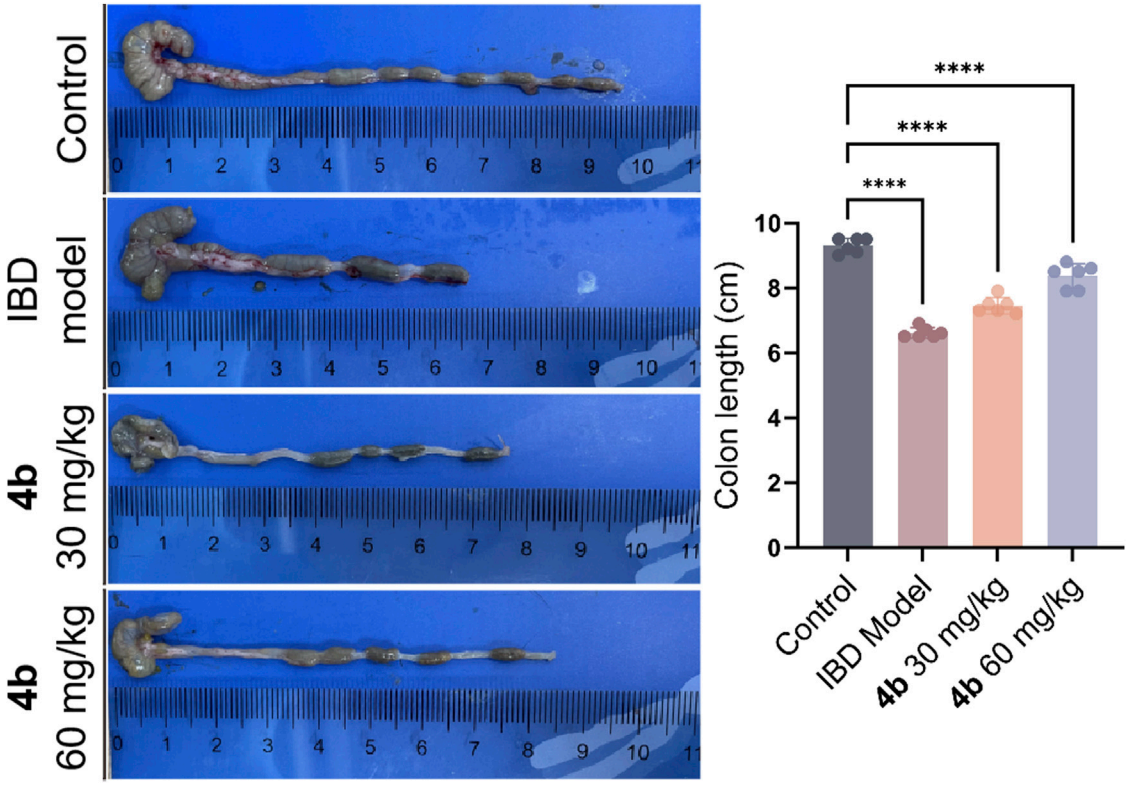

FIGURE 5
The positive effects of compound **4b** in mitigating TNBS-induced colitis in rat models. The length of the colon was measured following dissection. The error bar indicated the SD, $^{****}p < 0.0001$, compared with the control groups.

influenced by potential cytotoxic effects of the compound. Collectively, this data indicates that **4b** possesses healing properties for IBD and may serve as a novel candidate for IBD treatment.

2.2.5 ADMET profile of synthesized compounds

To assess the drug-likeness and pharmacokinetic characteristics of the recently developed compounds, an *in silico* ADMET screening was conducted. The results, presented in Supplementary Table S1, include an evaluation of various factors such as molecular weight, hydrogen-bond acceptor/donor count, blood-brain barrier permeability, and drug-likeness. The anticipated outcomes indicated enhancements in the physical and chemical characteristics of the synthesized compound in comparison to chrysin. However, despite the favorable safety profile of the synthesized compounds, their absorption, distribution, and metabolic data are suboptimal. Additional investigations into the structure-activity relationship of this series of molecular structures

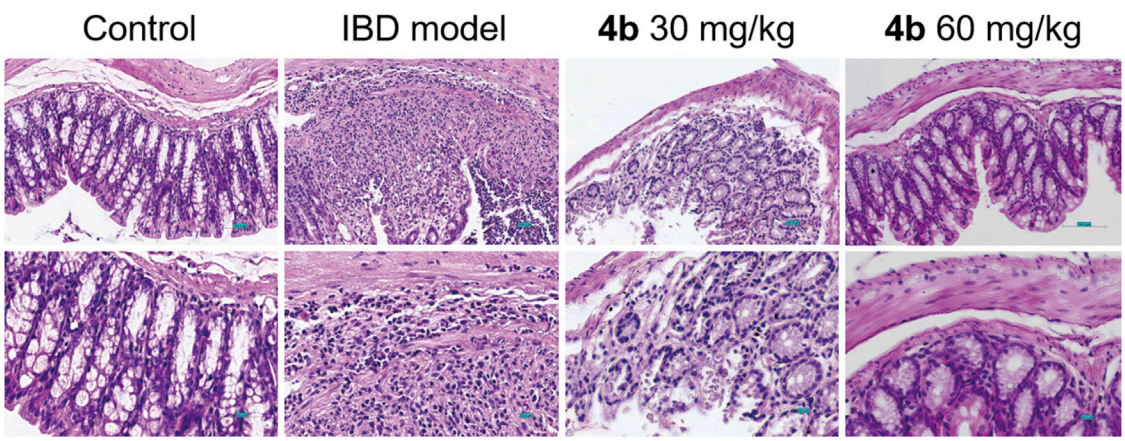

FIGURE 6
Representative H&E staining of colon sections from rat models with TNBS-induced colitis treated with **4b**. Scale bar = 100 μM.

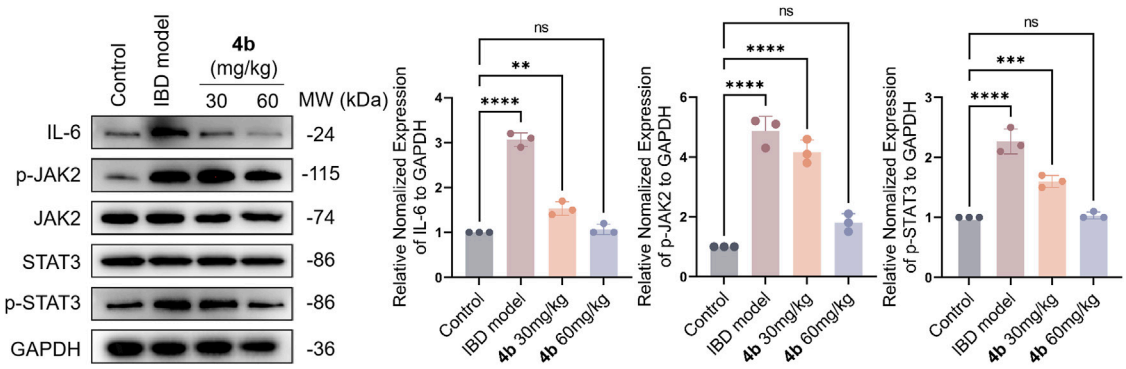

FIGURE 7
Western blotting assay. The impact of test compound on the modulation of TNF-α, p-JAK2, total JAK2, p-STAT3, and total STAT3 in colonic tissues was assessed, with the expression of GAPDH serving as an internal control. ns, not significant. The error bar indicated the SD, $^{**}p < 0.01$, $^{***}p < 0.001$ and $^{****}p < 0.0001$, compared with the control groups.

are warranted to identify promising derivatives with favorable ADMET properties for the management of IBD.

3 Experimental

3.1 Chemistry

Commercially available reagents and solvents were utilized without any additional purification. Column chromatography was performed using silica gel (100–200 mesh) as the medium for purification purposes. A fluorescent indicator was employed for real-time monitoring of the reaction, while UV light at wavelengths of 254 and 365 nM was utilized to visualize the markings on silica gel plates. A Bruker AV-600 spectrometer (^{1}H, 400 MHz; ^{13}C, 101 MHz) was utilized for the measurement of nuclear magnetic resonance (NMR) spectra, employing tetramethylsilane (TMS) as the internal reference compound. In NMR spectra analysis, spin multiplicities are denoted using the subsequent abbreviations. The values of coupling constants (*J*) are expressed in hertz units (Hz). Proton coupling patterns were denoted as singlet (s), doublet (d), triplet (t), quartet (q), multiplet (m), and doublet of doublets (dd). In reference to TMS, chemical shifts were reported using parts per million notation (ppm, *δ*). The test compounds were determined to have a purity exceeding 95% using an analytical high-performance liquid chromatography (HPLC) instrument (Agilent, Santa Clara, CA, United States). A GL-C18 reverse phase column (250 mm × 4.6 mm ×5 μM) was employed with ultra-pure water and methanol (chromatographic grade) as the mobile phase prior to assessing their biological activities. The HRMS analysis was carried out employing Agilent LC/MSD TOF mass spectrometers. Melting point was obtained by melting point apparatus (SGWX-4, Shanghai ShenGuang Instrument Co., Ltd, Shanghai, China).

General procedure for the synthesis of **4a–d** 5-[1, 2-Dithiolan-3-yl)-N-(2-(2-(2-(2-((5-hydroxy-4-oxo-2-phenyl-4H-chromen-7-yl)oxy)ethoxy)ethoxy)ethoxy)ethyl)pentanamide (**4a**).

Step 1: Chyrisn (1 mmol) was introduced into a vigorously stirred mixture containing tert-butyl (2-(2-(2-(2-bromoethoxy) ethoxy)ethoxy)ethyl)carbamate **2a** (1.05 mmol), K_2CO_3 (2 mmol), and KI (0.1 mmol) dissolved in acetone (20 mL). The reaction

mixture underwent stirring and reflux at a temperature of 65 °C for a duration of 16 h. Following the conclusion of the reaction, the mixture was cooled to ambient temperature. Subsequent filtration was conducted, and the resultant filtrate underwent further concentration and purification via column chromatography on silica gel utilizing a petroleum ether and ethyl acetate mixture in a 15:1 ratio. This procedure resulted in the formation of a yellow solid intermediate. Subsequently, the compound was dissolved in 5 mL of dichloromethane and subsequently treated with 2.5 mL of trifluoroacetic acid. The resulting mixture was stirred for 6 h at room temperature. To neutralize the reaction solution, saturated aqueous sodium bicarbonate was employed, followed by extraction with three portions of dichloromethane, each consisting of 30 mL. After being separated, the organic layer was washed with a saturated sodium chloride solution, dried with anhydrous Na_2SO_4, and evaporated, leading to the production of a yellow solid. This solid was utilized in the subsequent reaction without further purification steps.

Step 2: A solution comprising compound **3a** (0.25 mmol), HATU (0.25 mmol), α-LA (0.27 mmol), and DIPEA (0.5 mmol) in 30 mL of DMF was subjected to gentle stirring at room temperature for 20 h. Upon completion of the reaction, the resulting mixture was quenched by addition to 150 mL of ice-cold water, leading to the formation of a solid product upon filtration. The crude product was purified via silica gel chromatography utilizing a solvent system composed of methylene chloride and methanol in a 30:1 ratio, resulting in the isolation of pale yellow solid **4a** (0.49 g, 32% yield). mp 223.5°C–225.4°C. ^{1}H NMR (400 MHz, DMSO-d_6) δ 12.72 (s, 1H), 7.95–7.80 (m, 3H), 7.56–7.47 (m, 3H), 6.83 (s, 1H), 6.59 (s, 1H), 6.25 (s, 1H), 4.13 (s, 2H), 3.62–3.40 (m, 11H), 3.26–3.20 (m, 2H), 3.13—3.00 (m, 2H), 2.39–2.29 (m, 1H), 2.07 (t, *J* = 7.3 Hz, 2H), 1.84–1.73 (m, 1H), 1.64–1.43 (m, 5H), 1.34–1.24 (m, 2H). ^{13}C NMR (101 MHz, DMSO-d_6) δ 182.25, 172.65, 172.60, 164.79, 163.65, 161.62, 157.55, 132.33, 130.93, 129.37, 126.65, 126.60, 105.60, 105.31, 98.75, 93.37, 70.88, 70.45, 70.09, 70.04, 69.73, 69.06, 68.44, 56.59, 38.64, 38.52, 35.62, 34.59, 32.46, 28.81, 25.52. HRMS (ESI) (*m/z*): [M + H]$^+$ calcd for $C_{31}H_{40}NO_8S_2$ 618.2190, found 618.2197. Purity: 98.00% (HPLC, t_R = 11.13 min).

7-(2-(4-(5-(1,2-Dithiolan-3-yl)pentanoyl)piperazin-1-yl)ethoxy)-5-hydroxy-2-phenyl-4H-chromen-4-one (**4b**) yellow solid (0.20 g, 15% yield); mp 194.7°C–197.0°C. ^{1}H NMR (400 MHz, Chloroform-*d*) δ 12.66 (s, 1H), 7.79 (d, *J* = 7.3°Hz, 2H), 7.52–7.45 (m, 3H), 6.56 (s, 1H), 6.41 (s, 1H), 6.25 (d, *J* = 1.9 Hz, 1H), 4.12 (t, *J* = 5.5°Hz, 2H), 3.64 (t, *J* = 4.7 Hz, 2H), 3.49 (d, *J* = 5.1 Hz, 2H), 3.22—3.01 (m, 2H), 2.88—2.73 (m, 5H), 2.59–2.52 (m, 4H), 2.47–2.39 (m, 1H), 2.33 (t, *J* = 7.5 Hz, 2H), 1.93–1.85 (m, 1H), 1.66–1.59 (m, 2H), 1.54—1.38 (m, 2H). ^{13}C NMR (101 MHz, Chloroform-*d*) δ 181.83, 170.78, 164.26, 163.33, 161.62, 157.19, 131.63, 130.67, 128.80, 125.91, 105.24, 98.38, 92.69, 66.29, 56.43, 56.26, 53.51, 53.06, 45.27, 41.27, 40.03, 38.41, 38.33, 36.22, 34.56, 32.65, 31.14, 28.85, 24.80. HRMS (ESI) (*m/z*): [M + H]$^+$ calcd for $C_{29}H_{35}N_2O_5S_2$ 555.1982, found 555.1982. Purity: 99.36% (HPLC, t_R = 11.84 min).

7-((1-(5-(1,2-Dithiolan-3-yl)pentanoyl)piperidin-4-yl)methoxy)-5-hydroxy-2-phenyl-4H-chromen-4-one (**4c**) yellow solid (0.33 g, 28% yield); mp 189.0°C–191.5°C. ^{1}H NMR (400 MHz, Chloroform-*d*) δ 12.70 (s, 1H), 7.95—7.78 (m, 2H), 7.57–7.49 (m, 3H), 6.65 (s, 1H), 6.50 (d, *J* = 2.3 Hz, 1H), 6.35 (d, *J* = 2.1 Hz, 1H), 6.14 (d, *J* = 5.8 Hz, 1H), 4.19 (dd, *J* = 5.6, 3.3 Hz, 2H), 3.85 (dd, *J* = 5.6, 3.3 Hz, 2H), 3.64 (t, *J* = 5.0 Hz, 2H), 3.58—3.45 (m, 4H), 3.19—3.03 (m, 2H), 2.81 (s, 1H), 2.45–2.38 (m, 1H), 2.19 (t, *J* = 7.5 Hz, 2H), 1.91–1.83 (m, 2H), 1.68—1.59 (m, 3H), 1.52—1.34 (m, 2H). ^{13}C NMR (101 MHz, Chloroform-*d*) δ 182.37, 172.96, 164.63, 164.03, 162.06, 157.64, 131.94, 131.11, 129.11(2), 126.25(2), 105.75, 98.61, 93.18, 70.14, 69.08, 67.92, 56.43, 40.22 (2), 39.14, 38.45, 36.38, 34.60 (2), 28.88, 25.40 (2). HRMS (ESI) (*m/z*): [M + H]$^+$ calcd for $C_{29}H_{34}NO_5S_2$ 540.1890, found 540.1946. Purity: 99.36% (HPLC, t_R = 11.84 min).

7-[(1-(5-(1,2-Dithiolan-3-yl)pentanoyl)azetidin-3-yl)methoxy)-5-hydroxy-2-phenyl-4H-chromen-4-one (**4d**ays)]

Yellow solid (0.26 g, 19% yield); mp 176.7°C–178.9°C. ^{1}H NMR (400 MHz, Chloroform-*d*) δ 12.67 (s, 1H), 7.78 (t, *J* = 5.6 Hz, 2H), 7.48 (dd, *J* = 12.5, 7.3 Hz, 3H), 6.55 (d, *J* = 4.3 Hz, 1H), 6.42 (s, 1H), 6.25 (t, *J* = 2.6 Hz, 1H), 4.29 (t, *J* = 8.5 Hz, 1H), 4.20—3.97 (m, 4H), 3.87 (dd, *J* = 10.1, 5.2 Hz, 1H), 3.66—3.50 (m, 1H), 3.18–3.03 (m, 3H), 2.48–2.39 (m, 1H), 2.12 (t, *J* = 7.2 Hz, 2H), 1.94–1.85 (m, 1H), 1.74–1.64 (m, 4H), 1.55—1.39 (m, 2H). ^{13}C NMR (101 MHz, $CDCl_3$) δ 182.18, 173.08, 164.33, 163.81, 162.00, 157.48, 131.87, 130.90, 129.02(2), 126.13(2), 105.57, 98.47, 92.97, 92.94, 69.38, 56.40, 52.47, 49.81, 40.20, 38.48, 34.65, 30.98, 28.97, 27.73, 24.49. HRMS (ESI) (*m/z*): [M + Na]$^+$ calcd for $C_{27}H_{29}NNaO_5S_2$ 534.1379, found 534.1388. Purity: 100% (HPLC, t_R = 10.63 min).

3.2 Biology

3.2.1 Cell culture and antibodies

The HT29 and U937 cell lines, representing a human colonic epithelial cell line and a pre-monocytic cell line respectively, were acquired from the Shanghai Cell Bank of the Chinese Academy of Science (Shanghai, China). The cells were cultured in RMPI 1640 media supplemented with 10% fetal bovine serum and 1% Penicillin/Streptomycin. The incubation was carried out at a temperature of 37°C in a CO_2-humidified incubator with a concentration of 5%.

The following antibodies were used in this study: GAPDH (CST, no. 2118), IL-6 (CST, no. 12912), JAK2 (CST, no. 3230), Phospho-JAK2 (CST, no. 3771), STAT3 (CST, no. 12640), Phospho-JAK2 (CST, no. 9145), TNF-α (CST, no. 11948), ICAM-1 (CST, no. 67836S), MCP-1 (CST, no. 2029), and E-cadherin (CST, no. 3195).

3.2.2 TNF-α-stimulated adhesion of monocytic cells to colonic epithelial cells

A previously established method was employed to conduct the adhesion assay, utilizing a cultured monolayer of HT29 cells and non-adherent monocytic cell U937 cells. The adhesion of U937 monocytic cells to colonic epithelial cells was assessed by utilizing human U937 pre-monocytic cells. These cells were previously labeled with BCECF/AM (10 μg/mL) for 1 h at a temperature of 37°C. The HT-29 cells were cultured in 24-well plates and treated with the test compound for 60 min before being exposed to TNF-α (10 ng/mL) and IL-6 (5 ng/mL) for an additional 180 min. Following this, the cells were co-incubated with U937 cells that had been prelabeled with BCECF/AM (1×10^6 cells/well) for a duration of 30 min at a temperature of 37°C. The U937 cells that did not adhere were eliminated, while the HT-29 cells and U937 cells that adhered were rinsed twice with PBS. For quantitative analysis,

additional cell samples were subjected to lysis using a solution containing 0.1% Triton X-100 in Tris (0.1 M). The resulting fluorescence was then measured utilizing a fluorescence-detecting microplate reader (Synergy MX, Biotek) with excitation and emission wavelengths set at 580 nm.

3.2.3 NF-κB reporter assay

To assess the activation of NF-κB, HT-29 cells were subjected to transfection with an NF-κB reporter gene utilizing the CignalTM NF-κB Reporter luciferase Kit (Qiagen Ltd., Manchester, UK). Initially, the cells were seeded onto a 24-well culture plate in a medium supplemented with 10% fetal bovine serum and devoid of antibiotics. Following a 24-h incubation period, the cells were transfected with the constructs utilizing Lipofectamine 2000 (Invitrogen, United States) in accordance with the manufacturer's guidelines. Following a 24-h period, the transfection media was substituted with RPMI 1640 supplemented with 10% fetal bovine serum, allowing the cells an additional day for proliferation. Prior to subjecting the transfected cells to TNF-α treatment for a duration of 3 h, they were pre-treated with various compounds for 1 hour. Subsequently, TNF-α was administered and incubated for another 3 hours. The cell lysates were obtained using a lysis buffer and analyzed following the manufacturer's instructions.

3.2.4 TNBS-stimulated colitis

The animal experiments conducted in this study were approved by the relevant committee at Chengdu University of Traditional Chinese Medicine and were carried out in accordance with institutional guidelines for animal research (ethical review number: 20231012). Female Sprague-Dawley (SD) rats were utilized to assess the *in vivo* anti-IBD activity of the test compounds. Experimental colitis was induced using 2, 4, 6-trinitrobenzenesulfonic acid (TNBS) as previously described. Prior to the administration of TNBS, rats underwent a 24-h fasting period and were lightly anesthetized with diethyl ether. Subsequently, a solution containing 1.0 mL of TNBS at a concentration of 5% was gently introduced into the colon, approximately 7 cm away from the anus. This is achieved by affixing a polyethylene catheter to a 1 mL syringe. In contrast, the animal models in the control group underwent a similar procedure but were administered with ethanol at a concentration of 50% instead. Following the administration of TNBS, the rats were placed in an upright position for a duration of 60 s before being returned to their enclosure. Compound **4 d**ays, at doses of 30 or 60 mg/kg/day and suspended in a solution of 10% DMSO, 15% sulfobutylether-β-cyclodextrin, and 75% saline, was orally administered on the day of TNBS administration. On the 15th day of the experiment, the rats were euthanized, and the severity of colitis and visible ulcers in the mice was assessed by trained professionals. The colon tissue located 6–9 cm proximal to the rectum was surgically removed, followed by analysis of myeloperoxidase content and histological examination.

3.2.5 Western blotting

The rat colon tissue, weighing 45 mg, was pulverized and homogenized in 1X PBS using the Bead blaster from Benchmark Scientific. Following centrifugation of the homogenates, the lysate was resuspended in RIPA buffer supplemented with a cocktail of protease inhibitors and phosphatase inhibitors to extract the proteins. The BCA protein assay kit (Beyotime Biotechnology, Jiangsu, China) was utilized to quantify the concentration of protein samples. Nitrocellulose membranes were employed for transferring equivalent quantities of total protein resolved on SDS-PAGE gels. Afterwards, the membranes were obstructed using skim milk with a concentration of 5%. Subsequently, primary antibodies and their corresponding secondary antibodies were introduced to the membranes for incubation. Ultimately, the protein bands were made visible by utilizing the ECL chemiluminescent HRP substrate.

3.2.6 Hematoxylin and eosin (H&E) staining

The colon samples were surgically removed, preserved in a 4% formaldehyde solution, encased in paraffin wax, and sliced into sections. After the removal of paraffin and restoration of moisture, longitudinal sections with a thickness of 5 μM were subjected to hematoxylin staining for a duration of 5 min. Subsequently, they underwent incubation in acid ethanol solution (1% HCl in 70% ethanol) followed by rinsing with distilled water. The sections were subsequently stained with eosin for 5 min, dehydrated using a graded series of alcohol solutions, and cleared in xylene. The slides that were mounted underwent examination, photography, and observation for any pathological alterations utilizing a digital bright-field microscope (BZ-9000, Keyence, Japan).

3.2.7 Analysis of intracellular ROS production

As per the guidelines provided by the manufacturer, the ROS assay kit from Beyotime Biotechnology was utilized to assess the levels of intracellular ROS following treatment with the test compounds. Following this, intracellular ROS production was assessed using a fluorescence microscopy (MZ16FA, Leica, Germany). Statistical analysis was performed using GraphPrism software.

3.2.8 Quantification of levels of cytokines associated with inflammation

Serum samples were obtained from mice blood through centrifugation at 4,000 *g* for 12 min, followed by measurement of serum cytokine levels using specific ELISA kits from Abcam (ab181421, ab178013, and ab214025).

3.2.9 Statistical analysis

The validity of the findings was verified through replication in a minimum of three independent experiments. Data were presented as means ± standard deviation and subjected to statistical analysis using GraphPad Prism 8.0 software. Significance levels were determined by either one-way analysis of variance (ANOVA) or Student's t-test, with a threshold of $p < 0.05$ indicating statistical significance.

3.2.10 *In-silico* ADMET analysis

In this research, the utilization of ADMETlab facilitated the prediction of ADMET properties for synthesized molecules (https://admetmesh.scbdd.com). ADMETlab, an online computational tool, offers a variety of models for calculating molecular properties and pharmacokinetics, encompassing solubility, plasma protein binding, liver metabolism, renal excretion, among others. These models

enable the prediction of drug absorption, distribution, metabolism, and excretion processes within the human body, as well as the assessment of potential toxicity and safety.

4 Conclusion

At present, natural products are great treasures for the identification of the novel lead molecules for IBD treatment. Although chrysin demonstrates a range of biological activities, studies have shown that the compound has limited water solubility and low bioavailability. Hence, the use of chrysin as a precursor for structural modification holds significant promise in the identification of potential therapeutic agents. In this study, the incorporation of the essential pharmacophore into α-lactalbumin has led to the identification of a series of novel chrysin derivatives derived from α-lactalbumin. These derivatives have shown promising efficacy in inhibiting the adhesion of monocytes to colon epithelium induced by TNF-α. Compound **4b** exhibited the highest inhibitory potency compared to the other compounds, with an IC_{50} value of 4.71 μM. *In vitro* experiments demonstrated that compound 4b effectively inhibited monocyte adhesion to epithelial cells, reduced ROS production induced by TNF-α, suppressed the levels of ICAM-1 and MCP-1, decreased NF-κB activity, and ameliorated TNBS-induced colitis in rat models. This study offers a novel approach for identifying chrysin-based compounds with potential therapeutic activity for the treatment of IBD.

Data availability statement

The original contributions presented in the study are included in the article/Supplementary Material, further inquiries can be directed to the corresponding authors.

Ethics statement

Ethical approval was not required for the studies on humans in accordance with the local legislation and institutional requirements because only commercially available established cell lines were used. The animal study was approved by Chengdu University of Traditional Chinese Medicine. The study was conducted in accordance with the local legislation and institutional requirements.

Author contributions

PZ: Writing–original draft, Writing–review and editing. YH: Writing–original draft, Writing–review and editing. TY: Data curation, Formal Analysis, Software, Writing–review and editing. JK: Formal Analysis, Methodology, Project administration, Writing–review and editing. YT: Investigation, Software, Writing–review and editing. JL: Methodology, Writing–review and editing. CZ: Conceptualization, Investigation, Project administration, Validation, Writing–review and editing. FG: Data curation, Formal Analysis, Funding acquisition, Methodology, Project administration, Resources, Supervision, Validation, Visualization, Writing–original draft, Writing–review and editing. QL: Conceptualization, Data curation, Formal Analysis, Funding acquisition, Investigation, Methodology, Project administration, Resources, Software, Supervision, Validation, Visualization, Writing–original draft, Writing–review and editing.

Funding

The author(s) declare financial support was received for the research, authorship, and/or publication of this article. This work was supported by the National Natural Science Foundation Regional Innovation and Development Joint Fund, Grant numbers: U21A20409; Outstanding Youth Fund of Sichuan Natural Science Foundation of China, Grant numbers: 23NSFJQ0019.

Conflict of interest

Authors YT and CZ were employed by Guizhou Yunfeng Pharmaceutical Co., Ltd. Author JK was employed by Yunnan Shengke Pharmaceutical Co., Ltd.

The remaining authors declare that the research was conducted in the absence of any commercial or financial relationships that could be construed as a potential conflict of interest.

Publisher's note

Supplementary material

The Supplementary Material for this article can be found online at: https://www.frontiersin.org/articles/10.3389/fchem.2024.1406051/full#supplementary-material

References

Ahad, A., Ganai, A. A., Mujeeb, M., and Siddiqui, W. A. (2014). Chrysin, an anti-inflammatory molecule, abrogates renal dysfunction in type 2 diabetic rats. *Toxicol. Appl. Pharmacol.* 279, 1–7. doi:10.1016/j.taap.2014.05.007

Atanasov, A. G., Zotchev, S. B., Dirsch, V. M., and Supuran, C. T. (2021). Natural products in drug discovery: advances and opportunities. *Nat. Rev. Drug Discov.* 20, 200–216. doi:10.1038/s41573-020-00114-z

Bhowmik, S., Anand, P., Das, R., Sen, T., Akhter, Y., Das, M. C., et al. (2022). Synthesis of new chrysin derivatives with substantial antibiofilm activity. *Mol. Divers.* 26, 137–156. doi:10.1007/s11030-020-10162-7

Chen, N., Wang, R., Lu, L. J., Yan, L. J., Bai, L. L., Fu, Y., et al. (2020). Synthesis of chrysin derivatives and screening of antitumor activity. *J. Asian Nat. Prod. Res.* 22, 444–451. doi:10.1080/10286020.2019.1586677

Faheem, M. A., Akhtar, T., Naseem, N., Aftab, U., Zafar, M. S., Hussain, S., et al. (2023). Chrysin is immunomodulatory and anti-inflammatory against complete freund's adjuvant-induced arthritis in a pre-clinical rodent model. *Pharmaceutics* 15, 1225. doi:10.3390/pharmaceutics15041225

Ghorab, M. M., Msoliman, A., El-Sayyad, G. S., Abdel-Kader, M. S., and El-Batal, A. I. (2023). Synthesis, antimicrobial, and antibiofilm activities of some novel 7-methoxyquinoline derivatives bearing sulfonamide moiety against urinary tract infection-causing pathogenic microbes. *Int. J. Mol. Sci.* 24, 8933. doi:10.3390/ijms24108933

Hemperly, A., and Vande Casteele, N. (2018). Clinical pharmacokinetics and pharmacodynamics of infliximab in the treatment of inflammatory bowel disease. *Clin. Pharmacokinet.* 57, 929–942. doi:10.1007/s40262-017-0627-0

Jang, D. I., Lee, A. H., Shin, H. Y., Song, H. R., Park, J. H., Kang, T. B., et al. (2021). The role of tumor necrosis factor alpha (TNF-α) in autoimmune disease and current TNF-α inhibitors in therapeutics. *Int. J. Mol. Sci.* 22, 2719. doi:10.3390/ijms22052719

Larabi, A., Barnich, N., and Nguyen, H. T. T. (2020). New insights into the interplay between autophagy, gut microbiota and inflammatory responses in IBD. *Autophagy* 16, 38–51. doi:10.1080/15548627.2019.1635384

Li, R. (2016). Natural product-based drug discovery. *Med. Res. Rev.* 36, 3. doi:10.1002/med.21380

Li, Y., Li, Y. P., He, J., Liu, D., Zhang, Q. Z., Li, K., et al. (2019). The relationship between pharmacological properties and structure-activity of chrysin derivatives. *Mini. Rev. Med. Chem.* 19, 555–568. doi:10.2174/1389557518666180424094821

Li, Y., Zhang, Q. Z., He, J., Yu, W., Xiao, J., Guo, Y., et al. (2021). Synthesis and biological evaluation of amino acid derivatives containing chrysin that induce apoptosis. *Nat. Prod. Res.* 35, 529–538. doi:10.1080/14786419.2019.1582043

Navaei-Alipour, N., Mastali, M., Ferns, G. A., Saberi-Karimian, M., and Ghayour-Mobarhan, M. (2021). The effects of honey on pro- and anti-inflammatory cytokines: a narrative review. *Phytother. Res.* 35, 3690–3701. doi:10.1002/ptr.7066

Naz, S., Imran, M., Rauf, A., Orhan, I. E., Shariati, M. A., Ul-Haq, I., et al. (2019). Chrysin: pharmacological and therapeutic properties. *Life Sci.* 235, 116797. doi:10.1016/j.lfs.2019.116797

Oršolić, N., Nemrava, J., Jeleč, Ž., Kukolj, M., Odeh, D., Jakopović, B., et al. (2022). Antioxidative and anti-inflammatory activities of chrysin and naringenin in a drug-induced bone loss model in rats. *Int. J. Mol. Sci.* 23, 2872. doi:10.3390/ijms23052872

Parigi, T. L., D'Amico, F., Peyrin-Biroulet, L., and Danese, S. (2021). Evolution of infliximab biosimilar in inflammatory bowel disease: from intravenous to subcutaneous CT-P13. *Expert. Opin. Biol. Ther.* 21, 37–46. doi:10.1080/14712598.2020.1811849

Peng, J. C., Shen, J., and Ran, Z. H. (2014). Novel agents in the future: therapy beyond anti-TNF agents in inflammatory bowel disease. *J. Dig. Dis.* 15, 585–590. doi:10.1111/1751-2980.12193

Prieto-Hontoria, P. L., Pérez-Matute, P., Fernández-Galilea, M., López-Yoldi, M., Sinal, C. J., Martínez, J. A., et al. (2015). Effects of alpha-lipoic acid on chemerin secretion in 3T3-L1 and human adipocytes. *Biochim. Biophys. Acta.* 1861, 260–268. doi:10.1016/j.bbalip.2015.12.011

Radaei, Z., Zamani, A., Najafi, R., Saidijam, M., Jalilian, F. A., Ezati, R., et al. (2020). Promising effects of zerumbone on the regulation of tumor-promoting cytokines induced by TNF-α-activated fibroblasts. *Curr. Med. Sci.* 40, 1075–1084. doi:10.1007/s11596-020-2289-7

Saez, A., Gomez-Bris, R., Herrero-Fernandez, B., Mingorance, C., Rius, C., and Gonzalez-Granado, J. M. (2021). Innate lymphoid cells in intestinal homeostasis and inflammatory bowel disease. *Int. J. Mol. Sci.* 22, 7618. doi:10.3390/ijms22147618

Salehi, B., Berkay, Y. Y., Antika, G., Boyunegmez, T. T., Fawzi, M. M., Lobine, D., et al. (2019). Insights on the use of α-lipoic acid for therapeutic purposes. *Biomolecules* 9, 356. doi:10.3390/biom9080356

Seyedian, S. S., Nokhostin, F., and Malamir, M. D. (2019). A review of the diagnosis, prevention, and treatment methods of inflammatory bowel disease. *J. Med. Life* 12, 113–122. doi:10.25122/jml-2018-0075

Thoma, A., and Lightfoot, A. P. (2018). NF-kB and inflammatory cytokine signalling: role in skeletal muscle atrophy. *Adv. Exp. Med. Biol.* 1088, 267–279. doi:10.1007/978-981-13-1435-3_12

Wang, J., Macoritto, M., Guay, H., Davis, J. W., Levesque, M. C., and Cao, X. (2023a). The Clinical Response of upadacitinib and risankizumab is associated with reduced inflammatory bowel disease anti-TNF-α inadequate response mechanisms. *Inflamm. Bowel Dis.* 29, 771–782. doi:10.1093/ibd/izac246

Wang, Q. Q., Cheng, N., Yi, W. B., Peng, S. M., and Zou, X. Q. (2014). Synthesis, nitric oxide release, and α-glucosidase inhibition of nitric oxide donating apigenin and chrysin derivatives. *Bioorg. Med. Chem.* 22, 1515–1521. doi:10.1016/j.bmc.2014.01.038

Wang, Y., Ye, R. W., Fan, L. M., Zhao, X., Li, L. X., Zheng, H., et al. (2023b). A TNF-α blocking peptide that reduces NF-κB and MAPK activity for attenuating inflammation. *Bioorg. Med. Chem.* 92, 117420. doi:10.1016/j.bmc.2023.117420

Wang, Z., Iida, N., Seishima, J., Okafuji, H., Yutani, M., Fujinaga, Y., et al. (2022). Patient-derived Enterococcus faecium with inflammatory genotypes promote colitis. *J. Gastroenterol.* 57, 770–783. doi:10.1007/s00535-022-01905-4

Willrich, M. A., Murray, D. L., and Snyder, M. R. (2015). Tumor necrosis factor inhibitors: clinical utility in autoimmune diseases. *Transl. Res.* 165, 270–282. doi:10.1016/j.trsl.2014.09.006

Zeinali, M., Rezaee, S. A., and Hosseinzadeh, H. (2017). An overview on immunoregulatory and anti-inflammatory properties of chrysin and flavonoids substances. *Biomed. Pharmacother.* 92, 998–1009. doi:10.1016/j.biopha.2017.06.003

Zhang, L., Jin, Y., Peng, J., Chen, W., Lisha, L., and Lin, J. (2019). Qingjie Fuzheng Granule attenuates 5-fluorouracil-induced intestinal mucosal damage. *Biomed. Pharmacother.* 118, 109223. doi:10.1016/j.biopha.2019.109223

frontiers | Frontiers in Chemistry

TYPE Original Research
PUBLISHED 03 July 2024
DOI 10.3389/fchem.2024.1424637

OPEN ACCESS

EDITED BY
Afzal Basha Shaik,
Jawaharlal Nehru Technological University, India

REVIEWED BY
Pavitra Suresh Thacker,
Stanford University, United States
Sathish Kumar Konidala,
Vignan's Foundation for Science, Technology and Research, India

*CORRESPONDENCE
Sadia Sarwar,
Sadia.Sarwar@riphah.edu.pk
Amir Faisal,
amir.faisal@lums.edu.pk

RECEIVED 28 April 2024
ACCEPTED 29 May 2024
PUBLISHED 03 July 2024

CITATION
Arif MN, Sarwar S, Firdous F, Saleem RSZ, Nadeem H, Alamro AA, Alghamdi AA, Alshammari AH, Farooq O, Khan RA and Faisal A (2024), Discovery and prospects of new heterocyclic Isatin-hydrazide derivative with a novel role as estrogen receptor α degrader in breast cancer cells.
Front. Chem. 12:1424637.
doi: 10.3389/fchem.2024.1424637

Discovery and prospects of new heterocyclic Isatin-hydrazide derivative with a novel role as estrogen receptor α degrader in breast cancer cells

Muhammad Nouman Arif[1], Sadia Sarwar[2]*, Farhat Firdous[3,4], Rahman Shah Zaib Saleem[3], Humaira Nadeem[1], Abir Abdullah Alamro[5], Amani Ahmad Alghamdi[5], Atekah Hazza Alshammari[5], Omer Farooq[6], Rashid Ali Khan[6] and Amir Faisal[4]*

[1]Pharmaceutical Chemistry Research Lab, Department of Pharmaceutical Chemistry, Riphah Institute of Pharmaceutical Sciences, Riphah International University, Islamabad, Pakistan, [2]Cell Culture Laboratory, Department of Pharmacognosy, Riphah Institute of Pharmaceutical Sciences, Riphah International University, Islamabad, Pakistan, [3]Department of Chemistry and Chemical Engineering, Syed Babar Ali School of Science and Engineering, Lahore University of Management Sciences (LUMS), Defence Housing Authority, Lahore, Pakistan, [4]Department of Life Sciences, Syed Babar Ali School of Science and Engineering, Lahore University of Management Sciences (LUMS), Lahore, Pakistan, [5]Department of Biochemistry, College of Science, King Saud University, Riyadh, Saudi Arabia, [6]Shifa College of Pharmaceutical Sciences, Shifa Tameer-e-Millat University, Islamabad, Pakistan

Introduction: Isatin, a heterocycle scaffold, is the backbone of many anticancer drugs and has previously been reported to engage multiple cellular targets and mechanisms, including angiogenesis, cell cycle, checkpoint pathways and multiple kinases. Here, we report that a novel isatin derivative, 5i, degrades estrogen receptor alpha (ERα) in estrogen-dependent breast cancer cells. This effect of the isatin nucleus has not been previously reported. Tamoxifen and fulvestrant represent standard therapy options in estrogen-mediated disease but have their own limitations. Isatin-based triple angiokinase inhibitor BIBF1120 (Nintedanib) and multikinase inhibitor Sunitinib (Sutent) have been approved by the FDA.

Methods: Keeping this in view, we synthesized a series of N'-(1-benzyl-2-oxo-1, 2-dihydro-3H-indol-3-ylidene) hydrazide derivatives and evaluated them *in vitro* for antiproliferative activities in MCF-7 (ER+) cell line. We further investigated the effect of the most potent compound (5i) on the Erα through Western Blot Analysis. We used *in silico* pharmacokinetics prediction tools, particularly pkCSM tool, to assess the activity profiles of the compounds.

Results and discussion: Compound 5i showed the best antiproliferative activity (IC50 value; 9.29 ± 0.97 μM) in these cells. Furthermore, 5i downregulated ERα protein levels in a dose-dependent manner in MCF-7. A multifaceted analysis of physicochemical properties through Data Warrior software revealed some prominent drug-like features of the synthesized compounds. The docking studies predicted the binding of ligands (compounds) with the target protein

(ERα). Finally, molecular dynamics (MD) simulations indicated stable behavior of the protein-ligand complex between ERα and its ligand 5i. Overall, these results suggest that the new isatin derivative 5i holds promise as a new ERα degrader.

KEYWORDS

isatin–hydrazide derivatives, antiproliferative activity, molecular docking, molecular dynamics simulations, estrogen receptor, breast cancer

1 Introduction

Breast cancer is the leading malignancy causing the highest death rate among women (Guissi et al., 2017). Most BC patients have an estrogen receptor (ER)-positive form of the disease, with postmenopausal women accounting for 75% of the cases (Shoda et al., 2015). The initial line of treatment for ER-positive BC is endocrine therapy. Selective estrogen receptor modulators (SERMs) are a predominant class of endocrine therapeutic agents, including tamoxifen (brand name: Soltamox), raloxifene (brand name: Evista), and toremifene (brand name: Farestone). These pharmacological substances bind to the ER (ERα or ERβ subtypes) in cells, acting as agonists/antagonists in an organ-specific manner (Dandriyal et al., 2016). The first-generation SERM, tamoxifen, dramatically decreased BC mortality rates and the risk of recurrence. Although tamoxifen remained a gold standard in BC treatment, its use was restricted once its agonistic action on endometrial cells was shown to be associated with moderately increased risk of endometrial cancer growth, progression, and resistance (Duffy, 2006; Hiscox et al., 2006; Lewis-Wambi et al., 2011; Welsh et al., 2012; Han et al., 2016). Second-generation SERMs have also been associated with hot flashes, increased blood clot risk, deep vein thrombosis, and pulmonary embolism. Bazedoxifene, a third-generation SERM, was launched to treat BC and osteoporosis due to the toxicity and unfavorable side effects associated with the earlier SERMs (Lewis-Wambi et al., 2011; Payton-Stewart et al., 2014) by replacing the benzothiophene core of raloxifene by indole (Harris et al., 2003). Bazedoxifene binds to both ERα and ERβ, with a stronger affinity for the former. The inhibitory impact of bazedoxifene is linked to cell cycle arrest and ERα downregulation (Lewis-Wambi et al., 2011). Recently, bazedoxifene was used in combination with palbociclib to treat stage IV metastatic BC (Lindsay et al., 2009; Gupta et al., 2014; Jeselsohn et al., 2019).

Selective estrogen receptor degraders (SERDs), another class of ER-binding small molecules, bind to the ER and downregulate ER-mediated transcriptional activity. Fulvestrant and elacestrant are FDA-approved SERDs for clinical use in ER+ BC patients. Some small-molecule examples of SERDs have been disclosed in the literature (e.g., WO2005073204, WO2014205136, and WO2016097071). There has been a recent shift of focus in research on endocrine therapies toward SERDs as the development of resistance against SERMs grows (Bhatia et al., 2023). These SERDs can be used either as single agents or in combination with other classes of drugs, including SERMs, aromatase inhibitors, CDK4/CDK6 inhibitors, PI3K inhibitors, and mTOR inhibitors to treat hormone receptor-positive BC. The quest for new molecules to treat ER+ cancers that display better pharmacokinetic and pharmacodynamic properties, including oral bioavailability and higher efficiency in the clinic, is highly desirable.

Isatin stands out as an important class of heterocyclic compounds. It is a versatile scaffold present in human and other mammalian tissues. Isatin is a common structural feature in various dyes, agrochemicals, and pharmacologically active molecules. The synthetic ingenuity of isatin makes it a perfect platform for structural alterations and derivatization. Isatin-based compounds have displayed diverse biological properties, such as anticancer, antidepressant, anticonvulsant, antifungal, anti-HIV, and antiangiogenic activities (Pandeya et al., 1999; Sridhar and Ramesh, 2001; Verma et al., 2004; Selvam et al., 2008; Rohini et al., 2011; Ibrahim et al., 2015). Isatin–quinazoline hybrids have demonstrated antiproliferative activities against HepG2, MCF-7, and HT-29 cancer cell lines (Fares et al., 2015). Several isatin-based compounds have gone through clinical trials (shown in Figure 1), including triple angiokinase inhibitor BIBF1120 (Nintedanib, Vargatef), Sunitinib (Sutent), a multikinase inhibitor targeting VEGFR-1, VEGFR-2, PDGFRb and c-Kit. Sunitinib was approved by FDA for treating gastrointestinal stromal tumors (GIST) and advanced renal cell carcinoma (RCC) (Motzer et al., 2006; Le Tourneau et al., 2007).

The main objective of the present research was to synthesize a new series of compounds based on the isatin nucleus and to investigate their antiproliferative activity and potential to degrade ER, inspired by the uniqueness of the isatin scaffold and its demonstrated biological activities. The present study describes the synthesis of N'-(1-benzyl-2-oxo-1, 2-dihydro-3H-indol-3-ylidene) hydrazide derivatives along with their antiproliferative evaluation against MCF-7 (ER+) cell-lines using MTT assay. Predictions of physicochemical and pharmacokinetic properties of synthesized compounds were conducted using *in silico* approaches. Molecular docking and molecular dynamics simulations further explored the binding modes of test compounds into the ligand binding domain (LBD) of estrogen receptor (ERα).

The main objective of the present research was to synthesize new series of an isatin-based nucleus and to investigate the candidates as potential ER degraders, inspired by the deficiencies and side effects of first, second, and third generations of endocrine therapeutic agents for the treatment of ER+ BC. Thus, inspired by the uniqueness of the isatin scaffold and its demonstrated biological activities, this study was aimed at the synthesis of new compounds that will have even better pharmacokinetics and pharmacodynamics profiles than the current regimen.

The present study describes the synthesis of N′-(1-benzyl-2-oxo-1, 2-dihydro-3H-indol-3-ylidene) hydrazide derivatives, along with their antiproliferative evaluation against MCF-7 (ER+) cell lines using the MTT assay. The physicochemical and pharmacokinetic properties of synthesized compounds were predicted using *in silico* approaches. Molecular docking and molecular dynamics (MD) simulations further explored the binding modes of the test compounds into the ligand-binding domain (LBD) of estrogen receptor alpha (ERα).

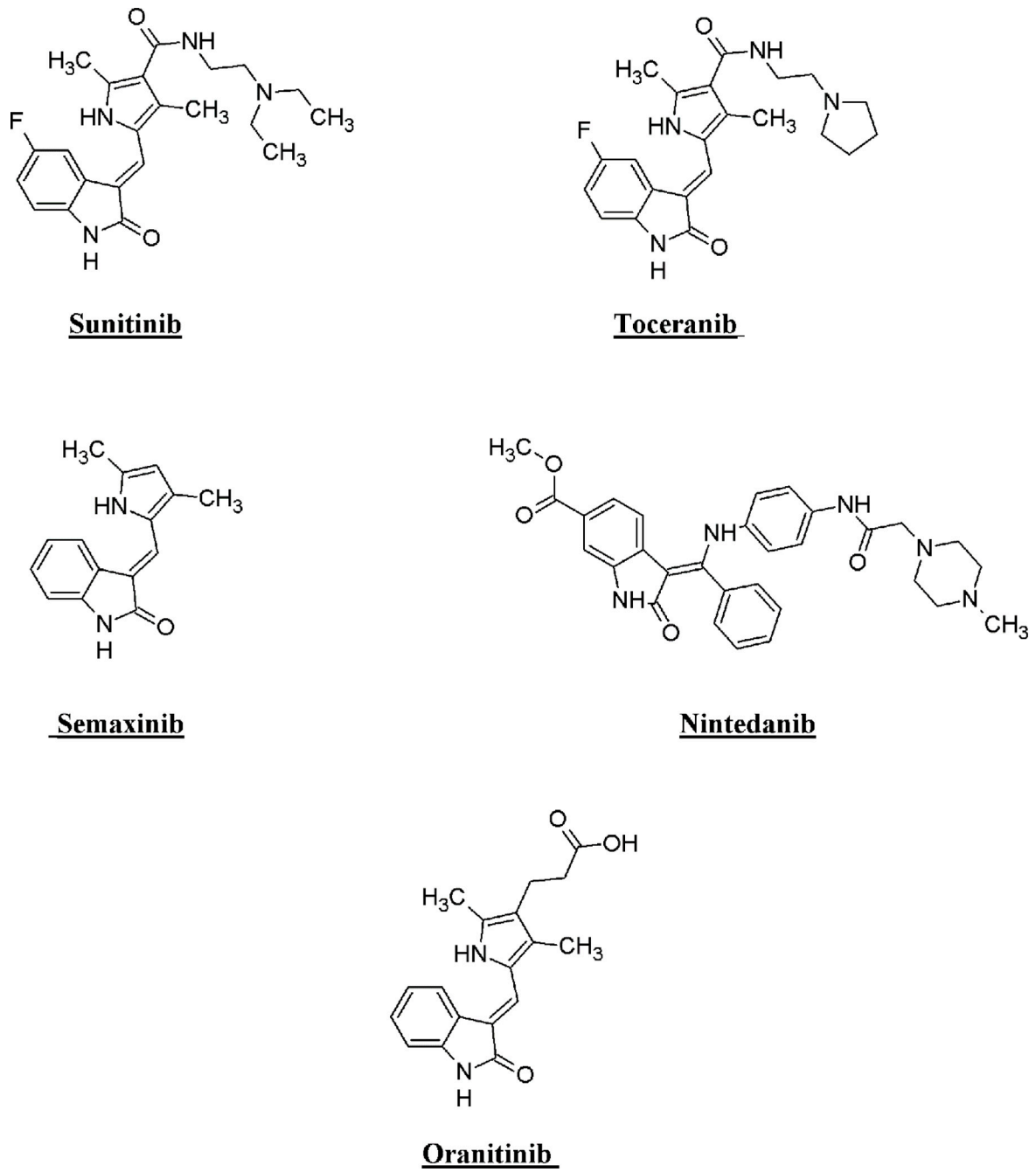

FIGURE 1
Structure of few isatin derivatives in clinical application/clinical trials.

2 Materials and methods

2.1 Synthetic chemistry

Solvents and chemicals from Merck and Sigma-Aldrich were used without further purification. All the synthesized compounds were purified by recrystallization in suitable solvents. The boiling points of the esters were determined using a microscale condenser apparatus. Elemental analyses (C, H, and N) were in agreement with the proposed structures and within ±0.5% of the theoretical values. Thin-layer chromatography (TLC) was used to monitor the reaction progress and purity of the final products using silica gel-precoated aluminum sheets (60 F254; Merck Schuchardt, Darmstadt, Germany). The TLC plates were visualized with ultraviolet light at 365 and 254 nm. The synthesized compounds were characterized using spectrophotometric analysis employing Fourier-transform infrared (FTIR) spectroscopy (Nicolet iS10 spectrophotometer, Thermo Fisher Scientific) and ^{1}H NMR and ^{13}C NMR spectroscopy (Bruker AM-300 spectrophotometer).

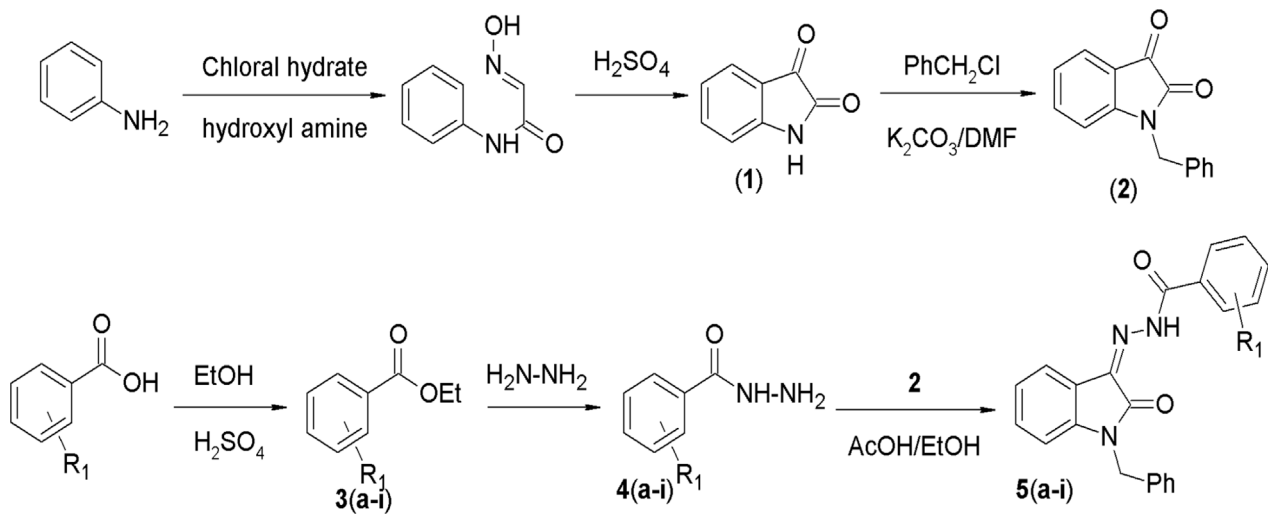

FIGURE 2
General scheme for the synthesis of compounds.

TABLE 1 Cytotoxicity of test compounds against cancer cell line MCF-7.

Compound	Name	R	IC_{50} (μM ± SD)
5a	N'-(1-benzyl-2-oxo-1,2-dihydro-3H-indol-3-ylidene)pyridine-4-carbohydrazide	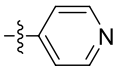	31.00 ± 11.50
5b	N'-(1-benzyl-2-oxo-1,2-dihydro-3H-indol-3-ylidene)-3-bromobenzohydrazide	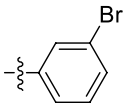	48.90 ± 24.6
5c	N'-(1-benzyl-2-oxo-1,2-dihydro-3H-indol-3-ylidene)-3-iodobenzohydrazide	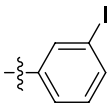	33.13 ± 9.57
5d	N'-(1-benzyl-2-oxo-1,2-dihydro-3H-indol-3-ylidene)-2-hydroxybenzohydrazide	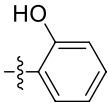	13.34 ± 2.53
5e	N'-(1-benzyl-2-oxo-1,2-dihydro-3H-indol-3-ylidene)-4-fluorobenzohydrazide	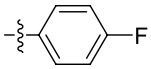	39.47 ± 12.58
5f	N'-(1-benzyl-2-oxo-1,2-dihydro-3H-indol-3-ylidene)pyridine-2-carbohydrazide	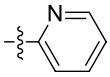	12.35 ± 0.65
5g	N'-(1-benzyl-2-oxo-1,2-dihydro-3H-indol-3-ylidene)-3,4,5trihydroxybenzohydrazide	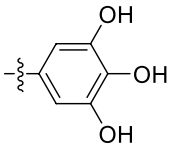	12.09 ± 4.08
5h	N'-(1-benzyl-2-oxo-1,2-dihydro-3H-indol-3-ylidene)-2-chlorobenzohydrazide	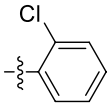	22.99 ± 2.75
5i	N'-(1-benzyl-2-oxo-1,2-dihydro-3H-indol-3-ylidene)benzohydrazide	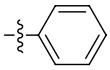	9.29 ± 0.97

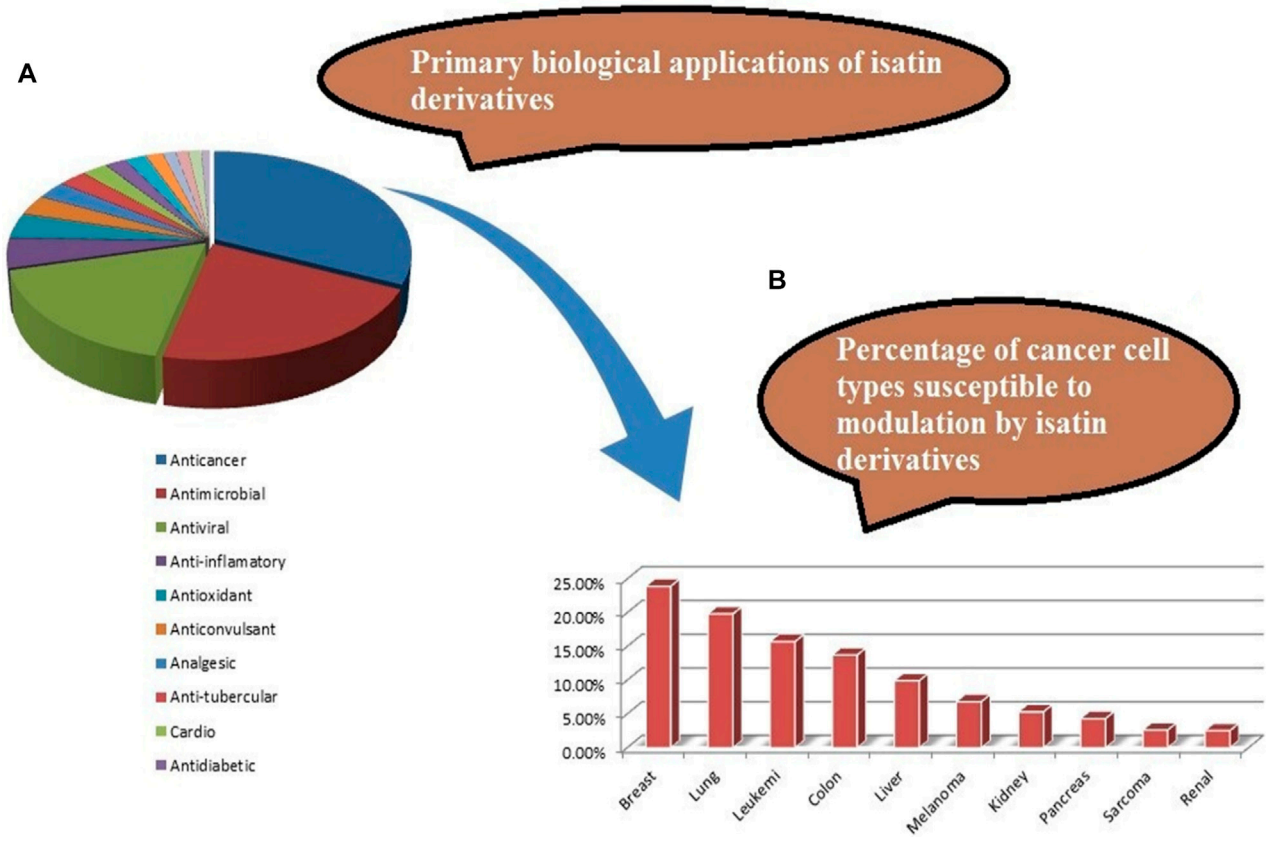

FIGURE 3
(A) Reported pharmacological actions of isatin derivatives. **(B)** Percentage of different types of target cancers (adapted from the study by Ferraz de Paiva et al., 2021).

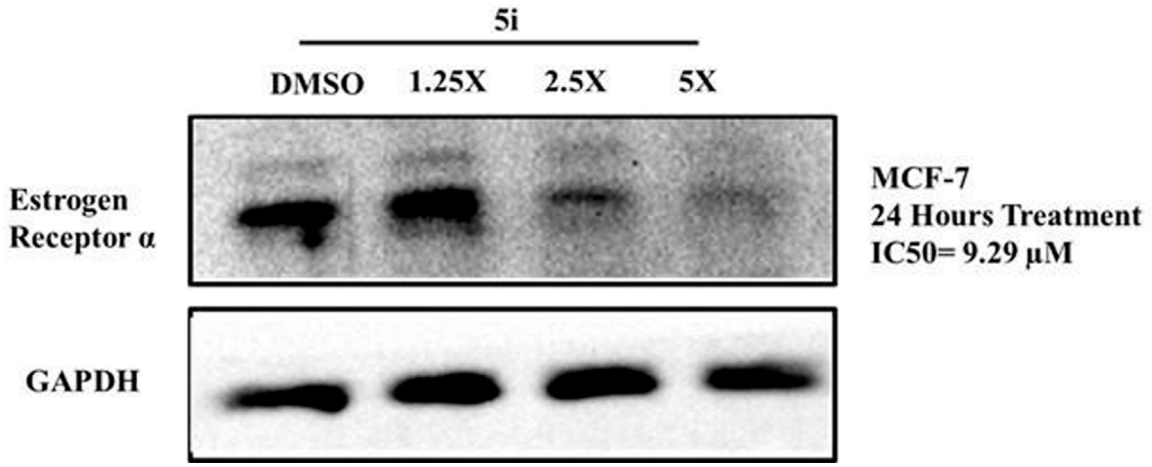

FIGURE 4
Compound 5i downregulates ERα levels in MCF-7 cells. Cells were treated with IC_{50} concentrations of 1.25X, 2.5X, and 5X of 5i for 24 h. Treatment with DMSO served as a solvent control. Cells were then lysed, and equal amounts of protein for all samples were analyzed for ERα levels through Western blotting using specific antibodies. GAPDH was used as a loading control.

TABLE 2 Chemoinformatics analysis of synthesized compounds.

Column name	5a	5b	5c	5d	5e	5f	5 g	5 h	5i
Total mol. weight	356.384	434.292	481.288	371.395	373.386	356.384	403.393	389.841	355.396
Monoisotopic mass	356.127	433.0325	481.028	371.126	373.122	356.127	403.1168	389.093	355.132
cLogP	2.602	4.3284	4.403	3.257	3.704	2.6563	2.5661	4.2092	3.6032
cLogS	−4.475	−6.102	−6.284	−4.972	−5.582	−4.497	−4.38	−6.004	−5.268
H acceptors	6	5	5	6	5	6	8	5	5
H donors	1	1	1	2	1	1	4	1	1
Total surface area	272.03	291.9	299.55	279.62	279.62	272.03	292.32	288.69	273.27
Relative PSA	9.2336	0.1802	0.1756	0.23496	0.188	9.2336	0.31348	0.1822	0.19248
Polar surface area	74.66	61.77	61.77	82	61.77	74.66	122.46	61.77	61.77
Drug-likeness	6.5269	4.7369	6.9034	6.4978	5.1869	6.5269	6.4978	6.5395	6.5269
Irritant	None	None	None	None	None	None	None	None	None
Nasty functions	Acyl hydrazone	Acyl hydrazones	Acyl hydrazones	Acyl hydrazones	Acyl hydrazones	Acyl hydrazone	Acyl hydrazones	Acyl hydrazones	Acyl hydrazones
Shape index	0.55556	0.53571	0.53571	0.53571	0.57143	0.55556	0.53333	0.53571	0.55556
Molecular flexibility	0.31329	0.31467	0.31467	0.31467	0.31467	0.31329	0.317	0.3183	0.31329
Molecular complexity	0.82315	0.83059	0.83059	0.83059	0.82582	0.82315	0.84087	0.83554	0.82132
Fragments	1	1	1	1	1	1	1	1	1
Non-hydrogen atoms	27	28	28	28	28	27	30	28	27
Non-C/H atoms	6	6	6	6	6	6	8	6	5
Metal atoms	0	0	0	0	0	0	0	0	0
Electronegative atom	6	6	6	6	6	6	8	6	5
Stereo lefts	0	0	0	0	0	0	0	0	0
Rotatable bonds	4	4	4	4	4	4	4	4	4
Ring closures	4	4	4	4	4	4	4	4	4
Aromatic atoms	18	18	18	18	18	18	18	18	18
Sp3 carbon fraction	0.047619	0.045455	0.045455	0.045455	0.045455	0.047619	0.045455	0.045455	0.045455
Sp3 atoms	1	1	1	2	1	1	4	1	1
Symmetric atom	4	2	2	2	4	4	5	2	4
Small rings	4	4	4	4	4	4	4	4	4
Carbo rings	2	3	3	3	3	2	3	3	3
Hetero rings	2	1	1	1	1	2	1	1	1
Saturated rings	0	0	0	0	0	0	0	0	0
Non-aromatic ring	1	1	1	1	1	1	1	1	1
Aromatic rings	3	3	3	3	3	3	3	3	3
Saturated carbon rings	0	0	0	0	0	0	0	0	0
Non-aromatic carbon ring	0	0	0	0	0	0	0	0	0
Carbon aromatic ring	2	3	3	3	3	2	3	3	3

(Continued on following page)

TABLE 2 (*Continued*) Chemoinformatics analysis of synthesized compounds.

Column name	5a	5b	5c	5d	5e	5f	5 g	5 h	5i
Saturated hetero ring	0	0	0	0	0	0	0	0	0
Non-aromatic hetero ring	1	1	1	1	1	1	1	1	1
Hetero aromatic ring	1	0	0	0	0	1	0	0	0
Amide	1	1	1	1	1	1	1	1	1
Amines	0	0	0	0	0	0	0	0	0
Alkyl amines	0	0	0	0	0	0	0	0	0
Aromatic amines	0	0	0	0	0	0	0	0	0
Aromatic nitrogen	1	0	0	0	0	1	0	0	0
Basic nitrogen	0	0	0	0	0	0	0	0	0
Acidic oxygen	0	0	0	0	0	0	0	0	0
Globularity SVD	0.33914	0.3235	0.32945	0.34663	0.33395	0.33914	0.33756	0.34848	0.33564
Globularity vol	0.69798	0.6829	0.68036	0.6924	0.69143	0.69798	0.67078	0.69103	0.69396
VDW surface	340.61	364.17	371.16	352.06	349.99	340.61	384.53	359.13	345.27
VDW volume	344.58	368.75	377.24	357.78	353.88	344.58	389.41	367.49	348.66
Lipinski rule validation	Yes	Yes	Yes	Yes	Yes	Yes	Yes	Yes	Yes

2.1.1 Preparation of isatin (1H-indole-2,3-dione) (**1**)

The synthesis of isatin involved the reaction of chloral hydrate, hydroxylamine, and aniline to yield α-isonitrosoacetanilide and subsequent electrophilic cyclization in the presence of a strong acid such as concentrated sulfuric acid. The synthesis is generally known as the Sandmeyer isatin synthesis (Sumpter, 1944). A yield of 84.7% was obtained, with m.p. 200°C and R_f 0.85 (ethyl acetate: petroleum ether, 2:1).

2.1.2 Synthesis of N-benzyl indole-2,3-dione (N-benzyl isatin) (**2**)

In a round bottom flask, indole-2,3-dione (**1**, 0.8 gm, 3.37 mM) and an equimolar quantity of benzyl chloride (6.5 mL, 3.7 mM) were mixed in DMF (20 mL). K_2CO_3 (2 g) was added to this mixture, and the mixture was refluxed for 2 h. The flask was cooled, and the contents of the flask were poured onto ice-cold water (100 mL), leading to the formation of an orange–red precipitate, which was collected, washed with water, and dried. The compound was then purified by recrystallization from acetonitrile. A yield of 83.6% was obtained, with m.p. 134°C and R_f 0.65 (ethyl acetate:petroleum ether, 2:1); ^{1}H NMR: (300 MHz, $CDCl_3$) δ 5.09 (s, 2H, CH_2 benzyl group), 7.18 (d, J = 7.8 Hz, 1H, Ar-H), 7.23 (t, J = 7.6 Hz, 1H, Ar-H), 7.41 (s, 5H, Ar-H), 7.52 (t, J = 8.4 Hz, 1H, Ar-H), and 7.69 (d, J = 7.9 Hz, 1H, Ar-H). The NMR spectral data are congruent with previously documented findings (El-Faham et al., 2014).

2.1.3 General procedure for the preparation of esters 3(a–i)

Appropriately substituted benzoic acid (0.032 mol) was dissolved in absolute ethanol (20 mL) in a round bottom flask. Concentrated sulfuric acid (1 mL) was added to the reaction mixture, and the mixture was refluxed. The reaction progress was monitored through TLC. Upon completion of the reaction, the mixture was cooled and poured onto ice-cold water, and the product was extracted with ethyl acetate. The ethyl acetate layer was washed with water and 10% $NaHCO_3$ solution, dried over anhydrous sodium sulfate, and evaporated to dryness to obtain the respective ester (Guzowski Jr et al., 2012). The NMR spectral data of all synthesized ester derivatives 3(a–i) are congruent with previously documented findings (Samanta et al., 2014).

Methyl pyridine-4-carboxylate (3a): Yield, 75%; b.p., 207°C–208°C; and IR (KBr) cm^{-1}, 1,720 (C=O). ^{1}H NMR: (300 MHz, $CDCl_3$) δ: 3.74 (s, 3H, OCH_3), 7.91 (d, J = 8.4 Hz, 2H, Ar-H), and 8.73 (d, J = 7.8 Hz, 2H, Ar-H).

Methyl 3-bromobenzoate (3b): Yield, 68%; b.p., 233°C–237°C; and IR (KBr) cm^{-1}, 1,729 (C=O). ^{1}H NMR: (300 MHz, $CDCl_3$) δ: 3.84 (s, 3H, OCH_3), 7.62–7.68 (m, 1H, Ar-H), 7.73–7.79 (m, 1H, Ar-H), and 7.82 (d, J = 7.8 Hz, 2H, Ar-H).

Methyl 3-iodobenzoate (3c): Yield, 65%; b.p., 263°C–267°C; and IR (KBr) cm^{-1}, 1,730 (C=O). ^{1}H NMR: (300 MHz, $CDCl_3$) δ: 3.86 (s, 3H, OCH_3), 7.68–7.77 (m, 1H, Ar-H), 7.82–7.86 (m, 1H, Ar-H), and 7.95 (d, J = 7.8 Hz, 2H, Ar-H).

Methyl 2-hydroxybenzoate (3d): Yield, 75%; b.p., 214°C–216°C; and IR (KBr) cm^{-1}, 1,720 (C=O). ^{1}H NMR: δ: 3.83 (s, 3H, OCH_3), 5.29 (s, 1H of OH), 7.05 (d, J = 8.3 Hz, 1H, Ar-H), 7.83 (d, J = 8.1 Hz, 1H, Ar-H), 7.85 (d, J = 8.3 Hz, 1H, Ar-H), and 7.94 (d, J = 8.1 Hz, 1H, Ar-H).

Methyl 4-fluorobenzoate (3e): Yield, 75%; b.p., 196°C–198°C; and IR (KBr) cm^{-1}, 1,720 (C=O). ^{1}H NMR: (300 MHz, $CDCl_3$) δ: 3.83 (s, 3H, OCH_3), 7.50 (d, J = 7.8 Hz, 2H, Ar-H), and 7.83 (d, J = 7.8 Hz, 2H, Ar-H).

10.3389/fchem.2024.1424637

TABLE 3 Pharmacokinetics profile of synthesized compounds (5a–5i).

Property	Model name	5a	5b	5c	5d	5e	5f	5 g	5 h	5i	Unit
Absorption	Water solubility	−3.989	−5.661	−5.647	−4.434	−5.453	−3.872	−3.623	−5.585	−5.133	Numeric (log mol/L)
Absorption	$CaCO_2$ permeability	1.235	1.315	1.313	1.034	1.319	1.037	0.118	1.317	1.321	Numeric (log Papp in 10–6 cm/s)
Absorption	Intestinal absorption (human)	96.501	92.916	93.552	93.482	93.894	96.442	73.742	92.983	94.644	Numeric (% absorbed)
Absorption	Skin permeability	−2.742	−2.729	−2.731	−2.822	−2.75	−2.707	−2.736	−2.729	−2.732	Numeric (log Kp)
Absorption	P-glycoprotein substrate	No	Yes	Yes	Yes	Yes	No	Yes	Yes	Yes	Categorical (yes/no)
Absorption	P-glycoprotein I inhibitor	Yes	Yes	Yes	Yes	Yes	Yes	Yes	Yes	Yes	Categorical (yes/no)
Absorption	P-glycoprotein II inhibitor	Yes	Yes	Yes	Yes	Yes	Yes	Yes	Yes	Yes	Categorical (yes/no)
Distribution	VDss (human)	−0.083	−0.175	−0.165	−0.332	−0.361	−0.132	−0.146	−0.192	−0.208	Numeric (log L/kg)
Distribution	Fraction unbound (human)	0	0	0	0	0	0	0	0	0	Numeric (Fu)
Distribution	BBB permeability	−0.291	−0.078	−0.083	0.132	−0.044	−0.309	−1.013	−0.077	−0.076	Numeric (log BB)
Distribution	CNS permeability	−2.296	−1.788	−1.821	−2.104	−1.958	−2.303	−2.508	−1.81	−1.925	Numeric (log PS)
Metabolism	CYP2D6 substrate	No	No	No	No	No	No	No	No	No	Categorical (yes/no)
Metabolism	CYP3A4 substrate	Yes	Yes	Yes	Yes	Yes	Yes	Yes	Yes	Yes	Categorical (yes/no)
Metabolism	CYP1A2 inhibitor	Yes	No	No	Yes	Yes	Yes	No	No	Yes	Categorical (yes/no)
Metabolism	CYP2C19 inhibitor	Yes	Yes	Yes	Yes	Yes	Yes	No	Yes	Yes	Categorical (yes/no)
Metabolism	CYP2C9 inhibitor	Yes	Yes	Yes	Yes	Yes	Yes	Yes	Yes	Yes	Categorical (yes/no)
Metabolism	CYP2D6 inhibitor	No	No	No	No	No	No	No	No	No	Categorical (yes/no)
Metabolism	CYP3A4 inhibitor	Yes	Yes	Yes	Yes	Yes	Yes	No	Yes	Yes	Categorical (yes/no)
Excretion	Total clearance	0.468	−0.121	−0.411	0.208	0.151	0.345	−0.126	0.106	0.424	Numeric (log mL/min/kg)
Excretion	Renal OCT2 substrate	Yes	No	No	No	No	Yes	No	No	No	Categorical (yes/no)
Toxicity	Max. tolerated dose (human)	0.051	0.221	0.208	−0.417	0.232	−0.05	0.001	0.218	0.203	Numeric (log mg/kg/day)

Methyl pyridine-2-carboxylate (3f): Yield, 75%; b.p., 204°C–206°C; and IR (KBr) cm^{-1}, 1,720 (C=O). ^1H NMR: (300 MHz, $CDCl_3$) δ: 3.72 (s, 3H, OCH_3), 7.57–7.60 (m, 1H, Ar-H), 7.62 (d, J = 7.8 Hz, 2H, Ar-H), and 7.65–7.69 (m, 1H, Ar-H).

Methyl 3,4,5-trihydroxybenzoate (3g): Yield, 67%; b.p, 201°C–203°C; and IR (KBr) cm^{-1}, 1,725 (C=O). ^1H NMR: (300 MHz, $CDCl_3$) δ: 3.87 (s, 3H, OCH_3), 5.34 (m, 3H of OH), and 7.25 (d, J = 7.2, 2H, Ar-H).

Methyl 2-chlorobenzoate (3h): Yield, 60%; b.p, 217°C–219°C; and IR (KBr) cm^{-1}, 1,725 (C=O). ^1H NMR: (300 MHz, $CDCl_3$) δ: 3.81 (s, 3H, OCH_3), 7.35 (d, J = 8.5 Hz, 1H, Ar-H), 7.43 (d, J = 8.3 Hz, 1H, Ar-H), 7.57 (d, J = 8.5 Hz, 1H, Ar-H), and 7.94 (d, J = 8.3 Hz, 1H, Ar-H).

Methyl benzoate (3i): Yield, 75%; b.p., 188°C–190°C; and IR (KBr) cm^{-1}, 1,725 (C=O). ^1H NMR: (300 MHz, $CDCl_3$) δ: 3.81 (s, 3H, OCH_3), 7.45 (d, J = 8.5 Hz, 2H, Ar-H), 7.57–7.61 (m, 1H, Ar-H), and 8.02 (d, J = 8.5 Hz, 2H, Ar-H).

2.1.4 General procedure for the preparation of hydrazide 4(a–i)

Respective ester **3(a–i)** was dissolved in absolute ethanol (50 mL), and hydrazine monohydrate (15 mL) was added to the solution. The mixture was thoroughly stirred and heated under reflux for 10–12 h. The reaction progress was monitored through TLC (chloroform:methanol, 3:1). Upon completion of the reaction, excess ethanol and hydrazine were evaporated under reduced pressure, yielding the corresponding hydrazide.

The NMR spectral data are congruent with previously documented findings (Khan et al., 2003).

Pyridine-4-carbohydrazide (4a): Light yellow solid; yield, 80%; m.p., 169°C–171°C; and IR (KBr) cm^{-1}, 1,675 (C=O). ^1H NMR: (300 MHz, $CDCl_3$) δ: 4.45 (s, 2H, NH_2), 7.88 (d, J = 8.5 Hz, 2H, Ar-H), 8.34 (d, J = 8.5 Hz, 2H, Ar-H), and 9.53 (s, 1H, NH).

3-Bromobenzohydrazide (4b): White solid; yield, 75%; m.p., 183°C–187°C; and IR (KBr) cm^{-1}, 1,650 (C=O). ^1H NMR: (300 MHz, $CDCl_3$) δ: 4.51 (s, 2H, NH_2), 7.43–7.48 (m, 1H, Ar-H), 7.65–7.71 (m, 1H, Ar-H), 7.94 (d, J = 7.4 Hz, 2H, Ar-H), and 9.60 (s, 1H, NH).

3-Iodobenzohydrazide (4c): White solid; yield, 70%; m.p., 208°C–211°C; and IR (KBr) cm^{-1}, 1,645 (C=O). ^1H NMR: (300 MHz, $CDCl_3$) δ: 4.49 (s, 2H, NH_2), 7.26–7.31 (m, 1H, Ar-H), 7.42–7.47 (m, 1H, Ar-H), 8.08 (d, J = 8.2 Hz, 2H, Ar-H), and 10.02 (s, 1H, NH).

2-Hydroxybenzohydrazide (4d): Light yellow solid; yield, 80%; m.p., 146°C–148°C; and IR (KBr) cm^{-1}, 1,635 (C=O). ^1H NMR: (300 MHz, $CDCl_3$) δ: 4.49 (s, 2H, NH_2), 5.41 (s, 1H of OH), 7.03 (d,

J = 8.6 Hz, 1H, Ar-H), 7.22 (d, J = 8.3 Hz, 1H, Ar-H), 7.52 (d, J = 8.6 Hz, 1H, Ar-H), 7.89 (d, J = 8.3 Hz, 1H, Ar-H), and 10.02 (s, 1H, NH).

4-Fluorobenzohydrazide (4e): White solid; yield, 70%; m.p., 176°C–178°C; IR (KBr) cm^{-1}, 1,644 (C=O). ^1H NMR: (300 MHz, $CDCl_3$) δ: 4.39 (s, 2H, NH_2), 7.47 (d, J = 8.4 Hz, 2H, Ar-H), 7.81 (d, J = 8.4 Hz, 2H, Ar-H), and 9.97 (s, 1H, NH).

Pyridine-2-carbohydrazide (4f): Light yellow solid; yield, 70%; m.p., 164°C–166°C; and IR (KBr) cm^{-1}, 1,670 (C=O). ^1H NMR: (300 MHz, $CDCl_3$) δ: 4.43 (s, 2H, NH_2), 7.57–7.63 (m, 1H, Ar-H), 7.71 (d, J = 8.0 Hz, 2H, Ar-H), 8.52–7.69 (m, 1H, Ar-H), and 9.87 (s, 1H, NH).

3,4,5-Trihydroxybenzohydrazide (4g): Light brown solid; yield, 55%; m.p., 159°C–161°C; and IR (KBr) cm^{-1}, 1,665 (C=O). 1H NMR: (300 MHz, $CDCl_3$) δ: 4.36 (s, 2H, NH_2), 5.51 (m, 3H of OH), 7.17 (d, J = 7.4, 2H, Ar-H), and 10.19 (s, 1H, NH).

2-Chlorobenzohydrazide (4h): White solid; yield, 75%; m.p., 114°C–116°C; and IR (KBr) cm^{-1}, 1,647 (C=O). ^1H NMR: (300 MHz, $CDCl_3$) δ: 4.35 (s, 2H, NH_2), 7.47 (d, J = 8.8 Hz, 1H, Ar-H), 7.59 (d, J = 8.4 Hz, 1H, Ar-H), 7.66 (d, J = 8.8 Hz, 1H, Ar-H), 8.94 (d, J = 8.4 Hz, 1H, Ar-H), and 9.99 (s, 1H, NH).

Benzohydrazide (4i): White solid; yield, 75%; m.p., 109°C–111°C; and IR (KBr) cm^{-1}, 1,667 (C=O). ^1H NMR: (300 MHz, $CDCl_3$) δ: 4.49 (s, 2H, NH_2), 7.45 (d, J = 8.5 Hz, 2H, Ar-H), 7.55–7.58 (m, 1H, Ar-H), 7.77 (d, J = 8.5 Hz, 2H, Ar-H), and 10.21 (s, 1H, NH).

2.1.5 N'-(1-benzyl-2-oxo-1, 2-dihydro-3H-indol-3-ylidene) hydrazide derivatives (5a–i)

A solution of appropriate hydrazide **4(a–i)** (316 mg, 2 mmol) was prepared in ethanol (20 mL). Another solution was prepared containing benzylisatin (**2**) (1 mmol) in ethanol (20 mL) and glacial acetic acid (two drops). The two solutions were mixed and refluxed for 3–4 h. Upon completion of the reaction, the mixture was cooled, and the product was filtered and purified by recrystallization from ethanol.

N'-(1-benzyl-2-oxo-1,2-dihydro-3H-indol-3-ylidene)pyridine-4-carbohydrazide (5a): Yellowish orange; 89% yield; m.p., 182°C–184°C. IR (KBr) cm^{-1}: 3,227 (NH), 1,612 (C=N), 1,713, 1,682 (amide C=O). ^1H NMR (300 MHz, $CDCl_3$) δ: 14.32 (s, 1H, NH of hydrazide), 8.77 (s, 2H, Ar-H), 8.31–8.25 (m, 1H, Ar-H), 7.74 (d, 2H, *J* = 6.4 Hz, Ar-H), 7.58 (t, 1H, Ar-H), 7.57–7.43 (m, 2H, Ar-H), 7.42–7.27 (m, 4H, Ar-H), 7.24–7.17 (m, 1H, Ar-H), and 5.22 (s, 2H, CH_2 of the benzyl group). ^{13}C NMR: δ: 170.46, 164.71, 151.17, 141.39, 139.65, 136.80, 136.77, 129.86, 128.76, 127.50, 127.40, 125.73, 122.82, 121.49, 120.89, 109.95, and 53.38. GC–MS (EI) *m/z* 356 $[M]^+$. Elemental analysis: $C_{21}H_{16}N_4O_2$, calculated: C (70.77%), H (4.53%), N (15.72%), and O (8.98%); found: C (70.71%), H (4.51%), N (15.69%), and O (8.88%).

N'-(1-benzyl-2-oxo-1,2-dihydro-3H-indol-3-ylidene)-3-bromobenzohydrazide (5b): Yellowish orange; 84% yield; m.wt: 434.3. m.p., 186°C–190°C. IR (KBr) cm^{-1}: 3,225 (NH), 1,617 (C=N), 1,710, 1,679 (amide C=O); ^1H NMR (300 MHz, $CDCl_3$) δ: 13.96 (s, 1H, NH of hydrazide), 8.30–8.20 (m, 1H, Ar-H), 8.05 (s, 1H, Ar-H), 7.85–7.71 (m, 1H, Ar-H), 7.62 (t, 1H, J = 6.2 Hz, Ar-H), 7.57 (d, 1H, J = 4.3 Hz, Ar-H), 7.45–7.40 (m, 3H, Ar-H), 8.38–8.27 (m, 5H, Ar-H), and 5.18 (s, 2H, CH_2 benzyl group). ^{13}C NMR: δ: 167.47, 162.82, 153.60, 142.25, 136.77, 134.46, 133.86, 132.14, 130.87, 128.86, 128.76, 127.80, 127.40, 126.83, 125.73, 122.82, 122.26, 118.93, 114.60, and 46.77. GC–MS (EI) *m/z* 433 $[M]^+$. Elemental analysis: $C_{22}H_{16}BrN_3O_2$; calculated: C (60.84%), H (3.71%), Br (18.40%), N (9.68%), and O (7.37%); found: C (60.79%), H (3.73%), Br (18.33%), N (9.64%), and O (7.35%).

N'-(1-benzyl-2-oxo-1,2-dihydro-3H-indol-3-ylidene)-3-iodobenzohydrazide (5c): Yellowish orange; 77% yield; m.p., 201°C–203°C. IR (KBr) cm^{-1}: 3,238 (NH), 1,615 (C=N), 1,717, 1,678 (amide C=O). ^1H NMR (300 MHz, $CDCl_3$) δ: 13.91 (s, 1H, NH of hydrazide), 8.31–8.20 (m, 1H, Ar-H), 8.12 (s, 1H, Ar-H), 7.60 (d, 1H, J = 6.2 Hz, Ar), 7.58–7.53 (m, 2H, Ar-H), 7.43–7.38 (m, 2H, Ar-H), 7.35–7.24 (m, 6H, Ar-H), and 5.18 (s, 2H, CH_2 benzyl group). ^{13}C NMR: δ: 165.18, 160.45, 140.46, 138.96, 138.42, 136.70, 135.34, 135.24, 131.14, 129.72, 128.76, 127.80, 127.34, 126.68, 125.06, 122.63, 120.43, 110.74, 93.74, and 43.64. GC–MS (EI) *m/z* 481 $[M]^+$. Elemental analysis:

TABLE 4 Predicted toxicity parameters of synthesized compounds 5a–i.

Compound	Toxicity						Metabolism
	Cramer's rule	*In vitro* mutagenicity and carcinogenicity	Skin irritation/ corrosion	Eye irritation/ corrosion	Alert for DNA binding	Structure alerts for the *in vivo* micronucleus assay in rodents	Cytochrome P450-mediated drug metabolism
5a	Negative	Negative	Negative	Negative	Negative	Negative	Positive
5b	Negative	Negative	Negative	Negative	Negative	Negative	Positive
5c	Negative	Negative	Negative	Negative	Negative	Negative	Positive
5d	Negative	Negative	Negative	Negative	Negative	Negative	Positive
5e	Negative	Negative	Negative	Negative	Negative	Negative	Positive
5f	Negative	Negative	Negative	Negative	Negative	Negative	Positive
5g	Negative	Negative	Negative	Negative	Negative	Negative	Positive
5h	Negative	Negative	Negative	Negative	Negative	Negative	Positive
5i	Negative	Negative	Negative	Negative	Negative	Negative	Positive

TABLE 5 Docking scores of ligands with estrogen receptor α.

Compound	Binding affinity (kcal/mol)	Amino acid residue
5a	−8.3	VAL418, ARG394, LEU391, MET388, LEU387, LEU384, and TRP383
5b	−8.2	TRP383, ARG394, LEU391, MET388, LEU387, and LEU384
5c	−8.3	GLU419, ARG394, LEU391, MET388, LEU387, LEU384, and TRP383
5d	−9.2	ARG394, LEU391, MET388, LEU387, LEU384, TRP383, GLU353, ALA350, LEU349, PHE404, THR347, LEU346, and MET353
5e	−8.8	MET443, ARG394, LEU391, MET388, LEU387, LEU384, and TRP383
5f	−8.5	ARG394, LEU391, MET388, LEU387, LEU384, and TRP383
5g	−8.8	ARG394, LEU391, MET388, LEU387, LEU384, and TRP383
5h	−8.2	ARG394, LEU391, MET388, LEU387, LEU384, and TRP383
5i	−8.9	ARG394, LEU391, MET388, LEU387, LEU384, TRP383, LYS 520, GLY521, MET522, HID524, LEU525, and MET528

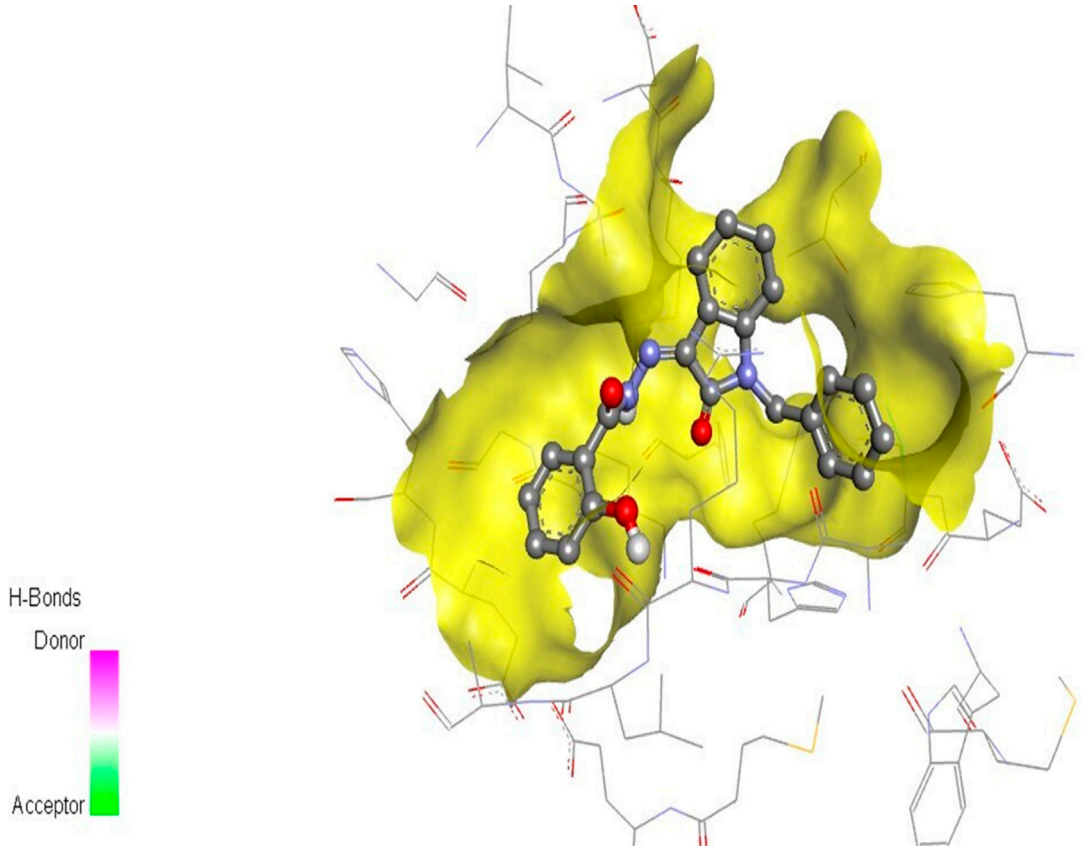

FIGURE 5
Compound 5d docked with ERα (PDB ID: 3ERT) 3D pose.

$C_{22}H_{16}IN_3O_2$; calculated: C (54.90%), H (3.35%), I (26.37%), N (8.73%), and O (6.65%); found: C (54.88%), H (3.30%), I (26.37%), N (8.68%), and O (6.61%).

N'-(1-benzyl-2-oxo-1,2-dihydro-3H-indol-3-ylidene)-2-hydroxybenzohydrazide (5d): Yellowish orange; 78% yield; m.p., 193°C–195°C. IR (KBr) cm^{-1}: 3,233 (NH), 1,623 (C=N), 1,726, 1,677 (amide C=O). ^1H NMR (300 MHz, $CDCl_3$) δ: 14.07 (s, 1H, NH of hydrazide), 8.31–8.20 (m, 1H, Ar-H), 7.80–7.78, (d, 2H, J = 8.1 Hz, Ar-H), 7.62–7.52 (m, 1H, Ar-H), 7.43–7.40 (m, 2H, Ar-H), 7.36–7.26 (m, 5H, Ar-H), 6.95–6.93 (m, 2H of

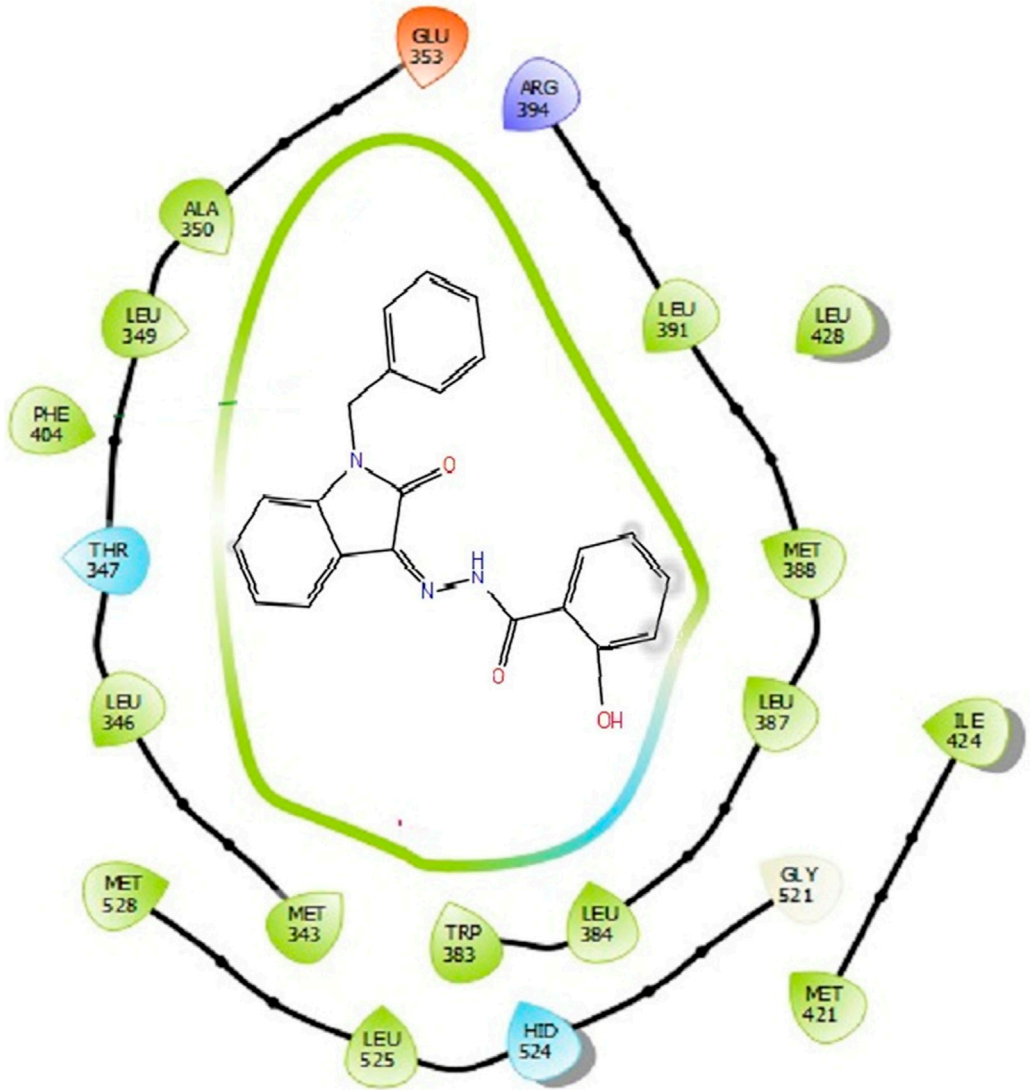

FIGURE 6
Binding interactions of compound 5d with ERα (PDB ID: 3ERT) 2D pose.

Ar-H), 5.63 (s, 1H of OH), and 5.07 (s, 2H, CH_2 benzyl group). ^{13}C NMR: δ: 166.84, 162.11, 156.99, 138.81, 136.96, 136.77, 134.11, 130.08, 129.86, 128.76, 127.80, 127.40, 125.73, 122.82, 120.89, 119.58, 117.18, 116.09, 111.86, and 45.51. GC–MS (EI) *m/z* 371 [M]+. Elemental analysis: $C_{22}H_{17}N_3O_3$; calculated: C (71.15%), H (4.61%), N (11.31%), and O (12.92%); found: C (71.05%), H (4.55%), N (11.29%), and O (12.90%).

N'-(1-benzyl-2-oxo-1,2-dihydro-3H-indol-3-ylidene)-4-fluorobenzohydrazide (5e): Yellowish orange; 74% yield; m.p., 185°C–188°C. IR (KBr) cm^{-1}: 3,239 (NH), 1,620 (C=N), 1,719, 1,685 (amide C=O). ^1H NMR (300 MHz, $CDCl_3$) δ: 14.16 (s, 1H, NH of hydrazide), 8.51–8.46 (m, 1H, Ar-H), 7.97 (t, 2H, J = 7.2 Hz, Ar-H), 7.63–7.52 (m, 1H, Ar-H), 7.41–7.36 (m, 3H, Ar-H), 7.34–7.29 (m, 6H, Ar-H), and 5.18 (s, 2H, CH_2 benzyl group). ^{13}C NMR: δ: 165.88, 164.04, 163.90, 163.51, 138.81, 136.80, 136.77, 130.98, 130.96, 130.65, 130.58, 129.86, 128.76, 127.80, 127.40, 125.73, 122.82, 120.89, 116.13, 115.95, 111.96, and 44.52. GC–MS (EI) *m/z* 373 $[M]^+$. Elemental analysis: $C_{22}H_{16}FN_3O_2$; calculated: C (70.77%), H (4.32%), F (5.09%), N (11.25%), and O (8.57%); found: C (70.71%), H (4.29%), F (5.09%), N (11.22%), and O (8.53%).

N'-(1-benzyl-2-oxo-1,2-dihydro-3H-indol-3-ylidene)pyridine-2-carbohydrazide (5f): Yellowish orange; 86% yield; m.p., 187°C–189°C. IR (KBr) cm^{-1}: 3,198 (NH), 1,631 (C=N), 1,707, 1,680 (amide C=O). ^1H NMR (300 MHz, $CDCl_3$) δ: 14.17 (s, 1H, NH of hydrazide), 8.67–8.66 (m, 1H, Ar-H), 8.30–8.21 (m, 1H, Ar-H), 8.03 (d, 1H, J = 8.3 Hz, Ar-H), 7.89–7.63 (m, 1H, Ar-H), 7.58–7.53 (m, 1H, Ar-H), 7.43–7.37 (m, 3H, Ar-H), 7.34–7.24 (m, 5H, Ar-H), and 5.15 (s, 2H, CH_2 benzyl group). ^{13}C NMR: δ: 163.95, 159.39, 149.99, 149.62, 138.81, 137.76, 136.96, 136.77, 129.86, 128.76, 127.80, 127.40, 125.94, 125.61, 123.75, 122.82, 120.89, 111.96, and 44.52. GC–MS (EI) *m/z* 356 $[M]^+$. Elemental

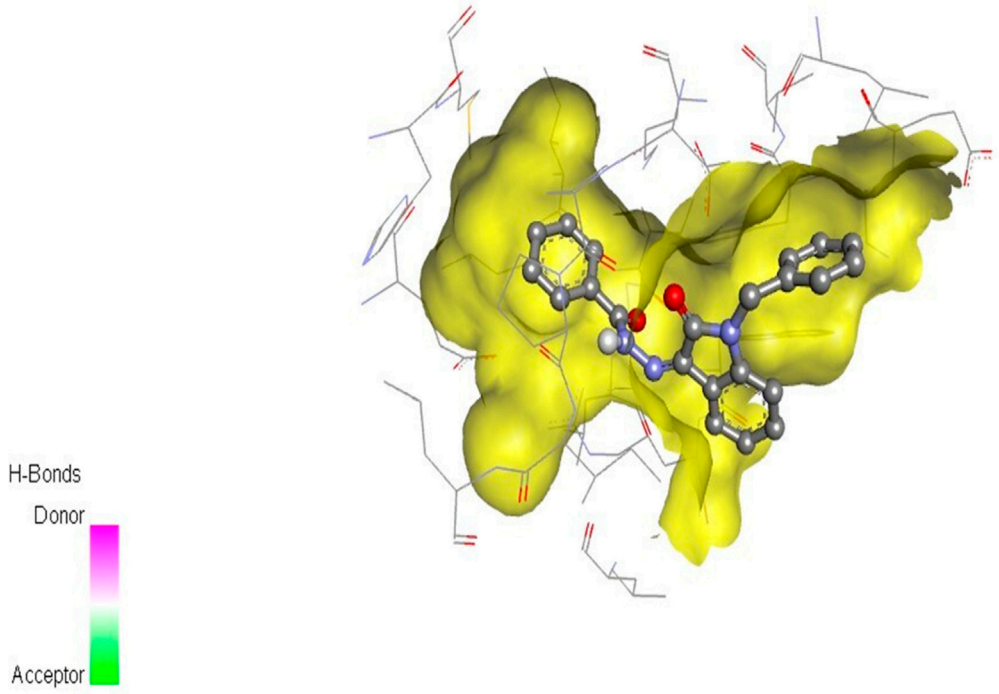

FIGURE 7
Compound 5i docked with ERα (PDB ID: 3ERT) 3D pose.

analysis: $C_{21}H_{16}N_4O_2$; calculated: C (70.77%), H (4.53%), N (15.72%), and O (8.98%); found: C (70.74%), H (4.51%), N (15.66%), and O (8.91%).

N'-(1-benzyl-2-oxo-1,2-dihydro-3H-indol-3-ylidene)-3,4,5 trihydroxybenzohydrazide (5g): Yellowish orange; 72% yield; m.p., 204°C–206°C. IR (KBr) cm^{-1}: 3,230 (NH), 1,619 (C=N), 1,714, 1,674 (amide C=O); ^1H NMR (300 MHz, $CDCl_3$) δ: 14.10 (s, 1H, NH of hydrazide), 8.30–7.20 (m, 1H, Ar-H), 7.62–7.53 (m, 1H, Ar-H), 7.43–7.38 (m, 2H, Ar-H) 7.36–7.24 (m, 5H, Ar-H), 7.15 (s, 2H of OH), 7.01 (s, 2H of Ar-H), 5.40 (s, 1H of OH), and 5.18 (s, 2H, CH_2 benzyl group). ^{13}C NMR: δ: 167.94, 162.11, 146.73, 138.81, 138.55, 136.82, 136.77, 129.86, 128.76, 127.80, 127.40, 126.88, 125.73, 122.82, 120.82, 113.25, 105.58, and 44.52. GC–MS (EI) *m/z* 403 $[M]^+$. Elemental analysis: $C_{22}H_{17}N_3O_5$; calculated: C (65.5%), H (4.25%), N (10.42%), and O (19.83%); found: C (65.11%), H (4.22%), N (10.38%), and O (19.79%).

N'-(1-benzyl-2-oxo-1,2-dihydro-3H-indol-3-ylidene)-2-chlorobenzohydrazide (5h): Yellowish orange; 70% yield; m.p., 197°C–200°C. IR (KBr) cm^{-1}: 3,237 (NH), 1,604 (C=N), 1,723, 1,683 (amide C=O); ^1H NMR (300 MHz, $CDCl_3$): δ: 14.26 (s, 1H, NH of hydrazide), 8.04–7.98 (m, 1H, Ar-H), 7.88–7.82 (t, 1H, J = 7.3 Hz, Ar) 7.58–7.42 (m, 1H, Ar), 7.38–7.36 (m, 4H, Ar-H), 7.34–7.32 (m, 6H, Ar-H), and 4.96 (s, 2H, CH_2 benzyl group). ^{13}C NMR: δ: 169.20, 162.58, 149.27, 140.52, 136.88, 136.77, 133.35, 132.58, 131.59, 129.98, 129.86, 129.53, 128.76, 127.80, 127.58, 127.40, 125.73, 122.82, 111.96, and 48.74. GC–MS (EI) *m/z* 389 $[M]^+$. Elemental analysis: $C_{22}H_{16}ClN_3O_2$, calculated: C (67.78%), H (4.14%), Cl (9.09%), N (10.78%) and O (8.21%); found: C (67.71%), H (4.09%), Cl (9.04%), N (10.72%), and O (8.18%).

N'-(1-benzyl-2-oxo-1,2-dihydro-3H-indol-3-ylidene) benzohydrazide (5i): Yellowish orange; 73% yield; m.p., 188°C–190°C. IR (KBr) cm^{-1}: 3,196 (NH), 1,606 (C=N), 1,721, 1,681 (amide C=O). ^1H NMR (300 MHz, $CDCl_3$) δ: 14.10 (s, 1H, NH of hydrazide), 8.31–8.25 (m, 1H, Ar-H), 7.94–7.90 (m, 2H, Ar-H), 7.62–7.51 (m, 4H, Ar-H), 7.49–7.43 (m, 2H, Ar-H), 7.38–7.24 (m, 5H, Ar-H), and 5.10 (s, 2H, CH_2 benzyl group). ^{13}C NMR: δ: 168.81, 163.66, 151.87, 141.39, 136.77, 135.96, 132.14, 129.86, 128.76, 128.68, 128.19, 127.80, 127.40, 125,73, 122.82, 120.89, 112.24, and 51.25. GC–MS (EI) *m/z* 355 $[M]^+$. Elemental analysis: $C_{22}H_{17}N_3O_2$, calculated: C (74.35%), H (4.82%), N (11.82%), and O (9.00%); found: C (74.32%), H (4.79%), N (11.77%), and O (8.97%).

2.2 Cytotoxicity assay

The impact of novel derivatives was determined in the MCF-7 BC cell line using the sulforhodamine B (SRB) assay, as described previously at the Department of Life Sciences, Syed Babar Ali School of Science and Engineering, Lahore University of Management Sciences (LUMS), Lahore, Pakistan. The cell line was originally from ATCC and was validated through STR profiling by Microsynth AG. The cell line used in this study was obtained from ATCC® HTB-22™. In this procedure, cells were plated in 96-well plates and subjected to different concentrations of derivatives (5a–5i) for 72 h. Subsequently,

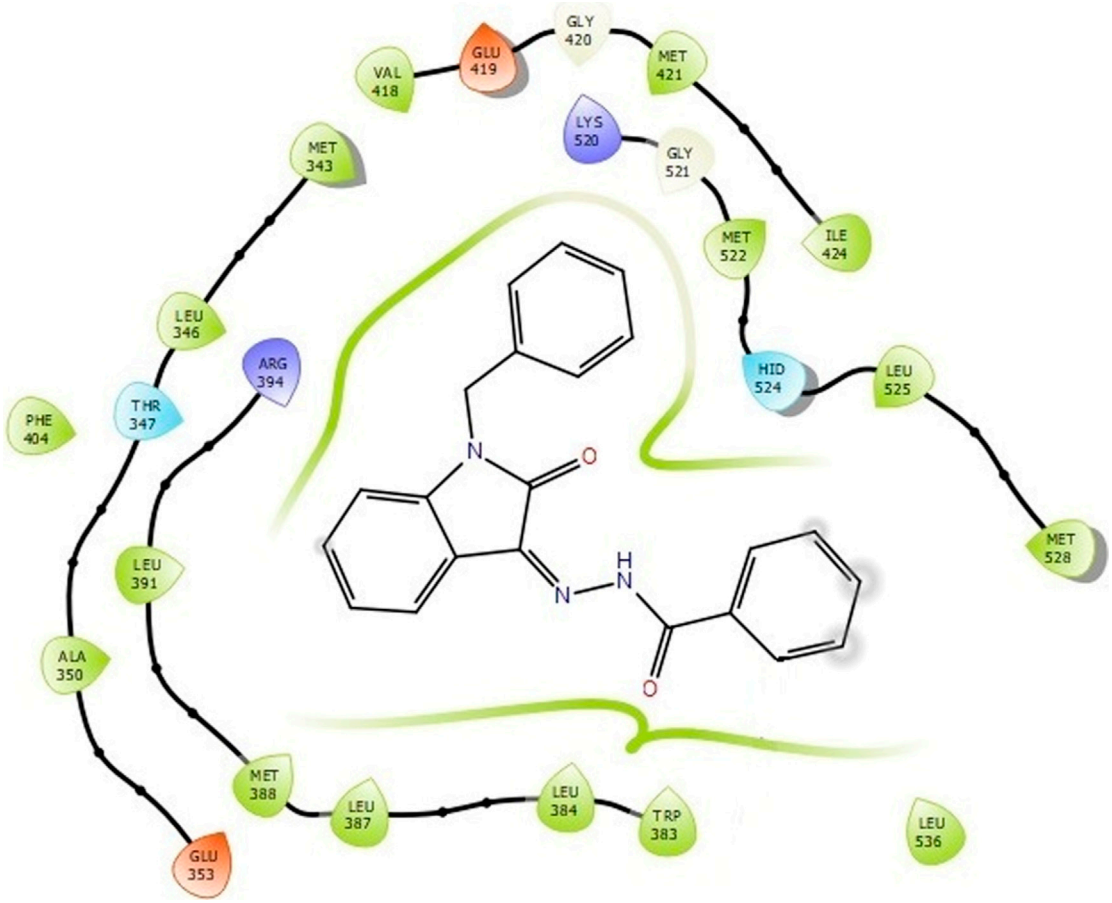

FIGURE 8
Binding interactions of compound 5i with ERα (PDB ID: 3ERT) 2D pose.

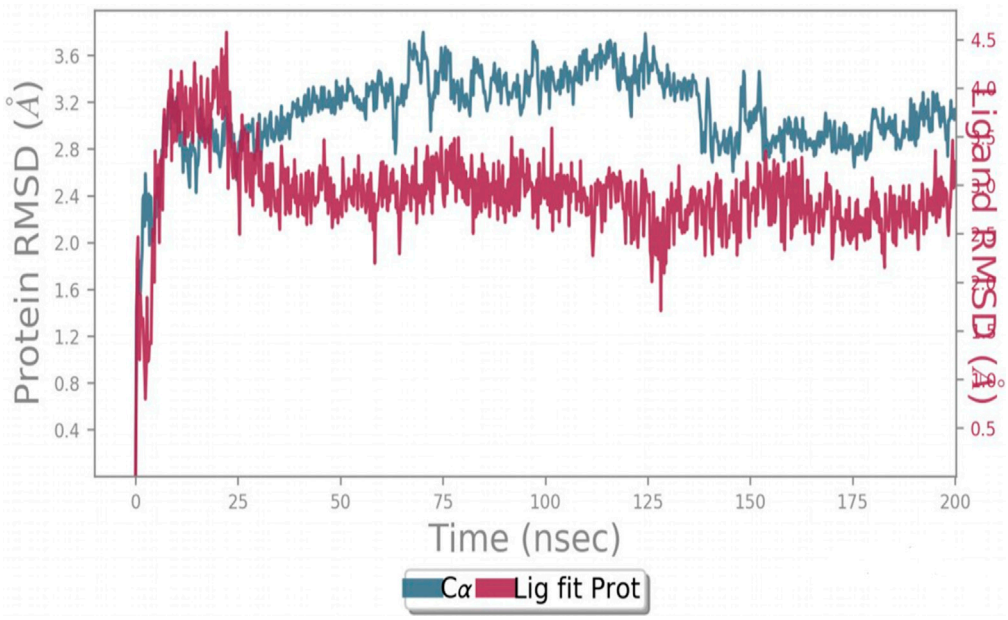

FIGURE 9
Protein–ligand RMSD.

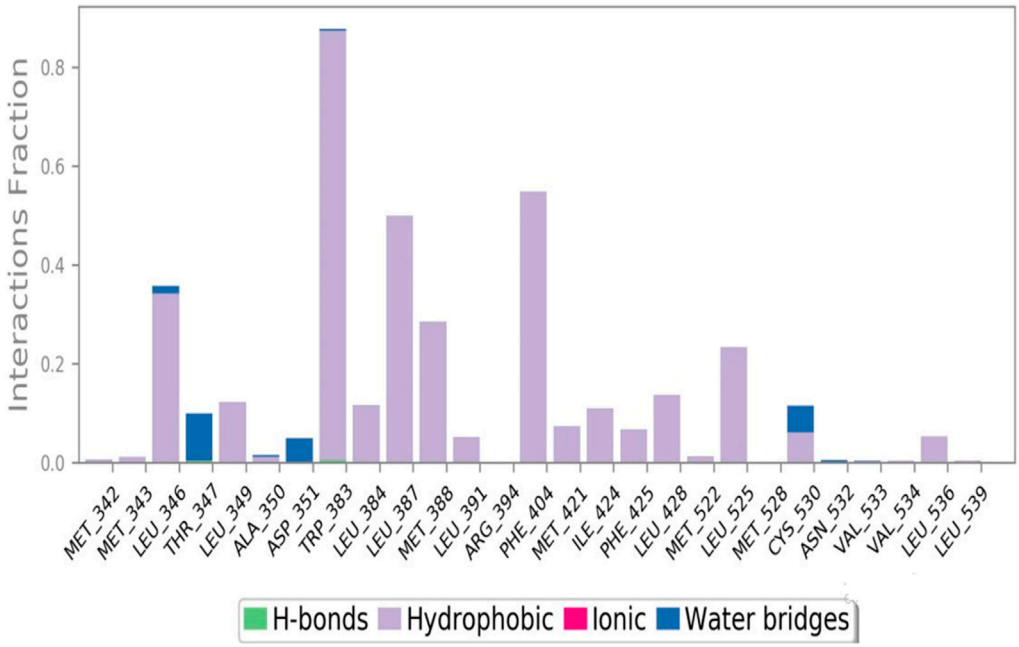

FIGURE 10
Protein–ligand contact stacked bar chart.

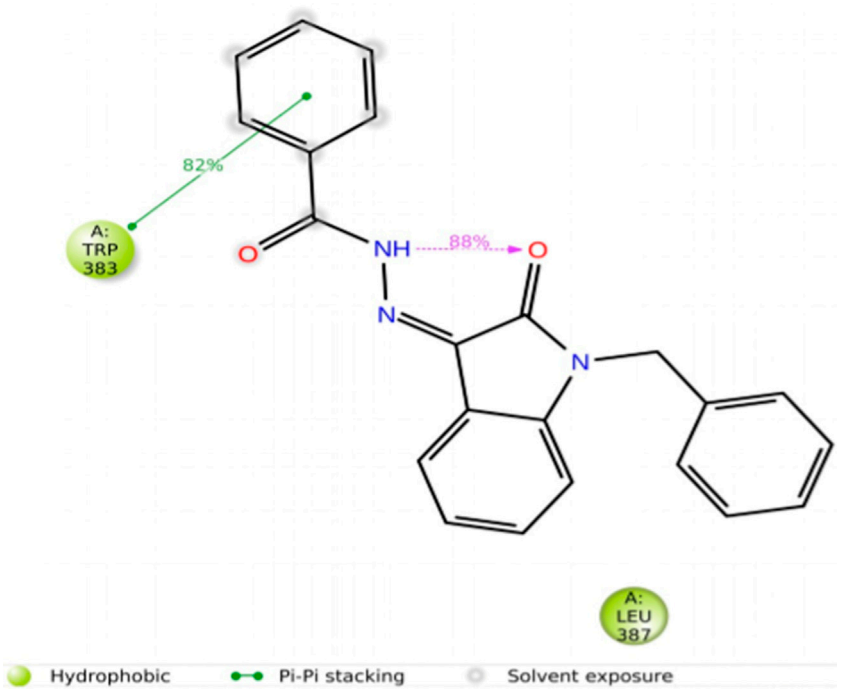

FIGURE 11
Protein–ligand contacts.

the cells were fixed by treatment with 3% ice-cold trichloroacetic acid (TCA) at 4°C for 2 h. Following fixation, the cells were washed and stained with 0.06% SRB for 30 min at room temperature. The SRB bound to the cells was then dissolved in 100 μL of Tris buffer (10 mM) at pH 10.5. The optical density (OD) was measured at 490 nm using a microplate reader (BioTek), and the percentage viability was calculated with reference to DMSO. The data represent the average from three independent experiments (Manzoor et al., 2018).

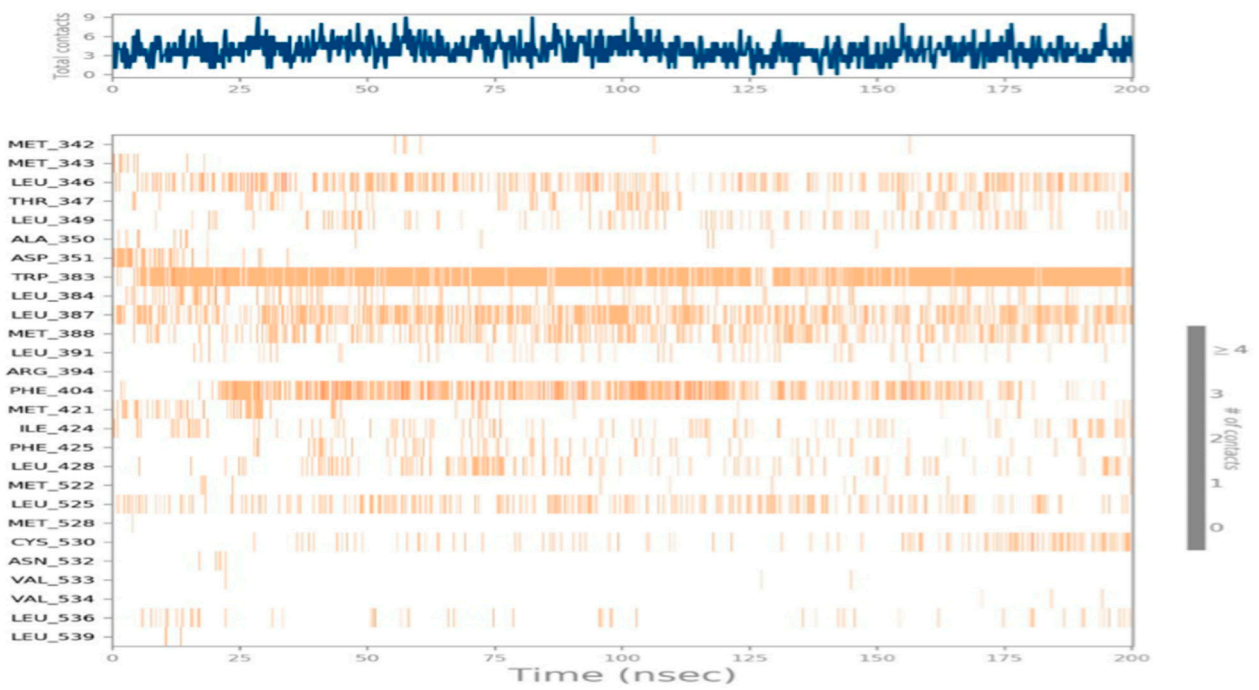

FIGURE 12
Total time simulation versus amino acid interactions.

2.3 Immunoblotting

BC cells (MCF-7) were subjected to treatment with three different concentrations of **5i** (1.25X, 2.5X, and 5X of IC_{50}) for 24 h. Afterward, cell lysis was performed with lysis buffer (50 mM NaCl, 20 mM Tris, pH 7.5, 1 mM EDTA, 1% Triton, 50 mM NaF supplemented with protease, and phosphatase inhibitors). The resulting cell lysates were cleared by centrifugation, and the protein concentration was determined using the Bradford reagent. An equal amount of proteins for each sample was separated by 10% SDS-PAGE and transferred to nitrocellulose membranes. These membranes were then blocked with skimmed milk and incubated with ERα and GAPDH (Millipore) antibodies. Following the incubation period, the membranes were washed with PBST and then exposed to a secondary antibody labeled with HRP for 1 h. The blots were subsequently washed again and developed using the ECL reagent using the Bio-Rad ChemiDoc system (Firdous et al., 2023).

2.4 Chemical space, drug-likeness prediction, and pharmacokinetics profiling of compounds 5a–5i

The chemical space and drug-like potential of the synthesized compounds were studied using DataWarrior (Sander et al., 2015), which is an open-source cheminformatics tool. The physicochemical properties of these compounds were evaluated using the cutoff criteria proposed by Lipinski (2004) and Veber et al. (2002). Lead-like molecules with favorable bioavailability typically exhibit the following characteristics: (a) molecular weight <500 g/mol; (b) ≤5 hydrogen bond donors; (c) ≤10 hydrogen bond acceptors; and (d) log(octanol/water) partition coefficient ≤5. In addition to the other requirements, Veber introduced the related issues of the number of rotatable bonds (10 or less) and the polar surface area (≤140 A2). The use of these parameters as a reference value was thus justified in the determination. To gain an understanding of the pharmaceutical properties of compounds 5a–5i, their structures were analyzed using pkCSM (Pires et al., 2015), a graph-based structural signature modeling server. At the beginning, ligand-based ADMET predictions were made to assist the structure screening using molecular docking and MD simulations with their information.

2.5 Assessment of toxicity *via* Toxtree software

Toxtree, an open-source software, was used on a Windows platform to predict the toxicity of the compounds. The software processed chemical structures by interacting with established toxic compounds, enabling predictive toxicology evaluations. Molecular structures were imported in MOL file format into the Toxtree navigator, subsequently undergoing processing via diverse interacting software modules. These modules encompassed Cramer's rule, carcinogenicity, *in vitro* mutagenicity, skin corrosion/irritation, eye corrosion/irritation, cytochrome P450-mediated drug metabolism, and structure alerts for the *in vivo* micronucleus assay in rodents. Post-processing, comprehensive decision support was obtained in portable document format (Patlewicz et al., 2008).

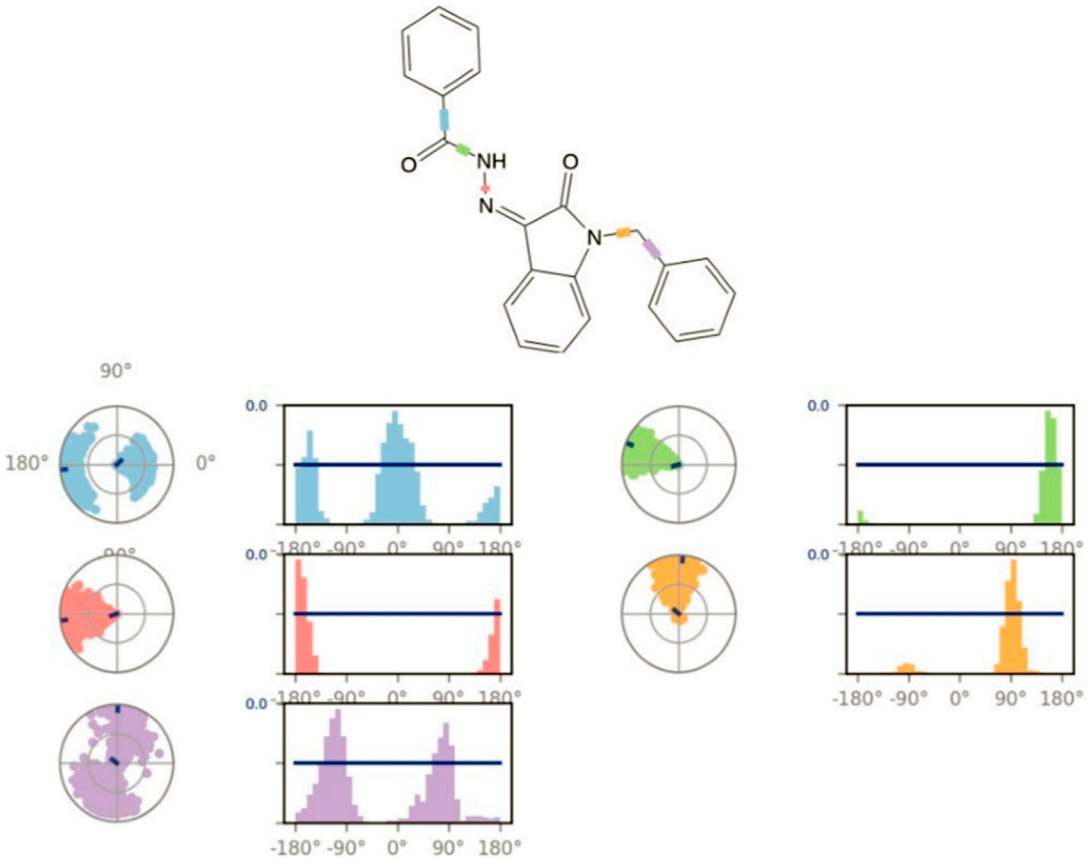

FIGURE 13
Ligand torsion profile.

2.6 Molecular docking analysis

The crystal structure of ERα (PDB ID: 3ERT) was analogized from the RCSB Protein Data Bank. The formation of nine distinct ligands, which were the derivatives of the isatin nucleus, was achieved using ChemSketch (version 12.0). Gridding parameters were determined using AutoDock Tools (v 1.5.6). Enhancements included the fusion of non-polar hydrogen; Gasteiger partial charges were added, and rotatable bonds were assigned. The spacing of 0.375 Å between the grid box dimensions included in the receptor site. After these preparations, the docking protocols were validated through a re-docking procedure using the ERα crystallographic structure (PDB ID: 3ERT). This process implied the docking of ligands into the active site of ERα, followed by the comparison of the resultant poses to the original crystallographic structure. In addition, The re-docked ligand had binding mode and interactions similar to the those of the original crystallographic structure. The actual protein–ligand docking was carried out using AutoDock Vina, and Open Babel GUI, Discovery Studio 4.1 Visualizer, and PyMOL were used for the preparation and conversion of the protein molecule into its structures by eliminating ligands and water. The results of the analysis were shown as binding affinity.

2.7 Molecular dynamics simulation analysis

In order to investigate the potential working mechanisms of the synthesized compound, MD simulations were carried out for compound 5i that demonstrated a theoretical docking score of −8.9 kcal/mol. The docking complex that involves ERα and the ligand was studied through MD simulations for its stability (Alajmi et al., 2018). The MD simulation was performed in the ligand–protein complex with the lowest MM-GBSA binding free energy value. The MD simulation was executed for 200 ns using Desmond software (Zamzami, 2023). First, a cubic simulation box was selected for the system builder panel of the Desmond–Schrodinger interface. Then, the TIP3P explicit water model was built. The distance between the simulation box and the protein surface remained equal to 10 Å. Additionally, to neutralize the system and to make the electrolyte environment isotonic with the NaCl, we added 150 mM (mM) of NaCl. Approximately 2,000 iterations were required for the system to achieve its minimum configuration. The minimized system was then subjected to a 200-ns MD simulation using the default relaxation option, at 300 K and 1 Bar under the NpT ensemble, Trevor 272. The Nose–Hoover chain (Brańka, 2000) thermostat and the Martyna–Tobias–Klein barostat (Martyna et al., 1994) were used to set the temperature and pressure at the desired levels. Energy and structural information were collected every 10 ps and stored in trajectory files. The MD simulation was performed in fs using a 2-fs

time step. Maestro software was used to analyze the trajectories and three-dimensional structure.

3 Results and discussion

In this study, a series of N'-(1-benzyl-2-oxo-1, 2-dihydro-3H-indol-3-ylidene) hydrazide derivatives (5a–i) was synthesized, spectroscopically analyzed, and then subjected to the study of anticancer effects in BC cell line MCF-7. The synthesis involved several steps, as outlined (given as Figure 2). The synthesis started with the reaction of aniline with chloral hydrate and hydroxylamine to yield α-isonitrosoacetanilide, which was then cyclized using a strong acid. Isatin thus prepared was benzylated using benzyl chloride in the presence of potassium carbonate in DMF. In parallel, a range of substituted and unsubstituted aromatic carboxylic acid hydrazides were prepared through esterification of the respective carboxylic acid and subsequent reaction with hydrazine hydrate. In the last step, these hydrazides were condensed with benzylisatin to yield a novel series of N-substituted isatin compounds. All synthesized compounds exhibited solubility in chloroform ($CHCl_3$) at room temperature and displayed a singular chromatographic spot in various solvent systems on TLC, indicative of their homogeneity as individual compounds.

The structures of 5(a–i) were characterized based on FTIR spectroscopy, ^{1}H NMR, ^{13}C NMR, and elemental analysis (provided as Supplementary Material). The FTIR spectra showed a major peak attributed to the carbonyl (C=O) group in each of the compounds within the range 1,720 cm^{-1}– 1,733 cm^{-1}. Furthermore, in each of the compounds under consideration, a particular spectral feature stands out as a peak within the wavenumber range 3,189 cm^{-1}–3,195 cm^{-1} that is assigned to the vibrational mode connected to the N-H group. In addition, a big peak related to the azomethine (C=N) functionality was visible in each compound between 1,663 cm^{-1} and 1,666 cm^{-1}. C–O bond stretching was also observed in all the synthesized derivatives.

In NMR spectroscopy, the appearance of a broad singlet signal within the range 13–14 ppm, corresponding to the NH protons of the hydrazide moiety, substantiated the formation of the condensation product. The methylenic protons that directly bonded to the nitrogen of isatin displayed deshielded resonances as a singlet between 4.53 and 4.73 ppm. The aromatic protons of the aryl rings exhibited upfield shifts between 6 and 9 ppm, with multiplicity consistent with their substitution patterns. Further confirmation of the structural attributes was derived from ^{13}C NMR spectroscopy. Notably, the characteristic carbonyl signal of isatin vanished at 183 ppm, and a new signal assigned to the C=N group appeared within the range 135–140 ppm. The persistence of other carbon signals in their respective chemical shift regions provided clear evidence for the formation of the condensation products **5(a–i)**.

3.1 Anticancer activity

The *in vitro* anticancer potential of the synthesized compounds (**5a–i**) was assessed against the MCF-7 cell line using the SRB proliferation assay. All the tested compounds showed notable cytotoxicity against the MCF-7 cell line, as indicated by their IC_{50} values presented in Table 1. Among them, N'-(1-benzyl-2-oxo-1,2-dihydro-3H-indol-3-ylidene)benzohydrazide (**5i**) exhibited the highest potency, with an IC_{50} value of 9.29 ± 0.97 μM. Compounds N'-(1-benzyl-2-oxo-1,2-dihydro-3H-indol-3-ylidene)-2-hydroxybenzohydrazide (**5d**), N'-(1-benzyl-2-oxo-1,2-dihydro-3H-indol-3-ylidene)pyridine-2-carbohydrazide (**5f**), and N'-(1-benzyl-2-oxo-1,2-dihydro-3H-indol-3-ylidene)-3,4,5 trihydroxybenzohydrazide (**5g**) also exhibited inhibition at IC_{50} values of 13.34 ± 2.53, 12.35 ± 0.65, and 12.09 ± 4.08 μM, respectively.

Various isatin derivatives with different substitutions have been investigated and reported for the inhibition of the growth of BC cells to varying degrees (Figure 3). Several isatin derivatives, including semaxanib, sunitinib, nintedanib, and hesperadin, are in clinical use and have been reviewed recently (Kumar et al., 2018; Ding et al., 2020). In our study, the investigation into the structure–activity relationship (SAR) has revealed that the arrangement of substituent groups on the aryl ring and the placement of the heteroatom within the heteroaryl ring exert an influence on the cytotoxic potential of these compounds against MCF-7 cell lines.

The most potent compound, **5i**, characterized by an unsubstituted phenyl ring, showed an IC_{50} value of 9.29 ± 0.97 μM (Table 1). The introduction of halogen substituent groups onto the phenyl ring (5c, 5e, and 5 h) resulted in decreased activity compared to the unsubstituted compound **5i**. Remarkably, among the derivatives with phenyl substitutions, compounds with substituents at the 2-position of the phenyl ring displayed the highest activity level. For instance, compound **5d**, featuring an electron-donating hydroxyl group at the 2-position of the phenyl ring, demonstrated a pronounced IC_{50} value of 13.34 ± 2.53 μM. Similarly, compound **5h**, bearing a 2-chloro substitution, displayed a slightly reduced IC_{50} value of 22.99 ± 2.75 μM.

However, compounds containing the substitution at the 3-position of the phenyl ring were less active than their 2-substituted counterparts. For example, compounds such as **5b** and **5c**, with iodo and bromo groups of the phenyl ring as electron-withdrawing groups, showed decreased activity with IC_{50} values of 48.90 ± 24.6 μM and 33.13 ± 9.57 μM, respectively. Substitutions at the 4-position of the phenyl ring on **5e** yielded reduced reactivity, with an IC_{50} value of 39.47 ± 12.58 μM. In addition, a compound containing several substitutions on the phenyl ring, for example, compound **5g** with 3,4,5-trihydroxy configuration, had an IC_{50} value of 12.09 ± 4.08 μM, exceeding that of the 2-substituted, 3-substituted, and 4-substituted derivatives.

These findings collectively underscore the crucial role played by the inherent characteristics and strategic arrangement of substituent groups on the phenyl ring in determining the cytotoxic activity of these compounds.

Furthermore, compounds having a heteroaryl pyridyl ring instead of the phenyl ring are observed to be highly dependent on the spatial orientation of the heteroatom in this regulation. For instance, compound **5f**, garnished with a 2-pyridyl ring moiety, shows better activity, with an IC_{50} value of 12.35 ± 0.65 μM, while compound 5a, with 4-pyridyl ring substitution, showed a lower toxic effect (IC_{50} value: 31.00 ± 11.50 μM).

This discernible activity pattern conforms to the deductions on the location of the heteroatom made in the case of substitution on the phenyl ring. In particular, the presence of the heteroatom at the 2-position, analogically to the substitution at the 2-position of the phenyl

ring, results in superior activity compared to the 4-position, comparable to the substitution at the 4-position of the phenyl ring, thereby highlighting the role of the heteroatom position in cytotoxicity.

3.2 Downregulated estrogen receptor levels in MCF-7 cells

To determine the mechanism of action for the antiproliferative activity of 5i, we determined its effect on the expression levels of ERα in ER+ MCF-7 cells. Cells were treated with IC_{50} concentrations of 1.25X, 2.5X, and 5X of **5i** for 24 h, and the expression of ERα was analyzed through Western blotting. Treatment with concentrations of 2.5X and 5X of **5i** robustly reduced ERα expression compared to DMSO-treated solvent control cells (Figure 4). The loading control GAPDH remained unchanged at all the concentrations, indicating equal loading of whole-cell lysate in all the wells.

In a recent review on the pharmacological profile of isatin derivatives, Ferraz de Paive et al. (2020) claimed that among different biological activities, the anticancer effect was more pronounced (Ferraz de Paiva et al., 2021). The main cancer type where isatin derivatives were tested was BC. It is well established that more than 70% cases of BC are estrogen-mediated (Fujiki et al., 2014). Our results strongly support that a major contributing mechanism underlying the cytotoxic effect of isatin derivatives in estrogen-responsive cancer cells is the degradation of ERα. However, no previous report on the antagonistic/inhibitory action of any isatin derivative on ERs, ERα or ERβ, in estrogen-responsive BC or in any other system (*in vitro* or *in vivo*) has been published. So, these results strongly suggest that this derivative with isatin moiety has the potential to be further developed into a SERD to be used alone or in combination with other anti-angiogenesis agents, checkpoint, or kinase inhibitors.

3.3 Chemical space, drug-likeness prediction, and pharmacokinetics profiling of compounds 5a–5i

Table 2 provides a general view of the main physicochemical properties measured using DataWarrior software. These features take care of numerous traits important to the assessment of the synthetic compounds as drug candidates. The multifaceted analysis of these properties points out some very prominent features that qualify the synthesized compounds as promising drug candidates. First, the molecular weight and monoisotopic mass offer significant information about the size and mass distribution of compounds that elucidate the chemically important properties affecting the drug absorption, distribution, metabolism, and excretion (ADME). Furthermore, properties such as lipophilicity and solubility in the water, represented by cLogP and cLogS, respectively, are key determinants of how the compounds will behave pharmacokinetically. Compounds with ideal lipophilicity and solubility often exhibit much better ADME properties, contributing to the improved bioavailability and efficacy. Moreover, the existence of functional groups like H acceptors and H donors governs the ability of the molecule to bind to the target biomolecules through hydrogen bonding, which is one of the key aspects of the molecular recognition and binding affinity of molecule. This analysis includes the molecular surface area and polarity descriptors that reflect the capability of the compound to permeate the biological membranes and to reach intracellular targets, which in turn engender its pharmacodynamic profile. In addition, parameters like drug-like propensity, irritant potential, and molecular complexity play many important roles in the evaluation of the drug-like quality, safety properties, and synthetic accessibility of the compound, which are very crucially relevant to the drug development. The presence of important structural elements such as aromaticity, cycles, and stereochemistry additionally enhances its bioactivity and also therapeutic potential. In general, the complete assessment of these physicochemical characteristics suggests that the synthesized compounds have the potential to be very promising drugs; hence, further detailed studies on their pharmacological activities and therapeutic applications are necessary.

Recognition and minimization of illegitimate actions of pharmacological entities are an issue that programs aiming at the procurement of druggable molecule candidates need to deal with. The initial characterization of PK behavior represents a critical tool to address safety issues likely to be associated with hit compounds. We used *in silico* pharmacokinetics prediction tools, particularly the pkCSM tool, for the assessment of the activity profiles of the compounds 5a–5i in this study. The initial evaluation of compounds 5a–5i through pkCSM prediction showed very promising activity profiles (Table 3). Importantly, all the compounds 5a–5i fell within the safe limits for the ADME parameters. The results imply that the synthetic substances have good PK characteristics, a key factor in drug discovery and development. Despite the predictions of ADME profiles, in the case of multiple models, more effort should be taken to enrich the literature with consensus ADME profiling and experimental data relevant to the pharmacokinetics of the synthesized compounds.

3.4 Toxicity prediction using Toxtree

The toxicity prediction by Toxtree, a widely deployed *in silico* toxicological approach, indicates good toxicity/safety profiles of tested compounds. Traditionally, such results are obtained only through the use of a large number of model animals. Additionally, animal experimentation is a major obstacle in terms of cost and time consumed (Rim, 2020). An intensive *in silico* computational examination sheds light on the molecular intricacy of each compound. The investigated series of the compounds has shown a one-way tendency towards the non-toxic traits across various tests performed, as shown in Table 4.

The components showed a negative potential for ocular irritation and the nullification of skin sensitization alerts, thus supporting their safety for dermal use. Moreover, the compounds showed no genotoxic carcinogenicity, thus implying their compatibility with the biological system at the genetic level (non-DNA binding). The compounds were also found harmless in other assessments, such as non-genotoxic carcinogenicity.

3.5 Molecular docking

The docking studies were undertaken to predict the binding affinities of the ligands (compounds) with the target protein (ERα),

as shown in Table 5. The docking scores were calculated in terms of binding affinities. These findings substantiate the prominence of hydrophobic interactions, specifically pi–sigma, pi–pi, pi–anion, and pi–alkyl interactions, involving the indolinone and aromatic ring constituents of the isatin–hydrazide conjugates and the binding residues within the target proteins. This assertion is reinforced by the graphical representations shown in Figures 5–8. The origin of these hydrophobic interactions can be attributed to the optimal positioning of the indolinone ring within a hydrophobic pocket.

Compounds 5i and 5d exhibited the best *in vitro* inhibition, which is further supported by the outcome of docking simulations. The binding affinity of compound 5i was attributed to van der Waals interactions with lysine (521), hydrogen bonding with histidine (524), as well as pi–alkyl and pi–sulphur interactions with methionine (522). Additionally, a pi–pi interaction was observed with leucine (387), while a pi–sigma bond was formed between the indolylidene ring and methionine (388). Furthermore, a pi–pi interaction was evident between the indolylidene ring and the hydrazide phenyl ring with tryptophan (383).

3.6 Molecular dynamics simulation analysis

MD simulation was used to analyze and evaluate the stability and dynamic behavior of the protein–ligand complex between ERα and its ligand. The docked ERα–ligand complex was simulated for 200 ns. As shown in Figure 9, RMSD exhibited comparable traces during the latter part of the initial half (75–100 ns) and the latter half (135–200 ns) of the simulation, implying that the whole system became effectively equilibrated. In contrast, during 10–25 ns, the movement of the complex completely repeated the trajectory of the Apo form (without ligand). Along the simulation, the RMSD values for the complex and Apo forms varied between 0 Å and 3.7 Å and 0 Å and 3.8 Å, respectively. Taken together, these results reflect a steady binding association between the ligand (compound 5i) and the ERα protein, facilitated by considerable interactions with key amino acids within the binding pocket.

The interactions between the ligand and the protein were constantly surveyed during the whole of the simulation. These interactions were classified into four main categories, namely, hydrogen bonds, ionic interactions, water bridges, and hydrophobic interactions, schematically shown in Figures 10, 11. The normalized stacked bar chart (Figure 10) represents the fraction of time whenever particular interactions were sustained. For example, a value of 0.9 implies that the specific interactions were observed during 90% of the simulation period.

In accordance with the stacked bar charts, the ligand interaction fraction of TRP383 was approximately 0.9, and hydrogen bonds, electrostatic, and pi–alkyl interactions were the contributing types of interaction. In the beginning, there were hydrogen bonds with an interaction fraction of 0.01, then hydrophobic interactions from 0.01 to 0.88, and finally, there were water bridges for a short period of time. The mole fraction of the ligand with PHE404 was approximately 0.6, mainly including hydrophobic compensation. Analogously, the binding fraction with LEU387 was also high and consisted only of hydrophobic contacts. The interaction energy with LEU346 was approximately 0.38, which was mainly due to hydrophobic interactions and water bridges. A few other amino acids with minor interactions during short durations are presented in the stacked bar charts.

Importantly, hydrophobic interactions determine the binding of ligands. The fact that these hydrophobic interactions have a profound effect on the specificity of the drug, its metabolism, and its adsorption requires them to be taken into account when developing new drugs. Hydrophobic contacts can be categorized into three subtypes: π–cation, π–π, and other nonspecific interactions. Generally, it is a hydrophobic amino acid that interacts with an aromatic or aliphatic group on the ligand. This category has now been expanded to include π–cation interactions.

The current geometric criteria for hydrophobic interactions are defined as follows: π–cation, aromatic and charged groups less than 4.5 Å; π–π, two aromatic group stacked face to face or face to edge; and other, an uncharacterized hydrophobic side chain within 3.6 Å of the aromatic or aliphatic carbons of a ligand.

The criteria outlined herein constitute a foundation upon which to anchor mechanistic frameworks of hydrophobic interactions in the design and development of drugs (Sadiq et al., 2020).

The duration of the simulation is shown on the *x*-axis, and the interaction of each amino acid with the ligand is shown on the *y*-axis, as shown in Figure 12. The figure shows the interaction time of each amino acid involved across 200 ns of simulation. This analysis indicates that TRP383 showed one of the strongest interactions with the ligand. LEU387 displays a continuous interaction with negligible interruptions throughout the simulation, suggesting a stable interaction. However, the second important amino acid, PHE404, also displays a significant interaction with a ligand. Moreover, other amino acids that show strong and continuous interactions including LEU346, MET388, and LEU525 are also notable.

CYS530 initiates interaction in the second part of the simulation and maintains strong interaction afterward with only minor interruptions until the end of the simulation. In addition, LEU349 is significant and strong that has many minor interruptions throughout the simulation run.

Moreover, THR347, which did not show any interaction during the molecular docking phase, shows interactions during MD simulations. Such an event can be related to the dynamic nature of the environment and the presence of water molecules. THR347 creates a water bridge and then makes contact with the ligand atom, as shown in Figure 13.

Figure 13 displays the torsional profile of compound 5i obtained from MD simulations. The compound is made up of five rotatable bonds, each color-coded for clarity. Two types of plots are depicted in this figure: bar graphs and radial charts. These plots illustrate the distribution of torsional angles and the conformation of torsion, respectively, during the simulation (0–200 ns). The radial and line plots of the rotatable bond between the benzene ring and CH_2 (in purple) show a significant degree of rotational freedom, with the bond rotating almost completely by 180° in both negative and positive *x*-axes. Furthermore, in both cases of positive and negative *x*-axes, a complete rotation of 180° in the bond between the carbonyl carbon and benzene ring is also shown in both the bar and radial plots (shown in blue).

In addition, the rotatable bond between the nitrogens of the hydrazide (pink) rotates approximately 90° around the negative *x*-axis. Similarly, the rotatable bond located between indolidine and CH_2 (marked in orange) has a specific rotation of approximately 90° with both positive and negative *x*-axes. Additionally, other rotatable bonds are

color-coded, and their torsional plots are shown in both radial and bar charts for a thorough inspection.

4 Conclusion

In summary, a new series of isatin–hydrazide conjugates, 5a–5i, were designed, synthesized, and evaluated for their *in vitro* cytotoxicity in the BC cell line MCF-7. All the compounds displayed moderate-to- good growth inhibitory potential. Compound 5i was most active with an IC_{50} value 9.29 ± 0.97 μM. This compound was shown to downregulate ERα levels robustly. The molecular docking results suggested the potential binding ability of the synthesized compounds. Furthermore, the accuracy and reliability of this molecule to bind with ERα were confirmed through MD simulations. MD simulations revealed the significant stability of the synthesized compound within the active site of ERα. In addition to that, *in silico* ADMET studies indicated that the compound entails drug-like properties. Collectively, these findings imply that the investigated compounds can serve as promising candidates for developing potent SERDs like anticancer agents against ER+ BC.

Data availability statement

The original contributions presented in the study are included in the article/Supplementary Material; further inquiries can be directed to the corresponding authors.

Ethics statement

Ethical approval was not required for the studies on humans in accordance with the local legislation and institutional requirements because only commercially available established cell lines were used. Ethical approval was not required for the studies on animals in accordance with the local legislation and institutional requirements because only commercially available established cell lines were used.

Author contributions

MA: investigation and writing–original draft. SS: conceptualization, supervision, and writing–review and editing. FF: data curation, methodology, formal analysis, and writing–review and editing. RS: formal analysis, validation, and writing–review and editing. HN: conceptualization, supervision, writing–original draft, and writing–review and editing. AbA: funding acquisition, validation, visualization, and writing–review and editing. AmA: data curation, formal analysis, resources, and writing–review and editing. AtA: data curation, methodology, formal analysis, writing–review and editing. OF: formal analysis, validation, and writing–review and editing. RK: data curation, formal analysis, and writing–review and editing. AF: investigation, resources, supervision, and writing–review and editing.

Funding

The author(s) declare financial support was received for the research, authorship, and/or publication of this article. The authors acknowledge the HEC, Pakistan, for partially funding this project under NRPU project # 6224.

Conflict of interest

The authors declare that the research was conducted in the absence of any commercial or financial relationships that could be construed as a potential conflict of interest.

Publisher's note

All claims expressed in this article are solely those of the authors and do not necessarily represent those of their affiliated organizations, or those of the publisher, the editors, and the reviewers. Any product that may be evaluated in this article, or claim that may be made by its manufacturer, is not guaranteed or endorsed by the publisher.

Supplementary material

The Supplementary Material for this article can be found online at: https://www.frontiersin.org/articles/10.3389/fchem.2024.1424637/full#supplementary-material

References

Alajmi, M. F., Rehman, M. T., Hussain, A., and Rather, G. M. (2018). Pharmacoinformatics approach for the identification of Polo-like kinase-1 inhibitors from natural sources as anti-cancer agents. *Int. J. Biol. Macromol.* 116, 173–181. doi:10.1016/j.ijbiomac.2018.05.023

Bhatia, N., Hazra, S., and Thareja, S. (2023). Selective Estrogen receptor degraders (SERDs) for the treatment of breast cancer: an overview. *Eur. J. Med. Chem.* 256, 115422. doi:10.1016/j.ejmech.2023.115422

Branka, A. (2000). Nosé-Hoover chain method for nonequilibrium molecular dynamics simulation. *Phys. Rev. E* 61, 4769–4773. doi:10.1103/PhysRevE.61.4769

Dandrial, J., Singla, R., Kumar, M., and Jaitak, V. (2016). Recent developments of C-4 substituted coumarin derivatives as anticancer agents. *Eur. J. Med. Chem.* 119, 141–168. doi:10.1016/j.ejmech.2016.03.087

Ding, Z., Zhou, M., and Zeng, C. (2020). Recent advances in isatin hybrids as potential anticancer agents. *Arch. Pharm.* 353, 1900367. doi:10.1002/ardp.201900367

Duffy, M. J. (2006). Estrogen receptors: role in breast cancer. *Crit. Rev. Clin. Lab. Sci.* 43, 325–347. doi:10.1080/10408360600739218

El-faham, A., Elzathahery, A. A., Al-Othman, Z. A., and Elsayed, E. A. (2014). Facile method for the synthesis of silver nanoparticles using 3-hydrazino-isatin derivatives in aqueous methanol and their antibacterial activity. *Int. J. Nanomedicine* 9, 1167–1174. doi:10.2147/IJN.S58571

Fares, M., Eldehna, W. M., Abou-seri, S. M., Abdel-Aziz, H. A., Aly, M. H., and Tolba, M. F. (2015). Design, synthesis and *in vitro* antiproliferative activity of novel isatin-quinazoline hybrids. *Arch. Pharm.* 348, 144–154. doi:10.1002/ardp.201400337

Ferraz De Paiva, R. E., Vieira, E. G., Rodrigues da silva, D., Wegermann, C. A., and Costa Ferreira, A. M. (2021). Anticancer compounds based on isatin-derivatives: strategies to ameliorate selectivity and efficiency. *Front. Mol. Biosci.* 7, 627272. doi:10.3389/fmolb.2020.627272

Firdous, F., Riaz, S., Furqan, M., Fozail, S., Fatima, K., Pohl, S. O. T.-G., et al. (2023). Design, synthesis, and biological evaluation of SSE1806, a microtubule destabilizer that overcomes multidrug resistance. *ACS Med. Chem. Lett.* 14, 1369–1377. doi:10.1021/acsmedchemlett.3c00258

Fujiki, N., Konno, H., Kaneko, Y., Gohno, T., Hanamura, T., Imami, K., et al. (2014). Estrogen response element-GFP (ERE-GFP) introduced MCF-7 cells demonstrated the coexistence of multiple estrogen-deprivation resistant mechanisms. *J. Steroid Biochem. Mol. Biol.* 139, 61–72. doi:10.1016/j.jsbmb.2013.08.012

Guissi, N. E. I., Li, H., Xu, Y., Semcheddine, F., Chen, M., Su, Z., et al. (2017). Mitoxantrone-and folate-TPGS2k conjugate hybrid micellar aggregates to circumvent toxicity and enhance efficiency for breast cancer therapy. *Mol. Pharm.* 14, 1082–1094. doi:10.1021/acs.molpharmaceut.6b01009

Gupta, V. K., Bhalla, Y., and Jaitak, V. (2014). Impact of ABC transporters, glutathione conjugates in MDR and their modulation by flavonoids: an overview. *Med. Chem. Res.* 23, 1–15. doi:10.1007/s00044-013-0612-6

Guzowski, J. R., Delaney, E. J., Humora, M. J., Irdam, E., Kiesman, W. F., Kwok, A., et al. (2012). Understanding and control of dimethyl sulfate in a manufacturing process: kinetic modeling of a fischer esterification catalyzed by H2SO4. *Org. Process Res. Dev.* 16, 232–239. doi:10.1021/op200323j

Han, S. J., Begum, K., Foulds, C. E., Hamilton, R. A., Bailey, S., Malovannaya, A., et al. (2016). The dual estrogen receptor α inhibitory effects of the tissue-selective estrogen complex for endometrial and breast safety. *Mol. Pharmacol.* 89, 14–26. doi:10.1124/mol.115.100925

Harris, H. A., Albert, L. M., Leathurby, Y., Malamas, M. S., Mewshaw, R. E., Miller, C. P., et al. (2003). Evaluation of an estrogen receptor-β agonist in animal models of human disease. *Endocrinology* 144, 4241–4249. doi:10.1210/en.2003-0550

Hiscox, S., Morgan, L., Green, T. P., Barrow, D., Gee, J., and NicholsonI, R. I. (2006). Elevated Src activity promotes cellular invasion and motility in tamoxifen resistant breast cancer cells. *Breast Cancer Res. Treat.* 97, 263–274. doi:10.1007/s10549-005-9120-9

Ibrahim, H. S., Abou-seri, S. M., Tanc, M., Elaasser, M. M., Abdel-Aziz, H. A., and Supuran, C. T. (2015). Isatin-pyrazole benzenesulfonamide hybrids potently inhibit tumor-associated carbonic anhydrase isoforms IX and XII. *Eur. J. Med. Chem.* 103, 583–593. doi:10.1016/j.ejmech.2015.09.021

Jeselsohn, R., Guo, H., Rees, R., Barry, W., Barlett, C., Tung, N., et al. (2019). Abstract PD1-05: results from the phase Ib/II clinical trial of bazedoxifene and palbociclib in hormone receptor positive metastatic breast cancer. *Cancer Res.* 79, PD1. PD1-05. doi:10.1158/1538-7445.SABCS18-PD1-05

Khan, K. M., Rasheed, M., Ullah, Z., Hayat, S., Kaukab, F., Choudhary, M. I., et al. (2003). Synthesis and *in vitro* leishmanicidal activity of some hydrazides and their analogues. *Bioorg Med. Chem.* 11, 1381–1387. doi:10.1016/S0968-0896(02)00611-9

Kumar, S., Gu, L., Palma, G., Kaur, M., Singh-Pillay, A., Singh, P., et al. (2018). Design, synthesis, anti-proliferative evaluation and docking studies of 1 H-1, 2, 3-triazole tethered ospemifene–isatin conjugates as selective estrogen receptor modulators. *New J. Chem.* 42, 3703–3713. doi:10.1039/C7NJ04964A

Le Tourneau, C., Raymond, E., and Faivre, S. (2007). Sunitinib: a novel tyrosine kinase inhibitor. A brief review of its therapeutic potential in the treatment of renal carcinoma and gastrointestinal stromal tumors (GIST). *Ther. Clin. Risk Manag.* 3, 341–348. doi:10.2147/tcrm.2007.3.2.341

Lewis-Wambi, J. S., Kim, H., Curpan, R., Grigg, R., Sarker, M. A., and Jordan, V. C. (2011). The selective estrogen receptor modulator bazedoxifene inhibits hormone-independent breast cancer cell growth and down-regulates estrogen receptor α and cyclin D1. *Mol. Pharmacol.* 80, 610–620. doi:10.1124/mol.111.072249

Lindsy, R., Gallagher, J. C., Kagan, R., PickarI, J. H., and Constantine, G. (2009). Efficacy of tissue-selective estrogen complex of bazedoxifene/conjugated estrogens for osteoporosis prevention in at-risk postmenopausal women. *Fertil. Steril.* 92, 1045–1052. doi:10.1016/j.fertnstert.2009.02.093

Lipinski, C. A. (2004). Lead-and drug-like compounds: the rule-of-five revolution. *Drug Discov. Today Technol.* 1, 337–341. doi:10.1016/j.ddtec.2004.11.007

Manzoor, S., Bilal, A., Khan, S., Ullah, R., Iftikhar, S., Emwas, A.-H., et al. (2018). Identification and characterization of SSE15206, a microtubule depolymerizing agent that overcomes multidrug resistance. *Sci. Rep.* 8, 3305. doi:10.1038/s41598-018-21642-0

Martyna, G. J., Tobias, D. J., and Klein, M. L. (1994). Constant pressure molecular dynamics algorithms. *J. Chem. Phys.* 101, 4177–4189. doi:10.1063/1.467468

Motzer, R. J., MichaelsonI, M. D., Redman, B. G., Hudes, G. R., Wilding, G., Figin, R. A., et al. (2006). Activity of SU11248, a multitargeted inhibitor of vascular endothelial growth factor receptor and platelet-derived growth factor receptor, in patients with metastatic renal cell carcinoma. *J. Clin. Oncol.* 24, 16–24. doi:10.1200/jco.2005.02.2574

Pandeya, S., Sriram, D., Nath, G., and Declerc, E. (1999). Synthesis, antibacterial, antifungal and anti-HIV activities of Schiff and Mannich bases derived from isatin derivatives and N-[4-(4′-chlorophenyl) thiazol-2-yl] thiosemicarbazide. *Eur. J. Pharm. Sci.* 9, 25–31. doi:10.1016/S0928-0987(99)00038-X

Patlewicz, G., Jeliazkova, N., Safford, R., Worth, A., and Aleksiev, B. (2008). An evaluation of the implementation of the Cramer classification scheme in the Toxtree software. *Sar. QSAR Environ. Res.* 19, 495–524. doi:10.1080/10629360802083871

Payton-Stewart, F., Tilghman, S. L., Williams, L. G., and Winfield, L. L. (2014). Benzimidazoles diminish ERE transcriptional activity and cell growth in breast cancer cells. *Biochem. Biophys. Res. Commun.* 450, 1358–1362. doi:10.1016/j.bbrc.2014.06.130

Pires, D. E., Blundell, T. L., and Ascher, D. B. (2015). pkCSM: predicting small-molecule pharmacokinetic and toxicity properties using graph-based signatures. *J. Med. Chem.* 58, 4066–4072. doi:10.1021/acs.jmedchem.5b00104

Rim, K.-T. (2020). *In silico* prediction of toxicity and its applications for chemicals at work. *Toxicol. Environ. Health Sci.* 12, 191–202. doi:10.1007/s13530-020-00056-4

Rohini, R., Reddy, P. M., Shanker, K., Kanthaiah, K., Ravinder, V., and Hu, A. (2011). Synthesis of mono, bis-2-(2-arylideneaminophenyl) indole azomethines as potential antimicrobial agents. *Arch. Pharm. Res.* 34, 1077–1084. doi:10.1007/s12272-011-0705-z

Roth, G. J., Heckel, A., Colbatzky, F., Handschuh, S., Kley, J. R., Lehmann-Lintz, T., et al. (2009). Design, synthesis, and evaluation of indolinones as triple angiokinase inhibitors and the discovery of a highly specific 6-methoxycarbonyl-substituted indolinone (BIBF 1120). *J. Med. Chem.* 52, 4466–4480. doi:10.1021/jm900431g

Samanta, S., Pappula, V., Dinda, M., and Adimurthy, S. (2014). Transition metal-free oxidative esterification of benzylic alcohols in aqueous medium. *Org. Biomol. Chem.* 12, 9453–9456. doi:10.1039/C4OB01524J

Sander, T., Freyss, J., Von Korff, M., and Ruffner, C. (2015). DataWarrior: an open-source program for chemistry aware data visualization and analysis. *J. Chem. Inf. Model* 55, 460–473. doi:10.1021/ci500588j

Selvam, P., Murugesh, N., Chandramohan, M., Debyser, Z., and Witvrouw, M. (2008). Design, synthesis and antiHIV activity of novel isatine-sulphonamides. *Indian J. Pharm. Sci.* 70, 779. doi:10.4103/0250-474X.49121

Shoda, T., Kato, M., Harada, R., Fujisato, T., Okuhira, K., Demizu, Y., et al. (2015). Synthesis and evaluation of tamoxifen derivatives with a long alkyl side chain as selective estrogen receptor down-regulators. *Bioorg Med. Chem.* 23, 3091–3096. doi:10.1016/j.bmc.2015.05.002

Sridhar, S. K., and Ramesh, A. (2001). Synthesis and pharmacological activities of hydrazones, Schiff and Mannich bases of isatin derivatives. *Biol. Pharm. Bull.* 24, 1149–1152. doi:10.1248/bpb.24.1149

Sumpter, W. C. (1944). The chemistry of isatin. *Chem. Rev.* 34, 393–434. doi:10.1021/cr60109a003

Veber, D. F., Johnson, S. R., Cheng, H.-Y., Smith, B. R., Ward, K. W., and Kopple, K. D. (2002). Molecular properties that influence the oral bioavailability of drug candidates. *J. Med. Chem.* 45, 2615–2623. doi:10.1021/jm020017n

Verma, M., Pandeya, S. N., Singh, K. N., and Stables, J. P. (2004). Anticonvulsant activity of Schiff bases of isatin derivatives. *Acta Pharm.* 54, 49–56.

Welsh, A. W., Lannin, D. R., Young, G. S., Sherman, M. E., FigueroaI, J. D., Henry, N. L., et al. (2012). Cytoplasmic estrogen receptor in breast cancer. *Clin. Cancer Res.* 18, 118–126. doi:10.1158/1078-0432.CCR-11-1236

Zamzami, M. A. (2023). Molecular docking, molecular dynamics simulation and MM-GBSA studies of the activity of glycyrrhizin relevant substructures on SARS-CoV-2 RNA-dependent-RNA polymerase. *J. Biomol. Struct. Dyn.* 41, 1846–1858. doi:10.1080/07391102.2021.2025147

frontiers | Frontiers in Chemistry

TYPE Original Research
PUBLISHED 06 August 2024
DOI 10.3389/fchem.2024.1418975

OPEN ACCESS

EDITED BY
Afzal Basha Shaik,
Jawaharlal Nehru Technological University,
Kakinada, India

REVIEWED BY
Mallesh Pandrala,
Stanford University, United States
Ahmed A. Al-Karmalawy,
Ahram Canadian University, Egypt

*CORRESPONDENCE
Sanmati Kumar Jain,
sanmatijain72@yahoo.co.in

RECEIVED 17 April 2024
ACCEPTED 04 July 2024
PUBLISHED 06 August 2024

CITATION
Gupta AK, Vaishnav Y, Jain SK, Annadurai S and Kumar N (2024), Exploring novel Apalutamide analogues as potential therapeutics for prostate cancer: design, molecular docking investigations and molecular dynamics simulation.
Front. Chem. 12:1418975.
doi: 10.3389/fchem.2024.1418975

Exploring novel Apalutamide analogues as potential therapeutics for prostate cancer: design, molecular docking investigations and molecular dynamics simulation

Ajay Kumar Gupta[1], Yogesh Vaishnav[1], Sanmati Kumar Jain [1]*, Sivakumar Annadurai[2] and Neeraj Kumar[3]

[1]Drug Discovery and Research Laboratory, Department of Pharmacy, Guru Ghasidas Vishwavidyalaya (A Central University), Bilaspur, Chhattisgarh, India, [2]Department of Pharmacognosy, College of Pharmacy, King Khalid University, Abha, Saudi Arabia, [3]Department of Pharmaceutical Chemistry, Bhupal Nobles' College of Pharmacy, Udaipur, Rajasthan, India

Introduction: Prostate cancer (PC) ranks as the second most frequent type of cancer in men and is the fourth largest cause of mortality worldwide. Androgenic hormones such as testosterone and dihydrotestosterone are crucial for the development and progression of the prostate gland. Androgenic hormones bind to androgen receptors (AR) and trigger the synthesis of many genes that stimulate the growth of prostate cells, initiating PC growth. Apalutamide (APL) is a non-steroidal antiandrogen drug used to treat PC; however, it also causes a variety of toxicities and resistance during the treatment.

Methods: The purpose of this study was to computationally identify new and safer analogues of APL, focusing on improved pharmacokinetic properties and reduced toxicity. Drug likeness (DL) and drug score (DS) were also calculated. Docking studies on the designed analogues were conducted to predict their binding affinities and compare their orientations with the ligands in the original crystal structure. Molecular dynamics (MD) simulation of docked ligands was done using Schrödinger suite.

Results: We generated a total of 1,415 analogues for different groups of APL using the bioisosteric approach. We selected 80 bioisosteres based on pharmacokinetic profiles, DL and DS score predictions, and found that the designed APL bioisosteres were optimal to good compared to APL. Analogues APL19, APL35, APL43, APL76, and APL80, formed hydrogen bonds with protein (*PDB ID: 5T8E*) which is similar hydrogen bonding to the standard (APL). The MD simulation result confirmed that APL43 and APL80 complexes were stable during the 100 nS run.

Discussion: The results suggest that the APL analogues, particularly APL43 and APL80, are predicted to be potential antiandrogen drugs for the treatment of prostate cancer.

KEYWORDS

Apalutamide, prostate cancer, bioisosteric approach, molecular dynamics simulation, molecular docking 1

1 Introduction

The prevention of cancer is a significant priority in public health in the 21st century, considering the increasing worldwide effect of the illness. In 2022, the International Agency for Research on Cancer (IARC) estimated that there would be around 20 million cases of cancer diagnosed and 9.7 million deaths linked to cancer globally. Prostate cancer is second in terms of frequency among all malignancies in men, and fourth overall. In the year 2022, there were about 1.46 million numbers of prostate cancer and 0.39 million deaths (Bray et al., 2021; Chen et al., 2023; Guida et al., 2022; Ferlay et al., 2024; Sung et al., 2021; Ferlay et al., 2021). In India, the incidence of prostate cancer (PC) is projected to increase from 43,691 cases in 2022 to 47,068 cases in 2025. Furthermore, it has been recognized as the second most common form of cancer among males who are 65 years of age or older, with a total of 33,695 cases and a prevalence rate of 12.3% (Sathishkumar et al., 2022; Kulothungan et al., 2022). Androgens, which are male sex hormones, are a group of hormones that regulate the growth and sustain the traits associated with male characteristics. Testosterone and dihydrotestosterone are the most prevalent androgens in males which are necessary for the proper development and operation of the prostate gland. Androgens stimulate the proliferation of both healthy and malignant prostate cells by attaching to and activating the androgen receptor (AR). Upon activation, the AR induces the production of several genes that promote the proliferation of prostate cells (Mohler et al., 2011; Zhang et al., 2016; Stabile and Dicks, 2003). During the early stage of PC, it is often classified into four stages: The early stage, or localized (Stages I and II: When the tumor remains confined to the prostate and has not spread beyond it), locally advanced (Stage III: Cancer has metastasized beyond the prostate but is limited to adjacent tissues) and advanced (Stage IV: Cancer has metastasized beyond the prostate to distant sites such as the lymph nodes, bones, liver, or lungs). A blood test often diagnoses PC by measuring levels of prostate-specific antigen (PSA), with a threshold of PSA >4 ng/mL. In addition, the diagnostic process may also include a digital rectal examination (Belkahla et al., 2022). Metastatic disease, discovered either during the diagnostic process or after local therapy-induced recurrence, causes most PC deaths. Castration-resistant prostate cancer (CRPC) is the last stage of advanced PC that results from the tumor's adaptability to a low-testosterone environment. It typically takes three to 8 years for individuals to respond to androgen deprivation therapy (ADT), at which point they often start to exhibit symptoms of metastatic CRPC (Harris et al., 2009; Tran et al., 2009; Murray et al., 2022; Huang et al., 2023a).

ADT used to be thought of as the standard treatment for metastatic hormone-sensitive prostate cancer (mHSPC), but in 2015, new information showed that ADT was not always effective and that some patients were actually resistant to it (López-Abad et al., 2024; Gan et al., 2018; Huang et al., 2023b). Antiandrogen drugs are used to treat PC. Flutamide and bicalutamide, which were among the first non-steroidal antiandrogen drugs, showed efficacy in treating PC in their early stages. However, their effectiveness diminished when the disease progressed to a hormone-resistant stage. Flutamide and bicalutamide, in a cases of cancer that do not respond to therapy, function as agonists to stimulate the excessive production of androgen receptors (AR), thereby facilitating the advancement of the disease (Kelly et al., 1997). Consequently, the development of second-generation drugs has prioritized the adjustment of agonist activity while maintaining antiandrogen action in cells that have an excessive amount of AR (Tran et al., 2009; Gao et al., 2021). Apalutamide (APL) is a second-generation nonsteroidal antiandrogen drug or androgen signaling inhibitor (ASI) that was developed by the group of Sawyers and Jung at the University of California, Los Angeles (UCLA). The approval was granted by the United States in February 2018 and by the European Union in January 2019 (Hughes, 2020; Chi et al., 2019). Animal studies indicate that APL is somewhat more effective than enzalutamide and may have a reduced risk of seizures due to its lesser ability to enter the brain, which is four times lesser than enzalutamide (Clegg et al., 2012). By acting as an AR inhibitor, APA stops the nuclear translocation of AR. AR hinders transcription and DNA binding and is hindered by APL. APL demonstrated a significant clinical response in a Phase-II trial treating males with non-metastatic castration-resistant prostate cancer (nmCRPC), with 89% of patients with high-risk nmCRPC seeing a reduction in PSA of at least 50% by the 12-weeks mark (Borno et al., 2019; Shen et al., 2023; Zhu et al., 2023).

APL is quickly absorbed after being taken orally, and it reaches its maximum concentration (T-max) within 2 h. It is metabolised by the enzymes CYP2C8 and CYP3A4 (cytochrome P450) to produce its active metabolite, N-desmethyl apalutamide. After a period of 70 days after the administration of the radiolabeled dosage, it was discovered that 65% of the medicine was excreted in urine and 24% was retrieved in feces (Pérez-Ruixo et al., 2020; Huang et al., 2023c). During the Spartan study, APL causes hypertension to varying degrees. Cardiac toxicities resulted in treatment cessation and, specifically, hypertension and atrial fibrillation in a limited number of patients. During the Titan study, APL also causes hypertension of varying severity. Ischemic heart disease, characterized by a minor abnormality in the QT interval, has also been seen in patients and resulted in the death of two individuals. In the Spartan study, a few individuals had treatment stoppages due to renal toxicities such as hematuria and acute kidney damage. Urinary retention was also seen in participants during the Titan experiment (Belderbos et al., 2018; Lv et al., 2024). Although

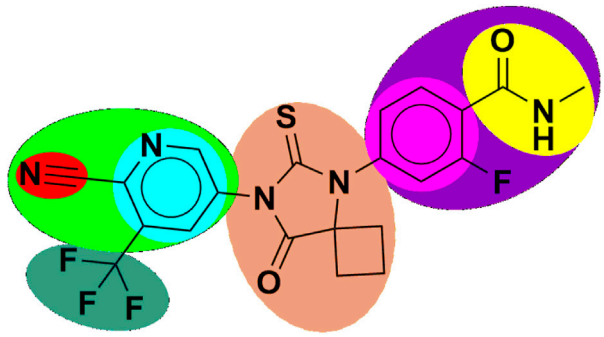

FIGURE 1
Structure of apalutamide and its modified groups, including cyano (red colour), cyano-pyridinyl (green colour), pyridinyl (cyan colour), cyclobutyl-thiohydantoin (coral colour), phenyl (pink colour), 2-fluoro-N-methylbenzamide (purple colour), N-methyl formamide (yellow colour), and trifluoromethyl (aquamarine colour).

APL is generally regarded as safe, concerns arise regarding its potential impact on the central nervous system (CNS). CNS effects might be diminished the overall quality of life, result in permanent effects, or required the discontinuation of therapy. However, it is crucial to acknowledge, the spreading of tumors may have significantly contribute to the emergence of neurological symptoms. These characteristics have prompted the publication of several studies about the safety of novel hormonal therapy for metastatic castration-resistant prostate cancer (mCRPC). However, there is little data regarding to the occurrence of seizures and neuropsychiatric symptoms in patients with nmCRPC (Sutil et al., 2021; Slovin et al., 2018; Gillessen et al., 2018; Pilon et al., 2017).

Therefore, it is imperative to change the structure of APL (Figure 1) in order to design newer APL analogues with safer and less toxic antiandrogen drugs for the treatment of PC. In this work, we designed the newer analogues of APL by the use of scaffold-transforming techniques. It is a unique technique in medicinal chemistry for the lucid design of drugs by gradually altering the parent component to develop a variety of different compounds with improved therapeutic potential (Manjunatha et al., 2019; Zheng et al., 2022). The scaffold-transforming techniques (bioisosteric approach) were applied to design APL analogues that exhibit a comparatively higher level of safety, followed by *in silico* pharmacokinetic (ADMET), docking studies and molecular dynamics (MD) simulation.

2 Materials and methods

The smile notation of the APL was taken from DrugBank, a widely-utilized chemical information library. In addition, the MolOpt was used to generate the several bioisosteres for the APL molecule. The chemical structures of APL and these analogues were drawn using ChemDraw software. The ADMETLab 2.0 online tool was used to predict the pharmacokinetic and toxicological properties. The Osiris property explorer (PEO) was used to determine the drug likeness (DL) and drug score (DS). The docking investigation was performed using AutoDock Vina (ADV), and the docking results were analyzed using Discovery Studio.

2.1 Designing of apalutamide bioisosteres

APL is used as a second-generation antiandrogen medication for the treatment of PC. On the other hand, people receiving this medication often experienced a variety of toxicities. Therefore, it is essential to alter the APL structure to mitigate its hazardous effects. MolOpt is an online program that uses deep generative models, data mining, and similarity comparisons to generate bioisosteres. It utilizes bioisosteric transformation rules. MolOpt has capability to explore the historical bioisosteric group space and discover novel bioisosteric transformation concepts (Shan and Ji, 2020). A total of 1,415 bioisosteres were generated by replacing various groups in the APL molecule. We then subjected these bioisosteres to further screening, including ADMET, DL, DS prediction, and docking investigations.

2.2 Pharmacokinetic and toxicological (ADMET) properties predictions

The prediction of ADMET properties of generated APL bioisosteres were computed using ADMETlab 2.0. It is an integrated online platform with eighty-four quantitative and four qualitative regression models with authentic and extensive predictions of ADMET properties for novel ligands that mimic mammalian ADMET properties (Xiong et al., 2021; Dong et al., 2018; Wang et al., 2016; Lei et al., 2016).

2.3 Drug likeness (DL) and drug score (DS) prediction

DL and DS evaluations are essential in the first phase of the drug development process. They assist researchers in selecting and prioritizing compounds, allowing them to concentrate on candidates that have a greater chance of success in subsequent development and clinical testing. PEO (Sander et al., 2009) helped to calculate DL and DS.

2.4 Molecular docking analysis

Molecular docking is commonly used technique in the field of drug development that aims to find potential lead molecules, enhance their binding interactions, and forecast their binding affinities to particular biological targets. This tool is beneficial for understanding the basic foundation of protein-ligand interactions and designing novel therapeutic drugs (Feher and Williams, 2012; Forli et al., 2016). We performed a molecular docking study to investigate the interactions between the crystal structure of the AR and the designed APL bioisosteres. This work involved several stages, including ligand preparation, protein preparation, and investigation of protein-ligand interactions (Trott and Olson, 2010).

TABLE 1 Medicinal Properties, DL and DS of analogues.

Entry no.	QED	Synth	MCE-18	Lipinski	Pfizer	GT	DL	DS
APL1	0.544	3.527	96	Accepted	Accepted	Accepted	−12.82	0.15
APL2	0.512	4.115	124	Accepted	Accepted	Accepted	−11.47	0.17
APL3	0.512	4.115	124	Accepted	Accepted	Accepted	−11.47	0.17
APL4	0.526	3.81	109	Accepted	Accepted	Accepted	−7.65	0.14
APL5	0.529	3.667	96	Accepted	Accepted	Accepted	−10.38	0.14
APL6	0.512	3.571	91	Accepted	Rejected	Accepted	−9.51	0.14
APL7	0.514	3.563	96	Accepted	Accepted	Accepted	−10.48	0.14
APL8	0.439	3.57	93	Accepted	Accepted	Accepted	−13.62	0.13
APL9	0.523	4.922	131	Accepted	Accepted	Accepted	−6.21	0.17
APL10	0.515	4.116	99	Accepted	Accepted	Accepted	−9.14	0.20
APL11	0.528	4.585	124	Accepted	Accepted	Accepted	−12.72	0.17
APL12	0.527	3.867	96	Accepted	Accepted	Accepted	−9.77	0.16
APL13	0.537	3.965	98	Accepted	Accepted	Accepted	−7.09	0.19
APL14	0.545	4.051	96	Accepted	Accepted	Accepted	−6.98	0.12
APL15	0.662	3.888	99	Accepted	Accepted	Accepted	−4.85	0.09
APL16	0.649	5.432	153	Accepted	Accepted	Accepted	−7.68	0.07
APL17	0.653	5.294	153	Accepted	Accepted	Accepted	−8.15	0.16
APL18	0.674	5.318	153	Accepted	Accepted	Accepted	−8.17	0.17
APL19	0.712	5.29	151	Accepted	Accepted	Accepted	−8.15	0.20
APL20	0.694	4.834	126	Accepted	Accepted	Accepted	−9.71	0.19
APL21	0.683	3.854	100	Accepted	Accepted	Accepted	−6.0	0.08
APL22	0.674	3.718	100	Accepted	Accepted	Accepted	−6.13	0.2
APL23	0.654	4.578	128	Accepted	Accepted	Accepted	−7.28	0.21
APL24	0.63	4.759	127	Accepted	Accepted	Accepted	−7.78	0.22
APL25	0.63	4.822	127	Accepted	Accepted	Accepted	−7.39	0.22
APL26	0.624	4.287	145	Accepted	Accepted	Rejected	−7.94	0.15
APL27	0.531	3.615	80	Accepted	Accepted	Rejected	−6.86	0.15
APL28	0.538	3.54	96	Accepted	Accepted	Rejected	−9.5	0.15
APL29	0.517	3.565	97	Accepted	Accepted	Rejected	−11.19	0.14
APL30	0.556	3.539	64	Accepted	Accepted	Rejected	−8.25	0.16
APL31	0.552	3.073	54	Accepted	Accepted	Rejected	−8.57	0.16
APL32	0.675	3.983	80	Accepted	Accepted	Rejected	−5.09	0.09
APL33	0.456	3.767	80	Accepted	Accepted	Rejected	−8.5	0.12
APL34	0.702	3.758	85	Accepted	Accepted	Rejected	−6.15	0.21
APL35	0.746	3.558	77	Accepted	Accepted	Rejected	−6.73	0.17
APL36	0.705	3.537	77	Accepted	Accepted	Rejected	−5.26	0.17
APL37	0.483	3.135	23	Accepted	Accepted	Rejected	−9.09	0.19
APL38	0.705	3.536	77	Accepted	Accepted	Rejected	−6.54	0.17

(Continued on following page)

TABLE 1 (*Continued*) Medicinal Properties, DL and DS of analogues.

Entry no.	QED	Synth	MCE-18	Lipinski	Pfizer	GT	DL	DS
APL39	0.504	3.592	80	Accepted	Accepted	Rejected	−4.95	0.16
APL40	0.572	3.005	54	Accepted	Accepted	Rejected	−8.28	0.17
APL41	0.614	3.033	24	Accepted	Accepted	Rejected	−8.18	0.19
APL42	0.572	3.01	54	Accepted	Accepted	Rejected	−8.28	0.17
APL43	0.709	3.578	36	Accepted	Rejected	Rejected	−9.17	0.25
APL44	0.629	3.026	23	Accepted	Accepted	Rejected	−8.5	0.2
APL45	0.436	4.166	108	Accepted	Accepted	Accepted	−8.88	0.33
APL46	0.534	4.423	124	Accepted	Accepted	Accepted	−8.72	0.09
APL47	0.531	4.048	100	Accepted	Accepted	Accepted	−5.87	0.14
APL48	0.522	3.817	98	Accepted	Accepted	Accepted	−6.89	0.17
APL49	0.516	3.855	95	Accepted	Accepted	Accepted	−9.87	0.23
APL50	0.522	3.837	95	Accepted	Accepted	Accepted	−4.33	0.29
APL51	0.518	3.988	95	Accepted	Accepted	Accepted	−7.1	0.24
APL52	0.551	3.345	92	Accepted	Accepted	Accepted	−4.14	0.32
APL53	0.551	3.425	92	Accepted	Accepted	Accepted	−4.14	0.32
APL54	0.535	3.547	95	Accepted	Accepted	Accepted	−3.78	0.31
APL55	0.569	3.392	92	Accepted	Accepted	Accepted	−5.22	0.30
APL56	0.569	3.387	92	Accepted	Accepted	Accepted	−5.22	0.30
APL57	0.528	3.545	94	Accepted	Accepted	Accepted	−10.13	0.23
APL58	0.531	3.543	95	Accepted	Accepted	Accepted	−5.2	0.30
APL59	0.569	3.52	92	Accepted	Accepted	Accepted	−5.22	0.31
APL60	0.569	3.476	92	Accepted	Accepted	Accepted	−5.22	0.31
APL61	0.548	3.607	92	Accepted	Accepted	Accepted	−5.59	0.29
APL62	0.528	3.614	95	Accepted	Accepted	Accepted	−5.17	0.29
APL63	0.518	3.625	95	Accepted	Accepted	Accepted	−12.46	0.15
APL64	0.502	3.522	94	Accepted	Accepted	Accepted	−5.37	0.16
APL65	0.503	3.881	94	Accepted	Accepted	Accepted	−4.16	0.27
APL66	0.496	4.001	128	Accepted	Accepted	Accepted	−6.27	0.17
APL67	0.502	3.536	113	Accepted	Rejected	Accepted	−4.76	0.13
APL68	0.518	3.625	95	Accepted	Accepted	Accepted	−12.46	0.15
APL69	0.395	3.526	98	Accepted	Accepted	Accepted	−5.32	0.15
APL70	0.425	3.672	104	Accepted	Accepted	Rejected	−8.14	0.13
APL71	0.298	3.608	99	Accepted	Accepted	Accepted	−10.20	0.14
APL72	0.457	3.632	105	Accepted	Rejected	Rejected	−8.78	0.1
APL73	0.53	3.439	95	Accepted	Rejected	Accepted	−5.17	0.15
APL74	0.365	3.71	106	Accepted	Accepted	Rejected	−9.66	0.11
APL75	0.734	3.589	86	Accepted	Accepted	Accepted	−3.65	0.29
APL76	0.705	3.626	89	Accepted	Accepted	Accepted	−5.35	0.26

(Continued on following page)

TABLE 1 (*Continued*) Medicinal Properties, DL and DS of analogues.

Entry no.	QED	Synth	MCE-18	Lipinski	Pfizer	GT	DL	DS
APL77	0.554	3.554	76	Accepted	Accepted	Accepted	−13.66	0.23
APL78	0.734	3.671	76	Accepted	Accepted	Accepted	−11.74	0.21
APL79	0.674	3.678	86	Accepted	Rejected	Accepted	−10.26	0.16
APL80	0.668	4.296	136	Accepted	Rejected	Accepted	−8.27	0.15
APL	0.538	3.54	96	Accepted	Accepted	Accepted	−9.5	0.15

QED, quantitative estimate of druglikeness; Synth, synthetic accessibility score; Fsp3, The number of sp3 hybridized carbons/total carbon count; MCE-18, medicinal chemistry evolution in 2018; GT, golden triangle; DL, drug likeness; DS, drug score.

2.4.1 Protein preparation

The three-dimensional structure of protein was retrieved from the Protein Data Bank (PDB) database (https://www.rcsb.org/). The selective androgen receptor modulator (*PDB ID: 5T8E*, Resolution = 2.71 Å) was used as a protein to identify the interaction between ligand and protein binding domain (Asano et al., 2017). The protein was first prepared for docking studies by removing water molecules, adding hydrogen atoms, and adding Kollman charges, followed by the repair of missing atoms, and saved in PDBQT format.

2.4.2 Ligand preparation

ChemDraw was used to draw the 2D chemical structure of the ligands. Chem3D for APL and their designed analogues (ligands) converted the 2D structure into a 3D structure. The ligands were subjected to energy minimization using Chem3D and stored in SDF format. The OpenBabel (O'Boyle et al., 2011) software was used for the conversion into MOL2 format. Then, ligands were introduced into ADV and then stored in PDBQT format for the docking procedure. Furthermore, the introduction of protein into a solvent called ADV facilitates the arrangement of grid boxes, ensuring that the ligand remains in the core.

2.4.3 Molecular docking

We performed the docking simulations between the ligands and the protein using the ADV software. The whole protein's active site was then the focus of a grid box that had a grid spacing of 1.0 Å and dimensions of size x = 40, size y = 40, and size z = 40. The grid centre was located at X = 23, Y = 7, and Z = 7. The default settings for other docking parameters, including ADV and the rates of crossover and gene mutation, remained in place. The resulting files were analyzed using Discovery studio (Kemmish et al., 2017) to generate 2D and 3D protein-ligand interactions.

2.5 Molecular dynamics simulation

The top two complexes, based on docking scores and interactions, were selected for the molecular dynamics (MD) simulation. The MD simulation was conducted on an Acer workstation running Ubuntu 22.04. The Desmond software in the Schrödinger suite is used to run the MD simulation to elucidate the effectiveness of the screened compounds by molecular docking (Alturki et al., 2022; Van Der Spoel et al., 2005). The protein-ligand complexes were prepared using the 'System Builder'. After reducing its volume, the SPC water model with an orthorhombic shape was selected. It has 10 × 10 × 10 Å periodic boundary conditions in the protein-ligand complex's x, y, and *z*-axes. Moreover, the androgen receptor modulator protein (*PDB ID: 5T8E*) received additions of 25 sodium ions and 30 chloride ions. Ion and salt placements within 20 Å were excluded from neutralizing the simulation. Also, the complex's energies were lowered using the OPLS2005 forcefield by heating and reaching an equilibrium state before the MD simulations were run (Banks et al., 2005). We used the steepest descent method-based minimization protocol against the complexes and then heated them at 0–300 K. Further, with the time step of 100 nS, the system normalized into an equilibrium state at 1,000 steps. We kept the final production run for 100 nS at time steps of 100 ps, 300 K temperature, and 1.0325 bar pressure for both complexes, applying the Nose-Hoover method with the NPT ensemble (Huang et al., 2011).

3 Results and discussion

3.1 Bioisosteres of Apalutamide

Scientists or chemists often use the bioisosteric strategy to enhance pharmacokinetic characteristics and reduce undesired toxicities. MolOpt generated 1,415 replaceable groups for various groups in the APL molecule. The screened compounds are shown in Supplementary Table S1.

3.2 Prediction of molecular properties

The prediction of molecular properties for APL bioisosteres were computed and is shown in Supplementary Table S1. The Lipinski rule of five comprises the molecular weight (MW), number of hydrogen bond acceptors (nHA), number of hydrogen bond donors (nHD), and logarithm of partition coefficient value (logP). All analogues meet the Lipinski's rule of five, indicating appropriate absorption and bioavailability of the drug candidates. So, all analogues may be considered as drug candidates. All analogues exhibited excellent topological polar surface areas (TPSA), suggesting their potential to penetrate cells.

3.3 Prediction of medicinal properties

A quantitative estimate of druglikeness (QED) is a property that measures the druglikeness properties of drug candidates. It is based

TABLE 2 ADME properties of the analogues.

Entry no.	Caco-2	MDCK	HIA	BBB	PPB (%)	VD	CYP3A4	CL	$T_{1/2}$
APL1	−5.256	Ex	0.008	0.49	94.20	0.456	sub	1.383	0.172
APL2	−5.062	Ex	0.005	0.832	85.95	0.978	sub	4.292	0.175
APL3	−5.062	Ex	0.005	0.832	85.95	0.978	sub	4.292	0.175
APL4	−5.203	Ex	0.006	0.688	81.69	2.279	sub	4.827	0.062
APL5	−5.107	Ex	0.007	0.609	93.86	1.403	sub	5.058	0.077
APL6	−5.265	Ex	0.008	0.487	74.68	2.65	sub	6.753	0.107
APL7	−5.282	Ex	0.005	0.355	94.48	0.923	sub	3.63	0.167
APL8	−5.04	Ex	0.006	0.474	90.46	1.488	sub	6.308	0.131
APL9	−5.122	Ex	0.016	0.875	78.30	0.881	sub	8.422	0.229
APL10	−5.15	Ex	0.018	0.577	72.81	0.983	sub	4.9	0.29
APL11	−5.424	Ex	0.037	0.226	62.86	0.66	sub	7.038	0.33
APL12	−4.747	Ex	0.011	0.634	83.59	1.033	sub	6.72	0.256
APL13	−5.204	Ex	0.023	0.963	89.47	1.645	sub	6.922	0.157
APL14	−5.008	Ex	0.018	0.481	93.25	0.656	sub	6.932	0.288
APL15	−5.626	Ex	0.015	0.401	70.40	0.913	sub	5.814	0.208
APL16	−5.489	Ex	0.014	0.506	80.29	0.746	sub	7.259	0.202
APL17	−5.179	Ex	0.011	0.827	85.49	1.01	sub	7.628	0.162
APL18	−5.126	Ex	0.013	0.911	75.20	1.025	sub	7.527	0.211
APL19	−5.128	Ex	0.015	0.837	73.06	0.981	sub	7.129	0.177
APL20	−5.288	Ex	0.04	0.967	71.14	1.15	sub	3.799	0.305
APL21	−5.682	Ex	0.01	0.711	59.80	0.942	sub	6.049	0.184
APL22	−5.628	Ex	0.013	0.932	77.97	0.937	sub	6.348	0.227
APL23	−5.456	Ex	0.014	0.417	60.99	0.926	sub	5.195	0.36
APL24	−5.408	Ex	0.015	0.191	46.90	0.795	sub	4.049	0.438
APL25	−5.377	Ex	0.018	0.200	44.78	0.853	sub	3.74	0.363
APL26	−5.407	Ex	0.011	0.500	95.81	0.922	sub	5.03	0.18
APL27	−5.088	Ex	0.019	0.941	91.67	1.021	sub	7.157	0.189
APL28	−5.091	Ex	0.01	0.931	93.53	1.203	sub	6.294	0.123
APL29	−5.077	Ex	0.008	0.855	94.63	1.101	sub	6.354	0.102
APL30	−5.095	Ex	0.011	0.927	93.04	1.188	sub	6.142	0.141
APL31	−5.188	Ex	0.018	0.962	91.18	1.126	sub	6.782	0.183
APL32	−5.068	Ex	0.011	0.651	94.54	0.484	sub	7.466	0.039
APL33	−5.026	Ex	0.018	0.708	95.25	0.953	sub	7.568	0.129
APL34	−5.039	Ex	0.032	0.719	65.66	1.408	sub	6.595	0.27
APL35	−5.008	Ex	0.006	0.949	90.92	0.779	sub	7.576	0.058
APL36	−4.912	Ex	0.006	0.743	90.45	0.708	sub	6.763	0.093
APL37	−4.933	Ex	0.013	0.105	81.27	0.449	inh	4.584	0.623
APL38	−4.96	Ex	0.006	0.909	90.75	0.75	sub	7.999	0.071

(Continued on following page)

TABLE 2 (*Continued*) ADME properties of the analogues.

Entry no.	Caco-2	MDCK	HIA	BBB	PPB (%)	VD	CYP3A4	CL	$T_{1/2}$
APL39	−5.158	Ex	0.022	0.913	89.81	0.915	sub	7.826	0.213
APL40	−4.934	Ex	0.015	0.99	84.34	0.943	sub	6.335	0.154
APL41	−4.81	Ex	0.009	0.518	79.78	0.486	sub	3.739	0.696
APL42	−4.92	Ex	0.015	0.99	84.78	0.944	sub	6.315	0.16
APL43	−4.723	Ex	0.005	0.448	97.92	1.255	sub	8.788	0.062
APL44	−4.913	Ex	0.006	0.301	75.59	0.511	sub	3.418	0.697
APL45	−5.028	Ex	0.016	0.965	86.72	0.524	sub	5.619	0.16
APL46	−4.985	Ex	0.013	0.909	90.23	1.117	sub	4.822	0.117
APL47	−5.063	Ex	0.017	0.876	49.73	1.092	sub	2.724	0.485
APL48	−5.118	Ex	0.013	0.978	76.24	1.817	sub	2.933	0.112
APL49	−4.876	Ex	0.013	0.308	94.54	1.134	sub	7.069	0.221
APL50	−4.922	Ex	0.013	0.989	87.40	2.027	sub	5.135	0.107
APL51	−4.811	Ex	0.023	0.956	88.56	1.953	sub	5.899	0.137
APL52	−4.977	Ex	0.006	0.968	93.03	1.918	sub	6.612	0.14
APL53	−5.034	Ex	0.006	0.97	92.29	2.239	inh	6.627	0.135
APL54	−5.31	Ex	0.01	0.409	89.38	1.178	sub	4.904	0.191
APL55	−4.925	Ex	0.005	0.973	89.24	2.215	sub	3.659	0.12
APL56	−4.927	Ex	0.005	0.967	88.90	2.228	sub	3.931	0.132
APL57	−4.886	Ex	0.006	0.992	91.44	2.191	sub	3.83	0.12
APL58	−4.991	Ex	0.008	0.767	92.50	1.998	sub	2.287	0.229
APL59	−4.838	Ex	0.007	0.959	89.48	1.571	sub	4.114	0.108
APL60	−4.806	Ex	0.007	0.974	86.63	1.959	sub	3.154	0.088
APL61	−4.84	Ex	0.007	0.785	94.10	2.293	sub	7.835	0.142
APL62	−4.78	Ex	0.011	0.982	93.67	1.887	sub	4.206	0.106
APL63	−5.083	Ex	0.012	0.985	85.52	2.206	sub	3.45	0.177
APL64	−4.965	Ex	0.007	0.976	89.84	2.131	sub	3.662	0.149
APL65	−5.131	Ex	0.009	0.891	92.44	1.851	sub	7.14	0.156
APL66	−5.096	Ex	0.007	0.991	86.52	1.744	sub	3.119	0.203
APL67	−5.142	Ex	0.005	0.982	95.24	1.747	sub	2.716	0.05
APL68	−5.083	Ex	0.012	0.985	85.52	2.206	sub	3.45	0.177
APL69	−5.061	Ex	0.008	0.919	91.55	2.405	sub	2.836	0.129
APL70	−5.368	Ex	0.009	0.989	94.41	1.962	sub	2.63	0.085
APL71	−4.924	Ex	0.008	0.583	94.17	1.379	sub	3.612	0.133
APL72	−5.138	Ex	0.008	0.510	97.46	4.615	sub	5.005	0.055
APL73	−4.908	Ex	0.011	0.846	95.08	1.87	sub	5.253	0.073
APL74	−5.318	Ex	0.011	0.951	95.00	1.991	sub	1.803	0.094
APL75	−5.099	Ex	0.026	0.972	90.43	0.859	sub	7.002	0.247
APL76	−5.172	Ex	0.016	0.972	91.75	0.882	sub	6.428	0.138

(Continued on following page)

TABLE 2 (*Continued*) ADME properties of the analogues.

Entry no.	Caco-2	MDCK	HIA	BBB	PPB (%)	VD	CYP3A4	CL	$T_{1/2}$
APL77	−4.993	Ex	0.01	0.952	66.95	0.943	sub	7.191	0.439
APL78	−4.983	Ex	0.008	0.986	85.02	0.94	sub	6.26	0.26
APL79	−4.984	Ex	0.004	0.947	93.89	0.917	sub	5.892	0.192
APL80	−4.968	Ex	0.005	0.716	95.23	2.754	inh	8.184	0.105
APL	−5.091	Ex	0.01	0.931	93.53	1.203	sub	6.294	0.123

Caco-2, the human colon adenocarcinoma cell lines; MDCK, Madin–Darby canine kidney cells; HIA, human intestinal absorption; PPB, plasma protein binding; BBB, blood–brain barrier; VD, volume distribution; Fu, the fraction unbound in plasms; Ex, Excellent; sub, substrate for human cytochrome P450 (CYP3A4); CL, the clearance of a drug; $T_{1/2}$, the half-life of a drug.

on the idea of desirability, which encompasses eight drug-like-related properties. The QED score of the designed analogues, such as APL32, APL74-76, APL38, APL43, APL75, APL76, APL78-80, and APL18-22, is in the good range (>0.67), but the QED score for APL is 0.538. The QED score shows that all analogues are attractive compounds. MCE-18 is an abbreviation for the concept of medicinal chemistry evolution in the year 2018. This metric is capable of accurately assessing the novelty of compounds based on their overall sp3 complexity. The MCE-18 score of newly designed analogues such as APL1-8, APL9-14, APL15-26, APL27-30, APL32-34, APL45-76, APL79, and APL80 found more than 78, as these analogues need to be visually examined to evaluate their target profile and drug-likeness. Lipinski's rule [Karami et al., 2022] has been accepted for all analogues, suggesting the potential for proper absorption or permeability. Pfizer's rule of all analogues were also found under the accepted criteria, with some exceptions, including APL6, APL43, APL69, APL72, APL73, APL79, and APL80, which indicate favorable ADMET profiles. The Golden Triangle (GT) rule comprises of two parameters, including MW (≤200 and ≥50) and LogP (≤5 and ≥ −2). All analogues, except for APL26, APL27-44, APL70, APL71, and APL74, met the acceptance criteria of the GT rule. The calculated medicinal properties of all APL analogues are being in Table 1.

3.4 Prediction of DS and DL score

The definitions of DL and DS have been established according to certain physicochemical properties of the known drug compounds and how they influence the molecular behavior *in-vitro*. The DL and DS scores predict the properties, such as solubility, permeability, metabolic stability, and transporter effects, of the drug candidates. The DL score of the compounds may provide information about their safety and efficacy. The DS is a comprehensive metric that compiles properties including druglikeness, cLogP, logS, MW, and toxicity concerns into a single number. This value may be used to assess the overall possibility of an unknown compound meeting the criteria for becoming a drug (Bickerton et al., 2012; Lagu et al., 2022). Among all analogues, APL75 has a higher DL score, followed by APL54 with scores of −3.65 and −3.78, respectively, compared to APL (−9.5). On the other hand, APL45 (0.33) has a higher DS, followed by ADL54, ADL59, and ADL60 with a score of 0.31, which is superior to APL (0.15). The predicted DL and DS scores are shown in Table 1.

3.5 Prediction of pharmacokinetic (ADME) properties

Pharmacokinetic parameters play a crucial role in drug development, and they provide valuable information on the absorption, distribution, metabolism, and excretion of a drug inside the body. We have calculated the pharmacokinetic parameters, including absorption (caco-2, MDCK, and HIA), distribution (BBB, PPB, and VD), metabolism (CYP3A4), and excretion (CL and $T_{1/2}$), for the designed analogues. The scores for these parameters are tabulated in Table 2. The human colon adenocarcinoma cell line (Caco-2) is a widely used *in-vitro* method for predicting the intestinal permeability of drugs and assessing their potential for oral absorption. Therefore, the assessment of Caco-2 cell permeability has emerged as a crucial criterion in determining the suitability of a therapeutic molecule. Results reflecting the caco-2 score of analogues APL2, APL3, APL5, APL8, APL9, APL12, APL14, APL18, APL19, APL27-30, APL32-38, APL40-53, APL55-69, APL71-73, APL75, and APL77-80 found more than −5.15, which may be predicted as proper *in-vivo* drug permeability. An excellent MDCK score suggests that all analogues have the ability to permeate and transport across the cell. Human intestinal absorption (HIA) scores found in the range between 0 and 0.3 indicate analogues might have good oral bioavailability. The blood-brain barrier (BBB) score for analogues such as APL11, APL24, APL25, and APL37 is less than 0.03, indicating that these analogues might be safe from CNS side effects.

The designed analogues, including APL2-4, APL6, APL9-13, APL15-25, APL34, APL37, APL39-42, APL44, APL45, APL47, APL48, APL50, APL51, APL53, APL54-56, APL59, APL60, APL64, APL66, APL68, APL77, and APL78, exhibited plasma protein binding (PPB) of less than 90%. Therefore, these compounds may have proper PPB, indicating that they can distribute easily throughout the body. The volume of distribution (VD) of all analogues shows a score in the range between 0.04 and 20, which means that these analogues may have a proper distribution amount in body fluid and an uptake amount in tissues. Cytochrome P450 (CYT P450) is a group of isozymes that plays a crucial role in phase-I and phase-II drug metabolism. All analogues show a higher substrate score and a lower inhibitor score for CYP3A4, with the exception of APL80, which means they might be easily metabolized in the body. Analyses have found that the clearance (CL) score of analogues such as APL5-6, APL8, APL9, APL11-14, APL15-19, APL21-23, APL26, APL27-36, APL42,

TABLE 3 Toxicity screening of analogues.

Entry no.	H-HT	DILI	Ames	ROA	Carc.	NR-AR	NR-AR-LBD
APL1	0.984	0.996	0.02	0.939	0.877	0.375	0.243
APL2	0.969	0.988	0.042	0.893	0.862	0.319	0.13
APL3	0.969	0.988	0.042	0.893	0.862	0.319	0.13
APL4	0.985	0.99	0.026	0.911	0.597	0.015	0.369
APL5	0.987	0.994	0.022	0.739	0.906	0.047	0.217
APL6	0.984	0.983	0.02	0.947	0.712	0.056	0.062
APL7	0.979	0.995	0.042	0.938	0.875	0.472	0.114
APL8	0.984	0.989	0.045	0.911	0.898	0.09	0.527
APL9	0.981	0.984	0.043	0.634	0.893	0.012	0.007
APL10	0.982	0.993	0.055	0.605	0.892	0.034	0.04
APL11	0.964	0.997	0.061	0.644	0.754	0.015	0.004
APL12	0.966	0.994	0.083	0.766	0.605	0.01	0.181
APL13	0.971	0.989	0.087	0.633	0.878	0.026	0.048
APL14	0.975	0.994	0.043	0.238	0.842	0.011	0.022
APL15	0.99	0.986	0.358	0.943	0.983	0.329	0.014
APL16	0.989	0.98	0.25	0.73	0.95	0.004	0.004
APL17	0.936	0.978	0.029	0.607	0.931	0.017	0.013
APL18	0.933	0.98	0.027	0.645	0.934	0.011	0.012
APL19	0.939	0.981	0.034	0.609	0.936	0.009	0.015
APL20	0.963	0.986	0.372	0.925	0.972	0.009	0.078
APL21	0.986	0.982	0.247	0.836	0.969	0.206	0.02
APL22	0.982	0.984	0.046	0.944	0.945	0.27	0.01
APL23	0.985	0.978	0.052	0.864	0.896	0.008	0.005
APL24	0.982	0.984	0.298	0.844	0.9	0.002	0.008
APL25	0.973	0.981	0.202	0.817	0.877	0.005	0.005
APL26	0.958	0.987	0.07	0.583	0.838	0.032	0.27
APL27	0.97	0.99	0.026	0.754	0.852	0.027	0.087
APL28	0.975	0.991	0.039	0.843	0.841	0.037	0.285
APL29	0.973	0.99	0.038	0.838	0.84	0.036	0.262
APL30	0.976	0.992	0.046	0.828	0.851	0.039	0.406
APL31	0.976	0.989	0.03	0.778	0.786	0.036	0.05
APL32	0.9	0.48	0.397	0.649	0.214	0.262	0.603
APL33	0.964	0.774	0.52	0.31	0.069	0.137	0.425
APL34	0.968	0.935	0.021	0.118	0.107	0.001	0.002
APL35	0.931	0.485	0.604	0.787	0.431	0.121	0.661
APL36	0.931	0.485	0.604	0.787	0.431	0.121	0.661
APL37	0.978	0.982	0.718	0.288	0.609	0.072	0.587
APL38	0.967	0.334	0.463	0.857	0.517	0.139	0.417

(Continued on following page)

TABLE 3 (*Continued*) Toxicity screening of analogues.

Entry no.	H-HT	DILI	Ames	ROA	Carc.	NR-AR	NR-AR-LBD
APL39	0.969	0.986	0.245	0.677	0.875	0.013	0.027
APL40	0.969	0.989	0.056	0.869	0.173	0.409	0.041
APL41	0.977	0.957	0.423	0.583	0.168	0.112	0.476
APL42	0.97	0.989	0.061	0.87	0.17	0.409	0.043
APL43	0.978	0.251	0.088	0.758	0.175	0.017	0.565
APL44	0.982	0.977	0.658	0.419	0.124	0.086	0.187
APL45	0.976	0.99	0.228	0.194	0.932	0.034	0.009
APL46	0.98	0.995	0.671	0.517	0.924	0.008	0.003
APL47	0.987	0.99	0.149	0.318	0.963	0.009	0.009
APL48	0.95	0.986	0.068	0.673	0.9	0.097	0.063
APL49	0.979	0.99	0.491	0.975	0.861	0.021	0.318
APL50	0.973	0.985	0.028	0.972	0.439	0.027	0.008
APL51	0.971	0.991	0.044	0.993	0.438	0.035	0.011
APL52	0.887	0.982	0.031	0.839	0.681	0.023	0.005
APL53	0.903	0.986	0.081	0.82	0.524	0.034	0.005
APL54	0.926	0.99	0.03	0.892	0.692	0.037	0.008
APL55	0.911	0.992	0.037	0.849	0.518	0.024	0.006
APL56	0.916	0.991	0.034	0.867	0.615	0.025	0.005
APL57	0.939	0.986	0.032	0.637	0.881	0.116	0.011
APL58	0.915	0.992	0.046	0.547	0.721	0.037	0.035
APL59	0.979	0.985	0.046	0.878	0.884	0.068	0.038
APL60	0.952	0.993	0.038	0.596	0.744	0.029	0.007
APL61	0.951	0.989	0.433	0.964	0.772	0.018	0.008
APL62	0.968	0.994	0.049	0.68	0.742	0.035	0.013
APL63	0.951	0.993	0.039	0.804	0.803	0.046	0.064
APL64	0.939	0.99	0.041	0.677	0.785	0.042	0.021
APL65	0.965	0.987	0.02	0.963	0.326	0.021	0.005
APL66	0.907	0.987	0.024	0.784	0.854	0.121	0.019
APL67	0.925	0.986	0.033	0.866	0.881	0.028	0.032
APL68	0.951	0.993	0.039	0.804	0.803	0.046	0.064
APL69	0.929	0.99	0.025	0.81	0.859	0.049	0.017
APL70	0.945	0.996	0.028	0.765	0.794	0.015	0.017
APL71	0.938	0.989	0.119	0.699	0.912	0.3	0.09
APL72	0.984	0.992	0.024	0.95	0.809	0.018	0.065
APL73	0.949	0.989	0.023	0.864	0.782	0.155	0.019
APL74	0.956	0.993	0.108	0.795	0.885	0.022	0.037
APL75	0.989	0.989	0.069	0.9	0.956	0.017	0.063
APL76	0.978	0.991	0.024	0.383	0.755	0.007	0.023

(Continued on following page)

TABLE 3 (*Continued*) Toxicity screening of analogues.

Entry no.	H-HT	DILI	Ames	ROA	Carc.	NR-AR	NR-AR-LBD
APL77	0.95	0.987	0.207	0.811	0.863	0.156	0.12
APL78	0.939	0.984	0.045	0.832	0.916	0.085	0.043
APL79	0.951	0.988	0.057	0.343	0.86	0.019	0.725
APL80	0.972	0.992	0.317	0.981	0.863	0.005	0.176
APL	0.975	0.991	0.039	0.843	0.841	0.037	0.285

H-HT, the human hepatotoxicity; DILI, drug-induced liver injury; Ames, Test for mutagenicity; ROA, rat oral acute toxicity; NR-AR, androgen receptor - a nuclear hormone receptor; NR-AR-LBD, molecule bind with LBD, of androgen receptor; Carc., carcinogenicity.

APL43, APL45, APL49-53, APL61, APL65, APL72, APL73, and APL75-80 is greater than 5. The clarity of the drug candidates indicates the dosing frequency of a drug. Half-life ($T_{1/2}$) score of all analogues found in the range from 0 to 0.3 with some exception of APL11, APL20, APL23-25, APL37, APL41, APL44, APL47, and APL77, which indicates proper clearance from the body.

3.6 Prediction of the toxicity properties

The toxicological properties of analogues, including drug-induced liver injury (DILI), mutagenicity (Ames test), acute oral toxicity in rats (ROA), binding of the molecule with the ligand-binding domain (LBD) of the androgen receptor (NR-AR-LBD), and carcinogenicity (Carc.), were calculated, and their scores are shown in Table 3. All designed analogues had identical human hepatotoxicity (H-HT) scores to APL, indicating they may have shown harmful effects. Analogue APL29 was predicted to have a safer DILI score, while APL exhibited toxicity (0.99). However, counterparts such as APL32, APL35, APL36, and APL38 predicted mild toxicity levels ranging from 0.3 to 0.7. However, the prediction of a safer mutagenic score for all analogues indicates that they are unlikely to induce mutagenesis. However, there are several exceptions, including APL15, APL20, APL32, APL33, APL35, APL36, APL38, APL41, APL44, APL46, APL49, APL51, APL61, and APL80.

Analogues APL14, APL34, APL45, and APL77 exhibited ROA prediction scores within a safer range (0–0.3), a crucial safety characteristic for potential drug candidates. In contrast, ROA score of APL found in toxic range. APL9-11, APL13, APL17-19, APL26, APL32-33, APL39, APL41, APL44, APL46-48, APL53, APL57, APL58, APL60, APL62, APL64, APL71, and APL76 exhibited lower levels of hazards compared to APL. The carcinogenic nature of analogues is a significant concern due to their potent impact on health and their ability to harm the genome or disturb cellular metabolism. The NR-AR receptor plays a vital function in androgen receptor-dependent PC and other disorders connected to androgens. Researchers determined that the analogues APL4-6, APL8, APL9-16, APL27-39, APL41, and APL43-80 have a lower NR-AR score, suggesting their potential non-toxicity to the AR.

3.7 Molecular docking study

Our objective was to examine the possible interaction between newly designed APL analogues and the protein. We acquired the 3D crystallographic structure of the protein from the protein data bank (*PDB ID: 5T8E*). The ADV program successfully aligned the protein with the ligands (Supplementary Table S1), resulting in uniform grid box dimensions that enhanced the understanding of the inhibitors' binding affinities. The designed ligands exhibited docking scores ranging from −6.2 to −8.5 *Kcal/mol* (Table 4).

APL8 is a bioisostere of APL, where the amide group in the phenyl ring is substituted with an amine group in the phenyl ring. The overall structure of APL8 is comparable to that of APL. Ligand APL8 had the second highest binding affinity score (−8.4 *Kcal/mol*). Residues ARG752 and GLN711 of the target protein form hydrogen bonds with CN and CF_3 groups in the ligand's pyridinyl ring in the docked ADV complex. These hydrogen bonds are similar to those found in APL. TRP751 also formed a carbon-hydrogen bond with the phenyl ring of the ligand. On the other hand, it formed an additional hydrogen bond between the GLU678 residue and the N-H group of the methyl amide in the ligand. It was also easy for PRO682 to form strong bonds with the F of the CF_3 group and the nitrogen of the pyridinyl in the ligand. GLU681 and GLY683 formed a halogen interaction with the F of the CF_3 group in the ligand. Additionally, ligands formed alkyl (PRO682) and pi-alkyl (VAL684 and ARG752) interactions. Figures 2A, 3A show the 2D and 3D interactions of the ligand APL8, respectively.

APL35 is the bioisostere of APL in which the cyclobutyl-thiohydantoin group is replaced with 3-ethyl-5-oxopyrrolidine, and the resting structure is similar to that of APL. The docking score of APL35 was −7.1 *Kcal/mol*. The APL35 analogue showed four conventional hydrogen bonds with amino acid residues (GLN711, ARG752, ASN756, and TYR763). ARG752 formed a hydrogen bond with fluorine (F) in the trifluoromethyl (CF_3) group attached to the pyridine ring. GLN711 formed another hydrogen bond with F of CF_3. The N-H of the amide group formed two hydrogen bonds with ASN756 and TYR763. A carbon-hydrogen bond was also seen between TRP751 and 3-ethyl-5-oxopyrrolidine. ARG752 formed a pi-cation bond with the pyridine ring as well. We identified an alkyl bond between the carbons of CF_3 and Val685 as well as PRO682. We observed a pi-alkyl bond between the pyridine ring and PRO682, as well as ALA748. There is a halogenic bond form between Gly683 and GLN711 and the F in the CF_3 group. The 2D and 3D interactions of the ligand APL35 are shown in Figures 2C, 3C, respectively.

A docking study revealed that APL42 shows the highest binding score (−8.5 *Kcal/mol*) among selected analogues. There are cyano

TABLE 4 Docking score and interactions of the analogues.

Entry no.	Docking score (*Kcal/mol*)	Interactions	
		H-binding	Other
APL1	-	NHB	NHB
APL2	−6.9	ARG752, THR755, TRP751	ARG752, GLU681, ALA748, PRO801, PHE804, PRO801
APL3	−6.8	ARG752, THR755	GLU681, ALA748, ARG752, LEU805, PRO801
APL4	−6.9	ARG752, THR755	GLY683, PRO801, VAL684, LEU805, ARG752
APL5	−6.6	ARG752, THR755, GLN802, GLU678	GLU678, PRO682, GLY683, VAL684, TRP751, ARG752
APL6	−6.8	VAL685, GLN711, ARG752, THR755, PRO682	GLU681, PRO682, GLY683, TRP751, PHE754, ARG752
APL7	−8.1	GLN711, ARG752, GLU678, VAL684	PRO682, GLU681, GLY683
APL8	−8.4	GLN711, ARG752, PRO682, TRP751	VAL684, GLU681, GLY683
APL9	−7.1	ARG752, THR755, TRP751, ILE799	GLU681, ALA748, PRO801, ARG752, TRP751, PHE804
APL10	−7.2	ARG752, THR755, TRP751, PRO682	GLU681, ALA748, PRO748, ARG752, TRP751
APL11	-	NHB	NHB
APL12	-	NHB	NHB
APL13	−7.6	ARG752, VAL685, TRP751, GLN711	GLU678, GLU681, PRO682, GLY683, TRP751, ARG752
APL14	−7.1	ARG752, PRO682, TRP751, GLN711	GLU681, ARG752, ALA748, PRO682, TRP751
APL15	−7.6	GLN711, ARG752, THR755, ASN756, GLU678, VAL684	GLU681, PRO682, GLY683, TRP751, VAL684, ARG752
APL16	−7.1	ARG752, TRP751, TRP751	GLU681, ALA748, ARG752, TRP751, PHE804
APL17	−7.6	GLN711, ARG752, THR755, GLU678, VAL684	GLU681, PRO682, GLY683, VAL684, ARG752
APL18	−7.6	ARG752, TRP751	GLU681, ALA748, PRO801, ARG752, LEU805, TRP751, TRP751, PHE804, ARG752
APL19	−7.7	VAL685, GLN711, TRP751, ARG752, PRO682	GLU681, PRO682, GLY683, TRP751, PRO682, ARG752
APL20	−7.0	VAL685, GLN711, ARG752	GLU681, PRO682, GLY683, TRP751, ARG752
APL21	−7.9	GLN711, ARG752, GLU678, VAL684	GLU681, PRO682, GLY683, VAL684, ARG752
APL22	−7.7	GLN711, ARG752, PRO682, TRP751, GLU678	GLU681, PRO682, GLY683, TRP751, ARG752
APL23	−7.4	GLN711, ARG752, THR755, ASN756, PRO682	GLU681, PRO682, GLY683, ARG752
APL24	−6.7	GLN711, ARG752, ASN756, VAL684	GLU681, PRO682, GLY683, VAL684, ARG752
APL25	−7.6	ARG752, THR755, TRP751	GLU681, ALA748, ARG752, PHE804
APL26	−7.8	GLN711, ARG752, PRO682	GLU681, PRO682, GLY683, TRP751, VAL684, ARG752
APL27	−8.2	ARG752, THR755, GLU678, PRO682, GLN711	GLU681, PRO682, GLY683, TRP751, VAL684, ARG752
APL28	-	NHB	NHB
APL29	−7.3	ARG752, THR755, VAL685, PRO682, GLN711	GLU681, PRO682, GLY683, THR755, TRP751, ARG752
APL30	−8.2	ARG752, THR755, VAL685, PRO682, GLN711	GLU681, PRO682, GLY683, THR755, TRP751, ARG752
APL31	-	NHB	NHB
APL32	-	NHB	NHB
APL33	−7.4	ARG752, THR755, VAL684, GLN711, GLU678	GLU678, GLU681, PRO682, ARG752, GLU678, TRP751, ALA748, VAL684
APL34	-	NHB	NHB
APL35	−7.1	GLN711, ARG752, ASN756, TYR763, TRP751	GLY683, GLN711, ARG752, VAL684, PRO682, VAL685, ALA748

(Continued on following page)

TABLE 4 (*Continued*) Docking score and interactions of the analogues.

Entry no.	Docking score (*Kcal/mol*)	Interactions	
		H-binding	Other
APL36	-	NHB	NHB
APL37	-	NHB	NHB
APL38	-	NHB	NHB
APL39	-	NHB	NHB
APL40	-	NHB	NHB
APL41	-	NHB	NHB
APL42	−8.5	GLN711, ARG752, GLU678, PRO682, VAL684	GLU681, PRO682, GLY683, VAL684, ARG752
APL43	−6.6	GLN711, ARG752, TRP751, THR755	GLU681, GLN711, ARG752, ALA748, LEU805, PRO682
APL44	-	NHB	NHB
APL45	-	NHB	NHB
APL46	-	NHB	NHB
APL47	−8.3	GLN711, ARG752, TRP751	GLU681, ALA748, TRP751, ARG752
APL48	-	NHB	NHB
APL49	-	NHB	NHB
APL50	-	NHB	NHB
APL51	−7.3	GLN711, ARG752, TRP751, THR755, PRO682, GLY683	GLU681, ALA748, ARG752, PRO801, LEU805
APL52	-	NHB	NHB
APL53	-	NHB	NHB
APL54	−7.7	GLU678, ARG752, TRP751, PRO682	GLU678, GLU681, ALA748, ARG752, TRP751, PHE804
APL55	-	NHB	NHB
APL56	-	NHB	NHB
APL57	-	NHB	NHB
APL58	−7.0	ARG752, TRP751, THR755	GLU681, ARG752, PRO682, GLY683, ALA748, VAL684
APL59	-	NHB	NHB
APL60	-	NHB	NHB
APL61	-	NHB	NHB
APL62	−6.6	GLN711, ARG752, VAL685, GLY683, PHE764	GLU681, PRO682, VAL684, ARG752, VAL685, VAL684
APL63	-	NHB	NHB
APL64	−7.5	GLN711, ARG752, TRP751, GLU678	GLU678, GLU681, ALA748, ARG752, TRP751, PHE804
APL65	-	NHB	NHB
APL66	-	NHB	NHB
APL67	−6.7	TRP751, ARG752, GLU678	GLU681, ALA748, GLU678, PRO682, ARG752, TRP751, PHE804
APL68	-	NHB	NHB
APL69	-	NHB	NHB
APL70	−8.3	GLN711, ARG752, VAL685	GLU678, PRO682, TRP751, ALA748, VAL715, LEU744, LYS808, TRP718, GLY683
APL71	-	NHB	NHB

(Continued on following page)

TABLE 4 (*Continued*) Docking score and interactions of the analogues.

Entry no.	Docking score (*Kcal/mol*)	Interactions	
		H-binding	Other
APL72	−7.6	GLN711, ARG752, TRP751	PRO682, TRP751, ALA748, GLU681, GLY683
APL73	-	NHB	NHB
APL74	-	NHB	NHB
APL75	-	NHB	NHB
APL76	−7.2	GLN711, ARG752, VAL685. ASN756, PRO682	ARG752, GLU681, TRP751
APL77	−6.2	GLN711, ARG752, VAL685. TRP751, VAL684, PRO682	TRP751, LEU805, PHE804, PRO801, VAL684, GLU681, PRO682, ARG752, GLY683
APL78	−7.4	GLN711, ARG752, VAL685	PRO685, GLU681, ARG752, GLY683, TRP751, PRO801, PHE804, LEU805
APL79	−7.9	GLN711, ARG752, VAL684	LEU684, GLY683, PRO682, GLU681, ARG752, GLU678, LEU805
APL80	−8.0	GLN711, ARG752, VAL684. PRO682	TRP751, VAL684, GLY683, PRO682, GLU681, ARG752, GLU678
APL	−7.1	GLN711, ARG752, THR755	GLU681, PRO682, TRP751, ALA748, ARG752

NHB, no hydrogen bonds were seen as being found in apalutamide.

(CN) and CF_3 groups that form hydrogen bonds with GLN711 and ARG752, respectively. There are also hydrogen bonds in APL. Surprisingly, GLU678 forms additional hydrogen bonds with the N-H group of the amide in the ligand. PRO682 shows a carbon-hydrogen bond interaction with the F of CF_3 groups. The two F atoms of CF_3 formed halogen bonding with the amino acid residues GLU681, PRO682, and GLY683. Residues VAL684 and ARG752 show pi-alkyl interactions with the pyridinyl group in the ligand. Residue PRO682 also formed an alkyl interaction with F of CF_3. The 2D and 3D interactions of the ligand APL42 are shown in Figures 2D, 3D, respectively.

APL43 is a bioisostere of APL, where the cyclobutyl-thiohydantoin group is substituted with 1-fluoropent-1-ene. The overall structure of APL43 is comparable to that of APL. The docking score of APL43 was −6.6 *Kcal/mol*. A docking study revealed that APL43 formed three conventional hydrogen bonds with THR755, ARG752, and GLN711. Ligand APL43 formed a hydrogen bond with THR755 through the oxygen attached to the carbon next to the phenyl ring. ARG752 formed a hydrogen bond with one of the F in the CF_3 group attached to the pyridine ring. The CN group attached to the pyridine ring formed a hydrogen bond with GLN711. The F attached to the double-bonded carbon next to the pyridine ring forms a carbon-hydrogen bond with TRP751. The nitrogen of the pyridine group forms a carbon-hydrogen bond with ARG752. GLU681 and GLN711 form three halogen bonds. GLU681 forms halogen bonds with a double-bonded carbon adjacent to the pyridine ring and one of the F from the CF_3 group. LEU805 forms an alkyl bond with the last carbon of the ethyl group attached to the carbon next to the phenyl group. The carbon of the CF_3 group forms alkyl bonds with ALA748 and PRO682. Figures 2E, 3E show the 2D and 3D interactions of the ligand APL43, respectively.

The structure of APL47 is like that of APL, but the 6-cyano-5-(trifluoromethyl)pyridin-3-yl group is changed to 1-cyano-2-oxo-3-(trifluoromethyl)-2,3-dihydro-1H-imidazol-4-yl. The resting structure of APL47 is the same as that of APL. The docking score of APL47 was −8.3 *Kcal/mol*. It was found that residues ARG752 and GLN711 connect with CN and carbonyl groups in 1-cyano-2-oxo-3-(trifluoromethyl)-2,3-dihydro-1H-imidazol, which is the same as APL. TRP751 formed a carbon-hydrogen bond with F of the CF_3 side chain. Glu681 and ALA748 interacted with the F of CF_3 through halogen bonds. Hydrophobic interactions formed between the phenyl ring of the ligand and TRP751. Additionally, ARG752 and TRP751 exhibited hydrophobic interactions with the F of CF_3 and 1,3-dihydro-1H-imidazol, respectively. Figures 2F, 3F show the 2D and 3D interactions of the ligand APL47, respectively.

APL76 is a bioisostere of APL, where the CF_3 group is substituted with an CF_2 group in the pyridine ring. The docking score for APL76 was −7.2 *Kcal/mol*. Through ADV, four regular hydrogen bonds were seen between the ligand APL76 and the amino acid residues ASN756, ARG752, GLN711, and VAL685. The hydrogen bonds with VAL685 and GLN711 were via the nitrogen triple bond with the carbon next to the pyridine ring. A hydrogen bond was established between ARG752 and one of the F presents in CF_2 that was attached to the pyridine ring. ASN756 formed a hydrogen bond with the hydrogen atom attached to the nitrogen atom of the amide group. GLU681 forms a halogen bond with F of the CF_2. The same F also forms carbon-hydrogen bonds with PRO682. With ARG682, the pyridine ring forms an alkyl bond. TRP751 forms an alkyl bond with the cyclobutene attached to the imidazolidine. Figures 2G, 3G show the 2D and 3D interactions of the ligand APL76, respectively.

APL80 is a bioisostere of APL, where the 6-cyano-5-(trifluoromethyl)pyridin-3-yl group is substituted with a benzothiazoles-2-yl group in the pyridine ring. The docking score for APL80 was −8.0 *Kcal/mol*. According to the study, the CN group of the pyridinyl ring in the ligand formed a hydrogen bond with the GLN711 residue. On the other hand, F of the CF_3 group also formed a hydrogen bond with the ARG752 residue. Both PRO682 and VAL684 formed a carbon-hydrogen bond with the F of CF_3 and the

TABLE 5 QED, MCE-18, docking score and docking interactions of selected analogues.

Entry no.	QED score	MCE-18 score	Docking score (*Kcal/mol*)	Interactions	
				H-binding	Other
APL19	0.712	151	−7.7	VAL685, GLN711, TRP751, ARG752, PRO682	GLU681, PRO682, GLY683, TRP751, PRO682, ARG752
APL35	0.746	77	−7.1	GLN711, ARG752, ASN756, TYR763, TRP751	GLY683, GLN711, ARG752, VAL684, PRO682, VAL685, ALA748
APL43	0.709	36	−6.6	GLN711, ARG752, TRP751, THR755	GLU681, GLN711, ARG752, ALA748, LEU805, PRO682
APL76	0.705	89	−7.2	GLN711, ARG752, VAL685. ASN756, PRO682	ARG752, GLU681, TRP751
APL80	0.668	136	−8.0	GLN711, ARG752, VAL684. PRO682	TRP751, VAL684, GLY683, PRO682, GLU681, ARG752, GLU678
APL	0.538	96	−7.1	GLN711, ARG752, THR755	GLU681, PRO682, TRP751, ALA748, ARG752

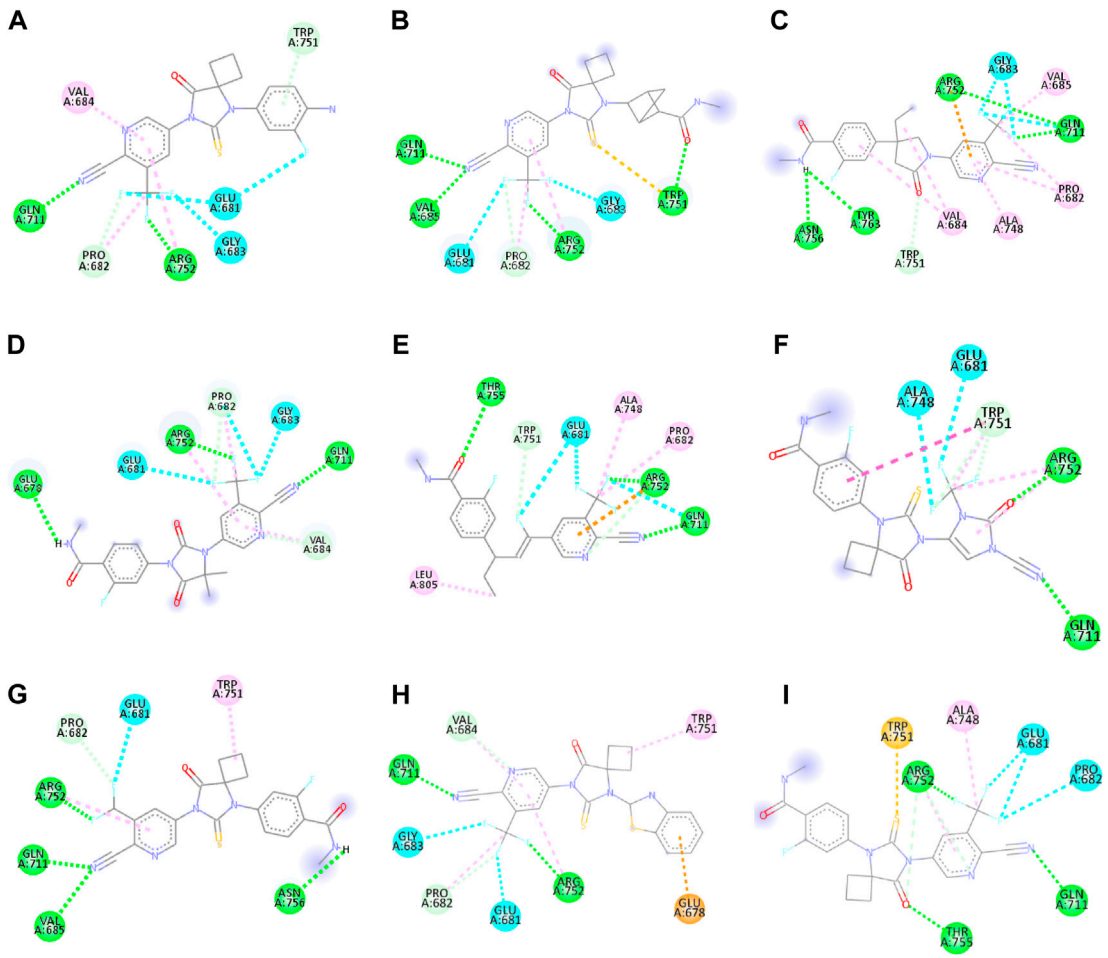

FIGURE 2
2D interactions of ligand APL8 **(A)**, APL19 **(B)**, APL35 **(C)**, APL 42 **(D)**, APL43 **(E)**, APL47 **(F)**, APL76 **(G)**, APL80 **(H)**, and Apalutamide **(I)**.

nitrogen of the pyridinyl ring in the ligand. Pi-alkyl interactions formed between TRP751 and the cyclobutyl ring of thiohydantoins. GLU681 and GLU683 show interaction with F of CF_3 through halogenic bonds. A pi-anion bond was formed between the indolyl ring and GLU678. 2D and 3D interactions of the ligand APL80 are shown in Figures 2H, 3H, respectively.

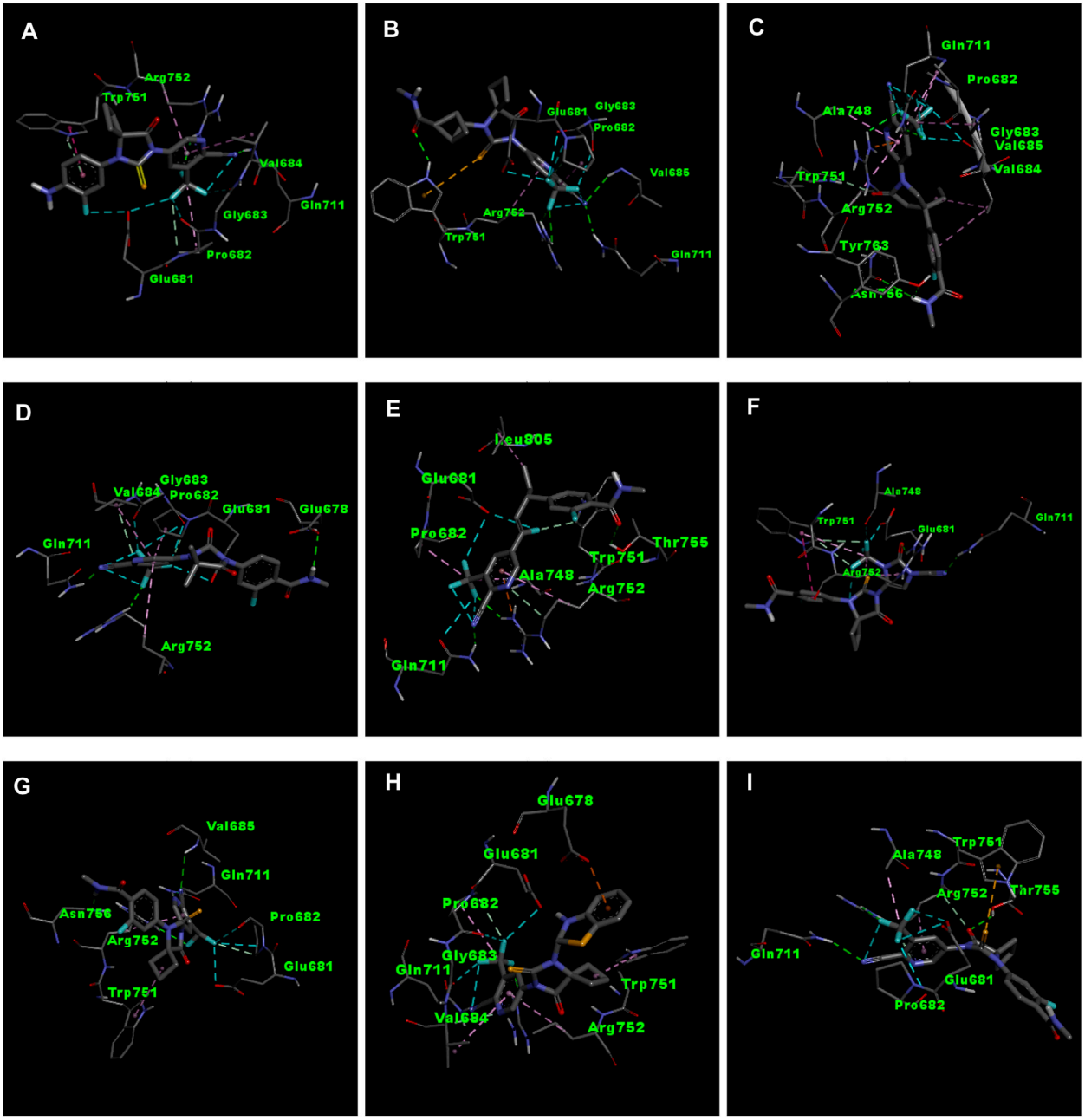

FIGURE 3
3D interactions of ligand APL8 **(A)**, APL19 **(B)**, APL35 **(C)**, APL 42 **(D)**, APL43 **(E)**, APL47 **(F)**, APL76 **(G)**, APL80 **(H)**, and Apalutamide **(I)**.

In APL19, the fluoro-phenyl group is replaced with bicyclo [1.1] pentane groups, which is based on the literature (Subbaiah and Meanwell, 2021). The docking score of APL19 was −7.7 *Kcal/mol*. Based on the result of the docking study of APL19, it shows the hydrogen bonding interaction of CN and CF_3 with GLN711 and F of CF_3, respectively. Surprisingly, the CN group also forms hydrogen with the VAL685 amino acid residue. On the other hand, the carbonyl group also formed a hydrogen bond with TRP 751. TRP751 also formed a pi-Sulfur interaction with the Sulphur of the thiohydantoin scaffold. GLU681 and GLY683 show halogen bonding with F in CF_3. The 2D and 3D interactions of the ligand APL19 are shown in Figures 2B, 3B, respectively.

The standard APL shows three conventional hydrogen bonds with the amino acid residues ARG752, THR755, and GLN711. The hydrogen bond with ARG752 was established with one of the F presents in the CF_3 that was attached to the pyridine ring. The hydrogen bond with GLN711 was via the nitrogen triple bond with the carbon next to the pyridine ring. The hydrogen bond with THR755 was established via the oxygen group attached to the imidazolidine ring. The CF_3 group's F formed three halogen bonds with the amino acid residues PRO682 and GLU681. ARG752 forms two carbon-hydrogen bonds, one with the nitrogen of the pyridine ring and the other with the oxygen attached to the imidazolidine ring. The first carbon-hydrogen

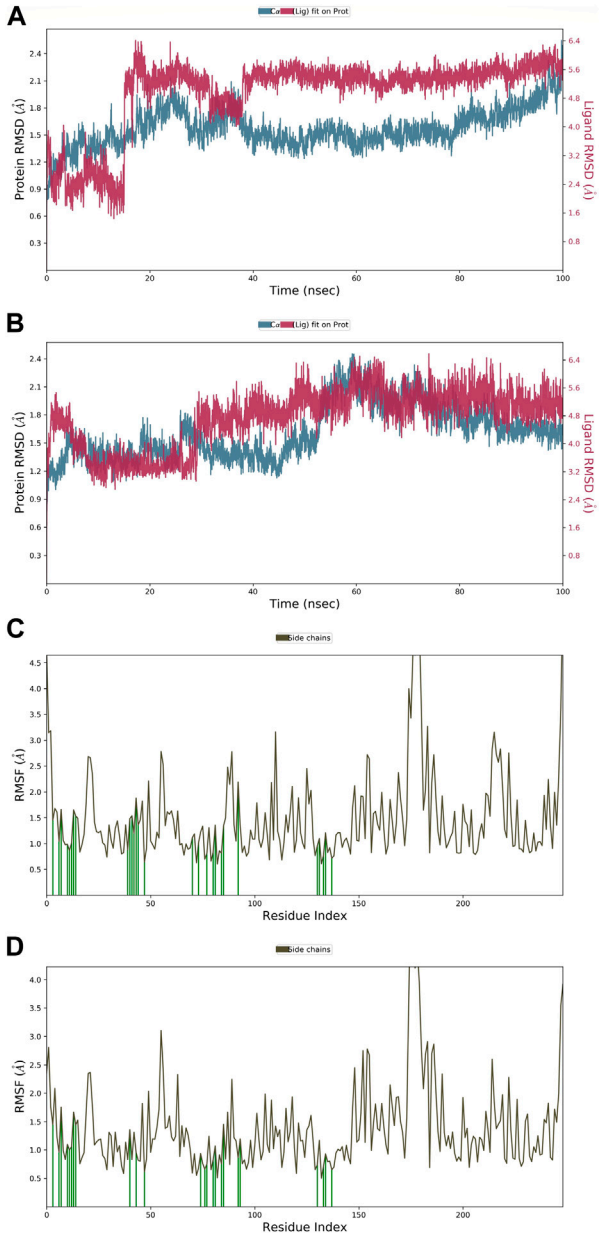

FIGURE 4
The root mean square deviation (RMSD) of the protein relative to the starting complexes during the 100 nS MD trajectory for APL43 **(A)** and APL80 **(B)**; The root mean square fluctuation (RMSF) of the protein during 100 ns MD, representing local changes along the protein chain for APL43 **(C)** and APL80 **(D)**.

bond with ARG752 was with the nitrogen of the pyridine ring, and the other was with the oxygen attached to the imidazolidine ring. ARG752 also formed an alkyl bond with the pyridine ring. ALA748 formed another alkyl bond with the carbon of the CF_3 group. Lastly, there is a pi-Sulfur bond between the THR751 and the sulfur attached to the imidazolidine ring. 2D and 3D interactions of the ligand APL are shown in Figures 2I, 3I, respectively.

In conclusion, ligands APL19, APL35, APL43, APL76, and APL80 show good docking scores of −7.7, −7.1, −6.6, −7.2, and −8.0 *Kcal/mol*, respectively (Table 5). In contrast, APL has a binding affinity score of −7.1 *Kcal/mol*. We found that hydrogen bond interactions in APL involved the two common protein residues (ARG752 and GLN711), which are similar to these ligands. According to the literature, docking studies of APL were carried out with protein (*PDB ID: 5T8E*). APL formed the hydrogen bonding and carbon hydrogen bonding with the ARG752, THR755, and GLN711 protein residues. On the other hand, it shows interaction with ALA748 and ARG752 through halogenic and hydrophobic pi-alkyl interactions, respectively (Ikwu et al., 2020). ARG752 and GLN711 protein residues were the active residues of protein which might be the reason behind the antagonistic activity toward the AR. The QED, MCE-18, docking score, and docking interactions of selected newer APL analogues (APL19, APL35, APL43, APL76, and APL80) are shown in Table 5.

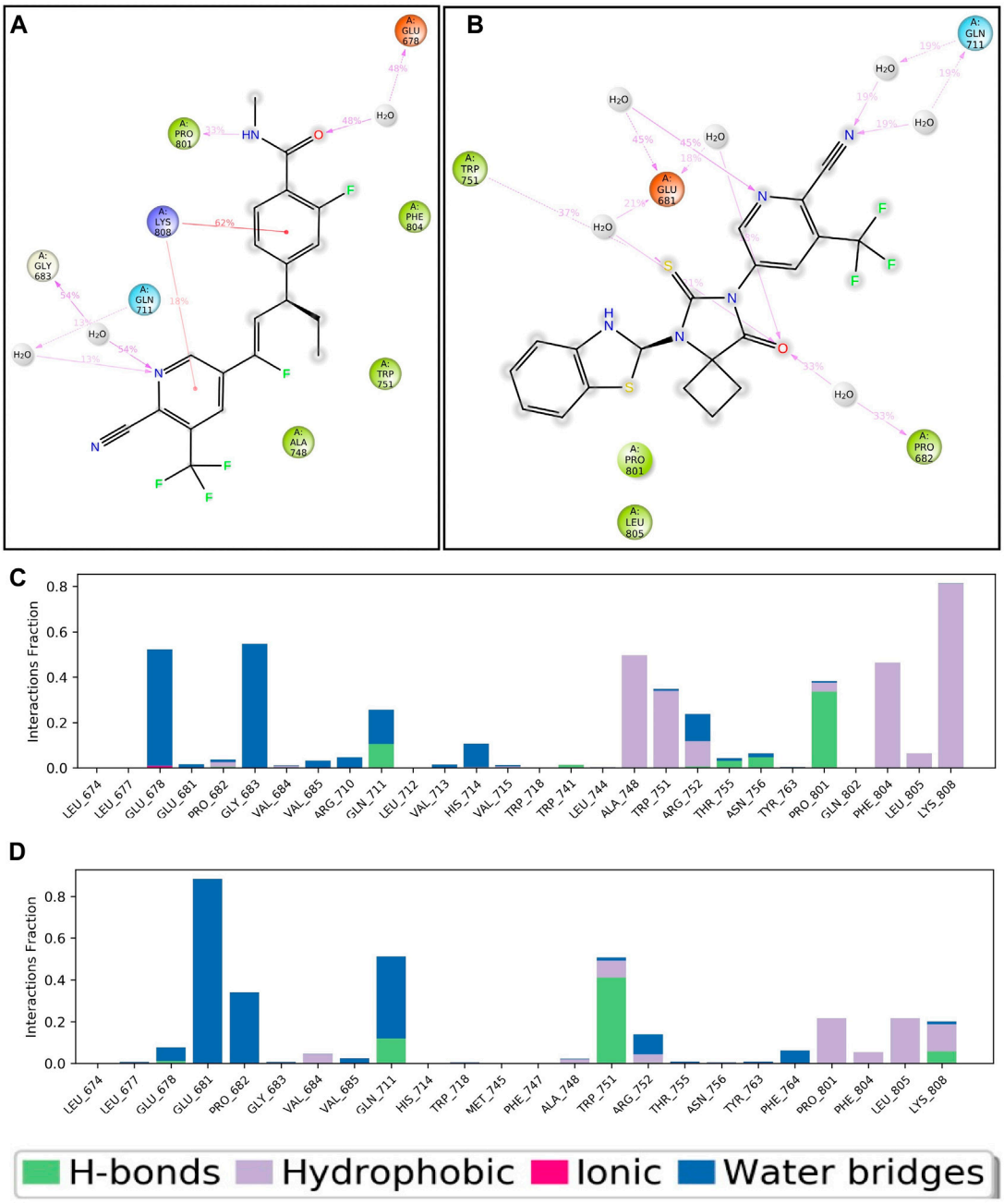

FIGURE 5
Two-dimensional interaction of APL43 **(A)** and APL80 **(B)** with respect to the protein during 100–nS MD simulation; Histogram represents the hydrogen bonding interactions of APL43 **(C)** and APL80 **(D)** with respect to residues of protein.

3.8 Molecular dynamics simulation

The MD simulation was performed to examine the dynamic behavior of atoms and molecules. It is a methodology and collection of algorithms that calculate and predict the stability of compounds. It is a very effective independent method for accurately capturing molecular and atomistic-level changes. This mechanism is very important for studying how ligand molecules interact with proteins to understand the stability of protein-ligand complexes. Structure-based drug design, which uses standard methods such as molecular docking and virtual screening, has yielded a selection of potential medications in the field of bioscience. The MD simulation is crucial for comprehending the ligand's dynamic behavior and its stability in relation to the protein. We used the simulation interaction diagram (SID) to examine the MD simulation trajectories of a 100 nS SPC water model-based simulation. This allowed us to get insights into the deviation, fluctuation, and intermolecular interaction occurring throughout the simulation. The MD simulations for ligands APL19, APL35, APL43, APL76, and APL80 were carried out. The MD simulation of ligand

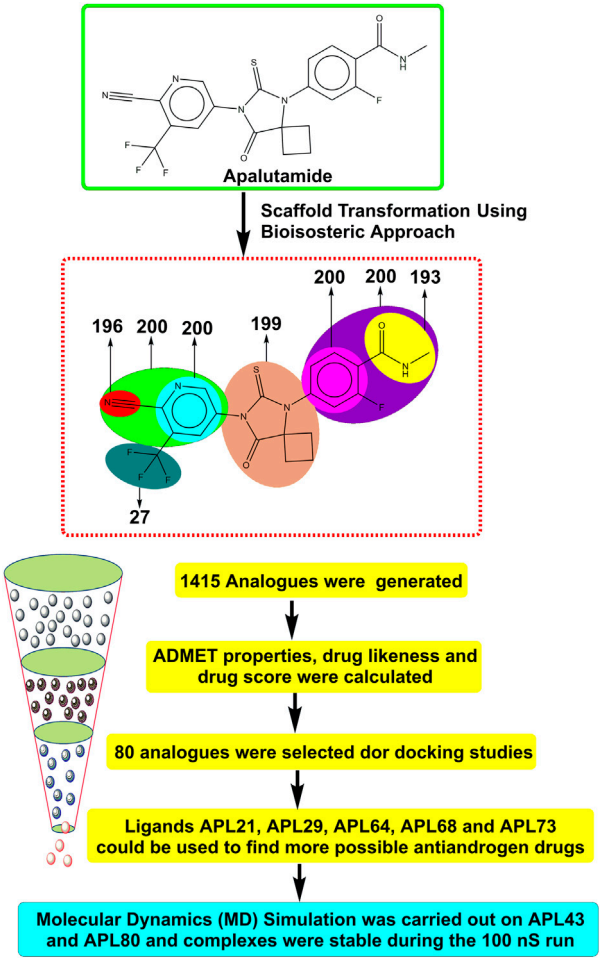

FIGURE 6
Overall workflow of the present study.

APL43 and APL80 were found stable. MD runs for the other molecules (APL19, APL35, and APL76) did not fall within the desired range.

3.8.1 RMSD and RMSF

The root mean square deviation (RMSD) quantifies the average displacement of a chosen set of atoms in a certain frame compared to a reference frame. The calculation is performed for every frame in the trajectory. The RMSD value was used to calculate the deviation in the protein's backbone (C and N) during the 100 nS simulative period. Throughout the MD run, very slight or minute fluctuations in RMSD values were observed as compared to the protein backbone. In the case of a protein in a complex with a ligand (APL43), the backbone RMSD initially fluctuated from 0 to 0.7 Å in 0.50 nS, and the ligand fluctuated 0.8 Å (Figure 4A). We saw that when the protein was in a complex with the ligand (APL80), the protein RMSD changed from 0 to 0.8 Å in 0.50 nS, while the ligand's changed by 1.1 Å (Figure 4B). The overall RMSD is satisfactory for both complexes. After the initial fluctuation, the complexes throughout the MD run were found stable. The androgen receptor modulator protein in complex with APL43 shows an average RMSD of 1.57 Å, while the ligand shows 2.03 Å at 100 nS. While the androgen receptor modulator protein in complex with APL80 shows an average RMSD of 1.61 Å, the ligand shows 0.75 Å at 100 nS. Initially, we observed a lower RMSD deviation (average RMSD) from 0 to 15 nS; we noticed a slight fluctuation for two frames, followed by stable complexes (APL43) from 15 to 40 nS. After that, we observed a stable RMSD value with minute deviations from 40 to 100 nS. Conversely, we observed a lower RMSD deviation (average RMSD) for APL80 from 0 to 30 nS, a slight fluctuation for three frames, and stable complexes (APL80) from 30 to 60 nS. After that, we observed a stable RMSD value with minute deviations from 60 to 100 nS. This means that both complexes are completely stable for the 100 nS simulation.

Later, the root mean square fluctuation (or RMSF) analysis gives the complex fluctuation with time evolution against amino acid residues. Figures 4C, D show the protein-RMSF and protein-ligand contacts for the complete simulation. We showed how the androgen receptor modulator works with APL43 and APL80 by focusing on how their proteins interact with ligands during 100 nS simulation. On the protein-RMSF plot, peaks indicate areas of the protein that fluctuate the most during the simulation. Typically, we will observe that the tails (N- and C-terminal) fluctuate more than any other part

of the protein. Secondary structure elements like alpha helices and beta strands are usually more rigid than the unstructured part of the protein and thus fluctuate less than the loop regions. Green-colored vertical bars mark protein residues that interact with the ligand. In proteins, some amino acid residues have fluctuated (Figures 4C, D). The rest of the amino acid residues have shown a significantly lower level of fluctuations. During the complete 100 nS simulation, ligands APL43 and APL80 showed interaction with lower fluctuation due to the formation of favorable interactions with different amino acid residues. Furthermore, the overall observed fluctuation is very low, providing valuable information for future studies against proteins using both ligands, APL43 and APL80. In addition, the protein molecule is stiffer because of its H-bonds, pi-pi stacking, and secondary structure elements. In both conditions, the fluctuation shown in Figures 4C, D (for ligand APL43 and APL80) is found below 2 Å, indicating promising results.

3.8.2 Intermolecular interactions

Throughout the entire simulation process, it is crucial to understand the atoms' interactions with each other in order to predict how the protein and ligand will bind. Throughout the entire 100 nS simulation, we examined numerous binding interactions between the protein and ligand molecules. These included hydrogen bonds, ionic interactions, hydrophobic contact, and the salt bridge. This study demonstrates the involvement of numerous intramolecular interactions, including hydrogen bonds, phosphorylation, and water molecules in water bridges. Figure 5A depicts the ligand-APL43 interaction with protein amino acids and other relevant fragments. Even though we have not noticed any direct interaction with carbon molecules, the interaction with the N, O, and NH groups formed hydrophilic, hydrophobic, and hydrogen bonding interactions with respective percentiles. Furthermore, the direction of the arrows shows both donors and acceptors. The H_2O molecules interacted widely, forming water bridges, while the amino acids interacted directly, as well as through hydrophilic and other interactions. There are three water molecules involved in the interaction, along with GLU678, GLY683, and GLN711. The GLN711 showed a hydrogen bond, LYS808 forms a pi-cation bond with the phenyl and pyridinyl rings, PRO801 forms a single hydrophobic bond, and GLU678 forms a pi-anion bond (Figure 5A).

Figure 5B shows the APL80 ligand interaction with protein amino acids. The interaction with the O, S, and N groups resulted in hydrophilic, hydrophobic, and hydrogen bonding interactions with respective percentiles. Furthermore, the direction of the arrows shows both donors and acceptors. The H_2O molecules interacted widely, forming water bridges, while the amino acids interacted directly, as well as through hydrophilic and other interactions. There are six water molecules involved in the interaction, along with GLU681, TRP751, PRO682, and GLN711. GLN711 formed the hydrogen bond, GLU681 made the pi-anion bond, and PRO682 and TRP751 made the hydrophobic bond. During 100 nS run, we displayed the percentiles of interaction for each type of bond. Figures 5C, D show more statistical explanations by dividing protein-ligand interactions (contacts) into four groups: ionic, hydrophobic, hydrogen bonds, and water bridges. Overall, the MD simulation results suggested that both complexes are stable and have lower RMDS, RMSF, and good interactions. The overall workflow of the study is summarized in Figure 6.

4 Conclusion

APL is one of the non-steroidal antiandrogen drug used in the management of PC. During therapy with APL, it causes several toxicities. So, structure modification of APL is required to get novel and less toxic analogues. By using the bioisosteric approach, *in silico* design of APL analogues was carried out using MolOpt. We selected newer bioisosteres of APL to calculate the pharmacokinetic and toxicological properties using ADMETlab 2.0. Additionally, the DL and DS scores of the designed analogues of APL were also computed using PEO. Docking studies of selected analogues were also carried out using ADV and Discovery Studio. Analogues APL19, APL35, APL43, APL76, and APL80 have shown good interactions with the protein (PDB ID: *5T8E*), which is similar to the standard drug (APL). The common amino acid residues ARG752, GLN711, THR755, GLU681, and PRO682 might play a crucial role in the binding affinity and antagonistic activity of androgen receptors. The molecular docking study has shown promising results with many ligands, such as APL19, APL35, APL43, APL76, and APL80. We ran the MD simulation on two ligands. We only selected the top two ligands for further simulation using the SPC water model. The MD simulation results for both ligands, APL43 and APL80, were promising. According to the data obtained from ADMET, DL, DS score, and docking studies, the ligands APL19, APL35, APL43, APL76, and APL80 can be used as potential antiandrogen agents for the treatment of prostate cancer. Further work is in progress in order to evaluate this hypothesis as an antiandrogen agent in the management of PC.

Data availability statement

The original contributions presented in the study are included in the article/Supplementary Material, further inquiries can be directed to the corresponding author.

Author contributions

AKG: Data curation, Investigation, Methodology, Writing–original draft; SKJ: Conceptualization, Formal Analysis, Supervision, Validation, Writing–review and editing; YV: Formal Analysis, Investigation, Project Administration, Validation, Writing–review and editing; SA: Formal Analysis, Validation, Writing–review and editing; NK: Data curation, Investigation, Methodology, Writing–review and editing.

Funding

The author(s) declare that no financial support was received for the research, authorship, and/or publication of this article. AKG, Senior Research Fellow (SRF), expressed his gratitude to the Indian Council of Medical Research (ICMR), New Delhi, for the award of SRF [Award Number: BMI/11 (89)/2022].

Acknowledgments

The authors wish to thank the Head, Department of Pharmacy, Guru Ghasidas Vishwavidyalaya (A Central University), Bilaspur (C.G.), India, for providing the required facilities to perform the research work. The author, SA, would like to express his gratitude to the Deanship of Research and Graduate Studies at King Khalid University, Abha, Saudi Arabia, for funding this work through small group research under grant number RGP1/161/45.

Conflict of interest

The authors declare that the research was conducted in the absence of any commercial or financial relationships that could be construed as a potential conflict of interest.

Publisher's note

All claims expressed in this article are solely those of the authors and do not necessarily represent those of their affiliated organizations, or those of the publisher, the editors and the reviewers. Any product that may be evaluated in this article, or claim that may be made by its manufacturer, is not guaranteed or endorsed by the publisher.

Supplementary material

The Supplementary Material for this article can be found online at: https://www.frontiersin.org/articles/10.3389/fchem.2024.1418975/full#supplementary-material

References

Alturki, N. A., Mashraqi, M. M., Alzamami, A., Alghamdi, Y. S., Alharthi, A. A., Asiri, S. A., et al. (2022). In-Silico Screening and Molecular Dynamics Simulation of Drug Bank Experimental Compounds against SARS-CoV-2. *Molecules* 27, 4391. doi:10.3390/molecules27144391

Asano, M., Hitaka, T., Imada, T., Yamada, M., Morimoto, M., Shinohara, H., et al. (2017). Synthesis and Biological Evaluation of Novel Selective Androgen Receptor Modulators (Sarms). Part II: Optimization of 4-(Pyrrolidin-1-Yl)Benzonitrile Derivatives. *Bioorg. Med. Chem. Lett.* 27 (9), 1897–1901. doi:10.1016/j.bmcl.2017.03.038

Banks, J. L., Beard, H. S., Cao, Y., Cho, A. E., Damm, W., Farid, R., et al. (2005). Integrated Modeling Program, Applied Chemical Theory (IMPACT). *J. Comput. Chem.* 26, 1752–1780. doi:10.1002/jcc.20292

Belderbos, B. P. S. I., Wit, R., Chien, C., Mitselos, A., Hellemans, P., Jiao, J., et al. (2018). An Open-Label, Multicenter, Phase Ib Study Investigating the Effect of Apalutamide on Ventricular Repolarization in Men with Castration-Resistant Prostate Cancer. *Cancer Chemother. Pharmacol.* 82, 457–468. doi:10.1007/s00280-018-3632-6

Belkahla, S., Nahvi, I., Biswas, S., Nahvi, I., and Amor, N. B. (2022). Advances and Development of Prostate Cancer, Treatment, and Strategies: A Systemic Review. *Front. Cell. Dev. Biol.* 10, 991330. doi:10.3389/fcell.2022.991330

Bickerton, G. R., Paolini, G. V., Besnard, J., Muresan, S., and Hopkins, A. L. (2012). Quantifying the Chemical Beauty of Drugs. *Nat. Chem.* 4 (2), 90–98. doi:10.1038/nchem.1243

Borno, H. T., and Small, E. J. (2019). Apalutamide and its Use in the Treatment of Prostate Cancer. *Future Oncol.* 15 (6), 591–599. doi:10.2217/fon-2018-0546

Bray, F., Laversanne, M., Weiderpass, E., and Soerjomataram, I. (2021). The Ever-Increasing Importance of Cancer as a Leading Cause of Premature Death Worldwide. *Cancer* 127 (16), 3029–3030. doi:10.1002/cncr.33587

Chen, S., Cao, Z., Prettner, K., Kuhn, M., Yang, J., Jiao, L., et al. (2023). Estimates and Projections of the Global Economic Cost of 29 Cancers in 204 Countries and Territories from 2020 to 2050. *JAMA Oncol.* 9 (4), 465–472. doi:10.1001/jamaoncol.2022.7826

Chi, K. N., Agarwal, N., Bjartell, A., Chung, B. H., Gomes, A. J. P. S., Given, R., et al. (2019). Apalutamide for Metastatic, Castration-Sensitive Prostate Cancer. *N. Engl. J. Med.* 381, 13–24. doi:10.1056/nejmoa1903307

Clegg, N. J., Wongvipat, J., Joseph, J. D., Tran, C., Ouk, S., Dilhas, A., et al. (2012). ARN-509: A Novel Antiandrogen for Prostate Cancer Treatment. *Cancer Res.* 72 (6), 1494–1503. doi:10.1158/0008-5472.can-11-3948

Dong, J., Wang, N. N., Yao, Z. J., Zhang, L., Cheng, Y., Ouyang, D., et al. (2018). ADMETlab: A Platform for Systematic ADMET Evaluation Based on a Comprehensively Collected ADMET Database. *J. Cheminform.* 10 (1), 29. doi:10.1186/s13321-018-0283-x

Feher, M., and Williams, C. I. (2012). Numerical Errors and Chaotic Behavior in Docking Simulations. *J. Chem. Inf. Model.* 52, 724–738. doi:10.1021/ci200598m

Ferlay, J., Colombet, M., Soerjomataram, I., Parkin, D. M., Piñeros, M., Znaor, A., et al. (2021). Cancer Statistics for the Year 2020: An Overview. *Int. J. Cancer* 149, 778–789. doi:10.1002/ijc.33588

Ferlay, J., Ervik, M., Lam, F., Laversanne, M., Colombet, M., Mery, L., et al. (2024). *Global Cancer Observatory: Cancer Today*. Lyon, France: International Agency for Research on Cancer. Available at: https://gco.iarc.who.int/today (Accessed June 14, 2024).

Forli, S., Huey, R., Pique, M. E., Sanner, M. F., Goodsell, D. S., and Olson, A. J. (2016). Computational Protein-Ligand Docking and Virtual Drug Screening with the AutoDock Suite. *Nat. Protoc.* 11 (5), 905–919. doi:10.1038/nprot.2016.051

Gan, Y., Li, L., Zhang, L., Yan, S., Gao, C., Hu, S., et al. (2018). Association between Shift Work and Risk of Prostate Cancer: A Systematic Review and Meta-Analysis of Observational Studies. *Carcinogenesis* 39 (2), 87–97. doi:10.1093/carcin/bgx129

Gao, Y., Liu, Y., Liu, Y., Peng, Y., Yuan, B., Fu, Y., et al. (2021). UHRF1 Promotes Androgen Receptor-Regulated CDC6 Transcription and Anti-Androgen Receptor Drug Resistance in Prostate Cancer through KDM4C-Mediated Chromatin Modifications. *Cancer Lett.* 520, 172–183. doi:10.1016/j.canlet.2021.07.012

Gillessen, S., Attard, G., Beer, T. M., Beltran, H., Bossi, A., Bristow, R., et al. (2018). Management of Patients with Advanced Prostate Cancer: The Report of the Advanced Prostate Cancer Consensus Conference APCCC 2017. *Eur. Urol.* 73 (2), 178–211. doi:10.1016/j.eururo.2017.06.002

Guida, F., Kidman, R., Ferlay, J., Schüz, J., Soerjomataram, I., Kithaka, B., et al. (2022). Global and Regional Estimates of Orphans Attributed to Maternal Cancer Mortality in 2020. *Nat. Med.* 28 (12), 2563–2572. doi:10.1038/s41591-022-02109-2

Harris, W. P., Mostaghel, E. A., Nelson, P. S., and Montgomery, B. (2009). Androgen Deprivation Therapy: Progress in Understanding Mechanisms of Resistance and Optimizing Androgen Depletion. *Nat. Clin. Pract. Urol.* 6 (2), 76–85. doi:10.1038/ncpuro1296

Huang, C., Li, C., Choi, P. Y., Nandakumar, K., and Kostiuk, L. W. (2011). A Novel Method for Molecular Dynamics Simulation in the Isothermal–Isobaric Ensemble. *Mol. Phys.* 109, 191–202. doi:10.1080/00268976.2010.513345

Huang, S., Yuan, J., Xie, Y., Qing, K., Shi, Z., Chen, G., et al. (2023a). Targeting Nano-Regulator Based on Metal–Organic Frameworks for Enhanced Immunotherapy of Bone Metastatic Prostate Cancer. *Cancer Nanotechnol.* 14 (1), 43. doi:10.1186/s12645-023-00200-y

Huang, X., Chen, X. X., Chen, X., Chen, Q. Z., Wang, L., Li, C., et al. (2023b). Feasibility of Anterior Lobe-Preserving Transurethral Enucleation and Resection of Prostate on Improving Urinary Incontinence in Patients with Benign Prostatic Hyperplasia: A Retrospective Cohort Study. *Medicine* 102 (7), e32884. doi:10.1097/MD.0000000000032884

Huang, R., Li, Y., Wu, H., Liu, B., Zhang, X., and Zhang, Z. (2023c). 68Ga-PSMA-11 PET/CT versus 68Ga-PSMA-11 PET/MRI for the Detection of Biochemically Recurrent Prostate Cancer: A Systematic Review and Meta-Analysis. *Front. Oncol.* 13, 1216894. doi:10.3389/fonc.2023.1216894

Hughes, D. L. (2020). Review of Synthetic Routes and Crystalline Forms of the Antiandrogen Oncology Drugs Enzalutamide, Apalutamide, and Darolutamide. *Org. Process Res. Dev.* 24 (3), 347–362. doi:10.1021/acs.oprd.0c00005

Ikwu, F. A., Shallangwa, G. A., and Mamza, P. A. (2020). QSAR, QSTR, and Molecular Docking Studies of the Anti-Proliferative Activity of Phenylpiperazine Derivatives against DU145 Prostate Cancer Cell Lines. *Beni-Suef. Univ. J. Basic Appl. Sci.* 9, 35. doi:10.1186/s43088-020-00054-y

Karami, T. K., Hailu, S., Feng, S., Graham, R., and Gukasyan, H. J. (2022). Eyes on Lipinski's Rule of Five: A New "Rule of Thumb" for Physicochemical Design Space of Ophthalmic Drugs. *J. Ocul. Pharmacol. Ther.* 38 (1), 43–55. doi:10.1089/jop.2021.0069

Kelly, W. K., Slovin, S., and Scher, H. I. (1997). Steroid Hormone Withdrawal Syndromes. Pathophysiology and Clinical Significance. *Urol. Clin. North Am.* 24 (2), 421–431. doi:10.1016/s0094-0143(05)70389-x

Kemmish, H., Fasnacht, M., and Yan, L. (2017). Fully Automated Antibody Structure Prediction Using BIOVIA Tools: Validation Study. *PLoS One* 12, e0177923. doi:10.1371/journal.pone.0177923

Kulothungan, V., Sathishkumar, K., Leburu, S., Ramamoorthy, T., Stephen, S., Basavarajappa, D., et al. (2022). Burden of Cancers in India - Estimates of Cancer Crude Incidence, YLLs, YLDs and DALYs for 2021 and 2025 Based on National Cancer Registry Program. *BMC Cancer* 22, 527. doi:10.1186/s12885-022-09578-1

Lagu, S. B., Yejella, R. P., Nissankararao, S., Bhandare, R. R., Golla, V. S., Lokesh, B. V. S., et al. (2022). Antitubercular Activity Assessment of Fluorinated Chalcones, 2-Aminopyridine-3-Carbonitrile and 2-Amino-4H-Pyran-3-Carbonitrile Derivatives: *In Vitro*, Molecular Docking and In-Silico Drug Likeliness Studies. *PLoS One* 17 (6), e0265068. doi:10.1371/journal.pone.0265068

Lei, T., Li, Y., Song, Y., Li, D., Sun, H., and Hou, T. (2016). ADMET Evaluation in Drug Discovery: 15. Accurate Prediction of Rat Oral Acute Toxicity Using Relevance Vector Machine and Consensus Modeling. *J. Cheminform.* 8, 6. doi:10.1186/s13321-016-0117-7

López-Abad, A., Backhaus, M. R., Gómez, G. S., Avellaneda, E. C., Alarcón, C. M., Cubillana, P. L., et al. (2024). Real-World Prostate-Specific Antigen Reduction and Survival Outcomes of Metastatic Hormone-Sensitive Prostate Cancer Patients Treated with Apalutamide: An Observational, Retrospective, and Multicentre Study. *Prostate Int.* 12 (1), 20–26. doi:10.1016/j.prnil.2023.10.003

Lv, Z., Hu, J., Huang, M., Pan, G., Xu, G., and Yang, M. (2024). Molecular Mechanisms of Cadmium-Induced Cytotoxicity in Human Ovarian Granulosa Cells Identified Using Integrated Omics. *Ecotoxicol. Environ. Saf.* 272, 116026. doi:10.1016/j.ecoenv.2024.116026

Manjunatha, M. R., Shandil, R., Panda, M., Sadler, C., Ambady, A., Panduga, V., et al. (2019). Scaffold Morphing to Identify Novel DprE1 Inhibitors with Antimycobacterial Activity. *ACS Med. Chem. Lett.* 10 (10), 1480–1485. doi:10.1021/acsmedchemlett.9b00343

Mohler, J. L., Titus, M. A., Bai, S., Kennerley, B. J., Lih, F. B., Tomer, K. B., et al. (2011). Activation of the Androgen Receptor by Intratumoral Bioconversion of Androstanediol to Dihydrotestosterone in Prostate Cancer. *Cancer Res.* 71 (4), 1486–1496. doi:10.1158/0008-5472.can-10-1343

Murray, N. P., Aedo, S., Fuentealba, C., Reyes, E., and Salazar, A. (2022). The CAPRA-S Score and Immune Dysfunction as a Guide to Outcome in Men Treated with Prostatectomy Radical as Mono-Therapy for Prostate Cancer. *Arch. Esp. Urol.* 75 (6), 507–516. doi:10.56434/j.arch.esp.urol.20227506.75

O'Boyle, N. M., Banck, M., James, C. A., Morley, C., Vandermeersch, T., and Hutchison, G. R. (2011). Open Babel: An Open Chemical Toolbox. *J. Cheminformatics* 3, 33. doi:10.1186/1758-2946-3-33

Pérez-Ruixo, C., Pérez-Blanco, J. S., Chien, C., Yu, M., Ouellet, D., Pérez-Ruixo, J. J., et al. (2020). Population Pharmacokinetics of Apalutamide and its Active Metabolite N-Desmethyl-Apalutamide in Healthy and Castration-Resistant Prostate Cancer Subjects. *Clin. Pharmacokinet.* 59 (2), 229–244. doi:10.1007/s40262-019-00808-7

Pilon, D., Behl, A. S., Ellis, L. A., Robitaille, M. N., Lefebvre, P., and Dawson, N. A. (2017). Assessment of Real-World Central Nervous System Events in Patients with Advanced Prostate Cancer Using Abiraterone Acetate, Bicalutamide, Enzalutamide, or Chemotherapy. *Am. Health Drug Benefits* 10 (3), 143–153.

Sander, T., Freyss, J., Korff, M. V., Reich, J. R., and Rufener, C. (2009). OSIRIS, an Entirely in-House Developed Drug Discovery Informatics System. *J. Chem. Inf. Model.* 49 (2), 232–246. doi:10.1021/ci800305f

Sathishkumar, K., Chaturvedi, M., Das, P., Stephen, S., and Mathur, P. (2022). Cancer Incidence Estimates for 2022 and projection for 2025: Result from National Cancer Registry Programme, India. *Indian J. Med. Res.* 156 (4and5), 598–607. doi:10.4103/ijmr.ijmr_1821_22

Shan, J., and Ji, C. (2020). MolOpt: A Web Server for Drug Design Using Bioisosteric Transformation. *Curr. Comput-Aided Drug Des.* 16 (4), 460–466. doi:10.2174/1573409915666190704093400

Shen, W., Pei, P., Zhang, C., Li, J., Han, X., Liu, T., et al. (2023). A Polymeric Hydrogel to Eliminate Programmed Death-Ligand 1 for Enhanced Tumor Radio-Immunotherapy. *ACS Nano* 17 (23), 23998–24011. doi:10.1021/acsnano.3c08875

Slovin, S., Clark, W., Carles, J., Krivoshik, A., Park, J. W., Wang, F., et al. (2018). Seizure Rates in Enzalutamide-Treated Men with Metastatic Castration-Resistant Prostate Cancer and Risk of Seizure: the UPWARD Study. *JAMA Oncol.* 4 (5), 702–706. doi:10.1001/jamaoncol.2017.3361

Stabile, R. G., and Dicks, A. P. (2003). Microscale Synthesis and Spectroscopic Analysis of Flutamide, an Antiandrogen Prostate Cancer Drug. *J. Chem. Educ.* 80 (12), 1439–1443. doi:10.1021/ed080p1439

Subbaiah, M. A. M., and Meanwell, N. A. (2021). Bioisosteres of the Phenyl Ring: Recent Strategic Applications in Lead Optimization and Drug Design. *J. Med. Chem.* 64 (19), 14046–14128. doi:10.1021/acs.jmedchem.1c01215

Sung, H., Ferlay, J., Siegel, R. L., Laversanne, M., Soerjomataram, I., Jemal, A., et al. (2021). Global Cancer Statistics 2020: GLOBOCAN Estimates of Incidence and Mortality Worldwide for 36 Cancers in 185 Countries. *CA Cancer J. Clin.* 71 (3), 209–249. doi:10.3322/caac.21660

Sutil, R. S., Ruiz, J. S., Gomez, B. G., Romero-Otero, J., Garcia-Gonzalez, L., Ojeda, J. M. D., et al. (2021). Seizures and Neuropsychiatric Toxicity in Patients with Non-Metastatic CRPC Treated with New Antiandrogens: Systematic Review and Meta-Analysis. *Oncol. Res. Treat.* 44 (4), 154–163. doi:10.1159/000515014

Tran, C., Ouk, S., Clegg, N. J., Chen, Y., Watson, P. A., Arora, V., et al. (2009). Development of a Second-Generation Antiandrogen for Treatment of Advanced Prostate Cancer. *Science* 324 (5928), 787–790. doi:10.1126/science.1168175

Trott, O., and Olson, A. J. (2010). AutoDock Vina: Improving the Speed and Accuracy of Docking with A New Scoring Function, Efficient Optimization, and Multithreading. *J. Comput. Chem.* 31, 455–461. doi:10.1002/jcc.21334

Van Der Spoel, D., Lindahl, E., Hess, B., Groenhof, G., Mark, A. E., and Berendsen, H. J. C. (2005). GROMACS: Fast, Flexible, and Free. *J. Comput. Chem.* 26, 1701–1718. doi:10.1002/jcc.20291

Wang, N. N., Dong, J., Deng, Y. H., Zhu, M. F., Wen, M., Yao, Z. J., et al. (2016). ADME Properties Evaluation in Drug Discovery: Prediction of Caco-2 Cell Permeability Using a Combination of NSGA-II and Boosting. *J. Chem. Inf. Model.* 56 (4), 763–773. doi:10.1021/acs.jcim.5b00642

Xiong, G., Wu, Z., Yi, J., Fu, L., Yang, Z., Hsieh, C., et al. (2021). ADMETlab 2.0: An Integrated Online Platform for Accurate and Comprehensive Predictions of ADMET Properties. *Nucleic. Acids Res.* 49 (W1), W5–W14. doi:10.1093/nar/gkab255

Zhang, A., Zhang, J., Plymate, S., and Mostaghel, E. A. (2016). Classical and Non-Classical Roles for Pre-Receptor Control of DHT Metabolism in Prostate Cancer Progression. *Horm. Cancer.* 7, 104–113. doi:10.1007/s12672-016-0250-9

Zheng, J., Yue, R., Yang, R., Wu, Q., Wu, Y., Huang, M., et al. (2022). Visualization of Zika Virus Infection via a Light-Initiated Bio-Orthogonal Cycloaddition Labeling Strategy. *Front. Bioeng. Biotechnol.* 1051, 940511. doi:10.3389/fbioe.2022.940511

Zhu, J., Jiang, X., Luo, X., Zhao, R., Li, J., Cai, H., et al. (2023). Combination of Chemotherapy and Gaseous Signaling Molecular Therapy: Novel β-elemene Nitric Oxide Donor Derivatives against Leukemia. *Drug Dev. Res.* 84 (4), 718–735. doi:10.1002/ddr.22051

frontiers | Frontiers in Chemistry

TYPE Original Research
PUBLISHED 07 August 2024
DOI 10.3389/fchem.2024.1424017

OPEN ACCESS

EDITED BY
Afzal Basha Shaik,
Jawaharlal Nehru Technological University,
Kakinada, India

REVIEWED BY
Adil Shareef Mohammed,
Temple University, United States
Vamshi Krishna Reddy Sammeta,
National Cancer Institute at Frederick (NIH),
United States

*CORRESPONDENCE
Wagdy M. Eldehna,
wagdy2000@gmail.com
Maha-Hamadien Abdulla,
mabdulla@ksu.edu.sa
Jaroslaw Dziadek,
jdziadek@cbm.pan.pl

RECEIVED 26 April 2024
ACCEPTED 12 June 2024
PUBLISHED 07 August 2024

CITATION
Sabt A, Abdulla M-H, Ebaid MS, Pawełczyk J, Abd El Salam HA, Son NT, Ha NX, Vaali Mohammed M-A, Traiki T, Elsawi AE, Dziadek B, Dziadek J and Eldehna WM (2024), Identification of 2-(*N*-aryl-1,2,3-triazol-4-yl) quinoline derivatives as antitubercular agents endowed with InhA inhibitory activity. *Front. Chem.* 12:1424017. doi: 10.3389/fchem.2024.1424017

Identification of 2-(*N*-aryl-1,2,3-triazol-4-yl) quinoline derivatives as antitubercular agents endowed with InhA inhibitory activity

Ahmed Sabt[1], Maha-Hamadien Abdulla[2]*, Manal S. Ebaid[1,3], Jakub Pawełczyk[4], Hayam A. Abd El Salam[5], Ninh The Son[6,7], Nguyen Xuan Ha[8], Mansoor-Ali Vaali Mohammed[2], Thamer Traiki[2], Ahmed E. Elsawi[9], Bozena Dziadek[10], Jaroslaw Dziadek[4]* and Wagdy M. Eldehna[9,11]*

[1]Chemistry of Natural Compounds Department, Pharmaceutical and Drug Industries Research Institute, National Research Center, Dokki, Egypt, [2]Colorectal Research Chair, Department of Surgery, College of Medicine, King Saud University, Riyadh, Saudi Arabia, [3]Department of Chemistry, College of Science, Northern Border University, Arar, Saudi Arabia, [4]Laboratory of Genetics and Physiology of Mycobacterium, Institute of Medical Biology of the Polish Academy of Sciences, Lodz, Poland, [5]Department of Green Chemistry, National Research Center, Dokki, Egypt, [6]Institute of Chemistry, Vietnam Academy of Science and Technology (VAST), Hanoi, Vietnam, [7]Department of Chemistry, Graduate University of Science and Technology, Hanoi, Vietnam, [8]Institute of Natural Products Chemistry, Vietnam Academy of Science and Technology, Hanoi, Vietnam, [9]Department of Pharmaceutical Chemistry, Faculty of Pharmacy, Kafrelsheikh University, Kafrelsheikh, Egypt, [10]Department of Molecular Microbiology, Faculty of Biology and Environmental Protection, University of Lodz, Lodz, Poland, [11]Department of Pharmaceutical Chemistry, Faculty of Pharmacy, Pharos University in Alexandria, Alexandria, Egypt

The spread of drug-resistant tuberculosis strains has become a significant economic burden globally. To tackle this challenge, there is a need to develop new drugs that target specific mycobacterial enzymes. Among these enzymes, InhA, which is crucial for the survival of *Mycobacterium tuberculosis*, is a key target for drug development. Herein, 24 compounds were synthesized by merging 4-carboxyquinoline with triazole motifs. These molecules were then tested for their effectiveness against different strains of tuberculosis, including *M. bovis BCG*, *M. tuberculosis*, and *M. abscessus*. Additionally, their ability to inhibit the InhA enzyme was also evaluated. Several molecules showed potential as inhibitors of *M. tuberculosis*. Compound **5n** displayed the highest efficacy with a MIC value of 12.5 μg/mL. Compounds **5g**, **5i**, and **5n** exhibited inhibitory effects on InhA. Notably, **5n** showed significant activity compared to the reference drug Isoniazid. Molecular docking analysis revealed interactions between these molecules and their target enzyme. Additionally, the molecular dynamic simulations confirmed the stability of the complexes formed by quinoline-triazole conjugate **5n** with the InhA. Finally, **5n** underwent *in silico* analysis to predict its ADME characteristics. These findings provide promising insights for developing novel small compounds that are safe and effective for the global fight against tuberculosis.

KEYWORDS

quinoline, triazole, biological evaluations, molecular docking, MD simulation

1 Introduction

Since its identification in 1882, *Mycobacterium tuberculosis* (MTB), commonly referred to as Koch's *bacillus*, has continued to exert a significant impact on global health (Barberis et al., 2017). Tuberculosis (TB), caused by the bacterium MTB is consistently listed among the leading 10 causes of mortality worldwide (Ravimohan et al., 2018). At present, approximately 1.7 billion people, constituting 23% of the world's population, grapple with MTB, resulting in over 10 million new TB cases annually (Daley, 2019). Current TB treatment is lengthy, arduous, and associated with numerous side effects; a course of antibiotics is typically prescribed for a duration of 6–9 months for drug-susceptible tuberculosis, while cases of multidrug-resistant tuberculosis (MDR-TB) or instances of emerging drug resistance may necessitate treatment durations of 9–20 months (Esmail et al., 2014). A strain of tuberculosis that exhibits resistance to the two primary drugs, rifampicin and isoniazid (INH), is classified as MDR-TB (Seung et al., 2015). Conversely, the extensively drug-resistant tuberculosis strain (XDR-TB) represents an MDR-TB form that is resistant not only towards additional fluoroquinolones but also to at least one of levofloxacin, moxifloxacin, bedaquiline, and linezolid (WHO Report, 2020).

TB agents cannot reach the target site due to the intricate structure and poor permeability of mycobacteria's cell envelope (Jackson, 2014). Fatty acid synthase type I and type II (FAS-I and FAS-II) control the synthesis of the mycobacterial cell envelope (Marrakchi et al., 2000; Lu and Tonge, 2008). While FAS-I is exclusive to eukaryotic cells, the FAS-II enzyme emerges as a viable candidate for pharmaceutical development. Enoyl acyl carrier protein reductase (InhA), an enzyme of the FAS-II system, assumes a pivotal role in the saturation of double bonds in fatty acid chains linked to acyl carrier protein (ACP) (Rožman et al., 2017). Isoniazid, a primary treatment for tuberculosis, inhibits

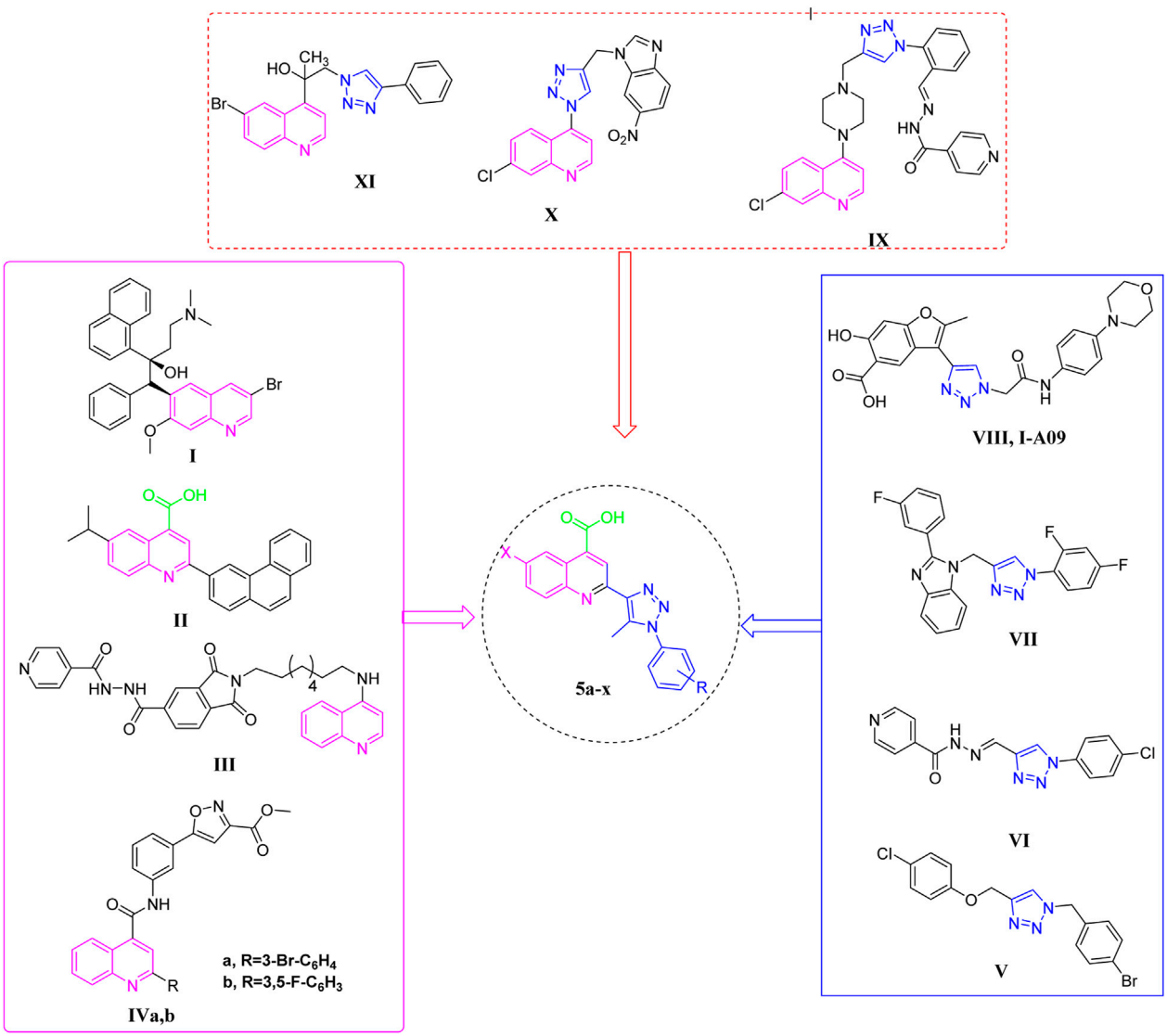

FIGURE 1
Reported antitubercular agents containing bioactive cores quinoline (**I-IV**), triazoles (**V-VIII**), quinoline-triazole hybrids (**IX-XI**), and our newly designed compounds (5a-x).

the enzyme InhA, thereby blocking mycolic acid production (Dessen et al., 1995). However, for INH to exhibit its pharmacological activity, it must undergo an activation process facilitated by the catalase-peroxidase enzyme KatG. Such a process entails the covalent INH binding to the NADH cofactor located in the InhA binding cavity (Munir et al., 2021). Over time, different strains of MTB have acquired resistance to INHdue to genetic mutations in the KatG gene (Muthaiah et al., 2017). Consequently, researchers have been motivated to explore new compounds that directly target InhA without relying on KatG activation (Almeida Da Silva and Palomino, 2011).

Quinoline is a commonly occurring structural framework present in many natural anti-tuberculosis products and medications (Keri and Patil, 2014), besides its diverse biological effects (Mohamede et al., 2015; Abdelrahman et al., 2022; Elbadawi et al., 2022; Elkaeed et al., 2022; Sabt et al., 2023a; Sabt et al., 2023b; Khaleel et al., 2024). Bedaquiline **I** (TMC207, Sirturo) (Figure 1) which contains a diarylquinoline core, received approval from the US-FDA for the treatment of pulmonary MDR-TB, marking the end of a 40-year delay. As an inhibitor of ATP synthase, this compound exhibits remarkable potency against both replicating and non-replicating strains (Pym et al., 2016). 1n 2023, Quimque and colleagues (Quimque et al., 2023) created and synthesized new arylated quinoline carboxylic acids (QCAs) that effectively inhibited the pathogen MTB. Compound **II** (Figure 1) was found to have the highest potency, with a minimum inhibitory concentration (MIC) of around 16 μM. Furthermore, anti-mycobacterial action was also demonstrated for 4-aminoquinoline-isoindolindione-isoniazidhybrid **III** (Figure 1), with a MIC of 5.1 μM (Zhou et al., 2010). Yaddanapudi and colleagues (Kumar Sahoo et al., 2022) exploited the quinoline motif and combined it with isoxazole alkyl ester to synthesize potent hybrid compounds **IVa-b** (Figure 1) with high activity towards MTB, exhibiting a MIC value of 1 μg/mL.

In recent times, triazole tethered small molecules have emerged as a significant category of organic compounds due to their diverse array of biological applications, e.g., anti-tubercular (Dhameliya et al., 2023), antibacterial (Li and Zhang, 2022), anti-viral (Senthil et al., 2015), and anticancer (Said et al., 2020; Azab et al., 2022; Elsawi et al., 2023; Elsawi et al., 2024). Notably, derivatives of 1,2,3-triazole have demonstrated promising anti-tubercular activity, prompting the development of numerous synthetic methodologies for their production (Zhang et al., 2017; El-Shoukrofy et al., 2023). Recent research has focused on the synthesis of a spectrum of small molecules containing conjugated 1,2,3-triazoles, which have exhibited various bioactivities. For instance, Shingate and colleagues have reported the inhibitory activities of 1,4-disubstituted 1,2,3-triazole-based molecules (Compound **V**, Figure 1) against MTB (Shaikh et al., 2015). Additionally, the clubbed 1,2,3-triazoles with INH, such as compound **VI** (Figure 1), have been identified as inhibitors of the MTB H37Rv strain MIC = 0.62 ug/mL (Boechat et al., 2011). Furthermore, the hybridization of fluorine-containing benzimidazole series and triazoles resulted in compound **VII** (Figure 1) that have also been reported to be a potent inhibitor of tuberculosis with MIC = 6.25 ug/mL (Gill et al., 2008). Notably, in clinical trials, **I-A09**, a compound containing triazole (**VIII**, Figure 1) is being studied as an anti-TB drug (Dadlani et al., 2022). In addition, certain quinoline-appended triazoles **IX-XI** (Figure 1) showed potent antitubercular actions (Alcaraz et al., 2022; Nyoni et al., 2023; Shinde et al., 2023).

Based on the facts mentioned above, along with the biological importance of quinoline and 1,2,3-triazole cores, coupled with the ongoing exploration for novel anti-infective compounds as potential anti-tubercular agents, the present investigation aims to explore the potential inhibitory impacts for 4-carboxy quinolino-triazole hybrids on the InhA target as anti-tuberculous agents. The current work employs a molecular hybridization strategy to design these molecules with the potential inhibitory antitubercular effects. The research involves the synthesis of a range of derivatives of 4-carboxy quinoline core, each featuring distinct substituents within the triazole moiety, such as halogens, methoxy, and nitro. Subsequently, the synthesized compounds undergo assessment for their effectiveness against various strains such as *Mycobacterium bovis BCG*, *M. abscesses*, and *M. tuberculosis*. The most potent molecules are subjected to further scrutiny for the inhibitory efficacy towards the MTB InhA. Furthermore, molecular docking investigations, as well as molecular dynamics (MD) studies, are performed to scrutinize the interactions between these biologically active analogues and the InhA enzyme. Lastly, the pharmacokinetics parameters for select analogues undergo exploration utilizing web-based ADMET predictors.

2 Results and discussion

2.1 Organic chemistry work

The synthetic procedures used to prepare the quinolino-triazole hybridized molecules **5** are described in Scheme 1. As previously reported, the key intermediates acetyl triazoles **3a-h** were prepared *via* a 1,3-dipolar cycloaddition reaction (Bekheit et al., 2021), that was performed through the diazotization of aniline derivatives **1a-h** before reacting with sodium azide to yield the corresponding azido derivatives **2a-h**. The reaction of azido compounds **2a-h** with acetylacetone was done in the presence of anhydrous potassium carbonate in refluxing ethanol, producing acetyl triazole derivatives **3a-h**. The desired products, quinoline triazole conjugates **5a-x**, were synthesized using Pfitzinger conditions (Elghamry and Al-Faiyz, 2016) by refluxing acetyl triazole derivatives **3a-h** with the isatin derivatives **4a-c** and adding an aqueous solution of KOH, then acidifying with dilute hydrochloric acid producing the 4-carboxyquinoline-triazole derivatives **5a-x**. The newly synthesized compounds underwent microanalyses and spectrum analysis, including 1H-NMR and 13C-NMR. The collected data aligned with the predetermined structures of the produced molecules.

2.2 Biological activities

2.2.1 Antimycobacterial assessment

All carboxy quinoline triazole compounds underwent assessment for potential anti-tubercular efficacy towards tubercle bacilli, encompassing both *M. bovis* BCG and MTB, as well as nontuberculous opportunistic pathogen represented by fast-growing mycobacteria, notably *M. abscessus*. This type of mycobacteria is

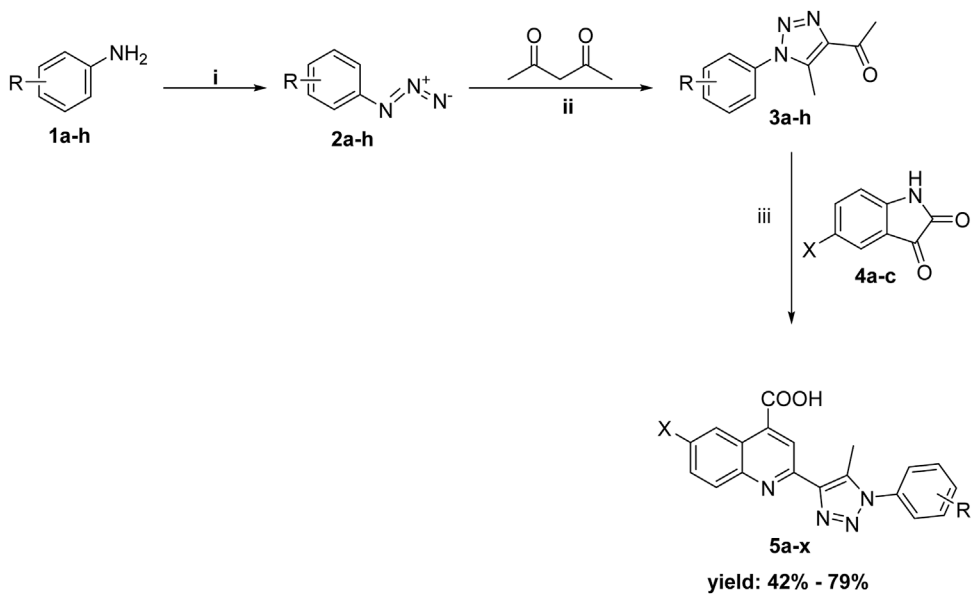

SCHEME 1
Synthesis of the target conjugates (**5a-x**); Reagents and conditions: (**i**) a) $NaNO_2$/HCl/0–5°C,1h, then r.t 1h b) NaN_3/stirring/rt/3h; (**ii**) K_2CO_3/EtOH/reflux; (**iii**) a) aq KOH/EtOH/reflux for 12 h, b) H_3O^+.

characterized by a heightened resistance to most anti-tuberculous drugs (Johansen et al., 2020). The primary screening was performed for all compounds at the same concentration of 125 μg/mL. None of the compounds displayed an anti-tubercular effect at the tested concentration against *M. abscessus*. Conversely, all 24 tested compounds suppressed the development of *M. bovis BCG* and MTB. Next, using MABA (microplate alamar blue assay), the MICs against MTB were assessed for all the reported molecules (Table 1). The majority of the compounds investigated demonstrated favorable to moderate anti-tubercular activity against MTB.

The derivative **5n** exhibited the most potent anti-tubercular effect toward MTB, with an MIC value of 12.5 μg/mL. Conversely, twelve of the compounds investigated (**5g**, **5i-l**, **5o**, **5q-t**, **5v**, and **7w**) demonstrated effective activity, with an MIC value equal 15 μg/mL. Additionally, seven compounds (**5b-d**, **5f**, **5m**, **5p**, and **5u**) displayed moderate anti-tubercular efficacy towards *Mycobacterium* (MIC = 62.5 μg/mL). The remaining derivatives (**5a**, **5e**, **5h**, and **5x**) exhibited lower activity, with the lowest MIC recorded at 125 μg/mL (Table 1). Moreover, compounds demonstrating the highest potency with MIC values ≤ 15 μg/mL underwent a more comprehensive assessment of their cytotoxicity effects. This evaluation adhered precisely to international standards (ISO 10993-5:2009(E)), employing L929 cells and the MTT protocol (Bekier et al., 2021). The determination of the half maximal inhibitory concentration (IC_{50}) values was carried out for 12 out of the 13 compounds tested, considering the occurrence of derivative precipitation in the growth medium for L929 cells (Table 1). With the exception of **5r**, the tested compounds showed low cytotoxicity at concentrations up to 10xMIC. For two compounds (**5g** and **5i**), the discriminatory index (IC_{50}/MIC) was identified at the level of 20.

Within the synthesized quinoline compounds with phenyltriazole substituents, compound **5g** containing a 4-bromo substituent showed the strongest anti-tubercular effects against *M. tuberculosis* with a MIC value of 15 μg/mL. Moreover, compounds **4b**, **5c**, **5d**, and **5f** with 4-methoxyphenyl, 3-chlorophenyl, 3-bromophenyl, and 4-chlorophenyl substituents, respectively exhibited decreased activity with MIC values of 62.5 μg/mL, whereas, compounds **5a**, **5e**, and **5h** with unsubstituted phenyltriazole, 4-fluorophenyl, and 4-nitrophenyl showed even lower activity with MIC values of 125 μg/mL.

In the case of 6-chloroquinoline compounds with phenyltriazole substituents, compound **5n** with a 4-chlorophenyl substituent demonstrated the highest activity with a MIC of 12.5 μg/mL. Substituting this chlorophenyl with unsubstituted, 4-methoxy, 3-chloro, 3-bromo, and 4-bromo in compounds **5i**, **5j**, **5k**, **5L**, and **5o**, respectively, led to a slight decrease in activity with a MIC of 15 μg/mL. However, compounds **5m** and **5p** with 4-fluorophenyl and 4-nitrophenyl substituents showed a significant decrease in activity with a MIC of 62.5 μg/mL.

For 6-bromoquinoline compounds with phenyltriazole substituents, compounds **5q**, **5r**, **5s**, **5t**, **5v**, and **5w** containing unsubstituted phenyl, 4-methoxyphenyl, 3-chlorophenyl, 3-bromophenyl, 4-chlorophenyl, and 4-bromophenyl, respectively exhibited the most potent anti-tubercular effects with MIC values of 15 μg/mL. On the other hand, counterparts **5u** and **5x** with 4-fluorophenyl and 4-nitrophenyl showed reduced activity with MIC values of 62.5 and 125 μg/mL. Overall, compounds with substituted quinoline containing chloro and bromo groups displayed significant activity.

2.2.2 Inhibitory effect toward MTB InhA

To assess the effectiveness of 4-carboxyquinoline-triazole hybrids **5g**, **5i**, and **5n**, which displayed notable cytotoxic effects and potent activity against MTB, further scrutiny was conducted to gauge their capacity to impede the InhA enzyme. In this analysis,

TABLE 1 The anti-tubercular effectiveness (MICs; μg/mL) of the reported compounds (5a-x) tested toward *Mycobacterium bovis* BCG, *M. tuberculosis,* and *M. abscessus* strains.

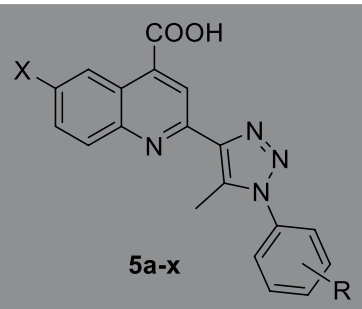

5a-x

Compounds	X	R	MIC [μg/mL]			IC_{50} -L929/MIC_{Mtb}
			M. bovis BCG	*M. tuberculosis*	*M. abscessus*	
5a	H	H	<125	125	>125	ND
5b		4-OCH_3	<125	62.5	>125	ND
5c		3-Cl	<125	62.5	>125	ND
5d		3-Br	<125	62.5	>125	ND
5e		4-F	<125	125	>125	ND
5f		4-Cl	<125	62.5	>125	ND
5g		4-Br	<125	15	>125	20
5h		4-NO_2	<125	125	>125	ND
5i	Cl	H	<125	15	>125	20
5j		4-OCH_3	<125	15	>125	10
5k		3-Cl	<125	15	>125	13
5L		3-Br	<125	15	>125	13
5m		4-F	<125	62.5	>125	ND
5n		4-Cl	<125	12.5	>125	16
5o		4-Br	<125	15	>125	10
5p		4-NO_2	<125	62.5	>125	ND
5q	Br	H	<125	15	>125	ND
5r		4-OCH_3	<125	15	>125	5
5s		3-Cl	<125	15	>125	13
5t		3-Br	<125	15	>125	13
5u		4-F	<125	62.5	>125	ND
5v		4-Cl	<125	15	>125	13
5w		4-Br	<125	15	>125	10
5x		4-NO_2	<125	125	>125	ND
INH			0.05	0.1	0.1	

ND, not determine.
MIC, IC_{50} – cytotoxicity index for L929 cell line.

INH served as a positive control. The outcomes, as displayed in Table 2, reveal that the examined derivatives effectively suppressed the InhA enzyme within the micromolar concentration ranges, recording IC_{50} values ranging from 0.72 ± 0.03 to 11.83 ± 0.49 μM. Remarkably, compound **5n**, exhibiting the best activity toward MTB with a MIC value of 12.5 μg/mL, also demonstrated substantial inhibition of the InhA enzyme (IC_{50} = 0.72 ± 0.03 μM), on par with that of INH (IC_{50} = 0.24 ± 0.01 μM). These results

10.3389/fchem.2024.1424017

TABLE 2 The IC_{50} values (μM) for the most effective counterparts (5g, 5i, and 5n) against InhA.

Compound	IC_{50} (μM)
5g	4.13 ± 0.17
5i	11.83 ± 0.49
5n	0.72 ± 0.03
INH	0.24 ± 0.01

validated the inhibitory activity of compound **5n** against the InhA enzyme. The plausible binding mode for these analogues (**5g**, **5i**, and **5n**) in their interaction with InhA was explored through molecular docking, a discussion of which follows in the subsequent section.

2.3 *In silico* insights

2.3.1 Molecular docking analysis

In order to enhance comprehension of the interaction mechanisms occurring at the binding site of a specific protein, molecular docking simulations were performed on compounds exhibiting strong *in vitro* effects towards the InhA enzyme of MTB. The docking results disclosed that 4-carboxyquinoline-triazole hybrids **5g**, **5i**, and **5n** exhibited binding affinities (ΔG_{dock}) of −8.182, −9.337, and −9.493 kcal/mol, respectively. Notably, compound **5n** demonstrated the highest binding affinity within the active site of InhA, consistent with *in vitro* experimental findings.

The 2D and 3D interactions of the three compounds (**5g**, **5i**, and **5n**) are detailed in Figure 2. These compounds formed hydrogen bonds between the oxygen atom of the carboxylic functionality in the molecule and the N-H of the amino acid residue Lys165. The hydrogen bond distances for these compounds with this residue were observed to be 2.51 Å, 2.45 Å, and 2.33 Å, respectively. Specifically, compound **5n** exhibited the shortest hydrogen bond distance, explaining its strongest affinity among the studied compounds due to the crucial role of hydrogen bonding in the protein-ligand complex. Furthermore, halogen bonding was identified in the InhA complex with this compound at residue Pro156. Various interactions, including pi-pi stacked, pi-sigma, alkyl, pi-alkyl, pi-sulfur, pi-donor hydrogen bonding, and van der Waals were observed in the binding site of InhA, contributing to the stability of the complex. Generally, the fused benzene ring of the quinoline scaffold in the studied compounds, and pi-sigma interactions with residue Ile21 were established.

In more detail, compound **5g** established alkyl interactions with residues Leu197 and Ala198, along with pi-sigma interactions with Ala198 and Ile21. Compound **5i** formed three pi-sulfur interactions with Met199 and pi-pi stacked interactions with Phe149. Pi-alkyl and alkyl interactions were also noticed in the InhA-**5i** complex with amino acid residues Ile215, Tyr158, and Ile21. This was also evident in the complexes InhA-**5n** and InhA-reference. Furthermore, compound **5n** exhibited additional pi-alkyl and alkyl interactions with other amino acid residues such as Met199 and Ala157.

2.3.2 Molecular dynamics simulation

The best-docked pose with the most negative binding affinity of the top-lead compound **5n** obtained from the AutoDock Vina program was utilized as the input structure for a 100 ns MD simulation. The output result of the best docking was used to establish this procedure in a high-throughput fashion and scrutinize the dynamic binding modes of the ligand at the protein's active site in explicit water conditions.

The examination of alterations in the conformation of the ligand-protein complex was evaluated by calculating the root-mean-square deviation (RMSD) from the original structure in order to assess the structural stability. The average RMSD value for the compound **5n** was determined to be approximately 0.229 nm, Figure 3A. From the protein RMSD chart, it can be observed that the structure undergoes slight changes, with the RMSD value increasing slightly over the first 20 ns and then stabilizing to form a well-defined complex throughout the simulation with an RMSD value around 2.3 Å. The accepted range for RMSD values is typically less than 3.0 Å, with lower RMSD values signifying enhanced stability within the system (Kufareva and Abagyan, 2012). In contrast, the ligand **5n** in the complex shows minor changes with an RMSD value less than 2.0 Å. Its average RMSD value is calculated as 0.11 nm, demonstrating the durability of the ligand within the active site of the InhA protein, which is illustrated in Figure 3B.

The root-mean-square fluctuation (RMSF) for the ligand-protein complex was graphed using the 100 ns MD trajectory to assess the mean fluctuation and flexibility of each specific amino acid (Figure 3C). The RMSF chart indicates the varying degrees of fluctuation observed in amino acid residues within the protein during the interaction state with the ligand over certain time intervals. This chart illustrates that the fluctuations in residues during interaction with compound 5n are greater compared to the residues of the apo-protein, particularly concentrated in the regions from 100 to 120 and 227 to 230. This observation implies that the compound 5n has a comparable stabilizing effect on this protein section.

The compactness of the InhA-**5n** complex was analyzed using a radius of gyration (Rg) chart. From the displayed results, a small change in Rg was observed at the 40–60 ns time point, followed by sustained stability for the ligand-protein complex during the simulation, with an average value of 1.841 nm, similar to the reference compound and apo-protein (Rg values of 1.841 and 1.819 nm, respectively), indicating the tightness of the structure (Figure 3D). In summary, the results indicate that the InhA-**5n** system remains stable throughout the 100 ns MD simulation under virtual physiological conditions.

2.3.3 ADMET

The compound **5n**, with its molecular weight of 399.23 g/mol, 5 hydrogen bond acceptors, 1 hydrogen bond donor, molar refractivity of 104.04, and LogP of 3.71, is being investigated for its potential to inhibit InhA, and its drug-likeness and pharmacokinetics are currently under research. According to Supplementary Table S1, all these parameter values meet Lipinski's proposed criteria (Lipinski et al., 1997). Additionally, the Absorption, Distribution, Metabolism, Excretion, and Toxicity (ADMET) profile of the synthesized compound **5n** has

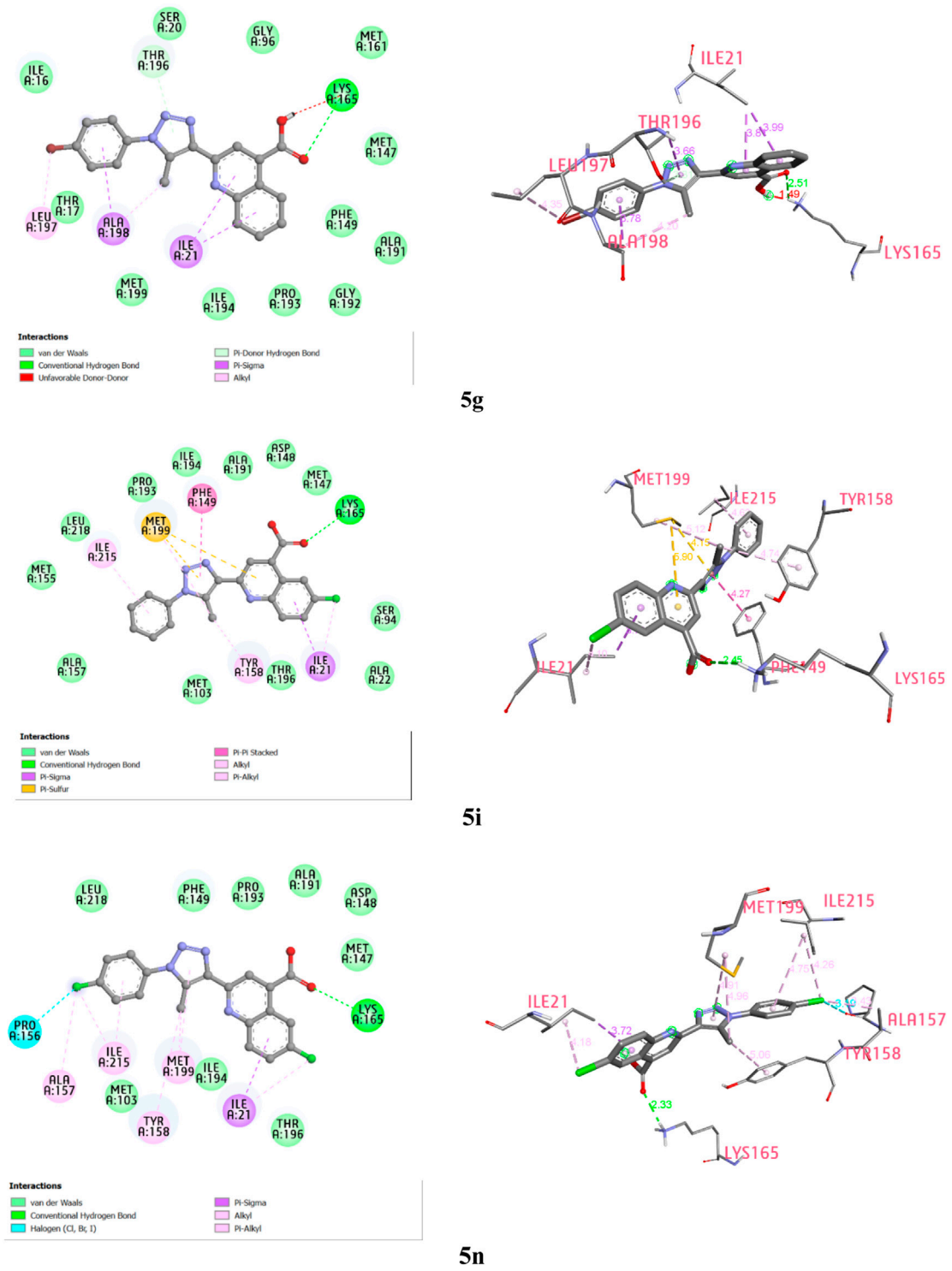

FIGURE 2
2D and 3D interactions of three compound **5g**, **5i**, and **5n** with InhA residues.

been preliminarily assessed to make pharmacokinetic predictions for potential drug candidates in clinical studies.

As shown in Supplementary Table S2, ADMET profiling results indicate that compound **5n** has a high human intestinal absorption value of 94.021%. It exhibits high permeability through Caco-2 with a predicted value of 1.389 (>0.90). The skin permeation ability is high with a logKp value of −2.735 (<−2.5). CNS permeability study demonstrates good penetration (logPS value of −1.934 > −2), while the compound cannot cross the blood-brain barrier (logBB = −1.043 < −1) (Supplementary Table S2, Figure 4). Cytochrome P450 enzymes in the liver are generally not inhibited, except for cytochrome P2C9, a key enzyme in drug

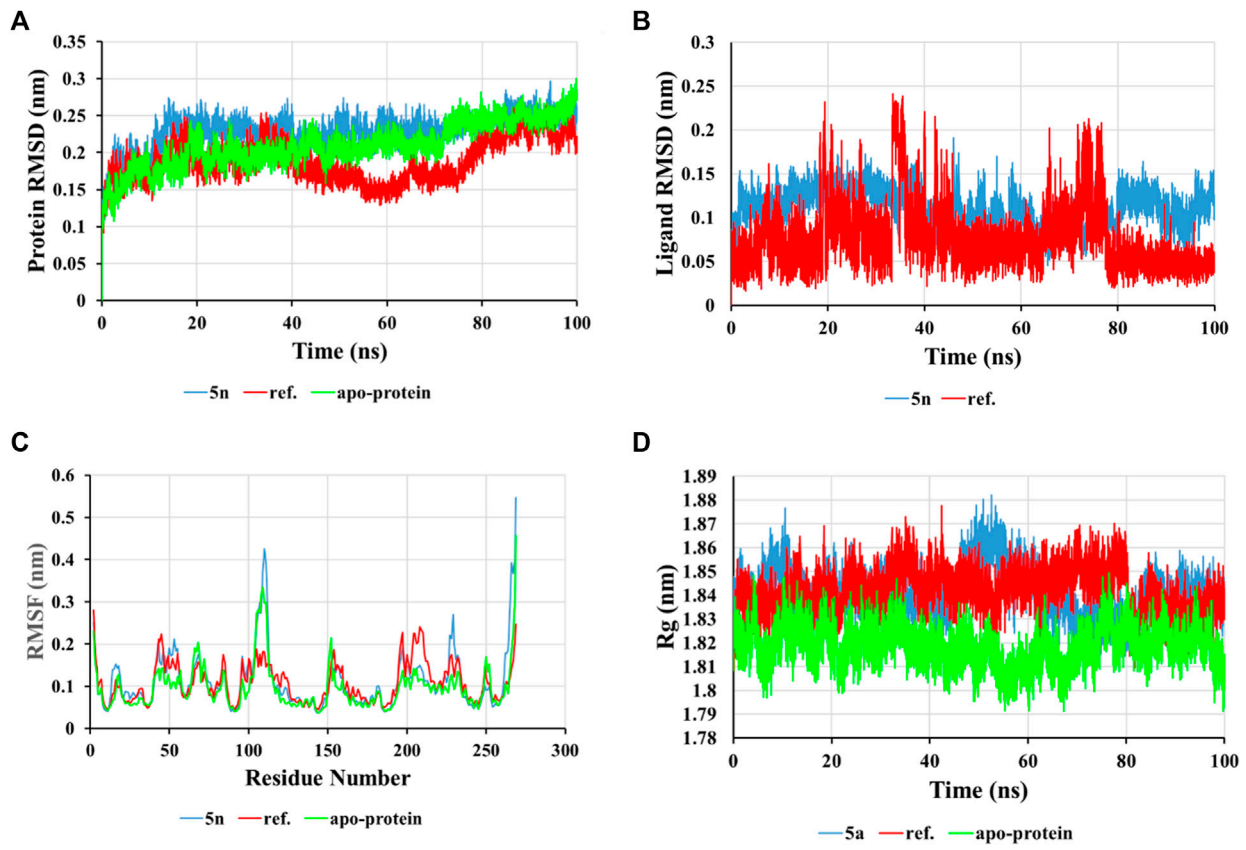

FIGURE 3
RMSD of protein backbone **(A)** and ligand **(B)** in solvated InhA-**5n** complex, RMSF values of the complex **(C)**, and Radius of gyration (Rg) of the complex **(D)** during 100 ns simulation time.

metabolism, which may be inhibited by this compound. The excretion is evaluated based on the total clearance, an important parameter in determining the dosing interval. Data indicates that the compound **5n** has a total clearance value of 0.192 log mL/min/kg. Toxicity parameters assessed in the ADMET profile of the new InhA inhibitor **5n** show inactivity with carcinogenicity, immunotoxicity, mutagenicity, cytotoxicity, no AMES toxicity, and no inhibition of hERG (I and II). However, it exhibits undesired hepatotoxicity. The toxicity level of 4, as indicated by the ProTox II web server, suggests the relative toxicity of compound **5n** (Banerjee et al., 2018a). Furthermore, the estimated Oral Rat Acute Toxicity (LD_{50}) and Oral Rat Chronic Toxicity values for the synthesized compound **5n** are 2.822 mol/kg and 0.528 log mg/kg_bw/day, respectively.

3 Conclusion

In conclusion, the synthesized carboxyquinoline-triazole compounds **5a-x** in this investigation demonstrated promising potential as anti-tubercular agents, particularly against MTB. Despite not exhibiting significant activity against the highly resistant *M. abscessus*, all 24 compounds effectively suppressed the growth of *M. bovis BCG* and MTB. Among them, derivative **5n** emerged as the most potent, with a MIC value of 12.5 μg/mL against MTB, comparable to the standard drug INH. Moreover, the cytotoxicity assessment revealed low toxicity for most compounds, with compound **5n** demonstrating a favorable IC_{50}-L929/MIC_{MTB} ratio of 16. Further investigation into the inhibition of the MTB InhA enzyme confirmed the efficacy of derivatives **5g**, **5i**, and **5n**, with compound **5n** displaying substantial inhibition with an IC_{50} value closely mirrored that of INH. Molecular docking simulations elucidated the binding affinities and interactions of these compounds within the active site of InhA, suggesting a comparable binding mode to reported InhA inhibitors and emphasizing the importance of hydrogen and halogen bonding, as well as various other interactions contributing to stability. Additionally, an MD analysis supported the stability of the InhA-**5n** complex over 100 ns, corroborating the binding mode observed in docking studies. ADMET profiling indicated favorable drug-like properties for compound **5n** that comply with Lipinski's rule of five, including high intestinal absorption, permeability, and minimal toxicity, albeit with some potential for hepatotoxicity. Overall, compound **5n** stands out as a promising lead compound warranting further exploration as a potential anti-tubercular agent with favorable pharmacokinetic properties and low toxicity profile, offering a potential avenue for the development of novel compounds to combat tuberculosis and mitigate the challenge of resistance.

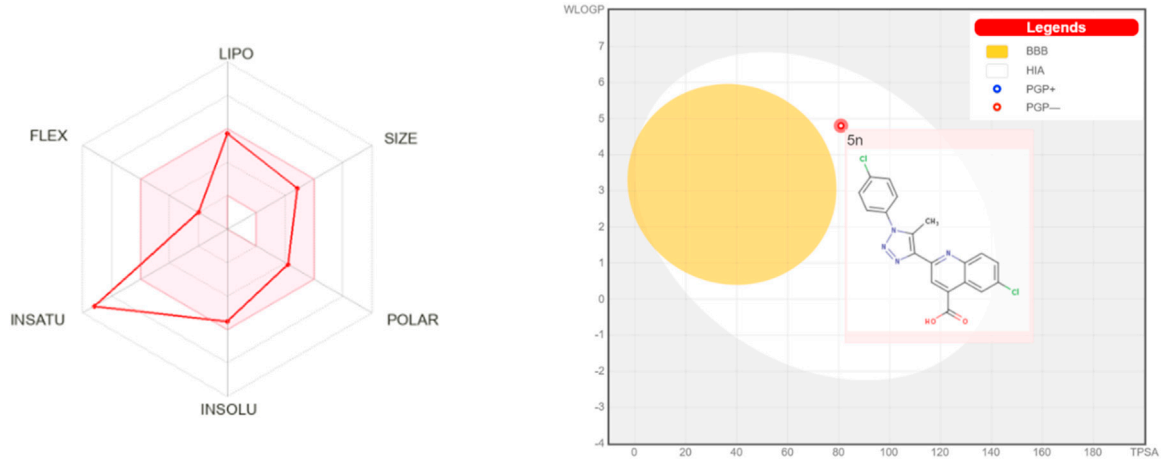

FIGURE 4
Swiss ADME bioavailability radar and BOILED-egg plot of compound **5n**.

4 Experimental section

4.1 Chemistry

Melting points have been determined using the Electrothermal IA-9000 apparatus and have been reported without correction. The ^{1}H NMR and ^{13}C NMR spectra were recorded using Bruker Avance 500 MHz spectrometer (500 MHz ^{1}H and 126 MHz ^{13}C NMR). Deuterated dimethylsulfoxide (DMSO-d_6) was used as a solvent in all samples. The progression of the reactions was observed through TLC using silica gel on aluminium sheets 60 F254 from Merck, with $CHCl_3$/MeOH (9.5: 0.5 v/v) as the eluent, and iodine-potassium for visualization. It is important to mention that compounds **3a-h** had been synthesized previously (Dong et al., 2010; Singh et al., 2013; Bekheit et al., 2021).

4.1.1 General procedures for preparing targeted 4-carboxyquinoline-triazole derivatives *(5a-x)*

Stirring a solution of isatin derivatives **4a-c** (1 mmol) and potassium hydroxide (2.5 mmol) in 5 mL of water was conducted at room temperature for 15–30 min. Following this, the reaction mixture received an addition of acetyl triazoles derivatives **3a-h** (1 mmol) and 10 mL of ethyl alcohol. Refluxing the reaction took place for a duration of 12 h, and subsequently, the mixture was acidified to achieve a pH of 2–3 using diluted HCl, resulting in the formation of a precipitate. This precipitate was then subjected to filtration, and underwent recrystallization after a water-washing process, ultimately yielding the pure target products 4-carboxyquinoline-triazole derivatives **5a-x**.

2-(5-Methyl-1-phenyl-1H-1,2,3-triazol-4-yl)benzo [b]pyridine-4-carboxylic acid (**5a**).

Orange powder; mp 278°C–280°C; yield (63%); ^{1}H NMR (500 MHz, DMSO-d$_6$) δ = 2.60 (s, 3H, triazole CH_3), 6.86-6.88 (m, 1H, H-Arm), 7.01-7.04 (m, 1H, H-Arm), 7.45-7.47 (m, 1H, H-Arm), 7.53-7.56 (m, 1H, H-Arm), 7.59-7.65 (m, 6H, H3 of quinoline and H-Arm), 11.00 (brs, 1H, C(O)OH); ^{13}C NMR (126 MHz, DMSO-d$_6$) δ 10.23 (triazole CH_3), 112.73, 118.35, 123.29, 125.20, 125.95 (2C), 130.27 (2C), 130.67, 135.54, 138.21, 138.90 (Arm), 143.38 (=C-N, triazole), 151.27 (C9 of quinoline), 159.88 (C2 of quinoline), 184.91 (C(O)OH); Analysis for $C_{19}H_{14}N_4O_2$, M.wt. (330.35 g/mol), Calcd.: % C, 69.08; H, 4.27; N, 16.96; Actual: % C, 68.96; H, 4.29; N, 17.03 (Pokhodylo et al., 2009).

2-(1-(4-Methoxyphenyl)-5-methyl-1H-1,2,3-triazol-4-yl)benzo [b]pyridine-4-carboxylic acid (**5b**).

Yellow powder; mp 222°C–224°C; yield (65%); ^{1}H NMR (500 MHz, DMSO-d$_6$) δ = 2.62 (s, 3H, triazole CH_3), 3.85 (s, 3H, OCH_3), 7.16 (d, 2H, J = 8.8 Hz, H-Arm), 7.50-7.56 (m, 5H, H-Arm), 7.58 (dd, 1H, J = 8.8 and 2.5 Hz, H-Arm), 8.73 (s, 1H, H3 of quinoline), 11.06 (s, 1H, C(O)OH); ^{13}C NMR (126 MHz, DMSO-d$_6$) = δ 9.67 (triazole CH_3), 55.65 (OCH_3), 112.25, 114.79 (2C), 117.80, 122.76, 124.67, 125.55, 126.92 (2C), 127.76, 134.60, 130.23, 137.74, 138.38 (Arm), 142.68 (=C-N, triazole), 150.79 (C9 of quinoline), 159.40 (C2 of quinoline), 167.38 (C(O)OH). Analysis for $C_{20}H_{16}N_4O_3$, M.wt. (360.37 g/mol), Calcd: % C, 66.66; H, 4.48; N, 15.55; Actual: % C, 66.78; H, 4.46; N, 15.49.

2-(1-(3-Chlorophenyl)-5-methyl-1H-1,2,3-triazol-4-yl)benzo [b]pyridine-4-carboxylic acid (**5c**).

Orange powder; mp 276°C–277°C; yield (51%); ^{1}H NMR (500 MHz, DMSO-d$_6$) δ = 2.59 (s, 3H, triazole CH_3), 6.86 (d, 1H, J = 7.5 Hz, H-Arm), 7.00-7.03 (m, 1H, H-Arm), 7.44 (d, 1H, J = 7.5 Hz, H-Arm), 7.52-7.55 (m, 1H, H-Arm), 7.59 (d, 1H, J = 7.5 Hz, H-Arm), 7.63-7.69 (m, 3H, H-Arm), 7.97 (s, 1H, H3 of quinoline), 11.01 (brs, 1H, C(O)OH); ^{13}C NMR (126 MHz, DMSO-d$_6$) δ = 10.13 (triazole CH_3), 112.74, 118.31, 123.27, 124.81, 125.17, 125.92, 130.71, 131.90, 134.48, 136.67, 138.51, 138.88 (Arm), 143.35 (=C-N, triazole), 151.27 (C9 of quinoline), 159.85 (C2 of quinoline), 185.06 (C(O)OH); Analysis for $C_{19}H_{13}ClN_4O_2$, M.wt. (364.79 g/mol), Calcd.: % C, 62.56; H, 3.59; N, 15.36; Actual: % C, 62.54; H, 3.60; N, 15.32.

2-(1-(3-Bromophenyl)-5-methyl-1H-1,2,3-triazol-4-yl)benzo [b]pyridine-4-carboxylic acid (**5d**).

Buff powder; mp 248°C–250°C; yield (78%); ^{1}H NMR (500 MHz, DMSO-d$_6$) δ = 2.60 (s, 3H, triazole CH_3), 6.87 (d, 1H, J = 8.0 Hz, H-Arm), 7.01–7.04 (m, 1H, H-Arm), 7.45 (d, 1H, J = 7.5 Hz, H-Arm), 7.53–7.60 (m, 2H, H-Arm), 7.64-7.65 (m, 1H, H-Arm),

7.81 (d, 2H, J = 8.0 Hz, H-Arm), 7.90 (s, 1H, H3 of quinoline); 11.01 (brs, 1H, C(O)OH); ^{13}C NMR (126 MHz, DMSO-D6) δ = 10.90 (triazole CH_3), 114.37, 115.30, 119.62, 121.52, 124.62, 125.02, 127.34, 127.47, 128.89, 131.09, 131.93, 132.84, 135.31, 137.78(Arm), 141.91(=C-N, triazole), 152.50 (C9 of quinoline), 160.67(C2 of quinoline), 183.87(C(O)OH).Analysis for $C_{19}H_{13}BrN_4O_2$, M.wt. (409.24 g/mol), Calcd.: % C, 55.76; H, 3.20; N, 13.69; Actual: % C, 55.95; H, 3.19; N, 13.63.

2-(1-(4-Fluorophenyl)-5-methyl-1H-1,2,3-triazol-4-yl)benzo [b]pyridine-4-carboxylic acid (**5e**).

Buff powder; mp 290°C–291°C; yield (62%); ^{1}H NMR (500 MHz, DMSO-d_6) δ = 2.81 (s, 3H, triazole CH_3), 7.49–7.52 (m, 2H, H-Arm), 7.67–7.70 (m, 1H, H-Arm), 7.75–7.84 (m, 3H, H-Arm), 8.09 (d, 1H, J = 8.0 Hz, H-Arm), 8.70-8.71 (m, 2H, H3 and H8 of quinoline), 13.98 (brs, 1H, C(O)OH); ^{13}C NMR (126 MHz, DMSO-d_6) δ = 11.01 (triazole CH_3), 117.12, 117.33, 120.22, 123.90, 126.11, 128.37, 128.50, 128.56, 129.99, 130.80, 135.31, 137.41, 142.41 (=C-N, triazole), 148.75 (C9 of quinoline), 151.88 (C-F), 157.21 (C2 of quinoline), 167.88 (C(O)OH); Analysis for $C_{19}H_{13}FN_4O_2$, M.wt. (348.34 g/mol), Calcd.: % C, 65.51; H, 3.76; N, 16.08; Actual: % C, 65.56; H, 3.78; N, 16.04.

2-(1-(4-Chlorophenyl)-5-methyl-1H-1,2,3-triazol-4-yl)benzo [b]pyridine-4-carboxylic acid (**5f**).

Yellow powder; mp 246°C–248 °C; yield (63%); ^{1}H NMR (500 MHz, DMSO-d_6) δ = 2.60 (s, 3H, triazole CH_3), 6.86 (d, 1H, J = 8.0 Hz, H-Arm), 7.01–7.10 (m, 1H, H-Arm), 7.45 (d, 1H, J = 7.5 Hz, H-Arm), 7.53–7.56 (m, 1H, H-Arm), 7.81–7.85 (m, 3H, H-Arm), 8.01 (d, 1H, J = 8.0 Hz, H-Arm), 8.7 (s, 1H, H3 of quinoline), 11.00 (brs, 1H, C(O)OH); ^{13}C NMR (126 MHz, DMSO-d_6) δ = 9.65 (triazole CH_3), 112.19, 122.74, 124.65, 125.55, 127.21, 127.78, 129.77, 130.22, 133.79, 134.81, 137.89, 138.35 (Arm), 142.85 (=C-N, triazole), 150.70 (C9 of quinoline), 159.46 (C2 of quinoline), 167.33 (C(O)OH). Analysis for $C_{19}H_{13}ClN_4O_2$, M.wt. (364.79 g/mol), Calcd.: % C, 62.56; H, 3.59; N, 15.36; Actual: % C, 62.58; H, 3.58; N, 15.40 (Pokhodylo et al., 2009).

2-(1-(4-Bromophenyl)-5-methyl-1H-1,2,3-triazol-4-yl)benzo [b]pyridine-4-carboxylic acid (**5g**).

Yellow powder; mp 228°C–229°C; yield (58%); ^{1}H NMR (500 MHz, DMSO-d_6) δ = 2.61 (s, 3H, triazole CH_3), 7.58–7.60 (m, 3H, H-Arm), 7.82–7.85 (m, 4H, H-Arm), 8.10 (d, 1H, J = 8.0 Hz, H-Arm), 8.71 (s, 1H, H3 of quinoline), 11.00 (brs, 1H, C(O)OH); ^{13}C NMR (126 MHz, DMSO-d_6) δ = 10.17 (triazole CH_3), 123.34, 123.88, 125.18, 127.97, 130.92, 133.44, 134.78, 135.18, 136.53, 138.41, 138.66, 138.94 (Arm), 143.49 (=C-N, triazole), 154.63 (C9 of quinoline), 158.83 (C2 of quinoline), 194.22 (C(O)OH); Analysis for $C_{19}H_{13}BrN_4O_2$, M.wt. (409.24 g/mol), Calcd.: % C, 55.76; H, 3.20; N, 13.69; Actual: % C, 55.60; H, 3.21; N, 13.75.

2-(5-Methyl-1-(4-nitrophenyl)-1H-1,2,3-triazol-4-yl)benzo [b] pyridine-4-carboxylic acid (**5h**).

Yellow powder; mp 265°C–267°C; yield (67%); ^{1}H NMR (500 MHz, DMSO-d_6) δ = 2.62 (s, 3H, triazole CH_3), 7.49–7.74 (m, 1H, H-Arm), 7.84–8.00 (m, 3H, H-Arm), 8.10–8.16 (m, 1H, H-Arm), 8.29 (d, 1H, J = 7.5 Hz, H-Arm), 8.44–8.52 (m, 2H, H-Arm), 8.72 (s, 1H, H3 of quinoline), 11.03 (brs, 1H, C(O)OH); ^{13}C NMR (126 MHz, DMSO-d_6) δ = 10.12 (triazole CH_3), 119.87, 122.75, 123.37, 125.64, 127.05, 130.32, 130.39, 132.40, 137.59, 138.65, 138.89, 140.35 (Arm), 143.71 (=C-N, triazole), 148.53 (CH-NO_2-CH), 157.95 (C2 of quinoline), 194.21 (C(O)OH); Analysis for $C_{19}H_{13}N_5O_4$, M.wt. (375.34 g/mol), Calcd.: % C, 60.80; H, 3.49; N, 18.66; Actual: % C, 60.81; H, 3.48; N, 18.69.

6-Chloro-2-(5-methyl-1-phenyl-1H-1,2,3-triazol-4-yl)benzo [b]pyridine-4-carboxylic acid (**5i**).

Yellow powder; mp > 300°C; yield (79%); ^{1}H NMR (500 MHz, DMSO-d_6) δ = 2.80 (s, 3H, triazole CH_3), 7.61–7.69 (m, 5H, H-Arm), 7.82 (d, 1H, J = 9.0 Hz, H-Arm), 8.09 (d, 1H, J = 8.5 Hz, H-Arm), 8.79 (s, 1H, H3 of quinoline), 8.82 (brs, 1H, H5 of quinoline), 14.17 (brs, 1H, C(O)OH); ^{13}C NMR (126 MHz, DMSO-d_6) δ = 10.97 (triazole CH_3), 121.56, 124.71, 125.05, 126.00, 130.27, 130.49, 131.19, 131.98, 132.93, 135.27, 135.99, 136.09, 142.16 (=C-N, triazole), 147.29 (C9 of quinoline), 152.40 (C2 of quinoline), 167.34 (C(O)OH); Analysis for $C_{19}H_{13}ClN_4O_2$, M.wt. (364.78 g/mol), Calcd.: % C, 62.56; H, 3.59; N, 15.36; Actual: % C, 62.67; H, 3.60; N, 15.30.

6-Chloro-2-(1-(4-methoxyphenyl)-5-methyl-1H-1,2,3-triazol-4-yl)benzo [b]pyridine-4-carboxylic acid (**5j**).

White powder; mp 287°C–289°C; yield (54%); ^{1}H NMR (500 MHz, DMSO-d_6) δ = 2.73 (s, 3H, triazole CH_3), 3.83 (s, 3H, OCH_3), 7.15 (d, 2H, J = 8.5 Hz, H-Arm), 7.56 (d, 2H, J = 8.5 Hz, H-Arm), 7.77 (d, 1H, J = 9.0 Hz, H-Arm), 8.01 (dd, 1H, J = 3.5 and 8.5 Hz, H7 of quinoline), 7.74 (d, 1H, J = 3.5 Hz, H5 of quinoline); 8.78 (s, 1H, H3 of quinoline); 11.11 (brs, 1H, C(O)OH); ^{13}C NMR (126 MHz, DMSO-d_6) δ = 10.90 (triazole CH_3), 56.17 (OCH_3), 114.37, 115.30, 119.62, 121.52, 124.62, 127.47, 131.09, 131.91, 132.84, 135.31, 137.78, 141.91 (=C-N, triazole), 149.77 (C9 of quinoline), 159.63 (C2 of quinoline), 160.67, 167.32 (C(O)OH); Analysis for $C_{20}H_{15}ClN_4O_3$, M.wt. (394.81 g/mol), Calcd.: % C, 60.84; H, 3.83; N, 14.19; Actual: % C, 60.90; H, 3.85; N, 14.15.

6-Chloro-2-(1-(3-chlorophenyl)-5-methyl-1H-1,2,3-triazol-4-yl)benzo [b]pyridine-4-carboxylic acid (**5k**).

Yellow powder; mp > 300°C; yield (62%); ^{1}H NMR (500 MHz, DMSO-d_6) δ = 2.79 (s, 3H, triazole CH_3), 7.66-7.69 (m, 3H, H-Arm), 7.78 (d, 1H, J = 9.0 Hz, H-Arm), 7.84 (s, 1H, H-Arm), 8.03 (d, 1H, J = 9.0 Hz, H-Arm), 8.73 (s, 1H, H3 of quinoline); 8.78 (brs, 1H, H5 of quinoline); 14.10 (brs, 1H, C(O)OH); ^{13}C NMR (126 MHz, DMSO-d_6) δ = 10.97 (triazole CH_3), 121.56, 124.71, 125.05, 126.00, 130.27, 130.49, 131.19, 131.98, 132.93, 135.27, 135.99, 136.09, 142.16 (=C-N, triazole), 147.29 (C9 of quinoline), 152.40 (C2 of quinoline), 167.34 (C(O)OH); Analysis for $C_{19}H_{12}Cl_2N_4O_2$, M.wt. (399.23 g/mol), Calcd.: % C, 57.16; H, 3.03; N, 14.03; Actual: % C, 57.29; H, 3.03; N, 13.99.

2-(1-(3-Bromophenyl)-5-methyl-1H-1,2,3-triazol-4-yl)-6-chlorobenzo [b]pyridine-4-carboxylic acid (**5L**).

Buff powder; mp 248°C–250°C; yield (71%); ^{1}H NMR (500 MHz, DMSO-d_6) δ = 2.80 (s, 3H, triazole CH_3), 7.55-7.63 (m, 1H, H-Arm), 7.71 (d, 1H, J = 9.0 Hz, H-Arm), 7.80–7.84 (m, 2H, H-Arm); 7.97–7.98 (m, 1H, H-Arm); 8.06 (d, 1H, J = 9.0 Hz, H-Arm), 8.76 (s, 1H, H3 of quinoline), 8.78 (d, 1H, J = 2.0 Hz, H-Arm), 14.10 (brs, 1H, C(O)OH); ^{13}C NMR (126 MHz, DMSO-d_6) δ = 10.86 (triazole CH_3), 121.46, 122.64, 124.59, 124.90, 125.07, 125.15, 128.61, 131.04, 131.85, 132.11, 132.93, 133.63, 135.36, 137.20, 142.06 (=C-N, triazole), 147.07 (C9 of quinoline), 151.99 (C2 of quinoline), 167.23 (C(O)OH); Analysis for $C_{19}H_{12}BrClN_4O_2$, M.wt. (443.68 g/mol), Calcd.: % C, 51.43; H, 2.73; N, 12.63; Actual: % C, 51.25; H, 2.74; N, 12.67.

6-Chloro-2-(1-(4-fluorophenyl)-5-methyl-1H-1,2,3-triazol-4-yl)benzo [b]pyridine-4-carboxylic acid (**5m**).

Yellow powder; mp 298°C–299°C; yield (64%); ^{1}H NMR (500 MHz, DMSO-d_6) δ = 2.77 (s, 3H, triazole CH_3), 7.48–7.51 (m, 2H, H-Arm), 7.74–7.76 (m, 2H, H-Arm), 7.79 (dd, 1H, *J* = 2.0 and 9.0 Hz, H-Arm), 8.04 (d, 1H, *J* = 9.0 Hz, H-Arm), 8.74 (s, 1H, H3 of quinoline), 8.79 (d, 1H, *J* = 2.0 Hz, H-Arm), 14.13 (brs, 1H, C(O)OH); ^{13}C NMR (126 MHz, DMSO-d_6) δ = 10.85 (triazole CH_3), 117.10, 117.29, 121.48, 124.63, 124.96, 128.38, 128.45, 131.01, 131.84, 132.87, 135.39, 135.66, 142.01 (=C-N, triazole), 147.14 (C9 of quinoline), 152.19 (C2 of quinoline), 162.02 (C-F), 167.26 (C(O)OH); Analysis for $C_{19}H_{12}ClFN_4O_2$, M.wt. (382.77 g/mol), Calcd.: % C, 59.62; H, 3.16; N, 14.64; Actual: % C, 59.54; H, 3.17; N, 14.67.

6-Chloro-2-(1-(4-chlorophenyl)-5-methyl-1H-1,2,3-triazol-4-yl)benzo [b]pyridine-4-carboxylic acid (**5n**).

Pale yellow powder; mp > 300°C; yield (48%); ^{1}H NMR (500 MHz, DMSO-d_6) δ = 2.78 (s, 3H, triazole CH_3), 7.72-7.73 (m, 4H, H-Arm), 7.79–7.82 (m, 1H, H-Arm), 8.04 (dd, 1H, *J* = 3.5 and 9.0 Hz, H-Arm), 8.74 (d, 1H, *J* = 3.5 Hz, H-Arm), 8.79 (brs, 1H, H3 of quinoline), 14.13 (brs, 1H, C(O)OH); ^{13}C NMR (126 MHz, DMSO-d_6) δ = 10.92 (triazole CH_3), 121.51, 124.71, 125.04, 127.78, 130.31, 131.16, 131.96, 132.94, 134.90, 135.14, 135.43, 135.98, 142.22 (=C-N, triazole), 147.24 (C9 of quinoline), 152.24 (C2 of quinoline), 167.31 (C(O)OH); Analysis for $C_{19}H_{12}Cl_2N_4O_2$, M.wt. (399.23 g/mol), Calcd.: % C, 57.16; H, 3.03; N, 14.03; Actual: % C, 57.13; H, 3.04; N, 14.01.

2-(1-(4-Bromophenyl)-5-methyl-1H-1,2,3-triazol-4-yl)-6-chlorobenzo [b]pyridine-4-carboxylic acid (**5o**).

White powder; mp > 300°C; yield (66%); ^{1}H NMR (500 MHz, DMSO-d_6) δ = 2.77 (s, 3H, triazole CH_3), 7.64 (d, 2H, *J* = 8.5 Hz, H-Arm), 7.77 (dd, 1H, *J* = 2.0 and 9.0 Hz, H-Arm), 7.84 (d, 2H, *J* = 8.0 Hz, H-Arm), 8.02 (d, 1H, *J* = 8.5 Hz, H-Arm), 8.73 (brs, 1H, H3 of quinoline), 8.78 (d, 1H, *J* = 1.5 Hz, H-Arm), 14.10 (brs, 1H, C(O)OH), ^{13}C NMR (126 MHz, DMSO-d_6) δ = 10.91 (triazole CH_3), 121.51, 123.66, 124.67, 125.00, 127.94, 131.08, 131.90, 132.93, 133.24, 135.30, 135.32, 135.78, 142.21 (=C-N, triazole), 147.18 (C9 of quinoline), 152.17 (C2 of quinoline), 167.26 (C(O)OH). Analysis for $C_{19}H_{12}BrClN_4O_2$, M.wt. (443.68 g/mol), Calcd.: % C, 51.43; H, 2.73; N, 12.63; Actual: % C, 51.45; H, 2.73; N, 12.60.

6-Chloro-2-(5-methyl-1-(4-nitrophenyl)-1H-1,2,3-triazol-4-yl) benzo [b]pyridine-4-carboxylic acid (**5p**).

Orange powder; mp 235°C–237°C; yield (47%); ^{1}H NMR (500 MHz, DMSO-d_6) δ = 2.90 (s, 3H, triazole CH_3), 6.88-6.90 (m, 3H, H-Arm), 7.52 (s, 1H, H-Arm), 7.57-7.59 (m, 1H, H-Arm), 7.86-8.16 (m, 2H, H-Arm), 8.44-8.50 (m, 1H, H-Arm), 11.10 (brs, 1H, C(O)OH); Analysis for $C_{19}H_{12}ClN_5O_4$, M.wt. (409.78 g/mol), Calcd.: % C, 55.69; H, 2.95; N, 17.09; Actual: % C, 55.79; H, 2.94; N, 17.04.

6-Bromo-2-(5-methyl-1-phenyl-1H-1,2,3-triazol-4-yl)benzo [b]pyridine-4-carboxylic acid (**5q**).

Yellow powder; mp > 300°C; yield (74%); ^{1}H NMR (500 MHz, DMSO-d_6) δ = 2.77 (s, 3H, triazole CH_3), 7.60-7.68 (m, 5H, H-Arm), 7.89 (dd, 1H, *J* = 2.0 and 9.0 Hz, H-Arm), 7.95 (d, 1H, *J* = 9.0 Hz, H-Arm), 8.74 (s, 1H, H3 of quinoline), 8.95 (s, 1H, H5 of quinoline), 14.11 (brs, 1H, C(O)OH); ^{13}C NMR (126 MHz, DMSO-d_6) δ = 11.39 (triazole CH_3), 121.49, 121.67, 125.12, 125.97, 128.26, 130.28, 130.46, 131.98, 133.64, 135.22, 135.67, 136.08, 142.13 (=C-N, triazole), 147.36 (C9 of quinoline), 152.40 (C2 of quinoline), 167.29 (C(O)OH); Analysis for $C_{19}H_{13}BrN_4O_2$, M.wt. (409.24 g/mol), Calcd.: % C, 55.76; H, 3.20; N, 13.69; Actual: % C, 55.69; H, 3.21; N, 13.66.

6-Bromo-2-(1-(4-methoxyphenyl)-5-methyl-1H-1,2,3-triazol-4-yl)benzo [b]pyridine-4-carboxylic acid (**5r**).

Yellow powder; mp 294°C–295°C; yield (53%); ^{1}H NMR (500 MHz, DMSO-d_6) δ = 2.74 (s, 3H, triazole CH_3), 3.84 (s, 3H, OCH_3), 7.15 (d, 2H, *J* = 9.5 Hz, H-Arm), 7.57 (d, 2H, *J* = 9.0 Hz, H-Arm), 7.90 (dd, 1H, *J* = 2.5 and 9.5 Hz, H-Arm), 7.97 (d, 1H, *J* = 9.5 Hz, H-Arm); 8.75 (s, 1H, H3 of quinoline), 8.96 (d, 1H, *J* = 2.5 Hz, H5 of quinoline), 14.13 (s, 1H, C(O)OH); ^{13}C NMR (126 MHz, DMSO-d_6) *δ* = 10.90 (triazole CH_3), 56.17 (OCH_3), 115.30, 121.48, 125.10, 127.46, 128.23, 128.90, 131.95, 133.63, 135.07, 135.31, 135.67, 141.89 (=C-N, triazole), 147.38 (C9 of quinoline), 152.49 (C2 of quinoline), 160.67, 167.29 (C(O)OH); Analysis for $C_{20}H_{15}BrN_4O_3$, M.wt. (439.26 g/mol), Calcd.: % C, 54.69; H, 3.44; N, 12.75; Actual: % C, 54.76; H, 3.43; N, 12.70.

6-Bromo-2-(1-(3-chlorophenyl)-5-methyl-1H-1,2,3-triazol-4-yl)benzo [b]pyridine-4-carboxylic acid (**5s**).

Yellow powder; mp > 300°C; yield (67%); ^{1}H NMR (500 MHz, DMSO-d_6) δ = 2.79 (s, 3H, triazole CH_3), 7.63-7.71 (m, 3H, H-Arm), 7.84-7.85 (m, 1H, H-Arm), 7.89 (dd, 1H, *J* = 2.0 and 9.0 Hz, H-Arm), 7.96 (d, 1H, *J* = 9.0 Hz, H-Arm), 8.73 (s, 1H, H3 of quinoline); 8.95 (s, 1H, H5 of quinoline), 14.14 (brs, 1H, C(O)OH); ^{13}C NMR (126 MHz, DMSO-d_6) δ = 10.90 (triazole CH_3), 121.45, 124.79, 125.92, 128.22, 130.51, 131.89, 131.97, 133.67, 134.48, 135.48, 135.71, 137.20, 142.18 (=C-N, triazole), 147.34 (C9 of quinoline), 152.21 (C2 of quinoline), 167.25 (C(O) OH); Analysis for $C_{19}H_{12}BrClN_4O_2$, M.wt. (443.69 g/mol), Calcd.: % C, 51.43; H, 2.73; N, 12.63; Actual: % C, 51.57; H, 2.74; N, 12.58.

6-Bromo-2-(1-(3-bromophenyl)-5-methyl-1H-1,2,3-triazol-4-yl)benzo [b]pyridine-4-carboxylic acid (**5t**).

Yellow powder; mp 299°C–300°C; yield (71%); ^{1}H NMR (500 MHz, DMSO-d_6) δ = 2.80 (s, 3H, triazole CH_3), 7.59-7.64 (m, 1H, H-Arm); 7.72-7.74 (m, 1H, H-Arm), 7.83-7.85 (m, 1H, H-Arm), 7.92-7.94 (m, 1H, H-Arm), 7.97-8.02 (m, 2H, H3 of quinoline and H-Arm), 8.75 (d, 1H, *J* = 5.0 Hz, H-Arm), 8.97 (d, 1H, *J* = 3.0 Hz, H5 of quinoline), 14.19 (brs, 1H, C(O)OH); ^{13}C NMR (126 MHz, DMSO-d_6) δ = 10.91 (triazole CH_3), 121.46, 121.70, 122.65, 125.15, 128.22, 128.69, 131.95, 132.10, 133.41, 133.64, 135.47, 135.64, 137.29, 142.15 (=C-N, triazole), 147.32 (C9 of quinoline), 152.20 (C2 of quinoline), 167.25 (C(O)OH); Analysis for $C_{19}H_{12}Br_2N_4O_2$, M.wt. (488.14 g/mol), Calcd.: % C, 46.75; H, 2.48; N, 11.48; Actual: % C, 46.86; H, 2.47; N, 11.45.

6-Bromo-2-(1-(4-fluorophenyl)-5-methyl-1H-1,2,3-triazol-4-yl)benzo [b]pyridine-4-carboxylic acid (**5u**).

Yellow powder; mp > 300°C; yield (42%); ^{1}H NMR (500 MHz, DMSO-d_6) δ = 2.77 (s, 3H, triazole CH_3), 7.45-7.52 (m, 2H, H-Arm), 7.66-7.70 (m, 1H, H-Arm), 7.74-7.76 (m, 1H, H-Arm), 7.90 (dd, 1H, *J* = 2.0 and 9.0 Hz, H-Arm), 7.97 (d, 1H, *J* = 9.0 Hz, H-Arm), 8.74 (s, 1H, H3 of quinoline), 8.96 (d, 1H, *J* = 2.5 Hz, H5 of quinoline), 14.13 (s, 1H, C(O)OH); ^{13}C NMR (126 MHz, DMSO-d_6) δ = 10.68 (triazole CH_3), 114.79, 115.03, 117.04, 117.23, 119.62, 121.21, 121.62, 127.33, 128.19, 131.68, 132.19, 135.21, 140.70, 141.87 (=C-N, triazole), 146.98 (C9 of quinoline), 151.82 (C2 of quinoline), 167.01 (C(O)OH); Analysis for $C_{19}H_{12}BrFN_4O_2$,

M.wt. (427.22 g/mol), Calcd.: % C, 53.42; H, 2.83; N, 13.11; Actual: % C, 53.43; H, 2.84; N, 13.08.

6-Bromo-2-(1-(4-chlorophenyl)-5-methyl-1H-1,2,3-triazol-4-yl)benzo [b]pyridine-4-carboxylic acid (**5v**).

Yellow powder; mp > 300°C; yield (57%); ^{1}H NMR (500 MHz, DMSO-d_6) δ = 2.78 (s, 3H, triazole CH_3), 7.65-7.73 (m, 4H, H-Arm); 7.89-7.92 (m, 1H, H-Arm), 7.97 (dd, 1H, *J* = 3.5 and 9.0 Hz, H-Arm), 8.73 (d, 1H, *J* = 4.0 Hz, H-Arm), 8.96 (d, 1H, *J* = 1.5 Hz, H5 of quinoline), 14.15 (brs, 1H, C(O)OH); ^{13}C NMR (126 MHz, DMSO-d_6) δ = 10.92 (triazole CH_3), 121.45, 121.67, 125.12, 127.72, 128.22, 130.29, 131.94, 133.63, 134.88, 135.12, 135.38, 135.67, 142.20 (=C-N, triazole), 147.32 (C9 of quinoline), 152.24 (C2 of quinoline), 167.26 (C(O)OH); Analysis for $C_{19}H_{12}BrClN_4O_2$, M.wt. (443.69 g/mol), Calcd.: % C, 51.43; H, 2.73; N, 12.63; Actual: % C, 51.61; H, 2.72; N, 12.59.

6-Bromo-2-(1-(4-bromophenyl)-5-methyl-1H-1,2,3-triazol-4-yl)benzo [b]pyridine-4-carboxylic acid (**5w**).

Yellow powder; mp > 300°C, yield (60%); ^{1}H NMR (500 MHz, DMSO-d_6) δ = 2.77 (s, 3H, triazole CH_3), 7.64 (d, 2H, *J* = 8.5 Hz, H-Arm), 7.84 (d, 2H, *J* = 8.5 Hz, H-Arm), 7.88 (dd, 1H, *J* = 2.0 and 9.0 Hz, H-Arm), 7.95 (d, 1H, *J* = 9.0 Hz, H-Arm), 8.72 (s, 1H, H3 of quinoline), 8.94 (d, 1H, *J* = 2.0 Hz, H5 of quinoline), 14.12 (s, 1H, C(O)OH); ^{13}C NMR (126 MHz, DMSO-d_6) δ = 10.93 (triazole CH_3), 121.46, 121.68, 123.65, 125.12, 127.93, 128.22, 131.95, 133.24, 133.64, 135.29, 135.35, 135.67, 142.22 (=C-N, triazole), 147.33 (C9 of quinoline), 152.23 (C2 of quinoline), 167.25 (C(O)OH); Analysis for $C_{19}H_{12}Br_2N_4O_2$, M.wt. (488.14 g/mol), Calcd.: % C, 46.75; H, 2.48; N, 11.48; Actual: % C, 46.56; H, 2.49; N, 11.51.

6-Bromo-2-(5-methyl-1-(4-nitrophenyl)-1H-1,2,3-triazol-4-yl) benzo [b]pyridine-4-carboxylic acid (**5x**).

Red powder; mp 236°C–238°C; yield (71%); ^{1}H NMR (500 MHz, DMSO-d_6) δ = 2.86 (s, 3H, triazole CH_3), 6.82 (d, 1H, *J* = 8.0 Hz, H-Arm), 7.58 (s, 1H, H-Arm), 7.67 (d, 1H, *J* = 8.5 Hz, H-Arm), 7.94-8.02 (m, 3H, H-Arm), 8.45 (d, 1H, *J* = 8.5 Hz, H-Arm), 8.72 (s, 1H, H3 of quinoline), 11.13 (s, 1H, C(O)OH); ^{13}C NMR (126 MHz, DMSO-d_6) δ = 11.10 (triazole CH_3), 114.83, 120.03, 121.84, 125.63, 126.90, 127.02, 127.39, 128.27, 132.05, 133.78, 135.68, 135.87, 140.58, 150.14 (C-NO_2), 159.44 (C2 of quinoline), 167.24 (C(O)OH); Analysis for $C_{19}H_{12}BrN_5O_4$, M.wt. (454.24 g/mol), Calcd.: % C, 50.24; H, 2.66; N, 15.42; Actual: % C, 50.27; H, 2.65; N, 15.47.

4.2 Biological evaluations

The experimental procedures for the antimycobacterial (Franzblau et al., 1998) and MTB InhA inhibition (He et al., 2007) biological experiments were conducted using the reported protocols (Supplementary Material).

4.3 *In silico* studies

In silico studies involved molecular docking and molecular dynamics (MD) simulations using AutoDock Vina v1.2.3 (Eberhardt et al., 2021) and GROMACS v2023 (Van Der Spoel et al., 2005), respectively. The methods employed for the preparation of the tested compounds and InhA protein (PDB ID: 4TZK (He et al., 2006)) in both simulations and all the subsequent steps are elaborated in detail in the Supplementary Material section. Additionally, drug-likeness analyses and ADMET predictions were made using SwissADME (Daina et al., 2017) and pkCSM (Pires et al., 2015), and toxicity assessments via ProTox II (Banerjee et al., 2018b), following established protocols for thorough evaluation (Supplementary Material).

Data availability statement

The original contributions presented in the study are included in the article/supplementary materials; further inquiries can be directed to the corresponding authors.

Author contributions

AS: Conceptualization, Validation, Writing–review and editing. M-HA: Conceptualization, Writing–review and editing, Funding acquisition. ME: Writing–review and editing, Investigation, Methodology. JP: Investigation, Methodology, Writing–review and editing, Formal Analysis. HA: Methodology, Writing–review and editing, Data curation. NS: Methodology, Writing–review and editing, Software. NX: Methodology, Writing–review and editing, Formal Analysis. M-AV: Data curation, Writing–original draft. TT: Data curation, Writing–original draft, Funding acquisition. AE: Data curation, Writing–original draft, Formal Analysis, Validation. BD: Formal Analysis, Validation, Investigation, Resources, Writing–review and editing. JD: Resources, Validation, Writing–review and editing, Conceptualization. WE: Conceptualization, Resources, Writing–review and editing, Supervision, Visualization.

Funding

The author(s) declare that financial support was received for the research, authorship, and/or publication of this article. The authors extend their appreciation to the Deanship of Scientific Research, King Saud University, for funding through the Vice Deanship of Scientific Research Chairs, Research Chair of Colorectal Surgery. JP & JD were supported by the Ministry of Science and Higher Education, POL-OPENSCREEN, DIR/WK/2018/06 and National Science Centre, Poland UMO-2023/49/B/NZ7/01421.

Conflict of interest

The authors declare that the research was conducted in the absence of any commercial or financial relationships that could be construed as a potential conflict of interest.

The author(s) declared that they were an editorial board member of Frontiers, at the time of submission. This had no impact on the peer review process and the final decision.

Publisher's note

All claims expressed in this article are solely those of the authors and do not necessarily represent those of their affiliated organizations, or those of the publisher, the editors and the reviewers. Any product that may be evaluated in this article, or claim that may be made by its manufacturer, is not guaranteed or endorsed by the publisher.

Supplementary material

The Supplementary Material for this article can be found online at: https://www.frontiersin.org/articles/10.3389/fchem.2024.1424017/full#supplementary-material

References

Abdelrahman, M. A., Almahli, H., Al-Warhi, T., Majrashi, T. A., Abdel-Aziz, M. M., Eldehna, W. M., et al. (2022). Development of novel isatin-tethered quinolines as anti-tubercular agents against multi and extensively drug-resistant mycobacterium tuberculosis. *Molecules* 27 (24), 8807. doi:10.3390/molecules27248807

Alcaraz, M., Sharma, B., Roquet-Baneres, F., Conde, C., Cochard, T., Biet, F., et al. (2022). Designing quinoline-isoniazid hybrids as potent anti-tubercular agents inhibiting mycolic acid biosynthesis. *Eur. J. Med. Chem.* 239, 114531. doi:10.1016/j.ejmech.2022.114531

Almeida Da Silva, P. E., and Palomino, J. C. (2011). Molecular basis and mechanisms of drug resistance in *Mycobacterium tuberculosis*: classical and new drugs. *J. Antimicrob. Chemother.* 66 (7), 1417–1430. doi:10.1093/jac/dkr173

Azab, A. E., Alesawy, M. S., Eldehna, W. M., Elwan, A., and Eissa, I. H. (2022). New [1, 2, 4] triazolo [4, 3-c] quinazoline derivatives as vascular endothelial growth factor receptor-2 inhibitors and apoptosis inducers: design, synthesis, docking, and antiproliferative evaluation. *Arch. Pharm.* 355 (10), 2200133. doi:10.1002/ardp.202200133

Banerjee, P., Eckert, A. O., Schrey, A. K., and Preissner, R. (2018a). ProTox-II: a webserver for the prediction of toxicity of chemicals. *Nucleic acids Res.* 46 (W1), W257–W263. doi:10.1093/nar/gky318

Banerjee, P., Eckert, A. O., Schrey, A. K., and Preissner, R. (2018b). ProTox-II: a webserver for the prediction of toxicity of chemicals. *Nucleic acids Res.* 46 (W1), W257–W263. doi:10.1093/nar/gky318

Barberis, I., Bragazzi, N. L., Galluzzo, L., and Martini, M. (2017). The history of tuberculosis: from the first historical records to the isolation of Koch's bacillus. *J. Prev. Med. Hyg.* 58, E9–E12. doi:10.15167/2421-4248/jpmh2017.58.1.728

Bekheit, M. S., Mohamed, H. A., Abdel-Wahab, B. F., and Fouad, M. A. (2021). Design and synthesis of new 1, 4, 5-trisubstituted triazole-bearing benzenesulphonamide moiety as selective COX-2 inhibitors. *Med. Chem. Res.* 30, 1125–1138. doi:10.1007/s00044-021-02716-7

Bekier, A., Kawka, M., Lach, J., Dziadek, J., Paneth, A., Gatkowska, J., et al. (2021). Imidazole-thiosemicarbazide derivatives as potent anti-Mycobacterium tuberculosis compounds with antibiofilm activity. *Cells* 10 (12), 3476. doi:10.3390/cells10123476

Boechat, N., Ferreira, V. F., Ferreira, S. B., Ferreira, M. L. G., da Silva, F. C., Bastos, M. M., et al. (2011). Novel 1,2,3-triazole derivatives for use against *Mycobacterium tuberculosis* H37Rv (ATCC 27294) strain. *J. Med. Chem.* 54, 5988–5999. doi:10.1021/jm2003624

Dadlani, V. G., Chhabhaiya, H., Somani, R. R., and Tripathi, P. K. (2022). Synthesis, molecular docking, and biological evaluation of novel 1,2,4-triazole-isatin derivatives as potential *Mycobacterium tuberculosis* shikimate kinase inhibitors. *Chem. Biol. Drug Des.* 100 (2), 230–244. doi:10.1111/cbdd.14060

Daina, A., Michielin, O., and Zoete, V. (2017). SwissADME: a free web tool to evaluate pharmacokinetics, drug-likeness and medicinal chemistry friendliness of small molecules. *Sci. Rep.* 7 (1), 42717. doi:10.1038/srep42717

Daley, C. L. (2019). The global fight against tuberculosis. *Surg. Clin.* 29, 19–25. doi:10.1016/j.thorsurg.2018.09.010

Dessen, A., Quemard, A., Blanchard, J. S., Jacobs, Jr W. R., and Sacchettin, J. C. (1995). Crystal structure and function of the isoniazid target of *Mycobacterium tuberculosis*. *Science* 267 (5204), 1638–1641. doi:10.1126/science.7886450

Dhameliya, T. M., Vekariya, D. D., Patel, H. Y., and Patel, J. T. (2023). Comprehensive coverage on anti-mycobacterial endeavour reported during 2022. *Eur. J. Med. Chem.* 255, 115409. doi:10.1016/j.ejmech.2023.115409

Dong, H. S., Wang, H. C., Gao, Z. L., Li, R. S., and Cui, F. H. (2010). Tandem Michael addition/imino-nitrile cyclization synthesis of 2-amino-6-(1-aryl-5-methyl-1*H*-1,2,3-triazol-4yl)-4-phenylpyridine-3-carbonitrile. *J. Heterocycl. Chem.* 47, 389–395. doi:10.1002/jhet.336

Eberhardt, J., Santos-Martins, D., Tillack, A. F., and Forli, S. (2021). AutoDock Vina 1.2. 0: new docking methods, expanded force field, and python bindings. *J. Chem. Inf. Model.* 61 (8), 3891–3898. doi:10.1021/acs.jcim.1c00203

Elbadawi, M. M., Eldehna, W. M., El-Hafeez, A. A. A., Somaa, W. R., Albohy, A., Al-Rashood, S. T., et al. (2022). 2-Arylquinolines as novel anticancer agents with dual EGFR/FAK kinase inhibitory activity: synthesis, biological evaluation, and molecular modelling insights. *J. Enzyme Inhibition Med. Chem.* 37 (1), 355–378. doi:10.1080/14756366.2021.2015344

Elghamry, I., and Al-Faiyz, Y. (2016). A simple one-pot synthesis of quinoline-4-carboxylic acids by the Pfitzinger reaction of isatin with enaminones in water. *Tetrahedron Lett.* 57, 110–112. doi:10.1016/j.tetlet.2015.11.070

Elkaeed, E. B., Taghour, M. S., Mahdy, H. A., Eldehna, W. M., El-Deeb, N. M., Kenawy, A. M., et al. (2022). New quinoline and isatin derivatives as apoptotic VEGFR-2 inhibitors: design, synthesis, anti-proliferative activity, docking, ADMET, toxicity, and MD simulation studies. *J. Enzyme Inhibition Med. Chem.* 37 (1), 2191–2205. doi:10.1080/14756366.2022.2110869

Elsawi, A. E., Elbadawi, M. M., Nocentini, A., Almahli, H., Giovannuzzi, S., Shaldam, M., et al. (2023). 1, 5-diaryl-1, 2, 4-triazole ureas as new SLC-0111 analogues endowed with dual carbonic anhydrase and VEGFR-2 inhibitory activities. *J. Med. Chem.* 66 (15), 10558–10578. doi:10.1021/acs.jmedchem.3c00721

Elsawi, A. E., Shahin, M. I., Elbendary, H. A., Al-Warhi, T., Hassan, F. E., and Eldehna, W. M. (2024). 1, 2, 4-triazole-tethered indolinones as new cancer-fighting small molecules targeting VEGFR-2: synthesis, biological evaluations and molecular docking. *Pharmaceuticals* 17 (1), 81. doi:10.3390/ph17010081

El-Shoukrofy, M. S., Atta, A., Fahmy, S., Sriram, D., Mahran, M. A., and Labouta, I. M. (2023). New tetrahydropyrimidine-1, 2, 3-triazole clubbed compounds: antitubercular activity and Thymidine Monophosphate Kinase (TMPKmt) inhibition. *Bioorg. Chem.* 131, 106312. doi:10.1016/j.bioorg.2022.106312

Esmail, H., Barry, C. E., Young, D. B., and Wilkinson, R. J. (2014). The ongoing challenge of latent tuberculosis. *Philos. Trans. R. Soc. Lond. B Biol. Sci.* 369, 20130437. doi:10.1098/rstb.2013.0437

Franzblau, S. G., Witzig, R. S., McLaughlin, J. C., Torres, P., Madico, G., Hernandez, A., et al. (1998). Rapid, low-technology MIC determination with clinical *Mycobacterium tuberculosis* isolates by using the microplate Alamar Blue assay. *J. Clin. Microbiol.* 36 (2), 362–366. doi:10.1128/jcm.36.2.362-366.1998

Gill, C., Jadhav, G., Shaikh, M., Kale, R., Ghawalkar, A., Nagargoje, D., et al. (2008). Clubbed [1,2,3] triazoles by fluorine benzimidazole: a novel approach to H37Rv inhibitors as a potential treatment for tuberculosis. *Bioorg. Med. Chem. Lett.* 18 (23), 6244–6247. doi:10.1016/j.bmcl.2008.09.096

He, X., Alian, A., and Ortiz de Montellano, P. R. (2007). Inhibition of the *Mycobacterium tuberculosis* enoyl acyl carrier protein reductase InhA by arylamides. *Bioorg Med. Chem.* 15 (21), 6649–6658. doi:10.1016/j.bmc.2007.08.013

He, X., Alian, A., Stroud, R., and Ortiz de Montellano, P. R. (2006). Pyrrolidine carboxamides as a novel class of inhibitors of enoyl acyl carrier protein reductase from *Mycobacterium tuberculosis*. *J. Med. Chem.* 49 (21), 6308–6323. doi:10.1021/jm060715y

Jackson, M. (2014). The mycobacterial cell envelope-lipids. *Cold Spring Harb. Perspect. Med.* 4 (10), a021105. doi:10.1101/cshperspect.a021105

Johansen, M. D., Herrmann, J. L., and Kremer, L. (2020). Non-tuberculous mycobacteria and the rise of Mycobacterium abscessus. *Nat. Rev. Microbiol.* 18 (7), 392–407. doi:10.1038/s41579-020-0331-1

Keri, R. S., and Patil, S. A. (2014). Quinoline: a promising antitubercular target. *Biomed. Pharmacother.* 68, 1161–1175. doi:10.1016/j.biopha.2014.10.007

Khaleel, E. F., Ahmed, S., Korycka-Machala, M., Mustafa Badi, R., Son, N. T., Xuan Ha, N., et al. (2024). Identification of new anti-mycobacterial agents based on quinoline-isatin hybrids targeting enoyl acyl carrier protein reductase (InhA). *Bioorg. Chem.* 144, 107138. doi:10.1016/j.bioorg.2024.107138

Kufareva, I., and Abagyan, R. (2012). Methods of protein structure comparison. *Methods Mol. Biol.* 857, 231–257. doi:10.1007/978-1-61779-588-6_10

Kumar Sahoo, S., Naiyaz Ahmad, M., Kaul, G., Nanduri, S., Dasgupta, A., Chopra, S., et al. (2022). Exploration of isoxazole-carboxylic acid methyl ester based 2-substituted

quinoline derivatives as promising antitubercular agents. *Chem. Biodivers.* 19 (7), e202200324. doi:10.1002/cbdv.202200324

Li, J., and Zhang, J. (2022). The antibacterial activity of 1, 2, 3-triazole-and 1, 2, 4-triazole-containing hybrids against *Staphylococcus aureus*: an updated review (2020-present). *Curr. Top. Med. Chem.* 22 (1), 41–63. doi:10.2174/1568026621666211111160332

Lipinski, C. A., Lombardo, F., Dominy, B. W., and Feeney, P. J. (1997). Experimental and computational approaches to estimate solubility and permeability in drug discovery and development settings. *Adv. Drug Deliv. Rev.* 23 (1–3), 3–25. doi:10.1016/S0169-409X(96)00423-1

Lu, H., and Tonge, P. J. (2008). Inhibitors of FabI, an enzyme drug target in the bacterial fatty acid biosynthesis pathway. *Acc. Chem. Res.* 41 (1), 11–20. doi:10.1021/ar700156e

Marrakchi, H., Lanéelle, G., and Ak, Q. (2000). InhA, a target of the antituberculous drug isoniazid, is involved in a mycobacterial fatty acid elongation system, FAS-II. *Microbiology* 146 (2), 289–296. doi:10.1099/00221287-146-2-289

Mohamede, A. S., Elneairy, M. A., and Eldine, S. M. (2015). 2, 4-Cycloaddition reactions: preparation and cytotoxicity of novel quinoline and pyrrolo [3, 4-f] quinoline derivatives. *Int. J. Pharm. Pharm. Sci.* 7 (12), 64–68.

Munir, A., Wilson, M. T., Hardwick, S. W., Chirgadze, D. Y., Worrall, J. A. R., Blundell, T. L., et al. (2021). Using cryo-EM to understand antimycobacterial resistance in the catalase-peroxidase (KatG) from *Mycobacterium tuberculosis*. *Structure* 29 (8), 899–912.e4. doi:10.1016/j.str.2020.12.008

Muthaiah, M., Shivekar, S. S., Cuppusamy Kapalamurthy, V. R., Alagappan, C., Sakkaravarthy, A., and Brammachary, U. (2017). Prevalence of mutations in genes associated with rifampicin and isoniazid resistance in *Mycobacterium tuberculosis* clinical isolates. *J. Clin. Tuberc. Other Mycobact. Dis.* 8, 19–25. doi:10.1016/j.jctube.2017.06.001

Nyoni, N. T., Ncube, N. B., Kubheka, M. X., Mkhwanazi, N. P., Senzani, S., Singh, T., et al. (2023). Synthesis, characterization, *in vitro* antimycobacterial and cytotoxicity evaluation, DFT calculations, molecular docking and ADME studies of new isomeric benzimidazole-1, 2, 3-triazole-quinoline hybrid mixtures. *Bioorg. Chem.* 141, 106904. doi:10.1016/j.bioorg.2023.106904

Pires, D. E., Blundell, T. L., and Ascher, D. B. (2015). pkCSM: predicting small-molecule pharmacokinetic and toxicity properties using graph-based signatures. *J. Med. Chem.* 58 (9), 4066–4072. doi:10.1021/acs.jmedchem.5b00104

Pokhodylo, N. T., Savka, R. D., Matiichuk, V. S., and Obushak, N. D. (2009). Synthesis and selected transformations of 1-(5-methyl-1-aryl-1 H-1, 2, 3-triazol-4-yl) ethanones and 1-[4-(4-R-5-methyl-1 H-1, 2, 3-triazol-1-yl) phenyl] ethanones. *Russ. J. General Chem.* 79, 309–314. doi:10.1134/s1070363209020248

Pym, A. S., Diacon, A. H., Tang, S.-J., Conradie, F., Danilovits, M., Chuchottaworn, C., et al. (2016). Bedaquiline in the treatment of multidrug- and extensively drug-resistant tuberculosis. *Eur. Respir. J.* 47 (2), 564–574. doi:10.1183/13993003.00724-2015

Quimque, M. T., Go, A. D., Lim, J. A., Vidar, W. S., and Macabeo, A. P. (2023). *Mycobacterium tuberculosis* inhibitors based on arylated quinoline carboxylic acid backbones with anti-mtb gyrase activity. *Int. J. Mol. Sci.* 24 (14), 11632. doi:10.3390/ijms241411632

Ravimohan, S., Kornfeld, H., Weissman, D., and Bisson, G. P. (2018). Tuberculosis and lung damage: from epidemiology to pathophysiology. *Eur. Respir. Rev.* 27 (147), 170077. doi:10.1183/16000617.0077-2017

Rožman, K., Sosič, I., Fernandez, R., Young, R. J., Mendoza, A., Gobec, S., et al. (2017). A new 'golden age'for the antitubercular target InhA. *Drug Discov. Today* 22 (3), 492–502. doi:10.1016/j.drudis.2016.09.009

Sabt, A., Abdelraof, M., Hamissa, M. F., and Noamaan, M. A. (2023b). Antibacterial activity of quinoline-based derivatives against methicillin-resistant *Staphylococcus aureus* and *Pseudomonas aeruginosa*: design, synthesis, DFT and molecular dynamic simulations. *Chem. Biodivers.* 20, e202300804. doi:10.1002/cbdv.202300804

Sabt, A., Eldehna, W. M., Ibrahim, T. M., Bekhit, A. A., and Batran, R. Z. (2023a). New antileishmanial quinoline linked isatin derivatives targeting DHFR-TS and PTR1: design, synthesis, and molecular modeling studies. *Eur. J. Med. Chem.* 246, 114959. doi:10.1016/j.ejmech.2022.114959

Said, M. A., Eldehna, W. M., Nocentini, A., Bonardi, A., Fahim, S. H., Bua, S., et al. (2020). Synthesis, biological and molecular dynamics investigations with a series of triazolopyrimidine/triazole-based benzenesulfonamides as novel carbonic anhydrase inhibitors. *Eur. J. Med. Chem.* 185, 111843. doi:10.1016/j.ejmech.2019.111843

Senthil, S., Gopi, R., and Raj, C. G. (2015). Synthesis, characterization and antimicrobial activity of somequinoline appended 1, 2, 3-triazoles. *J. INDIAN Chem. Soc.* 92 (6), 956–959.

Seung, K. J., Keshavjee, S., and Rich, M. L. (2015). Multidrug-resistant tuberculosis and extensively drug-resistant tuberculosis. *Cold Spring Harb. Perspect. Med.* 5 (9), a017863. þ. doi:10.1101/cshperspect.a017863

Shaikh, M. H., Subhedar, D. D., Nawale, L., Sarkar, D., Khan, F. A., Sangshetti, J. N., et al. (2015). 1, 2, 3-Triazole derivatives as antitubercular agents: synthesis, biological evaluation and molecular docking study. *MedChemComm* 6 (6), 1104–1116. doi:10.1039/c5md00057b

Shinde, A., Thakare, P. P., Nandurkar, Y., Bhoye, M., Chavan, A., and Mhaske, P. C. (2023). Synthesis of 2-(6-substituted quinolin-4-yl)-1-(4-aryl-1H-1, 2, 3-triazol-1-yl) propan-2-ol as potential antifungal and antitubercular agents. *Eur. J. Med. Chem. Rep.* 7, 100102. doi:10.1016/j.ejmcr.2023.100102

Singh, H., Sindhu, J., and Khurana, J. M. (2013). Synthesis of biologically as well as industrially important 1,4,5-trisubstituted-1,2,3-triazoles using a highly efficient, green and recyclable DBU–H2O catalytic system. *RSC Adv.* 3, 22360–22366. doi:10.1039/c3ra44440f

Van Der Spoel, D., Lindahl, E., Hess, B., Groenhof, G., Mark, A. E., and Berendsen, H. J. (2005). GROMACS: fast, flexible, and free. *J. Comput. Chem.* 26 (16), 1701–1718. doi:10.1002/jcc.20291

WHO Report (2020). WHO. Available at: https://www.who.int/publications/i/item/9789240018662.

Zhang, S., Xu, Z., Gao, C., Ren, Q. C., Chang, L., Lv, Z. S., et al. (2017). Triazole derivatives and their anti-tubercular activity. *Eur. J. Med. Chem.* 138, 501–513. doi:10.1016/j.ejmech.2017.06.051

Zhou, B., He, Y., Zhang, X., Xu, J., Luo, Y., Wang, Y., et al. (2010). Targeting mycobacterium protein tyrosine phosphatase B for antituberculosis agents. *Proc. Natl. Acad. Sci. USA.* 107, 4573–4578. doi:10.1073/pnas.0909133107

frontiers | Frontiers in Chemistry

TYPE Original Research
PUBLISHED 15 October 2024
DOI 10.3389/fchem.2024.1489253

OPEN ACCESS

EDITED BY
Afzal Basha Shaik,
Jawaharlal Nehru Technological University,
Kakinada, India

REVIEWED BY
Mithun Rudrapal,
Vignan's Foundation for Science, Technology and Research, India
Adil Shareef Mohammed,
Temple University, United States

*CORRESPONDENCE
Gurudutta Pattnaik,
gurudutta.pattnaik@cutm.ac.in
Krishna Prasad Shetty,
kprasad11@gmail.com

RECEIVED 31 August 2024
ACCEPTED 27 September 2024
PUBLISHED 15 October 2024

CITATION
Barik B, Satapathy BS, Pattnaik G, Bhavrao DV and Shetty KP (2024) Sustainable synthesis of silver nanoparticles from *Azadirachta indica*: antimicrobial, antioxidant and *in silico* analysis for periodontal treatment.
Front. Chem. 12:1489253.
doi: 10.3389/fchem.2024.1489253

Sustainable synthesis of silver nanoparticles from *Azadirachta indica*: antimicrobial, antioxidant and *in silico* analysis for periodontal treatment

Binapani Barik[1], Bhabani Sankar Satapathy[2], Gurudutta Pattnaik[1]*, Desai Vijay Bhavrao[3] and Krishna Prasad Shetty[3]*

[1]School of Pharmacy and Life Sciences, Centurion University of Technology and Management, Bhubaneswar, Odisha, India, [2]GITAM School of Pharmacy, GITAM Deemed to be University, Hyderabad Campus, Hyderabad, Telangana, India, [3]Department of Clinical Science, College of Dentistry, Centre of Medical and Bio-Allied Health Science Research, Ajman University, Ajman, United Arab Emirates

Introduction: This study explores potential application of silver nanoparticles (AgNPs) to treat periodontal infection using *Azadirachta indica* leaf extract. The eco-friendly green synthesis process uses *Azadirachta indica* as a natural stabilizer and reducer, allowing AgNPs to be formed.

Methods: Experimental AgNPs were characterized through transmission electron microscopy (TEM), Fourier-transform infrared spectroscopy (FTIR), Zeta potential, ultraviolet-visible spectroscopy (UV-Vis) etc. The antimicrobial, antioxidant potential of AgNPs was tested to identify its efficacy against periodontal infections.

Results and discussion: AgNPs were found spherical, nanosized (86 nm), with negative surface charge (–26.9 mV). TEM study depicted clear formation of discrete nanosize particles with smooth surface texture. Results showed strong antibacterial and anti-oxidant action of experimental AgNPs, preventing biofilm growth and bacterial viability. A higher binding affinity was observed between Quercetin and the selected protein, which is implicated in bacterial growth and biofilm formation on teeth. The study suggests that *Azadirachta indica* derived AgNPs could be a safe, efficacious, and eco-friendly alternative in place of conventional therapies to treat periodontal infection. Future *in vivo* studies are however warranted.

KEYWORDS

silver nanoparticles, *Azadirachta indica*, antimicrobial, antioxidant, molecular docking, ADMET

Abbreviations: AgNPs, Silver nanoparticle; FTIR, Fourier transmission infrared spectroscopy; TEM, Transmission electron microscopy; DPPH, 2-Phenyl-1-Picrylhydrazyl; SAED, Selected area electron diffraction, MIC, Minimum Inhibitory Concentration; TPSA, Topological surface area.

1 Introduction

Periodontal disease is a global issue affecting millions, with 10%–15% of adults experiencing severe periodontitis. It causes tooth loss, pain, and reduced quality of life and is linked to health disorders (Gidiagba et al., 2023). The financial impact is substantial, with medical treatment, tooth extraction, and reduced work efficiency (Osherov et al., 2023). Periodontal disease is primarily caused by the buildup of dental plaque, a viscous biofilm of bacteria on teeth and gumline (Shareef et al., 2019). Key pathogens include diverse range of parasites including *Treponema denticola, Prevotella intermedia, Fusobacterium nucleatum*, *Eikenella corrodens*, *Porphyromonas gingivalis*, causing inflammation and tissue damage (Malandrakis et al., 2022; Ozdal and Gurkok, 2022). Modern periodontal treatments have made significant progress in managing periodontal disease, but they still face challenges such as insufficient effectiveness in advanced cases, limited access to care, patient adherence, and the possibility of disease return (Hossain et al., 2024; Khan et al., 2022). The increasing incidence of dental implants has led to concerns about peri-implantitis, a disorder that resembles periodontitis but affects dental implants (Xu et al., 2022; Grizzo et al., 2023). Antibiotic resistance has also been wide spread incidence owing to irrational use of antibiotics in periodontal infections (Harish et al., 2023; Kumar et al., 2023).

Azadirachta indica, a plant largely popular for its unique flavonoids content and long history of use in traditional medicine system, has also been found to be effective in treating periodontal disease (Hu et al., 2023). Flavonoids content of the *Azadirachta indica* leaf extract have antibacterial, antifungal, and anti-inflammatory properties, preventing the development of infections and reducing inflammation (Bajpai et al., 2022; Singh and Mijakovic, 2022a). They also possess antioxidant properties, protecting gum tissues from oxidative stress. *Azadirachta indica* extracts can also enhance tissue regeneration and wound healing and can be used in oral hygiene practices (Gupta et al., 2023).

Nanoparticulate mediated delivery has been emerged as hopeful technologies in improving pharmacological effectiveness and also in modulating pharmacokinetic and pharmacodynamic properties of conventional therapeutics (Vijayaram et al., 2024). Silver nanoparticles (AgNPs) are being explored as a potential treatment for periodontal disease thanks to their strong antibacterial properties and ability to infiltrate bacterial biofilms. AgNPs have been found to reduce inflammatory responses, improve periodontal tissue regeneration (Habeeb Rahuman et al., 2022). Few reports have documented effective antimicrobial potency of AgNPs against periodontal infections (Halilu et al., 2023). A recent study by Hedayatipanah et al. (2024), reported green synthesis of AgNPs from propolis and its antimicrobial activity on the on the *Porphyromonas gingivalis* biofilm. Similarly, in another study, AgNPs conjugated with chlorhexidine or metronidazole demonstrated preferential antibacterial and anti-inflammatory potency *in vitro* (Ortega et al., 2022).

The work aims to explore the use of *Azadirachta indica* leaf extract as a reducing and stabilizing agent for producing AgNPs for periodontal therapy. Primary objective was to create a reliable method for generating AgNPs with controlled dimensions, morphology, and surface properties. To achieve the highest yield, stability, and antibacterial activity, the synthesis parameters were optimized. Experimental AgNPs were then examined using techniques like UV-Vis spectroscopy, FTIR, size analysis, zeta potential and TEM (Huq et al., 2022). The antimicrobial activity of AgNPs against common periodontal pathogens was assessed using standard microbiological tests and antioxidant potential was evaluated using DPPH assay (Huq et al., 2022). Additionally, docking and ADME analysis was performed to unveil the mechanism of interaction with key periodontal bacterial protein.

2 Materials and methods

2.1 Materials

The green leaves of *Azardircata indica* were gathered from the centurion university campus, odisha. The silver nitrate used in this study was acquired from Mahavir Chemical Supply, located in Bhubaneswar, Odisha.

Nutrient agar media, nutrient broth, and antibiotic assay media serve as standard substrates for antimicrobial studies. The free radical scavenging activity of the nanoparticles was assessed using the DPPH assay, employing methanol or ethanol as solvents and ascorbic acid obtained from Himedia, Mumbai, India. All the chemicals were of analytical grade.

2.2 Methods

2.2.1 Preparation of *Azadirachta indica* extract

The process of preparing an aqueous extract from *Azadirachta indica* leaves involved collecting the leaves and allowing them to dry completely in the shade. Once dried, the leaves were powdered and stored in an airtight container (Prakash et al., 2022; Adaramola et al., 2023). To make the extract, 5 gm of *Azadirachta indica* powder was boiled with 50 mL of distilled water for 30 min in a beaker. After cooling it to room temperature, the liquid extract was filtered and was stored at a temperature for future use.

2.2.2 Green synthesis of experimental silver nanoparticles

Green synthesis of AgNPs was carried out as per the method reported elsewhere. Briefly, a solution of silver nitrate was prepared by dissolving 10 mg of silver nitrate in 50 mL of double distilled water. The solution was heated to a temperature range of 50°C–60°C, and *Azadirachta indica* extract was slowly added. The solution was thereafter incubated at a temperature of 80°C for duration of 60 min until an identifiable change in color was seen. The presence of pale-yellow color in the solution suggested the creation of AgNps (Hameed et al., 2022; Dubey and Mittal, 2020). This was further confirmed by the visible absorbance peak at 438 nm.

2.2.3 Characterization of experimental silver nanoparticles

2.2.3.1 UV–visible spectroscopy

The UV-visible absorption spectra were used to determine the optimal time and temperature conditions for the reduction of silver ions by the colloidal mixture of prepared AgNPs and the substrate mixture of the plant extract. This spectroscopic technique allowed for precise control over the synthesis process, ensuring maximum

efficiency in the production of silver nanoparticles (Wade, 2021; Sedghi et al., 2021).

2.2.3.2 Zetapotential and particle size

The zetasizer equipment was used to assess the particle size range and polydispersity of the nanoparticles. The particle size was determined by analyzing the temporal fluctuations in the scattering of laser light while the particles were undergoing Brownian motion (Dutt et al., 2023; Chinnasamy et al., 2021). This tool allows for the analysis of the average size of the particles in the sample. Overall, these analyses provide valuable insights into the characteristics and behavior of the nanoparticles in the colloidal solution (Nesappan and Subramani, 2023).

2.2.3.3 Fourier transmission infrared spectroscopy (FTIR)

The FTIR spectroscopy was used to identify the functional groups and their interactions in the sample. The resultant peaks corresponding to specific chemical bonds provide valuable information about the composition of the reaction mixture. The resultant AgNPs was scanned over a wave length of 4,000 cm^{-1} to 600 cm^{-1} in an FTIR instrument (SHIMADZU IR Prestige-21, Mumbai, India).

2.2.3.4 Morphological examination

The morphological examination allowed for the observation of the size, shape, and surface features of the AgNPs using the Transmission electron microscopy (TEM) and Selected Area electron diffraction (SAED). The analysis provides high-resolution images of the AgNPs, allowing for a detailed examination of their surface morphology (Ijaz et al., 2022; Dashora et al., 2022). Additionally, SAED analysis helps to determine the crystalline nature of the nanoparticles by analyzing the diffraction patterns produced when electrons interact with the sample (Mallineni et al., 2023).

2.2.3.5 SAED analysis

The Tecnai G2 20 S-TWIN instrument was utilized to conduct measurements of selected area electron diffraction pattern. These measurements allowed for a detailed analysis of the crystal structure and orientation of the silver nanoparticles. This information is crucial in understanding the physical properties of the AgNPs (Hameed et al., 2022).

2.2.3.6 TEM analysis

TEM imaging allows for direct observation of the nanoparticles, enabling precise determination of their size and morphology. It is a powerful imaging technique that allows for high-resolution visualization of nanoscale structures, such as AgNPs (Amananti et al., 2022). TEM provides detailed information about the size, shape, and distribution of nanoparticles within a sample (Sharma et al., 2022). The specimens were prepared by applying a droplet of suspension with an approximate thickness of 60 nm onto a carbon membrane. The carbon membrane was then transferred onto a copper grid and allowed to dry before being inserted into the TEM (Hashemi et al., 2022).

2.2.3.7 Antimicrobial activity

Treponema denticola and *Porphyromonas gingivalis*, commonest pathogens associated with periodontal diseases are selected for the study (Hasan et al., 2022). These are known to be highly resistant to conventional antibiotics (Liaqat et al., 2022). Briefly, the agar plates were inoculated with the bacterial strains of *Staphylococcus. aureus* (ATCC 25923) *P. gingivalis* (ATCC 33277), *T. denticola* (ATCC 35405) and incubated at an optimal temperature for growth (Gonfa et al., 2023). A chlorhexidine suspension at an equivalent concentration was introduced into another sterile disc as a standard. The growth inhibition zones around each disc were measured after incubation. The nutrient broth medium provided essential nutrients for the bacteria to grow and multiply, allowing for an accurate assessment of their susceptibility to the AgNPs (Moges and Goud, 2022). 1 mg/mL solution of AgNPs was prepared using Milli Q water and subjected to appropriate sonication. Overnight grown culture in Luria-Bertani broth of the mentioned microorganisms was taken and diluted to an optical density of 1. A 500 μL volume of diluted bacterial suspension was evenly distributed across three distinct Luria-Bertani agar plates, each containing a different microorganism. Following the dispersion, two wells were created on each plate utilizing a well borer with an approximate diameter of 10 mm. Each of the three plates was filled with solutions of AgNPs at concentrations of 20 μg/mL, 50 μg/mL, and 75 μg/mL, and incubated for 24 h at 37°C. The antibacterial activity of AgNPs was assessed by measuring the presence of a clear zone of inhibition (ZOI) and from the minimum inhibitory concentration (MIC) (Chavan et al., 2023; Salem et al., 2022).

2.2.3.8 Antioxidant study

The DPPH (2-Phenyl-1-Picrylhydrazyl) technique with relatively small modifications was used to assess the antioxidant activity of the biosynthesized AgNPs. DPPH provides free radical with a prominent purple color which gets decolorized in presence of antioxidant. This approach is a dependable way to assess the radical scavenging activity of a molecule (Owaid et al., 2021; Imchen et al., 2022).

Briefly, five distinct concentrations of biosynthesized AgNPs were prepared, with concentrations ranging from 0.5, 1, 1.5, 2, and 2.5 mg/mL. Each concentration was kept in a separate volumetric flask to which about 3 mL of a 0.1 mM methanolic solution containing DPPH radical was added. The solution was then rapidly agitated and left undisturbed for 30 min in a dark place at ambient temperature. The control sample included all the reaction reagents except for the AgNPs. Methanol was used for the purpose of baseline correction. Subsequently, the spectrophotometer was used to measure the absorbance at a wavelength of 517 nm. The findings were quantified as the percentage of radical scavenging activity, with ascorbic acid as a standard antioxidant.

The antioxidant activity data were quantified and reported as IC_{50}values produced by linear regression analysis which is the minimum concentration (in micrograms) of the test sample needed to neutralize or block 50% of the radicals of DPPH concentration. Lower the IC_{50} value, the higher the antioxidant activity of the test sample.

The DPPH scavenging activity, expressed as a percentage of inhibition, is calculated using the formula:

$$\text{Antioxidant capacity (\%)} = \left\{\frac{\text{Abs. of control} - \text{Abs. of sample}}{\text{Abs. of control}}\right\} \times 100$$

2.2.3.9 Molecular docking

To depict the molecular interaction in between quercetin with virulence factor of selected periodontal causing bacteria's i.e., *P. gingivalis* and *T. denticola*, *in silico* docking analysis was employed. The molecular structure of the selected compound was constructed utilizing canonical smiles from the PubChem database PubChem CID: 5280343. The PDB structure of virulence factor of *P. gingivalis* and *T. denticola* was acquired from the RCSB Protein Data Bank (PDB id: 5Y1A and 3R15 respectively). Following that, the receptor and ligand structures were uploaded to the Argus Lab App for docking. The Argus Lab App outcome was modified for the optimal structure and visualized with Discovery studio visualizer 2.5. Subsequently, the relationship was verified by evaluation of the obtained binding energy, including ACE (atomic contact energy), global energy and attractive (vdw van der Waals). The proteins employed for the analysis included collagenase, protease, and urinase, which are responsible for catalyzing specific biochemical reactions in the oral cavity (Muraro et al., 2022; Satapathy et al., 2024).

2.2.3.10 Assessment of ADMET

The Swiss ADME offers a practical alternative to the traditional approach of designing drugs from natural materials or synthetic compounds. The Swiss ADME approach was used to assess the pharmacokinetics, bioavailability, drug-likeness, and medicinal chemistry compatibility of the quercetin in order to enhance its properties and determining the bioavailability and efficacy of quercetin as a potential drug candidate.

3 Results and discussion

The main goal is to prepare nanomaterial-based therapies that are effective, non-hazardous, and compatible with the human body, potentially improving treatment outcomes and patient care in periodontal dentistry (Wasilewska et al., 2023; Singh and Mijakovic, 2022b).

In the current study, we have used *Azadirachta indica* leaf extracts to show the production of AgNPs. The impact of different experimental conditions on the biogenesis of silver nanoparticles was also investigated. In addition, silver nanoparticles that were produced under the most favorable circumstances were analyzed using several aspects of analytical equipment. The antibacterial and antioxidant activities of the produced silver nanoparticles were assessed. The results demonstrated that the silver nanoparticles exhibited strong antibacterial properties against a variety of pathogens. Furthermore, the antioxidant activity of the nanoparticles was found to be significant, indicating potential applications in biomedical and environmental fields (Kemala et al., 2022; Sharifi-Rad et al., 2024).

3.1 Green synthesis of silver nanoparticle from leaf extract of *Azadirachta indica*

The formation of silver nanoparticles was confirmed by surface plasmon resonance activity with a peak of 429 nm which indicated the reduction of $AgNO_3$ and the subsequent formation of silver nanoparticles were validated, all achieved without the use of any hazardous substances (Karan et al., 2024; Hernández-Venegas et al., 2023). It can be determined that this is an ecofriendly friendly technique commonly referred to as green synthesis of silver nanoparticles using the *Azadirachta indica* extract as shown in Figure 1.

3.2 Characterization of optimized silver-nanoparticle

The characterization includes UV analysis, zetapotential, FTIR, SAED, and TEM. These techniques are used to determine the size, shape, and stability of the silver nanoparticles. UV analysis is used to measure the absorption spectrum of the nanoparticles, while zeta potential measures the surface charge. FTIR is used to analyze the chemical composition of nanoparticles, and SAED and TEM are used to visualize the crystal structure and morphology of the nanoparticles. Overall, these characterization techniques provide a comprehensive understanding of the optimized silver nanoparticles (Yun et al., 2022; Zhang et al., 2022a).

3.3 UV-visible spectroscopy

The UV-vis absorption spectra showed a peak at 438 nm, indicating the formation of silver nanoparticles. As shown in Figure 2. The yellow color of the reaction mixture confirmed the successful reduction of Ag^+ ions to AgNPs (Chavan et al., 2023). Analysis of the UV-vis spectra showed that the peak intensity at 438 nm increased with longer incubation time. This suggests that there were more AgNPs in the solution (Dutt et al., 2023). Additionally, the temperature had a significant effect on the reaction rate, with higher temperatures leading to faster synthesis of AgNPs. The stability and production of silver nanoparticles in water are tested using UV-Vis spectroscopy. Surface plasmon activity is detected during the formation of nanoparticles, as shown in Figure 2.

3.4 FTIR

The FTIR value of AgNPS suggested that the nanoparticles have a strong absorption peak at around 400 cm^{-1}, indicating the presence of silver-metal bonding. Additionally, the FTIR spectrum shows peaks at 1,348.96 cm^{-1} and 3,400 cm^{-1}, suggesting the presence of carbonyl groups and hydroxyl groups on the surface of the nanoparticles. Overall, the FTIR analysis indicates that the AgNPS are well-formed and have functional groups that could potentially be useful for various applications in nanotechnology (Shirmohammadi et al., 2023; Nelagadarnahalli et al., 2023). The FTIR characterization image of AgNPs has been shown in Figure 3.

3.5 Zetapotential and particle size

The zeta potential of optimized AgNPs was found to be −26.9 mV, and the particle size was 86 nm with a polydisopersibility index of about 0.6832. This result suggests

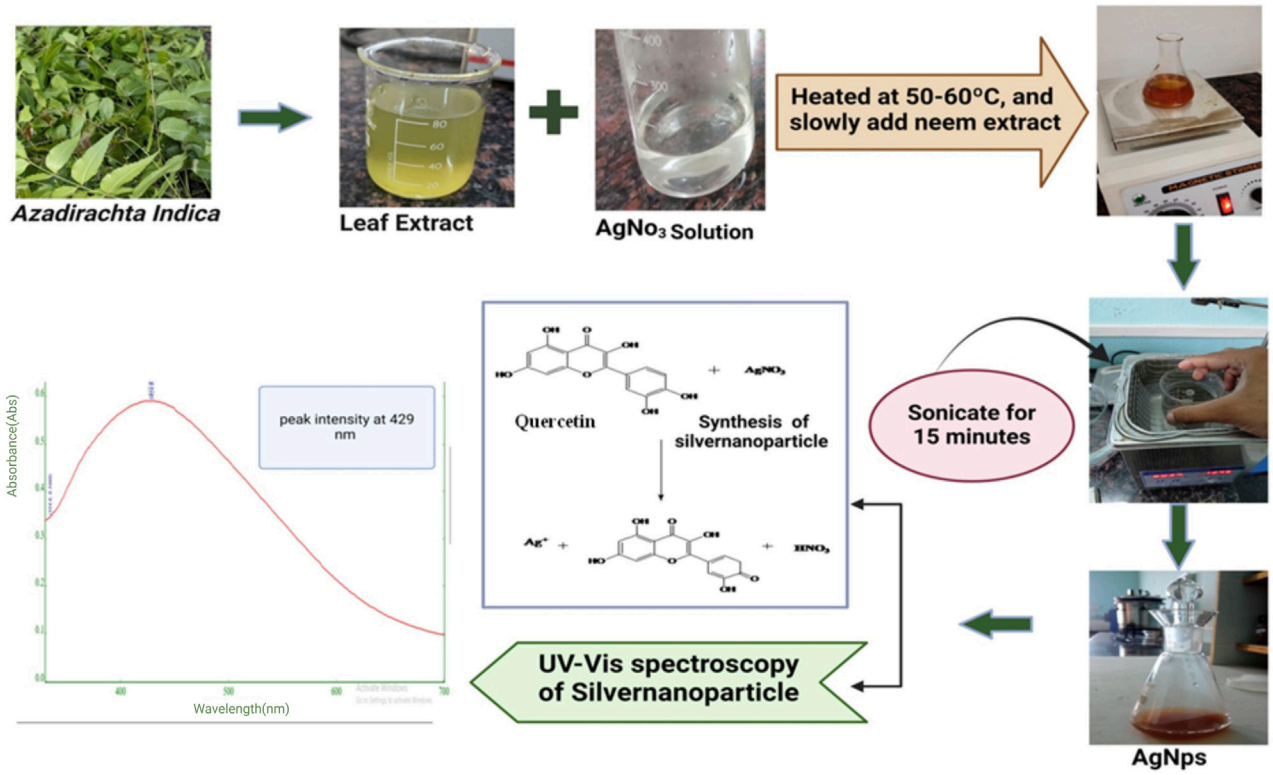

FIGURE 1
Outline of green synthesis steps of experimental Silver nanoparticles (AgNPs) from *Azadirachta indica* leaf extract.

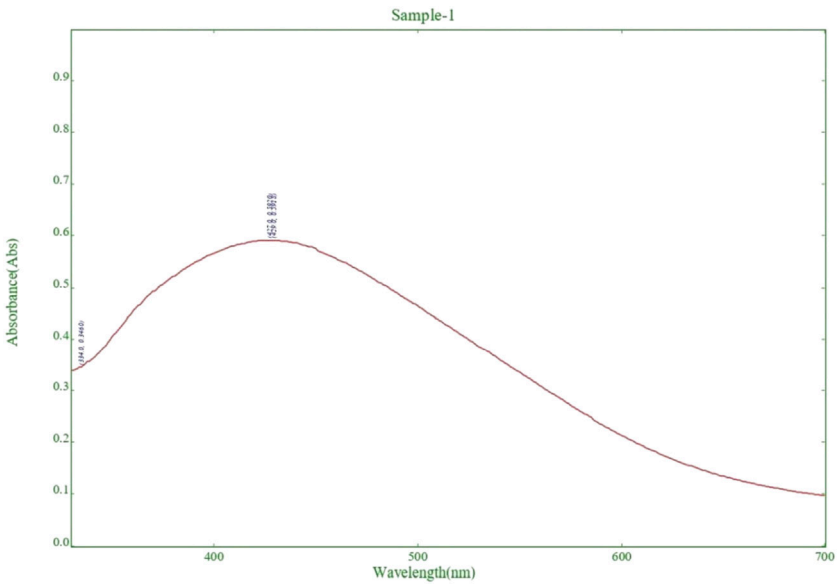

FIGURE 2
Detection of surface plasmon activity in experimental Silver nanoparticle (AgNPs) formation by UV-Visible spectroscopy.

that the AgNPs would stable in solution due to their high negative zeta potential, indicating repulsion between particles. The relatively small particle size suggests good dispersion and the potential for enhanced reactivity in various applications. The low polydispersibility index also indicated a relatively uniform size distribution, further supporting the stability and potential effectiveness of the AgNPs (Abdel-Aty et al., 2023; Singh et al., 2020). As shown in Figures 4A, B.

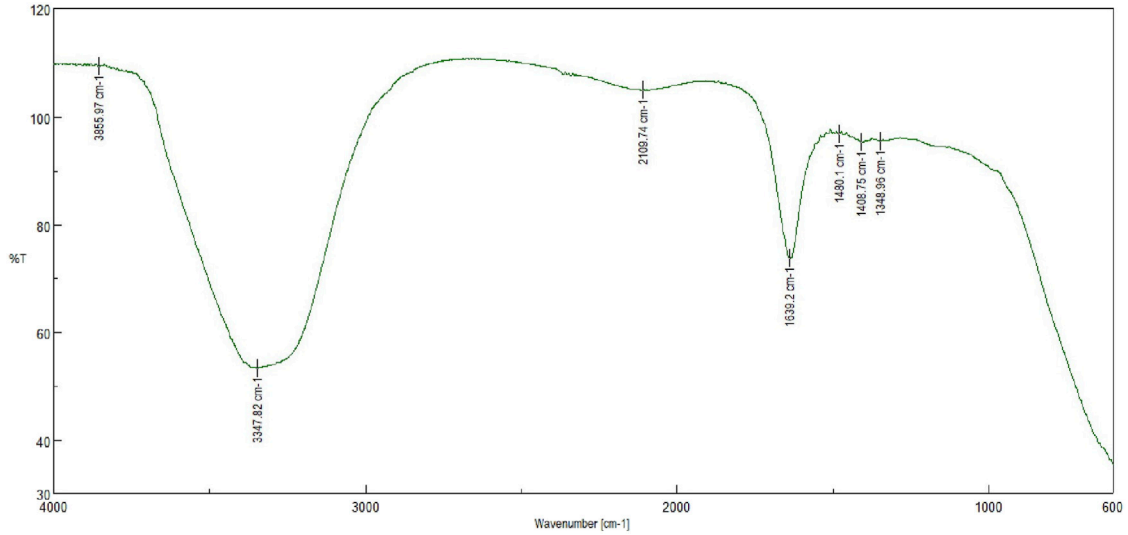

FIGURE 3
FTIR analysis of experimental Silver nanoparticles (AgNPs) showing characteristic peaks.

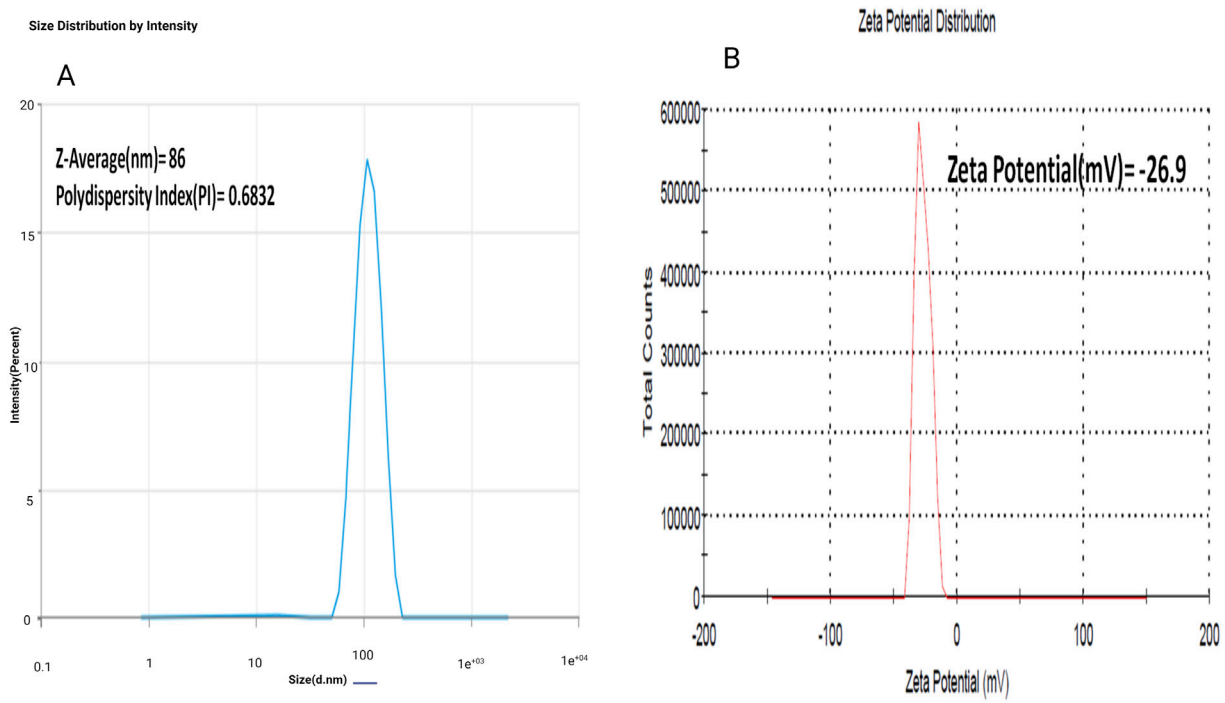

FIGURE 4
(A) Determination of avearge particle size (Z-avg), poly dispersity index (PDI) of experimental Silver nanoparticles (AgNPs); **(B)** Determination of zeta potential of experimental Silver nanoparticles (AgNPs).

3.6 SAED

The results showed that the AgNPs had a uniform size distribution and exhibited a face-centered cubic [FCC] crystal structure. The Selected area electron diffraction (SAED) data obtained from the optimized AgNPs exhibits a circular ring that exhibits the crystalline characteristics of the silver nanoparticles. The dimensions and morphology of the nanoparticles play a crucial role, since their functionalities are contingent upon their size and form. This suggests that the optimized AgNPs were well-formed and possess high purity Figures 5.

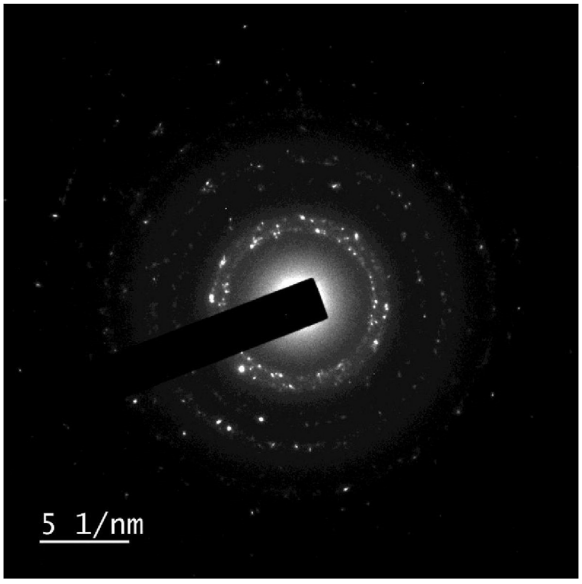

FIGURE 5
Selected area electron diffraction (SAED) characterization of experimental Silver. nanoparticles (AgNPs) to identify crystal structure and defects.

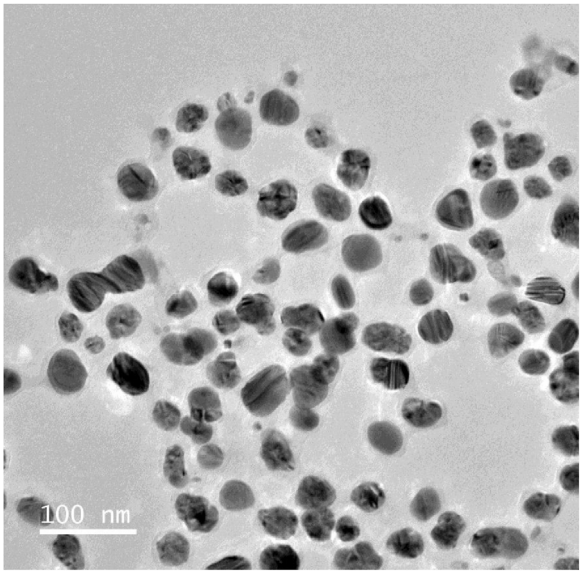

FIGURE 6
Transmision electron microscopic analysis of experimnetal Silver nanoparticles (AgNPs), showing uniform discrete nanosize particles.

3.7 TEM

This analysis determined the diameters ranging from 1 to 100 nm, revealed the existence of evenly distributed and highly crystalline silver nanoparticles. Most of them exhibited a roughly spherical morphology. The image showed that the periphery of the produced silver nanoparticles seemed to be less dense compared to the central region. Biomolecules function as capping agents, inhibiting the aggregation of nanoparticles (Ibrahim et al., 2021; Gontijo et al., 2020). As shown in Figure 6.

3.8 Antimicrobial activity

An antimicrobial study of silver nanoparticles showed promising results against a wide range of pathogenic bacteria and a standard drug to compare the effectiveness of AgNPs which shows a greater zone of inhibition against *P. gingivalish*, measuring 24 mm, *T. denticola*, measuring 22 mm; and *S. aureus*, measuring 20 mm, at a concentration of 75 μg/mL as shown in Table 1 (Donga and Chanda, 2021; Lomelí-Rosales et al., 2022). This research demonstrates that both Azadirachta indica and silver nanoparticles possess potent antibacterial abilities that successfully fight periodontal disorders (Yang et al., 2024; Zhang et al., 2022b). The large inhibition zone values showed that AgNPs could work well as an antibacterial agent against bacteria as shown in Figure 7.

3.9 Antioxidant activity

An Examination of the antioxidant properties of optimized silver nanoparticles (AgNPs) produced from *Azadirachta indica* demonstrated promising findings for possible medicinal uses. When 2.5 mg/mL of aqueous extract was added, the enzyme activity was inhibited by 45.11%. However, using AgNPs resulted in a substantially greater inhibition rate of 62%. By contrast, ascorbic acid, a well-recognized antioxidant, attained an inhibition rate of 72.48%. The results suggest that AgNPs

TABLE 1 *In vitro* antimicrobial efficacy evaluation of AgNPs on selected periodontal pathogens, viz., *S. aureus*, *T. denticola* and *P. gingivalis* through zone of inhibition assay.

Name of organism	Diameter of zone of inhibition [mm]					
	AgNPs (25 μg/mL)	Chlorhexidine (25 μg/mL)	AgNPs (50 μg/mL)	Chlorhexidine (50 μg/mL)	AgNPs (75 μg/mL)	Chlorhexidine (75 μg/mL)
S. aureus	15 ± 1.125	18 ± 2.052	18 ± 1.154	22 ± 1.456	24 ± 1.259	25 ± 1.961
T. denticola	14 ± 2.28	18 ± 1.32	17 ± 1.46	20 ± 2.45	26 ± 1.38	24 ± 1.34
P. gingivalis	18 ± 1.81	23 ± 1.61	22 ± 2.63	25 ± 1.95	25 ± 2.58	28 ± 2.67

Data are expressed Mean ± SD.

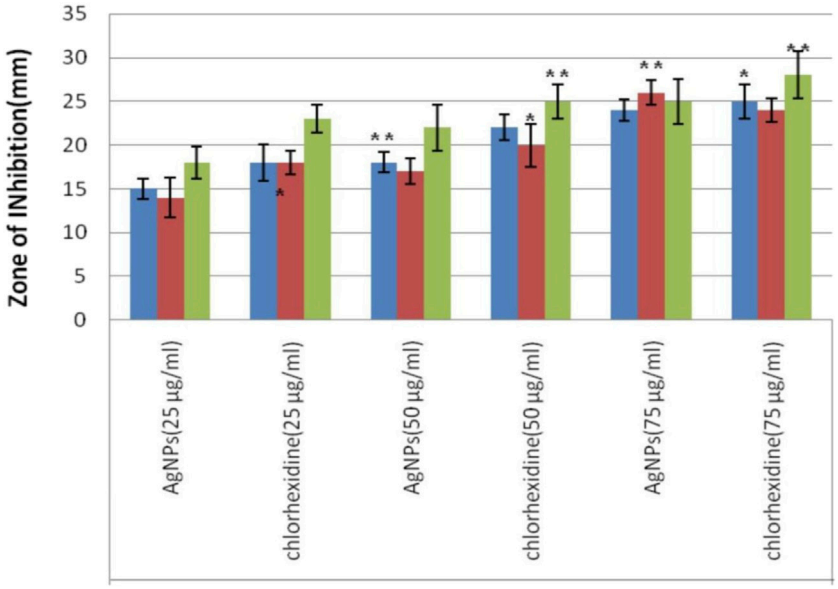

FIGURE 7
Evaluation of antimicrobial effect of experimental Silver nanoparticles (AgNPs) from measurement of zone of inhibition (ZOI) diameter against *S. aureus*, *T. denticola* and *P. gingivalis* at three different tested concentrations vs. Chlorhexidine as standard.

TABLE 2 ***In vitro*** **anti-oxidant activity analysis of experimental AgNPs vs. aqueous extract through DPPH free radical scavenging assay; Ascorbic acid taken as standard.**

Concentration mg/mL	%Inhibition (aqueous extract)	%Inhibition AgNPs	%Inhibition (Ascorbic acid)
0.5	19.27 ± 1.2	40.29 ± 2.4	51.78 ± 1.7
1	22.89 ± 2.3	45.98 ± 2.7	59.89 ± 1.3
1.5	28.49 ± 1.6	50.68 ± 1.4	64.28 ± 1.1
2	35.05 ± 2.1	56.89 ± 1.5	67.99 ± 1.4
2.5	45.11 ± 1.5	62.01 ± 1.9	72.48 ± 1.8

have a higher antioxidant capacity compared to the aqueous extract. The IC_{50} value, representing the concentration needed to block 50% of enzyme activity, was lower for AgNPs compared to the aqueous extract. This indicates that AgNPs have a greater ability to remove harmful free radicals and protect cells from oxidative stress. The study's findings highlight the strong ability of the AgNPs to scavenge DPPH free radicals, hence strengthening their potential for use in the treatment of many disorders associated with oxidative stress. As shown in Table 2. The study's findings highlight the strong ability of the AgNPs to scavenge DPPH free radicals, strengthening their potential for use in periodontal treatment as shown in Figure 8.

3.10 Molecular docking result

The presentation of the primary phytochemical was examined using *in silico* molecular docking simulation (Quercetin) on different virulence factor of selected periodontal causing bacteria's. The findings demonstrated that quercetin interacted with distinct amino acids of the alkyl group at the active site of virulence factor of selected periodontal causing bacteria. These visualizations help to understand quercetin's molecular interactions with enzymes, revealing its therapeutic potential. The docking algorithm was able to predict the Quercetin ligand pose with those mediators viz5Y1A and 3R15 binding energy score of-9.37151 kcal/mol and −9.04139 kcal/mol and amino acids in Collagenase, Protease, and Urease, resulting in binding energies of −7.3, −8.7, and −8.6 kcal/mol, respectively. The results indicate that a large negative score of the mediators viz5Y1A binding energy score of −9.37151 kcal/mol strongly binds with quercetin rather than other proteins (Wu et al., 2024; Keshari et al., 2020). In Figure 9A, the two-dimensional pictures illustrate how quercetin binds to specific sites on the enzymes, affecting their activity. The 3D visualizations in Figure 9B provide a more detailed look at the complex molecular interactions between quercetin and the enzymes, highlighting the specific structural changes that occur during the binding process (Aljelehawy et al., 2022).

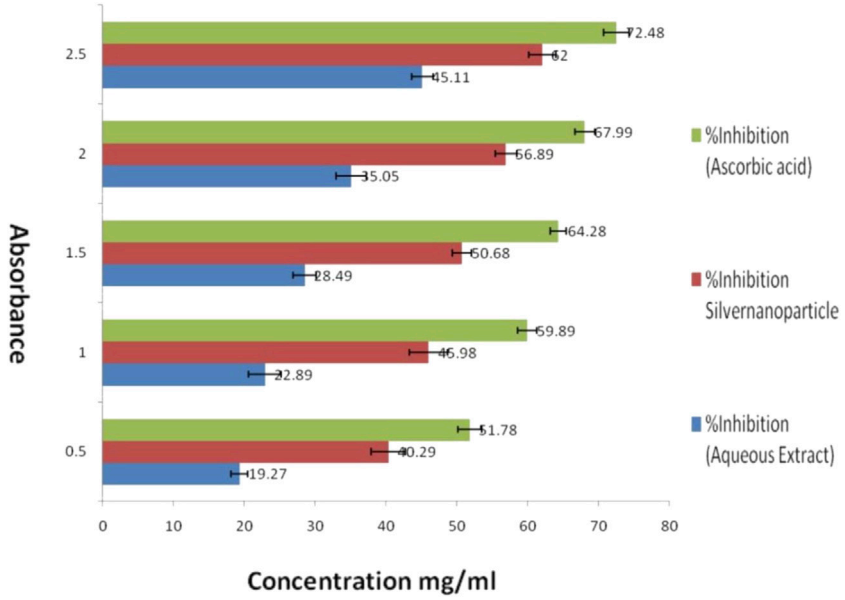

FIGURE 8
Evaluation of *in vitro* anti-oxidant activity of experimental Silver nanoparticles (AgNPs) by DPPH free radical scavenging assay against aqueous extract and ascorbic acid (standard).

3.11 *In-silico* Swiss-ADME analysis

The ADMET attribute of quercetin encompasses several characteristics, including physicochemical properties, lipophilicity, water solubility, pharmacokinetics, and drug-likeness. These attributes play a crucial role in determining the bioavailability and efficacy of quercetin as a potential drug candidate (Anwar et al., 2021).

As per Lipinski's rule, the molecular mass is always less than 500 Da. This rule helps in predicting the likelihood of a compound being orally bioavailable. As per the result, quercetin has a molecular mass of 302.24 Da, which indicates it is a good conductor for the process. The number of H-bond acceptors is below 10, which is 7, which follows Lipinski rule 5. The molar reactivity is about 78.03, which is in the range of 40–130. This suggests that the compound has a moderate reactivity level that indicate a balance between the desired activity of the drug and its potential safety profile, making it potentially suitable for further drug development. The topological surface area can predict the solubility parameter of a compound, which is about (TPSA) 131.36 $Å^2$. This value suggesting moderate absorption potential and the compound is unlikely to cross the BBB effectively, meaning it may not have central nervous system (CNS) effects. A TPSA under 140 $Å^2$ is generally favorable for oral bioavailability, so this result suggests that the compound suitable for oral administration. The log P value, which is less than 5, is what determines a compound's lipophilicity, and the average value is 1.22. The water solubility property of the compound shows that it is soluble in nature. The pharmacokinetic property shows high GI absorption; there is no blood-brain barrier permeation. The compound can be metabolized by the enzymes cytochrome P1A22, P2D6, P2D6, and P3A. The skin permeability log Kp is about 7.05 cm/s suggests that the compound has very high permeability through the skin. This is crucial for topical or transdermal drug delivery, as it indicates that the drug can effectively pass through the skin barrier and enter systemic circulation. Moderate reactivity and high skin permeability suggest that the compound could be effective in skin-based delivery methods.

The pharmacokinetics property shows the different parameters for designing a drug molecule and using the polymer to get more action. The drug-likeness property of the compound shows there is no violation of Lipinski, and the bioavailability score is about 0.55. A bioavailability score of 0.55 indicates that 55% of the orally administered compound reaches systemic circulation. This suggests that the compound has moderate oral absorption but may still be affected by factors like first-pass metabolism or poor permeability. The ADMET property of Quercetin was illustrated in the Table 3.

The BOILED-Egg model simplifies the calculation of molecular polarity and lipophilicity. According to the findings of the BOILED-Egg model, the molecules would appear in the white section of the egg, which would indicate that they were absorbed by the gastrointestinal tract. The BOILED-Egg model provides a visual representation of where the molecule is likely to be absorbed in the body, guiding further research and development efforts. Overall, the compound appears to have favorable properties for drug development, with high solubility, absorption, and metabolism rates. The skin permeability and pharmacokinetics data suggest that the compound could be effective when administered orally or through the skin.

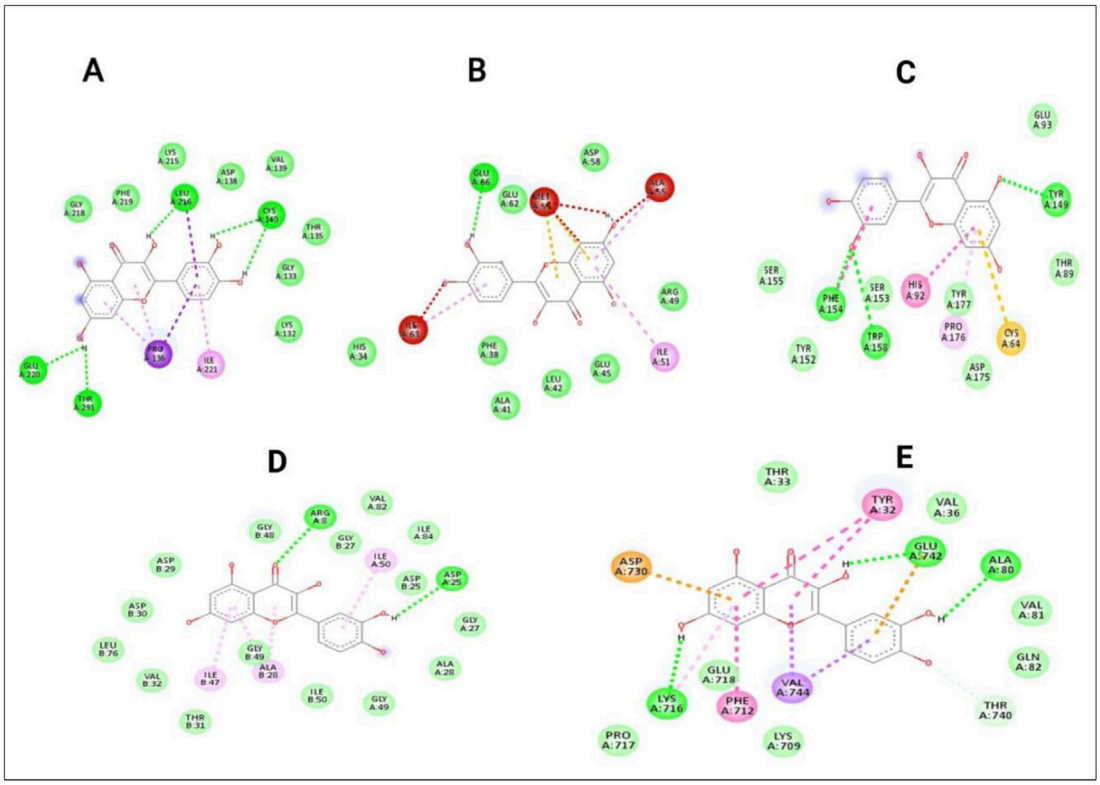

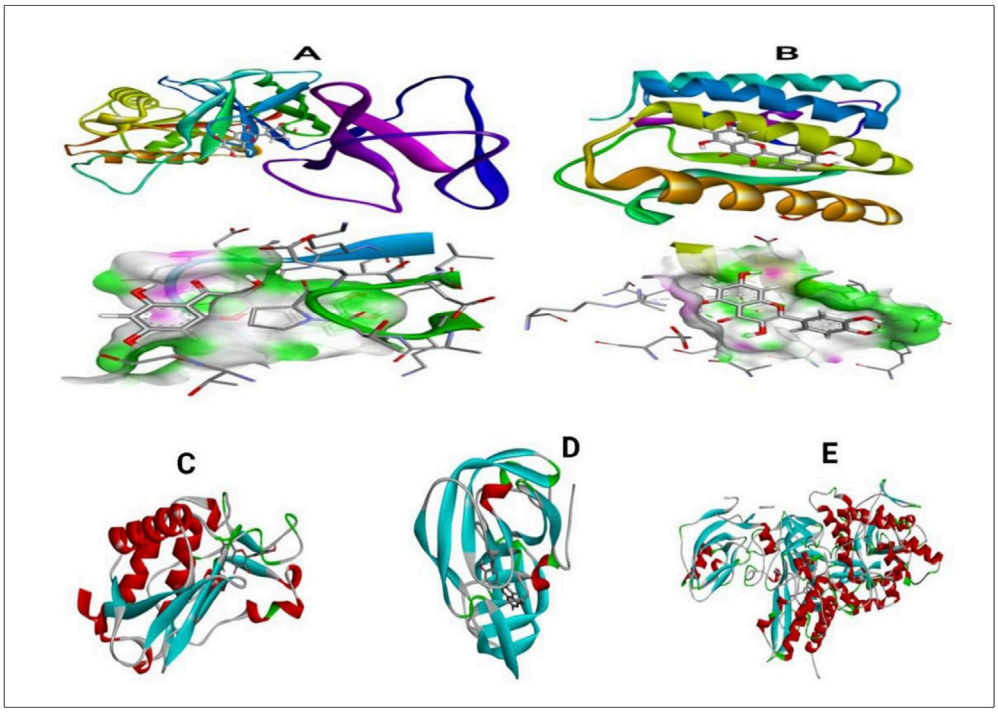

FIGURE 9
(A) In silico docking analysis of quercetin with five different selected proteins represented as two-dimensional images **(B)** Three-dimensional images of quercetin interacting with selected periodontal pathogenic proteins.

TABLE 3 Insight into ADMET property analysis of Quercetin using SWISS ADMET.

Physicochemical properties		Lipophilicity		Water solubility		Pharmaco-kinetics		Drug likeness	
Formula	$C_{15}H_{10}O_7$	Log $P_{o/w}$ (iLOGP)	1.63	Log S (ESOL)	−3.16	GI absorption	High	Lipinski	Yes; 0 violation
Molecular weight	302.24 g/mol	Log $P_{o/w}$ (XLOGP3)	1.54	Solubility	2.11e-01 mg/mL; 6.98e-04 mol/L	BBB permeation	No	Ghose	Yes
Num. heavy atoms	22	Log $P_{o/w}$ (WLOGP)	1.99	Class	Soluble	P-gp substrate	No	Veber	Yes
Num. arom. heavy atoms	16	Log $P_{o/w}$ (MLOGP)	−0.56	Log S (Ali)	−3.91	CYP1A2 inhibitor	Yes	Egan	Yes
Fraction Csp3	0.00	Log $P_{o/w}$ (SILICOS-IT)	1.54	Solubility	3.74e-02 mg/mL; 1.24e-04 mol/L	CYP2C19 inhibitor	No	Muegge	Yes
Num. rotatable bonds	1	Consensus Log $P_{o/w}$	1.23	Class	Soluble	CYP2C9 inhibitor	No	Bioavailability Score	0.55
Num. H-bond acceptors	7			Log S (SILICOS-IT)	−3.24	CYP2D6 inhibitor	Yes		
Num. H-bond donors	5			Solubility	1.73e-01 mg/mL; 5.73e-04 mol/L	CYP3A4 inhibitor	Yes		
Molar Refractivity	78.03			Class	Soluble	Log K_p (skin permeation)	−7.05 cm/s		
TPSA	131.36 Å^2								

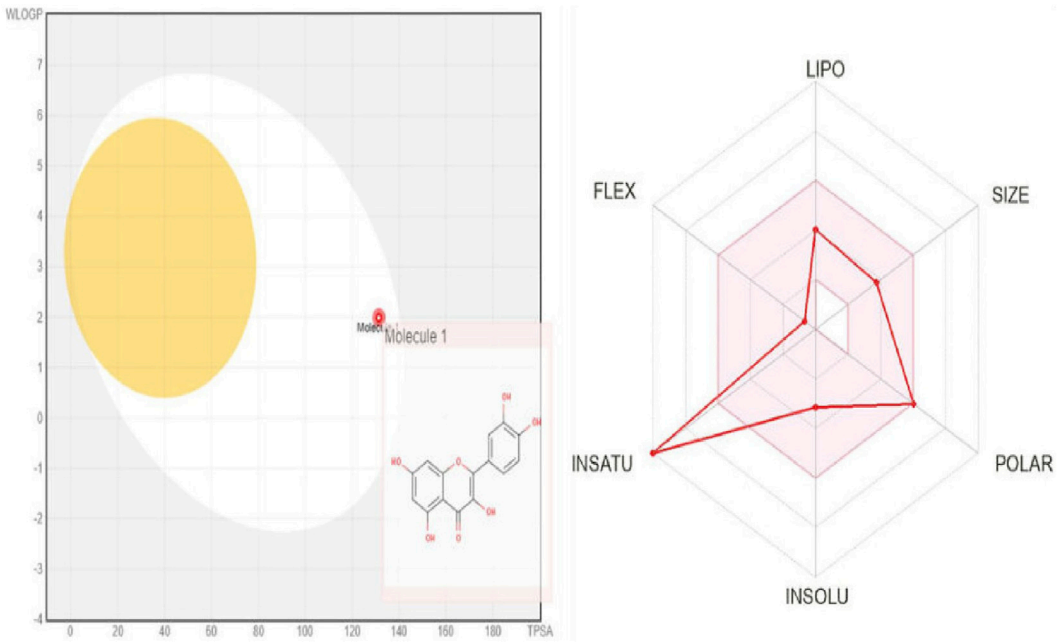

FIGURE 10
ADME analysis of quercetin using BOILED-Egg model.

Additionally, the lack of blood-brain barrier permeation indicates that the compound may have a lower risk of causing central nervous system side effects. The adherence to Lipinski's rule of five and favorable bioavailability score further support the potential of this compound as a drug candidate [69]. The BOILED-Egg model of Quercetin was illustrated (Figure 10).

4 Conclusion

One easy, green, and inexpensive way to make AgNPs is to use the extract from the leaves of the *Azadirachta indica* plant. The *Azadirachta indica* leaves contain phytochemicals, including flavonoid (Quercetin), which function as both reducing and capping agents throughout the synthesis process. The silver nanoparticles (AgNPs) show strong antibacterial efficacy against pathogenic gram-negative strains. The ability of AgNPs to break down bacterial cell membranes, stop metabolic processes, and make reactive oxygen species makes them antibacterial. The *Azadirachta indica* derived AgNPs not only possess antibacterial activities but also exhibit substantial antioxidant activity. The *Azadirachta indica* leaves include phytochemicals that enhance the ability of the AgNPs to neutralize free radicals and reduce them. Their size was determined to be 86 nm, with a potential of −26.9 mV. Furthermore, the SAED, FTIR, AFM, and TEM analyses demonstrated advantageous morphological properties of the silver nanoparticles. The promising results from *in silico* docking and ADME analyses demonstrated that Quercetin exhibits strong binding affinity to the target protein, which is critically involved in bacterial growth and biofilm formation on teeth. Additionally, ADME analysis indicated high skin permeability, supporting the potential of a synergistic combination of Quercetin and silver nanoparticles for effective topical application in periodontal therapy. The detailed study of the synthesized AgNPs gives us important information about their structure and function, which supports the idea that they could be used to treat gum disease. The study indicates that the synthesized AgNPs have acceptable pharmacokinetic features and low toxicity, making them appropriate for biomedical applications, particularly periodontal usage.

5 Future scope

Anticipating the future, the potential of this study is quite promising. Continued improvement of the synthesis process and optimization approaches may result in the powerful formulations that have improved medicinal benefits. Furthermore, exploring the possible synergistic impacts with other therapeutic agents might open up novel approaches for periodontal disorders. Additionally, continued research into the effectiveness and safety of these novel treatments will be crucial in advancing the field of periodontics.

Data availability statement

The original contributions presented in the study are included in the article/Supplementary Material, further inquiries can be directed to the corresponding authors.

Author contributions

BB: Software, Writing–review and editing. BS: Data curation, Methodology, Writing–original draft. GP: Investigation, Writing–original draft. DB: Data curation, Formal Analysis, Writing–original draft. KS: Conceptualization, Validation, Writing–original draft.

Funding

The author(s) declare that financial support was received for the research, authorship, and/or publication of this article. The work was funded by Ajman University, United Arab Emirates. Authors express their gratitude for the financial support.

Acknowledgments

I, KPS would thankful to the Deanship of graduate studies and research, Ajman University for necessary support towards Article Publication charges for this manuscript.

Conflict of interest

The authors declare that the research was conducted in the absence of any commercial or financial relationships that could be construed as a potential conflict of interest.

Publisher's note

All claims expressed in this article are solely those of the authors and do not necessarily represent those of their affiliated organizations, or those of the publisher, the editors and the reviewers. Any product that may be evaluated in this article, or claim that may be made by its manufacturer, is not guaranteed or endorsed by the publisher.

Supplementary material

The Supplementary Material for this article can be found online at: https://www.frontiersin.org/articles/10.3389/fchem.2024.1489253/full#supplementary-material

References

Abdel-Aty, A. M., Barakat, A. Z., Bassuiny, R. I., and Mohamed, S. A. (2023). Statistical optimization, characterization, antioxidant and antibacterial properties of silver nanoparticle biosynthesized by saw palmetto seed phenolic extract. *Sci. Rep.* 13 (1), 15605. doi:10.1038/s41598-023-42675-0

Adaramola, F., Adewole, S., and Adewole, O. (2023). Assessment of phytochemicals, antioxidant and antimicrobial activities of aqueous ethanol extract and fractions of Azadirachta indica stem bark. *Int. J. Sci. Glob. Sustain.* 9 (1), 13. doi:10.57233/ijsgs.v9i1.401

Aljelehawy, Q., Mal Allah, O. R., and Sourazur, G. (2022). Physicochemical properties, medicinal chemistry, toxicity, and absorption of quercetin and its interaction with spike glycoprotein of SARS-CoV-2: molecular docking. *Nano Micro Biosyst.* 1 (1), 32–39. doi:10.22034/nmbj.2022.163207

Amananti, W., Riyantal, A. B., Kusnadi, K., and Aledresi, K. A. M. S. (2022). Green synthesis and antibacterial activity of silver nanoparticles using turi (Sesbania grandiflora lour) leaf extract. *EKSAKTA Berk. Ilm. Bid. MIPA* 23 (04), 255–265. doi:10.24036/eksakta/vol23-iss04/337

Anwar, S. S., Al-Shmgani, H. S., Tawfeeq, A. T., Sulaiman, G. M., and Al-Mousawi, Y. H. (2021). *In silico* analysis of quercetin as potential anti-cancer agents. *Mater. Today Proc.* 42, 2521–2526. doi:10.1016/j.matpr.2020.12.573

Bajpai, R., Roy, S., and Verma, S. (2022). Microwave-assisted solid-state synthesis of dichalcogenide nanostructures for electrocatalytic hydrogen evolution. *ACS Appl. Nano Mater.* 5 (6), 8511–8525. doi:10.1021/acsanm.2c01908

Chavan, R. R., Bhutkar, M. A., and Bhinge, S. D. (2023). Design, synthesis, and optimization of silver nanoparticles using an Artocarpus heterophyllus Lam. leaf extract and its antibacterial application. *Nano Biomed. Eng.* 15 (3), 239–252. doi:10.26599/nbe.2023.9290011

Chinnasamy, G., Chandrasekharan, S., Koh, T. W., and Bhatnagar, S. (2021). Synthesis, characterization, antibacterial and wound healing efficacy of silver nanoparticles from Azadirachta indica. *Front. Microbiol.* 12, 611560. doi:10.3389/fmicb.2021.611560

Dashora, A., Rathore, K., Raj, S., and Sharma, K. (2022). Synthesis of silver nanoparticles employing Polyalthia longifolia leaf extract and their *in vitro* antifungal activity against phytopathogen. *Biochem. Biophysics Rep.* 31, 101320. doi:10.1016/j.bbrep.2022.101320

Donga, S., and Chanda, S. (2021). Facile green synthesis of silver nanoparticles using Mangifera indica seed aqueous extract and its antimicrobial, antioxidant and cytotoxic potential (3-in-1 system). *Artif. Cells, Nanomedicine, Biotechnol.* 49 (1), 292–302. doi:10.1080/21691401.2021.1899193

Dubey, P., and Mittal, N. (2020). Periodontal diseases-a brief review. *Int. J. Oral Heal Dent.* 6 (3), 177–187. doi:10.18231/j.ijohd.2020.038

Dutt, Y., Pandey, R. P., Dutt, M., Gupta, A., Vibhuti, A., Raj, V. S., et al. (2023). Silver nanoparticles phytofabricated through Azadirachta indica: anticancer, apoptotic, and wound-healing properties. *Antibiotics* 12 (1), 121. doi:10.3390/antibiotics12010121

Gidiagba, J. O., Daraojimba, C., Ofonagoro, K. A., Eyo-Udo, N. L., Egbokhaebho, B. A., Ogunjobi, O. A., et al. (2023). Economic impacts and innovations in materials science: a holistic exploration of nanotechnology and advanced materials. *Eng. Sci. and Technol. J.* 4 (3), 84–100. doi:10.51594/estj.v4i3.553

Gonfa, Y. H., Gelagle, A. A., Hailegnaw, B., Kabeto, S. A., Workeneh, G. A., Tessema, F. B., et al. (2023). Optimization, characterization, and biological applications of silver nanoparticles synthesized using essential oil of aerial part of Laggera tomentosa. *Sustainability* 15 (1), 797. doi:10.3390/su15010797

Gontijo, L. A. P., Raphael, E., Ferrari, D. P. S., Ferrari, J. L., Lyon, J. P., and Schiavon, M. A. (2020). pH effect on the synthesis of different size silver nanoparticles evaluated by DLS and their size-dependent antimicrobial activity. *Matéria (Rio de Janeiro)* 25 (04), e–12845. doi:10.1590/s1517-707620200004.1145

Grizzo, A., Dos Santos, D. M., da Costa, V. P., Lopes, R. G., Inada, N. M., Correa, D. S., et al. (2023). Multifunctional bilayer membranes composed of poly (lactic acid), beta-chitin whiskers and silver nanoparticles for wound dressing applications. *Int. J. Biol. Macromol.* 251, 126314. doi:10.1016/j.ijbiomac.2023.126314

Gupta, D., Boora, A., Thakur, A., and Gupta, T. K. (2023). Green and sustainable synthesis of nanomaterials: recent advancements and limitations. *Environ. Res.* 231, 116316. doi:10.1016/j.envres.2023.116316

Habeeb Rahuman, H. B., Dhandapani, R., Narayanan, S., Palanivel, V., Paramasivam, R., Subbarayalu, R., et al. (2022). Medicinal plants mediated the green synthesis of silver nanoparticles and their biomedical applications. *IET nanobiotechnology* 16 (4), 115–144. doi:10.1049/nbt2.12078

Halilu, E. M., Ngweh, V. A., and Airemwen, C. O. (2023). Green synthesis of silver nanoparticles from Parinari curatellifolia methanol stem bark extract and evaluation of antioxidant and antimicrobial activities. *Trop. J. Nat. Prod. Res.* 7 (3). doi:10.26538/tjnpr/v7i3.5

Hameed, A., Rehman, T. U., Rehan, Z. A., Noreen, R., Iqbal, S., Batool, S., et al. (2022). Development of polymeric nanofibers blended with extract of neem (Azadirachta indica), for potential biomedical applications. *Front. Mater.* 9, 1042304. doi:10.3389/fmats.2022.1042304

Harish, V., Ansari, M. M., Tewari, D., Yadav, A. B., Sharma, N., Bawarig, S., et al. (2023). Cutting-edge advances in tailoring size, shape, and functionality of nanoparticles and nanostructures: a review. *J. Taiwan Inst. Chem. Eng.* 149, 105010. doi:10.1016/j.jtice.2023.105010

Hasan, M. M., Khan, Z., Chowdhury, M. S., Khan, M. A., Moni, M. A., and Rahman, M. H. (2022). *In silico* molecular docking and ADME/T analysis of Quercetin compound with its evaluation of broad-spectrum therapeutic potential against particular diseases. *Inf. Med. Unlocked* 29, 100894. doi:10.1016/j.imu.2022.100894

Hashemi, Z., Shirzadi-Ahodashti, M., Mortazavi-Derazkola, S., and Ebrahimzadeh, M. A. (2022). Sustainable biosynthesis of metallic silver nanoparticles using barberry phenolic extract: optimization and evaluation of photocatalytic, *in vitro* cytotoxicity, and antibacterial activities against multidrug-resistant bacteria. *Inorg. Chem. Commun.* 139, 109320. doi:10.1016/j.inoche.2022.109320

Hedayatipanah, M., Gholami, L., Farmany, A., Alikhani, M. Y., Hooshyarfard, A., and Hashemiyan, F. S. (2024). Green synthesis of silver nanoparticles and evaluation of their effects on the Porphyromonas gingivalis bacterial biofilm formation. *Clin. Exp. Dent. Res.* 10 (3), e887. doi:10.1002/cre2.887

Hernández-Venegas, P. A., Martínez-Martínez, R. E., Zaragoza-Contreras, E. A., Domínguez-Pérez, R. A., Reyes-López, S. Y., Donohue-Cornejo, A., et al. (2023). Bactericidal activity of silver nanoparticles on oral biofilms related to patients with and without periodontal disease. *J. Funct. Biomaterials* 14 (6), 311. doi:10.3390/jfb14060311

Hossain, N., Islam, M. A., Ahmed, M. M. S., Chowdhury, M. A., Mobarak, M. H., Rahman, M. M., et al. (2024). Advances and significances of titaniumin dental implant applications. *Results Chem.* 7, 101394. doi:10.1016/j.rechem.2024.101394

Hu, X., Zuo, D., Cheng, S., Chen, S., Liu, Y., Bao, W., et al. (2023). Ultrafast materials synthesis and manufacturing techniques for emerging energy and environmental applications. *Chem. Soc. Rev.* 52 (3), 1103–1128. doi:10.1039/d2cs00322h

Huq, M. A., Ashrafudoulla, M., Rahman, M. M., Balusamy, S. R., and Akter, S. (2022). Green synthesis and potential antibacterial applications of bioactive silver nanoparticles: a review. *Polymers* 14 (4), 742. doi:10.3390/polym14040742

Ibrahim, S., Ahmad, Z., Manzoor, M. Z., Mujahid, M., Faheem, Z., and Adnan, A. (2021). Optimization for biogenic microbial synthesis of silver nanoparticles through response surface methodology, characterization, their antimicrobial, antioxidant, and catalytic potential. *Sci. Rep.* 11 (1), 770. doi:10.1038/s41598-020-80805-0

Ijaz, I., Bukhari, A., Gilani, E., Nazir, A., Zain, H., Saeed, R., et al. (2022). Green synthesis of silver nanoparticles using different plants parts and biological organisms, characterization and antibacterial activity. *Environ. Nanotechnol. Monit. and Manag.* 18, 100704. doi:10.1016/j.enmm.2022.100704

Imchen, P., Ziekhrü, M., Zhimomi, B. K., and Phucho, T. (2022). Biosynthesis of silver nanoparticles using the extract of Alpinia galanga rhizome and Rhus semialata fruit and their antibacterial activity. *Inorg. Chem. Commun.* 142, 109599. doi:10.1016/j.inoche.2022.109599

Karan, T., Gonulalan, Z., Erenler, R., Kolemen, U., and Eminagaoglu, O. (2024). Green synthesis of silver nanoparticles using Sambucus ebulus leaves extract: characterization, quantitative analysis of bioactive molecules, antioxidant and antibacterial activities. *J. Mol. Struct.* 1296, 136836. doi:10.1016/j.molstruc.2023.136836

Kemala, P., Idroes, R., Khairan, K., Ramli, M., Jalil, Z., Idroes, G. M., et al. (2022). Green synthesis and antimicrobial activities of silver nanoparticles using Calotropis gigantea from Ie Seu-Um Geothermal area, Aceh Province, Indonesia. *Molecules* 27 (16), 5310. doi:10.3390/molecules27165310

Keshari, A. K., Srivastava, R., Singh, P., Yadav, V. B., and Nath, G. (2020). Antioxidant and antibacterial activity of silver nanoparticles synthesized by Cestrum nocturnum. *J. Ayurveda Integr. Med.* 11 (1), 37–44. doi:10.1016/j.jaim.2017.11.003

Khan, Y., Sadia, H., Ali Shah, S. Z., Khan, M. N., Shah, A. A., Ullah, N., et al. (2022). Classification, synthetic, and characterization approaches to nanoparticles, and their applications in various fields of nanotechnology: a review. *Catalysts* 12 (11), 1386. doi:10.3390/catal12111386

Kumar, Y., Paswan, K. K., Nayan, K., Pandurangappa, G., Dwivedi, D., and Sangwai, J. S. (2023). "Introduction to functional materials: synthesis, properties, environmental sustainability, and general applications," in *Functional materials for the oil and gas industry* (London: CRC Press), 1–22.

Liaqat, N., Jahan, N., Anwar, T., and Qureshi, H. (2022). Green synthesized silver nanoparticles: optimization, characterization, antimicrobial activity, and cytotoxicity study by hemolysis assay. *Front. Chem.* 10, 952006. doi:10.3389/fchem.2022.952006

Lomelí-Rosales, D. A., Zamudio-Ojeda, A., Reyes-Maldonado, O. K., López-Reyes, M. E., Basulto-Padilla, G. C., Lopez-Naranjo, E. J., et al. (2022). Green synthesis of gold and silver nanoparticles using leaf extract of Capsicum chinense plant. *Molecules* 27 (5), 1692. doi:10.3390/molecules27051692

Malandrakis, A. A., Kavroulakis, N., and Chrysikopoulos, C. V. (2022). Metal nanoparticles against fungicide resistance: alternatives or partners? *Pest Manag. Sci.* 78 (10), 3953–3956. doi:10.1002/ps.7014

Mallineni, S. K., Sakhamuri, S., Kotha, S. L., AlAsmari, A. R. G. M., AlJefri, G. H., Almotawah, F. N., et al. (2023). Silver nanoparticles in dental applications: a descriptive review. *Bioengineering* 10 (3), 327. doi:10.3390/bioengineering10030327

Moges, A., and Goud, V. V. (2022). Optimization, characterization, and evaluation of antioxidant and antibacterial activities of silver nanoparticles synthesized from Hippophae salicifolia D. Don. *Inorg. Chem. Commun.* 146, 110086. doi:10.1016/j.inoche.2022.110086

Muraro, P. C. L., Pinheiro, L. D. S. M., Chuy, G., Vizzotto, B. S., Pavoski, G., Espinosa, D. C. R., et al. (2022). Silver nanoparticles from residual biomass: biosynthesis,

characterization and antimicrobial activity. *J. Biotechnol.* 343, 47–51. doi:10.1016/j.jbiotec.2021.11.003

Nelagadarnahalli, H. J., Jacob, G. K., Prakash, D., Iska, R. R., Iska, V. B. R., Ameen, F., et al. (2023). Optimization and fabrication of silver nanoparticles to assess the beneficial biological effects besides the inhibition of pathogenic microbes and their biofilms. *Inorg. Chem. Commun.* 156, 111140. doi:10.1016/j.inoche.2023.111140

Nesappan, T., and Subramani, A. (2023). Preparation of implant-prosthetic disinfectant solution by chitosan, green synthesized silver nanoparticles using cymbopogon citratus, azadirachta indica, melaleuca alternifolia and evaluation of its antimicrobial properties-an invitro study. *J. Pharm. Negat. Results* 14 (2). doi:10.47750/pnr.2023.14.02.241

Ortega, F., Versino, F., López, O. V., and García, M. A. (2022). Biobased composites from agro-industrial wastes and by-products. *Emergent Mater.* 5 (3), 873–921. doi:10.1007/s42247-021-00319-x

Osherov, A., Prasad, R., Chrzanowski, W., New, E. J., Brazaca, L., Sadik, O., et al. (2023). Responsible nanotechnology for a sustainable future. *One Earth* 6 (7), 763–766. doi:10.1016/j.oneear.2023.06.010

Owaid, M. N., Rabeea, M. A., Aziz, A. A., Jameel, M. S., and Dheyab, M. A. (2021). "Mycogenic fabrication of silver nanoparticles using Picoa," in *Pezizales, characterization and their antifungal activity*. doi:10.1016/j.enmm.2021.100612

Ozdal, M., and Gurkok, S. (2022). Recent advances in nanoparticles as antibacterial agent. *ADMET DMPK* 10 (2), 115–129. doi:10.5599/admet.1172

Prakash, V., Akhtar, S., Kumar, J., Mishra, S. K., and Pandey, R. R. (2022). "Azadirachta indica: the multifaceted and versatile tree," in *Current trends in medicinal chemistry*.

Salem, H. F., Nafady, M. M., Ewees, M. G. E. D., Hassan, H., and Khallaf, R. A. (2022). Rosuvastatin calcium-based novel nanocubic vesicles capped with silver nanoparticles-loaded hydrogel for wound healing management: optimization employing Box–Behnken design: *in vitro* and *in vivo* assessment. *J. Liposome Res.* 32 (1), 45–61. doi:10.1080/08982104.2020.1867166

Satapathy, B. S., Mishra, A., Biswal, S. K., Pattnaik, S., Parida, R., Biswal, B., et al. (2024). Encapsulation of Alpinia leaf essential oil in nanophytosome-embedded gel as novel strategy to treat periodontal infections: evaluation of antimicrobial effectiveness, pharmacokinetic, *in vitro-ex vivo* correlation and *in silico* studies. *J. Microencapsul.* 41, 327–344. doi:10.1080/02652048.2024.2354234

Sedghi, L., DiMassa, V., Harrington, A., Lynch, S. V., and Kapila, Y. L. (2021). The oral microbiome: role of key organisms and complex networks in oral health and disease. *Periodontology* 87 (1), 107–131. doi:10.1111/prd.12393

Shareef, M. A., Sirisha, K., Sayeed, I. B., Khan, I., Ganapathi, T., Akbar, S., et al. (2019). Synthesis of new triazole fused imidazo[2,1-b]thiazole hybrids with emphasis on *Staphylococcus aureus* virulence factors. *Bioorg. and Med. Chem. Lett.* 29 (19), 126621. doi:10.1016/j.bmcl.2019.08.025

Sharifi-Rad, M., Elshafie, H. S., and Pohl, P. (2024). Green synthesis of silver nanoparticles (AgNPs) by Lallemantia royleana leaf extract: their bio-pharmaceutical and catalytic properties. *J. Photochem. Photobiol. A Chem.* 448, 115318. doi:10.1016/j.jphotochem.2023.115318

Sharma, N. K., Vishwakarma, J., Rai, S., Alomar, T. S., AlMasoud, N., and Bhattarai, A. (2022). Green route synthesis and characterization techniques of silver nanoparticles and their biological adeptness. *ACS omega* 7 (31), 27004–27020. doi:10.1021/acsomega.2c01400

Shirmohammadi, A., Maleki Dizaj, S., Sharifi, S., Fattahi, S., Negahdari, R., Ghavimi, M. A., et al. (2023). Promising antimicrobial action of sustained released curcumin-loaded silica nanoparticles against clinically isolated Porphyromonas gingivalis. *Diseases* 11 (1), 48. doi:10.3390/diseases11010048

Singh, A., Gaud, B., and Jaybhaye, S. (2020). Optimization of synthesis parameters of silver nanoparticles and its antimicrobial activity. *Mater. Sci. Energy Technol.* 3, 232–236. doi:10.1016/j.mset.2019.08.004

Singh, P., and Mijakovic, I. (2022a). Green synthesis and antibacterial applications of gold and silver nanoparticles from Ligustrum vulgare berries. *Sci. Rep.* 12 (1), 7902. doi:10.1038/s41598-022-11811-7

Singh, P., and Mijakovic, I. (2022b). Strong antimicrobial activity of silver nanoparticles obtained by the green synthesis in Viridibacillus sp. extracts. *Front. Microbiol.* 13, 820048. doi:10.3389/fmicb.2022.820048

Vijayaram, S., Razafindralambo, H., Sun, Y. Z., Vasantharaj, S., Ghafarifarsani, H., Hoseinifar, S. H., et al. (2024). Applications of green synthesized metal nanoparticles—a review. *Biol. Trace Elem. Res.* 202 (1), 360–386. doi:10.1007/s12011-023-03645-9

Wade, W. G. (2021). Resilience of the oral microbiome. *Periodontology* 86 (1), 113–122. doi:10.1111/prd.12365

Wasilewska, A., Klekotka, U., Zambrzycka, M., Zambrowski, G., Święcicka, I., and Kalska-Szostko, B. (2023). Physico-chemical properties and antimicrobial activity of silver nanoparticles fabricated by green synthesis. *Food Chem.* 400, 133960. doi:10.1016/j.foodchem.2022.133960

Wu, T., Fu, Y., Guo, S., Shi, Y., Zhang, Y., Fan, Z., et al. (2024). Self assembly multifunctional DNA tetrahedron for efficient elimination of antibiotic resistant bacteria. *Aggregate* 5 (1), e402. doi:10.1002/agt2.402

Xu, Q., Cai, H., Li, W., Wu, M., Wu, Y., and Gong, X. (2022). Carbon dot/inorganic nanomaterial composites. *J. Mater. Chem. A* 10 (28), 14709–14731. doi:10.1039/d2ta02628g

Yang, B., Yang, H., Liang, J., Chen, J., Wang, C., Wang, Y., et al. (2024). A review on the screening methods for the discovery of natural antimicrobial peptides. *J. Pharm. Analysis*, 101046. doi:10.1016/j.jpha.2024.101046

Yun, Z., Qin, D., Wei, F., and Xiaobing, L. (2022). Application of antibacterial nanoparticles in orthodontic materials. *Nanotechnol. Rev.* 11 (1), 2433–2450. doi:10.1515/ntrev-2022-0137

Zhang, L., Shi, H., Tan, X., Jiang, Z., Wang, P., and Qin, J. (2022b). Ten-gram-scale mechanochemical synthesis of ternary lanthanum coordination polymers for antibacterial and antitumor activities. *Front. Chem.* 10, 898324. doi:10.3389/fchem.2022.898324

Zhang, S., Lin, L., Huang, X., Lu, Y. G., Zheng, D. L., and Feng, Y. (2022a). Antimicrobial properties of metal nanoparticles and their oxide materials and their applications in oral biology. *J. Nanomater.* 2022 (1), 2063265. doi:10.1155/2022/2063265

frontiers | Frontiers in Chemistry

TYPE Original Research
PUBLISHED 16 October 2024
DOI 10.3389/fchem.2024.1482852

OPEN ACCESS

EDITED BY
Oliviu Vostinaru,
University of Medicine and Pharmacy Iuliu Hatieganu, Romania

REVIEWED BY
Abdullah A. A. Ahmed,
Thamar University, Yemen
Valentin Duvauchelle,
Umeå University, Sweden

*CORRESPONDENCE
Avisek Mahapa,
avisek.mahapa@iiim.res.in
Prasoon Gupta,
guptap@iiim.ac.in
Jasha Momo H. Anal,
hmunshel.jasha@iiim.res.in

†These authors have contributed equally to this work

RECEIVED 18 August 2024
ACCEPTED 25 September 2024
PUBLISHED 16 October 2024

CITATION
Shahi A, Manhas R, Bhattacharya S, Rathore A, Kumar P, Samanta J, Sharma MK, Mahapa A, Gupta P and Anal JMH (2024) Synthesis and antibacterial potential of novel thymol derivatives against methicillin-resistant *Staphylococcus aureus* and *P. aeruginosa* pathogenic bacteria.
Front. Chem. 12:1482852.
doi: 10.3389/fchem.2024.1482852

Synthesis and antibacterial potential of novel thymol derivatives against methicillin-resistant *Staphylococcus aureus* and *P. aeruginosa* pathogenic bacteria

Ashutosh Shahi[1†], Rakshit Manhas[2†], Srija Bhattacharya[1], Arti Rathore[2,3], Puneet Kumar[1,3], Jayanta Samanta[4], Manish Kumar Sharma[1], Avisek Mahapa[2,3]*, Prasoon Gupta[1,3]* and Jasha Momo H. Anal[1,3]*

[1]Natural Products and Medicinal Chemistry Division, CSIR-Indian Institute of Integrative Medicine, (IIIM), Jammu, India, [2]Infectious Diseases Division, CSIR–IIIM, Jammu, India, [3]Academy of Scientific and Innovative Research (AcSIR), Ghaziabad, India, [4]Department of Chemistry, SRM Institute of Science and Technology, Kattankulathur, Tamil Nadu, India

The increasing threat of antibiotic resistance has created an urgent need for new antibacterial agents, particularly plant-based natural compounds and their derivatives. Thymol, a natural monoterpenoid phenolic compound derived from *Monarda citriodora*, is known for its aromatic and therapeutic properties, including antibacterial activity. This study focuses on synthesizing dihydropyrimidinone and dihydropyridine derivatives of thymol and exploring their antibacterial properties. The synthesized compounds were tested for their *in vitro* antibacterial potential against pathogenic microorganisms, specifically *Pseudomonas aeruginosa* (Gram-negative) and methicillin-resistant *Staphylococcus aureus* (MRSA) (Gram-positive). Among the synthesized derivatives, compound 3i (ethyl 4-(4-hydroxy-5-isopropyl-2-methylphenyl)-2-imino-6-methyl-1,2,3,4-tetrahydropyrimidine-5-carboxylate) exhibited the most promising antibacterial activity, with minimum inhibitory concentration (MIC) values of 12.5 μM against *P. aeruginosa* and 50.0 μM against MRSA. Additionally, compound 3i demonstrated a synergistic effect when combined with vancomycin, enhancing its antibacterial efficacy. The optimum fractional inhibitory concentration index (FICI) observed was 0.10 and 0.5 for MRSA and *P. aeruginosa*, respectively, in combination with vancomycin. *In silico* analysis of the physiochemical properties of 3i indicated compliance with all drug-likeness rules. Furthermore, molecular docking studies revealed that compound 3i has a stronger binding affinity to the target protein than thymol, providing valuable insights into its potential mechanism of action.

KEYWORDS

antibacterial, thymol derivatives, synergistic effect, antibiotic resistance, drug discovery

1 Introduction

Historically, natural products have played a crucial role in identifying and developing antibacterial agents. They have the potential to re-emerge as critical starting points in antibacterial discovery due to the emergence of antimicrobial resistance (AMR) in antibiotics (Moloney, 2016). Over the years, numerous studies have been extensively conducted on the antibacterial activity of natural sources, with a growing focus on plants, particularly herbs and spices (Abdou et al., 2007). Nowadays, more than 30,000 antibacterial compounds have been isolated from plants, and more than 1,340 plants have been found to exhibit specific antibacterial properties (Tajkarimi et al., 2010). The phytochemical compounds in these plants contain chemical functions or belong to families such as terpenes, isoflavonoids, aldehydes, ketones, and acids, which are critical constituents that exhibit antibacterial activity (Patra, 2006). Natural antibacterials can be used alone or in combinations as adjuvants in other applications like food preservation (Tiwari et al., 2009). *Monarda citriodora*, commonly known as Jammu Monarda, is a temperature-dependent plant. It is cultivated mainly in Jammu and Kashmir, Himachal Pradesh, Uttaranchal, and the higher lands of northeastern states (Figure 1). Recently, this plant has attracted the attention of research groups across the globe not only for its aromatic value but also for its potential as an antibacterial, antiviral, antifungal, antileishmanial, antitubercular, antioxidant, antiparasitic, and anticancer agent, as well as its use as kinase inhibitors and in few more drug applications all over the world (Mattarelli et al., 2017; Robledo et al., 2005; Sahoo et al., 2021). The essential oils collected from Monarda species have been analyzed and found to contain compounds like thymol, carvacrol, p-cymene, and their derivatives (Lawson et al., 2021). In the Lamiaceae family, thymol (2-isopropyl-5-methylphenol) is the main monoterpene phenol extracted from plants.

Multidrug-resistant bacterial strains have recently become a significant cause of persistent infections worldwide. This AMR has made effective drugs ineffective, making the bacterial infections untreatable. The emergence of AMR in bacterial pathogens has created an urgent need for novel antibacterial agents or alternative therapeutics (Ranjbar and Alam, 2024). According to a 2019 study, approximately 4.95 million deaths are associated with bacterial AMR, with AMR directly responsible for 1.27 million of these deaths (Murray et al., 2022). The ESKAPE group of pathogens (*Enterococcus faecium*, *Staphylococcus aureus*, *Klebsiella pneumoniae*, *Acinetobacter baumannii*, *P. aeruginosa*, and *Enterobacter* species) poses a global threat due to their concerningly rapid development of resistant properties. These pathogens are responsible for different deadly infections, eventually leading to death if left untreated (Ács et al., 2016). An earlier report showed the sensitivity of extracted essential oil containing thymol moiety from Monarda species against bacterial pathogens like *Pseudomonas aeruginosa* and methicillin-resistant *Staphylococcus aureus* (MRSA) (Utchariyakiat et al., 2016; Sahu and Siddiqui, 2016). In the present study, we have included *P. aeruginosa* (Gram-negative) and MRSA (Gram-positive bacteria, which are recognized as WHO priority pathogens. The

FIGURE 1
Jammu Monarda IIIM(J)MC-02.

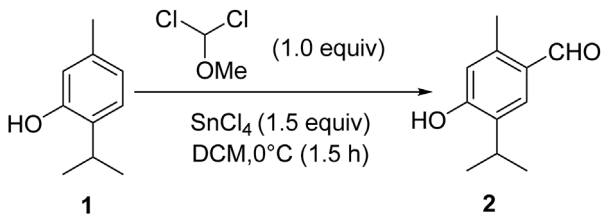

SCHEME 1
Synthesis of 4-hydroxy-5-isopropyl-2-methylbenzaldehyde (thymol aldehyde).

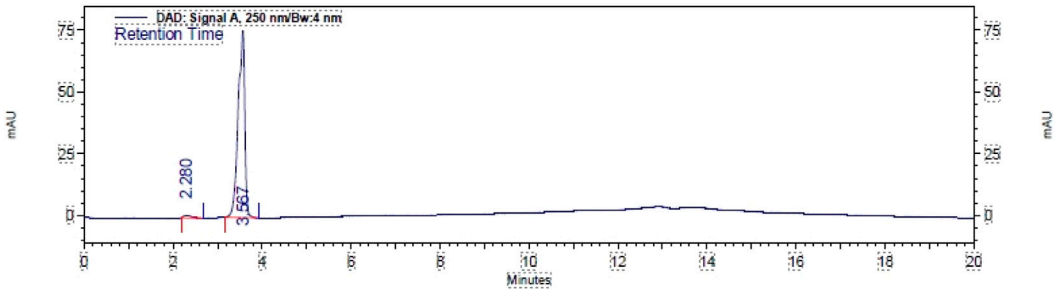

FIGURE 2
HPLC chromatogram of thymol aldehyde (2).

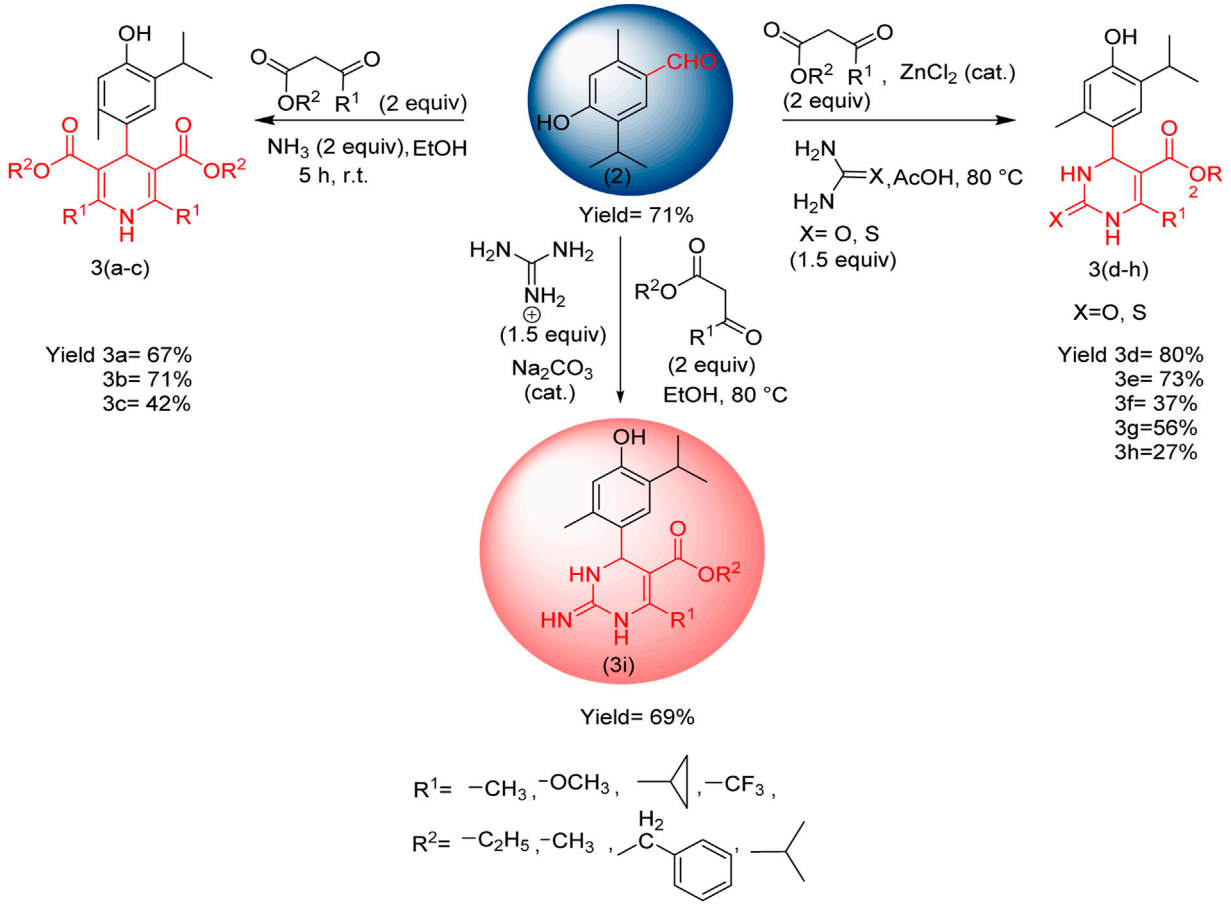

SCHEME 2
Synthesis of thymol derivatives.

TABLE 1 Energies and dipole moments of the compounds were calculated using the DFT/B3LYP method and 6-31G (d,*p*) basis set.

Compound	*R-configuration*		*S-configuration*	
	Energy (*Hartree*)	Dipole moment (*Debye*)	Energy (*Hartree*)	Dipole moment (*Debye*)
3 days	−1,110.852098	3.782651	−1,110.852146 (*min*)	3.674134
3e	−1,302.589632	3.840660	−1,302.589682 (*min*)	3.774777
3f	−1,447.871466	4.457909	−1,447.877407 (*min*)	3.765771
3g	−1,148.914783	3.840445	−1,148.914825 (*min*)	3.740330
3h	−1,433.814023 (*min*)	4.028652	−1,433.813994	4.100613
3i	−1,090.961189 (*min*)	1.677703	−1,090.961175	1.860417

development of novel therapies or adjuvants is urgently needed to combat resistant pathogens.

In this study, we isolated thymol, introduced an aldehyde group at the electron-rich *p*-position, and further derivatized thymol aldehyde to create a series of thymol dihydropyridine and dihydropyrimidinone derivatives. We synthesized nine thymol derivatives based on numerous potentials, which have antibacterial activities against Gram-negative and Gram-positive pathogens like *P. aeruginosa* and MRSA. These compounds have multiple implications in the pharmaceutical industry, and their derivatives possess different bioactivities. We further analyzed the synergistic potential of these derivatives using a checkerboard assay. This study explores the effectiveness of the newly synthesized thymol derivatives for their potential antibacterial properties that advance our battle against antibacterial resistance.

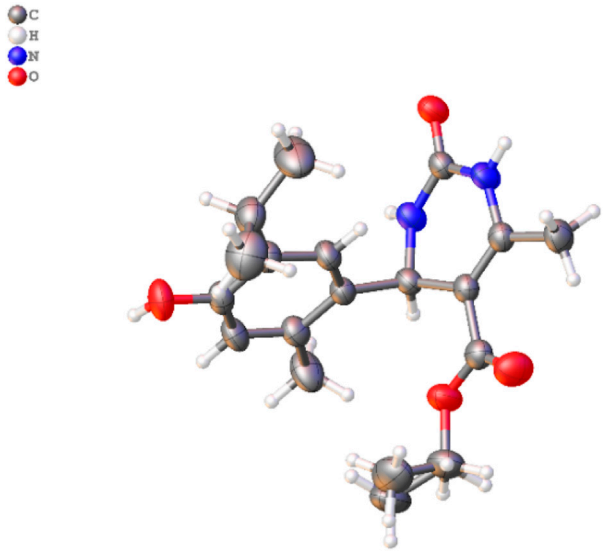

FIGURE 3
Molecular structure of 3d. The disordered part is removed for clarity. Thermal ellipsoids are shown at a 50% probability level (color code: C = gray, H = white, N = blue, and O = red) (CCDC2287405).

2 Materials and methods

2.1 Extraction and isolation

For isolation studies, 1.0 kg of dried marc of *Jammu Monarda* was collected from IIIM Farm (Chatha Farm) and was subjected to further extraction by ethyl acetate and methanol using a percolator. First, ethyl acetate was used for extraction. After filtration, ethyl acetate was evaporated completely using a rotary evaporator (Buchi R-200), and 55 gm of ethyl acetate extract was obtained. Similarly, after ethyl acetate, methanol was used for extraction, and after filtration, methanol was evaporated completely, and the MeOH extract (30.0 gm) was obtained. Upon further fractionation of the ethyl acetate fraction, six compounds were isolated, which were characterized as thymol, geraniol, limonene, carvacrol, cymene, and myrcene by using various spectroscopic techniques like NMR and mass spectroscopy. Thymol was found in the major quantity and all others in the minor quantity.

2.2 Preparation of 4-hydroxy-5-isopropyl-2-methylbenzaldehyde (thymol aldehyde)

Thymol (1.0 mmol), isolated from the marc of *Jammu Monarda*, and dichloromethyl methyl ether (1.0 mmol) in dichloromethane (25 mL) were mixed in a round bottom flask and stirred at 0°C for the initial half an hour. Then, tin chloride (1.5 mmol) was added dropwise to the reaction mixture, and stirring was carefully continued at room temperature for 3 h. After the completion of the reaction (monitored by TLC) to ascertain product formation, it was quenched slowly with ice water. The product was extracted using ethyl acetate. The combined organic layer was dried with anhydrous sodium sulfate and concentrated in rota-vapor, and the residue was subjected to silica gel column chromatography using hexane: ethyl acetate to afford the pure product, thymol aldehyde, 2 (Scheme 1).

High-performance liquid chromatography (HPLC) detected 98% of Figure 2, as shown in the chromatogram. HPLC was run using a gradient method to ensure the detection of any other products that may have formed on the C_{18} column. The mobile phase consisted of acetonitrile (MeCN) and water, with eluting conditions maintained throughout a run time of 20 min at a flow rate of 1.0 mL/min. The eluting solvent mixture MeCN/H_2O composition started at 70:30, then changed to 80:20 and 90:10, and returned to 80:20 and 70:30, with an interval of 5.0 min each, over a run time of 20.0 min. The retention time, t_R, of compound 2 was detected at 3.567 with an area percentage of 98.445.

2.3 General procedure for the synthesis of thymol derivatives

For the preparation of compounds 3(a–c), the prepared thymol aldehyde (1.0 mmol) and β-keto ester (2.0 mmol) in ethanol (25 mL) were placed in a round bottom flask. Then, ammonia (2.0 mmol) was added dropwise, and the mixture was stirred for 5 h at room temperature. After the completion of the reaction (product monitored by TLC), it was slowly quenched with H_2O. The product was extracted using ethyl acetate. The combined organic layer was dried with anhydrous sodium sulfate and concentrated in rota-vapor, and the residue was subjected to silica gel column chromatography using hexane: ethyl acetate to afford the pure product.

For compounds 3(d–h), thymol aldehyde (1.0 mmol), β-keto ester (2.0 mmol), and urea (1.5 mmol) or thio urea (1.5 mmol) in acetic acid (25 mL) were placed in a round bottom flask. Then, zinc chloride was added in a catalytic amount (0.3 mmol), and the mixture was reflexed at 80°C for 5 h After the completion of the reaction (product monitored by TLC), it was slowly quenched with sodium bicarbonate dissolved in water (for neutralizing acid), and the pure product was collected in the same manner as 1,4-dihydropyrimidine derivatives.

For the synthesis of compound 3i, thymol aldehyde 2 (1.0 mmol), β-keto ester (2.0 mmol), and guanidine (1.5 mmol) in ethanol (25 mL) were placed in the round bottom flask. Then, sodium carbonate was added in a catalytic amount (0.3 mmol), and the mixture was refluxed at 80°C for 5 h After the completion of the reaction (product monitored by TLC), the pure product was collected in the same manner as 1,4-dihydropyrimidinone derivatives.

2.4 Biology

2.4.1 Bacterial strain and growth

various bacterial strains were used for this study. These included *P. aeruginosa* (Schroeter) Migula 27,853, a Gram-negative strain, and MRSA, a Gram-positive strain. Additionally, *Escherichia coli*, *K. pneumoniae*, and *Mycobacterium smegmatis* were also included. The ESKAPE pathogens were grown in LB media, and MB7H9 media (supplemented with 2% glycerol) was used for mycobacterial

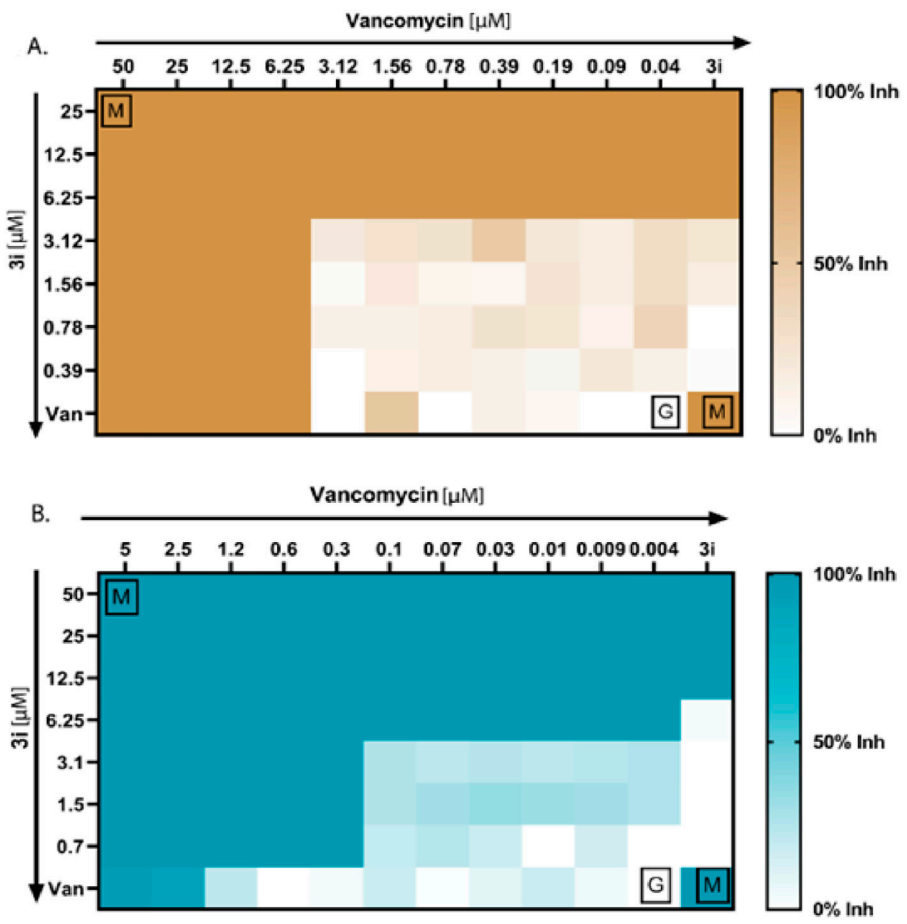

FIGURE 4
Antibacterial synergy of compound 3i. **(A)** Antibacterial synergy of compound 3i with vancomycin against *P. aeruginosa*. **(B)** Antibacterial synergy of compound 3i with vancomycin against MRSA.

TABLE 2 MIC values of compounds in μM against clinically isolated bacterial strains.

Compound	*Pseudomonas aeruginosa*	Methicillin-resistant *Staphylococcus aureus*
1	>100	>100
3i	12.5	50
Vancomycin	6.25	3.1

growth. All the strains were stored at −80°C (20% glycerol stock). A 20 μL sample of bacteria from the glycerol stock was added to 10 mL of LB/MB7H9 media to test their antibacterial properties. The cultures were then maintained at 37°C overnight with continuous shaking.

2.4.2 Minimum inhibitory concentration (MIC)

The thymol derivatives 3(a–i) were evaluated for their *in vitro* antibacterial potential using a 96-well microtiter plate method with some modifications according to the CLSI guidelines (Wang et al., 2021). Before the assay, the thymol derivatives 3(a–i) were dissolved in DMSO to prepare their (5 mg/mL) sample stocks, and reference drug vancomycin was dissolved in distilled water to prepare a stock of 1.0 mg/mL. The indicator solution of resazurin (indicator) was prepared as 0.04% in PBS. First, bacterial strains were grown overnight in LB broth at 37°C in a shaker incubator. In addition, 100 μL of LB media was added to a 96-well flat-bottom microtiter plate the next day. Two-fold concentrations of thymol derivatives were added horizontally in row 1, starting from well 1 to well 12. The compounds were then serially diluted vertically for each row up to the eighth well. Finally, 100.0 μL bacterial cultures at final OD_{600}~0.05 were added to each well. The plates were sealed with parafilm and incubated at 37 °C for 24 h. After incubation, 10 μL of the resazurin solution was added to each well, and the plates were incubated at 37 °C for 1 h. The optical density (OD) was observed at 570 nm on the microplate reader (TECAN Infinity 200 pro). The MIC is estimated as the minimum concentration of the compounds at which the resazurin's color did not reduce to pink. The

TABLE 3 Prediction of physicochemical properties of parent thymol and compound 3i.

Parameter	Thymol	3i
Molecular formula	$C_{10}H_{14}O$	$C_{18}H_{25}N_3O_3$
Molecular weight (g/mol)	150.100	331.190
H-bond acceptors	1	4
H-bond donors	1	4
TPSA (Å^2)	20.23	94.44
Log Po/w (iLOGP)	2.32	2.59
Solubility (mg/mL)	$9.74e^{-02}$	$1.36e^{-01}$
Drug-likeness Lipinski (violation)	Yes (0)	Yes (0)
Drug-likeness Ghose	No (1)	Yes
Drug-likeness Veber	Yes	Yes
Drug-likeness Egan	Yes	Yes
Drug-likeness Muegge (violation)	No (2)	Yes (0)
Lead-likeness	No	Yes
Bioavailability score	0.55	0.55
GI absorption	High	High
BBB permeation	Yes	No

experiment was performed in three biological replicates against all the pathogens.

2.4.3 Minimum bactericidal concentration (MBC)

MBC was considered the lowest compound concentration, where no visible colonies were observed. To perform the MBC assay, a total volume of 10 μL culture was removed from the wells of microtiter MIC plates (treated with compound 3i) and plated on LB agar. The plates were kept for 24-h incubation at 37°C (Rodríguez-Melcón et al., 2021). The MBC value was obtained from the plates, where no visible growth was observed at a particular concentration.

2.4.4 Synergistic activity

The synergistic study was performed between thymol derivatives and reference drug vancomycin against *P. aeruginosa* and MRSA, according to the National Committee for Clinical Laboratory Standards (NCCLS) guidelines (Utchariyakiat et al., 2016). In brief, a two-fold concentration of each drug combination and stock solution was prepared before testing (Orhan et al., 2005). Bacterial cultures were maintained in an LB medium overnight. The next day, one hundred microliters of LB media were added to 96-well microtiter plates, where compound 3i (vertically) and vancomycin (horizontally) were added and serially diluted. One hundred microliters (100 μL) of bacterial suspension (at OD 0.05) was added to the plates and incubated at 37°C for 24 h. To find the synergy, the fractional inhibitory concentration index (FICI) was calculated for each drug combination in a checkerboard assay. The FICI was calculated using the following formula:

$$\mathrm{FICI} = \mathrm{FICA} + \mathrm{FICB} = \left(\frac{\mathrm{CA}}{\mathrm{MICA}}\right) + \left(\frac{\mathrm{CB}}{\mathrm{MICB}}\right),$$

where CA and CB are the MICs of drugs A and B in combination (in a single well) and MICA and MICB are the MICs of each drug individually. The following interpretation criteria were followed for the checkerboard assay: the FICI value ≤0.5 indicated synergy, the FICI value between 0.5 and 4 indicated indifference or additive, and FICI >4 indicated antagonism.

3 Results

Thymol aldehyde (2) was synthesized from thymol, which is isolated from *Jammu Monarda* (Scheme 1) by the Rieche formylation, which is an important method for synthesizing aromatic aldehydes. In this process, dichloromethyl methyl ether acts as a formylation agent for electron-rich aromatic compounds in the presence of a Lewis acid such as titanium tetrachloride Polat and Cakici, 2022). In this reaction, we have used tin (iv) tetrachloride. This formylation method of converting thymol to its aldehyde allows further transformations to an extensive possibility for essential pharmaceutical ingredients.

Furthermore, a modification of thymol aldehyde and synthesis of compounds of pyridine and pyrimidinone derivatives are described (Scheme 2).

Compounds 3(a–c) were synthesized via the Hantzsch dihydropyridine (DPH) method using thymol aldehyde, β-keto ester (Supplementary Figure S1), and ammonia, which was added dropwise at room temperature in ethanol, and compounds 3(d–h) were synthesized using urea or thiourea instead of ammonia in acetic acid, with a catalytic amount of zinc chloride, and the mixture was refluxed at 80 °C for 5 h. In the case of compound 3i, guanidine was added in ethanol, with sodium carbonate acting as a catalyst, and the mixture at was refluxed 80 °C for 5 h (Tsvetkov et al., 2024).

A multicomponent reaction (MCR) is a synthetic methodology in which three or more reactants combine in a single vessel to form a new product. The defining aspect of MCRs is that the final products contain nearly all substrate portions, generating minimal by-products, which are helpful for drug discovery activities. MCR is a highly ideal and eco-friendly reaction system. Target compounds can be obtained in one pot with fewer steps (Weber, 2002). Thymol aldehyde converted from thymol is a highly electron-rich center susceptible to electrophilic aromatic substitution using the Rieche formylation method. Rieche formylation gives excellent yields and regiospecificity. It does not lead to further formylation (Garcıa and Nicolás, 2003; Alan et al., 2010; Jun and Yinjuan, 2002; Oliver, 2000; Majellaro et al., 2020).

The stereochemistry of the synthesized compounds 3 (a–c) and 3 (d–i) can theoretically determine whether they exist as racemic mixtures or exhibit enantiomeric excess. We optimized the 3D geometries of the synthesized molecules 3(d–i) using the DFT/B3LYP method and 6-31G (d,p) basis set. Our theoretical calculations indicate that in the case of compounds 3(d–g) (Table 1; Figure 3), the S-configuration exhibits lower energy and a decreased dipole moment compared to the R-configuration. This difference is attributed to a carbonyl group (C=O) within the dihydropyrimidine ring containing an electronegative oxygen atom. It confirms that the S-isomer is theoretically more stable and predominant compared to the R-isomer. Conversely, for compounds 3h and 3i (Table 1;

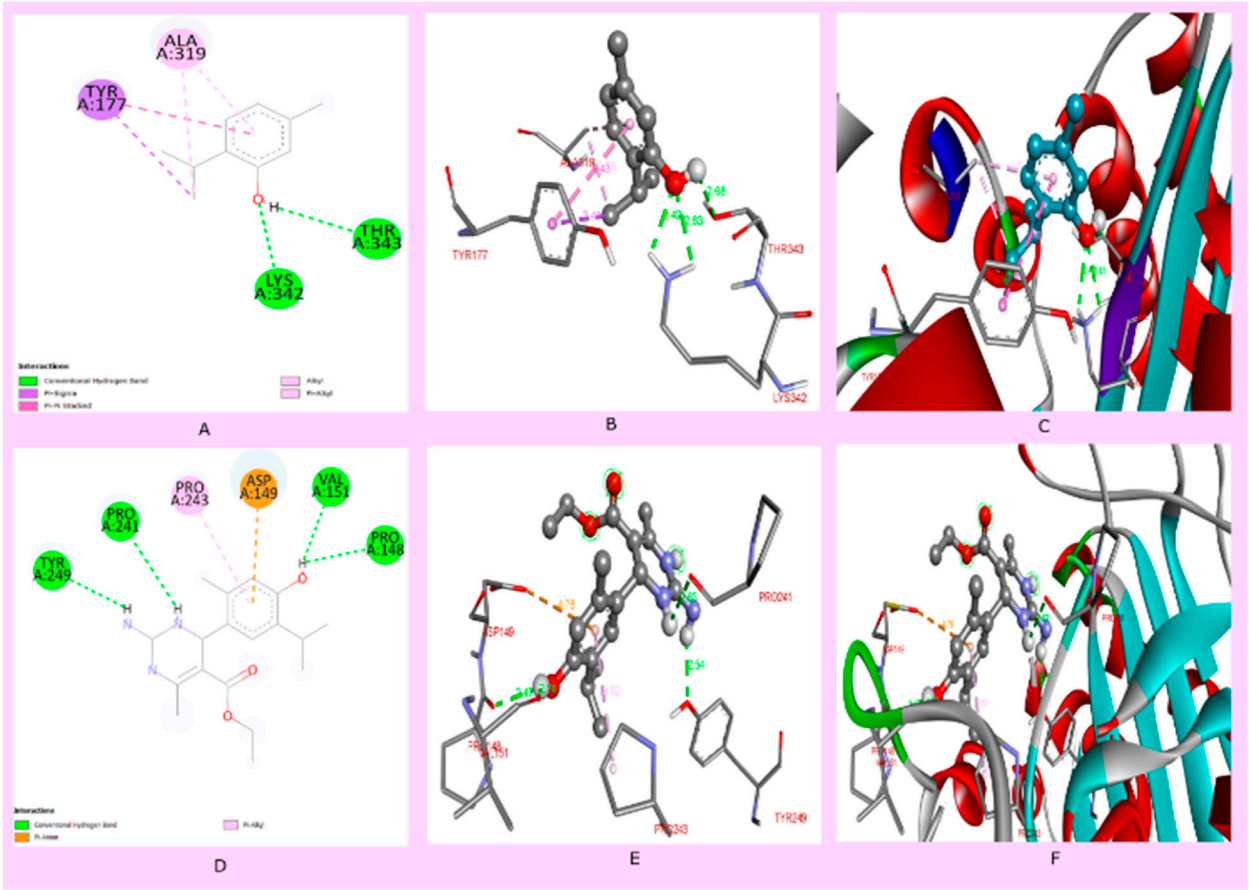

FIGURE 5
(A) Two-dimensional interaction of thymol with proteins (pdb id: 4HEF), (B) 3D interaction of thymol with amino acids of proteins, **(C)** 3D interaction of thymol with a protein receptor, **(D)** 2D interaction of compound 3i with proteins (PDB ID: 4HEF), **(E)** 3D interaction of compound 3i with amino acids of proteins, and **(F)** 3D interaction of thymol with a protein receptor.

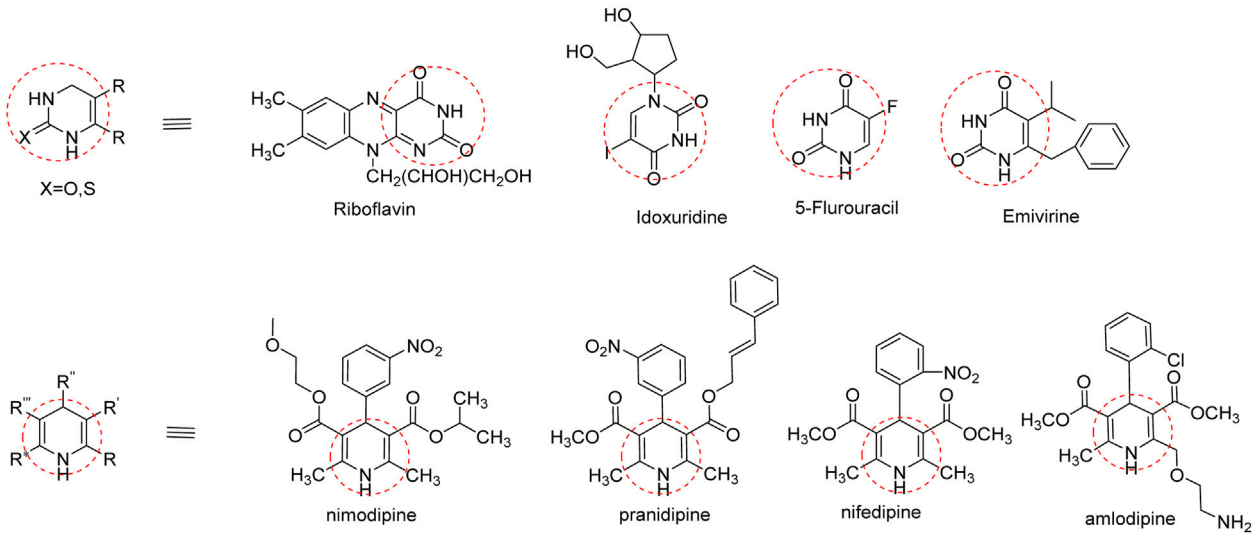

FIGURE 6
Dihydropyridine and dihydropyrimidinone pharmacophore-containing drugs.

Supplementary Figure S3), the R-isomer displays lower energy and dipole moment due to C=S and C=NH groups within the dihydropyrimidine ring, respectively. The reduced electronegativity of sulfur and nitrogen atoms compared to oxygen theoretically contributes to the stability and predominant presence of the R-isomer in these compounds.

3.1 Crystal study

A single X-ray diffraction technique validated the molecular structure of compound 3d. The crystal was grown in a diethyl ether: MeOH solvent mixture by slow evaporation at room temperature. The details of the crystal and data refinement are given in Supplementary Material, whereas the molecular structure and crystal (Figure 3) were determined further to verify the structure of the formation of this pharmacophore.

3.2 Antibacterial properties of thymol derivatives

The thymol derivatives were evaluated for their antibacterial efficacies against pathogens like *P. aeruginosa* and MRSA. We conducted MIC assays on the thymol derivatives, specifically compounds 3(a–i), to assess their antibacterial activity. Following the guidelines of the Clinical and Laboratory Standards Institute (CLSI) with some modifications (Humphries et al., 2018), we performed a microdilution assay and obtained MIC values for these compounds against different pathogens. The reference antibacterial drug, vancomycin, was also included in the assay. Compound 3i exhibited significant antibacterial activity against *P. aeruginosa* and MRSA among all the synthesized thymol derivatives. Compound 3i inhibited the growth of *P. aeruginosa* and MRSA with MIC values ranging from 12.5 to 50.0 μM, respectively. The remaining derivatives also demonstrated antibacterial efficacy; however, their antibacterial activity was observed at higher concentrations (>100 μM) against broad-spectrum pathogens such as *E. coli*, *K. pneumoniae*, and *M. smegmatis* (Supplementary Table S1).

We have also included standard positive control vancomycin in the study, with MIC values of 6.25 and 3.1 μM against *P. aeruginosa* and MRSA, respectively.

Next, we determined the bactericidal properties of the thymol derivative (3i). We performed MBC experiments. Figure 4 illustrates the MBC values of compound 3i. As depicted in the agar plate, no visible growth of MRSA was observed at concentrations of 50.0 and 100.0 μM, while bacterial colonies were observed at 25 μM. This suggests that compound 3i exhibits a bactericidal effect at 50 μM against MRSA. Additionally, no colonies of *Pseudomonas* were detected at concentrations of 12.5 μM or higher, indicating the potent bactericidal activity of compound 3i against *Pseudomonas* at the same concentration. The antibacterial activity of thymol and its derivative 3i against *P. aeruginosa* (Gram-negative) and MRSA (methicillin-resistant *S. aureus*) (Gram-positive) bacterial strains, with vancomycin used as the standard (Table 2), indicated good activity against clinically isolated bacterial strains.

3.3 Compound 3i synergizes vancomycin activity against MRSA and *P. aeruginosa*

We conducted checkerboard assays to determine whether the thymol derivative 3i and the reference drug vancomycin work synergistically against *P. aeruginosa* and MRSA. Combining drugs can synergistically reduce the need for higher doses of antibiotics and minimize adverse effects. We tested 77 possible combinations, as shown in Figures 4A, B, to determine the synergistic combinations among the thymol derivative 3i with vancomycin. We calculated the FICI using the standard formula specified in the method section to assess the number of synergies, additives, or antagonisms. Our result showed that for *P. aeruginosa*, four combinations of 3i and vancomycin were synergistic, with FICI values below 0.5. We also observed 36 no interactions with FICI values above 0.5 and up to 4, and 9 antagonistic combinations between the two drugs have been observed. Additionally, the checkerboard assay between 3i and vancomycin against MRSA yielded 32 possible synergistic combinations with FICI values below or equal to 0.5, indicating a synergy effect. We also identified 27 no interactions with FICI values above 0.5 and up to 4. Notably, no antagonism exists, as indicated by FICI values above 4. These findings suggest that combining 3i with vancomycin can enhance antibacterial activity. The synergistic combinations identified in this assay could explore the possibility of reducing drug doses and minimizing associated side effects while maintaining effective antibacterial activity against *P. aeruginosa* and MRSA.

The present study demonstrated the synthesis of novel thymol derivatives. It investigated the antibacterial potential of those thymol derivatives, focusing on bioactive compound 3i, against a panel of bacterial pathogens. Thymol is a natural compound with antibacterial properties, reported earlier in numerous studies (Zhang et al., 2021). Our MIC assays with the thymol derivatives revealed that compound 3i showed significant antibacterial activity among the tested molecules against *P. aeruginosa* and MRSA, WHO-priority pathogens. Significantly, compound 3i displayed lower MIC values of 12.5 μM/1.9 μg/mL and 50 μM/7.5 μg/mL against MRSA and *P. aeruginosa*, respectively, indicating improved potency compared to thymol and its derivatives 3(a-i). The MIC and MBC values of the native thymol ranged from 250 μg/mL to 1,000 μg/mL, respectively, against *S. aureus*, whereas for *P. aeruginosa*, they were greater than 1,000 μg/mL (Gan et al., 2023; Kim et al., 2022). This suggests that specific modifications in the chemical structure, as seen in compound 3i, can lead to heightened antibacterial efficacy against the examined pathogens. Additionally, our MBC experiments further supported the strong bactericidal effects of compound 3i at lower concentrations (50.0 μM against MRSA and 12.5 μM against *Pseudomonas*). The effective bactericidal activity at such low concentrations is a notable advantage and indicates compound 3i's potential as an antibacterial compound. Another significant feature of this study was investigating the synergy between compound 3i and the reference antibacterial, vancomycin. It is used to treat MRSA infections. The usefulness of drug combinations has become an essential strategy to combat antibacterial resistance and improve treatment outcomes (Liang et al., 2007). The checkerboard assay allowed us to search a wide range of combinations (77 combinations) and determine suitable antibacterial synergy. Our checkerboard assay revealed that for *P.*

aeruginosa, four combinations of compound 3i and vancomycin were synergistic (FICI values below 0.5). Similarly, for MRSA, 32 synergistic combinations were observed. The relative analysis between the natural product thymol and compound 3i reveals its antibacterial potency, especially against *P. aeruginosa* and MRSA (Table 2). Additionally, the synergistic effect observed when combining compound 3i with vancomycin highlights its potential in combination therapies. Our findings emphasize the significance of chemical modifications in enhancing the antibacterial properties of natural compounds and their potential contribution to combating antibacterial resistance.

3.4 Molecular docking analysis and *in silico* physicochemical studies

In the current drug development approaches, computational processes are utilized to predict potentially effective drug similarity molecules to direct or avoid synthesizing more active compounds. Physicochemical properties play an essential role during the development of drugs. The prediction of parameters using SwissADME to evaluate pharmacokinetics, drug-likeness, and medicinal chemistry supports the *in vitro* analysis of compounds, which exhibited that compound 3i displayed more drug-like properties than thymol. Compound 3i obeys all drug-likeness rules, including Lipinski's rule, Ghose's rule, Veber's rule, Egan's rule, and Muegge's rule, while thymol violates Ghose's rule and Muegge's rule of drug-likeness. Moreover, the Lipinski rule of five (RO5), based on molecular properties, molecular weight, numbers of hydrogen acceptors (H-ba), number of hydrogen donors (H-bd), and LogP values, was widely used in the selection criterion for an active drug molecule (Table 3). Compound 3i has a better binding affinity (docking score −6.9 kcal/mol), whereas thymol 1 shows a binding affinity (docking score −5.2 kcal/mol) to the protein interaction. Thymol interacted with amino acids LYS342 and, THR343 by conventional hydrogen bond, TRY177 by pi-sigma bond, and ALA319 by pi–pi stacking interaction. It is evident that docking compound 3i interacts with the amino acids of proteins, including TYR249, PRO241, VAL151, and PRO148 by conventional hydrogen bond, PRO243 by pi-alkyl bonding, and ASP149 by pi-sigma bonding. Compound 3i displayed better hydrogen bonding interaction than the parent compound (thymol) with the protein (Figure 5).

4 Discussion

Thymol exhibits significant antibacterial properties, inhibiting the growth of Gram-positive and Gram-negative bacteria (Palaniappan et al., 2010). The hydroxyl group in thymol and the LogP ratio of thymol, measured at 3.37, also contribute significantly to the antibacterial effect (Koroch et al., 2007; Anna et al., 2016). According to previous studies, the presence of the 1,4-dihydropyridine (1,4-DHP) central core is essential for antibacterial activity (Malhi et al., 2022). Investigations into dihydropyrimidine derivatives indicate that compounds containing thio- and oxo-groups possess enhanced potency (Yadlapalli et al., 2012). Thymol, pyridine derivatives, and pyrimidine derivatives each have individual antibacterial activity, suggesting the potential for enhanced activity by combining them.

In addition to natural thymol, the antibacterial efficacies of the derivatives were reported against different pathogens; the aryl-azo-thymol derivatives, which were synthesized, showed promising activity against MRSA, with an MIC value of 40 μg/mL. Another thymol oxypropanolamine compound (1-([cyclohex-1-en-1-ylmethyl] amino)-3-(2-isopropyl-5-methylphenoxy) propan-2-ol) exhibited efficient activity against *A. baumannii,* with a zone of inhibition of 3 mm. A halogenated thymol derivative, chloro-thymol (4-chloro-2-isopropyl-5-methylphenol), possesses significant activity at 12.5 and 25 μg/mL against *S. aureus* and *Staphylococcus epidermis*, respectively (Si et al., 2023).Therefore, we incorporated a nitrogen base into these pharmacophores to improve their activity. This base is essential for the nucleic acid biosynthesis pathway and is crucial for cell survival and various biological processes (Sienkiewicz et al., 2013). Interestingly, several FDA-approved drugs contain dihydropyridine, and dihydropyrimidine pharmacophores are presented in Figure 6 (Kaur et al., 2017).

5 Conclusion

Three dihydropyridine and six dihydropyrimidinone derivatives were obtained by converting thymol into its thymol aldehyde (Scheme 2). The antibacterial evaluation against various pathogenic bacteria led to a significant finding: among the nine compounds 3(a–i), compound 3i exhibited significant activity against *P. aeruginosa* and MRSA, with MIC values of 12.5 μM and 50.0 μM, respectively. Compound 3i shows broad-spectrum bactericidal activity against Gram-negative and Gram-positive pathogens and a synergistic effect for its combination therapy. The antibacterial characterization of compound 3i as a potent antibacterial agent offers valuable information for further studies and drug development. These findings indicate that these thymol derivatives have the potential to be novel antibacterial agents in combating microbial infections and contribute to the fight against antibiotic resistance by using biomass-derived waste from plant sources in a sustainable manner. Furthermore, the exploration of structural optimization for its better efficacy, toxicity, and safety will be carried out in future *in vivo* studies. We believe that such endeavors play a crucial role in strategizing the continuous battle against antibacterial resistance, emphasizing the significance of natural products as a reservoir for innovative drug discovery and development with potential pharmaceutical industrial applications.

Data availability statement

The datasets presented in this study can be found in online repositories. The names of the repository/repositories and accession number(s) can be found in the article/Supplementary Material.

Author contributions

AS: investigation, methodology, and writing–original draft. RM: formal analysis, investigation, methodology, and writing–review and editing. SB: investigation and writing–review and editing. AR:

formal analysis, investigation, and writing–review and editing. PK: investigation and writing–review and editing. JS: investigation and writing–review and editing. MS: investigation and writing–review and editing. AM: investigation, supervision, validation, and writing–review and editing. PG: validation, conceptualization, supervision, and writing–review and editing. JA: conceptualization, funding acquisition, project administration, supervision, writing–original draft, and writing–review and editing.

Funding

The author(s) declare that no financial support was received for the research, authorship, and/or publication of this article. The authors are grateful for financial support through CSIR-Aroma Mission Project Phase-II (HCP-0007) and the Department of Science and Technology (DST), Science and Engineering Research Board (SERB), Government of India, Start-up Research Grant (SRG) File no. SRG/2023/000,145.

Acknowledgments

All authors acknowledge the support provided by the Director, CSIR-Indian Institute of Integrative Medicine, Jammu, India. The authors also acknowledge the technical support from the central instrumentation facility of CSIR-IIIM, Jammu. The institutional manuscript communication number is CSIR-IIIM/IPR/00649.

Conflict of interest

The authors declare that the research was conducted in the absence of any commercial or financial relationships that could be construed as a potential conflict of interest.

Publisher's note

All claims expressed in this article are solely those of the authors and do not necessarily represent those of their affiliated organizations, or those of the publisher, the editors, and the reviewers. Any product that may be evaluated in this article, or claim that may be made by its manufacturer, is not guaranteed or endorsed by the publisher.

Supplementary material

The Supplementary Material for this article can be found online at: https://www.frontiersin.org/articles/10.3389/fchem.2024.1482852/full#supplementary-material

References

Abdou, A. M., Higashiguchi, S., Aboueleinin, A., Kim, M., and Ibrahim, H. R. (2007). Antimicrobial peptides derived from hen egg lysozyme with inhibitory effect against Bacillus species. *Food control.* 18 (2), 173–178. doi:10.1016/j.foodcont.2005.09.010

Ács, K., Bencsik, T., Böszörményi, A., Kocsis, B., and Horváth, G. (2016). Essential oils and their vapors as potential antibacterial agents against respiratory tract pathogens. *Nat. Product. Commun.* 11, 1934578X1601101. doi:10.1177/1934578X1601101121

Alan, R., Christopher, A. R., John, A., and Viktor, V. (2010) "Synthesis of monocyclic rings with one heteroatom," in *Handbook of heterocyclic. Chemistry*. Third Edition. Elsevier, 652–703. doi:10.1016/S0065-2725(08)60747-3

Anna, M., Ilkay, E. O., Maria, D., Ramona, B., Arianna Di Lorenzo, S., Fazel, N., et al. (2016). Antibacterial and antifungal activities of thymol: a brief review of the literature. *Food Chem.* 210, 402–414. doi:10.1016/j.foodchem.2016.04.111

Frisch, M. J. E. (2009). *A Gaussian 09, Revision d. 01*. Wallingford CT: Gaussian. Inc, 201.

Gan, C., Elisa, L., Antonio, V., Diego, B., and Rosa, P.-O. (2023). Synergistic activity of thymol with commercial antibiotics against critical and high WHO priority pathogenic bacteria. *Plants* 12, 1868. doi:10.3390/plants12091868

Garcıa, O., Nicolás, E., and Albericio, F. (2003). o-Formylation of electron-rich phenols with dichloromethyl methyl ether and TiCl4. *Tetrahedron Lett.* 44 (27), 4961–4963. doi:10.1016/S0040-4039(03)01168-7

Humphries, R. M., Jane, A., Stephanie, L., Mitchell, M., Tanis, D., Janet, A. H., et al. (2018). CLSI methods development and standardization working group best practices for evaluation of antimicrobial susceptibility tests. *J. Clin. Microbiol.* 56, 10–1128. doi:10.1128/jcm.01934-17

Jun, Lu., and Yinjuan, B. (2002). Catalysis of the biginelli reaction by ferric and nickel chloride hexahydrates. One-pot synthesis of 3,4-dihydropyrimidin-2(1H)-ones. *Synthesis* 4, 466–470. doi:10.1055/s-2002-20956

Kaur, R., Chaudhary, S., Kumar, K., Gupta, M. K., and Rawal, R. K. (2017). Recent synthetic and medicinal perspectives of dihydropyrimidinones: a review. *Eur. J. Med. Chem.* 132, 108–134. doi:10.1016/j.ejmech.2017.03.025

Kim, B., Hyerim, K., Hye, S., Su, H., Do-Hyun, C., Hee, Ju, et al. (2022). 4-Chloro-2-isopropyl-5-methylphenol exhibits antimicrobial and adjuvant activity against methicillin-resistant *Staphylococcus aureus*. *J. Microbiol. Biotechnol.* 32, 730–739. doi:10.4014/jmb.2203.03054

Koli, B., Gochar, R., Meena, S. R., Chandra, S., and Bindu, K. (2018). Domestication and nutrient management of Monarda citriodora Cer. ex-Lag. in sub-tropical region of Jammu (India). *Int. J. Chem. Stud.* 6, 1259–1263. P-ISSN: 2349–8528 E-ISSN: 2321–4902.

Koroch, A. R., Juliani, H., and Zygadlo, J. A. (2007). Bioactivity of essential oils and their components. *Flavours Fragrances Chemistry,Bbioprocessing Sustain.*, 87–115. doi:10.1007/978-3-540-49339-6_5

Lawson, S. K., Satyal, P., and Setzer, W. N. (2021). The volatile phytochemistry of Monarda species growing in South Alabama. *Plants* 10 (3), 482. doi:10.3390/plants10030482

Liang., Hengxing., Fukai, B., Xiaoping, D., Rui, T., Caijun, Z., et al. (2007). Antibacterial thymol derivatives isolated from Centipeda minima. *Molecules* 12, 1606–1613. doi:10.3390/12081606

Majellaro, M., Jespers, W., Crespo, A., Núñez, M. J., Novio, S., Azuaje, J., et al. (2020). 3,4-Dihydropyrimidin-2 (1 H)-ones as antagonists of the human A2B adenosine receptor: optimization, structure–activity relationship studies, and enantiospecific recognition. *J. Med. Chem.* 64 (1), 458–480. doi:10.1021/acs.jmedchem.0c01431

Malhi, D. S., Sohal, H. S., Singh, K., Almarhoon, Z. M., Bacha, A. B., and Al-Zaben, M. I. (2022). Highly efficient electrocarboxylation method to synthesize novel acid derivatives of 1,4-dihydropyridines and to study their antimicrobial activity. *ACS omega* 7, 16055–16062. doi:10.1021/acsomega.2c01316

Mattarelli, P., Epifano, F., Minardi, P., Vito, M., Modesto, M., Barbanti, L., et al. (2017). Chemical composition and antimicrobial activity of essential oils from aerial parts of*Monarda didyma*and*Monarda fistulosa*cultivated in Italy. *J. Essent. Oil- Bear. Plants* 20, 76–86. doi:10.1080/0972060X.2016.1278184

Moloney, M. G. (2016). Natural products as a source for novel antibiotics. *Trends Pharmacol. Sci.* 37, 689–701. doi:10.1016/j.tips.2016.05.001

Murray, C. J., Ikuta, K. S., Sharara, F., Swetschinski, L., Aguilar, G. R., Gray, A., et al. (2022). Global burden of bacterial antimicrobial resistance in 2019: a systematic analysis. *Lancet* 399 (10325), 629–655. doi:10.1016/S0140-6736(21)02724-0

Oliver, KAPPE. (2000). Recent advances in the biginelli dihydropyrimidine synthesis. New tricks from an old dog. *Acc. Chem. Res.* 33, 879–888. doi:10.1021/ar000048h

Orhan, G., Bayram, A., Zer, Y., and Balci, I. (2005). Synergy tests by E test and checkerboard methods of antimicrobial combinations against Brucella melitensis. *J. Clin. Microbiol. Jan.* 43 (1), 140–143. doi:10.1128/jcm.43.1.140-143.2005

Palaniappan, K., and Holley, R.A. (2010). Use of natural antimicrobial to increase antibiotic susceptibility of drug-resistant bacteria. *Int. J. Food Microbiol.* 140, 164–168. doi:10.1016/j.ijfoodmicro.2010.04.001

Patra, A. K. (2006). An overview of antimicrobial properties of different classes of phytochemicals. *Diet. phytochemicals microbes*, 1–32. doi:10.1007/978-94-007-3926-0_1

Polat, E., and Cakici, M. (2022). Deoxygenative chlorination of aldehydes and alcohols with dichloromethyl methyl ether and TiCl4. *Eur. J. Org. Chem.* 45, e202201106. doi:10.1002/ejoc.202201106

Ramos-Tomillero, I., Paradís-Bas, M., De Pinho Ribeiro Moreira, I., Bofill, J. M., Nicolas, E., and Albericio, F. (2015). Formylation of electron-rich aromatic rings mediated by dichloromethyl methyl ether and TiCl4: scope and limitations. *Molecules* 20 (4), 5409–5422. doi:10.3390/molecules20045409

Ranjbar, R., and Alam, M. (2024). Antimicrobial Resistance Collaborators (2022). Global burden of bacterial antimicrobial resistance in 2019: a systematic analysis. *Evid. Based Nurs.* 27 16–16. doi:10.1136/ebnurs-2022-103540

Robledo, S., Osorio, E., Munoz, D., Jaramillo, L. M., Restrepo, A., Arango, G., et al. (2005). *In vitro* and *in vivo* cytotoxicities and antileishmanial activities of thymol and hemisynthetic derivatives. *Antimicrob. agents Chemother.* 49, 1652–1655. doi:10.1128/AAC.49.4.1652–1655.2005

Rodríguez-Melcón, C., Carlos, A.-C., Camino, G.-F., Javier, C., and Rosa, C. (2021). Minimum inhibitory concentration (MIC) and minimum bactericidal concentration (MBC) for twelve antimicrobials (biocides and antibiotics) in eight strains of Listeria monocytogenes. *Biology* 11 (1), 46. doi:10.3390/biology11010046

Sahoo, C. R., Paidesetty, S. K., and Padhy, R. N. (2021). The recent development of thymol derivative as a promising pharmacological scaffold. *Drug Dev. Res.* 82, 1079–1095. doi:10.1002/ddr.21848

Sahu, M., and Siddiqui, N. (2016). A review on biological importance of pyrimidines in the new era. *Int. J. Pharm. Pharm. Sci.* 8 (5), 8–21. ISSN- 0975-1491.

Si, Z., Kevin, P., and Chan-Park, M.B. (2023). Chemical basis of combination therapy to combat antibiotic resistance. *J. Am. Chem. Soc. Au* 3, 276–292. doi:10.1021/jacsau.2c00532

Sienkiewicz, M., Łysakowska, M., Pastuszka, M., Bienias, W., and Kowalczyk, E. (2013). The potential of use basil and rosemary essential oils as effective antibacterial agents. *Molecules* 18, 9334–9351. doi:10.3390/molecules18089334

Sirianni, D. A., Alenaizan, A., Cheney, D. L., and Sherrill, C. D. (2018). Assessment of density functional methods for geometry optimization of bimolecular van der Waals complexes. *J. Chem. Theory Comput.* 14 (6), 3004–3013. doi:10.1021/acs.jctc.8b00114

Swain., Shasank, S., Sudhir, K., and Rabindra, N. (2019). Synthesis of novel thymol derivatives against MRSA and ESBL producing pathogenic bacteria. *Nat. Prod. Res.* 33, 3181–3189. doi:10.1080/14786419.2018.1474465

Tajkarimi, M. M., Ibrahim, S. A., and Cliver, D. O. (2010). Antimicrobial herb and spice compounds in food. *Food control.* 21, 1199–1218. doi:10.1016/j.foodcont.2010.02.003

Tiwari, B. K., Valdramidis, V. P., O'Donnell, C. P., Muthukumarappan, K., Bourke, P., and Cullen, P. J. (2009). Application of natural antimicrobials for food preservation. *J. Agric. food Chem.* 57 (14), 5987–6000. doi:10.1021/jf900668n

Tsvetkov, Y. E., Volkov, T. M., Eremin, S. A., Sklyarov, O. D., Kulakov, Y. K., Krylov, V. B., et al. (2024). New synthesis of oligosaccharides modelling the M epitope of the Brucella O-polysaccharide. *Front. Chem.* 12, 1424157. doi:10.3389/fchem.2024.1424157

Utchariyakiat, I., Surassmo, S., Jaturanpinyo, M., Khuntayaporn, P., and Chomnawang, M. T. (2016). Efficacy of cinnamon bark oil and cinnamaldehyde on anti-multidrug resistant *Pseudomonas aeruginosa* and the synergistic effects in combination with other antimicrobial agents. *BMC complementary Altern. Med.* 16, 6. doi:10.1186/s12906-016-1134-9

Wang, Y., Zhang, X., Wang, X., and Lai, X. (2021). Appropriateness of empirical fluoroquinolones therapy in patients infected with *Escherichia coli*, *Klebsiella pneumoniae*, or *Pseudomonas aeruginosa*: the importance of the CLSI breakpoints revision. *Infect. Drug Resist* 14, 3541–3552. doi:10.2147/idr.s329477

Weber, L. (2002). The application of multi-component reactions in drug discovery. *Curr. Med. Chem.* 9, 2085–2093. doi:10.2174/0929867023368719

Yadlapalli, R., Krishna, O. P., Kiranmayi, V., Manjula, S., and Ramu, S. P. (2012). Synthesis and *in vitro* anticancer and antitubercular activity of diarylpyrazole ligated dihydropyrimidines possessing lipophilic carbamoyl group. *Bioorg. and Med. Chem. Lett.* 22, 2708–2711. doi:10.1016/j.bmcl.2012.02.101

Zhang, M., Ouyang, J.-K., Xu, Q.-L., Liu, S.-B., Qian, T., Dong, L.-M., et al. (2021). Thymol derivatives with antibacterial and cytotoxic activity from the aerial parts of *Ageratina adenophora*. *RSC Adv.* 11, 5755–5761. doi:10.1039/D0RA08885D

frontiers | Frontiers in Chemistry

TYPE Original Research
PUBLISHED 12 November 2024
DOI 10.3389/fchem.2024.1493906

OPEN ACCESS

EDITED BY
Diego Brancaccio,
University of Naples Federico II, Italy

REVIEWED BY
Penke Vijaya Babu,
Tikvah Pharma Solutions Pvt Ltd., India
Navidha Aggarwal,
Maharishi Markandeshwar University, India

*CORRESPONDENCE
Bahaa G. M. Youssif,
bahaa.youssif@pharm.aun.edu.eg,
bgyoussif2@gmail.com
Stefan Bräse,
braese@kit.edu

RECEIVED 09 September 2024
ACCEPTED 30 October 2024
PUBLISHED 12 November 2024

CITATION
Al-Wahaibi LH, Mahmoud MA, Alzahrani HA, Abou-Zied HA, Abdelmoez A, Youssif BGM, Bräse S and Rabea SM (2024) Synthesis, enzyme inhibition, and docking studies of new schiff bases of disalicylic acid methylene-based derivatives as dual-target antibacterial agents. *Front. Chem.* 12:1493906.
doi: 10.3389/fchem.2024.1493906

Synthesis, enzyme inhibition, and docking studies of new schiff bases of disalicylic acid methylene-based derivatives as dual-target antibacterial agents

Lamya H. Al-Wahaibi[1], Mohamed A. Mahmoud[2], Hayat Ali Alzahrani[3], Hesham A. Abou-Zied[4], Alshaimaa Abdelmoez[2], Bahaa G. M. Youssif[2]*, Stefan Bräse[5]* and Safwat M. Rabea[6,7]

[1]Department of Chemistry, College of Sciences, Princess Nourah bint Abdulrahman University, Riyadh, Saudi Arabia, [2]Pharmaceutical Organic Chemistry Department, Faculty of Pharmacy, Assiut University, Assiut, Egypt, [3]Applied Medical Science College, Medical Laboratory Technology Department, Northern Border University, Arar, Saudi Arabia, [4]Medicinal Chemistry Department, Faculty of Pharmacy, Deraya University, Minia, Egypt, [5]Institute of Biological and Chemical Systems - Functional Molecular Systems (IBCS-FMS), Karlsruhe Institute of Technology, Karlsruhe, Germany, [6]Medicinal Chemistry Department, Faculty of Pharmacy, Minia University, Minia, Egypt, [7]Apogee Pharmaceuticals, Burnaby, BC, Canada

Introduction: Bacteria have acquired resistance to almost all antibiotics currently in use due to their extensive, broad, and improper utilization over a prolonged period. DNA gyrase and DHFR exhibit significant promise as targets for antibacterial therapeutics.

Methods: We have developed a series of disalicylic acid methylene/Schiff bases hybrids (**6a-l**) that function as antibacterial agents by targeting DNA gyrase and DHFR.

Results and discussion: The findings showed that **6a-l** have significant antibacterial activity against both Gram-positive and Gram-negative bacteria, with inhibition zones (IZ) comparable to or even higher than the reference Ciprofloxacin. MIC testing revealed that **6h** and **6l** were 1.5 times as effective than ciprofloxacin against *S. aureus*. Compounds **6h** and **6l** had MBC values of 28 and 33 nM for *S. aureus*, compared to Ciprofloxacin's 45 nM, indicating that they are more potent bactericidal agents. The MIC values for compounds **6c**, **6e**, **6h**, **6j**, and **6l** against *A. flavus* were between 14.50 and 19.50 μM, while the MIC value for fluconazole was 11.50 μM. Also, the studied compounds had MIC values between 18.20 and 22.90 μM against *C. albicans*, while Fluconazole had a MIC value of 17.50 μM. Compound **6h** showed a MIC value of 1.70 μM against the clinical strain *S. aureus* (ATCC 43300) (MRSA), making it an effective antibacterial agent. Compounds **6h**, **6j**, and **6l** inhibited *E. coli* DNA gyrase with IC_{50} values of 79, 117, and 87 nM, respectively, compared to the reference novobiocin (IC_{50} = 170 nM). Additionally, compounds **6h** and **6l**, the most potent *E. coli* gyrase

inhibitors, showed encouraging results on DHFR. Compounds **6h** and **6l** exhibit IC_{50} values of 3.80 μM and 4.25 μM, respectively. These values are significantly lower and hence more effective than Trimethoprim's IC_{50} of 5.20 μM.

KEYWORDS

bacterial resistance, biofilm, DNA, isatin, salicylic acid, bactericidal

1 Introduction

Bacterial infections, caused by either Gram-positive or Gram-negative pathogens, are the most common type of infections acquired in hospitals or by the general public (Chu et al., 2019; Abdel-Aziz et al., 2023). Moreover, bacteria have developed resistance to nearly all currently used antibiotics as a result of their long-term, widespread, and incorrect use, complicating the situation (Gao C. et al., 2018; Gao F. et al., 2018; Kumar et al., 2023a). Annually, some 0.7 million deaths occur worldwide due to drug-resistant infections, and this figure might rise to 10 million by the year 2050 if current patterns persist (Agrawal and Patel, 2024; Kumar et al., 2023b). Therefore, it is imperative to expedite the development of novel antibacterials that demonstrate exceptional efficacy against both susceptible and resistant infections (Kumar et al., 2022).

The enzyme dihydrofolate reductase (DHFR) is a crucial target for numerous anticancer and antibacterial medications. It holds significant value in the field of medicinal chemistry due to its role as a cofactor in the production of nucleic acids and amino acids (Roth, 1986; Abdolmaleki and Maddah, 2023). The mechanism of action for DHFR involves the inhibition of DNA, RNA, and protein synthesis, which leads to the stop of cell growth (Alrohily et al., 2019; Chawla et al., 2021). On the other hand, DNA gyrase is a type II topoisomerase enzyme that catalyzes modifications in the topology of DNA (Abdel-Aziz et al., 2023; Hirsch and Klostermeier, 2021). Furthermore, it consists of two chains, GyrA and GyrB subunits, which are accountable for the temporary disruption of two DNA strands and the induction of negative supercoiling in DNA during replication. Antibacterial drugs that specifically target DNA gyrase exert their activity through two mechanisms: gyrase poisoning, as seen in ciprofloxacin, or by blocking the ATP binding site, as observed in novobiocin (Tiz et al., 2019). Due to its crucial role, DNA gyrase has become an appealing target for the development of antibacterial drugs (Elbastawesy et al., 2023). As a result, DHFR and DNA topoisomerases have a demonstrated track record of supporting their function in microbial disorders (Hassan et al., 2020; Alqurashi et al., 2023).

The development of biofilms is another contributing component to bacterial resistance's pathogenicity. Biofilms consist of an intricate community of bacteria enclosed within a polysaccharide matrix (Singh et al., 2021; Shree et al., 2023). A significant portion of bacterial pathogens generate biofilms as a pathogenic mechanism to adhere to surfaces and protect themselves from antimicrobial agents. More than 80% of persistent microbial infections are associated with biofilms, which pose a significant health concern (Vestby et al., 2020). As a result, given the significant role biofilms play in infection transmission and resistance evolution, there is an urgent need for the discovery of new chemotherapeutic drugs that interfere with biofilm formation and/or break pre-formed ones.

The investigation of medically advantageous heterocyclic frameworks is an essential arena in the field of drug discovery. The compound is referred to as isatin (1*H*-indole-2,3-dione, Figure 1) moiety is widely present in nature, and its derivatives exhibit a wide range of pharmacological effects, with anti-bacterial activity (Zhang et al., 2018; Liu et al., 2022) being the most prominent.

The isatin moiety offers a wide range of modification possibilities, with the N-1, C-3, and C-5 positions being the most important ones for chemical modification (Wang et al., 2018). Additionally, a number of isatin-based medications, such as Semaxanib and Indirubin, are currently in clinics or undergoing clinical trials for the treatment of a variety of disorders (Xu et al., 2017a; Xu et al., 2017b). The extensive variety of biological activities, along with the ability to make various structural alterations, and the effective use in clinical practice, have motivated researchers to investigate isatins and develop many derivatives with different structures.

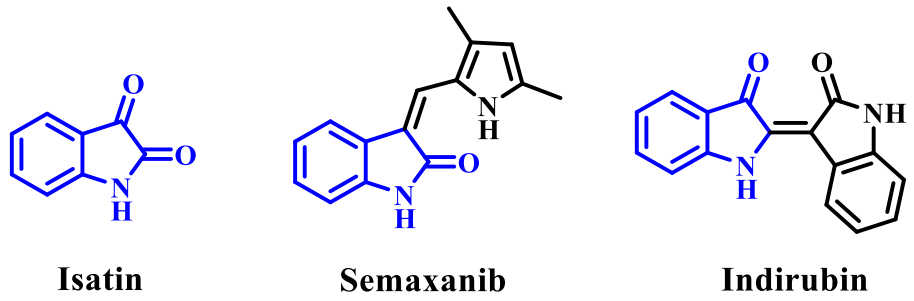

FIGURE 1
Structures of isatin, semaxanib, and indirubin.

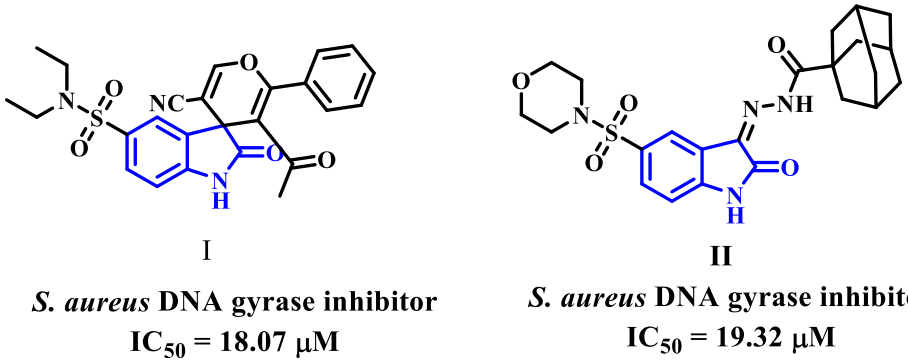

FIGURE 2
Isatin-based DNA gyrase inhibitors **I** and **II**.

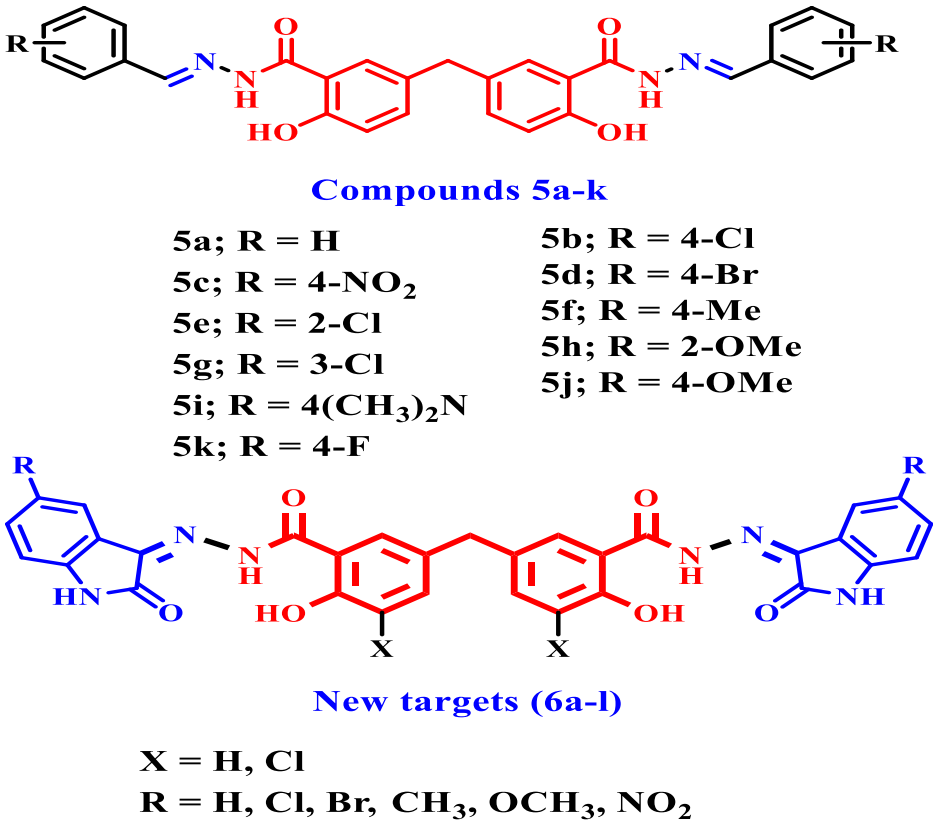

FIGURE 3
Structures of compounds **5a-k** and new targets **6a-l**.

Recently, researchers investigated various isatin compounds to establish their efficacy against bacteria. Some of these compounds (**I** and **II**, Figure 2) have demonstrated promise *in vitro* assays as DNA gyrase inhibitors (Alzahrani et al., 2022).

Schiff base structures are becoming increasingly popular among researchers due to their ease of synthesis, versatility, and diverse range of activities, including antibacterial properties (Bayeh et al., 2020). In addition, the imine bond found in Schiff base offers the potential to form interactions with various nucleophiles and electrophiles, thereby impeding the activity of enzymes or the replication of DNA (Nastasă et al., 2018).

The combination of multiple pharmacophores into a single hybrid molecule is a promising approach to the development of innovative drugs. This approach has the potential to overcome cross-resistance and increase the effectiveness of the original medications (Hisham et al., 2023; Frejat et al., 2022). In addition, many hybrids, such as **Ro 23-9424** and **TD-1792**, are currently undergoing clinical studies to help battle a variety of diseases. So, combining isatin with other antibacterial pharmacophores could

result in very potent options that function against both drug-sensitive and drug-resistant Gram-positive and Gram-negative bacteria.

1.1 Rational design

In a recent work from our lab (Al-Wahaibi et al., 2024), we reported on the design, synthesis, and antibacterial activity of a new series of Schiff bases of disalicylic acid methylene hybrid with various aldehydes as DNA gyrase and Topoisomerase IV inhibitors. The novel hybrids **5a-k**, Figure 3, were tested for antibacterial efficacy against Gram-positive pathogens *S. aureus* (*S. aureus*) and *B. subtilis* (*B. subtilis*), as well as Gram-negative organisms *E. coli* (*E. coli*) and *P. aeruginosa* (*P. aeruginosa*). Ciprofloxacin was utilized as the reference medication.

The *in vitro* assay test showed that compound **5h** (X = 2-OMe) had the highest potency among the compounds examined, with MIC values of 0.030, 0.065, and 0.060 μg/mL against *S. aureus*, *E. coli*, and *P. aeruginosa*. It was as effective as ciprofloxacin against the studied species but had a MIC value of 0.050 μg/mL against *B. subtilis*, making it five times less potent than ciprofloxacin. Additionally, compound **5i** (X = 4-dimethylamino) exhibited the second greatest activity. At the MIC level, it was equally effective against *S. aureus*, *E. coli*, and *P. aeruginosa* as compound **5h** and ciprofloxacin were. However, against *B. subtilis*, it was 7 times less effective than ciprofloxacin. Additionally, the inhibitory efficacy of **5h** and **5i** against *E. coli* DNA gyrase was assessed using the *E. coli* DNA gyrase test. Compounds **5h** and **5i** exhibited greater inhibitory activity against *E. coli* DNA gyrase, with IC_{50} values of 92 ± 5 nM and 97 ± 6 nM, respectively, compared to the positive control novobiocin (IC_{50} = 170 nM). Compounds **5h** and **5i** also demonstrated promising effects on Topoisomerase IV. Compounds **5h** and **5i** exhibit IC_{50} values of 3.50 μM and 5.80 μM, respectively. These results are much lower and more potent than Novobiocin's IC_{50} value of 11 μM.

In the present study, the newly synthesized compounds **(6a-l)** were developed by making two modifications to the previously disclosed **5a-k** compounds. Our first modification involves replacing aldehydes with isatin or isatin derivatives during the synthesis of our new hybrids. Second, in compounds **6j-l**, we use a dichloro-disalicylic acid methylene derivative rather than disalicylic acid methylene to increase the antibacterial activity.

Based on the data above and our ongoing research into developing medicinally active antimicrobials (Abdel-Aziz et al., 2023; Elbastawesy et al., 2023; Frejat et al., 2022; Al-Wahaibi et al., 2024; Al-Wahaibi et al., 2021a; Al-Wahaibi et al., 2021b; Aly et al., 2024; Abdu-Allah et al., 2017; Alkhaldi et al., 2018; Alkhaldi et al., 2019; Youssif, 2013; Hofny et al., 2021; Youssif et al., 2016), we report the design and synthesis of new isatin-based Schiff bases **6a–l** (Figure 3), obtained from methylene disalicylic acid hydrazide. The novel compounds **6a-l** were tested for antibacterial activity against Gram-positive pathogens *S. aureus* and *B. subtilis*, as well as Gram-negative organisms *E. coli* and *P. aeruginosa*. Ciprofloxacin was utilized as the reference medication. Furthermore, the synthetic compounds **6a-l** were tested for antifungal activity against Aspergillus flavus (*A. flavus*) and *Candida* albicans (*C. albicans*), using fluconazole as a reference medication. The minimum inhibitory concentrations (MICs), bactericidal concentrations (MBCs), and fungicidal concentrations (MFCs) of the most active derivatives against the tested microorganisms were compared to ciprofloxacin and/or fluconazole. This study looked at the antibacterial efficacy of the most potent Schiff bases against a panel of multi-drug resistant bacteria (MDRB), which included one clinical strain of *S. aureus* (ATCC 43300) (MRSA), two standard strains of *E. coli* (ATCC BAA-196), and *P. aeruginosa* (ATCC BAA-2111). Norfloxacin, a broad-spectrum antibiotic, was used as the positive control. Additionally, the evaluation focused on assessing the inhibitory potency of the most active compounds against *E. coli* DNA gyrase and DHFR, which were identified as potential targets. Finally, the cell viability and antibiofilm assays for the most potent compounds were evaluated.

2 Results and discussion

2.1 Chemistry

Scheme 1 depicts the synthesis steps for the key intermediates **4a** and **4b**, as well as the target compounds **6a-l**. Compounds **2**, **3**, and **4b** were previously synthesized and well described (Al-Wahaibi et al., 2024). The procedures used in the current investigation differ slightly from those used in Cushman and Suseela's study (Cushman and Kanamathareddy, 1990). The synthesis commenced by preparing the methylene bridged 3-chlorosalicylic acid dimer **2** (DSA-Cl_2) with a yield of 98%. This was achieved through the condensation of two molecules of 3-chlorosalicylic acid **1** with paraformaldehyde in concentrated sulfuric acid. The chlorine atom was used as a protective group to control the regio-chemistry in the dimerization reaction and prevent further interaction of DSA-Cl_2 with formaldehyde in the presence of acid. This interaction would lead to the formation of phenol-formaldehyde polymers.

The subsequent step involved the reduction of compound **2** through reductive dehalogenation using potassium formate as a source of hydride and Pd/C as a catalyst, resulting in the formation of disalicylic acid dimer **3** with a yield of 92%. Initially, the hydrodehalogenation of the chlorine atom in compound **2** to produce disalicylic acid dimer **3** was attempted using molecular hydrogen (Youssif, 2013). However, this reaction proceeded slowly and was incomplete even after 24 h. To overcome this, catalytic transfer hydrogenation (CTH) was employed, utilizing organic hydrogen donors such as potassium formate (HCOOK) as a reducing agent. CTH demonstrated a significantly higher reaction rate with potassium formate compared to molecular hydrogen. Additionally, potassium formate is easily manageable, less toxic, and less flammable, making it more advantageous for large-scale synthesis.

Compound **4a** was prepared from compound **2** using a two-step process. Firstly, compound **2** was heated in absolute ethanol with a catalytic amount of concentrated sulfuric acid. Then, the resulting ester product was further refluxed with an excess of hydrazine hydrate. Compound **4a** was obtained in a 65% yield as white crystals after purification. The structure of compound **4a** was confirmed using IR spectroscopy, which showed a strong

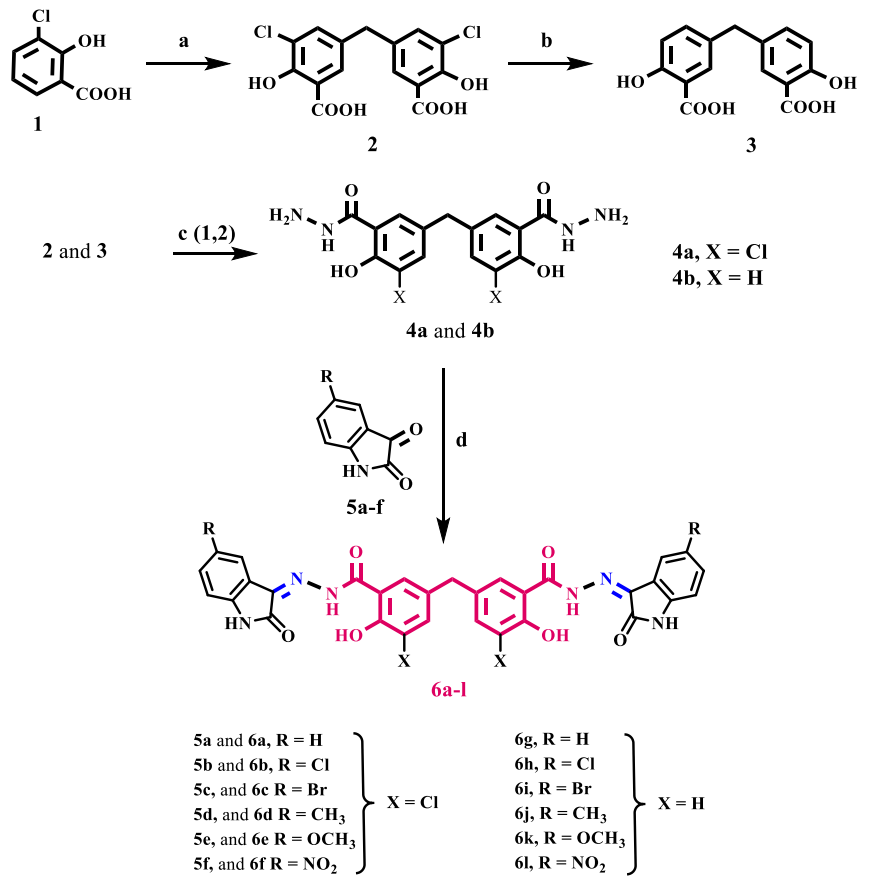

SCHEME 1
Reagents and reaction conditions: **(A)** HCHO, H2SO4, 35°C, 18 h, 98%; **(B)** KHCOO, Pd/C, KOH, 2- PrOH/H2O, 70°C, 4 h, 92%; **(C)** 1-EtOH/Conc. H2SO4, 2- Hydrazine hydrate, reflux 6 h; **(D)** isatin derivative, EtOH, reflux overnight.

absorption peak at υ 2,616–3,370 cm^{-1}, of phenolic OH groups. In addition, the spectrum exhibited prominent absorption peaks at υ 3,370 and 3,286 cm^{-1}, corresponding to the NH_2 group. Additionally, the spectrum revealed a characteristic peak at υ 1,654 cm^{-1}, corresponding to the amidic C=O bond. Unfortunately, due to solubility issues, we were unable to obtain a distinct ^{1}H NMR or ^{13}C NMR spectrum for **4a** using commonly used NMR solvents. We use LC-MS spectroscopy, which revealed the molecular ion peak of **4a** in the anticipated region of the mass spectrum (See Supplementary Material).

Schiff base derivatives, **6a-l**, were prepared by refluxing compounds **4a** and **4b** with proper (un) substituted isatin in ethanol for 14–18 h, giving **6a-l** in good yields. The validity of the structures of **6a-l** was verified by employing ^{1}H NMR, ^{13}C NMR, and elemental microanalysis experiments. The ^{1}H NMR spectrum of compound **6k**, as a representative example, displayed five distinct singlet signals, which are characteristic of this compound. There is a singlet at δ 14.38 ppm which corresponds to two phenolic OH groups. There is another singlet at δ 11.52 ppm which corresponds to amidic NH groups. Additionally, there is a singlet at δ 10.93 ppm which corresponds to isatin NH groups. There is also a singlet at δ 3.95 ppm which corresponds to an aryl methylene group (Ar-CH_2). Lastly, there is a singlet at δ 3.76 ppm which corresponds to six protons of two methoxy groups. Additionally, aromatic protons have distinct signals.

2.2 Biology

2.2.1 *In vitro* antimicrobial activities

The antimicrobial effects of the currently synthesized Schiff bases (**6a-l**) were tested against two Gram-positive bacteria (*S. aureus* and *B. subtilis*), two Gram-negative bacteria (*E. coli* and *P. aeruginosa*), and two strains of fungus (*A. flavus* and *C. albicans*). The modified disk diffusion method (Alkhaldi et al., 2019; Manso et al., 2021) was used to determine the inhibition zones (IZ, mm/mL) and the minimal inhibitory concentration (MIC, nM). Ciprofloxacin and Fluconazole was used as positive controls. Tables 1–3 display the findings.

Based on the inhibition zones (IZ) measurements in Table 1, we can conclude that five Schiff bases (**6c**, **6e**, **6h**, **6j**, and **6l**) had inhibition zones that were either greater than or comparable to the inhibition zones of the reference medications (ciprofloxacin and fluconazole) against pathogenic organisms. Schiff bases **6a-l** were found to have strong antibacterial activity against both Gram-positive and Gram-negative bacteria, with inhibition zones (IZ) ranging from 22 to 48 mm for all pathogens tested,

TABLE 1 Inhibition zone diameter (mm/mg) of compounds 6a-l and reference drugs.

Sample	Inhibition zone (IZ) diameter (mm/mg)					
	Bacterial species				Fungi	
	(G^+)		(G^-)			
	B. subtilis	*S. aureus*	*E. Coli*	*P. aeruginosa*	*A. flavus*	*C. albicans*
6a	36	36	34	35	18	28
6b	26	27	26	26	11	18
6c	38	38	37	38	22	31
6d	30	31	30	30	13	20
6e	37	38	36	38	21	30
6f	34	35	35	32	16	25
6g	23	25	22	22	9.0	15
6h	45	48	45	45	31	36
6i	31	32	33	32	15	22
6j	40	41	40	40	25	33
6k	29	31	27	25	14	20
6l	43	46	43	42	29	35
Ciprofloxacin	40	40	40	40	NA	NA
Fluconazole	NA	NA	NA	NA	40	40

NA: no activity (8 mm), weak activity (8–15 mm), moderate activity (15–20 mm), strong activity (>20 mm), DMSO, as solvent (8 mm), and *Bacillus subtilis* (*B. subtilis*), *Staphylococcus aureus* (*S. aureus*), *Escherichia coli* (*E. coli*), *Pseudomonas aeruginosa* (*P. aeruginosa*), *Candida albicans* (*C. albicans*), and *Aspergillus flavus* (*A. flavus*).

TABLE 2 MICs and MBCs of compounds 6c, 6e, 6h, 6j, and 6l.

Compound	Bacterial species							
	(G^+)				(G^-)			
	B. subtilis		*S. aureus*		*E. coli*		*P. aeruginosa*	
	MIC	*MBC*	*MIC*	*MBC*	*MIC*	*MBC*	*MIC*	*MBC*
6c	33 ± 2	51 ± 3	29 ± 2	45 ± 2	66 ± 4	88 ± 6	65 ± 5	85 ± 6
6e	37 ± 2	58 ± 3	35 ± 2	54 ± 3	69 ± 4	95 ± 6	69 ± 5	97 ± 6
6 h	24 ± 2	38 ± 2	19 ± 1	28 ± 1	54 ± 3	74 ± 6	55 ± 4	74 ± 5
6j	31 ± 2	47 ± 2	25 ± 2	40 ± 2	62 ± 4	81 ± 6	61 ± 5	80 ± 6
6l	26 ± 2	43 ± 3	21 ± 2	33 ± 2	57 ± 4	77 ± 6	57 ± 4	78 ± 6
Ciprofloxacin	10 ± 1	19 ± 1	30 ± 2	45 ± 2	60 ± 4	90 ± 6	60 ± 5	90 ± 6

compared to Ciprofloxacin's IZ of 40 mm. Moreover, Table 1 demonstrated that compounds **6h** and **6l** had superior efficacy compared to the reference ciprofloxacin against both gram-positive and gram-negative bacteria. In addition, most of the newly synthesized Schiff bases **6a-l** had IZ values between 11 and 36 mm against *A. flavus* and *C. albicans*, whereas fluconazole, a broad spectrum antifungal medication, had a value of 40 mm. We proceeded with the investigation to ascertain the minimal inhibitory concentrations (MIC, nM) of the potent Schiff bases (**6c**, **6e**, **6h**, **6j**, and **6l**). The results are displayed in Tables 2, 3.

2.2.2 Minimum inhibitory concentration (MIC) assay

The most potent components **6c**, **6e**, **6h**, **6j**, and **6l** were evaluated for antibacterial activity using a twofold serial dilution method on a 96-well microtiter plate (Wiegand et al., 2008). Table 2 showed the MICs (nM) of these compounds against the tested

TABLE 3 MICs and MFCs of compounds 6c, 6e, 6h, 6j, and 6l.

Compound	Fungi (μM)			
	A. flavus		*C. albicans*	
	MIC	*MFC*	*MIC*	*MFC*
6c	18.20 ± 1	35.90 ± 2	21.30 ± 1	44.80 ± 3
6e	19.50 ± 1	40.20 ± 3	22.90 ± 1	50.20 ± 3
6 h	14.50 ± 1	28.50 ± 1	18.20 ± 1	36.50 ± 2
6j	16.90 ± 1	33.90 ± 2	20.70 ± 1	41.50 ± 3
6l	15.60 ± 1	31.10 ± 2	19.50 ± 1	39.20 ± 3
Fluconazole	11.50 ± 1	22.80 ± 1	17.50 ± 1	35.00 ± 2

bacteria, with ciprofloxacin as the reference medicine. The results of this *in vitro* assay test are consistent with the findings of the antimicrobial sensitivity test. Compound **6h** (R = Cl, X = H) was the most potent of the compounds examined, having MIC values of 19, 54, and 55 nM against *S. aureus*, *E. coli*, and *P. aeruginosa*. It displayed greater potency to ciprofloxacin against the investigated species but had a MIC value of 24 nM against *B. subtilis*, which is 2.5 times less effective than ciprofloxacin (MIC = 10 nM). Compound **6l** (R = NO_2, X = H) exhibited the second highest activity. Its MIC values were comparable to those of ciprofloxacin against *E. coli* and *P. aeruginosa*, Table 2. However, it was 2.5 times less effective than ciprofloxacin against *B. subtilis*. Compounds **6h** and **6l** were 1.5 times more effective than ciprofloxacin against *S. aureus*, with MIC values of 19 and 21 nM, respectively, whereas ciprofloxacin had a MIC value of 30 nM. Compounds **6c** (R = Br, X = Cl) and **6j** (R = CH_3, X = H) exhibited significant activity against the tested species, especially against *S. aureus*, with MICs values of 29 and 25 nM, respectively. These values were comparable to that of ciprofloxacin (MIC = 30 nM). Finally, compound **6e** (with R = OCH_3 and X = Cl) demonstrated the lowest level of efficacy. It has lower antimicrobial activity than ciprofloxacin against all pathogens tested.

2.2.3 Minimum bactericidal concentration (MBC) assay

The MBC differs from the MIC. The MIC test finds the lowest concentration of an antimicrobial agent that significantly inhibits growth, whereas the MBC identifies the lowest concentration that causes microbiological organisms to die. In contrast to the MBC, which does result in mortality, the MIC just inhibits, meaning that the antibacterial action does not cause death (Abdullahi et al., 2023). MBC is typically reported as MBC_{50}, indicating that the antibiotic concentration kills 50% of the initial bacterial population (Sun et al., 2019).

In general, components **6c**, **6e**, **6h**, **6j**, and **6l** had strong bactericidal activity. The MBC values for Gram-positive bacteria ranged from 28 to 58 nM, whereas ciprofloxacin MBC values were 19 and 45 nM, Table 2. Compounds **6h** (R = Cl, X = H) and **6l** (R = NO_2, X = H), the most potent antibacterial agents, displayed bactericidal activity of 28 and 33 nM, respectively, for *S. aureus*, compared to ciprofloxacin's MBC value of 45 nM, making **6h** and **6l** more effective as bactericidal agents. Compound **6j** (R = CH_3, X = H) scored third in bactericidal activity with MBC value of 40 nM against *S. aureus*, which was comparable to the reference ciprofloxacin. Regrettably, compounds **6h**, **6j**, and **6l** exhibited lower effectiveness as bactericidal agents compared to ciprofloxacin against *B. subtilis*. The MBC values for compounds **6h**, **6j**, and **6l** were 38, 47, and 43 nM, respectively, while ciprofloxacin had an MBC value of 19 nM.

In the case of Gram-negative bacteria, compounds **6h**, **6j**, and **6l** had higher MBC values than the other compounds examined. These compounds have MBC values of 74, 80, and 78 nM, making them more effective than ciprofloxacin (MBC = 90 nM) against both *E. Coli* and *P. aeruginosa* species. Again, compound **6e** (with R = OCH_3 and X = Cl) was the least effective as bactericidal agents against all of the bacterial species tested.

2.2.4 Antifungal assay

Compounds **6c**, **6e**, **6h**, **6j**, and **6l** were tested for antifungal activity with a twofold serial dilution method (Wiegand et al., 2008). Table 3 displays the MICs (μM) and MFCs (minimum fungicidal concentration, μM) of these derivatives against *A. flavus* and *C. albicans* fungus, using fluconazole as the reference medication. Overall, the investigated compounds displayed robust antifungal efficacy against the selected fungal species when compared to ciprofloxacin. Compounds **6c**, **6e**, **6h**, **6j**, and **6l** exhibited MIC values ranging from 14.50 to 19.50 μM against *A. flavus*, while fluconazole had a MIC value of 11.50 μM. Moreover, the tested compounds demonstrated MIC values ranging from 18.20 to 22.90 μM against *C. albicans*, while the reference fluconazole had a MIC of 17.50 μM.

Compound **6h** (R = Cl, X = H), the most potent antibacterial agent, was also the most potent antifungal agent, with MIC values of 14.50 μM against *A. flavus* and 18.20 μM against *C. albicans*, being comparable to the reference fluconazole, which had MIC values of 11.50 and 17.50 μM, respectively. Compound **6l** (R = NO_2, X = H) demonstrated the second highest antifungal activity. It exhibited MIC values of 15.60 μM against *A. flavus* and 19.50 μM against *C. albicans*. Finally, Table 3 shows that all investigated compounds had fungicidal activity, with MFC/MIC ratios ranging around two.

2.2.5 Antibacterial assay against multi-drug resistant strains

The most potent Schiff bases **6c**, **6e**, **6h**, **6j**, and **6l** were examined for their antibacterial efficacy against a panel of MDRB (multi-drug resistant bacteria), including one clinical strain *S. aureus* (ATCC 43300) (MRSA), two standard strain *E. coli* (ATCC BAA-196) and *P. aeruginosa* (ATCC BAA-2111). Norfloxacin, a broad-spectrum antibiotic, worked as positive control. Results are displayed in Table 4.

The MIC values for the tested compounds vary from 1.70 to 7.15 μM, while the MBC values range from 3.50 to 10.40 μM against MDRB bacteria. These values are compared to the MIC values of norfloxacin, which range from 1.20 to 3.20 μM, and the MBC values, which range from 2.80 to 4.70 μM. The majority of the investigated Schiff bases, compounds **6c**, **6e**, **6h**, **6j**, and **6l**, had substantial broad-spectrum effects on both Gram-positive and Gram-negative bacteria, either by inhibiting their growth or by killing them (bactericidal effect). Notably, compounds **6h** and **6l** show the most potent actions compared to other derivatives. Compound

TABLE 4 MICs and MBCs of compounds 6c, 6e, 6h, 6j, and 6l against MDRB strains.

Compound	*S. aureus ATCC 43300*		*E. coli ATCC-BAA-196*		*P. aeruginosa ATCC-BAA-2111*	
	MIC	*MBC*	*MIC*	*MBC*	*MIC*	*MBC*
6c	4.70 ± 0.20	7.10 ± 0.50	5.30 ± 0.20	8.20 ± 0.60	6.85 ± 0.50	9.20 ± 0.60
6e	5.90 ± 0.20	7.80 ± 0.50	6.25 ± 0.25	9.30 ± 0.60	7.15 ± 0.50	10.40 ± 0.70
6h	1.70 ± 0.10	3.20 ± 0.15	1.90 ± 0.10	3.70 ± 0.20	3.40 ± 0.20	5.80 ± 0.30
6j	3.20 ± 0.15	5.90 ± 0.25	3.90 ± 0.15	6.10 ± 0.25	5.60 ± 0.25	7.80 ± 0.30
6l	2.20 ± 0.10	4.50 ± 0.20	2.70 ± 0.10	4.80 ± 0.20	4.50 ± 0.20	6.50 ± 0.25
Norfloxacin	1.20 ± 0.10	2.80 ± 0.10	1.60 ± 0.10	3.50 ± 0.10	3.20 ± 0.10	4.70 ± 0.20

TABLE 5 IC_{50} values of 6h, 6j, and 6l against *E. coli* DNA gyrase and DHFR.

Compound	IC_{50} (nM)	IC_{50} (μM)
	E. Coli DNA gyrase	DHFR *E. Coli*
6 h	79 ± 5	3.80 ± 0.10
6j	117 ± 8	5.10 ± 0.20
6l	87 ± 6	4.25 ± 0.10
Novobiocin	170 ± 20	--
Trimethoprim	--	5.20 ± 0.20

6h (R = Cl, X = H) showed a MIC value of 1.70 μM against the clinical strain *S. aureus* (ATCC 43300) (MRSA), making it an effective antibacterial agent. It was found to be approximately as potent as the reference drug norfloxacin, which had a MIC of 1.20 μM. Compound **6h**, on the other hand, exhibited an MBC of 3.90 μM, making it around 1.2 times more potent against the MRSA strain than the reference norfloxacin. Furthermore, compound **6h** demonstrated similar efficacy to norfloxacin against *E. coli* (ATCC BAA-196) and *P. aeruginosa* (ATCC BAA-2111), with MICs of 1.9 and 3.4 μM, respectively. Norfloxacin, on the other hand, showed MIC values of 1.6 and 3.2 μM. Additionally, compound **6l** (R = NO_2, X = H) showed significant antibacterial activity against MDRB strains, with MIC values ranging from 2.20 to 4.50 μM and MBC values ranging from 4.50 to 6.50 μM. Based on the MBC/MIC ratio, we identified that all of the compounds tested had values less than two, indicating bactericidal activity.

2.2.6 DNA gyrase and DHFR inhibitory assay

The inhibitory potency of derivatives **6h**, **6j**, and **6l**, the most potent antibacterial agents, against *E. coli* DNA gyrase and DHFR was determined using the *E. coli* DNA gyrase and DHFR assay (Durcik et al., 2018). The findings are shown as IC_{50} values for the investigated compounds and reference drugs (Table 5). The results of this assay complement those of the antibacterial activity investigation. Compounds **6h**, **6j**, and **6l** inhibited *E. coli* DNA gyrase at IC_{50} values of 79, 117, and 87 nM, respectively, compared to the reference novobiocin (IC_{50} = 170 nM). Compounds **6h**, **6j**, and **6l** exhibited greater potency compared to the reference compound novobiocin, with compounds **6h** and **6l** being twice as potent as novobiocin against DNA gyrase.

TABLE 6 Antibiofilm assay of compound 6h.

6 h	Biofilm inhibition %	SD (±)
1/4 of MIC	64	0.49
1/2 MIC	88	0.64
MIC	97	0.42

Compounds **6h**, **6j**, and **6l** were further evaluated against the DHFR enzyme as indicated in Table 5. Compounds **6h** and **6l**, the most potent *E. coli* gyrase inhibitors, also demonstrated promising effects on DHFR. Compounds **6h** and **6l** have IC_{50} values of 3.80 μM and 4.25 μM, respectively. These values are much lower and more potent than trimethoprim's IC_{50} value of 5.20 μM. Based on these observations, we may infer that both compounds **6h** and **6j** show promise as dual-target inhibitors against DNA gyrase and DHFR, especially after optimization.

2.2.7 Antibiofilm assay

Bacterial biofilms provide health risks in hospitals, the food industry, and drinking water systems. In the current work, we investigated the antibiofilm activity of compound **6h**, the most potent derivative, against *S. aureus* using Microtiter plate assay for biofilm quantification (Antunes et al., 2010; Niu and Gilbert, 2004). The assay was performed with three different concentrations, the first of which was equivalent to the MIC of **6h** against *S. aureus* ATCC 43300 (Table 4), the second of which was equivalent to 1/2 MIC, and finally 1/4 MIC. The results were presented in Table 6 as Biofilm inhibition%.

The results showed that **6h** has significant antibiofilm action, with biofilm inhibition percentage equal to 97 at the MIC dose. Compound **6h** inhibited biofilms by 88% and 64% at ½ and ¼ MIC levels, respectively.

Blank represented absorbance of media only.

Control represented absorbance of test organism without any treatment.

2.2.8 Cell viability assay

This test examines the impact of compounds **6c**, **6e**, **6h**, **6j**, and **6l**, which are the most potent derivatives, on normal cell lines in order to assess the safety level of these compounds. The vitality of the investigated compounds was assessed using the MCF-10A cell line,

TABLE 7 Cell viability assay of compounds 6c, 6e, 6h, 6j, and 6l

Comp	Cell viability %
6c	91
6e	92
6 h	93
6j	92
6l	89

which is a normal human mammary gland epithelial cell line. Following a 4-day incubation period on MCF-10A cells with a concentration of 50 μM for each compound being studied, the viability of the cells was assessed using the MTT test (Hisham et al., 2022; Mahmoud et al., 2022). The results from Table 7 indicate that none of the compounds tested exhibited cytotoxicity, and all compounds show a cell viability of more than 89% at a concentration of 50 μM.

2.3 Docking studies

2.3.1 Docking study of *E. Coli* DNA gyrase B

This investigation performed an extensive computational docking analysis to determine the binding affinities of compounds **6b**, **6h**, and **6l** with *E. coli* DNA gyrase B and *E. coli* DHFR. Novobiocin served as the reference drug for *E. coli* DNA gyrase B, while trimethoprim was used as the reference for *E. coli* DHFR. Utilizing Discovery Studio software (Baroroh et al., 2023), the study provided an in-depth examination of the interaction mechanisms between these compounds and their respective target proteins. To ensure the accuracy and relevance of our investigation, we incorporated the crystallographic structure of the *E. coli* DNA gyrase B ligand complex (PDB ID: 4DUH) from the Protein Data Bank (Marinho et al., 2023). The OPLS-AA (Optimized Potentials for Liquid Simulations - All Atom) force field was utilized during the energy minimization process for the molecular systems under examination. Implementing this force field was crucial for achieving conformational stability of the molecular structures, thereby enhancing the precision and reliability of our computational analyses (Hazarika et al.; Kumar H. et al., 2023). Prior to initiating the docking procedure, the protein structure underwent comprehensive preparation to ensure its accuracy. This preparation included protonation, a critical step that significantly contributed to the robustness and reliability of the subsequent docking analysis. A comparative analysis between docking scores and *in vitro* activity levels of *E. coli* DNA gyrase B for the compounds studied revealed a direct correlation. Compound **6h**, which demonstrated the highest *in vitro* activity against *E. coli* DNA gyrase B, achieved a docking score of −7.88 kcal/mol. In contrast, compound **6b**, with lower *in vitro* antibacterial activity and a smaller inhibition zone (IZ) measurement compared to the ciprofloxacin, had a docking score of −5.78 kcal/mol. Compound **6l** recorded a docking score of −7.51 kcal/mol, reflecting its relatively strong binding affinity and correlating with its moderate *in vitro* activity. Moreover, Novobiocin, used as a reference drug in the study, displayed a docking score of −7.26 kcal/mol, indicating its considerable binding affinity. In analyzing interactions between the tested compounds and the *E. coli* DNA gyrase B protein, compound **6h** has exhibited notable binding characteristics. An important hydrogen bond interaction between the carbonyl oxygen of the salicylate moiety and Arg136 stabilizes **6h** within the active site. This hydrogen bond is crucial as it anchors the compound, preventing its dissociation from the active site and enhancing its inhibitory efficacy (Figure 4). Moreover, the absence of a bulky atom, such as the 3-chloro group on the di-salicylate nucleus of **6h**, facilitates the free rotation of the two salicylate moieties around the methylene axis. This rotational freedom is crucial as it enables the compound to adopt a conformation that effectively blocks the entrance to the active site. By fitting more snugly into the binding pocket, **6h** can comprehensively obstruct substrate access, thereby enhancing its ability to inhibit *E. coli* gyrase activity. The isatin nucleus within **6h** significantly enhances its binding affinity. The docking interactions reveal that the isatin moiety forms essential interactions with several amino acid residues within the active site. Notably, the π-π T-shaped interactions with residues such as His55 and Lys103 underscore the crucial role of the isatin nucleus in stabilizing the enzyme-inhibitor complex. The aromatic nature of isatin allows for these non-covalent interactions, which strengthen the overall binding and stability of **6h** within the active site (Figure 4). Furthermore, the presence of substituents like the 5-chloro group on the isatin nucleus of **6h** further amplifies its binding affinity. The 5-chloro substituent increases hydrophobic interactions with the active site residues and contributes to the electronic distribution of the molecule. The electron-withdrawing nature of the 5-chloro group enhances interactions with residues like His99. Additionally, this substituent helps position the isatin moiety in an optimal orientation for interaction with the enzyme, thereby boosting the inhibitory potential of **6h** (Figure 4).

In contrast, compound **6l**, which also lacks the bulky 3-chloro group on the di-salicylate nucleus like 6 h, exhibits less binding affinity due to fewer interactions with the active site. The absence of the 3-chloro group allows **6l** to have a certain degree of rotational freedom, but not as effectively as **6h**. This results in a less snug fit within the binding pocket, making it less efficient in blocking substrate access (Figure 5). Arg136 forms a Pi-donor hydrogen bond with the salicylate moiety, while Gly77 and Arg76 interact with the isatin moiety. Thr165 and Asp73 contribute to stabilizing the binding conformation through additional hydrogen bonds.

In addition, Novobiocin exhibited notable interactions with the *E. coli* DNA gyrase B protein, with its amide nitrogen functioning as a hydrogen bond acceptor in conjunction with Gly 101, as depicted in Figure 6. However, this significant interaction results in Novobiocin having a comparatively lower binding affinity to the active site than compounds **6h** and **6l**. This reduced affinity can be attributed to the lack of additional stabilizing interactions that compounds **6h** and **6l** possess, such as the π-π interactions with His55 and Lys103 in compound **6h** and the hydrophobic interactions facilitated by the 5-chloro group in compound **6h** (Figure 4). Moreover, the rigid structure of Novobiocin, which might limit its flexibility and ability to adopt an optimal conformation within the active site. This structural rigidity can result in fewer contacts with key residues within the binding pocket, leading to weaker overall binding interactions (Figure 6).

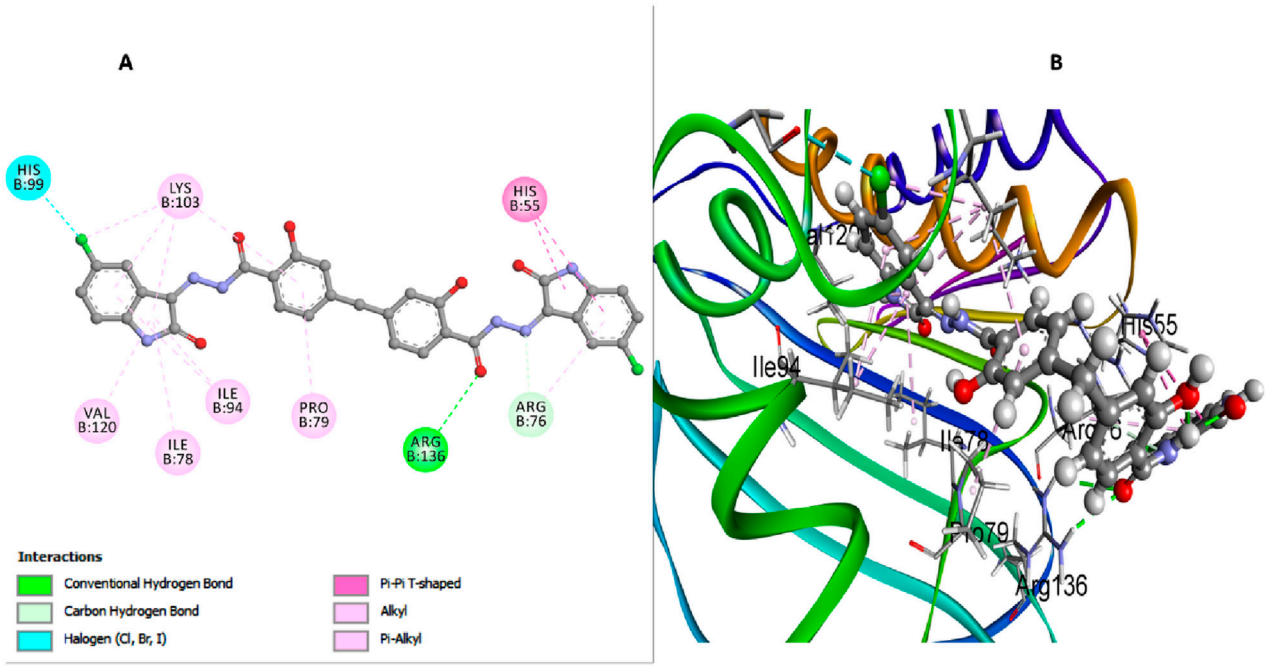

FIGURE 4
Docking representation models of compound **6h** within the binding site of *E. coli* DNA gyrase B protein; **(A)** 2D-docked model of compound **6h**; **(B)** 3D-docked model of compound **6h**.

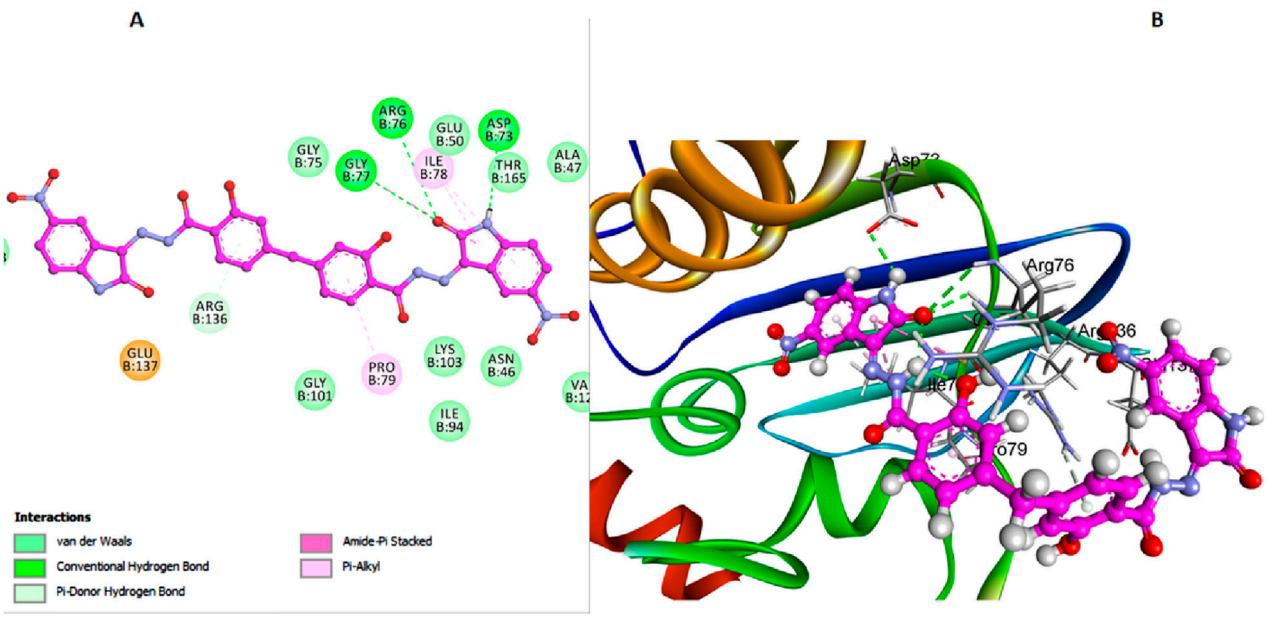

FIGURE 5
Docking representation models of compound **6l** within the binding site of *E. coli* DNA gyrase B protein; **(A)** 2D-docked model of compound **6l**; **(B)** 3D-docked model of compound **6l**.

On the other hand, compound **6b** features a bulky atom, the 3-chloro group on the di-salicylate nucleus, which significantly influences its interaction with *E. coli* gyrase. The presence of the 3-chloro group restricts the free rotation of the salicylate moieties around the methylene axis. This restriction limits the conformational flexibility of **6b**, potentially reducing its ability to snugly fit into the binding pocket and block substrate access as effectively as **6h** (Figure 7).

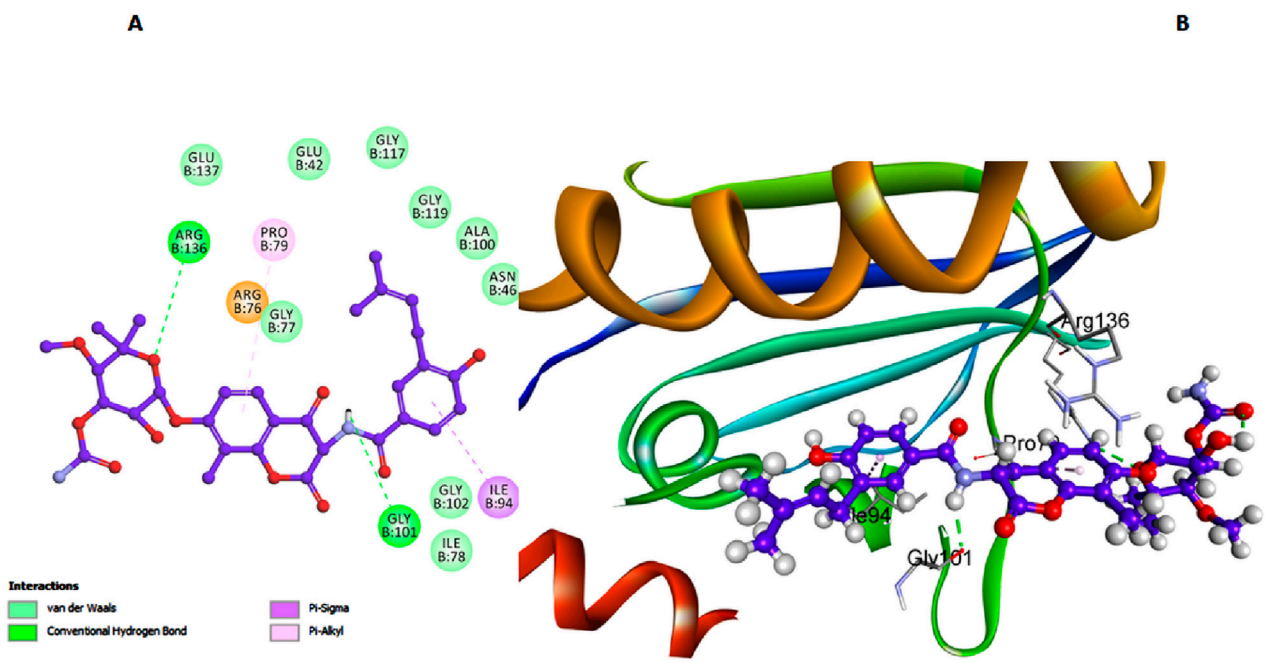

FIGURE 6
Docking representation models of Novobiocin within the binding site of *E. coli* DNA gyrase B protein; **(A)** 2D-docked model of Novobiocin; **(B)** 3D-docked model of Novobiocin.

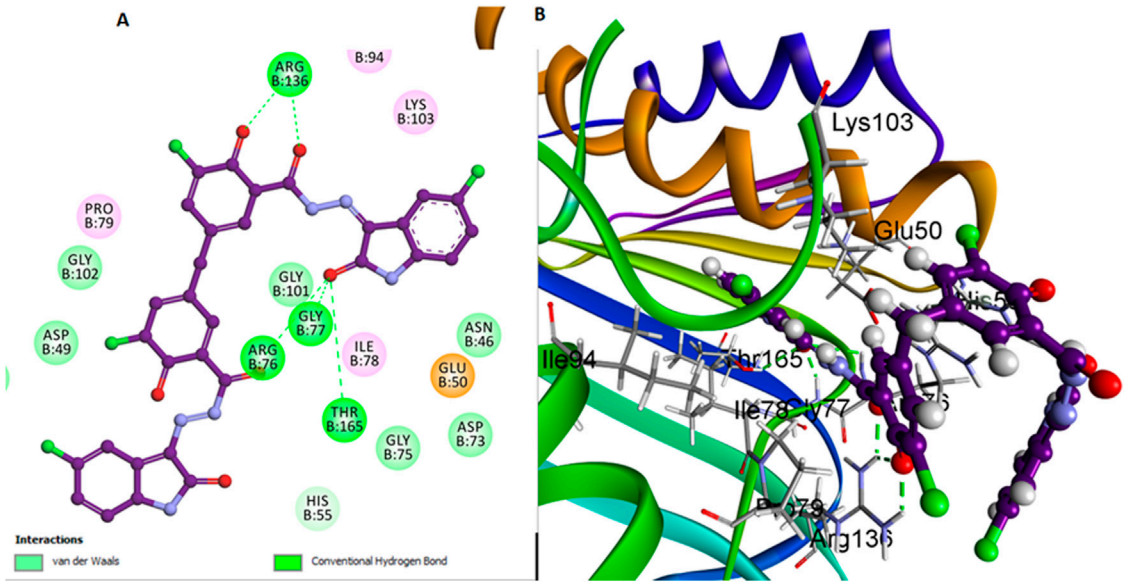

FIGURE 7
Docking representation models of compound **6b** within the binding site of *E. coli* DNA gyrase B protein; **(A)** 2D-docked model of compound **6b**; **(B)** 3D-docked model of compound **6b**.

Comparative analysis between compounds **6h**, **6l**, and **6b** reveals insights into their flexibility and stability. Compound **6h** benefits from the absence of bulky substituents, allowing for greater conformational flexibility and a snugger fit within the active site, leading to potentially higher inhibitory efficacy. Compound **6l**, while also lacking the bulky 3-chloro group on salicylate, forms fewer interactions within the active site, resulting in reduced binding affinity and inhibitory potency compared to **6h**. On the other hand, compound **6b**, with its bulky 3-chloro group on salicylate, faces a steric hindrance that reduces its conformational adaptability.

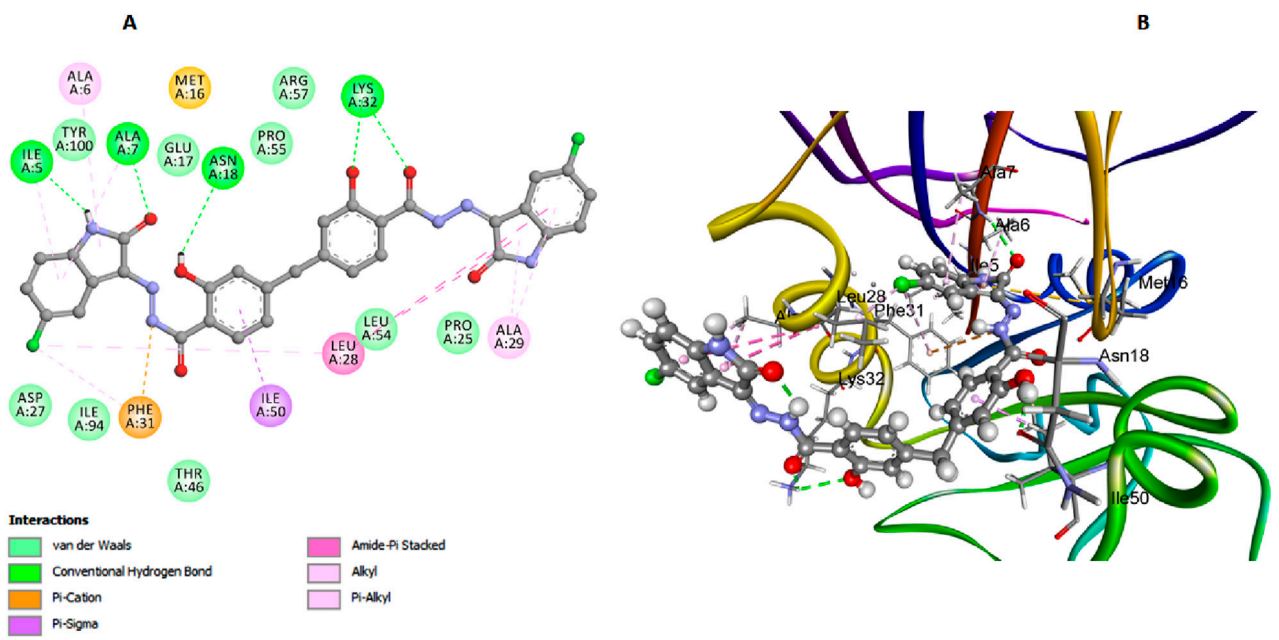

FIGURE 8
Docking representation models of compound **6h** within the binding site of *E. coli* DHFR enzyme; **(A)** 2D-docked model of compound **6h**; **(B)** 3D-docked model of compound **6h**.

2.3.2 Docking study of *E. Coli* DHFR

In our study on *E. coli* DHFR, we utilized the crystallographic structure of its ligand complex (PDB ID: 6CXK) from the Protein Data Bank as a foundational framework for computational modeling (Bhati, 2024). Compound **6h**, which demonstrated the highest *in vitro* activity against *E. coli* DHFR, achieved a docking score of −7.42 kcal/mol. Similarly, compound **6l**, with nearly comparable *in vitro* activity, recorded a docking score of −7.28 kcal/mol. Trimethoprim, used as the reference compound in this study, exhibited a docking score of −6.94 kcal/mol. The significance of the docking score of trimethoprim lies in its role as a benchmark, highlighting that compounds **6h** and **6l** exhibit stronger binding affinities, as evidenced by their lower docking scores, which correlates with their higher *in vitro* activities against *E. coli* DHFR. In the comprehensive analysis focusing on the interaction profiles between the investigated compounds and *E. coli* DHFR, compound **6h** exhibited significant binding characteristics. The docking interactions of compound **6h** with the DHFR *E. coli* enzyme provide detailed insights into its inhibitory potential. The carbonyl and phenolic oxygens of the salicylate moiety form two crucial hydrogen bonds with Lys32, anchoring **6h** within the active site (Figure 8). Additionally, π-stacked interactions with Leu28 and Leu54 further enhance the binding affinity of **6h**, while hydrogen bonds with Ile5 and Asn18 help stabilize its overall conformation within the active site. These interactions highlight the importance of specific residues in stabilizing the binding of compound **6h**, allowing it to fit snugly and effectively block substrate access, thereby enhancing its inhibitory efficacy against the DHFR *E. coli* enzyme.

Similarly, compound **6l** exhibits a binding affinity to DHFR *E. coli* enzyme that is comparable to **6h**. The docking interactions of **6l** reveal several key interactions contributing to its stability and inhibitory potential. The carbonyl oxygen of the salicylate moiety in **6l** forms a crucial hydrogen bond with Lys32, mirroring the interaction seen with **6h** (Figure 9). Pi-cation interactions between the aromatic ring of the salicylate moiety and Ala29 further stabilize the enzyme-inhibitor complex. Additionally, isatin-pi stacked interactions with Leu54, and Pro25 enhance the binding affinity of **6l**, while hydrogen bonds with Asn23 and Ile50 contribute to the overall stability of the compound within the active site. These interactions allow **6l** to occupy the DHFR active site effectively, forming stable bonds with key residues and blocking substrate access, thus inhibiting enzyme activity.

Trimethoprim exhibited notable interactions with the *E. coli* DHFR enzyme, with its amino nitrogen functioning as a hydrogen bond acceptor in conjunction with Asp27, as depicted in Figure 10. However, this significant interaction results in Trimethoprim having a comparatively lower binding affinity to the active site than compounds **6h** and **6l**. This reduced affinity can be attributed to the lack of additional stabilizing interactions that compounds **6h** and **6l** possess, such as the π-π stacking interactions with Ala29 and Lys32 of di-salicylate and also, the network interactions facilitated by the isatin nucleus.

This dual modeling against *E. coli* DNA gyrase B and DHFR enzymes has crucial implications for antibacterial drug development. Particularly, the favorable docking poses of **6h** suggest its potential as dual inhibitor against *E. coli* DNA gyrase B and DHFR enzymes.

In conclusion, The molecular docking results provided crucial insights into the binding affinities and interaction mechanisms of the compounds with *E.* coli DNA gyrase B and DHFR enzymes. As summarized in Table 8, compound **6h** demonstrated the strongest binding affinity due to key hydrogen bonds and π-π interactions with active site residues, making it particularly effective in blocking substrate access. Comparatively, compound **6l** and reference drugs like Novobiocin and Trimethoprim exhibited fewer stabilizing interactions, resulting in relatively lower binding affinities.

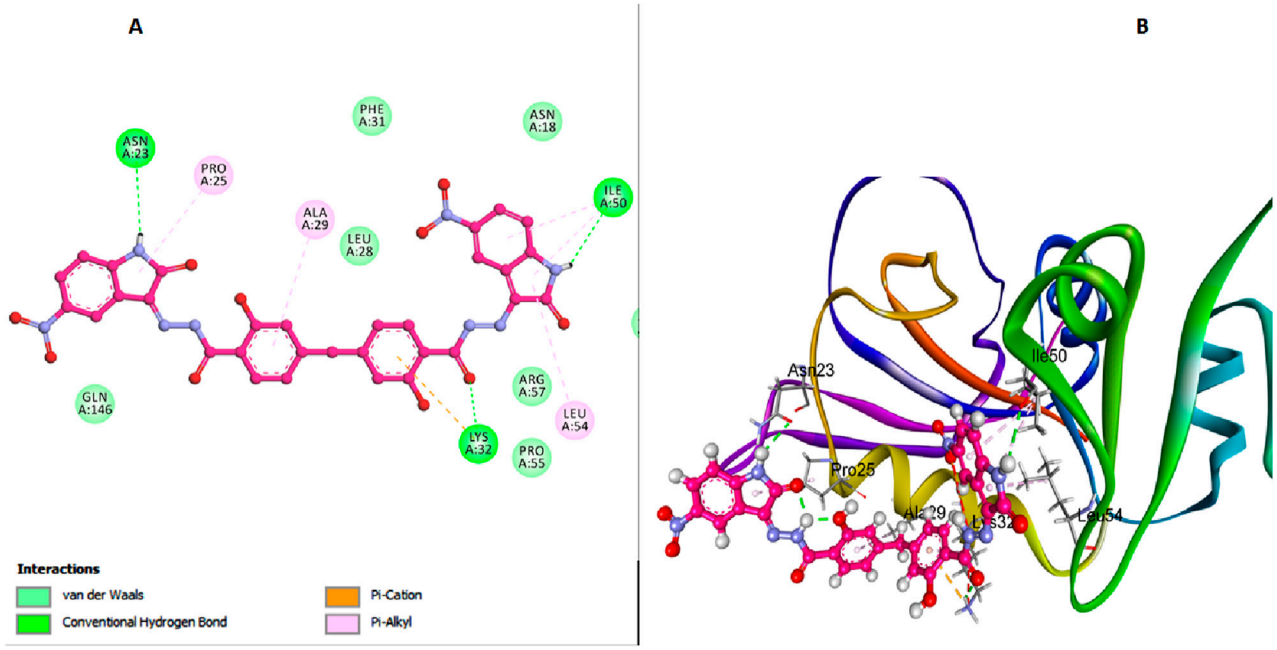

FIGURE 9
Docking representation models of compound **6l** within the binding site of *E. coli* DHFR enzyme; **(A)** 2D-docked model of compound **6l**; **(B)** 3D-docked model of compound **6L**.

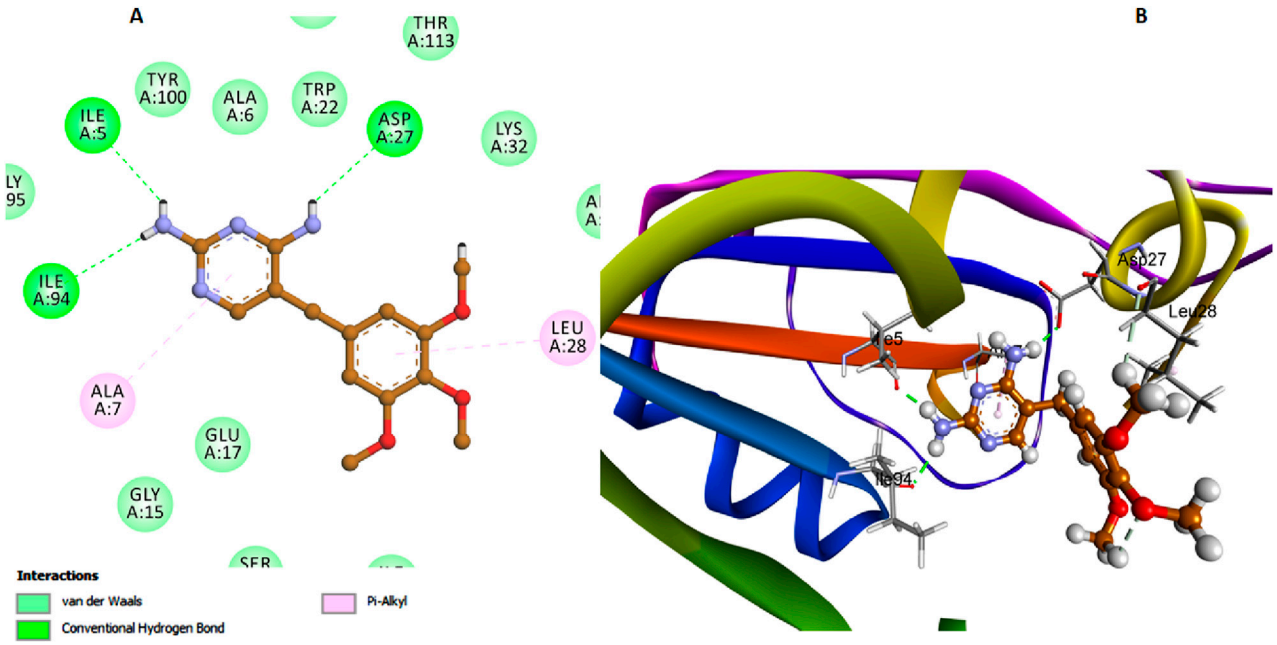

FIGURE 10
Docking representation models of Trimethoprim within the binding site of *E. coli* DHFR enzyme; **(A)** 2D-docked model of Trimethoprim; **(B)** 3D-docked model of Trimethoprim.

TABLE 8 Binding affinity and molecular interactions of compounds 6b, 6h and 6l with *E.* coli DNA gyrase B and DHFR enzymes in molecular docking studies.

Compound	Target enzyme	Docking score (kcal/mol)	Hydrogen bonding	Amino acids involved	Other important parameters
6h	*E. coli* DNA gyrase B	−7.88	Carbonyl oxygen of salicylate ↔ Arg136	His55, Lys103, Arg136	π-π interactions with His55 and Lys103, hydrophobic interactions by 5-chloro group, flexibility due to no 3-chloro group
	E. coli DHFR	−7.42	Carbonyl and phenolic oxygens ↔ Lys32	Leu28, Leu54, Ile5, Asn18	π-stacked with Leu28 and Leu54, stabilization through hydrogen bonds with Ile5 and Asn18
6l	*E. coli* DNA gyrase B	−7.51	Salicylate ↔ Arg136	Gly77, Arg76, Thr165, Asp73	Lacks 3-chloro, π-donor hydrogen bond with Arg136, reduced binding due to fewer active site interactions
	E. coli DHFR	−7.28	Salicylate oxygen ↔ Lys32	Ala29, Leu54, Pro25, Asn23, Ile50	π-cation interaction with Ala29, isatin π-stacked with Leu54, Pro25
6b	*E. coli* DNA gyrase B	−5.78	-	-	Presence of bulky 3-chloro group on di-salicylate nucleus reduces flexibility and binding effectiveness
Novobiocin	*E. coli* DNA gyrase B	−7.26	Amide nitrogen ↔ Gly101	-	Limited interactions due to rigidity, lacks flexibility for optimal binding
Trimethoprim	*E. coli* DHFR	−6.94	Amino nitrogen ↔ Asp27	Ala29, Lys32	Lower affinity due to fewer stabilizing interactions compared to 6h and 6l

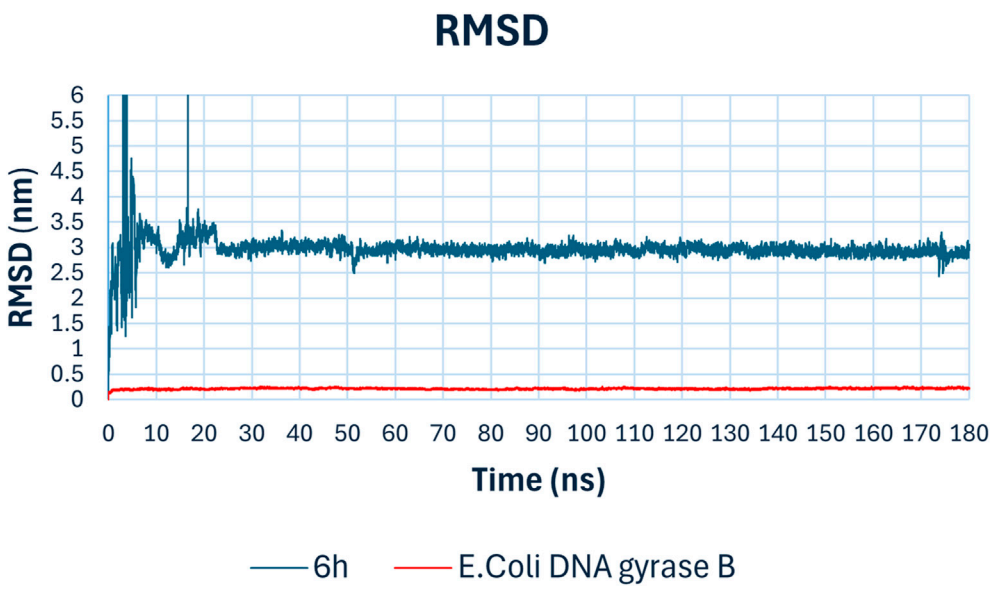

FIGURE 11
Rmsd analysis of compound **6h** with *E. coli* DNA gyrase B.

2.4 Molecular dynamics (MD) simulation against *E. coli* DNA gyrase B

To validate the docking study results, a molecular dynamics (MD) simulation was performed using GROMACS 2023 (Vieira et al., 2023). The MD simulations for compound **6h**, the top hit against *E. coli* DNA gyrase B enzyme, provided comprehensive insights into the stability and binding interactions of the compound within the active site over 180 ns simulation period. The key parameters analyzed include RMSD, RMSF, radius of gyration, hydrogen bonds, and potential energy. The Root Mean Square Deviation (RMSD) plot (Figure 11) indicates the stability of the compound-enzyme complex over the 180 ns simulation period. The RMSD of the backbone atoms of *E. coli* DNA gyrase B (red line) remained stable around 0.5 nm, signifying minimal fluctuations and indicating that the protein structure was well-maintained throughout the simulation. The RMSD of compound **6h** (blue line) showed initial fluctuations within the first 20 ns, stabilizing thereafter around 2.5 nm. This initial fluctuation is typical as the compound adjusts within the binding pocket, after which the stable RMSD suggests a consistent binding conformation.

The Root Mean Square Fluctuation (RMSF) chart (Figure 12) provides insights into the flexibility of individual amino acid residues. Peaks in the RMSF plot indicate regions of higher flexibility. Most residues showed low fluctuations, suggesting a

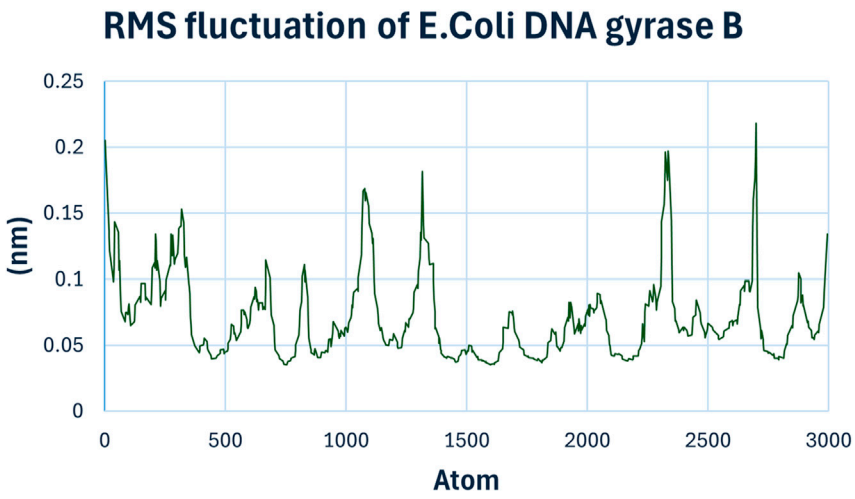

FIGURE 12
RMSF Analysis of compound **6h** with *E. coli* DNA Gyrase B.

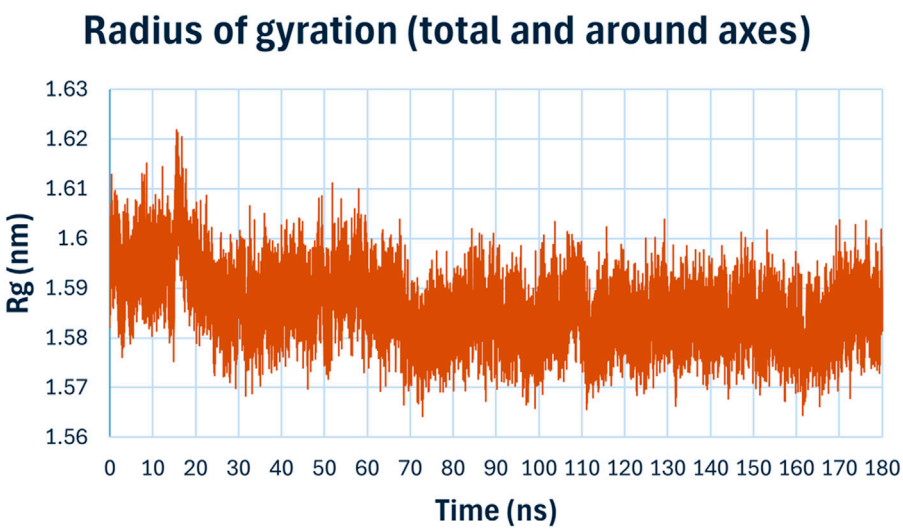

FIGURE 13
Radius of gyration (Rg) of compound **6h** with *E. coli* DNA Gyrase B.

rigid binding environment. However, certain residues around the binding site exhibited slightly higher fluctuations, indicating their involvement in dynamic interactions with compound **6h**.

The radius of gyration (Rg), (Figure 13), measures the compactness of the protein structure over time. The Rg values for the complex remained consistently around 1.59 nm, with minor fluctuations, indicating that the overall compactness and tertiary structure of the protein were maintained during the simulation. This suggests that the binding compound **6h** does not induce significant conformational changes in the protein structure.

Hydrogen bonding analysis (Figure 14) is crucial for understanding the stability and specificity of ligand binding. The number of hydrogen bonds between compound **6h** and *E. coli* DNA gyrase B fluctuated between 1 and 4 throughout the simulation, stabilizing mostly around 2 hydrogen bonds. These persistent hydrogen bonds are indicative of strong and stable interactions between the ligand and the protein, contributing to the high binding affinity observed in docking studies.

The potential energy (Figure 15) of the system remained relatively stable throughout the simulation, fluctuating around −438000 kJ/mol. The stability in potential energy further confirms the stability of the protein-ligand complex during the MD simulation, indicating that no significant energetic disturbances occurred, and the system was equilibrated.

The MD simulation results demonstrate that compound **6h** forms a stable complex with *E. coli* DNA gyrase B. The consistent RMSD, stable radius of gyration, persistent hydrogen bonding, and stable potential energy all point towards a robust binding interaction. These findings support the potential of compound **6h** as a promising lead compound for further development as an

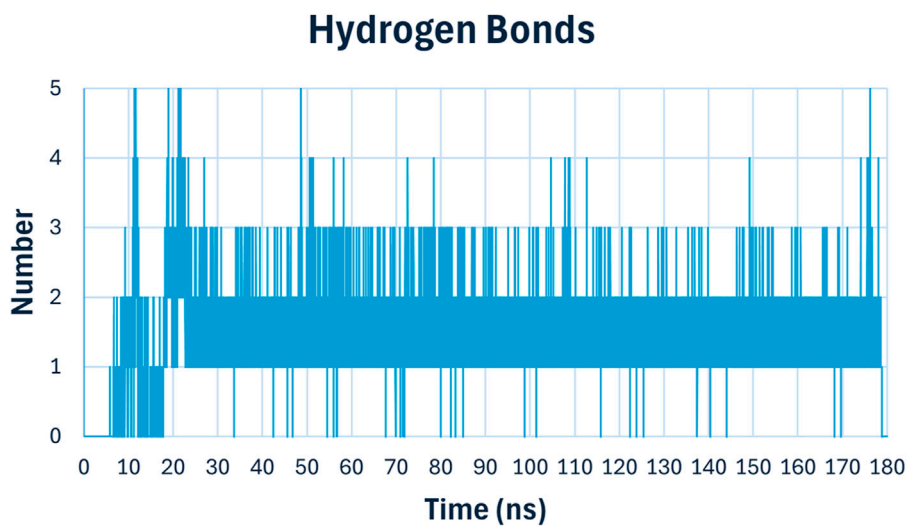

FIGURE 14
Hydrogen bonding analysis of compound **6h** with *E. coli* DNA Gyrase B.

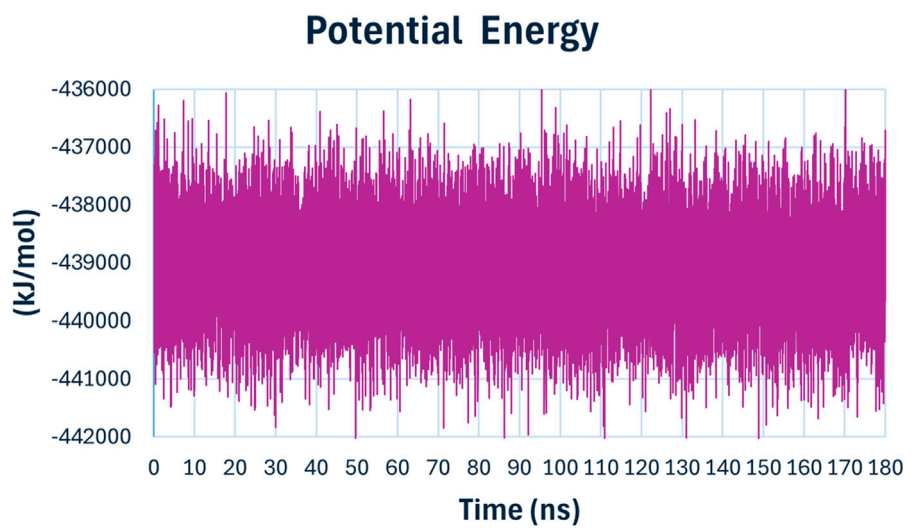

FIGURE 15
The potential energy of compound **6h** with *E. coli* DNA Gyrase B.

antibacterial agent targeting replication mechanisms. The observed molecular interactions and stability underscore its efficacy and provide a strong foundation for subsequent experimental validation and optimization studies.

3 Conclusion

Twelve compounds **(6a-l)** were developed by combining disalicylic acid methylene hydrazide with various isatin derivatives. The antibacterial activity of newly synthesized compounds **6a-l** was assessed against a variety of gram-negative and gram-positive bacterial strains, as well as fungal species. These novel targets were tested for DNA gyrase and DHFR inhibitory activities. The results showed that Compounds **6h** and **6l** were the most potent antibacterial agents, with MIC and MBC values comparable to or even lower than the reference Ciprofloxacin. Compound **6h** had a promising MIC value against the clinical strain *S. aureus* (ATCC 43300) (MRSA), indicating that it is an efficient antibacterial agent. It was shown to be about as potent as the reference medication, Norfloxacin. DNA gyrase and DHFR inhibitory experiments revealed that compounds **6h** and **6l** were twice as potent as novobiocin against DNA gyrase and more potent as DHFR inhibitors than the standard trimethoprim. Based on these data, we may conclude that both compounds **6h** and **6j** show promise as dual-target inhibitors of DNA gyrase and DHFR, especially following optimization. Additionally, compound 6 h demonstrated substantial antibiofilm effect, with a biofilm

inhibition percentage of 97 at the MIC level. Docking experiments demonstrated that compound **6h** has a high affinity for both the DNA gyrase and the DHFR enzyme. MD simulations lasting 180 nanoseconds demonstrated compound **6h**′s stability and binding interactions in the active region of DNA gyrase. The computational results, together with the promising antibacterial activity exhibited in laboratory tests for compound **6h**, indicate that it has the potential to be developed as a lead compound in combating bacterial infections that are resistant to many treatments. Subsequent study will focus on improving the molecular structure of **6h** to optimize its pharmacokinetic characteristics and efficacy in biological systems.

Data availability statement

The original contributions presented in the study are included in the article/Supplementary Material, further inquiries can be directed to the corresponding authors.

Author contributions

LA-W: Funding acquisition, Methodology, Resources, Software, Writing–review and editing. MM: Methodology, Writing–original draft, Writing–review and editing. HA: Formal Analysis, Methodology, Writing–review and editing. HA-Z: Methodology, Software, Writing–original draft, Writing–review and editing. AA: Data curation, Formal Analysis, Software, Writing–review and editing. BY: Conceptualization, Formal Analysis, Investigation, Methodology, Software, Validation, Visualization, Writing–original draft, Writing–review and editing. SB: Supervision, Visualization, Writing–review and editing. SR: Methodology, Resources, Supervision, Validation, Writing–original draft, Writing–review and editing.

Funding

The author(s) declare financial support was received for the research, authorship, and/or publication of this article. The authors acknowledge the support by Princess Nourah bint Abdulrahman University Researchers Supporting Project Number (PNURSP2023R3), Princess Nourah bint Abdulrahman University, Riyadh, Saudi Arabia. The authors also acknowledge support from the KIT-Publication Fund of the Karlsruhe Institute of Technology.

Conflict of interest

Author SR was employed by Apogee Pharmaceuticals.

The remaining authors declare that the research was conducted in the absence of any commercial or financial relationships that could be construed as a potential conflict of interest

Publisher's note

Supplementary material

The Supplementary Material for this article can be found online at: https://www.frontiersin.org/articles/10.3389/fchem.2024.1493906/full#supplementary-material

References

Abdel-Aziz, S. A., Cirnski, K., Herrmann, J., Abdel-Aal, M. A., Youssif, B. G., and Salem, O. I. (2023). Novel fluoroquinolone hybrids as dual DNA gyrase and urease inhibitors with potential antibacterial activity: design, synthesis, and biological evaluation. *J. Mol. Struct.* 1271, 134049. doi:10.1016/j.molstruc.2022.134049

Abdolmaleki, B., and Maddah, M. (2023). Screening of indole derivatives as the potent anticancer agents on dihydrofolate reductase: pharmaco-informatics and molecular dynamics simulation. *J. Biomol. Struct. Dyn.* 41 (8), 3667–3679. doi:10.1080/07391102.2022.2053745

Abdu-Allah, H. H., Youssif, B. G., Abdelrahman, M. H., Abdel-Hamid, M. K., Reshma, R. S., Yogeeswari, P., et al. (2017). Synthesis and anti-mycobacterial activity of 4-(4-phenyl-1 H-1, 2, 3-triazol-1-yl) salicylhydrazones: revitalizing an old drug. *Archives pharmacal Res.* 40, 168–179. doi:10.1007/s12272-016-0882-x

Abdullahi, Z. U., Musa, S. S., Abu-Odah, H., Ahmed, A., Lawan, A. A., and Bello, U. M. (2023). Bactericidal effects of snake venom phospholipases A2: a systematic review and analysis of minimum inhibitory concentration. *Physiologia* 3 (1), 30–42. doi:10.3390/physiologia3010003

Agrawal, A., and Patel, A. K. (2024). *Antibiotic resistance profile and detection in ESKAPE pathogens, ESKAPE pathogens: detection, mechanisms and treatment strategies*, 33–77. Springer2024.

Alkhaldi, A. A., Abdelgawad, M. A., and Youssif, B. G. (2018). Synthesis, antimicrobial evaluation and docking studies of new pyrazolone derivatives. *Trop. J. Pharm. Res.* 17 (11), 2235–2241. doi:10.4314/tjpr.v17i11.18

Alkhaldi, A. A., Abdelgawad, M. A., Youssif, B. G., El-Gendy, A. O., and De Koning, H. P. (2019). Synthesis, antimicrobial activities and GAPDH docking of novel 1, 2, 3-triazole derivatives. *Trop. J. Pharm. Res.* 18 (5), 1101–1108. doi:10.4314/tjpr.v18i5.27

Alqurashi, R. M., Farghaly, T. A., Sabour, R., and Shaabana, M. R. (2023). Design, Synthesis, antimicrobial screening and molecular modeling of novel 6, 7 dimethylquinoxalin-2 (1H)-one and thiazole derivatives targeting DNA gyrase enzyme. *Bioorg. Chem.* 134, 106433. doi:10.1016/j.bioorg.2023.106433

Alrohily, W. D., Habib, M. E., El-Messery, S. M., Alqurshi, A., El-Subbagh, H., and Habib, E.-S. E. (2019). Antibacterial, antibiofilm and molecular modeling study of some antitumor thiazole based chalcones as a new class of DHFR inhibitors. *Microb. Pathog.* 136, 103674. doi:10.1016/j.micpath.2019.103674

Al-Wahaibi, L. H., Amer, A. A., Marzouk, A. A., Gomaa, H. A., Youssif, B. G., and Abdelhamid, A. A. (2021a). Design, synthesis, and antibacterial screening of some novel heteroaryl-based ciprofloxacin derivatives as DNA gyrase and topoisomerase IV inhibitors. *Pharmaceuticals* 14 (5), 399. doi:10.3390/ph14050399

Al-Wahaibi, L. H., Mahmoud, M. A., Alzahrani, H. A., Abou-Zied, H. A., Gomaa, H. A., Youssif, B. G., et al. (2024). Discovery of new Schiff bases of the disalicylic acid scaffold as DNA gyrase and Topoisomerase IV inhibitors endowed with antibacterial properties. *Front. Chem.* 12, 1419242. doi:10.3389/fchem.2024.1419242

Al-Wahaibi, L. H., Mostafa, A., Mostafa, Y. A., Abou-Ghadir, O. F., Abdelazeem, A. H., Gouda, A. M., et al. (2021b). Discovery of novel oxazole-based macrocycles as anti-coronaviral agents targeting SARS-CoV-2 main protease. *Bioorg. Chem.* 116, 105363. doi:10.1016/j.bioorg.2021.105363

Aly, A. A., Abdallah, E. M., Ahmed, S. A., Rabee, M. M., Fuhr, O., Ibrahim, M. A., et al. (2024). Synthesis and characterization of new palladium (II) and silver (I) thiosemicarbazone derived by acenaphthenequinone complexes and their antimicrobial activity. *Polyhedron* 251, 116851. doi:10.1016/j.poly.2024.116851

Alzahrani, A. Y., Ammar, Y. A., Salem, M. A., Abu-Elghait, M., and Ragab, A. (2022). Design, synthesis, molecular modeling, and antimicrobial potential of novel 3-[(1H-

pyrazol-3-yl) imino] indolin-2-one derivatives as DNA gyrase inhibitors. *Arch. Pharm.* 355 (1), 2100266. doi:10.1002/ardp.202100266

Antunes, A. L. S., Trentin, D. S., Bonfanti, J. W., Pinto, C. C. F., Perez, L. R. R., Macedo, A. J., et al. (2010). Application of a feasible method for determination of biofilm antimicrobial susceptibility in staphylococci. *Apmis* 118 (11), 873–877. doi:10.1111/j.1600-0463.2010.02681.x

Baroroh, U., Biotek, M., Muscifa, Z. S., Destiarani, W., Rohmatullah, F. G., and Yusuf, M. (2023). Molecular interaction analysis and visualization of protein-ligand docking using Biovia Discovery Studio Visualizer. *Indonesian J. Comput. Biol. (IJCB)* 2 (1), 22–30. doi:10.24198/ijcb.v2i1.46322

Bayeh, Y., Mohammed, F., Gebrezgiabher, M., Elemo, F., Getachew, M., and Thomas, M. (2020). Synthesis, characterization and antibacterial activities of polydentate Schiff bases, based on salicylaldehyde. *Adv. Biol. Chem.* 10 (05), 127–139. doi:10.4236/abc.2020.105010

Beu, T. A., and Farcaş, A. (2017). CHARMM force field and molecular dynamics simulations of protonated polyethylenimine. *J. Comput. Chem.* 38 (27), 2335–2348. doi:10.1002/jcc.24890

Bhati, S. (2024). Synthesis, characterization, antimicrobial screening and in-silico studies of thiadiazole derivatives. *J. Mol. Struct.* 1316, 138793. doi:10.1016/j.molstruc.2024.138793

Chawla, P., Teli, G., Gill, R. K., and Narang, R. K. (2021). An insight into synthetic strategies and recent developments of dihydrofolate reductase inhibitors. *ChemistrySelect* 6 (43), 12101–12145. doi:10.1002/slct.202102555

Chu, X.-M., Wang, C., Liu, W., Liang, L.-L., Gong, K.-K., Zhao, C.-Y., et al. (2019). Quinoline and quinolone dimers and their biological activities: an overview. *Eur. J. Med. Chem.* 161, 101–117. doi:10.1016/j.ejmech.2018.10.035

Cushman, M., and Kanamathareddy, S. (1990). Synthesis of the covalent hydrate of the incorrectly assumed structure of aurintricarboxylic acid (ATA). *Tetrahedron* 46 (5), 1491–1498. doi:10.1016/s0040-4020(01)81957-8

Durcik, M., Tammela, P., Barančoková, M., Tomašič, T., Ilaš, J., Kikelj, D., et al. (2018). Synthesis and evaluation of N-phenylpyrrolamides as DNA gyrase B Inhibitors. *ChemMedChem* 13 (2), 186–198. doi:10.1002/cmdc.201700549

Elbastawesy, M. A., Mohamed, F. A., Zaki, I., Alahmdi, M. I., Alzahrani, S. S., Alzahrani, H. A., et al. (2023). Design, synthesis and antimicrobial activity of novel quinoline-2-one hybrids as promising DNA gyrase and topoisomerase IV inhibitors. *J. Mol. Struct.* 1278, 134902. doi:10.1016/j.molstruc.2023.134902

Frejat, F. O., Cao, Y., Wang, L., Zhai, H., Abdelazeem, A. H., Gomaa, H. A., et al. (2022). New 1, 2, 4-oxadiazole/pyrrolidine hybrids as topoisomerase IV and DNA gyrase inhibitors with promising antibacterial activity. *Arch. Pharm.* 355 (7), 2100516. doi:10.1002/ardp.202100516

Gao, C., Fan, Y.-L., Zhao, F., Ren, Q.-C., Wu, X., Chang, L., et al. (2018a). Quinolone derivatives and their activities against methicillin-resistant *Staphylococcus aureus* (MRSA). *Eur. J. Med. Chem.* 157, 1081–1095. doi:10.1016/j.ejmech.2018.08.061

Gao, F., Wang, P., Yang, H., Miao, Q., Ma, L., and Lu, G. (2018b). Recent developments of quinolone-based derivatives and their activities against *Escherichia coli*. *Eur. J. Med. Chem.* 157, 1223–1248. doi:10.1016/j.ejmech.2018.08.095

Hassan, A. S., Askar, A. A., Naglah, A. M., Almehizia, A. A., and Ragab, A. (2020). Discovery of new Schiff bases tethered pyrazole moiety: design, synthesis, biological evaluation, and molecular docking study as dual targeting DHFR/DNA gyrase inhibitors with immunomodulatory activity. *Molecules* 25 (11), 2593. doi:10.3390/molecules25112593

Hazarika, Z., Rajkhowa, S., and Jha, A. N. "Role of force fields in protein function prediction," in *Homol. Mol. modeling-perspectives Appl.*

Hirsch, J., and Klostermeier, D. (2021). What makes a type IIA topoisomerase a gyrase or a Topo IV? *Nucleic Acids Res.* 49 (11), 6027–6042. doi:10.1093/nar/gkab270

Hisham, M., Hassan, H. A., Gomaa, H. A., Youssif, B. G., Hayalah, A. M., and Abdel-Aziz, M. (2023). Design, synthesis, and antiproliferative activity of quinazolin-4-one/chalcone hybrids via the EGFR inhibition pathway. *Anti-Cancer Agents Med. Chem. Former. Curr. Med. Chemistry-Anti-Cancer Agents* 23 (17), 1932–1943. doi:10.2174/1871520623666230727104933

Hisham, M., Hassan, H. A., Gomaa, H. A., Youssif, B. G., Hayallah, A. M., and Abdel-Aziz, M. (2022). Structure-based design, synthesis and antiproliferative action of new quinazoline-4-one/chalcone hybrids as EGFR inhibitors. *J. Mol. Struct.* 1254, 132422. doi:10.1016/j.molstruc.2022.132422

Hofny, H. A., Mohamed, M. F., Gomaa, H. A., Abdel-Aziz, S. A., Youssif, B. G., El-Koussi, N. A., et al. (2021). Design, synthesis, and antibacterial evaluation of new quinoline-1, 3, 4-oxadiazole and quinoline-1, 2, 4-triazole hybrids as potential inhibitors of DNA gyrase and topoisomerase IV. *Bioorg. Chem.* 112, 104920. doi:10.1016/j.bioorg.2021.104920

Kumar, D., Aggarwal, N., Kumar, H., Kapoor, G., Deep, A., Bibi, S., et al. (2023a). 2-Substituted-3-(5-Substituted-1,3,4-oxadiazol/thiadiazol-2-yl) thiazolidin-4-one derivatives: synthesis, anticancer, antimicrobial, and antioxidant potential. *Pharmaceuticals* 16 (6), 805. doi:10.3390/ph16060805

Kumar, D., Aggarwal, N., Kumar, V., Kumar, H., Deep, A., Bibi, S., et al. (2023b). Synthesis, anticancer, antimicrobial and antioxidant potential of novel 4-(substituted phenyl-1,3,4-oxadiazol/thiadiazol-2-yl)-4-(4-substituted phenyl) azetidin-2-one derivatives. *Pharmaceuticals* 16 (4), 517. doi:10.3390/ph16040517

Kumar, H., Aggarwal, N., Marwaha, M. G., Deep, A., Chopra, H., Matin, M. M., et al. (2022). Thiazolidin-2,4-Dione scaffold: an insight into recent advances as antimicrobial, antioxidant, and hypoglycemic agents. *Molecules* 27 (19), 6763. doi:10.3390/molecules27196763

Kumar, H., Sharma, A., Kumar, D., Marwaha, M. G., Dhanawat, M., Aggarwal, N., et al. (2023c). Synthesis, biological evaluation and *in silico* studies of some new analogues of 3, 5-disubstituted thiazolidin-2, 4-dione. *Future Med. Chem.* 15 (24), 2257–2268. doi:10.4155/fmc-2023-0237

Liu, B., Jiang, D., and Hu, G. (2022). The antibacterial activity of isatin hybrids. *Curr. Top. Med. Chem.* 22 (1), 25–40. doi:10.2174/1568026621666211116090456

Mahmoud, M. A., Mohammed, A. F., Salem, O. I., Gomaa, H. A., and Youssif, B. G. (2022). New 1, 3, 4-oxadiazoles linked with the 1, 2, 3-triazole moiety as antiproliferative agents targeting the EGFR tyrosine kinase. *Arch. Pharm.* 355 (6), 2200009. doi:10.1002/ardp.202200009

Manso, T., Lores, M., and de Miguel, T. (2021). Antimicrobial activity of polyphenols and natural polyphenolic extracts on clinical isolates. *Antibiotics* 11 (1), 46. doi:10.3390/antibiotics11010046

Marinho, A. M. d.R., de Oliveira, C. M. S., Silva-Silva, J. V., de Jesus, S. C. A., Siqueira, J. E. S., de Oliveira, L. C., et al. (2023). Antimicrobial activity and molecular docking studies of the biotransformation of diterpene acanthotic acid using the fungus Xylaria sp. *Antibiotics* 12 (8), 1331. doi:10.3390/antibiotics12081331

Nastasă, C., Vodnar, D. C., Ionuţ, I., Stana, A., Benedec, D., Tamaian, R., et al. (2018). Antibacterial evaluation and virtual screening of new thiazolyl-triazole Schiff bases as potential DNA-gyrase inhibitors. *Int. J. Mol. Sci.* 19 (1), 222. doi:10.3390/ijms19010222

Niu, C., and Gilbert, E. (2004). Colorimetric method for identifying plant essential oil components that affect biofilm formation and structure. *Appl. Environ. Microbiol.* 70 (12), 6951–6956. doi:10.1128/aem.70.12.6951-6956.2004

Pettersen, E. F., Goddard, T. D., Huang, C. C., Meng, E. C., Couch, G. S., Croll, T. I., et al. (2021). UCSF ChimeraX: structure visualization for researchers, educators, and developers. *Protein Sci.* 30 (1), 70–82. doi:10.1002/pro.3943

Roth, B. (1986). Design of dihydrofolate reductase inhibitors from X-ray crystal structures. *Fed. Proc.* 45, 2765–2772.

Shree, P., Singh, C. K., Sodhi, K. K., Surya, J. N., and Singh, D. K., Biofilms: understanding the structure and contribution towards bacterial resistance in antibiotics, Medicine in Microecology (2023). 100084.

Singh, S., Datta, S., Narayanan, K. B., and Rajnish, K. N. (2021). Bacterial exo-polysaccharides in biofilms: role in antimicrobial resistance and treatments. *J. Genet. Eng. Biotechnol.* 19, 1–19. doi:10.1186/s43141-021-00242-y

Sun, N., Li, M., Cai, S., Li, Y., Chen, C., Zheng, Y., et al. (2019). Antibacterial evaluation and mode of action study of BIMQ, a novel bacterial cell division inhibitor. *Biochem. biophysical Res. Commun.* 514 (4), 1224–1230. doi:10.1016/j.bbrc.2019.05.086

Tiz, D. B., Skok, Ž., Durcik, M., Tomašič, T., Mašič, L. P., Ilaš, J., et al. (2019). An optimised series of substituted N-phenylpyrrolamides as DNA gyrase B inhibitors. *Eur. J. Med. Chem.* 167, 269–290. doi:10.1016/j.ejmech.2019.02.004

Vestby, L. K., Grønseth, T., Simm, R., and Nesse, L. L. (2020). Bacterial biofilm and its role in the pathogenesis of disease. *Antibiotics* 9 (2), 59. doi:10.3390/antibiotics9020059

Vieira, I. H. P., Botelho, E. B., de Souza Gomes, T. J., Kist, R., Caceres, R. A., and Zanchi, F. B. (2023). Visual dynamics: a web application for molecular dynamics simulation using GROMACS. *BMC Bioinforma.* 24 (1), 107. doi:10.1186/s12859-023-05234-y

Wang, G., Chen, M., Qiu, J., Xie, Z., and Cao, A. (2018). Synthesis, *in vitro* α-glucosidase inhibitory activity and docking studies of novel chromone-isatin derivatives. *Bioorg. and Med. Chem. Lett.* 28 (2), 113–116. doi:10.1016/j.bmcl.2017.11.047

Wiegand, I., Hilpert, K., and Hancock, R. E. (2008). Agar and broth dilution methods to determine the minimal inhibitory concentration (MIC) of antimicrobial substances. *Nat. Protoc.* 3 (2), 163–175. doi:10.1038/nprot.2007.521

Xu, Z., Song, X.-F., Hu, Y.-Q., Qiang, M., and Lv, Z.-S. (2017b). Azide-alkyne cycloaddition towards 1H-1, 2, 3-triazole-tethered gatifloxacin and isatin conjugates: design, synthesis and *in vitro* anti-mycobacterial evaluation. *Eur. J. Med. Chem.* 138, 66–71. doi:10.1016/j.ejmech.2017.05.057

Xu, Z., Zhang, S., Song, X., Qiang, M., and Lv, Z. (2017a). Design, synthesis and *in vitro* anti-mycobacterial evaluation of gatifloxacin-1H-1, 2, 3-triazole-isatin hybrids. *Bioorg. and Med. Chem. Lett.* 27 (16), 3643–3646. doi:10.1016/j.bmcl.2017.07.023

Youssif, B. G., Mohamed, Y. A., Salim, M. T., Inagaki, F., Mukai, C., and Abdu-Allah, H. H. (2016). Synthesis of some benzimidazole derivatives endowed with 1, 2, 3-triazole as potential inhibitors of hepatitis C virus. *Acta Pharm.* 66 (2), 219–231. doi:10.1515/acph-2016-0014

Youssif, B. G. M. (2013). Synthesis and biological evaluation of some new coumarin derivatives as antimicrobial agents. *Bull. Pharm. Sci. Assiut Univ.* 36 (2), 105–116. doi:10.21608/bfsa.2013.63201

Zhang, G.-F., Liu, X., Zhang, S., Pan, B., and Liu, M.-L. (2018). Ciprofloxacin derivatives and their antibacterial activities. *Eur. J. Med. Chem.* 146, 599–612. doi:10.1016/j.ejmech.2018.01.078

frontiers | Frontiers in Chemistry

TYPE Original Research
PUBLISHED 13 December 2024
DOI 10.3389/fchem.2024.1505272

Check for updates

OPEN ACCESS

EDITED BY
Mukhlesur Rahman,
University of East London, United Kingdom

REVIEWED BY
Yogesh Vaishnav,
Guru Ghasidas Vishwavidyalaya, India
Adnan Cetin,
Yüzüncü Yıl University, Türkiye
Pavitra Suresh Thacker,
Stanford University, United States

*CORRESPONDENCE
Mithun Rudrapal,
rsmrpal@gmail.com,
drmr_pharma@vignan.ac.in
Vijaya Jyothi Mallela,
drmvjyothiriper@gmail.com
Sahar M. Aldosari,
s.aldosari@mu.edu.sa

RECEIVED 02 October 2024
ACCEPTED 22 November 2024
PUBLISHED 13 December 2024

CITATION
Mallela VJ, Rudrapal M, Prasanth DSNBK, Pasala PK, Bendale AR, Bhattacharya S, Aldosari SM and Khan J (2024) Lotus seed *(Nelumbinis semen)* extract: anticancer potential and chemoprofiling by *in vitro*, *in silico* and GC-MS studies.
Front. Chem. 12:1505272.
doi: 10.3389/fchem.2024.1505272

Lotus seed *(Nelumbinis semen)* extract: anticancer potential and chemoprofiling by *in vitro*, *in silico* and GC-MS studies

Vijaya Jyothi Mallela[1]*, Mithun Rudrapal[2]*, D. S. N. B. K. Prasanth[3], Praveen Kumar Pasala[1], Atul R. Bendale[4], Soumya Bhattacharya[5], Sahar M. Aldosari[6,7]* and Johra Khan[6,7]

[1]Raghavendra Institute of Pharmaceutical Education and Research, Jawaharlal Nehru Technological University Anantapur, Anantapur, India, [2]Department of Pharmaceutical Sciences, School of Biotechnology and Pharmaceutical Sciences, Vignan's Foundation for Science, Technology and Research, Guntur, India, [3]School of Pharmacy and Technology Management, SVKM's Narsee Monjee Institute of Management Studies (NMIMS), Hyderabad, India, [4]Mahavir Institute of Pharmacy, Nashik, India, [5]Guru Nanak Institute of Pharmaceutical Science and Technology, Kolkata, India, [6]Department of Medical Laboratory Sciences, College of Applied Medical Laboratory Sciences, Majmaah University, Al Majma'ah, Saudi Arabia, [7]Health and Basic Science Research Center, Majmaah University, Al Majma'ah, Saudi Arabia

Lotus seeds, also known as Nelumbinis semen, has been utilized for over 7,000 years as vegetable, functional food and medicine. In this study, we primarily investigated the anticancer effects of lotus seed extracts, particularly of the methanolic extract (MELS) on cell proliferation inhibition, apoptosis induction and cell cycle arrest in ovarian cancer cell lines. Further, we studied the phytochemical composition of the MELS by gas chromatography-mass spectrometry (GC-MS) analysis. Additionally, molecular docking was performed in order to substantiate the *in vitro* anticancer effect by *in silico* inhibitory study of human survivin protein. Our *in vitro* study demonstrated significant inhibition of SKOV3 (IC_{50}: 79.73 ± 0.91), A2780 (IC_{50}: 100.18 ± 2.42), SKOV3-CisR (IC_{50}: 115.87 ± 2.2) and A2780-CisR (IC_{50}: 138.86 ± 2.46) cells by MELS, compared to acetone, petroleum ether, n-hexane extracts, and the standard drug, cisplatin. Furthermore, MELS resulted in a substantial increase in apoptosis cell count to 78% in A2780-CisR cells and 82% in SKOV3-CisR cells, whereas a significant reduction in the G1 and G2/M phases of cells treated with MELS when compared to the control group. To identify the potential phytocompounds present in the MELS, we conducted GC-MS analysis, which led to the identification of 14 compounds. Molecular docking analysis revealed that oleic acid, stigmast-5-en-3-ol, phytol and glyceryl linolenate exhibited remarkable binding affinities of −6.1, −5.9, −5.8 and −5.6 kcal/mol, respectively against survivin. Our findings suggest that certain phytochemicals presented above found in MELS may have therapeutic potential for management of ovarian cancer.

KEYWORDS

lotus seeds, methanolic extract, GC-MS, chemoprofiling, anticancer, phytochemicals, molecular docking

1 Introduction

Ovarian cancer (OC) is the fourth most common cause of cancer-related death among women in the Western world (Kohn et al., 2003; Mills et al., 2003). In the year 2020, there were an estimated 21,750 newly diagnosed cases of ovarian cancer, accounting for around 1.2% of all cancer cases. The expected death toll is at 13,940. The incidence of ovarian cancer risk is 1 in 70 women. Annually, OC causes 150,000 fatalities worldwide, making it the most lethal among various gynaecological cancers. Chemotherapy, laser therapy, radiation, gene therapy and surgery are some of the interventions now being used or tested to disrupt the proliferation of cancer cells (Ruibin et al., 2017; Senapati et al., 2018). Most ovarian cancer patients experience a recurring and worsening condition, as they develop a resistance to different types of standard chemotherapy medicines (Grosso et al., 2013). Furthermore, a majority of synthetic drugs employed in cancer therapy exhibit substantial harm to healthy cells. Conversely, diverse naturally-occurring phytochemicals found in plants have exhibited specific toxicity towards certain types of human cancer cells, while causing minimal harm to normal cells (Devi et al., 2015).

Survivin is a member of the inhibitor of apoptosis (IAP) protein family and plays a significant role in controlling the mitotic process and defending against apoptosis inhibition, which has been linked to mast cells (MCs) in squamous cell carcinoma (SCC) and non-small cell lung cancer. However, its expression is rarely detected in normal adult tissues, making it a potential target for selective cancer therapy (Kapellos et al., 2013; Khan et al., 2017). Over expression of survivin leads to increased cell survival by inactivating Apaf-1, caspase-9 and Mdm2, which in turn suppresses p53, resulting in uncontrolled cell division due to Cdk1 activation and promotes tumor growth (Mobahat et al., 2014). Additionally, studies have revealed that survivin interacts with Second Mitochondria-derived Activator of Caspase/Direct Inhibitor of Apoptosis-binding Protein with Low pI (Smac/DIABLO), which acts as an antagonist to apoptotic inhibitors and aggregates survivin. This interaction breaks up the protein-protein interaction (PPI) between survivin and other proteins, which is difficult to achieve through small molecules (Mobahat et al., 2014; Pavlyukov et al., 2011).

Nelumbo nucifera, or the sacred lotus, possesses numerous biological and pharmacological properties, making it a plant of scientific interest. The seeds of lotus are also known as *Nelumbinis semen*. *In vitro* studies have reported the anticancer activity of *N. nucifera*. For example, Paudel and Panth (Paudel and Panth, 2015) established that the leaf extract of *N. nucifera* exhibited potent anticancer activity against melanoma, prostate, and gastric cancer cells owing to the presence of 7-hydroxydehydronuciferine compounds in the leaves (Liu et al., 2014). In another study, aporphine alkaloids in leaves were shown to be effective antioxidant and anticancer agents. In addition, Dasari et al. examined the anticancer effect of neferine, an alkaloid compound from lotus seeds (Dasari et al., 2020). Neferine showed strong anticancer activity, inducing apoptosis and autophagy as reported in their study. The results of the studies described above, *N. nucifera* has potential as an agent of clinically significant bioactive compounds.

Chemo-profiling of plant extracts through gas chromatography-mass spectrometry (GC-MS) is gaining increasing demand because of such multitude of applications for the analysis of herbals and botanicals of medicinal interest (Altameme et al., 2015). Docking enables the identification of novel compounds of therapeutic interest based upon compound's binding affinity for the target protein or the compound-target interactions at a molecular level (Meng et al., 2011). The current study aimed to evaluate the phytoconstituents present in the methanolic extract of lotus seeds, which has been claimed to possess antitumor activity and induce apoptosis by functionally blocking survivin via molecular docking studies coupled with an *in vitro* study. The methanolic extract was used in the study as methanol has been found to be superior or more efficient in the extract of lower molecular weight polyphenols having anticancer or antioxidant potential. The methanol extract was found more active than other extracts. This may be attributed to the polar strength of methanol and it capability to extract more phenolic or polyphenolic compounds from the plant material. There are a plenty of literature (Paudel and Panth, 2015) that claim the superiority of methanolic extract over other extracts.

2 Materials and methods

2.1 Plant collection and authentication

The seeds of *N. nucifera* (lotus seeds) cultivar were selected for the study and were collected from the Gudlavalleru lake, Krishna District, Andhra Pradesh, India. They were authenticated by Dr. P. Srinivasa Rao, Assistant Professor, Department of Botany, P. B. Siddhartha College of Arts and Science (Autonomous), Vijayawada, Andhra Pradesh, India. A sample specimen was submitted to the Department to maintain a reference of the same and was marked as voucher specimen ID of PBS/BOT/004. The collection of plant material, its authentication and experiments conducted on the plant species comply with institutional and national guidelines.

2.2 Extraction of plant material

The seed material was washed with distilled water and dried under room temperature. It was finally grinded to obtain a powder using a blender. The powder sample was subjected to maceration with varying polarity solvents, namely, petroleum ether, *n*-hexane, acetone and methanol. The yields of four crude extracts were determined by the following formula. Following their extraction, the samples were kept at 4°C in a refrigerator for further analysis.

2.3 *In vitro* studies

The *in vitro* anticancer activities (anti-proliferative activity) of the extracts were carried out on ovarian cell lines.

2.3.1 Cell culture

Two human ovarian cancer cell lines, namely, SKOV3 and A2780, were obtained from the National Centre for Cell Sciences (NCCS), Pune, India. These cells were cultured as a monolayer in McCoy's 5A medium modified supplemented with 10% foetal bovine serum, 100 U/mL penicillin and 100 mg/mL

streptomycin. The SKOV3-CisR and A2780-CisR cell lines were derived by culturing the original SKOV3 and A2780 cell lines, respectively, over 12 months with gradually increasing doses of cisplatin. The cells were enzymatically cultured for 2 minutes using a solution of 0.25% trypsin and 1 mM EDTA. Furthermore, 125 cm^2 flasks of 75 cm^2 plastic flasks were sub-cultured at a density of 2.2 × 104 cells/cm^2. The culture medium was changed at 48 h intervals. The cell confluence was determined based on microscopic examination focusing on 80% confluence. The cells were then treated after being seeded for 12 h to prevent cell differentiation.

2.3.2 MTT assay

In a 96-well tissue culture plate, SKOV3, A2780, SKOV3-CisR and A2780-CisR cells (100 µL per well) were placed. The cell count per well was 105 cells. Test samples of petroleum ether, n-hexane and acetone extracts were added to SKOV3 and A2780 ovarian cancer cells. The concentrations of the extracts ranged from 5 to 320 µg/mL (5, 10, 20, 40, 80, 160, and 320 µg/mL). The cells were seeded and incubated for 12 h, and then further incubated for 24, 48, and 72 h. The methanolic extract of lotus seeds (MELS) was tested against SKOV3, A2780, SKOV3-CisR, and A2780-CisR cells at concentrations ranging from 5 to 320 µg/mL (5, 10, 20, 40, 80, 160 and 320 µg/mL). The cells were seeded in triplicate and incubated for 12 h, followed by incubation for 24, 48, and 72 h. All test samples were prepared using a 20 µL amount of culture media. Injected 15 µL of MTT reagent each well, prepared in PBS medium, resulting in a final concentration of 0.5 mg/mL. The reagent volume was modified in accordance with the cell culture volume. The cells were cultured for the duration of 3 h at a temperature of 37°C until the presence of intracellular purple formazan crystals was observed using a microscope. To reach well 100 µL of DMSO was introduced. The mixture was gently agitated on an orbital shaker for 1 h at room temperature. The amount of DMSO was modified according to the volume of the cell culture. An absorbance plate reader was used to quantify the absorbance at OD570 nm for each well. The percentage of cell viability (Mosmann, 1983; Turan et al., 2017) was calculated as follows:

$$\text{Cell viability rate (\%)} = \frac{\begin{pmatrix}\text{experimental group OD}\\ -\text{zero adjustment group OD}\end{pmatrix}}{\begin{pmatrix}\text{control group OD}\\ -\text{zero adjustment group OD}\end{pmatrix}} \text{X } 100$$

2.3.3 Apoptosis assay

Apoptosis was assessed using FITC-labeled Annexin V/PI double labelling and flow cytometry analysis. In brief, SKOV-3, A2780 SKOV3-CisR, and A2780-CisR cells were exposed to the methanolic extract at the concentration that inhibits 50% of cell growth (IC_{50}) for a duration of 24 h. Cells were collected and preserved at the specified period. Apoptosis was subsequently assessed using the FITC Annexin V Apoptosis Detection Kit II (BD Biosciences, Mississauga, ON) as per the instructions provided by the manufacturer. The BD Biosciences C6 flow cytometer was used to measure the proportions of cells in the early and late phases of apoptosis. The data were processed utilizing FlowJo 10.1 software. A minimum of 10,000 cells were enumerated for each measurement. The following controls were used to set up gates: unstained cells, cells with FITC Annexin V only, and cells with PI only (Demir et al., 2018).

2.3.4 Cell cycle analysis

The cell cycle distribution of SKOV3-CisR and A2780-CisR cells after treatment with MELS was determined using flow cytometry. Before the experiment, the cells were adjusted to a density of 5 × 106 cells/mL and left to bind for 24 h before drug application. The cells were fixed after 24 h of exposure to MELS at IC_{50}. The cell pellet was resuspended in 500 µL of PBS and fixed in 70% cold ethanol at −20°C for at least 2 h. After centrifugation at 1,000 rpm for 10 min followed by double rinsing with PBS, the cells were treated with 500 µL PI/RNase solution containing 400 µL propidium iodide and 100 µL ribonuclease A. The mixture was then incubated for 10 min at room temperature and PI/RNase mixture was added into it. The equipment selected for measuring the amount of DNA in cells was the BD Biosciences C6 flow cytometer, with an argon laser light source at 488 nm and a 630 nm band-pass filter. A total of 10,000 events were registered per sample and evaluated in terms of percentage relative to the untreated control population of the cells using a BD FACSDiva (BD Biosciences) (Li et al., 2019).

2.4 GC-MS analysis

GC-MS analysis was performed on a GC Clarus 500 Perkin Elmer system, which included an AOC-20i autosampler and a gas chromatograph interfaced with a mass spectrophotometer (GC-MS) instrument. The analysis used the following conditions: a column with an Elite-1 fused silica capillary column (30 × 0.25 mm ID x 1EM df, consisting of 100% dimethyl polysiloxane), operated in electron impact mode at 70 eV; helium (99.999%) was used as the carrier gas at a constant flow of 1 mL/min, and an injection volume of 0.5 EI was employed (split ratio of 10:1). The injector temperature was set at 250°C, and the ion-source temperature was set at 280°C. The oven temperature was programmed to start at 110°C (isothermal for 2 min), then increase by 10 °C/min to 200°C, followed by a 5 °C/min increase to 280°C, ending with a 9-min isothermal period at 280°C. Mass spectra were recorded at 70 eV, with a scan interval of 0.5 s and fragments ranging from 40 to 550 Da (Fitrianto et al., 2020; Shah et al., 2023).

2.5 *In silico* studies

2.5.1 Molecular docking

The docking of GC-MS eluted phytocompounds to human survivin protein (PDB: 3UIH) was carried out using AutoDock Vina (Prasanth et al., 2023). The input files needed for running this program were prepared using AutoDock software. The AutoDock files were prepared by adding polar hydrogen atoms and Gasteiger charges. For X, Y and Z dimensions, the grid box size in AutoDock Vina was maintained at 15, and the binding center was x = −34.831; y = −8.98 and z = 3.038 (Killari et al., 2023). However, the energy range was maintained at eight,

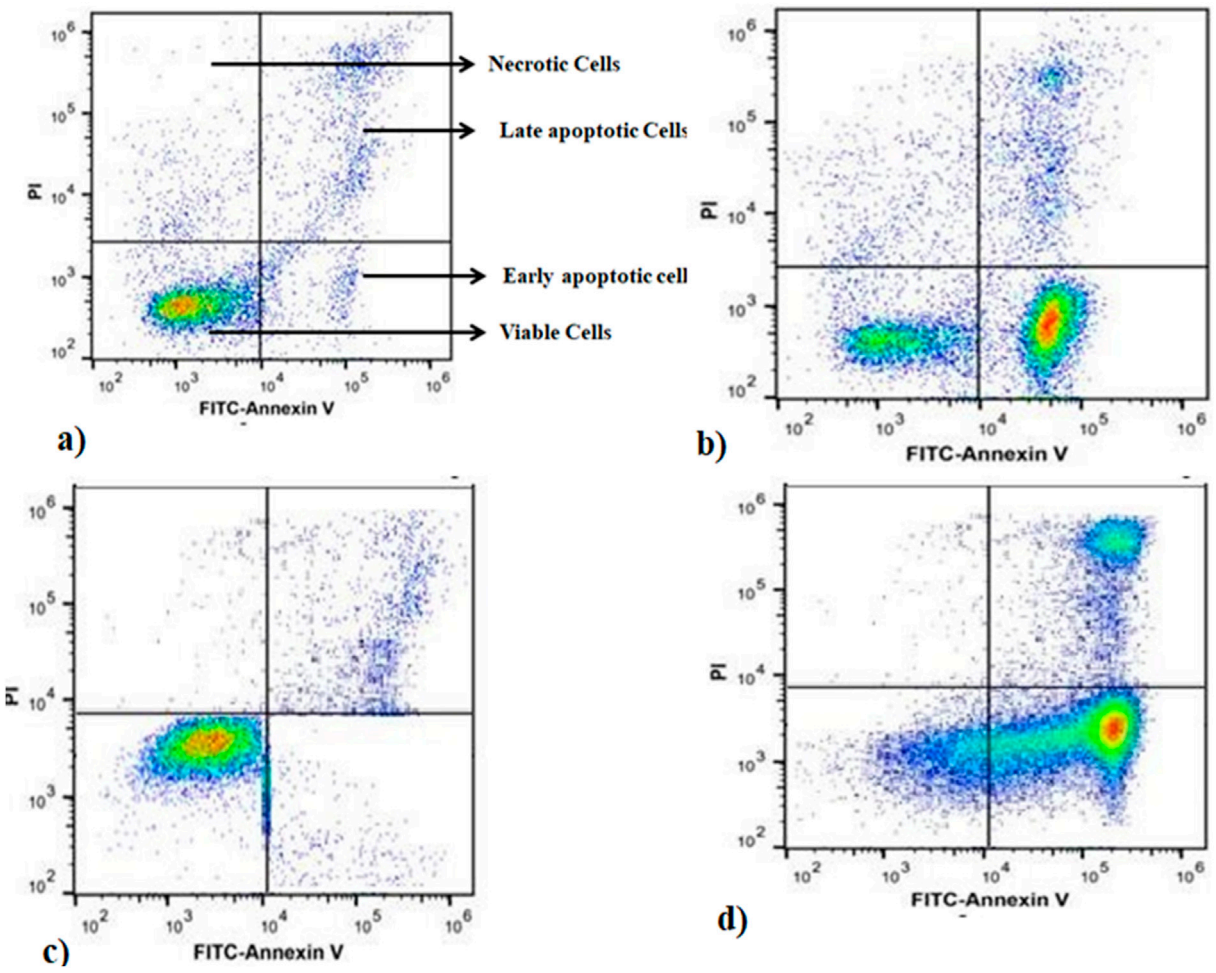

FIGURE 1
Annexin-V FITC/PI staining of apoptosis at 24 h of incubation. **(A)** SKOV3-CisR control, **(B)** A2780-CisR cells, **(C)** A2780-CisR control, **(D)** MELS treated SKOV3-CisR cells.

which was the default setting (DSNBK et al., 2023; Prasanth et al., 2021). The ligand-binding affinity was expressed as a negative score, with kcal/mol as a unit. Each ligand input generated nine ligand poses with different binding energies, as did the AutoDock Vina script. The pose with the highest binding affinity was extracted from the docked complex using an in-house Perl script. Using the Biovia Discovery Studio 2020 Visualizer, we studied ligand-protein interactions. The rationale for the selection of human survivin protein (3UIH) is that it a prominent anti-apoptotic protein which acts by directly binding and inhibiting caspase 3 activity.

2.5.2 Drug-likeliness and ADMET analysis

The structures of phytochemical compounds were acquired in SDF format from PubChem. Subsequently, these compounds were subjected to drug-likeness predictions using the DruLiTo software (Ezugwu et al., 2024; Singh et al., 2024). Investigating the pharmacokinetic properties of the ligands is necessary to understand their roles in the body. To assess the ADMET profiles of the ligands, the Swiss ADME, admetSAR and ProTox-II open source web servers were employed (Singh et al., 2024; Archana et al., 2023).

3 Results and discussion

3.1 Extraction and percentage of yield

The lotus seeds were extracted using various solvents such as petroleum ether, n-hexane, acetone and methanol by maceration method. The yields of the petroleum ether extract (PELS), n-hexane extract (HELS), acetone extract (AELS), and methanol extract (MELS) were determined to be 3.44%, 2.85%, 5.98%, and 8.25% w/w, respectively.

3.2 MTT assay

Significant positive findings were obtained while testing the anti-proliferative effects of Nelumbinis semen extract on ovarian cancer

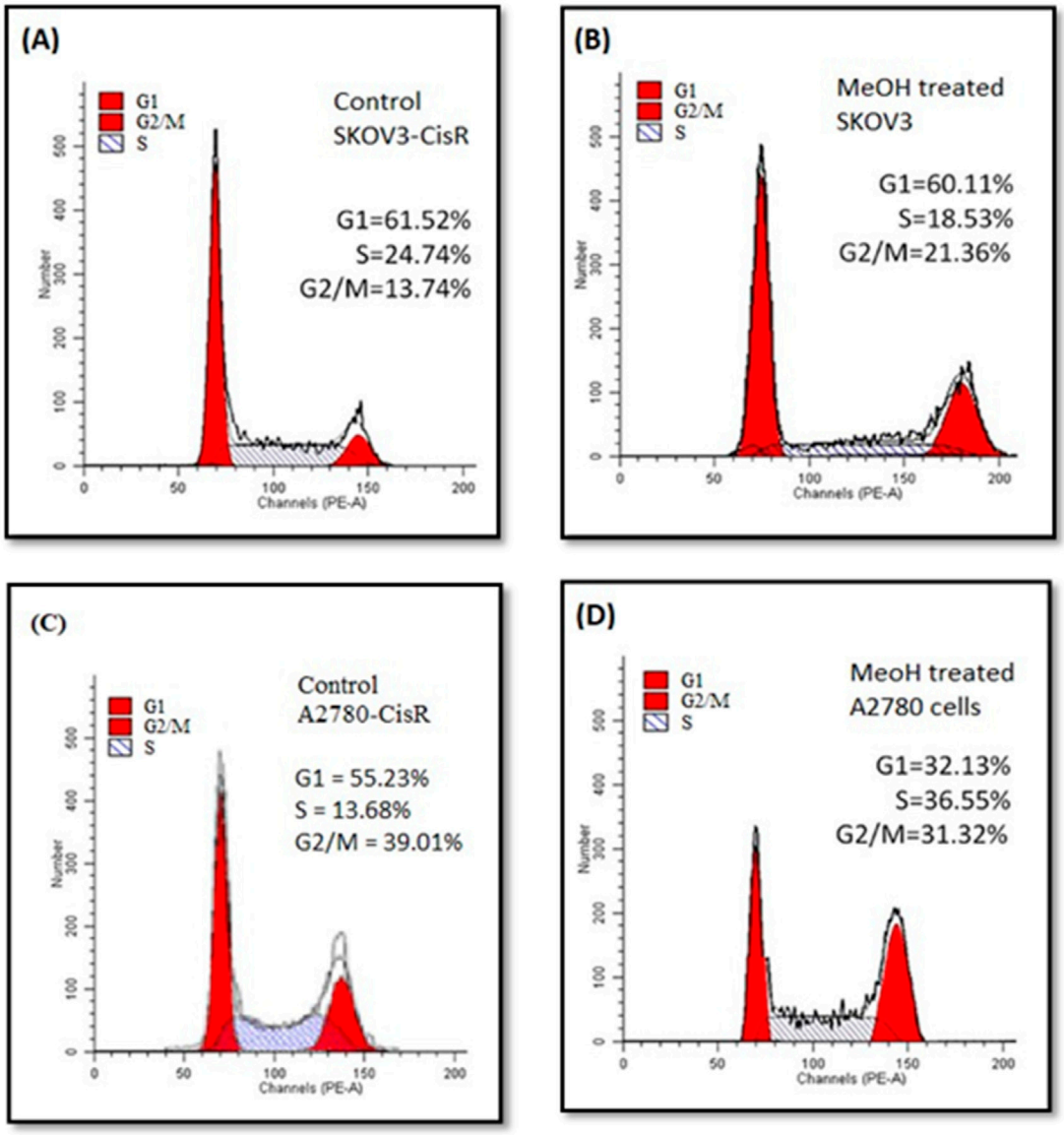

FIGURE 2
Flow cytometric cell cycle distribution analysis. **(A)** SKOV3-CisR control cells, **(B)** MELS treated SKOV3-CisR, **(C)** Control cells of A2780-CisR, **(D)** MELS treated A2780-CisR cells.

cells (Meng et al., 2011; Shah et al., 2023). Various concentrations of MELS, AELS, PELS, NELS and cisplatin, ranging from 5 to 320 μg/mL, were incubated with SKOV3 and A2780 cells. The findings demonstrated that the extracts had cytotoxic action against ovarian cancer cell types. After 72 h of incubation, MELS, AELS exhibited dose dependent decreased cell viability to 2.4%, 45.3% respectively on SKOV3 cells, decreased cell viability to 5.3%, 46.4% respectively after 48h of incubation on A2780 cells. MELS also exhibited significant decrease cell viability to 9.7% after 72 h of incubation on SKOV3 resistance cells and decrease cell viability to 10.3% after 48 h of incubation on A2780 resistance cells. The Lotus seed extracts demonstrate anticancer action, as evidenced by their IC_{50} value, which is the concentration at which 50% of cellular proliferation is inhibited. The study found that MELS had a substantial effect on SKOV3, A2780, SKOV3-CisR, and A2780-CisR cells, with IC_{50} values of 79.73 ± 0.91, 100.18 ± 2.42, 115.87 ± 2.2, and 138.86 ± 2.46 μg/mL correspondingly, compared to other extracts (Supplementary Figure S1; Supplementary Table S1).

3.3 Apoptosis assay

Apoptosis is a form of cell death. Disruption of the normal regulation of apoptosis results in the development of pathological states, such as cancer and autoimmune disorders. Consequently, scientists have concentrated their endeavours on devising strategies aimed at specifically triggering apoptosis in cancer cells (Baru Venkata et al., 2023). To assess apoptotic activity and quantify the rate of apoptosis, MELS was introduced to the cells at a dose that produces half of the maximum effect (EC_{50}) for duration of 72 h.

TABLE 1 Phytoconstituents identified in MELS by GC-MS.

Name of phytoconstituent	R. Time	I. Time	F. Time	Area	Area%	Height	A/H
Lupeol	1.061	1.030	1.105	685259	3.43	168066	4.08
Carotene-1.1′,2.2′- tetrahydro-1.1′-dimethoxy	1.392	1.375	1.430	72449	0.36	27522	2.63
Isocolchicine	10.160	10.155	10.210	77835	0.39	25035	3.11
Lupanol	10.220	10.210	10.280	108983	0.55	26833	4.06
Stigmast-5-en-3-ol	10.505	10.440	10.540	162031	0.81	28753	5.64
Oleanolic acid	11.200	11.150	11.240	52566	0.26	22136	2.37
Glyceryl linolenate	16.728	16.695	16.770	98823	0.49	51686	1.91
Lucenin 2	17.256	17.055	17.525	2711916	13.57	694269	3.91
Betulin	18.606	18.545	18.640	191201	0.96	94199	2.03
1-Oxo-forskolin	18.672	18.640	18.715	221003	1.11	120602	1.83
Beta-amyrin	20.775	20.720	20.815	84646	0.42	32095	2.64
Phytofluene	20.967	20.935	21.055	229449	1.15	91980	2.49
Phytol	26.032	25.995	26.095	51785	0.26	18385	2.82
Oleic acid	27.470	27.465	27.610	43525	0.22	6,606	6.59

TABLE 2 Results of molecular docking of 14 phytochemicals [with survivin (PDB: 3UIH)] identified in MELS by GC-MS.

Ligand	Binding energy (kcal/mol)
Oleic acid	−6.1
Stigmast-5-en-3-ol	−5.9
Phytol	−5.8
Glyceryl linolenate	−5.6
Lupeol	−4.9
Oleanolic acid	−4.9
Lupanol	−4.8
Phytofluene	−4.4
Beta amyrin	−4.1
Betulin	−3.8
Isocolchicine	−3.8
Lucenin 2	−3.7
1-Oxo-forskolin	−3.2
Carotene-1.1′,2.2′- tetrahydro-1.1′-dimethoxy	−3.2

The cells were then examined using annexin V and propidium iodide (PI) staining. Annexin V was utilised to identify cells in the initial phases of apoptosis by detecting the externalised phosphatidylserine (PS) on the cell membrane, which is a distinctive alteration during apoptosis. Conversely, PI was employed to identify cells in the later stages of apoptosis and dead cells. PI is used to label cells that have a compromised cell membrane. Living cells do not exhibit binding to annexin V and PI, as indicated by the annexin-V−/PI− phenotype. Early apoptotic cells specifically bind to annexin V but not PI, resulting in the annexin-V+/PI− phenotype. Late apoptotic cells exhibit binding to both molecules, leading to the annexin-V+/PI + phenotype. Dead cells alone bind to PI, as indicated by the annexin-V−/PI + phenotype (Mahassni and Al-Reemi, 2013). After incubating the A2780-CisR cells with the MELS for 72 h, we observed that 78% of the cells in the treatment group tested positive for annexin V. In contrast, only 0.5% of the cells in the control group tested positive for annexin V. The treatment of SKOV3-CisR cells resulted in 82% of the cells exhibiting annexin V positivity, while the control group showed only 0.4% annexin V positivity compared to the control. The observations suggest that MELS has a substantial effect in triggering apoptosis in A2780-CisR and SKOV3-CisR cells (Figure 1).

3.4 Cell cycle analysis

The results of cell cycle analysis using flow cytometry are presented in Figure 2. Treatment of SKOV3-CisR cells with MELS at a concentration of 100 μg/mL led to a significant reduction in the proportion of cells in G1 and S phases, from 61.52% to 60.11% and 24.75%–18.53%, respectively, compared to the control. Similarly, treatment of A2780-CisR cells with MELS resulted in a significant decrease in the proportion of cells in G1/S and G2/M phases, from 55.23% to 32.13% and 39.01%–31.32%, respectively, compared to the control. The cell cycle encompasses several checkpoints that enable the cell to repair its damaged DNA. Checkpoints at the G1/S and G2/M transitions play a crucial role in regulating cell cycle progression. However, the loss of these checkpoints prior to completing DNA repair can trigger the apoptotic cascade, leading to cell death (Hartwell and Kastan, 1994; Kastan and Bartek, 2004). Hence, it is

TABLE 3 Binding energies and interaction details of top-scored phytochemicals with survivin protein (PDB: 3UIH).

Ligands	Protein	Binding affinity ΔG (kcal/mol)	Amino acids involved and distance (Å)	
			Hydrogen-bond interactions	Hydrophobic interactions
Oleic acid	Survivin (PDB: 3UIH)	−6.1	ASP A:71 (3.34), ASP A:72 (4.65), GLU A: 76 (3.98)	LEU A:64 (4.15, 6.25), TRP A:67 (3.38), HIS A:80 (6.31, 6.56)
Stigmast-5-en-3-ol		−5.9	-	TRP A:67 (3.57), HIS A:80 (5.26)
Phytol		−5.8	ASP A:72 (3.48), GLU A:76 (3.49)	LEU A:64 (3.80), HIS A:80 (5.01)
Glyceryl linolenate		−5.6	LYS A:79 (5.45), GLU A:76 (4.48, 5.17)	GLU A:65 (6.36), GLY A:66 (4.55), ASP A: 72 (4.13)

clear that targeting the cell cycle will serve as an excellent source of novel anticancer chemicals (Carnero, 2002). After treatment with MELS, the cell-cycle distributions were found to be greatly aggregated at the G2/M phase. This indicates that MELS has the ability to cause cell-cycle arrest in ovarian cancer cells.

3.5 GC-MS analysis of MELS

The identified compounds in the MELS, as determined by GC-MS analysis, are listed in order of their column elution time (Supplementary Figure S2). A total of 14 compounds were detected (Table 1), accounting for 64.97% of the whole extract. Among the detected compounds, oleic acid (6.59%), stigmast-5-en-3-ol (5.64%), 2,3-dihydroxypropyl-cis-13-docosenoate (4.8%), lupeol (4.08%), and lupanol (4.06%) were the most dominant. The most representative compounds identified were lucenin 2 (3.91%), isocolchicine (3.11%), phytol (2.82%), β-amyrin (2.64%), 3,4,3′,4′-tetrahydrospirilloxanthin (2.63%), phytofluene (2.49%), oleanolic acid (2.37%), betulin (2.03%), glyceryl linolenate (1.91%), and 1-oxo-forskolin (1.83%).

3.6 Molecular docking

Molecular docking is an essential tool in computer-aided drug design, which aids in explaining ligand's binding affinity towards a protein target. It aids in identifying new therapeutic drugs and predicting ligand-protein interactions (Cetin, 2022; Cetin et al., 2023). It further enables structure-activity relationship studies and combinatorial library design to yield faster and more cost-effective drug discovery. The validation of molecular docking protocol was done by re-docking of the co-crystal ligand into the active site of receptor molecule (PDB: 3UIH) and confirming the conformation and orientation of a specific pose having a RMD value of not more than 2%. For protein-ligand docking, the active binding site (binding pocket) known as Smac/DIABLO of survivin was chosen for the docking study as it has pro-apoptotic function.

In the present study, MELS exhibited remarkable anticancer properties compared to other solvent extracts. GC-MS analysis was performed to discern the phytoconstituents responsible for the anticancer activity. Fourteen compounds were identified, and their docking score and interactions with survivin were evaluated through molecular docking study, as shown in Tables 2, 3. Based on the molecular docking studies, the binding affinity of ligands were oleic acid (−6.1 kcal/mol) > stigmast-5-en-3-ol (−5.9 kcal/mol) > phytol (−5.8 kcal/mol) > glyceryl linolenate (−5.6 kcal/mol).

Table 3 illustrates the binding affinities and interactions of various ligands with the survivin protein (PDB: 3UIH) (Figure 3). Among the ligands examined, oleic acid exhibited the strongest binding affinity with the survivin protein at −6.1 kcal/mol. Oleic acid formed hydrogen-bond interactions with ASP A:71, ASP A:72, and GLU A:76, while engaging in hydrophobic interactions with LEU A:64, TRP A:67, and HIS A:80. Stigmast-5-en-3-ol, with a binding affinity of −5.9 kcal/mol, interacted primarily through hydrophobic contacts with TRP A:67 and HIS A:80. Phytol, with a binding affinity of −5.8 kcal/mol, engaged in hydrogen-bond interactions with ASP A:72 and GLU A:76, while participating in hydrophobic interactions with LEU A:64 and HIS A:80. Glyceryl linolenate, with a binding affinity of −5.6 kcal/mol, formed hydrogen-bond interactions with LYS A:79, GLU A:76, and ASP A:72, and established hydrophobic contacts with GLU A:65, GLY A: 66, and ASP A:72.

According to previous research conducted by Foroughi and colleagues (Singh et al., 2024), several phytoconstituents, including berberine, carvacrol, crocetin, crocin, curcumin, picrocrocin, piperine, and thymol, have been found to have stronger binding affinities with survivin. A SAR study of docking results demonstrate that the most bioactive phytochemicals (lead scaffolds of their structures are presented in Figure 4) inhibit survivin by binding with Asp71, Glu76, Glu65, Lys62, and Glu63 through hydrogen bond interactions. In our study, we also observed that these phytoconstituents, specifically stigmast-5-en-3-ol and phytol interact with Asp71, Asp72, Glu76, and Lys79 through hydrogen bond interactions, which confirms that they inhibit survivin by interacting with some of the aforementioned amino acids. A results of *in vitro* anticancer activity (IC_{50} values) concords the inhibitory potential (binding affinity, kcal/mol) observed in the docking study. Looking into the lead structural scaffolds one can be apparently believe that the steroidal framework or pentacyclic triterpenoid structural framework is essentially important for the anticancer potential of MELS along with the inhibition of human survivin protein. The cyclic hydrocarbon structure is involved in hydrophobic interactions and the hydroxyl groups participates in polar

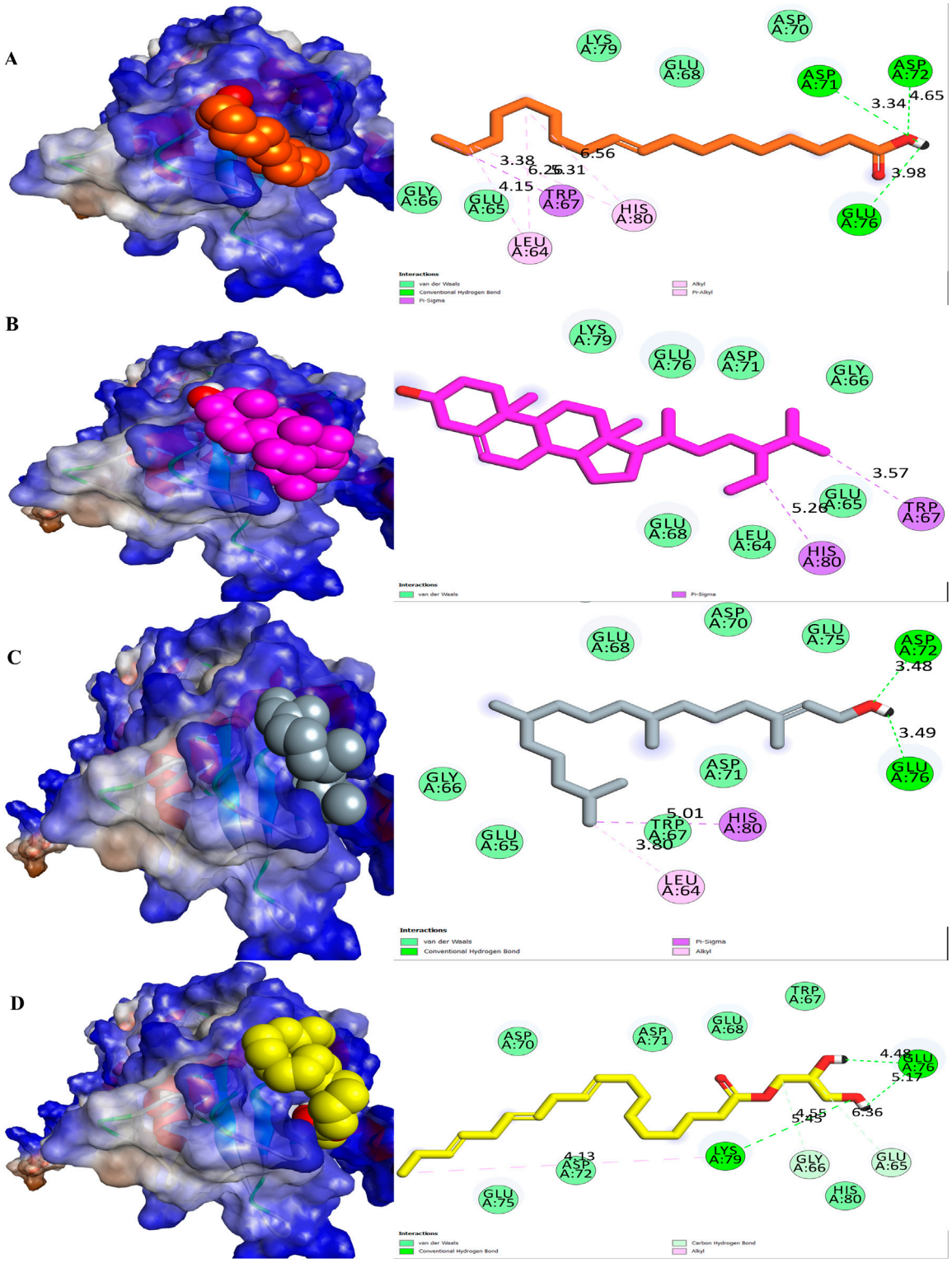

FIGURE 3
Molecular surface view and 2D representation of interactions between phytochemicals with the survivin. **(A)** Oleic acid, **(B)** Stigmast-5-en-3-ol, **(C)** Phytol and **(D)** Glyceryl linolenate.

hydrogen bonding with the amino acid residues (catalytic active site) of surviving protein molecule as depicted in the preceding section.

The binding energy of oleic acid, a phytoconstituent, was found to be higher than that of other phytocompounds studied by Foroughi et al. (Singh et al., 2024) with a value of −6.1 kcal/mol.

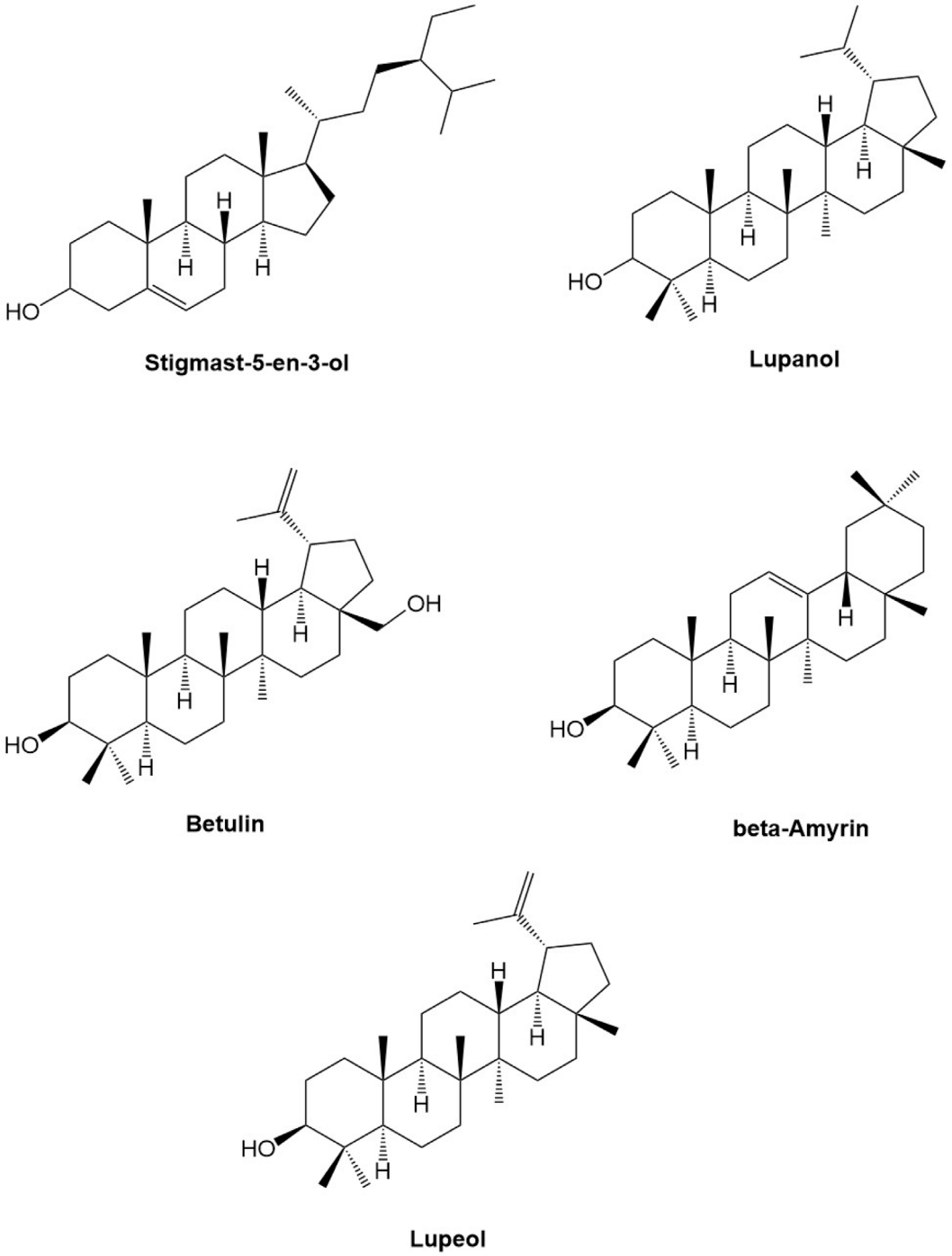

FIGURE 4
Lead scaffolds of some representative bioactive phytochemicals.

The anticancer properties of oleic acid have been demonstrated through its ability to inhibit the expression of HER2, a well-known oncogene that is involved in the development, progression, and spread of several human cancer. The previous study conducted by Fernando et al. demonstrated that stigmast-5-en-3-ol exhibited significant antiproliferative effects on HL-60 (leukemia) and MCF-7 (breast cancer) cell lines. Specifically, it was found to have IC_{50} values of 37.82 and 45.17 μg/mL for these cell lines, respectively (Fernando et al., 2018). As per the study conducted by the de Alencar et al. (2023), phytol has been demonstrated to exhibit potent anticancer properties, as evidenced by its ability to inhibit the growth of sarcoma −180 and human leukemia (HL-60) cells with IC_{50} values of 18.98 ± 3.79 and 1.17 ± 0.34 μM, respectively. The presence of oleic acid, stigmast-5-en-3-ol and phytol in MELS is likely responsible for its potent anticancer activity, as reported in previous studies. Our study presents a novel finding, as we report for

the first time the inhibition of survivin with oleic acid, stigmast-5-en-3-ol, and phytol. To validate their potential as an anticancer agent through the inhibition of survivin, additional experimental research is necessary in the future.

3.7 Drug-likeliness

The results of the GC-MS analysis of MELS revealed the presence of 14 phytocompounds that were evaluated for drug-likeness using the DruLiTo method. These drug-like properties were assessed in accordance with Lipinski's rule of five, which includes criteria such as logP ≤ 5, HBD ≤ 5, HBA ≤ 10, MW ≤ 500, TPSA ≤ 140, and AMR between 40 and 130 (Kumar Pasala et al., 2023). These parameters are important for considering a molecule as drug-like, as they affect its bioavailability, absorption, receptor-drug interactions, metabolism, and toxicity, which are all important factors for drug candidates to possess (Schneider, 2013). Additionally, the molecule size is also a crucial factor, especially for transmembrane transportation (Kumar Pasala et al., 2023). The study of drug likeness, based on the physicochemical nature of bioactive compounds, is an initial criterion for judging drug likeness. Lipinski's rule of five provides a structural similarity between an idealistic/rationalized drug synthetic structure and a bioactive compound. However, it is important to note that a drug candidate does not necessarily need to follow all the rules to be considered a potential drug candidate. Previous studies have shown that the lack of oral bioavailability does not necessarily affect the activity or pharmacokinetic potencies of a drug (Bickerton et al., 2012). From this analysis, two compounds, isocolchicine, and 1-oxo-forskolin, were identified as ideal molecules for further examination as they obey Lipinski's rule of five. However, it is important to note that the majority of natural products have been found to deviate from the Lipinski rule of five, as evidenced by various studies (James et al., 2023; Gandhi et al., 2022). The results of physicochemical properties are listed in Supplementary Table S2.

3.8 ADMET analysis

ADMET is a process that assesses the pharmacokinetic properties of a drug and its potential for clinical use. One of the advantages of ADMET analysis is that it can help identify issues in the early stages of drug development, which can reduce the likelihood of clinical trial failures (Schneider, 2013). This study examined for three lead compounds, with solubility, intestinal absorption, dermal permeability, and Caco2 permeability being key parameters (Dahlgren and Lennernäs, 2019).

Supplementary Table S3 provides a detailed summary of the phytoconstituents and their pharmacokinetic properties, which were obtained using different computational tools, *viz.*, SwissADME, admetTSAR, and ProTox-II. The compounds identified through molecular docking, including oleic acid, stigmast-5-en-3-ol, phyol and glyceryl linolenate, showed moderate to poor solubility, which resulted in low absorption in the gastrointestinal tract. However, according to the ProTox-II studies, all four of these compounds were found to be safe, and none of them exhibited hepatotoxicity, carcinogenicity, mutagenicity, or cytotoxicity. In terms of LD_{50}, oleic acid falls in Class 4 with a dose of 480 mg/kg, stigmast-5-en-3-ol belongs to Class 4 with a dose of 890 mg/kg, phytol falls in Class 5 with a dose of 5,000 mg/kg and glyceryl linolenate is in Class 6 with a dose of 39800 mg/kg. Based on this information, it can be concluded that all of these compounds are safe for human use.

4 Conclusion

The methanolic extract of lotus seeds (MELS) possesses anti-proliferative effects against ovarian cancer cells, possibly by inducing cell death and hindering the cell cycle. *In vitro* study demonstrated significant inhibition of SKOV3 (IC50: 79.73 ± 0.91), A2780 (IC50: 100.18 ± 2.42), SKOV3-CisR (IC50: 115.87 ± 2.2) and A2780-CisR (IC50: 138.86 ± 2.46) cells by MELS, compared to acetone, petroleum ether, n-hexane extracts, and the standard drug, cisplatin. Furthermore, MELS resulted in a substantial increase in apoptosis cell count to 78% in A2780-CisR cells and 82% in SKOV3-CisR cells, whereas a significant reduction in the G1 and G2/M phases of cells treated with MELS when compared to the control group. To identify the potential phytocompounds present in the MELS, we conducted GC-MS analysis, which led to the identification of 14 phytochemical compounds. Molecular docking analysis revealed that oleic acid, stigmast-5-en-3-ol, phytol and glyceryl linolenate exhibited remarkable binding affinities of -6.1, -5.9, -5.8 and -5.6 kcal/mol, respectively against human survivin. Our findings suggest that phytochemicals present in MELS might have potential anticancer effect against ovarian cancer, and further investigation is required in order to fully elucidate the mechanisms of anticancer action.

Data availability statement

The original contributions presented in the study are included in the article/Supplementary Material, further inquiries can be directed to the corresponding authors.

Author contributions

VM: Writing–original draft, Methodology, Investigation, Formal Analysis, Data curation, Conceptualization. MR: Writing–review and editing, Supervision, Resources, Investigation, Conceptualization. DP: Writing–original draft, Visualization, Validation, Methodology, Investigation, Formal Analysis, Data curation, Conceptualization. PP: Writing–original draft, Visualization, Supervision, Resources, Project administration, Conceptualization. AB: Writing–original draft, Visualization, Validation, Investigation, Formal Analysis. SB: Writing–original draft, Visualization, Validation, Investigation, Formal Analysis. SA: Writing–original draft, Visualization, Methodology, Investigation, Funding acquisition, Formal Analysis. JK: Writing–original draft, Project administration, Methodology, Investigation, Funding acquisition, Formal Analysis.

Funding

The author(s) declare that financial support was received for the research, authorship, and/or publication of this article. This research was funded by the Ministry of Education in Saudi Arabia, grant number IFP-2022-14.

Acknowledgments

The authors extend their appreciation to the Deputyship for research and innovation, the Ministry of Education in Saudi Arabia, for funding this research work through the project number, IFP-2022-14.

Conflict of interest

The authors declare that the research was conducted in the absence of any commercial or financial relationships that could be construed as a potential conflict of interest.

Generative AI statement

The author(s) declare that no Generative AI was used in the creation of this manuscript.

Publisher's note

All claims expressed in this article are solely those of the authors and do not necessarily represent those of their affiliated organizations, or those of the publisher, the editors and the reviewers. Any product that may be evaluated in this article, or claim that may be made by its manufacturer, is not guaranteed or endorsed by the publisher.

Supplementary material

The Supplementary Material for this article can be found online at: https://www.frontiersin.org/articles/10.3389/fchem.2024.1505272/full#supplementary-material

References

Altameme, H. J., Hameed, I. H., Idan, S. A., and Hadi, M. Y. (2015). Biochemical analysis of *Origanum vulgare* seeds by fourier-transform infrared (FT-IR) spectroscopy and gas chromatography-mass spectrometry (GC-MS). *J. Pharmacogn. Phytotherapy*. doi:10.5897/jpp2015.0362

Archana, V. P., Armaković, S. J., Armaković, S., Celik, I., Bhagyasree, J. B., Babu, K. D., et al. (2023). Exploring the structural, photophysical and optoelectronic properties of a diaryl heptanoid curcumin derivative and identification as a SARS-CoV-2 inhibitor. *J. Mol. Struct.* 1281, 135110. doi:10.1016/j.molstruc.2023.135110

Baru Venkata, R., Prasanth, D. S. N. B. K., Pasala, P. K., Panda, S. P., Tatipamula, V. B., Mulukuri, S., et al. (2023). Utilizing Andrographis paniculata leaves and roots by effective usage of the bioactive andrographolide and its nanodelivery: investigation of antikindling and antioxidant activities through *in silico* and *in vivo* studies. *Front. Nutr.* 10, 1185236. doi:10.3389/fnut.2023.1185236

Bickerton, G. R., Paolini, G. V., Besnard, J., Muresan, S., and Hopkins, A. L. (2012). Quantifying the chemical beauty of drugs. *Nat. Chem.* 4, 90–98. doi:10.1038/nchem.1243

Carnero, A. (2002). Targeting the cell cycle for cancer therapy. *Br. J. Cancer* 87, 129–133. doi:10.1038/sj.bjc.6600458

Cetin, A. (2022). Some flavolignans as potent Sars-Cov-2 inhibitors via molecular docking, molecular dynamic simulations and ADME analysis. *Curr. Computer-Aided Drug Des.* 18 (5), 337–346. doi:10.2174/1573409918666220816113516

Cetin, A., Donmez, A., Dalar, A., and Bildirici, I. (2023). Amino acid and dicyclohexylurea linked pyrazole analogues: synthesis, *in silico* and *in vitro* studies. *ChemistrySelect* 8 (6), e202204926. doi:10.1002/slct.202204926

Dahlgren, D., and Lennernäs, H. (2019). Intestinal permeability and drug absorption: predictive experimental, computational and *in vivo* approaches. *Pharmaceutics* 11, 411. doi:10.3390/pharmaceutics11080411

Dasari, S., Bakthavachalam, V., Chinnapaka, S., Venkatesan, R., Angela Lincy Prem Antony, S., and Munirathinam, G. (2020). Neferine, an alkaloid from lotus seed embryo targets HeLa and SiHa cervical cancer cells via pro-oxidant anticancer mechanism. *Phytotherapy Res.* 34, 2366–2384. doi:10.1002/ptr.6687

de Alencar, M. V. O. B., Islam, M. T., da Mata, A. M. O. F., dos Reis, A. C., de Lima, R. M. T., de Oliveira Ferreira, J. R., et al. (2023). Anticancer effects of phytol against Sarcoma (S-180) and Human Leukemic (HL-60) cancer cells. *Environ. Sci. Pollut. Res.* 30, 80996–81007. doi:10.1007/s11356-023-28036-4

Demir, S., Turan, I., Aliyazicioglu, R., Yaman, S. O., and Aliyazicioglu, Y. (2018). Primula vulgaris extract induces cell cycle arrest and apoptosis in human cervix cancer cells. *J. Pharm. Anal.* 8, 307–311. doi:10.1016/j.jpha.2018.05.003

Devi, K. P., Rajavel, T., Habtemariam, S., Nabavi, S. F., and Nabavi, S. M. (2015). Molecular mechanisms underlying anticancer effects of myricetin. *Life Sci.* 142, 19–25. doi:10.1016/j.lfs.2015.10.004

Dsnbk, P., Bhavanam, P. R., Pasala, P. K., Panda, S. P., Achanti, S., Jash, R., et al. (2023). In-silico study of Cassia tora linn in the treatment of gaucher disease: a scientific ethnomedical study. *Bull. Pharm. Sci. Assiut Univ.* 46, 0–815. doi:10.21608/bfsa.2023.184206.1620

Ezugwu, J. A., Okoro, U. C., Ezeokonkwo, M. A., Hariprasad, K. S., Rudrapal, M., Gogoi, N., et al. (2024). Design, synthesis, molecular docking, drug-likeness/ADMET and molecular dynamics studies of thiazolyl benzenesulfonamide carboxylates as antimalarial agents. *Chem. Afr.* 7, 2353–2368. doi:10.1007/s42250-024-00904-7

Fernando, I. P. S., Sanjeewa, K. K. A., Ann, Y.-S., Ko, C.-i., Lee, S.-H., Lee, W. W., et al. (2018). Apoptotic and antiproliferative effects of Stigmast-5-en-3-ol from Dendronephthya gigantea on human leukemia HL-60 and human breast cancer MCF-7 cells. *Toxicol. Vitro* 52, 297–305. doi:10.1016/j.tiv.2018.07.007

Fitrianto, N., Proklamasiningsih, E., and Muljowati, J. S. (2020). Phytochemical diversity and antimicrobial properties of methanol extract of several cultivars of Catharanthus roseus using GC-MS. *Biodiversitas J. Biol. Divers.* 21. doi:10.13057/biodiv/d210409

Gandhi, A. J., Rupareliya, J. D., Shukla, V., Donga, S. B., and Acharya, R. (2022). An ayurvedic perspective along with *in silico* study of the drugs for the management of SARS-CoV-2. *J. Ayurveda Integr. Med.* 13, 100343. doi:10.1016/j.jaim.2020.07.002

Grosso, G., Buscemi, S., Galvano, F., Mistretta, A., Marventano, S., La Vela, V., et al. (2013). Mediterranean diet and cancer: epidemiological evidence and mechanism of selected aspects. *BMC Surg.* 13 (Suppl. 2), S14. doi:10.1186/1471-2482-13-S2-S14

Hartwell, L. H., and Kastan, M. B. (1994). Cell cycle control and cancer. *Science* 266, 1821–1828. doi:10.1126/science.7997877

James, J. P., Ail, P. D., Crasta, L., Kamath, R. S., Shura, M. H., and T.j, S. (2023). *In silico* ADMET and molecular interaction profiles of phytochemicals from medicinal plants in dakshina Kannada. *J. Health Allied Sci. N. U.* 14, 190–201. doi:10.1055/s-0043-1770057

Kapellos, G., Polonifi, K., Farmakis, D., Spartalis, E., Tomos, P., Aessopos, A., et al. (2013). Overexpression of survivin levels in circulation and tissue samples of lung cancer patients. *Anticancer Res.* 33, 3475–3480.

Kastan, M. B., and Bartek, J. (2004). Cell-cycle checkpoints and cancer. *Nature* 432, 316–323. doi:10.1038/nature03097

Khan, Z., Khan, A. A., Yadav, H., Prasad, G. B. K. S., and Bisen, P. S. (2017). Survivin, a molecular target for therapeutic interventions in squamous cell carcinoma. *Cell. and Mol. Biol. Lett.* 22, 8. doi:10.1186/s11658-017-0038-0

Killari, K. N., Polimati, H., Prasanth, D., Singh, G., Panda, S. P., Vedula, G. S., et al. (2023). Salazinic acid attenuates male sexual dysfunction and testicular oxidative damage in streptozotocin-induced diabetic albino rats. *RSC Adv.* 13, 12991–13005. doi:10.1039/d3ra01542d

Kohn, E. C., Mills, G. B., and Liotta, L. (2003). Promising directions for the diagnosis and management of gynecological cancers. *Int. J. Gynaecol. Obstet.* 83 (1), 203–209. doi:10.1016/s0020-7292(03)90122-6

Kumar Pasala, P., Donakonda, M., Dintakurthi, P. S., Rudrapal, M., Gouru, S. A., and Ruksana, K. (2023). Investigation of cardioprotective activity of silybin: network

pharmacology, molecular docking, and *in vivo* studies. *ChemistrySelect* 8 (20), e202300148. doi:10.1002/slct.202300148

Li, Y., Pan, J., and Gou, M. (2019). The anti-proliferation, cycle arrest and apoptotic inducing activity of peperomin E on prostate cancer PC-3 cell line. *Molecules* 24, 1472. doi:10.3390/molecules24081472

Liu, C.-M., Kao, C. L., Wu, H., Li, W.-J., Huang, C.-T., Li, H.-T., et al. (2014). Antioxidant and anticancer aporphine alkaloids from the leaves of Nelumbo nucifera gaertn. Cv. Rosa-plena. *Molecules* 19, 17829–17838. doi:10.3390/molecules191117829

Mahassni, S. H., and Al-Reemi, R. M. (2013). Apoptosis and necrosis of human breast cancer cells by an aqueous extract of garden cress (Lepidium sativum) seeds. *Saudi J. Biol. Sci.* 20, 131–139. doi:10.1016/j.sjbs.2012.12.002

Meng, X.-Y., Zhang, H.-X., Mezei, M., and Cui, M. (2011). Molecular docking: a powerful approach for structure-based drug discovery. *Curr. Computer-aided Drug Des.* 7, 146–157. doi:10.2174/157340911795677602

Mills, G. B., Fang, X., Lu, Y., Hasegawa, Y., Eder, A., Tanyi, J., et al. (2003). Specific keynote: molecular therapeutics in ovarian cancer. *Gynecol. Oncol.* 88, S88–S92. doi:10.1006/gyno.2002.6692

Mobahat, M., Narendran, A., and Riabowol, K. (2014). Survivin as a preferential target for cancer therapy. *Int. J. Mol. Sci.* 15, 2494–2516. doi:10.3390/ijms15022494

Mosmann, T. (1983). Rapid colorimetric assay for cellular growth and survival: application to proliferation and cytotoxicity assays. *J. Immunol. Methods* 65, 55–63. doi:10.1016/0022-1759(83)90303-4

Paudel, K. R., and Panth, N. (2015). Phytochemical profile and biological activity of *Nelumbo nucifera*. *Evidence-Based Complementary Altern. Med.* 2015, 1–16. doi:10.1155/2015/789124

Pavlyukov, M. S., Antipova, N. V., Balashova, M. V., Vinogradova, T. V., Kopantzev, E. P., and Shakhparonov, M. I. (2011). Survivin monomer plays an essential role in apoptosis regulation. *J. Biol. Chem.* 286, 23296–23307. doi:10.1074/jbc.m111.237586

Prasanth, D., Murahari, M., Chandramohan, V., Bhavya, G., Lakshmana Rao, A., Panda, S. P., et al. (2021). In-silico strategies of some selected phytoconstituents from Melissa officinalis as SARS CoV-2 main protease and spike protein (COVID-19) inhibitors. *Mol. Simul.* 47, 457–470. doi:10.1080/08927022.2021.1880576

Prasanth, D. S. N. B. K., Singh, G., Panda, S. P., Achanti, S., Soni, H., Chaudhuri, T. K., et al. (2023). *In silico* screening of plant-derived anti-virals from shorea hemsleyana (king) king ex foxw against SARS CoV-2 main protease. *Chem. Afr.* 6, 345–366. doi:10.1007/s42250-022-00521-2

Ruibin, J., Bo, J., Danying, W., Chihong, Z., Jianguo, F., and Linhui, G. (2017). Therapy effects of wogonin on ovarian cancer cells. *Biomed. Res. Int.* 2017, 1–8. doi:10.1155/2017/9381513

Schneider, G. (2013). Prediction of drug-like properties, in *Madame curie bioscience database* (Landes Bioscience).

Senapati, S., Mahanta, A. K., Kumar, S., and Maiti, P. (2018). Controlled drug delivery vehicles for cancer treatment and their performance. *Signal Transduct. Target Ther.* 3, 7. doi:10.1038/s41392-017-0004-3

Shah, M., Khan, F., Ullah, S., Mohanta, T. K., Khan, A., Zainab, R., et al. (2023). GC-MS profiling and biomedical applications of essential oil of Euphorbia larica boiss.: a new report. *Antioxidants* 12, 662. doi:10.3390/antiox12030662

Singh, K. D., Chetia, D., Gogoi, N., Gogoi, B., and Rudrapal, M. (2024). *In vivo* and *in silico* based evaluation of antidiabetic potential of an isolated flavonoid from *Allium hookeri* in type 2 diabetic rat model. *Chem. and Biodivers.* 21 (1), e202301299. doi:10.1002/cbdv.202301299

Turan, I., Demir, S., Kilinc, K., Aliyazicioglu, Y., Alver, A., Mısır, S., et al. (2017). *Morus rubra* extract induces G (1) cell cycle arrest and apoptosis in human lung and prostate cancer cells. *Indian J. Pharm. Educ. Res.* 51, 51–58. doi:10.5530/ijper.51.1.8

frontiers | Frontiers in Chemistry

TYPE Original Research
PUBLISHED 06 January 2025
DOI 10.3389/fchem.2024.1515424

OPEN ACCESS

EDITED BY
Richie Bhandare,
Ajman University, United Arab Emirates

REVIEWED BY
Pradeep Kumar Jaiswal,
Texas A&M University College Station, United States
Subhash Chander,
Amity University, India
Srinath Pashikanti,
Idaho State University, United States

*CORRESPONDENCE
Kevser Kübra Kırboğa,
kubra.kirboga@bilecik.edu.tr
Aman Karim,
aman.karim@numspak.edu.pk
Mithun Rudrapal,
rsmrpal@gmail.com

RECEIVED 22 October 2024
ACCEPTED 10 December 2024
PUBLISHED 06 January 2025

CITATION
Kırboğa KK, Karim A, Küçüksille EU, Rudrapal M, Khan J, Achar RR, Silina E, Manturova N and Stupin V (2025) Exploring the antifungal potential of *Cannabis sativa*-derived stilbenoids and cannabinoids against novel targets through *in silico* protein interaction profiling. *Front. Chem.* 12:1515424.
doi: 10.3389/fchem.2024.1515424

Exploring the antifungal potential of *Cannabis sativa*-derived stilbenoids and cannabinoids against novel targets through *in silico* protein interaction profiling

Kevser Kübra Kırboğa[1]*, Aman Karim[2]*, Ecir Uğur Küçüksille[3], Mithun Rudrapal[4]*, Johra Khan[5], Raghu Ram Achar[6], Ekaterina Silina[7], Natalia Manturova[8] and Victor Stupin[8]

[1]Faculty of Engineering, Department of Bioengineering, Bilecik Şeyh Edebali University, Bilecik, Türkiye, [2]Faculty of Multidisciplinary Studies, Department of Biological Sciences, National University of Medical Sciences, Rawalpindi, Pakistan, [3]Faculty of Engineering, Department of Computer Engineering, Isparta Suleyman Demirel University, Isparta, Türkiye, [4]Department of Pharmaceutical Sciences, School of Biotechnology and Pharmaceutical Sciences, Vignan's Foundation for Science, Technology and Research, Guntur, India, [5]Department of Medical Laboratory Sciences, College of Applied Medical Sciences, Majmaah University, Al Majmaah, Saudi Arabia, [6]Division of Biochemistry, School of Life Sciences, JSS Academy of Higher Education and Research, Mysuru, India, [7]Institute of Digital Biodesign and Modeling of Living Systems, I. M. Sechenov First Moscow State Medical University (Sechenov University), Moscow, Russia, [8]Department of Surgery, Pirogov Russian National Research Medical University, Moscow, Russia

Cannabinoid and stilbenoid compounds derived from *Cannabis sativa* were screened against eight specific fungal protein targets to identify potential antifungal agents. The proteins investigated included Glycosylphosphatidylinositol (GPI), Enolase, Mannitol-2-dehydrogenase, GMP synthase, Dihydroorotate dehydrogenase (DHODH), Heat shock protein 90 homolog (Hsp90), Chitin Synthase 2 (CaChs2), and Mannitol-1-phosphate 5-dehydrogenase (M1P5DH), all of which play crucial roles in fungal survival and pathogenicity. This research evaluates the binding affinities and interaction profiles of selected cannabinoids and stilbenoids with these eight proteins using molecular docking and molecular dynamics simulations. The ligands with the highest binding affinities were identified, and their pharmacokinetic profiles were analyzed using ADMET analysis. The results indicate that GMP synthase exhibited the highest binding affinity with Cannabistilbene I (−9.1 kcal/mol), suggesting hydrophobic solid interactions and multiple hydrogen bonds. Similarly, Chitin Synthase 2 demonstrated significant binding with Cannabistilbene I (−9.1 kcal/mol). In contrast, ligands such as Cannabinolic acid and 8-hydroxycannabinolic acid exhibited moderate binding affinities, underscoring the variability in interaction strengths among different proteins. Despite promising *in silico* results, experimental validation is necessary to confirm

therapeutic potential. This research lays a crucial foundation for future studies, emphasizing the importance of evaluating binding affinities, pharmacokinetic properties, and multi-target interactions to identify promising antifungal agents.

KEYWORDS

cannabinoids, stilbenoids, antifungal agents, molecular docking, molecular dynamics simulation, *Cannabis sativa*

1 Introduction

The increasing prevalence of fungal infections and antifungal-resistant strains necessitates discovering new and effective antifungal agents. *Cannabis sativa* has high therapeutic potential due to its diverse biologically active compounds (Clarke and Merlin, 2015). Stilbenoids and cannabinoids are significant compounds derived from *Cannabis sativa* that exhibit various biological activities. Previous studies have highlighted their anti-inflammatory, anticancer, and antibacterial properties (Glodowska, 2016; Hanane and Mohammed, 2021; Hourfane et al., 2023; Reiss, 2010; Sun, 2023). Research on the effects of stilbenoids and cannabinoids in different biological systems has shown that these compounds can be used in a broad therapeutic spectrum (Jeong et al., 2019). However, studies investigating the interactions of stilbenoids and cannabinoids with fungal proteins and the antifungal efficacy of these interactions are limited.

Recent studies have explored the potential of natural metabolites derived from plants and fungi for antiviral, antidiabetic, and receptor-targeted purposes using *in silico* techniques. For example, Khan et al. conducted a molecular docking (MD) and dynamics simulation (MDS) study on secondary metabolites derived from medicinal fungi as potential inhibitors for COVID-19 treatment. This study highlighted several compounds that effectively targeted viral proteins such as the main protease and TMPRSS2, demonstrating the efficacy of fungi-derived natural products in combating viral infections (Khan et al., 2023). Additionally, another study investigated *Cannabis* constituents as potential candidates against diabetes mellitus using MD, dynamics simulations, and ADMET investigations, showing promising therapeutic potential (Abchir et al., 2023). Moreover, a recent study by Aissaoui et al. explored the anticancer potential of cannabidiol using computational methods, including MD, which are similar to the methodologies applied in this study. Their results

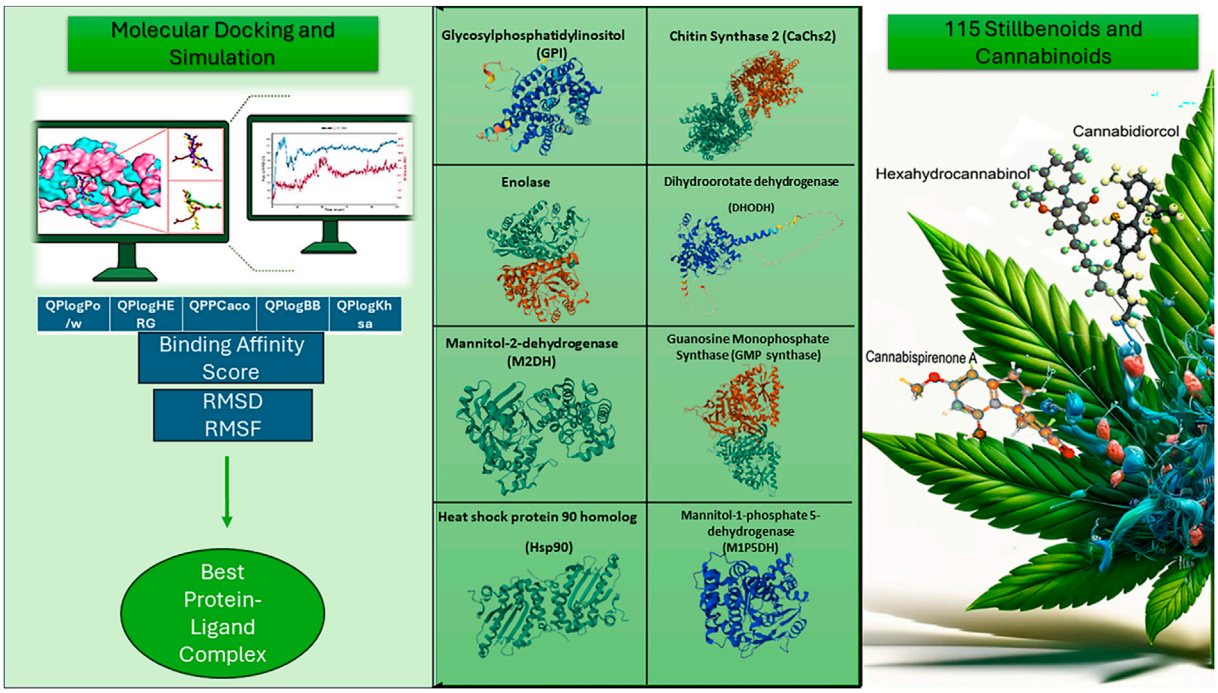

GRAPHICAL ABSTRACT
The objective of this study is to identify novel antifungal agents by exploring the interactions between cannabinoids and stilbenoids derived from Cannabis sativa and eight fungal protein targets that play critical roles in fungal pathogenicity and survival. These proteins were chosen based on their essential functions of cell wall integrity, metabolic processes, stress response, and other vital cellular activities essential for the proliferation and virulence of fungal pathogens. Targeting multiple pathways aims to evaluate whether these natural compounds can effectively inhibit crucial mechanisms in fungal cells, thereby offering a potential strategy to combat antifungal resistance. Through molecular docking and dynamics simulations, this study seeks to determine these compounds' specific binding affinities, stability, and pharmacokinetic properties, laying the groundwork for future experimental validation and potential therapeutic development.

indicated significant binding energies and interactions with targeted proteins, suggesting that cannabidiol could be synthesized and tested as a potential treatment for various types of human cancer (Aissaoui et al., 2024). Furthermore, virtual screening of cannabinoid analogs against CB1 and CB2 receptors using MD and MDS has also shown that these compounds interact significantly with key targets associated with these receptors, underscoring the therapeutic potential of cannabinoids beyond their known uses (Aviz-Amador et al., 2021).

This study aims to identify antifungal compounds by screening stilbenoids and cannabinoids reported from *Cannabis sativa* against new protein targets. A comprehensive literature review indicates a lack of extensive studies on the interactions of stilbenoids and cannabinoids with fungal proteins and their antifungal potential.

In this study, cannabinoid and stilbenoid compounds derived from *Cannabis sativa* were selected considering their structural diversity, biological activities and documented antifungal potential. Cannabiorcol ($C_{17}H_{18}O_2$) was included due to its unique structure and antimicrobial activities against various microorganisms. In the literature, it has been reported that this compound binds to the fungal cell membrane, destabilizes the cell wall and inhibits the growth of pathogenic cells (Appendino et al., 2008). Δ9-trans-Tetrahydrocannabinol (Δ9-trans-THC) ($C_{17}H_{22}O_2$) is an isomer of tetrahydrocannabinol (THC) and can establish strong interactions with cellular membranes due to its lipophilic properties. This compound was included in the study due to its antifungal potential, considering the known antimicrobial effects of THC (Kogan and Mechoulam, 2007). Cannabidiol ($C_{17}H_{22}O_2$) is a Cannabidiol (CBD) analog that exhibits potent antibiofilm activity against fungal species such as *Candida* albicans, offering the potential to target biofilm-based resistance mechanisms of pathogens (Feldman et al., 2021). CBD was selected in our study to evaluate its potential interactions with antifungal target proteins. In the literature, CBD has been shown to exhibit strong anti-inflammatory effects in human keratinocyte (HaCaT) cells stimulated with polyinosinic-polycytidylic acid [poly-(I:C)]. CBD suppresses the production of inflammatory markers such as monocyte chemotactic protein-2 (MCP-2), interleukin-6 (IL-6), interleukin-8 (IL-8), and tumor necrosis factor-α (TNF-α) in these cells in a dose-dependent manner (Petrosino et al., 2018). These effects have been shown to occur by activating cannabinoid type-2 (CB2) and transient receptor potential vanilloid type-1 (TRPV1) receptors. In addition, the absence of cytotoxic effects of CBD suggests that it can be considered a safe anti-inflammatory agent. CBD is predicted to have the potential to regulate cytokine and chemokine production during fungal infections. These properties make CBD a candidate that may support multiple binding mechanisms with antifungal target proteins and warrants comprehensive investigation in our study (Petrosino et al., 2018).

The pharmacokinetic properties of stilbenoids were decisive in the selection of certain compounds in our study. For example, Cannabistilbene I was a strong candidate, exhibiting properties such as high permeability through human skin (32.755 cm/s × 10^7), jejunal permeability (5.229 cm/s × 10^4) and high penetration into the blood-brain barrier (BBB) (81% reliability). Canniprene and 3,4′-Dihydroxy-5,3′-dimethoxy-5′-isoprenylbibenzyl fully comply with Lipinski's "Rule of 5" criteria (0 violations) and have an effective pharmacokinetic profile in terms of both skin and intestinal permeability. The high BBB penetration of stilbenoids (80%–96%) and their potential to bind to antifungal target proteins are consistent with their biological activities. In particular, it is anticipated that these compounds will support multiple target mechanisms with their capacity to form hydrogen bonds, lipophilic profiles and antifungal proteins (O'Croinin et al., 2023).

In the selection of stilbenoids, their strong antioxidant properties and cell membrane destabilization potential were taken into consideration. Cannabidivarin (CBDV) was selected in our study to evaluate its potential interactions with antifungal target proteins. In the literature, CBDV has been reported to be a non-psychoactive phytocannabinoid and to have both activation and desensitization effects on the TRPA1 (Transient Receptor Potential Ankyrin 1) channel family. This feature reveals its capacity to regulate inflammation-related parameters, especially cytokine production and intestinal permeability (Pagano et al., 2019). In studies conducted in mice, CBDV has been shown to reduce neutrophil infiltration, correct imbalances in the intestinal microbiota, and suppress the expression of inflammatory cytokines (IL-1β, IL-6, MCP-1). In addition, the ability of CBDV to reduce cytokine expression has been reported in biopsies taken from pediatric patients with active ulcerative colitis (UC). It is predicted that this compound may also show similar interactions with fungal proteins through mechanisms related to the control of inflammatory processes at the cellular level. CBDV, which is considered a safe phytocannabinoid in humans, was included in our study as a strong candidate for the evaluation of interactions with antifungal target proteins due to both its biological activity and pharmacokinetic profile (Pagano et al., 2019). These compounds were evaluated in the study due to their chemical diversity and potential for developing multi-target antifungal agents. In particular, their hydrogen bonding capacity (O'Croinin et al., 2023), lipophilic profiles (Akinwumi et al., 2018; Castellano et al., 2014; Lucas et al., 2018) and binding compatibility (Platella et al., 2021) with target proteins (Wahedi et al., 2020) constituted an important part of the selection criteria.

Accordingly, this research evaluates the interactions between eight proteins, critical in fungal pathogenicity, and specific stilbenoids and cannabinoids. The selected proteins include Glycosylphosphatidylinositol (GPI) from *Candida albicans*, which plays a vital role in cell wall structure and function. Inhibition of GPI proteins can disrupt fungal cell wall synthesis and reduce virulence (Chaffin, 2008). Enolase (AfEno1) from *Aspergillus fumigatus* is crucial in glycolysis and energy metabolism of pathogenic fungi, with inhibition shown to halt fungal growth (Dasari et al., 2019). Mannitol-2-dehydrogenase (M2DH) from Aspergillus fumigatus is involved in mannitol metabolism and osmoregulation, where inhibition increases sensitivity to osmotic stress (Suvarna et al., 2000). Guanosine Monophosphate Synthase (GMP synthase) from *A. fumigatus* is essential in guanine nucleotide synthesis, and its inhibition can impede cell division and pathogenicity (Kingsbury and McCusker, 2010). DHODH from *Aspergillus nidulans* is crucial in pyrimidine biosynthesis, with inhibition shown to stop fungal growth effectively (Nara et al., 2000). Heat shock protein 90 homolog (Hsp90) from *Candida* albicans assists in protein folding and stress response, with inhibition disrupting pathogenicity (Cowen and Lindquist, 2005). Chitin Synthase 2 (CaChs2) from *C. albicans* plays a role in chitin synthesis, with

inhibition leading to weakened cell walls (Munro and Gow, 2001). Mannitol-1-phosphate 5-dehydrogenase (M1P5DH) from *Neosartorya fumigata* is involved in mannitol metabolism, where inhibition affects osmoregulation and survival (Ruijter et al., 2004). These proteins are critical in fungal cells' survival and pathogenic mechanisms, making them suitable targets. These eight specific proteins were selected based on their crucial roles in fungal cell survival, pathogenicity, and resistance mechanisms. Each protein represents a key biological pathway or structural component essential for fungal virulence and survival, such as cell wall synthesis, energy metabolism, stress response, and nucleotide synthesis. Targeting multiple vital pathways simultaneously increases the likelihood of identifying potential antifungal agents that can overcome existing drug resistance mechanisms. The inhibition of these proteins involved in diverse but essential functions provides a broad spectrum approach to compromising fungal pathogenicity and highlights their significance as promising antifungal drug targets. Docking studies were conducted using PyRx software and the AutoDock Vina algorithm, followed by advanced MDS with Schrödinger Maestro 2021–3 software and the Desmond module. Simulation data were analyzed to evaluate protein-ligand interactions, binding energies, and stabilities. Additionally, ADMET analysis was performed using the Schrödinger QikProp module to assess the drug-like properties of the compounds. The novelty of this study lies in its comprehensive *in silico* approach to identify potential antifungal agents among stilbenoids and cannabinoids, focusing on eight essential fungal proteins that play key roles in pathogenicity. Unlike previous studies, which largely focused on these compounds' anti-inflammatory or anticancer properties, this research explores the antifungal potential by systematically evaluating binding affinities, dynamic behaviors, and pharmacokinetic properties. This integrated approach provides a novel insight into the potential of *Cannabis sativa*-derived compounds as antifungal agents, offering a foundation for future *in-vitro* and *in-vivo* validations. Ultimately, this study aims to contribute to developing new therapeutic strategies targeting antifungal resistance, an emerging global health challenge.

2 Materials and methods

The primary objective of this study is to investigate the potential antifungal compounds by screening stilbenoid and cannabinoid compounds derived from *Cannabis sativa* against novel protein targets. To this end, MD analyses were conducted utilizing PyRx software (Dallakyan and Olson, 2015). Furthermore, the assessment of drug-like properties, encompassing absorption, distribution, metabolism, excretion, and toxicity (ADMET), alongside MDS, was performed using Schrödinger software (Schrödinger, 2016). These extensive analyses have provided a deeper insight into the efficacy and safety profiles of the investigated compounds.

2.1 Data collection

This study investigates the antifungal potential of stilbenoid and cannabinoid compounds derived from Cannabis sativa, utilizing eight fungal protein targets (Table 1; Table 2, and Supplementary Data S1). Eight fungal proteins selected in this study were identified due to their critical roles in the survival and pathogenicity mechanisms of fungal pathogens and were used as primary targets to evaluate the efficacy of antifungal compounds. GPI protein plays a central role in cell wall biosynthesis, ensuring fungal cell stability; targeting this protein allowed weakening of cellular structural integrity (Samalova et al., 2020). Enolase is a key enzyme in glycolysis and energy metabolism and has been evaluated as a potential target for inhibition of energy production (Avilán et al., 2011; Langenhorst et al., 2023). M2DH and M1P5DH proteins play an important role in the adaptation of fungal cells to stress conditions by participating in osmoregulation and mannitol metabolism; inhibition of these proteins contributed to the disruption of osmotic balance (Meena et al., 2015). GMP synthase (Rodriguez-Suarez et al., 2007) ve DHODH (Zameitat et al., 2007) proteins are essential for genetic material production and cell division by participating in purine and pyrimidine biosynthesis, respectively; targeting these proteins has demonstrated the potential to limit fungal growth by interfering with DNA/RNA synthesis. Heat Shock Protein 90 (Hsp90), a chaperone protein that regulates stress responses and protein folding processes, has been targeted to reduce adaptability to environmental stresses (Gupta, 1995). CaChs2 protein has a critical role in the synthesis of chitin in the cell wall and has been used as an important target in weakening cellular mechanical stability (Banks et al., 2005). These proteins represent vital fungal processes such as energy metabolism, cell wall stability, genetic material synthesis and osmoregulation and have made significant contributions to the main aim of the study to develop multi-target antifungal strategies and overcome antifungal resistance mechanisms.

While most of the analyzed targets had experimentally resolved structures available in the RCSB PDB database (Berman et al., 2000), two of the proteins lacked structural data. For these two proteins, AlphaFold's state-of-the-art protein structure prediction algorithm (Varadi et al., 2021) was employed to generate high-confidence models. This integration of AlphaFold predictions addressed a critical gap by enabling the inclusion of these fungal proteins, significantly enhancing the study's comprehensiveness. Structural validation showed that AlphaFold-predicted models aligned well with similar proteins from the PDB, as indicated by low RMSD values, ensuring the reliability of the predicted structures. Additionally, these models revealed critical binding sites and conformational details that facilitated robust molecular docking and dynamics simulations. By incorporating AlphaFold predictions, this study broadened the target protein repertoire, allowing for a more complete assessment of the antifungal potential of the tested compounds. The use of AlphaFold not only supplemented missing structural data but also enabled comparative analyses with human homologs, aiding in the identification of selective antifungal targets (Varadi and Velankar, 2022). While AlphaFold models require experimental validation (Mirabello et al., 2024), their inclusion provided a strong foundation for hypothesis-driven research and highlighted the transformative potential of this tool in drug discovery for less-characterized fungal targets. The comprehensive integration of AlphaFold-predicted models not only enhanced the study's ability to explore diverse fungal protein structures but also provided a robust framework for evaluating their critical roles in pathogenicity and survival.

TABLE 1 Proteins and their sources were used in this study.

Protein name	Source database	Source organism	Reference
Glycosylphosphatidylinositol (GPI)	AlphaFold	Candida albicans	UniProt ID: Q873N2
Enolase (AfEno1)	RCSB PDB	Aspergillus fumigatus	7rhv.pdb
Mannitol-2-dehydrogenase (M2DH) (AfM1PDH)	RCSB PDB	Aspergillus fumigatus	7rk4.pdb
Guanosine Monophosphate Synthase (GMP synthase)	RCSB PDB	Aspergillus fumigatus	7mo6.pdb
Dihydroorotate dehydrogenase (DHODH)	AlphaFold	Aspergillus nidulans	UniProt ID: Q12610
Heat shock protein 90 homolog (Hsp90)	RCSB PDB	Candida albicans	6cjs.pdb
Chitin Synthase 2 (CaChs2)	RCSB PDB	*Candida* albicans	7STO.pdb
Mannitol-1-phosphate 5-dehydrogenase (M1P5DH) AfM2DH	AlphaFold	Neosartorya fumigata	UniProt ID: A0A222WJM7

TABLE 2 List of Cannabinoid and Stilbenoid compounds analyzed in this study. The continuation of the list can be found in the supplementary materials.

Compound type	Name of compound	Molecular formula
Cannabinoid	Cannabiorcol	C17H18O2
Cannabinoid	Δ9-trans-Tetrahydrocannabiorcol	C17H22O2
Cannabinoid	Cannabidiorcol	C17H22O2
Cannabinoid	Nor-Cannabivarin (cannabinol-C2)	C18H20O2
Cannabinoid	Δ9-trans-Tetrahydrocannabiorcolic acid	C18H22O4
Stilbenoid	Cannabispirone	C15H18O3
Stilbenoid	Cannabispirenone-A	C15H16O3
Stilbenoid	Isocannabispirenone	C15H20O3
Stilbenoid	Isocannabispiradienone	C15H14O3
Stilbenoid	Cannabispirenone-B	C15H16O3

2.2 Biological roles and signaling pathways of eight proteins

In this study, Cytoscape (v. 3.10.3) was used for network-based visualization and analysis together with KEGG Pathway (Varadi and Velankar, 2022), UniProt (Coudert et al., 2022) and Reactome (Milacic et al., 2023) databases to determine the molecular and cellular functions of eight fungal protein targets and to analyze the signaling pathways associated with these proteins. The roles of proteins in biological processes, molecular functions and cellular components were analyzed based on the information obtained from these databases. First, the functional properties and associated biological processes of each protein were characterized in detail using the UniProt database. The KEGG Pathway database was used to identify and detail the metabolic pathways and possible signaling mechanisms in which these proteins are involved. The Reactome database was used for in-depth analysis of specific biological pathways in which the proteins are involved, and a comprehensive and systematic evaluation of these pathways was performed.

In addition, Cytoscape software (Shannon et al., 2003) was used to visualize the obtained data relationships and interactions between proteins more clearly. This software was used as a critical tool in detailing the relationships and common functional pathways of proteins, providing the opportunity to effectively visualize the connections and shared biological processes between proteins. These comprehensive database searches and network analyses provided information about the cellular locations and molecular functions of the proteins, as well as revealed their interrelationships and common functional pathways. This methodological approach allowed for extensive functional analysis to understand both independent and coordinated roles of the proteins and provided a multifaceted perspective to evaluate the antifungal therapeutic potential of related proteins.

2.3 Molecular docking

Docking studies were performed using the PyRx software, incorporating the AutoDock Vina algorithm (Morris et al., 2009). Before docking, proteins were prepared by removing water molecules and cofactors, followed by energy minimization to optimize their structure. Ligands were retrieved from chemical databases in SMILES format, and their initial structures were subjected to a systematic workflow for generating conformations. Using Open Babel's systematic rotor search method, multiple ligand

conformations were generated by exploring rotatable bonds to ensure a comprehensive sampling of conformational space, vital for accurately representing biologically relevant poses. The best conformer based on energy minimization was selected for docking. For each protein, a grid box around the active site was defined, with dimensions set to adequately encompass the binding region (x = 40 Å, y = 40 Å, z = 40 Å). The docking procedure was carried out using the AutoDock Vina algorithm, with specific center coordinates and grid dimensions settings. Parameters such as exhaustiveness (set at 8) and the number of binding modes to be analyzed (set at 10) were adjusted to ensure thorough exploration of potential ligand orientations. The outcomes of the docking process, including binding affinity values and binding positions, were carefully evaluated to identify the most promising candidates. Ligands showing the highest binding affinities were subsequently selected for further MDS.

2.4 Molecular dynamics simulations (MDS)

In this study, MDS was conducted on eight target proteins, each paired with two ligands, to evaluate each protein-ligand complex's binding stability and interaction profiles. The simulations were performed using the Schrödinger Maestro 2021–3 software suite for 100 nanoseconds (ns) at 310 K (K) temperature within the NPT ensemble. Schrödinger's Desmond module facilitated the simulations, allowing for the analysis of structural stability, dynamic behavior, and specific interactions at the protein-ligand binding sites.

The selected protein-ligand complexes underwent solvation and ionization processes following the initial docking. The TIP3P water model was used for solvation, and the systems were neutralized with Na+ and Cl-ions to maintain physiological conditions. The simulation protocol consisted of three main phases: a heating phase from 0 to 10 ns, an equilibration phase from 10 to 20 ns, and a production phase from 20 to 100 ns. Data from the simulations were analyzed to calculate Root Mean Square Deviation (RMSD) and Root Mean Square Fluctuation (RMSF) values, providing insights into protein-ligand interactions, binding energies, and overall system stability.

Further analysis was conducted using Schrödinger's Prime MM-GBSA and Maestro modules to calculate the binding free energy and to characterize ligand binding modes. The force field parameters for the small molecules were generated using the OPLS3e force field within the Schrödinger software. This parameterization utilized the molecular structures of the ligands, and the automatic force field assignment ensured an accurate representation of intramolecular and intermolecular interactions. These comprehensive analyses provided profound insights into the protein-ligand complexes' interaction profiles and binding stabilities.

2.5 ADMET analysis

The ADMET (Absorption, Distribution, Metabolism, Excretion, and Toxicity) analysis was performed using the Schrödinger QikProp module to assess the drug-like properties of the selected compounds. This analysis aimed to evaluate various pharmacokinetic parameters crucial for determining the safety and efficacy of potential drug candidates. Specifically, QikProp was used to calculate parameters such as molecular weight (mol_MW), solvent-accessible surface area (SASA), the number of hydrogen bond donors (donorHB) and acceptors (accptHB), logP (partition coefficient), potential for hERG inhibition (QPlogHERG), Caco-2 cell permeability (QPPCaco), BBB permeability (QPlogBB), and plasma protein binding affinity (QPlogKhsa). These pharmacokinetic descriptors comprehensively evaluated the compounds' ADMET profiles, allowing for an informed assessment of their drug-likeness, bioavailability, and potential safety profiles. In addition to pharmacokinetic evaluations, toxicity analyses were also performed using the Schrödinger QikProp module to provide safety profiles of the tested compounds. QikProp provided reliable estimates of toxicity-related parameters such as Ames test results (mutagenicity potential), LD50 values (acute oral toxicity, in mg/kg), and cardiotoxicity potential via hERG channel inhibition (QPlogHERG). These parameters were calculated together with other descriptors such as accessible surface area in solution (SASA), logP (partition coefficient), and hydrogen bonding capacity (donorHB and accptHB), providing a comprehensive understanding of the safety profile of each compound. While Ames test estimates were classified as mutagenic or non-mutagenic, LD50 values provided quantitative information on the risk of acute toxicity. The integration of these toxicity descriptors with pharmacokinetic properties provided a balanced assessment of the therapeutic potential of compounds and allowed informed decisions to be made during the antifungal drug development process.

3 Results

3.1 Biological roles and signaling pathways

This study provides a comprehensive evaluation of the functional roles and involvement of eight different fungal target proteins in biological processes (Table 3; Figure 1). GPI (Glycosylphosphatidylinositol) is localized in the endoplasmic reticulum and membrane, playing a central role in GPI anchor biosynthesis, which is critical for regulating protein attachment to the cell surface. Enolase is found in the cytoplasm and cytosol, contributing to fundamental energy metabolism pathways, specifically glycolysis and ribonucleotide catabolism. M2DH exhibits oxidoreductase activity involved in the metabolism of mannitol and other polyol derivatives, supporting energy storage and osmotic balance. GMP Synthase plays a key role in nucleotide metabolic pathways, such as ribonucleotide and purine biosynthesis, while also contributing to cellular biosynthesis through diverse molecular activities like ATP binding. DHODH localizes the mitochondrial inner membrane, where it facilitates *de novo* pyrimidine biosynthesis, which is crucial for nucleotide production. Hsp90 plays a role in protein folding, stabilization, and biological regulation processes, regulating stress responses and cellular growth. CaChs2 is involved in chitin biosynthesis and glycosyltransferase activities, participating in cell wall biosynthesis and maintaining cellular stability. M1P5DH is involved in mannitol

TABLE 3 Comprehensive representation of the molecular functions, biological processes, and cellular localizations of eight target proteins.

Go category	GPI (glycosylphosphatidylinositol)	Enolase (AfEno1)	M2DH	GMP synthase	DHODH	Hsp90	Chitin synthase (CaChs2)	M1P5DH
Molecular Function	O-acyltransferase activity, acyltransferase activity, glucosaminyl-phosphatidylinositol O-acyltransferase activity	cation binding, magnesium ion binding, ion binding, metal ion binding, lyase activity, catalytic activity, protein-containing complex binding, hydro-lyase activity, phosphopyruvate hydratase activity	catalytic activity, oxidoreductase activity, mannitol 2-dehydrogenase activity, oxidoreductase activity acting on the CH-OH group of donors, hexitol dehydrogenase activity	ion binding, binding, nucleoside phosphate binding, purine nucleotide binding, organic cyclic compound binding, adenyl nucleotide binding, nucleotide binding, heterocyclic compound binding, ATP binding, carbohydrate derivative binding, anion binding	oxidoreductase activity, dihydroorotate dehydrogenase activity, dihydroorotate dehydrogenase (quinone) activity	ion binding, ATP-dependent protein folding chaperone, protein folding chaperone	UDP-glycosyltransferase activity, glycosyltransferase activity, chitin synthase activity, acetylglucosaminyltransferase activity, transferase activity, hexosyltransferase activity	oxidoreductase activity, mannitol-1-phosphate 5-dehydrogenase activity
Biological Process	GPI anchor biosynthetic process	glycolytic process, ribonucleotide catabolic process, carbohydrate catabolic process, pyridine nucleotide catabolic process, small molecule metabolic process, organic acid metabolic process, nucleoside phosphate catabolic process	carbohydrate catabolic process, small molecule metabolic process, mannitol metabolic process, hexitol metabolic process, polyol metabolic process, organic hydroxy compound metabolic process, alcohol metabolic process, alditol metabolic process, metabolic process	carbohydrate derivative metabolic process, ribose phosphate metabolic process, purine ribonucleoside monophosphate biosynthetic process, nucleotide biosynthetic process, purine ribonucleotide biosynthetic process, nucleobase-containing compound metabolic process, ribonucleotide biosynthetic process, purine nucleoside monophosphate biosynthetic process, purine ribonucleoside monophosphate metabolic process, purine nucleotide metabolic process, ribonucleotide metabolic process, ribonucleoside monophosphate metabolic process,	'*de novo*' pyrimidine nucleobase biosynthetic process, pyrimidine ribonucleotide biosynthetic process, '*de novo*' UMP biosynthetic process	primary metabolic process, metabolic process, cellular process, regulation of protein stability, protein stabilization, protein folding, biological regulation, growth	carbohydrate derivative metabolic process, metabolic process, cellular process	mannitol metabolic process

(Continued on following page)

10.3389/fchem.2024.1515424

TABLE 3 (*Continued*) Comprehensive representation of the molecular functions, biological processes, and cellular localizations of eight target proteins.

Go category	GPI (glycosylphosphatidylinositol)	Enolase (AfEno1)	M2DH	GMP synthase	DHODH	Hsp90	Chitin synthase (CaChs2)	M1P5DH
				nucleobase-containing small molecule metabolic process, purine-containing compound biosynthetic process				
Cellular Component	endoplasmic reticulum, endoplasmic reticulum membrane, membrane	cytoplasm, catalytic complex, cytosol, phosphopyruvate hydratase complex, protein-containing complex, cellular anatomical structure	cytoplasm	cytoplasm, intracellular anatomical structure	mitochondrial inner membrane, intracellular anatomical structure	membrane, cytoplasm, cytosol, plasma membrane, fungal-type cell wall, cell wall, external encapsulating structure, hyphal cell wall, cell periphery, cell surface, membrane-bounded organelle	membrane, cell wall, external encapsulating structure, cellular anatomical structure	cytoplasm, cytosol

metabolism and operates in the cytoplasm to regulate energy storage and osmotic balance.

The analysis of shared biological processes and cellular components highlights how these proteins interact with each other and the potential synergistic relationships among them (Supplementary Data S2). For instance, Enolase and GMP Synthase share similar molecular functions, such as "ATP binding" and "organic compound binding," indicating parallel roles in energy metabolism. Additionally, GMP Synthase and Hsp90 both localize in the cytosol and plasma membrane, whereas CaChs2 and GPI contribute to cell wall biosynthesis, maintaining cellular stability and regulating membrane-associated structural processes. This comprehensive assessment underscores the coordinated roles of these eight fungal proteins in biological processes and highlights their importance as potential targets for antifungal strategies.

3.2 Molecular docking

As a result of the MD and MDS, the ligands with the best binding affinities and their pharmacokinetic profiles were evaluated. According to Table 4, the docking studies reveal the binding affinities between various proteins and selected cannabinoid and stilbenoid compounds, measured in kcal/mol. Using PyRx software and the AutoDock Vina (Morris et al., 2009) algorithm, we assessed the interaction strengths of these protein-ligand pairs. The proteins included Hsp90, GMP synthase, Enolase, Mannitol-2-dehydrogenase, CaChs2, Glycosylphosphatidylinositol, M1P5DH, and DHODH. For Hsp90, the binding affinities with Hexahydrocannabinol and 5-OH-7-MeO-Indan-Spiro-Cyclohexane were −8.2 and −8.3 kcal/mol, respectively. GMP synthase showed a high binding affinity with Cannabistilbene I at −9.1 kcal/mol and a lower affinity with Δ9-cis-THC at −7.2 kcal/mol. Enolase had binding affinities of −7.1 kcal/mol with Cannabinolic acid and −7.8 kcal/mol with 8-hydroxycannabinolic acid. Mannitol-2-dehydrogenase interacted with Δ9-trans-THC and 8a-Hydroxy-Δ9-trans-THC showing affinities of −7.1 and −7.7 kcal/mol, respectively. CaChs2 strongly binds with Cannabistilbene I at −9.1 kcal/mol and moderate binding with Cannabidivarinic acid (CBDVA) at −7.6 kcal/mol. Glycosylphosphatidylinositol had affinities of −8.2 kcal/mol with both 3-Butyl-Δ9-THC and Δ9-trans-THC. M1P5DH showed affinities of −7.1 kcal/mol with Cannabinolic acid and −7.8 kcal/mol with 8-hydroxycannabinolic acid. Lastly, DHODH exhibited affinities of −7.6 kcal/mol with Cannabiglendol and −7.5 kcal/mol with Cannabicitran. The highest binding affinities were observed with GMP synthase and CaChs2 interacting with Cannabistilbene I, both at −9.1 kcal/mol, indicating a strong interaction. In comparison, the lowest affinity values were noted at −7.1 kcal/mol for several protein-ligand pairs, suggesting moderate interactions. These results highlight the potential of these compounds as antifungal agents and provide a basis for further MDS and biological validations.

As shown in Figure 2, the binding affinities and interaction profiles of eight different proteins with selected cannabinoid and stilbenoid compounds were evaluated. Hydrogen bonds and hydrophobic interactions play significant roles in the interactions of Hsp90 with Hexahydrocannabinol and 5-OH-7-MeO-Indan-

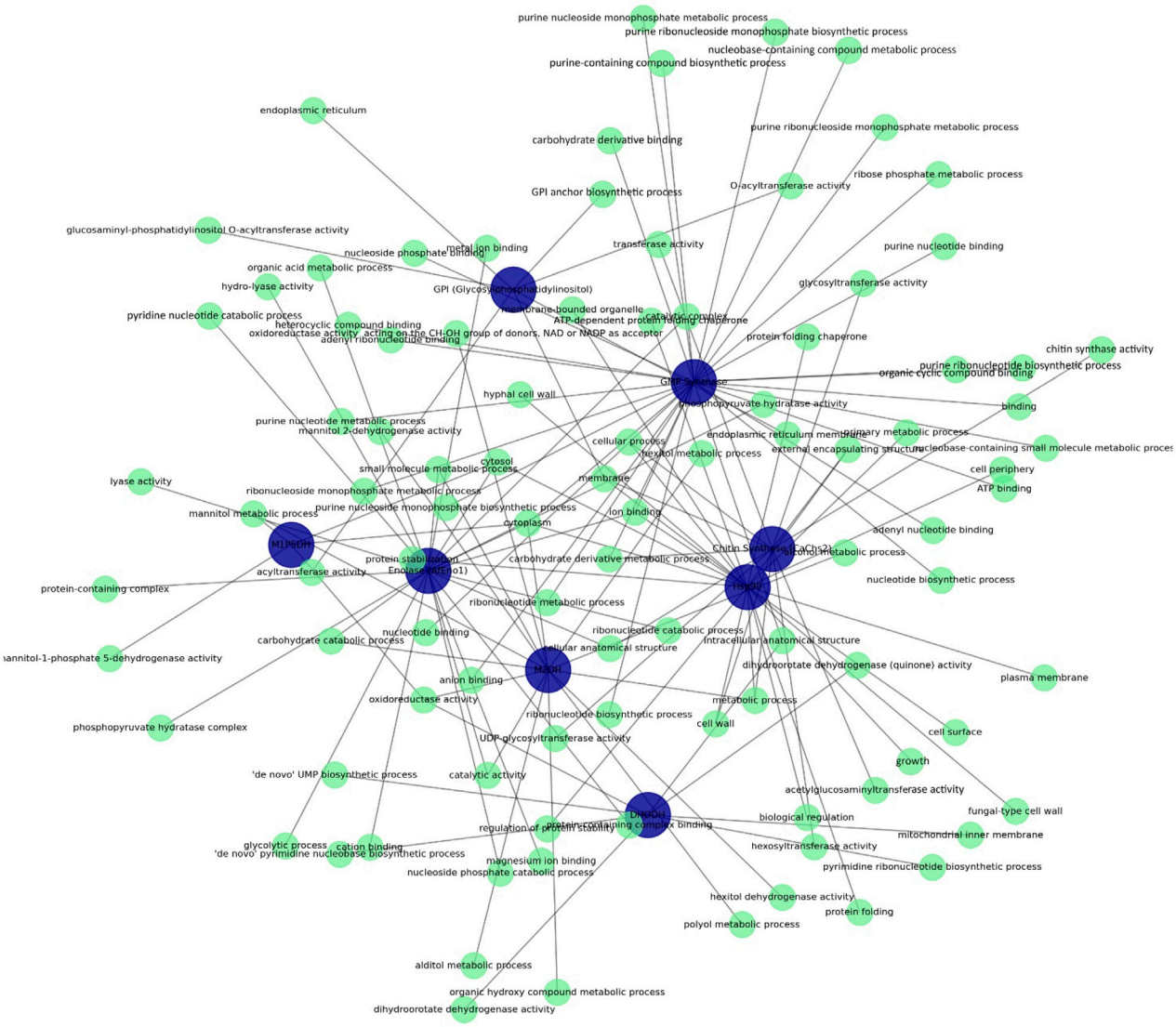

FIGURE 1
Functional interaction network of target proteins highlighting molecular functions, biological processes, and cellular components.

Spiro-Cyclohexane. GMP synthase exhibited a high binding affinity with Cannabistilbene I at −9.1 kcal/mol, indicating strong hydrophobic interactions and multiple hydrogen bonds with the ligand. Significant contributions from hydrogen bonds and hydrophobic regions characterized enolase interactions with Cannabinolic acid and 8-hydroxycannabinolic acid. Mannitol-2-dehydrogenase demonstrates moderate binding affinities (−7.1 to −7.7 kcal/mol) with Δ9-trans-THC and 8a-Hydroxy-Δ9-trans-THC, where hydrogen bonds and hydrophobic interactions are crucial. CaChs2 strongly binds with Cannabistilbene I (−9.1 kcal/mol) but has a lower affinity with CBDVA (−7.6 kcal/mol). Glycosylphosphatidylinositol has binding affinities of −8.2 kcal/mol with both 3-Butyl-Δ9-THC and Δ9-trans-Tetrahydrocannabiorcol. M1P5DH exhibited binding affinities of −7.1 kcal/mol with Cannabinolic acid and −7.8 kcal/mol with 8-hydroxycannabinolic acid. Finally, DHODH showed binding affinities of −7.6 kcal/mol with Cannabiglendol and −7.5 kcal/mol with Cannabicitran. Solvent exposure is observed in the DHODH-Cannabicitran and GMP synthase-Δ9-cis-THC complexes.

3.3 ADMET profile prediction

Table 4 displays the ADMET properties of various ligands, highlighting significant differences in their pharmacokinetic and toxicity profiles. Hexahydrocannabinol shows high lipophilicity (QPlogPo/w 5.724) and potential HERG inhibition (−4.8), with excellent intestinal permeability (QPPCaco 4,522.262) but moderate brain penetration (QPlogBB −0.096). Its non-mutagenic classification and moderate LD50 value of 2000 mg/kg suggest an acceptable safety profile. In contrast, Cannabistilbene I, a standout candidate, exhibits moderate lipophilicity (QPlogPo/w 4.004) and HERG inhibition risk (−3.435), with lower intestinal permeability

TABLE 4 Docking binding affinities, MM-GBSA binding free energies, and ADMET properties of protein-ligand complexes.

Protein	Ligand	Docking binding affinity (kcal/mol)	MM-GBSA ΔG (kcal/mol)	QPlogPo/w (lipophilicity)	QPlogHERG (hERG inhibition, log (mol/L))	QPPCaco (intestinal permeability, nm/s)	Ames test (mutagenicity)	LD50 (mg/kg)
Hsp90	Hexahydrocannabinol	−8.2	−82	5.724	−4.8	4,522.262	Non-Mutagenic	2000
Hsp90	5-OH-7-MeO-Indan-Spiro-Cyclohexane	−8.3	−83	3.45	−3.751	3,035.311	Non-Mutagenic	1500
GMP synthase	Cannabistilbene I	−9.1	−91	4.004	−3.435	1,318	Non-Mutagenic	2500
GMP synthase	Δ9-cis-Tetrahydrocannabinol	−7.2	−72	5.663	−4.894	4,571.459	Mutagenic	1000
Enolase	Cannabinolic acid	−7.1	−71	5.533	−3.228	276.554	Non-Mutagenic	2000
Enolase	8-hydroxycannabinolic acid	−7.8	−78	4.8	−3.197	95.563	Non-Mutagenic	1900
Mannitol-2-dehydrogenase	Δ9-trans-Tetrahydrocannabinol	−7.1	−71	5.466	−2.874	267.368	Non-Mutagenic	1800
Mannitol-2-dehydrogenase	8a-Hydroxy-Δ9-Transtetrahydrocannabinol	−7.7	−77	4.584	−4.819	1,915.497	Mutagenic	1200
Chitin Synthase 2	Cannabistilbene I	−9.1	−91	4.004	−3.435	1,318	Non-Mutagenic	2500
Chitin Synthase 2	Cannabidivarinic acid	−7.6	−76	4.874	−2.417	253.686	Non-Mutagenic	2000
Glycosylphosphatidylinositol	Butyl-Δ9-THC	−8.2	−82	5.262	−4.687	4,438.445	Mutagenic	1200
Glycosylphosphatidylinositol	Δ9-trans-Tetrahydrocannabiorcol	−8.2	−82	4.107	−4.049	4,453.091	Non-Mutagenic	1500
Mannitol-1-phosphate 5-dehydrogenase	Cannabinolic acid	−7.1	−71	5.533	−3.228	276.554	Non-Mutagenic	2000
Mannitol-1-phosphate 5-dehydrogenase	8-hydroxycannabinolic acid	−7.8	−78	4.8	−3.197	95.563	Non-Mutagenic	1900
DHODH	Cannabiglendol	−7.6	−76	4.258	−4.009	3,007.355	Non-Mutagenic	1700
DHODH	Cannabicitran	−7.5	−75	4.973	−4.511	9,906.038	Non-Mutagenic	1600

10.3389/fchem.2024.1515424

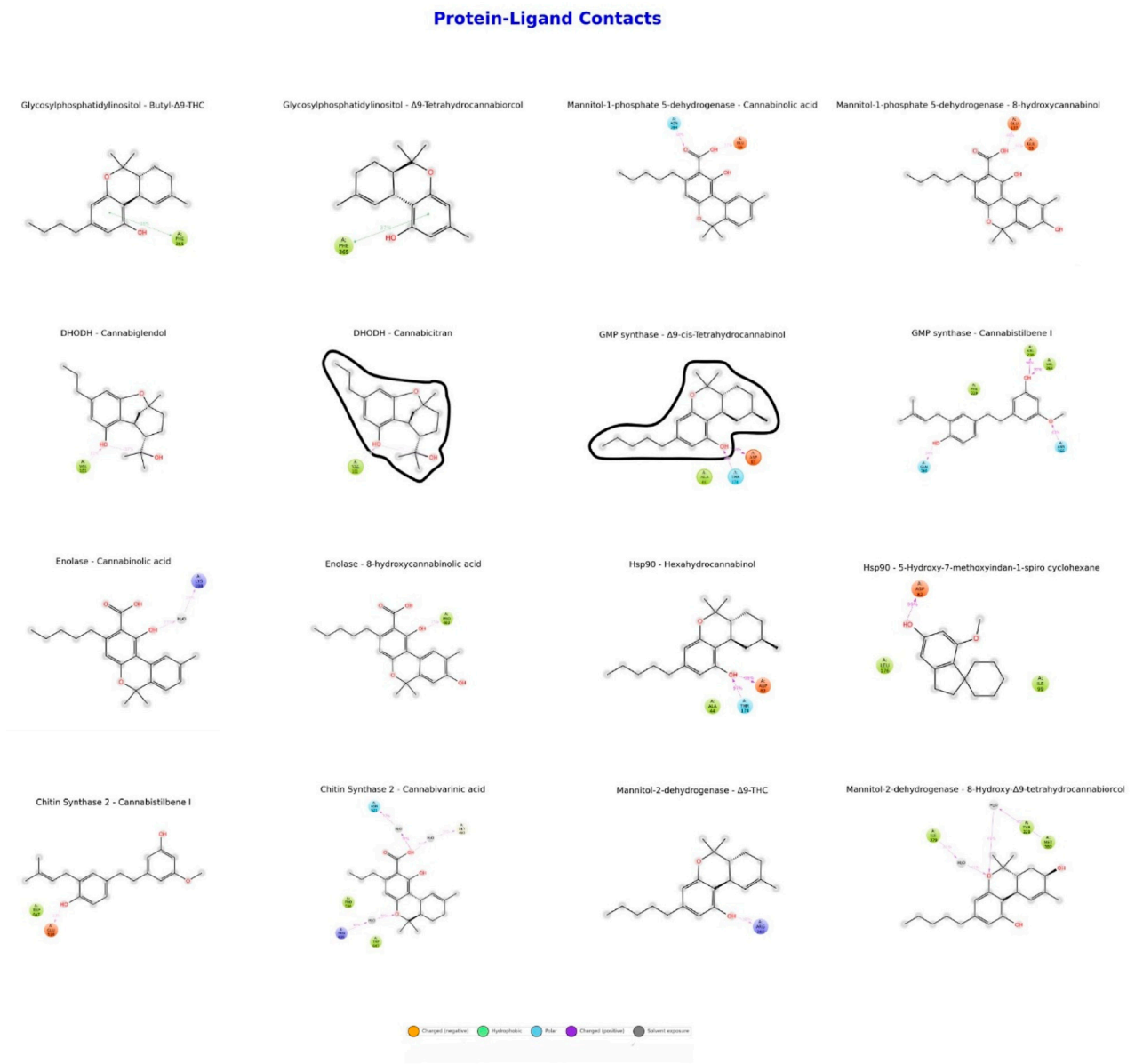

FIGURE 2
Binding affinities and interaction profiles of protein-ligand complexes.

(QPPCaco 1,318) but strong toxicity results, including a non-mutagenic Ames test outcome and a favorable LD50 of 2,500 mg/kg, indicating low acute toxicity. Δ9-cis-THC and 3-Butyl-Δ9-THC both demonstrate high lipophilicity and HERG inhibition risk, coupled with mutagenic potential and lower LD50 values (1,000–1,200 mg/kg), raising safety concerns despite their substantial intestinal permeability.Enolase ligands, Cannabinolic acid, and 8-hydroxycannabinolic acid, display moderate lipophilicity, low intestinal permeability, and a non-mutagenic profile, with LD50 values of 2,000 mg/kg and 1,900 mg/kg, respectively, supporting their safety. DHODH ligands, Cannabiglendol and Cannabicitran, show moderate lipophilicity and HERG inhibition, with Cannabicitran standing out due to its notably higher intestinal permeability (QPPCaco 9,906.038) and an LD50 of 1,600 mg/kg, indicating potential safety concerns compared to Cannabiglendol (LD50 1,700 mg/kg).Overall, these results underline the balance between efficacy and safety, with Cannabistilbene I emerging as a promising candidate due to its favorable ADMET and toxicity profile, while compounds such as Δ9-cis-THC and 3-Butyl-Δ9-THC require caution due to their mutagenicity and lower LD50 values.

3.4 Molecular dynamics simulation analysis

The RMSD analyses presented in Figure 3 have assessed the structural changes of protein-ligand complexes over time. In the GMP synthase-Δ9-cis-THC complex, the protein RMSD values remain steady between 2–4 Å, indicating structural stability, while the ligand RMSD values vary between 1–2 Å, suggesting a

high binding stability of the ligand. Conversely, the CaChs2-Cannabistilbene I complex exhibits protein RMSD values fluctuating between 6–10 Å, indicating some flexibility in the protein structure. The ligand RMSD values, ranging from 4 to 7 Å, reflect movements within the ligand binding site. For the CaChs2-Cannabivarinic acid complex, the protein RMSD values are stable between 6–9 Å, while the ligand RMSD values range from 5 to 8 Å, indicating moderate ligand stability. In the DHODH-Cannabicitran complex, the protein RMSD values remain consistent between 1–2 Å, demonstrating a very stable structure, but the ligand RMSD values fluctuate significantly between 10–20 Å, indicating substantial movements within the ligand binding site. The Enolase-Cannabinolic acid complex displays protein RMSD values consistently between 1–2 Å, reflecting high structural stability, with ligand RMSD values between 2–6 Å, indicating good ligand stability. The M1P5DH-Cannabinolic acid complex exhibits protein RMSD values stable between 2–3 Å, indicating structural stability, with ligand RMSD values ranging from 2 to 4 Å, reflecting high ligand stability. The Mannitol-2-dehydrogenase-Δ9-THC complex displays protein RMSD values stable between 2–3 Å, indicating structural stability, with ligand RMSD values between 2–4 Å, reflecting high ligand stability. For the Hsp90-5-Hydroxy-7-methoxyindan-1-spiro cyclohexane complex, protein RMSD values remain steady between 2–3 Å, indicating structural stability, while ligand RMSD values range from 3 to 6 Å, reflecting moderate ligand stability. In the Hsp90-Hexahydrocannabinol complex, protein RMSD values are stable between 3–4 Å, indicating structural stability, while ligand RMSD values vary between 5–8 Å, indicating moderate ligand stability. This detailed analysis provides insights into the stability and flexibility of protein-ligand interactions across various complexes, highlighting the importance of both protein and ligand dynamics in the context of structural biology. The GMP synthase-Δ9-cis-THC, Enolase-Cannabinolic acid, M1P5DH-Cannabinolic acid, Mannitol-2-dehydrogenase-Δ9-THC, and Hsp90-5-Hydroxy-7-methoxyindan-1-spiro cyclohexane complexes stand out for their excellent performance, reflecting high stability and strong binding interactions, crucial factors for future structural or therapeutic considerations.

The evaluations presented in Figure 4 are crucial for assessing these interactions. During the interaction between CaChs2 and Cannabidiolene I, high protein stability was observed, with slight increases in ligand RMSF (Root Mean Square Fluctuation) values at specific atoms. Conversely, the interaction with Cannabidiolic acid showed very low ligand RMSF values. In the interactions of DHODH protein with Cannabidiolic acid and Cannabidiolid, moderate protein mobility was noted, but the ligand RMSF values were lower compared to the protein. For Enolase, interactions with 9-Hydroxycannabidiolic acid exhibited increased mobility at certain atoms, whereas interactions with Cannabidiolic acid showed that the ligand stabilized the protein. The Glycosylphosphatidylinositol protein did not exhibit significant mobility differences in interactions with Bu-9-Δ9-THC and Δ9-Tetrahydrocannabidiolic acid. During the interaction of GMP Synthase with Cannabidiolene I, there was an increase in protein RMSF values, while there was no significant difference with cis-3-Hexenylcannabidiol. The Hsp90 protein displayed high mobility when interacting with 5-Hydroxy-7-methoxycoumarin-4-piperidone, whereas it exhibited low RMSF values with Hexahydrocannabinol. The M1P5DH protein showed low RMSF values and stability in interactions with both 8-Hydroxycannabidiolic acid and Cannabidiolic acid. However, in the interaction of Mannitol-2-dehydrogenase protein with 8-Hydroxy-Δ9-Tetrahydrocannabidiolic acid, a significant increase in RMSF was observed, particularly after atom 25, whereas no significant difference was noted with Δ9-THC. These results elucidate the impact of ligands on protein stability and reveal dynamic interactions in specific regions.

4 Discussion

This study aims to investigate the potential of selected cannabinoid and stilbenoid compounds as antifungal agents by evaluating their binding affinities and interaction profiles with eight fungal proteins. The eight fungal proteins investigated are associated with signaling pathways and biochemical functions that play critical roles in cellular homeostasis and pathogenic processes. Important information is included to uncover the antifungal potential of these targets by describing the molecular roles, biological mechanisms, and cellular locations of these proteins. The selected proteins include GPI, Enolase, M2DH, GMP Synthase, DHODH, Hsp90, Chitin Synthase, and M1P5DH. These proteins were included in the study because they contribute to a wide range of biological functions. In particular, GPI plays a central role in GPI anchor biosynthesis by regulating the binding of proteins to the cell surface and maintains the stability of the cellular structure (Álvarez-Sánchez et al., 2024). Therefore, GPI was selected as an antifungal target due to its potential to interfere with cell wall-associated biosynthetic processes. Enolase is involved in the basic pathways of energy metabolism such as glycolysis and ribonucleotide catabolism, and inhibition of these processes may prevent fungal growth by stopping energy production (Dasari et al., 2019; Díaz-Ramos et al., 2012). M2DH contributes to energy storage and osmotic balance by participating in the metabolism of mannitol and other polyol derivatives, which makes it an important strategic target that can weaken cellular stress resistance (Upadhyay et al., 2015). GMP Synthase plays a critical role in nucleotide biosynthesis pathways, especially ribonucleotide and purine biosynthesis, and inhibition of these processes can directly affect cell division (Oliver et al., 2013). DHODH supports *de novo* pyrimidine biosynthesis by localizing to the inner mitochondrial membrane, which is important for the production of nucleotides required for DNA and RNA synthesis (Hai et al., 2024; Rawls et al., 2000). Hsp90 regulates the resistance of pathogenic fungi to environmental stresses by acting in protein folding, stabilization and biological regulation processes, and therefore has significant potential as an antifungal target (Hoter et al., 2018; Wei et al., 2024). CaChs2 plays a critical role in cell wall biosynthesis through chitin synthesis and glycosyltransferase activities; since chitin is one of the main components of the fungal cell wall, inhibition of this protein may lead to weakening of the cell wall (Lenardon et al., 2010; Merzendorfer, 2011). M1P5DH is localized in the cytoplasm and contributes to energy storage and osmotic balance processes through mannitol metabolism; therefore, inhibition of mannitol may weaken the resistance of fungi to osmotic stress (Lim et al., 2021). Selecting

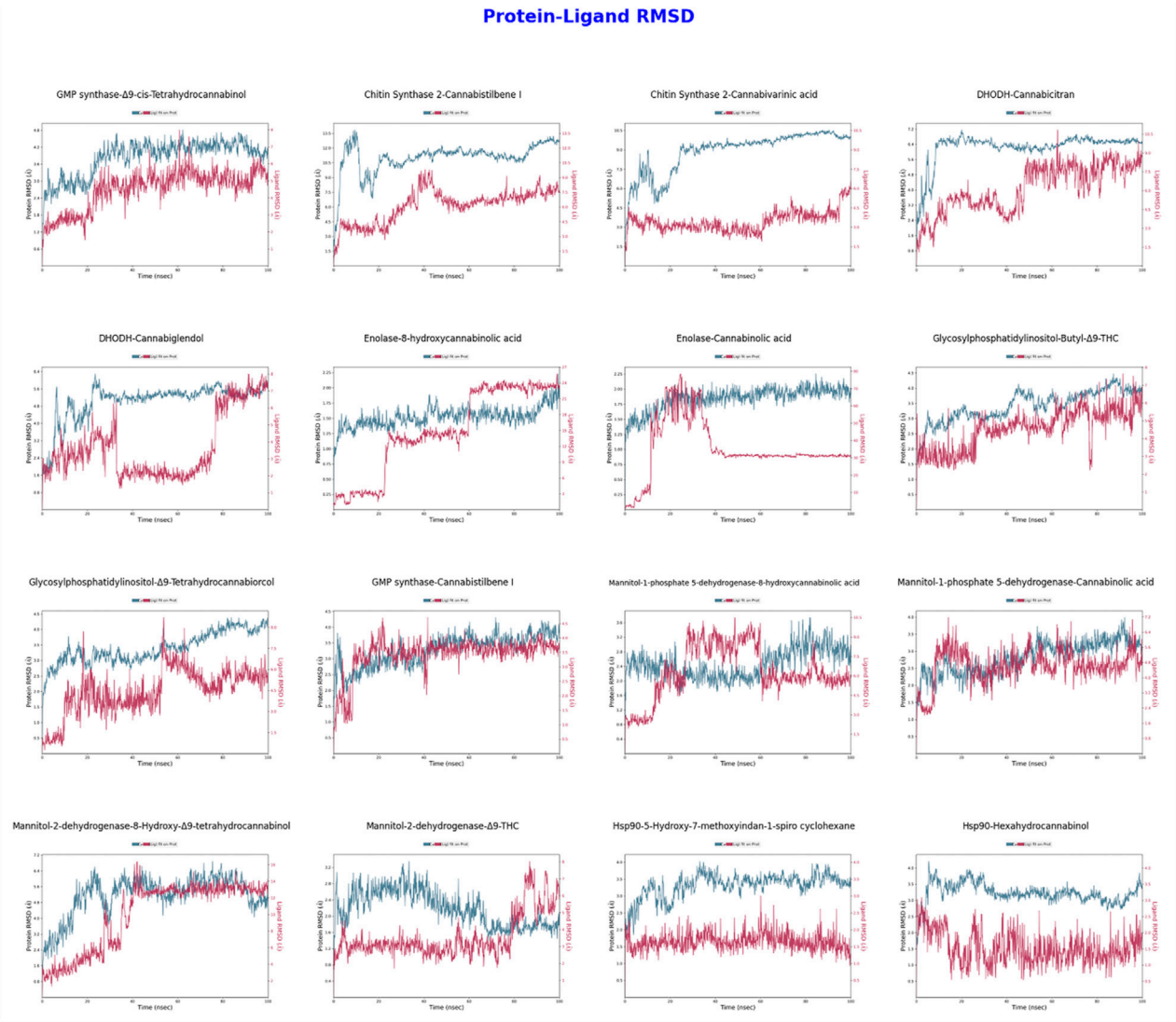

FIGURE 3
Protein-Ligand RMSD values obtained from molecular dynamics simulations conducted with two ligands for each of eight different proteins. The simulations were performed for 100 ns in the NPT ensemble at a temperature of 310 K. Each graph plots the RMSD values for both protein and ligand against time.

proteins from different fungal strains increases the versatility and scope of our study. There are phylogenetic differences between these strains, and it is anticipated that proteins from each strain may exhibit unique properties in ligand binding performance. This approach has allowed us to better understand the diversity of ligand trafficking in proteins from different strains and to conduct comprehensive analyses in a wide biological spectrum. In addition, this diversity is crucial for increasing the potential of the selected ligands to work in a wide range of fungi as their biological targets, thereby enhancing the overall applicability of our findings. Furthermore, the multi-target nature of this study highlights the potential for synergistic effects by simultaneously inhibiting multiple fungal proteins involved in distinct yet complementary pathways. For instance, targeting proteins associated with energy metabolism, cell wall synthesis, and stress response simultaneously could enhance antifungal efficacy by disrupting multiple critical functions (Fisher et al., 2024).In our study, the selected protein targets were evaluated as protein models that could provide potential therapeutic effects on clinically important pathogenic fungal species. These protein targets are particularly associated with pathogenic species such as *Candida* albicans and Aspergillus fumigatus, which are the main causes of hospital-associated infections and can develop resistance to treatment. For example, Hsp90 plays a critical therapeutic role in important fungal pathogens such as *Candida* albicans, and this pathogen is known for its nosocomial infections and resistance to treatment. Aspergillus fumigatus, where the other target protein is GMP synthase, is another important pathogen that can become resistant to treatment and commonly cause infections in hospitals. In addition, proteins such as CaChs2 and Enolase AfEno1 are proteins that can potentially contribute to treatment by targeting the resistance mechanisms exhibited by pathogens such as *Candida*

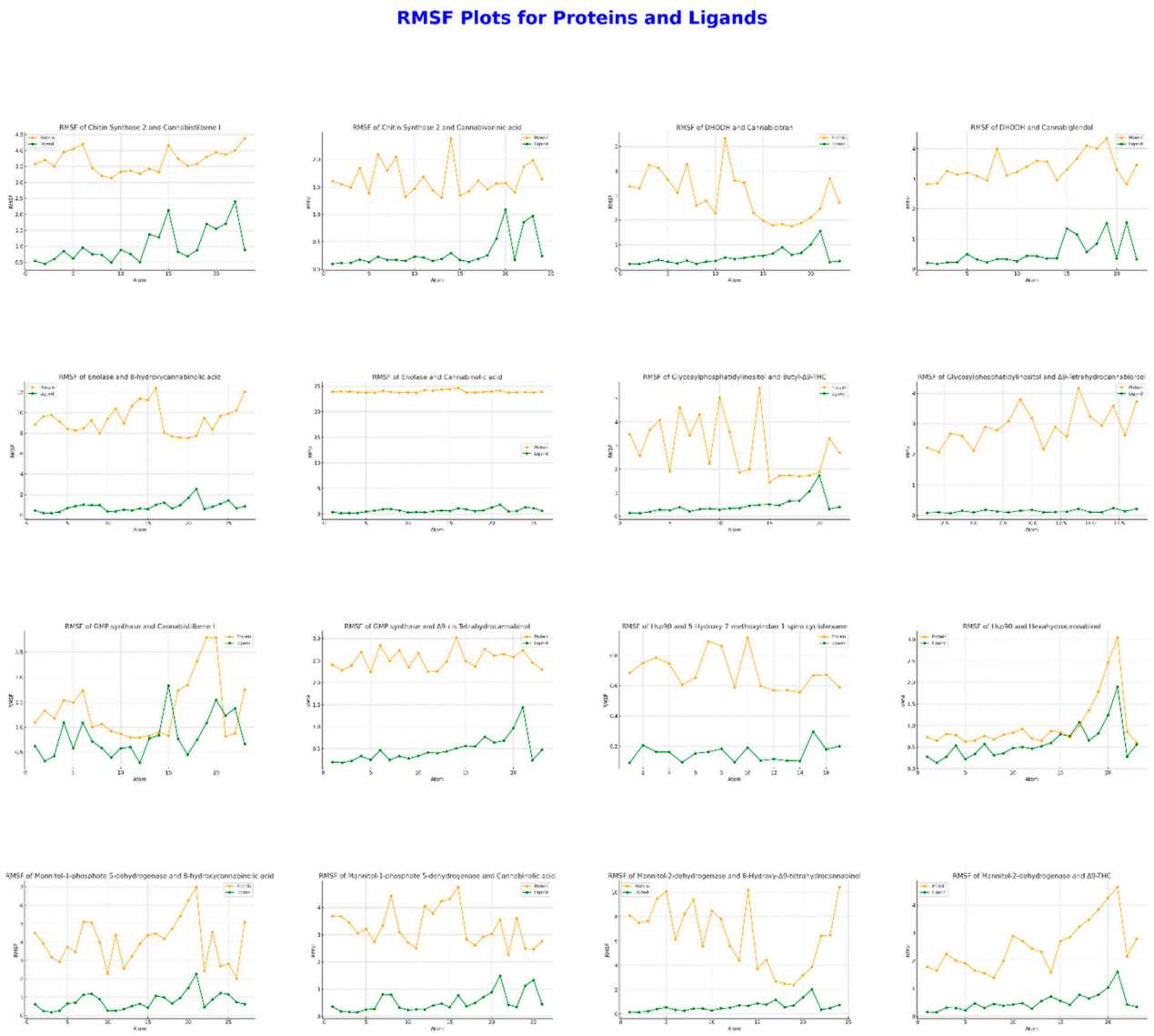

FIGURE 4
Protein-Ligand RMSF Values: Results Obtained from Molecular Dynamics Simulations with Two Ligands for Each of Eight Different Proteins. In Each Graph, the RMSF Values for Both Protein and Ligand are Plotted Against Atom Number.

spp. and Aspergillus spp. against antifungal treatment. The selected protein targets are of greater clinical importance due to the resistance of fungal infections to treatment. For example, GPI is a critical component of the cell wall of *Candida* albicans, while enzymes such as M2DH and M1P5DH are part of critical metabolic pathways in Aspergillus fumigatus, and DHODH is an important biosynthetic enzyme in other fungal species such as Aspergillus nidulans. Selection of these proteins is directly linked to resistance to therapy in different fungal species, and inhibition of these proteins may allow the development of new therapeutic strategies.

In light of recent comprehensive reviews, such as (Rabaan et al., 2023; Fisher et al., 2022), which emphasize the increasing prevalence of antifungal resistance, the importance of multi-target strategies becomes even more apparent. Antifungal resistance mechanisms, including efflux pump overexpression, biofilm formation, and genetic alterations in target sites, significantly hinder the efficacy of current therapies. Addressing these mechanisms through a multi-target approach not only has the potential to mitigate resistance but also aligns with global initiatives aimed at developing novel antifungal agents with broader activity spectra and reduced resistance potential. While the potential for antagonistic interactions between targets must be carefully evaluated to optimize combination therapies, such strategies represent a promising avenue for enhancing treatment efficacy and overcoming the limitations of current antifungal agents.

Functional network analyses have revealed potential synergistic interactions and shared functions of these proteins in biological processes. For example, Enolase and GMP Synthase play similar roles in energy metabolism by participating in molecular functions such as “ATP binding”; Chitin Synthase and GPI share similar functions in maintaining cellular stability by participating in cell wall biosynthesis. Hsp90 and GMP Synthase are localized in the

cytosol and plasma membrane, supporting cellular resistance mechanisms. These findings are important for our understanding of how proteins participate in various biological pathways and molecular functions and the coordination between them. By employing MD and MDS, ligands with the highest binding affinities were identified, and their pharmacokinetic profiles were analyzed using ADMET. The docking studies indicated that GMP synthase had the highest binding affinity with Cannabistilbene I (−9.1 kcal/mol), reflecting hydrophobic solid interactions and multiple hydrogen bonds. Similarly, CaChs2 demonstrated strong binding with Cannabistilbene I, suggesting its potential as an inhibitor. In contrast, ligands such as Cannabinolic acid and 8-hydroxycannabinolic acid exhibited moderate binding affinities with the target proteins, emphasizing the variability in interaction strengths among different compounds (Appendino et al., 2011; Kogan and Mechoulam, 2007).

ADMET analysis provided important information on the pharmacokinetic properties of the ligands. Hexahydrocannabinol and Δ9-cis-THC showed high lipophilicity and significant intestinal permeability; however, these ligands also carry the risk of HERG channel inhibition, which may limit their therapeutic applications. In contrast, ligands such as Cannabistilbene I and Cannabiglendol stand out as more suitable candidates, exhibiting lower risk of HERG inhibition and moderate lipophilicity. Solvent exposure analysis revealed significant differences in the binding environments of protein-ligand complexes. In particular, solvent exposure was observed for DHODH-Cannabicitran and GMP synthase-Δ9-cis-THC complexes, indicating potential changes in ligand stability and protein interactions in these environments (Jiang et al., 2019).

Consistent with the study by Mulia et al., Δ(9)-THC derivatives exhibited pharmacokinetic properties such as high lipophilicity (logP >5), intestinal permeability, and moderate brain penetration (Mulia et al., 2021). In our study, the calculated QPlogPo/w (5.663) and QPPCaco (4571.459) values for Δ9-cis-THC were found to be consistent with these results. The study of Thomas et al. examined the pharmacological properties of Δ(9)-THC analogs in more depth, and showed the effects of lipophilicity on a compound. In particular, it was stated that the addition of long side chains increased lipophilicity by approximately 3 times per CH2 group, and although no direct correlation with pharmacological activity was found, it was emphasized that lipophilicity plays a critical role in pharmacokinetic processes (Thomas et al., 1990). The QPlogPo/w value in our study (5.663) confirms the natural high lipophilicity of Δ(9)-THC, and as stated by Thomas et al., it also draws attention to the role of this lipophilicity in pharmacokinetic processes. However, the QPlogHERG value of Δ9-cis-THC (−4.894) indicates the risk of cardiotoxicity, complementing the findings of both Mulia and Thomas. Chetia et al., addressing the toxic effects of THC on brain dopamine levels and the attenuation of these effects with Cannabidiol, emphasized that THC affects the dopaminergic (DAergic) system in the brain, especially stimulating mesolimbic DA-containing neurons and increasing striatal dopamine levels. However, thanks to the anxiolytic and antipsychotic properties of CBD, it has been stated that THC has the potential to improve these variations on the DAergic system (Chetia and Borah, 2020). Δ9-cis-THC (Δ9-cis-THC) is an isomer that has attracted attention in low-THC Cannabis sativa cultivars, where it is found at levels comparable to Δ9-trans-THC (Jagannathan, 2020). This ligand was detected especially in low THC fiber hemp species but not in high THC medical cannabis varieties. This suggests that the natural abundance of Δ9-cis-THC may be related to genetic or environmental factors. It has been stated that Δ9-cis-THC has high enantiomeric purity (80%–90%) and this feature provides a significant advantage in the investigation of its biological effects (Schafroth et al., 2021). In our study, the selection of Δ9-cis-THC to evaluate its antifungal potential reveals the possible importance of both its natural abundance and chemical properties in interaction with target proteins. In particular, Δ9-cis-THC, which shows strong binding to targets such as GMP synthase, is considered a promising candidate for the development of new antifungal agents due to its potential to be easily obtained at low cost and its stability in biological systems. In this context, information on its natural abundance increases the importance of our study in terms of the sustainability and large-scale production of the compound.

The study by O'Croinin et al. addressing the pharmaceutical potential and predictive pharmacokinetic properties of stilbenes provides valuable data regarding the anti-inflammatory, antioxidant and anticancer effects of stilbenes, especially those derived from Cannabis sativa (O'Croinin et al., 2023). In the study, the pharmacokinetic profiles of Cannabistilbene I and other stilbenes were evaluated with parameters such as the potential to cross the BBB and the ability to pass through human skin and jejunal tissues. In this context, the high BBB permeability of Cannabistilbene I (84%) and its compliance with optimal Lipinski parameters indicate that the molecule is a promising candidate pharmacologically for neurological targets. In our study, ADMET analyses of Cannabistilbene I support its high lipophilicity and reliable bioavailability properties, and also emphasize the effects of the molecule especially on inflammatory mechanisms. The findings of both studies indicate that the physiochemical and pharmacokinetic properties of stilbenes increase the therapeutic potential, strengthening the consistency of the data in the current literature. These results reveal the need for further research to develop pharmaceutical formulations of stilbenes. The effect of Cannabistilbene I on Angiotensin II (Ang II)-induced cardiac hypertrophy was studied and how this effect was modulated by cytochrome P450 (CYP) enzymes and arachidonic acid (AA) metabolites. The findings indicate that Cannabistilbene I attenuates the cardiac hypertrophy-inducing effects of Ang II, reduces the increase in cellular surface area, and regulates the expression of hypertrophic marker genes. In addition, Cannabistilbene I was found to provide cardioprotective enzymatic activity by increasing CYP1A1 gene expression, increasing the levels of the metabolite 19(S)-HETE, and reversing the decline induced by Ang II (Alammari et al., 2024).

In our study, it was determined that stilbene derivatives such as Cannabistilbene I exhibit high lipophilicity and anti-inflammatory properties, and also show potential therapeutic effects in the cardiovascular system. In particular, ADMET analyses emphasized that Cannabistilbene I has BBB permeability, but its low lipophilic profile may reduce cardiotoxicity. The effects on Ang II-induced cardiac hypertrophy support the protective role of Cannabistilbene I against cardiovascular diseases and are consistent with our ADMET-based pharmacokinetic findings. In particular, stilbenes' effects on inflammation and cellular stress

response were emphasized, demonstrating a cardioprotective potential at both molecular and cellular levels. In our study, the ADMET profile of Cannabidiolic Acid (CBDA) was evaluated in detail. Our findings regarding the pharmacokinetic and pharmacodynamic properties of CBDA largely overlap with the research conducted by Formato et al. Formato et al. In their study, the molecular weight (MW) of CBDA was determined as 358.48, the logP value measuring hydrophobicity was 6.43, the number of hydrogen bond acceptors (HBA) was 4 and the number of donors (HBD) was 3. In addition, the topological polar surface area (TPSA) of CBDA was calculated as 77.75 and it was determined that it contained 7 rotatable bonds (NRTOB). They emphasized that these parameters were positive in terms of oral bioavailability and showed that CBDA has a good absorption potential (Formato et al., 2020).

The antifungal activities and ADMET profiles of selected compounds such as Cannabistilbene I and Δ9-cis-THC were compared with those of the widely used clinical antifungal agents fluconazole (Kauthale et al., 2017) and amphotericin B (Khosravi et al., 2022) in this study. In the literature, it has been reported that the minimum inhibitory concentration (MIC) values of fluconazole against fungal pathogens such as *Candida* albicans, Aspergillus niger, and Aspergillus flavus are between 3.12 and 25 μg/mL, while amphotericin B, despite its high activity, has serious disadvantages such as nephrotoxicity and high cost. In our study, Cannabistilbene I exhibited high binding affinity with GMP Synthase (−9.1 kcal/mol) and CaChs2 (−9.1 kcal/mol), while Δ9-cis-THC showed a lower binding affinity with GMP Synthase (−7.2 kcal/mol). ADMET analyses show that Cannabistilbene I has safety properties similar to fluconazole with a low risk of cardiotoxicity and a high bioavailability profile. On the other hand, Δ9-cis-THC carries pharmacokinetic advantages such as high lipophilicity (QPlogPo/w = 5.663) and intestinal permeability (QPPCaco = 4571.459), while its higher hERG channel inhibition potential (−4.894) compared to fluconazole and amphotericin B poses a possible risk in terms of cardiotoxicity. While the efficacy of fluconazole is supported by MIC values, the antifungal activities of the compounds in our study were based on their binding affinities, which requires *in vitro* and *in vivo* validation to better understand their clinical potential. Cannabistilbene I and Δ9-cis-THC can be considered as innovative and potential candidates in antifungal therapy; However, comprehensive pharmacokinetic and toxicological studies as well as experimental confirmations are needed before it can be considered as an alternative to fluconazole and amphotericin B (Elias et al., 2022; Ghobadi et al., 2023; Martínez et al., 2024; Parveen and Balamurugan, 2023).

In our study, similarly strong oral bioavailability signals were found for CBDA and it was shown that the logP value was calculated as 6.2, TPSA as 79.1, HBA as 4, and HBD as 3. In addition, in our protein target analyses, CBDA's G-protein coupled receptor (GPCR) binding score was evaluated as −0.41, ion channel modulator score as −0.06, kinase inhibitor score as −0.72, and nuclear receptor binding score as −0.28. These findings are very close to the values of −0.39, −0.05, −0.74, and −0.30 in the study by Formato et al. In addition, minimal deviations were observed in protease inhibitor and enzyme inhibitor activities, and the protease inhibitor score was found as −0.65 in our study and −0.63 in Formato et al. The pharmacokinetic profiles and antiseizure effects of phytocannabinoid acids (including CBDA) were examined in detail in the study by Lyndsey L. Anderson et al. (Anderson et al., 2019). In this study, it was reported that CBDA was rapidly absorbed and its brain-to-plasma ratio was low (≤0.04). However, when a different Tween 80-based carrier was used, this ratio increased to 1.9, emphasizing that this increased the brain penetration of CBDA. In addition, it was shown that CBDA delayed the occurrence of generalized tonic-clonic seizures by increasing the seizure threshold in mice with Dravet syndrome. Our study, on the other hand, examined the pharmacokinetic properties and biological activities of CBDA at the molecular level, including the evaluation of important pharmacokinetic parameters of CBDA such as QPlogPo/w, TPSA and NRTOB. The report of a low brain-to-plasma ratio by Anderson et al. and their emphasis on anti-seizure effects are parallel to our results confirming the pharmacokinetic potential of CBDA. In particular, the finding that the bioavailability and brain penetration of CBDA may vary depending on the carrier supports the relevance of our pharmacokinetic assessments for clinical applications. Current studies on cannabicitran have indicated that this compound is often found at levels of up to 10% in commercial "purified" CBD extracts. The literature suggests that cannabicitran is racemic in nature and may be formed during herbal extraction processes (Wood et al., 2023). In contrast, the evaluations made on the pharmacokinetic profile of cannabicitran in our study provided new information, especially on its structural and pharmacological properties. ADMET results obtained from the literature provide critical information regarding the bioavailability of cannabicitran and its interaction with target receptors. For example, it is known that this compound has affinity for receptors such as 5-HT1A. While our study provides preliminary information for a better understanding of the metabolic and biological effects of cannabicitran, it can be expanded to provide full compliance with the literature with more comprehensive ADMET analyses and abundance data. In this context, in-depth studies are required at both the biosynthesis and biological effects levels to evaluate the pharmacological potential of cannabicitran.

The analyses made on CBDVA in our study evaluated the pharmacokinetic properties and potential anticonvulsant effects of the compound. In our study, CBDVA significantly increased the thermal seizure threshold at certain doses (e.g., 100 mg kg^{-1}), indicating the antiseizure effect of the compound. These findings support a study by Anderson et al. (2021). In the study by Anderson et al., it was reported that CBDVA, as well as other phytocannabinoid acids such as CBGA and CBGVA, exhibited protective effects against thermal seizures in the Dravet syndrome mouse model. In particular, this study showed that CBDVA had a neuroprotective effect against thermal seizures after acute intraperitoneal administration, but Δ9-THCV (at a dose of 3 mg kg^{-1}) had a proconvulsant effect in contrast. Our study suggests that CBDVA may be a promising agent in the treatment of epileptic diseases such as Dravet syndrome, and

supports the fact that this compound should be considered in future drug development processes for epilepsy, together with the results of Anderson et al. Among the 16 ligands evaluated in our study, considering that certain ligands may be higher in natural abundance than others, this situation stands out as an important finding when considered together with RMSD and RMSF analyses. In particular, ligands exhibiting high RMSF stability and low RMSD values supported strong interactions with the target protein. These ligands, which are naturally more abundant, offer the potential to improve both their availability in biological systems and their pharmacokinetic profiles. Considering this relationship, the findings supported by protein-ligand contact and ADMET predictions suggest that naturally more abundant compounds may be more pharmacologically suitable candidates. For example, although the natural abundances of ligands such as cannabicitran have been reported in the literature, in this study they were found to support this assumption with their strong stability and interaction profiles. These findings demonstrate that our study is not only relevant to pharmacological profile assessments, but also to the effect of ligand abundance on therapeutic potential. RMSD analyses are crucial for evaluating the structural stability of protein-ligand complexes over time. In the GMP synthase-Δ9-cis-Tetrahydrocannabinol (Δ9-cis-THC) complex, the protein RMSD values remain stable between 2–4 Å, indicating the structural stability of the protein-ligand interaction. This suggests that the ligand binds firmly and stably to the protein. On the other hand, in the CaChs2-Cannabistilbene I complex, the protein RMSD values fluctuate between 6–10 Å, indicating some flexibility in the protein structure. This flexibility allows more movement in the ligand binding site, leading to higher ligand RMSD values (4–7 Å). In the DHODH-Cannabicitran complex, the protein RMSD values remain steady between 1–2 Å, demonstrating high structural stability; however, the ligand RMSD values fluctuate widely between 10–20 Å, indicating significant movements within the ligand binding site, which might be related to solvent exposure.

RMSF analyses are critical for evaluating protein-ligand interactions' dynamic flexibility and stability. During the interaction between CaChs2 and Cannabistilbene I, high protein stability was observed, with slight increases in ligand RMSF values at specific atoms. In contrast, the interaction with Cannabinolic acid showed very low ligand RMSF values, indicating that Cannabinolic acid stabilizes CaChs2, resulting in less dynamic flexibility in the protein-ligand interaction. In the interactions of DHODH protein with Cannabinolic acid and Cannabiglendol, moderate protein mobility was observed, but the ligand RMSF values were lower compared to the protein. These results highlight the impact of ligands on protein stability and reveal dynamic interactions in specific regions.

For Enolase, interactions with 8-hydroxycannabinolic acid showed increased mobility at certain atoms, whereas interactions with Cannabinolic acid indicated that the ligand stabilized the protein. The Glycosylphosphatidylinositol protein did not show significant mobility differences in interactions with 3-Butyl-Δ9-THC and Δ9-Tetrahydrocannabinorcol. During the interaction of GMP synthase with Cannabistilbene I, an increase in protein RMSF values was observed, while no significant difference was noted with Δ9-cis-THC. The Hsp90 protein displayed high mobility when interacting with 5-Hydroxy-7-methoxyindan-1-spiro cyclohexane, whereas it exhibited low RMSF values with Hexahydrocannabinol. The M1P5DH protein showed low RMSF values and stability in interactions with both 8-hydroxycannabinolic acid and Cannabinolic acid. However, in the interaction of Mannitol-2-dehydrogenase protein with 8-Hydroxy-Δ9-Tetrahydrocannabinol, a significant increase in RMSF was observed, particularly after atom 25, whereas no significant difference was noted with Δ9-THC. These results elucidate the impact of ligands on protein stability and reveal dynamic interactions in specific regions.

The differences between the binding affinities obtained in our study are due to the diversity in the chemical and structural properties of the protein targets and ligands. In particular, the hydrogen bonding potentials, hydrophobic surface areas and electrostatic interactions of the ligands are among the determining factors of these differences (Chen et al., 2016; Patil et al., 2010). Differences in the active sites of protein targets may also contribute to the changes observed in ligand binding affinities. For example, while extensive hydrogen bonding networks in proteins such as Hsp90 lead to high binding affinities, hydrophobic regions in targets such as GMP Synthase may be effective in ligand selection (Hoxie and Street, 2020). In similar studies in the literature, studies comparing the binding properties of different ligands to the same protein targets show that the changes in binding affinities are affected by the chemical modifications of the ligands or the conformational flexibility of the protein targets (Ferenczy and Kellermayer, 2022; Madushanka et al., 2023; Patil et al., 2010). In future studies, detailed examinations are planned with methods such as molecular dynamics simulations and energy component analysis of ligand-protein complexes to better understand the differences in binding affinities. This approach may contribute to the design of structural modifications that will increase the binding affinities of ligands.

The choice to employ MD and MDS in this study is well-founded due to their complementary nature in evaluating protein-ligand interactions. Molecular docking serves as an initial screening tool, allowing for the identification of the most promising ligand candidates based on binding affinities (Agu et al., 2023; Salmaso and Moro, 2018). However, docking alone cannot fully capture these interactions' dynamic and temporal aspects, which are crucial for understanding the stability and behavior of protein-ligand complexes in a physiological environment. Therefore, MDS was utilized to provide a more comprehensive assessment of the binding stability and dynamic interactions over time (Shukla and Tripathi, 2021). Furthermore, the decision to utilize a 100 ns simulation duration for MDS was based on a balance between computational feasibility and the ability to capture significant conformational changes and stabilization patterns within the protein-ligand complexes (Koshy et al., 2010). While longer simulations could potentially provide additional insights, previous studies have demonstrated that a 100 ns timeframe is sufficient to observe key interaction features, stabilize RMSD values, and gain meaningful insights into protein flexibility and

ligand binding modes. Therefore, this duration was considered appropriate for effectively investigating the dynamic behaviors of the complexes and their potential antifungal properties (Al-Karmalawy et al., 2021). The combination of MD followed by MDS ensured a robust evaluation of the selected ligands' potential as antifungal agents, supporting their future experimental exploration as promising drug candidates.

This study provides a comprehensive analysis of interactions between various fungal proteins and ligands, revealing the antifungal potential of selected compounds. Cannabistilbene I exhibited strong binding affinities (−9.1 kcal/mol) and stable dynamic profiles with GMP Synthase and CaChs2, while ADMET analyses highlighted its high bioavailability and low cardiotoxicity risk. Similarly, Δ9-cis-THC stood out as another promising candidate due to its natural abundance and protein-ligand stability. These findings suggest that both molecules are promising candidates for antifungal drug development and underscore the importance of further experimental validation.

5 Conclusion

This study provides a comprehensive assessment of how selected cannabinoid and stilbenoid compounds interact with eight different fungal proteins, highlighting the promising potential of these compounds as antifungal agents. Through MD simulations and analyses, ligands with high binding affinity, particularly interacting with GMP Synthase and CaChs2, were identified. These ligands stand out as strong candidates as potential inhibitors. In particular, Cannabistilbene I exhibited exceptional binding affinity with both GMP Synthase (−9.1 kcal/mol) and CaChs2, supported by stable RMSD values and significant hydrogen bond interactions. Furthermore, Δ9-cis-THC exhibited low RMSD values (2–4 Å) and strong hydrophobic interactions with GMP Synthase, demonstrating its potential as a potent initiator compound for antifungal applications. ADMET analysis reinforced these findings, revealing that Cannabistilbene I presented favorable pharmacokinetic profiles such as low risk of HERG inhibition and moderate lipophilicity, while Δ9-cis-THC showed a mild risk of cardiotoxicity despite high intestinal permeability and promising bioavailability. One of the major strengths of this study is the detailed establishment of interaction profiles between different proteins and ligands. This broad scope helps us to understand the biological activities and antifungal capacities of these compounds in more depth. The study showed that stable protein-ligand interactions with low RMSD and RMSF values are important indicators of antifungal potential. However, it should be noted that these promising *in silico* results need to be confirmed by *in vitro* and *in vivo* experiments to fully confirm the efficacy of these compounds. Future research should prioritize the experimental evaluation and optimization of lead candidates, particularly Cannabistilbene I and Δ9-cis-THC, to better understand the validity and efficacy of these compounds as clinical antifungal agents. In conclusion, this study highlights the therapeutic potential of cannabinoids and stilbenoids and provides a solid foundation for the development of new antifungal therapies.

Data availability statement

The original contributions presented in the study are included in the article/Supplementary Material, further inquiries can be directed to the corresponding authors.

Author contributions

KK: Methodology, Writing–original draft, Writing–review and editing. AK: Data curation, Formal Analysis, Writing–original draft, Writing–review and editing. EK: Supervision, Writing–original draft, Writing–review and editing. MR: Data curation, Writing–original draft, Writing–review and editing. JK: Formal Analysis, Writing–original draft, Writing–review and editing. RA: Software, Writing–original draft, Writing–review and editing. ES: Methodology, Writing–original draft, Writing–review and editing. NM: Conceptualization, Validation, Writing–original draft, Writing–review and editing. VS: Resources, Validation, Writing–original draft, Writing–review and editing.

Funding

The author(s) declare that no financial support was received for the research, authorship, and/or publication of this article.

Conflict of interest

The authors declare that the research was conducted in the absence of any commercial or financial relationships that could be construed as a potential conflict of interest.

Generative AI statement

The author(s) declare that no Generative AI was used in the creation of this manuscript.

Publisher's note

All claims expressed in this article are solely those of the authors and do not necessarily represent those of their affiliated organizations, or those of the publisher, the editors and the reviewers. Any product that may be evaluated in this article, or claim that may be made by its manufacturer, is not guaranteed or endorsed by the publisher.

Supplementary material

The Supplementary Material for this article can be found online at: https://www.frontiersin.org/articles/10.3389/fchem.2024.1515424/full#supplementary-material

References

Abchir, O., Daoui, O., Nour, H., Yamari, I., Elkhattabi, S., Errougui, A., et al. (2023). Exploration of Cannabis constituents as potential candidates against diabetes mellitus disease using molecular docking, dynamics simulations and ADMET investigations. *Sci. Afr.*, 21, e01745. doi:10.1016/j.sciaf.2023.e01745

Agu, P. C., Afiukwa, C. A., Orji, O. U., Ezeh, E. M., Ofoke, I. H., Ogbu, C. O., et al. (2023). Molecular docking as a tool for the discovery of molecular targets of nutraceuticals in diseases management. *Sci. Rep.* 13 (1), 13398. doi:10.1038/s41598-023-40160-2

Aissaoui, S., Hajji, H., Zaki, H., Alaqarbeh, M., Chtita, S., Lakhlifi, T., et al. (2024). Study of the anticancer potential of cannabidiol using computational methods. *Phys. Chem. Res.* 12 (3), 783–800. doi:10.22036/pcr.2024.425179.2450

Akinwumi, B. C., Bordun, K. M., and Anderson, H. D. (2018). Biological activities of stilbenoids. *Int. J. Mol. Sci.* 19 (3), 792. doi:10.3390/ijms19030792

Alammari, A. H., Isse, F. A., O'Croinin, C., Davies, N. M., and El-Kadi, A. O. S. (2024). Effect of Cannabistilbene I in attenuating Angiotensin II-induced cardiac hypertrophy: insights into cytochrome P450s and arachidonic acid metabolites modulation. *Cannabis Cannabinoid Res.* doi:10.1089/can.2024.0148

Al-Karmalawy, A. A., Dahab, M. A., Metwaly, A. M., Elhady, S. S., Elkaeed, E. B., Eissa, I. H., et al. (2021). Molecular docking and dynamics simulation revealed the potential inhibitory activity of ACEIs against SARS-CoV-2 targeting the hACE2 receptor. *Front. Chem.* 9, 661230. doi:10.3389/fchem.2021.661230

Álvarez-Sánchez, A., Grinat, J., Doria-Borrell, P., Mellado-López, M., Pedrera-Alcócer, É., Malenchini, M., et al. (2024). The GPI-anchor biosynthesis pathway is critical for syncytiotrophoblast differentiation and placental development. *Cell. Mol. Life Sci.* 81 (1), 246. doi:10.1007/s00018-024-05284-2

Anderson, L. L., Heblinski, M., Absalom, N. L., Hawkins, N. A., Bowen, M. T., Benson, M. J., et al. (2021). Cannabigerolic acid, a major biosynthetic precursor molecule in cannabis, exhibits divergent effects on seizures in mouse models of epilepsy. *Br. J. Pharmacol.* 178 (24), 4826–4841. doi:10.1111/bph.15661

Anderson, L. L., Low, I. K., Banister, S. D., McGregor, I. S., and Arnold, J. C. (2019). Pharmacokinetics of phytocannabinoid acids and anticonvulsant effect of cannabidiolic acid in a mouse model of Dravet syndrome. *J. Nat. Prod.* 82 (11), 3047–3055. doi:10.1021/acs.jnatprod.9b00600

Appendino, G., Chianese, G., and Taglialatela-Scafati, O. (2011). Cannabinoids: occurrence and medicinal chemistry. *Curr. Med. Chem.* 18 (7), 1085–1099. doi:10.2174/092986711794940888

Appendino, G., Gibbons, S., Giana, A., Pagani, A., Grassi, G., Stavri, M., et al. (2008). Antibacterial cannabinoids from Cannabis sativa: a structure-activity study. *J. Nat. Prod.* 71 (8), 1427–1430. doi:10.1021/np8002673

Avilán, L., Gualdrón-López, M., Quiñones, W., González-González, L., Hannaert, V., Michels, P. A., et al. (2011). Enolase: a key player in the metabolism and a probable virulence factor of trypanosomatid parasites-perspectives for its use as a therapeutic target. *Enzyme Res.* 2011, 1–14. doi:10.4061/2011/932549

Aviz-Amador, A., Contreras-Puentes, N., and Mercado-Camargo, J. (2021). Virtual screening using docking and molecular dynamics of cannabinoid analogs against CB1 and CB2 receptors. *Comput. Biol. Chem.*, 95, 107590. doi:10.1016/j.compbiolchem.2021.107590

Banks, I. R., Specht, C. A., Donlin, M. J., Gerik, K. J., Levitz, S. M., and Lodge, J. K. (2005). A chitin synthase and its regulator protein are critical for chitosan production and growth of the fungal pathogen Cryptococcus neoformans. *Eukaryot. Cell.* 4 (11), 1902–1912. doi:10.1128/ec.4.11.1902-1912.2005

Berman, H. M., Westbrook, J., Feng, Z., Gilliland, G., Bhat, T. N., Weissig, H., et al. (2000). The protein data bank. *Nucleic Acids Res.* 28 (1), 235–242. doi:10.1093/nar/28.1.235

Castellano, G., Lara, A., and Torrens, F. (2014). Classification of stilbenoid compounds by entropy of artificial intelligence. *Phytochemistry*, 97, 62–69. doi:10.1016/j.phytochem.2013.10.010

Chaffin, W. L. (2008). Candida albicans cell wall proteins. *Microbiol. Mol. Biol. Rev.* 72 (3), 495–544. doi:10.1128/mmbr.00032-07

Chen, D., Oezguen, N., Urvil, P., Ferguson, C., Dann, S. M., and Savidge, T. C. (2016). Regulation of protein-ligand binding affinity by hydrogen bond pairing. *Sci. Adv.* 2 (3), e1501240. doi:10.1126/sciadv.1501240

Chetia, S., and Borah, G. (2020). Δ 9-tetrahydrocannabinol toxicity and validation of cannabidiol on brain dopamine levels: an assessment on cannabis duplicity. *Nat. Prod. Bioprospecting* 10 (5), 285–296. doi:10.1007/s13659-020-00263-z

Clarke, R. C., and Merlin, M. D. (2015). Letter to the editor: small, ernest. 2015. Evolution and classification of cannabis sativa (marijuana, hemp) in relation to human utilization. Botanical review 81(3): 189-294. *Botanical Rev. Botanical Rev.* 81 (4), 295–305. doi:10.1007/s12229-015-9158-2

Coudert, E., Gehant, S., de Castro, E., Pozzato, M., Baratin, D., Neto, T., et al. (2022). Annotation of biologically relevant ligands in UniProtKB using ChEBI. *Bioinformatics* 39 (1), btac793. doi:10.1093/bioinformatics/btac793

Cowen, L. E., and Lindquist, S. (2005). Hsp90 potentiates the rapid evolution of new traits: drug resistance in diverse fungi. *Science* 309 (5744), 2185–2189. doi:10.1126/science.1118370

Dallakyan, S., and Olson, A. J. (2015). "Small-molecule library screening by docking with PyRx," in *Chemical biology: methods and protocols*. Editors J. E. Hempel, C. H. Williams, and C. C. Hong (New York: Springer), 243–250. doi:10.1007/978-1-4939-2269-7_19

Dasari, P., Koleci, N., Shopova, I. A., Wartenberg, D., Beyersdorf, N., Dietrich, S., et al. (2019). Enolase from Aspergillus fumigatus is a moonlighting protein that binds the human plasma complement proteins factor H, FHL-1, C4BP, and plasminogen. *Front. Immunol.* 10, 2573. doi:10.3389/fimmu.2019.02573

Díaz-Ramos, A., Roig-Borrellas, A., García-Melero, A., and López-Alemany, R. (2012). α-Enolase, a multifunctional protein: its role on pathophysiological situations. *J. Biomed. and Biotechnol.* 2012, 1–12. doi:10.1155/2012/156795

Elias, R., Basu, P., and Fridman, M. (2022). Fluconazole-COX inhibitor hybrids: a dual-acting class of antifungal azoles. *J. Med. Chem.* 65 (3), 2361–2373. doi:10.1021/acs.jmedchem.1c01807

Feldman, M., Sionov, R. V., Mechoulam, R., and Steinberg, D. (2021). Anti-biofilm activity of cannabidiol against Candida albicans. *Microorganisms* 9 (2), 441. doi:10.3390/microorganisms9020441

Ferenczy, G. G., and Kellermayer, M. (2022). Contribution of hydrophobic interactions to protein mechanical stability. *Comput. Struct. Biotechnol. J.*, 20, 1946–1956. doi:10.1016/j.csbj.2022.04.025

Fisher, M. C., Alastruey-Izquierdo, A., Berman, J., Bicanic, T., Bignell, E. M., Bowyer, P., et al. (2022). Tackling the emerging threat of antifungal resistance to human health. *Nat. Rev. Microbiol.* 20 (9), 557–571. doi:10.1038/s41579-022-00720-1

Fisher, M. C., Burnett, F., Chandler, C., Gow, N. A. R., Gurr, S., Hart, A., et al. (2024). A one health roadmap towards understanding and mitigating emerging Fungal Antimicrobial Resistance: fAMR. *npj Antimicrob. Resist.* 2 (1), 36. doi:10.1038/s44259-024-00055-2

Formato, M., Crescente, G., Scognamiglio, M., Fiorentino, A., Pecoraro, M. T., Piccolella, S., et al. (2020). (−)-Cannabidiolic acid, a still overlooked bioactive compound: an introductory review and preliminary research. *Molecules* 25 (11), 2638. doi:10.3390/molecules25112638

Ghobadi, E., Hashemi, S. M., Fakhim, H., Hosseini-Khah, Z., Badali, H., and Emami, S. (2023). Design, synthesis and biological activity of hybrid antifungals derived from fluconazole and mebendazole. *Eur. J. Med. Chem.* 249, 115146. doi:10.1016/j.ejmech.2023.115146

Glodowska, M. (2016). Cannabis sativa L. and its antimicrobial properties – a review.

Gupta, R. S. (1995). Phylogenetic analysis of the 90 kD heat shock family of protein sequences and an examination of the relationship among animals, plants, and fungi species. *Mol. Biol. Evol.* 12 (6), 1063–1073. doi:10.1093/oxfordjournals.molbev.a040281

Hai, Y., Fan, R., Zhao, T., Lin, R., Zhuang, J., Deng, A., et al. (2024). A novel mitochondria-targeting DHODH inhibitor induces robust ferroptosis and alleviates immune suppression. *Pharmacol. Res.*, 202, 107115. doi:10.1016/j.phrs.2024.107115

Hanane, Z., and Mohammed, B. (2021). Can cannabinoids suppress the cytokines cascade in patients with coronavirus disease COVID-19? A mini-review. *Coronaviruses*, 2(2), 187–192. doi:10.2174/2666796701999200915144255

Hoter, A., El-Sabban, M. E., and Naim, H. Y. (2018). The HSP90 family: structure, regulation, function, and implications in health and disease. *Int. J. Mol. Sci.* 19 (9), 2560. doi:10.3390/ijms19092560

Hourfane, S., Mechqoq, H., Bekkali, A. Y., Rocha, J. M., and El Aouad, N. (2023). A comprehensive review on cannabis sativa ethnobotany, phytochemistry, molecular docking and biological activities. *Plants (Basel)* 12 (6), 1245. doi:10.3390/plants12061245

Hoxie, R. S., and Street, T. O. (2020). Hsp90 chaperones have an energetic hot-spot for binding inhibitors. *Protein Sci.* 29 (10), 2101–2111. doi:10.1002/pro.3933

Jagannathan, R. (2020). Identification of psychoactive metabolites from cannabis sativa, its smoke, and other phytocannabinoids using machine learning and multivariate methods. *ACS omega* 5 (1), 281–295. doi:10.1021/acsomega.9b02663

Jeong, S., Yun, H. K., Jeong, Y. A., Jo, M. J., Kang, S. H., Kim, J. L., et al. (2019). Cannabidiol-induced apoptosis is mediated by activation of Noxa in human colorectal cancer cells. *Cancer Lett.*, 447, 12–23. doi:10.1016/j.canlet.2019.01.011

Jiang, X., Yu, J., Zhou, Z., Kongsted, J., Song, Y., Pannecouque, C., et al. (2019). Molecular design opportunities presented by solvent-exposed regions of target proteins: JIANG et al. *Med. Res. Rev.* 39, 2194–2238. doi:10.1002/med.21581

Kauthale, S., Tekale, S., Damale, M., Sangshetti, J., and Pawar, R. (2017). Synthesis, antioxidant, antifungal, molecular docking and ADMET studies of some thiazolyl hydrazones. *Bioorg Med. Chem. Lett.* 27 (16), 3891–3896. doi:10.1016/j.bmcl.2017.06.043

Khan, M. A. S., Miah, M. I., Islam, Z., Afrin, S., Ahmed, M. F., and Rahman, S. R. (2023). Molecular docking and dynamics simulation study of medicinal fungi derived secondary metabolites as potential inhibitor for COVID-19 treatment. *Inf. Med. Unlocked*, 41, 101305. doi:10.1016/j.imu.2023.101305

Khosravi, A., Sharifi, I., Tavakkoli, H., Molaakbari, E., Bahraminegad, S., Salarkia, E., et al. (2022). Cytotoxicity of amphotericin B and AmBisome: *in silico* and *in vivo*

evaluation employing the chick embryo model. *Front. Pharmacol.* 13, 860598. doi:10.3389/fphar.2022.860598

Kingsbury, J. M., and McCusker, J. H. (2010). Cytocidal amino acid starvation of *Saccharomyces cerevisiae* and Candida albicans acetolactate synthase (ilv2Δ) mutants is influenced by the carbon source and rapamycin. *Microbiol. Read.* 156 (Pt 3), 929–939. doi:10.1099/mic.0.034348-0

Kogan, N. M., and Mechoulam, R. (2007). Cannabinoids in health and disease. *Dialogues Clin. Neurosci.* 9 (4), 413–430. doi:10.31887/DCNS.2007.9.4/nkogan

Koshy, C., Parthiban, M., and Sowdhamini, R. (2010). 100 ns molecular dynamics simulations to study intramolecular conformational changes in bax. *J. Biomol. Struct. Dyn.* 28, 71–83. doi:10.1080/07391102.2010.10507344

Langenhorst, D., Fürst, A. L., Alberter, K., Vilhena, C., Dasari, P., Daud, M., et al. (2023). Soluble enolase 1 of Candida albicans and Aspergillus fumigatus stimulates human and mouse B cells and monocytes. *J. Immunol.* 211 (5), 804–815. doi:10.4049/jimmunol.2200318

Lenardon, M. D., Munro, C. A., and Gow, N. A. (2010). Chitin synthesis and fungal pathogenesis. *Curr. Opin. Microbiol.* 13 (4), 416–423. doi:10.1016/j.mib.2010.05.002

Lim, J. Y., Jang, S. H., and Park, H. M. (2021). Mannitol-1-phosphate dehydrogenase, MpdA, is required for mannitol production in vegetative cells and involved in hyphal branching, heat resistance of conidia and sexual development in Aspergillus nidulans. *Curr. Genet.* 67 (4), 613–630. doi:10.1007/s00294-021-01163-6

Lucas, C. J., Galettis, P., and Schneider, J. (2018). The pharmacokinetics and the pharmacodynamics of cannabinoids. *Br. J. Clin. Pharmacol.* 84 (11), 2477–2482. doi:10.1111/bcp.13710

Madushanka, A., Moura, R. T., Verma, N., and Kraka, E. (2023). Quantum mechanical assessment of protein–ligand hydrogen bond strength patterns: insights from semiempirical tight-binding and local vibrational mode theory. *Int. J. Mol. Sci.* 24 (7), 6311. doi:10.3390/ijms24076311

Martínez, I., Rivera-Santiago, L., Rodríguez-Hernández, K. D., Galván-Hernández, A., Rodríguez-Fragoso, L., Díaz-Peralta, L., et al. (2024). A promising amphotericin B derivative induces morphological alterations, mitochondrial damage, and oxidative stress *in vitro* and prevents mice from death produced by a virulent strain of trypanosoma cruzi. *Microorganisms* 12 (6), 1064. doi:10.3390/microorganisms12061064

Meena, M., Prasad, V., Zehra, A., Gupta, V. K., and Upadhyay, R. S. (2015). Mannitol metabolism during pathogenic fungal-host interactions under stressed conditions. *Front. Microbiol.* 6, 1019. doi:10.3389/fmicb.2015.01019

Merzendorfer, H. (2011). The cellular basis of chitin synthesis in fungi and insects: common principles and differences. *Eur. J. Cell. Biol.*, 90(9), 759–769. doi:10.1016/j.ejcb.2011.04.014

Milacic, M., Beavers, D., Conley, P., Gong, C., Gillespie, M., Griss, J., et al. (2023). The reactome pathway knowledgebase 2024. *Nucleic Acids Res.* 52 (D1), D672–D678. doi:10.1093/nar/gkad1025

Mirabello, C., Wallner, B., Nystedt, B., Azinas, S., and Carroni, M. (2024). Unmasking AlphaFold to integrate experiments and predictions in multimeric complexes. *Nat. Commun.* 15 (1), 8724. doi:10.1038/s41467-024-52951-w

Morris, G. M., Huey, R., Lindstrom, W., Sanner, M. F., Belew, R. K., Goodsell, D. S., et al. (2009). AutoDock4 and AutoDockTools4: automated docking with selective receptor flexibility. *J. Comput. Chem.* 30 (16), 2785–2791. doi:10.1002/jcc.21256

Mulia, A., Oktavia, S., and Ifora, I. (2021). Pharmacological properties of Δ (9)-tetrahydrocannabinol: a review.

Munro, C. A., and Gow, N. A. R. (2001). Chitin synthesis in human pathogenic fungi. *Med. Mycol.* 39 (1), 41–53. doi:10.1080/mmy.39.1.41.53

Nara, T., Hshimoto, T., and Aoki, T. (2000). Evolutionary implications of the mosaic pyrimidine-biosynthetic pathway in eukaryotes. *Gene* 257 (2), 209–222. doi:10.1016/s0378-1119(00)00411-x

O'Croinin, C., Garcia Guerra, A., Doschak, M. R., Löbenberg, R., and Davies, N. M. (2023). Therapeutic potential and predictive pharmaceutical modeling of stilbenes in cannabis sativa. *Pharmaceutics* 15 (7), 1941. doi:10.3390/pharmaceutics15071941

O'Croinin, C., Garcia Guerra, A., Doschak, M. R., Löbenberg, R., and Davies, N. M. (2023). Therapeutic potential and predictive pharmaceutical modeling of stilbenes in cannabis sativa. *Pharmaceutics* 15 (7), 1941. doi:10.3390/pharmaceutics15071941

Oliver, J. C., Linger, R. S., Chittur, S. V., and Davisson, V. J. (2013). Substrate activation and conformational dynamics of guanosine 5'-monophosphate synthetase. *Biochemistry* 52 (31), 5225–5235. doi:10.1021/bi3017075

Pagano, E., Romano, B., Iannotti, F. A., Parisi, O. A., D'Armiento, M., Pignatiello, S., et al. (2019). The non-euphoric phytocannabinoid cannabidivarin counteracts intestinal inflammation in mice and cytokine expression in biopsies from UC pediatric patients. *Pharmacol. Res.* 149, 104464. doi:10.1016/j.phrs.2019.104464

Parveen, S. T., and Balamurugan, B. J. (2023). QSPR analysis through graph models for predicting ADMET properties of antifungal drugs to treat fungal diseases. *Int. J. Quantum Chem.*, 123(22), e27211. doi:10.1002/qua.27211

Patil, R., Das, S., Stanley, A., Yadav, L., Sudhakar, A., and Varma, A. K. (2010). Optimized hydrophobic interactions and hydrogen bonding at the target-ligand interface leads the pathways of drug-designing. *PloS One* 5 (8), e12029. doi:10.1371/journal.pone.0012029

Petrosino, S., Verde, R., Vaia, M., Allarà, M., Iuvone, T., and Di Marzo, V. (2018). Anti-inflammatory properties of cannabidiol, a nonpsychotropic cannabinoid, in experimental allergic contact dermatitis. *J. Pharmacol. Exp. Ther.* 365 (3), 652–663. doi:10.1124/jpet.117.244368

Platella, C., Mazzini, S., Napolitano, E., Mattio, L. M., Beretta, G. L., Zaffaroni, N., et al. (2021). Plant-derived stilbenoids as DNA-binding agents: from monomers to dimers. *Chemistry* 27 (34), 8832–8845. doi:10.1002/chem.202101229

Rabaan, A. A., Sulaiman, T., Al-Ahmed, S. H., Buhaliqah, Z. A., Buhaliqah, A. A., AlYuosof, B., et al. (2023). Potential strategies to control the risk of antifungal resistance in humans: a comprehensive review. *Antibiot. (Basel)* 12 (3), 608. doi:10.3390/antibiotics12030608

Rawls, J., Knecht, W., Diekert, K., Lill, R., and Löffler, M. (2000). Requirements for the mitochondrial import and localization of dihydroorotate dehydrogenase. *Eur. J. Biochem.* 267 (7), 2079–2087. doi:10.1046/j.1432-1327.2000.01213.x

Reiss, C. S. (2010). Cannabinoids and viral infections. *Pharmaceuticals* 3 (6), 1873–1886. doi:10.3390/ph3061873

Rodriguez-Suarez, R., Xu, D., Veillette, K., Davison, J., Sillaots, S., Kauffman, S., et al. (2007). Mechanism-of-Action determination of GMP synthase inhibitors and target validation in Candida albicans and Aspergillus fumigatus. *Chem. Biol.*, 14(10), 1163–1175. doi:10.1016/j.chembiol.2007.09.009

Ruijter, G. J. G., Visser, J., and Rinzema, A. (2004). Polyol accumulation by Aspergillus oryzae at low water activity in solid-state fermentation. *Microbiol. Read.* 150 (Pt 4), 1095–1101. doi:10.1099/mic.0.26723-0

Salmaso, V., and Moro, S. (2018). Bridging molecular docking to molecular dynamics in exploring ligand-protein recognition process: an overview. *Front. Pharmacol.* 9, 923. doi:10.3389/fphar.2018.00923

Samalova, M., Carr, P., Bromley, M., Blatzer, M., Moya-Nilges, M., Latgé, J.-P., et al. (2020). "GPI anchored proteins in Aspergillus fumigatus and cell wall morphogenesis,". *GPI Anchored Proteins Aspergillus fumigatus Cell. Wall Morphog. Curr. Top. Microbiol. Immunol.*, 425, 167–186. doi:10.1007/82_2020_207

Schafroth, M. A., Mazzoccanti, G., Reynoso-Moreno, I., Erni, R., Pollastro, F., Caprioglio, D., et al. (2021). Δ(9)-cis-Tetrahydrocannabinol: natural occurrence, chirality, and pharmacology. *J. Nat. Prod.* 84 (9), 2502–2510. doi:10.1021/acs.jnatprod.1c00513

Schrödinger, E. (2016). Schrödinger. *Centen. Celebra*.

Shannon, P., Markiel, A., Ozier, O., Baliga, N. S., Wang, J. T., Ramage, D., et al. (2003). Cytoscape: a software environment for integrated models of biomolecular interaction networks. *Genome Res.* 13 (11), 2498–2504. doi:10.1101/gr.1239303

Shukla, R., and Tripathi, T. (2021). Molecular dynamics simulation in drug discovery: opportunities and challenges. 295–316). doi:10.1007/978-981-15-8936-2_12

Sun, X. (2023). Research progress on cannabinoids in cannabis (cannabis sativa L.) in China. *Molecules* 28 (9), 3806. doi:10.3390/molecules28093806

Suvarna, K., Bartiss, A., and Wong, B. (2000). Mannitol-1-phosphate dehydrogenase from Cryptococcus neoformans is a zinc-containing long-chain alcohol/polyol dehydrogenase the GenBank accession numbers for the nucleotide sequences for the C. neoformans mannitol-1-phosphate dehydrogenase cDNA and gene are AF175685 and AF186474, respectively. *Microbiol. Read.* 146 (Pt 10), 2705–2713. doi:10.1099/00221287-146-10-2705

Thomas, B. F., Compton, D. R., and Martin, B. R. (1990). Characterization of the lipophilicity of natural and synthetic analogs of delta 9-tetrahydrocannabinol and its relationship to pharmacological potency. *J. Pharmacol. Exp. Ther.* 255 (2), 624–630.

Upadhyay, R. S., Meena, M., Prasad, V., Zehra, A., and Gupta, V. K. (2015). Mannitol metabolism during pathogenic fungal–host interactions under stressed conditions. *Front. Microbiol.* 6, 1019. doi:10.3389/fmicb.2015.01019

Varadi, M., Anyango, S., Deshpande, M., Nair, S., Natassia, C., Yordanova, G., et al. (2021). AlphaFold Protein Structure Database: massively expanding the structural coverage of protein-sequence space with high-accuracy models. *Nucleic Acids Res.* 50 (D1), D439–D444. doi:10.1093/nar/gkab1061

Varadi, M., and Velankar, S. (2022). The impact of AlphaFold Protein Structure Database on the fields of life sciences. *PROTEOMICS* 23, 2200128. doi:10.1002/pmic.202200128

Wahedi, H., Ahmad, S., and Abbasi, S. (2020). Stilbene-based natural compounds as promising drug candidates against COVID-19. *J. Biomol. Struct. Dyn.* 39, 3225–3234. doi:10.1080/07391102.2020.1762743

Wei, H., Zhang, Y., Jia, Y., Chen, X., Niu, T., Chatterjee, A., et al. (2024). Heat shock protein 90: biological functions, diseases, and therapeutic targets. *MedComm* 5 (2), e470. doi:10.1002/mco2.470

Wood, J. S., Gordon, W. H., Morgan, J. B., and Williamson, R. T. (2023). Cannabicitran: its unexpected racemic nature and potential origins. *Chirality*, 35(9), 540–548. doi:10.1002/chir.23571

Zameitat, E., Freymark, G., Dietz, C. D., Löffler, M., and Bölker, M. (2007). Functional expression of human dihydroorotate dehydrogenase (DHODH) in pyr4 mutants of ustilago maydis allows target validation of DHODH inhibitors *in vivo*. *Appl. Environ. Microbiol.* 73 (10), 3371–3379. doi:10.1128/aem.02569-06

frontiers | Frontiers in Chemistry

TYPE Original Research
PUBLISHED 15 January 2025
DOI 10.3389/fchem.2024.1513150

OPEN ACCESS

EDITED BY
Afzal Basha Shaik,
Jawaharlal Nehru Technological University,
Kakinada, India

REVIEWED BY
Girish Kumar Gupta,
Sri Sai Group of Institutes Badhani, India
Srinath Pashikanti,
Idaho State University, United States

*CORRESPONDENCE
Zehra Edis,
z.edis@ajman.ac.ae

RECEIVED 17 October 2024
ACCEPTED 27 December 2024
PUBLISHED 15 January 2025

CITATION
Edis Z, Haj Bloukh S, Ashames AA, Al-Tabakha MM, Shahwan MJSA, Abu Sara H, Boddu SHS, Khan SN, Bloukh IH, Eladdasy M, Sadeghi S, Alkubaisi H, Bloukh IH and Hassan NAGM (2025) *Syzygium aromaticum* extract mediated, sustainable silver nanoparticle synergetic with heterocyclic antibiotic clarithromycin and their antimicrobial activities.
Front. Chem. 12:1513150.
doi: 10.3389/fchem.2024.1513150

Syzygium aromaticum extract mediated, sustainable silver nanoparticle synergetic with heterocyclic antibiotic clarithromycin and their antimicrobial activities

Zehra Edis[1,2]*, Samir Haj Bloukh[2,3], Akram A. Ashames[1,2], Moawia M. Al-Tabakha[1,2], Moyad J. S. A. Shahwan[2,3], Hamed Abu Sara[2,3], Sai H. S. Boddu[1,2], Sohaib N. Khan[1,2], Ibrahim Haj Bloukh[4], Maram Eladdasy[3], Somayeh Sadeghi[3], Haneen Alkubaisi[3], Iman Haj Bloukh[4] and Nageeb A. G. M. Hassan[2,3]

[1]Department of Pharmaceutical Sciences, College of Pharmacy and Health Sciences, Ajman University, Ajman, United Arab Emirates, [2]Center of Medical and Bio-Allied Health Sciences Research, Ajman University, Ajman, United Arab Emirates, [3]Department of Clinical Sciences, College of Pharmacy and Health Sciences, Ajman University, Ajman, United Arab Emirates, [4]College of Dentistry, Ajman University, Ajman, United Arab Emirates

Microorganisms are becoming resistant to drugs and antimicrobials, making it a significantly critical global issue. Nosocomial infections are resulting in alarmingly increasing rates of morbidity and mortality. Plant derived compounds hold numerous antimicrobial properties, making them a very capable source to counteract resistant microbial strains. *Syzygium aromaticum* (Clove) extract has been proven by studies to contain active ingredients that demonstrate antibacterial, antifungal, antioxidant, and insecticidal properties. It has also been used historically for its pain relief especially for tooth ache. Clove extract derived nanoparticle synthesis is a promising method of combining therapeutics with metals at nanoscale. Such nanostructured systems in combination with the heterocyclic antibiotic clarithromycin could potentiate the action of plant extracts, decrease drug side effects and improve antimicrobial activity. In this study, clove extract (C) was successfully used to synthesize silver nanoparticles (AgNP) to create AgNPC and AgNPCA (A = clarithromycin). The two compounds underwent different analytical methods consisting of SEM, EDS, DLS, UV-vis, FTIR and XRD. These nanoparticles were used against a variety of 10 pathogens and exhibited very good to intermediate antibacterial properties. AgNPC resulted in

Abbreviations: AMR, Antimicrobial Resistance; AgNP, Silver nanoparticle; C, Clove extract; A, Antibiotic Clarithromycin; EDS, Energy Dispersive Spectroscopy; FTIR, Fourier transmission infrared spectroscopy; Raman, Raman spectroscopy; SEM, Scanning electron microscopy; UV-vis, Ultraviolet-visible spectroscopy; WHO, World Health Organization; XRD, X-ray crystallography; ZOI, Zone of Inhibition.

better antibacterial properties and smaller nanoparticle size. This study demonstrates the potential of clove extract mediated AgNP synthesis in combination with and without the antibiotic clarithromycin.

KEYWORDS

silver nanoparticles, antibiotic resistance, clarithromycin, heterocyclic antibiotic, plant extract, clove

1 Introduction

Pathogenic microorganisms are a serious concern due to developing microbial resistance to antimicrobial agents (Baran et al., 2023; El-Sawy et al., 2024; Tang et al., 2023; Uddin et al., 2021). Pathogens learn to endure and survive what once were lethal concentrations, causing resistance to drugs, antibiotics and antimicrobials (Baran et al., 2023; El-Sawy et al., 2024; Tang et al., 2023; Uddin et al., 2021). This has become an alarming obstacle globally, causing a constant increase in the deaths from antimicrobial resistance (AMR) (Baran et al., 2023; El-Sawy et al., 2024; Tang et al., 2023; Uddin et al., 2021). Especially during COVID-19, AMR proved to be a major contributor to morbidity and mortality (Mahoney et al., 2021). Unfortunately, the uncontrolled use of antimicrobials to save COVID-19 patients in emergency wards and hospitals ameliorated AMR (Mahoney et al., 2021). Consequently, the search for new potent alternatives and synergistic agents to the commonly used antimicrobials and antibiotics has become an essential need for human survival (Uddin et al., 2021). Therefore, increasing numbers of investigations are dedicated to this pivotal pursuit, which include different approaches. Among the alternatives studied to combat antimicrobial resistant pathogens are plants with a rich spectrum of biocompounds (Adamczak et al., 2020; Ashraf et al., 2023; Barik et al., 2024; De Fazio et al., 2024; Di Lorenzo et al., 2021; Lalević al., 2023; Patanè et al., 2024). Many plants and essential oils have been used for medicine since ancient times due to their useful antimicrobial, antioxidative, anti-inflammatory and anticancer properties (Ashraf et al., 2023; Di Lorenzo et al., 2021; Edis et al., 2024). These medicinal plants integrate an abundance of bioactive compounds, which is an excellent defense that synergistically protects the plants against "opportunistic pathogens" and any other threats. Most medicinal plants and herbs are easy to find and low-cost, therefore convenient alternatives against AMR (Ashraf et al., 2023; Di Lorenzo et al., 2021; Edis and Bloukh, 2024; Edis et al., 2024; Edis et al., 2022; Edis and Bloukh, 2021; Edis and Bloukh, 2020; Hameed et al., 2021; Lakhan et al., 2020; Maggini et al., 2024; Mohammed et al., 2021; Murtaza et al., 2024; Ricardo-Rodrigues et al., 2024; Romanescu et al., 2023; Singh et al., 2024; Xu et al., 2023). Medicinal plants can be applied on wounds, as

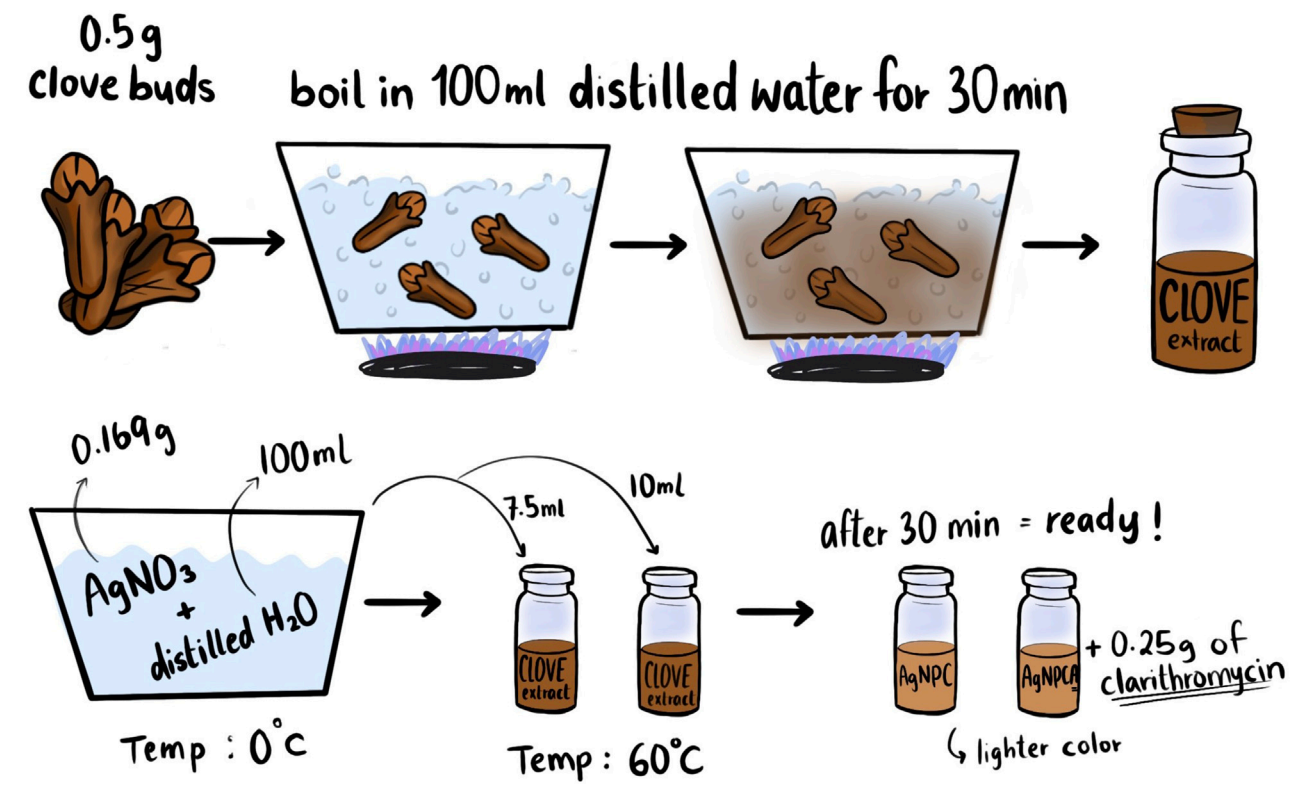

GRAPHICAL ABSTRACT

well as dental and oral care (Ashraf et al., 2023; Di Lorenzo et al., 2021; Edis and Bloukh, 2024; Edis et al., 2024; Edis et al., 2022; Edis and Bloukh, 2021; Edis and Bloukh, 2020; Hameed et al., 2021; Lakhan et al., 2020; Maggini et al., 2024; Mohammed et al., 2021; Murtaza et al., 2024; Ricardo-Rodrigues et al., 2024; Romanescu et al., 2023; Singh et al., 2024; Xu et al., 2023).

Clove (*Syzygium aromaticum*) is a commonly known plant belonging to the Myrtaceae family (Singh et al., 2024). Clove possesses effective antimicrobial properties and is a frequently used preservative (Hameed et al., 2021; Lakhan et al., 2020; Maggini et al., 2024; Mohammed et al., 2021; Murtaza et al., 2024; Ricardo-Rodrigues et al., 2024; Singh et al., 2024; Xu et al., 2023). The clove plant's flower buds contain the greatest essential oil concentration in the plant (Hameed et al., 2021; Maggini et al., 2024; Ricardo-Rodrigues et al., 2024; Singh et al., 2024; Xu et al., 2023). Clove attracted attention due to its antioxidant, antimicrobial, antinociceptive, antiviral, and cytotoxic properties (Hameed et al., 2021; Singh et al., 2024; Xu et al., 2023). It represents one of the main plant sources of phenolic compounds such as flavonoids, hydroxybenzoic acids, hydroxycinnamic acids and hydroxyphenyl propenes (Singh et al., 2024). Clove is one of the most valuable sources of phenolic compounds, such as quercetin and kaempferol, ellagic acid, caffeic acid, as well as ferulic acid (Singh et al., 2024). Eugenol is the main compound found in clove (Hameed et al., 2021; Lakhan et al., 2020; Singh et al., 2024). It has been used in dental applications for pain relieve and for its anti-inflammatory properties (Hameed et al., 2021; Maggini et al., 2024; Singh et al., 2024). The topical use of clove oil is a known and ancient remedy for the relief of tooth pain, which patients still utilize even in modern times (Hameed et al., 2021; Maggini et al., 2024; Singh et al., 2024). Clove is increasingly used for the biosynthesis of nanoparticles and offers interesting results (Hameed et al., 2021; Lakhan et al., 2020; Mohammed et al., 2021; Murtaza et al., 2024; Singh et al., 2024; Xu et al., 2023). Recently, nanoparticles and plant extracts are used as anti-cancer agents within different applications (Chen et al., 2023; Cheng et al., 2023; Lou et al., 2021; Shi et al., 2022; Tang et al., 2017; Wang et al., 2025; Wang et al., 2024; Zeng et al., 2020).

Another option against AMR is the utilization of nanotechnology with silver nanoparticles (Al Aboody, 2019; Al-Otibi et al., 2021; Ankegowda et al., 2020; Barik et al., 2024; Bloukh et al., 2020; Bruna et al., 2021; Corciovă et al., 2024; Desai et al., 2023; El-Kahky et al., 2021; Haj Bloukh et al., 2021; Hernández-Venegas et al., 2023; Mateo and Jiménez, 2022; Menichetti et al., 2023; Mussin and Giusiano, 2024; Nguyen et al., 2023; Pereira et al., 2024; Reda et al., 2019; Riau et al., 2019; Samuggam et al., 2021; Sukhanova et al., 2018; Suvandee et al., 2022). Silver (Ag) has been studied throughout history for its exceptionally potent bactericidal and antimicrobial properties, which can be used against AMR (Bruna et al., 2021; Desai et al., 2023; Haj Bloukh et al., 2021; Hernández-Venegas et al., 2023; Mateo and Jiménez, 2022; Nguyen et al., 2023; Pereira et al., 2024; Riau et al., 2019). Ag is generally unreactive, but ionizes due to the presence of oxygen and moisture in the tissues (Desai et al., 2023; Hernández-Venegas et al., 2023; Pereira et al., 2024; Riau et al., 2019; Singh et al., 2024). This ionization results in the release of silver cations (Ag^+), which are biologically active silver ions (Al Aboody, 2019; Desai et al., 2023; Haj Bloukh et al., 2021; Hernández-Venegas et al., 2023; Menichetti et al., 2023; Pereira et al., 2024; Riau et al., 2019; Singh et al., 2024). Ag^+-ions then attach themselves to thiol groups, anionic ligands of proteins and then to the bacterial cell membrane (Al Aboody, 2019; Desai et al., 2023; Haj Bloukh et al., 2021; Hernández-Venegas et al., 2023; Menichetti et al., 2023; Pereira et al., 2024; Riau et al., 2019; Singh et al., 2024). Once it binds to the cell membrane, it will induce pinocytosis which is the penetration of the bacterial cell wall, leading to denaturation of proteins and the growth arrest of bacteria by enzymes (Al Aboody, 2019; Desai et al., 2023; Haj Bloukh et al., 2021; Hernández-Venegas et al., 2023; Menichetti et al., 2023; Pereira et al., 2024; Riau et al., 2019; Singh et al., 2024).

Currently, the use of silver nanoparticles (AgNP) can be found in water treatments, wound care products, antiseptic sprays, medical devices and cosmetics, for the protection against pathogens (Al Aboody, 2019; Al-Otibi et al., 2021; Ankegowda et al., 2020; Barik et al., 2024; Bloukh et al., 2020; Bruna et al., 2021; Corciovă et al., 2024; Desai et al., 2023; El-Kahky et al., 2021; Haj Bloukh et al., 2021; Hernández-Venegas et al., 2023; Mateo and Jiménez, 2022; Menichetti et al., 2023; Mussin and Giusiano, 2024; Nguyen et al., 2023; Pereira et al., 2024; Reda et al., 2019; Riau et al., 2019; Samuggam et al., 2021; Sukhanova et al., 2018; Suvandee et al., 2022). Silver nanoparticles and plants can be used synergistically due to their outstanding individual properties, giving us greater benefits and an excellent chance to win the battle against AMR (Al Aboody, 2019; Desai et al., 2023; Haj Bloukh et al., 2021; Hernández-Venegas et al., 2023; Menichetti et al., 2023; Pereira et al., 2024; Riau et al., 2019; Singh et al., 2024).

Medicinal plants and nanoparticles can be used in combination with antibiotics to achieve a synergistic effect against resistant pathogens (Khan et al., 2022). Clarithromycin is a commonly used semisynthetic, heterocyclic macrolide antibiotic (Domanovich-Asor et al., 2021; Khan et al., 2022; Lebel, 1993; Takemori et al., 2020; Yamamoto et al., 2021). It is a part of the 14-membered macrolide antibiotic family along with erythromycin and roxithromycin (Domanovich-Asor et al., 2021; Khan et al., 2022; Lebel, 1993; Takemori et al., 2020; Yamamoto et al., 2021). Clarithromycin is an acid-stable equivalent of erythromycin having a methoxy substitution at C-6 of the erythronolide ring (Domanovich-Asor et al., 2021; Khan et al., 2022; Lebel, 1993; Takemori et al., 2020; Yamamoto et al., 2021). This structural difference inhibits the conversion to inactive spiroketal forms in the stomach and enhances the bioavailability and GI tolerance after taking a dose orally. This difference will increase its bactericidal activity when compared to erythromycin (Khan et al., 2022; Lebel, 1993; Takemori et al., 2020; Yamamoto et al., 2021). The antibacterial activity is correlated with its ability to inhibit protein synthesis in bacteria, which is achieved by the binding of the molecules to the subunit 50S of the bacterial ribosome (Khan et al., 2022; Lebel, 1993; Takemori et al., 2020; Yamamoto et al., 2021). The metabolism of clarithromycin in humans produces 14-hydroxy clarithromycin, which promotes an additive or synergistic action to the action of the parent compound against chosen pathogens (Khan et al., 2022; Lebel, 1993; Takemori et al., 2020; Yamamoto et al., 2021). Clarithromycin has a rapid first-pass effect in the liver following its intestinal absorption. Due to its acid stability property, it has a half-life of 5–7 h when taken orally with the dose of 500 mg, meaning it needs to be administered every 12 h (Khan et al., 2022; Lebel, 1993; Takemori et al., 2020; Yamamoto et al., 2021). Increasing antimicrobial resistance against clarithromycin in

comparison to other common antibiotics is alarming. Synergetic mixtures of AgNP and antibiotics in colloidal solutions are often governed by complex processes (Domanovich-Asor et al., 2021; Pani and Chandrasekaran, 2024; Ullah et al., 2023). Recently published studies combine AgNPs with antibiotics, including clarithromycin (Adil et al., 2023; Dove et al., 2023; Hasoon et al., 2024; Ormeño-Martínez et al., 2024; Samari-Kermani et al., 2021; Yang et al., 2017; Zúñiga-Miranda et al., 2023; Ruban et al., 2023). The target is to lower the dosages to mitigate AgNP toxicity and development of resistance towards these new compounds (Adil et al., 2023; Dove et al., 2023; Hasoon et al., 2024).

In this study, we used a clove bud extract (C) mediated silver nanoparticle (AgNP) synthesis in form of AgNPC. We also aimed at introducing clarithromycin into the formulation to study the changes within the compound. The antimicrobial properties of the two title compounds AgNPC and AgNPCA against a panel of 10 microorganisms were investigated. The study revealed higher antimicrobial activities and smaller nanoparticle size for AgNPC compared to AgNPCA. The reasons for these results were found in the molecular changes, when clarithromycin is present. Amalgamation of AgNPC with clarithromycin increases the size of the nanoparticles, causes aggregation (Adil et al., 2023; Dove et al., 2023; Hasoon et al., 2024; Ruban et al., 2023). A comparison between SEM and DLS sourced particle size measurements showed a slight difference and pointed out a possible organic layer around AgNPCA caused by the availability of clarithromycin (Tarrés et al., 2022). However, alleviated particle size in AgNPCA along with agglomeration did not counteract the antimicrobial properties. AgNPCA, the synergistic compound between clove-bud mediated AgNP and clarithromycin, inhibited pathogens, which are resistant to pure clarithromycin. Bacterial strains were in general more susceptible to AgNPC, followed by AgNPCA and lastly to clarithromycin alone. The results indicate possible applications for the title compounds in wound treatment. Further investigations like *in vitro* studies and cytotoxicity analysis are needed to confirm the uses in the medical field.

2 Materials and methods

2.1 Materials

Dry clove buds were purchased from the local market of UAE. Sterile filter paper Whatman 150 mm were purchased from GE Healthcare (Amersham Place Little Chalfont, Buckinghamshire, HP7 9NA, United States). Sodium hydroxide (NaOH) pellets, chlarithromycin and silver nitrate ($AgNO_3$) were provided from Sigma-Aldrich Chemical Co. (St. Louis, MO, United States). The same company supplied the reference strains *E. coli* WDCM 00013 Vitroids, *K. pneumoniae* WDCM 00097 Vitroids, *P. aeruginosa* WDCM 00026 Vitroids, *B. subtilis* WDCM 0003 Vitroids, and *C. albicans* WDCM 00054 Vitroids. Mueller Hinton Broth (MHB), Sabouraud Dextrose broth and ethanol were also procured from Sigma Aldrich. Further strains consisting of *P. mirabilis* ATCC 29906, *S. aureus* ATCC 25923, *S. pyogenes* ATCC 19615, *E. faecalis* ATCC 29212, and *S. pneumoniae* ATCC 49619 were purchased from Liofilchem (Roseto degli Abruzzi, TE, Italy). Himedia (Jaitala Nagpur, Maharashtra, India) provided sterile filter paper discs with a diameter of 6 mm. Liofilchem Diagnostici (Roseto degli Abruzzi (TE), Italy) supplied antibiotic discs of nystatin (9078, 100 IU/disc) and gentamicin (9125, 30 μg/disc), as well as disposable sterilized Petri dishes containing Mueller Hinton II agar and McFarland standard sets. All utilized reagents were of analytical grade. All experiments were done under sterile conditions with ultrapure water and absolute ethanol.

2.2 Preparation of clove (C) extract

The clove buds were finely grinded. 0.5 g of the obtained clove powder was filled into a 250 mL beaker with 100 mL of distilled water, covered and heated to 60°C with stirring for 30 min. The resulting light brown extract was cooled down to room temperature and filtered by a Whatman 150 mm filter paper into a 250 mL flask. 30 mL and 40 mL of clove extract were diluted with 70 mL and 60 mL ultra-distilled water, respectively. The prepared stock solution was transferred into brown, screw capped bottles and stored at 3°C in the fridge until further usage equations should be inserted in editable format from the equation editor.

2.3 Preparation of AgNPC and AgNPCA

$AgNO_3$ solution was prepared by adding 0.169 g of $AgNO_3$ into 100 mL of distilled water at 0°C and 10 min of constant stirring. After that, 7.5 mL and 10 mL of these $AgNO_3$ solutions were added into 100 mL of the prepared 30% and 40% clove stock solutions, respectively. The silver nitrate solution was added during constant stirring into the clove extract stock solution at a temperature of 60°C. After 30 min continuous stirring, color changes were observed in the solution from dark brown to light brown. Few drops (1-2 drops) of HCl at 0°C and 10 min of stirring were added into AgNPC to adjust the pH from 8.5 to 8.3. AgNPCA is prepared by first dissolving 0.125 g clarithromycin into 250 mL of distilled water. Then, 25 mL of this clarithromycin solution was added under constant stirring into a 40%-AgNPC solution at 0°C within 10 min.

2.4 Characterization of AgNPC and AgNPCA

Morphology and composition of AgNPC and AgNPCA were studied by SEM/EDS, UV-vis, FTIR, and x-ray diffraction (XRD).

2.4.1 Scanning electron microscopy (SEM) and energy-dispersive X-ray spectroscopy (EDS)

The SEM (scanning electron microscopy) and EDS (energy-dispersive X-ray spectroscopy) analysis was performed with the Thermofisher scientific APREO 2C SEM (Waltham, Massachusetts, United States 02451). The analysis was conducted at 10 kV after being diluted with distilled water, dropped onto a carbon-coated copper tape, dried and covered with a gold coating with the Quorum Technology Mini Sputter Coater.

2.4.2 Size and zeta potential analysis

Calculating the average size, size distribution, zeta potential, as well as polydispersity index (PDI) of AgNPC and AgNPCA was

achieved by Dynamic light scattering (DLS) analysis by a Horiba SZ-100 (Palaiseau, France).

2.4.3 UV-vis spectrophotometry (UV-Vis)

The UV-vis analysis of AgNPC and AgNPCA was done on a Shimadzu spectrophotometer model 2600i (Kyoto, Japan). Measurements included the wavelength spectrum from 195 to 800 nm.

2.4.4 Fourier-transform infrared spectroscopy (FTIR)

AgNPC and AgNPCA underwent Fourier Transform Infrared (FTIR) analysis within the spectral range of 400–4,000 cm^{-1} by utilizing a Shimadzu Attenuated Total Reflectance (ATR) IR spectrometer equipped with a Diamond window (Kyoto, Japan).

2.4.5 X-ray diffraction (XRD)

The X-ray diffraction analysis was performed by using a BRUKER D8 Advance (Karlsruhe, Germany). The study used a Two Theta configuration, with a time per step of 0.5 s and a step size of 0.03 equipped with Cu radiation at a wavelength of 1.54060 Å.

2.5 Antimicrobial studies

The title compounds AgNPC and AgNPCA were tested against the ten reference strains, which included *S. aureus* ATCC 25923, *S. pneumoniae* ATCC 49619, *E. faecalis* ATCC 29212, *S. pyogenes* ATCC 19615, *B. subtilis* WDCM 0003 Vitroids, *K. pneumoniae* WDCM 00097 Vitroids, *E. coli* WDCM 00013 Vitroids, *P. aeruginosa* WDCM 00026 Vitroids, *P. mirabilis* ATCC 29906 and *C. albicans* WDCM 00054 Vitroids. Nystatin and gentamicin and nystatin were utilized as positive controls. Negative controls included pure ethanol and ultrapure water. These negative controls showed no inhibition zone. Every test was done thrice, and the average results were reported.

2.5.1 Bacterial strains and culturing

AgNPC and AgNPCA were tested against ten reference, standard microbial strains consisting of *S. aureus* ATCC 25923, *S. pneumoniae* ATCC 49619, *E. faecalis* ATCC 29212, *S. pyogenes* ATCC 19615, *B. subtilis* WDCM 0003 Vitroids, *K. pneumoniae* WDCM 00097 Vitroids, *E. coli* WDCM 00013 Vitroids, *P. aeruginosa* WDCM 00026 Vitroids, *P. mirabilis* ATCC 29906 and *C. albicans* WDCM 00054 Vitroids. The reference strains were stored at −20°C and then revived by inoculating fresh microbes into Mueller Hinton Broth (MHB). These prepared strains were then kept at 4°C until further use.

2.5.2 Procedure for zone of inhibition (ZOI) plate studies

The zone of inhibition (ZOI) plate method was used to investigate the antimicrobial activities of AgNPC and AgNPCA against the 10 microbial reference strains (Bauer et al., 1959). All the nine bacterial reference strains were suspended in 10 mL of Mueller-Hinton broth (MHB) and then incubated for 2–4 h at 37°C. Only the fungus *C. albicans* WDCM 00054 was cultured in Sabouraud Dextrose broth at 30°C. The microbial cultures were adjusted to 0.5 McFarland standard and 100 μL of microbial culture was evenly seeded with sterile cotton swaps on ready-made disposable, sterilized Petri dishes. These plates were dried for 10 min at ambient conditions and then utilized for the antimicrobial testing.

2.5.3 Disc diffusion method (DD)

The antimicrobial testing of AgNPC and AgNPCA followed the guidelines of the Clinical and Laboratory Standards Institute (CLSI) (CLSI, 2019). Sterile filter paper discs were soaked in 2 mL AgNPC and AgNPCA solutions of various concentrations for 24 h at ambient conditions. Afterwards, the discs were dried at ambient conditions for 24 h. Nystatin and gentamycin antibiotic discs were utilized as positive controls. The clear area around the soaked disk is measured by a ruler to the nearest millimeter and is the diameter of zone of inhibition (ZOI). No inhibition zone around the disk is considered as resistant (R) against the reference strain.

2.6 Statistical analysis

The statistical analysis was done utilizing SPSS software (version 17.0, SPSS Inc., Chicago, IL, United States), with data presented in mean values. The significance between groups was determined through one-way ANOVA. Statistical significance value was defined as $p < 0.05$.

3 Results and discussion

AMR is a dangerous threat to human health the future of its existence (Baran et al., 2023; Tang et al., 2023; Uddin et al., 2021). Multi-drug resistant pathogens cause higher morbidity and mortality rates among immunocompromised patients worldwide (Baran et al., 2023; Tang et al., 2023; Uddin et al., 2021). Alternative agents are needed to support or replace antimicrobials. Following this trend, we present in this study biosynthesized silver nanoparticles AgNPC and AgNPCA and their antimicrobial properties. The two title compounds were characterized by diverse analytical methods, as well as tested against a selection of 10 reference microbial strains.

3.1 Electron microscope (SEM) and energy-dispersive X-ray spectroscopic (EDS) analysis

The morphology and composition of AgNPCA and AgNPC were studied by SEM and EDS analysis, respectively (Figure 1).

Figure 1A reveals a smooth surface texture morphology of AgNPC with small, spherical structures. In contrast, Figure 1C looks a bit more heterogeneous with slightly bigger, flatter entities in AgNPCA (Figure 1A, Supplementary Material S1–S4). These changes in size and morphology confirm the incorporation of clarithromycin into AgNPCA. The EDS displays in Figure 1B the presence of Al (55.6%), C (18.5%), O (13.0%), Ag (10.5%) and P (2.4%). Figure 1D presents Ag (39.1%), C (24.2%), Al (19.0%), O (9.4%), K (4.8%), Cl (2.5%) and Na (0.9%). In both samples, aluminum and gold are found due to the sample holder and the

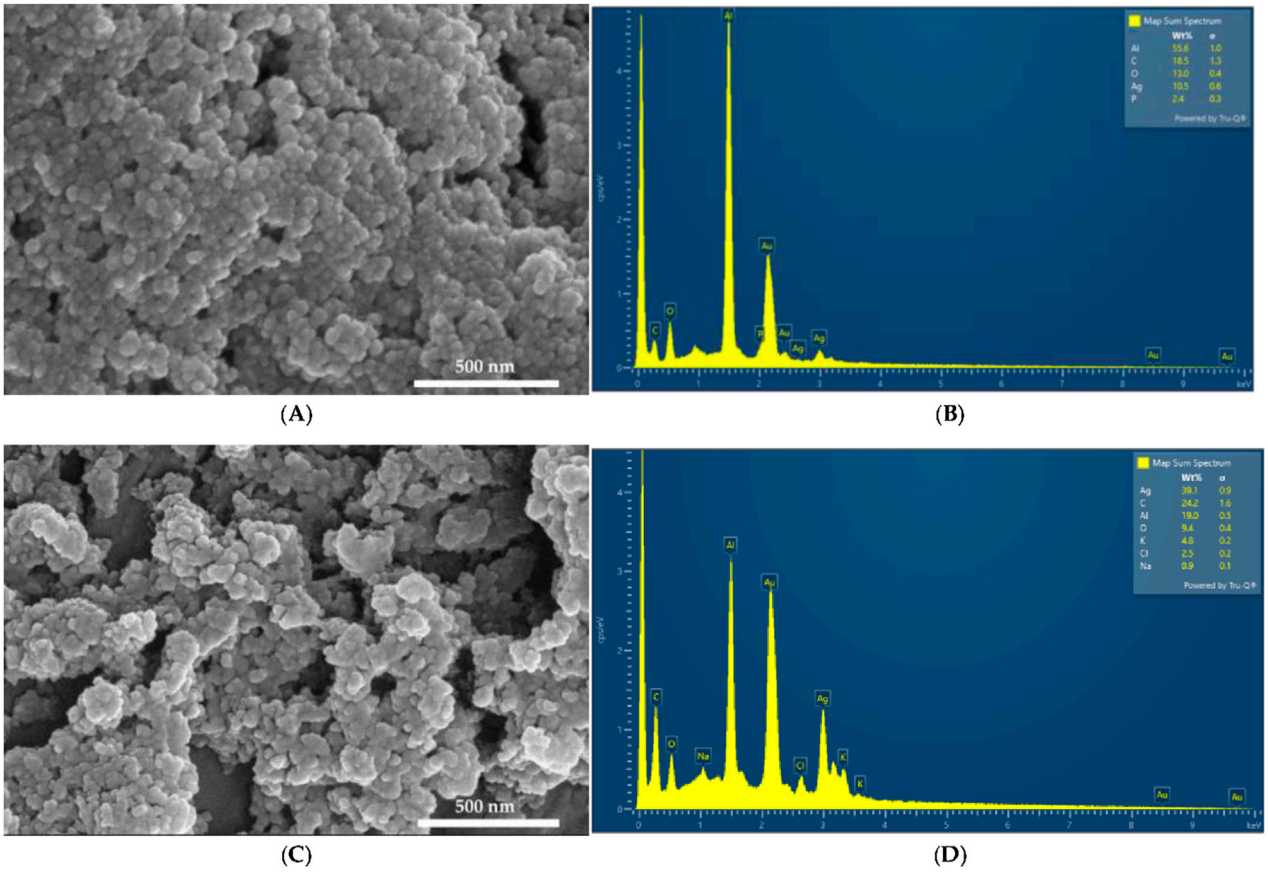

FIGURE 1
SEM and EDS analysis. AgNPC **(A)** SEM; **(B)** EDS; AgNPCA **(C)** SEM; **(D)** EDS.

coating process, respectively. Both samples show high purity by the EDS analysis. Oxygen and carbon are available in both samples due to the abundance of biomolecules originating from the clove extract. The peak of Ag appears in both EDS between 3 and 4 keV in agreement with previous reports (Bloukh et al., 2020; Haj Bloukh et al., 2021; Mussin and Giusiano, 2024; Singh et al., 2024). Figure 1D shows a small peak around 0.5 keV for AgNPCA, which indicates also the existence of Ag_2O through oxidation (Singh et al., 2024). K and Na, as well as Cl are introduced through clarithromycin in form of inactive ingredients within the antibiotic (Pani and Chandrasekaran, 2024). The addition of few drops of HCl to stabilize the pH, the nanoparticles and the clarithromycin contributed also to the detection of Cl (Ullah et al., 2023). The particle size measurements by SEM on both samples provided 7.3 ± 0.3 nm for AgNPC and 7.7 ± 0.6 nm for AgNPCA (Supplementary Material S4).

3.2 Dynamic light scattering (DLS) and zeta potential analysis

The DLS and Zeta Potential analysis provide crucial information regarding the size, agglomeration, distribution, and stability of nanoparticles in solution. Table 1 shows the results of the DLS measurements of AgNPC and AgNPCA.

The DLS results of the AgNPCA and AgNPC reveal an average size of 36.0 nm and 12.8 nm, respectively (Table 1). Further peak intensities are not available in the spectrum. Clarithromycin and AgNPC attract each other because of their opposite charges leading to aggregation and increase in particle size (Table 1).

AgNPC has a polydispersity index (PDI) of 0.458 additionally to the average size of 12.8 nm. This data verifies a polydisperse sample, in which the phenolic compounds in the clove extract effectively functioned as capping and reducing agents (Desai et al., 2023; Haj Bloukh et al., 2021). The PDI and Z-average for AgNPCA could not be calculated due to the increase in particle size, instability and agglomeration. Our DLS has a limit up to 50, any measurement above that will not be reported. Therefore, a PDI value increase above 50 is expected for AgNPCA. This increase in PDI from AgNPC to AgNPCA verifies, that the nanocompound is strongly polydisperse and clarithromycin contributed to their synthesis (Adil et al., 2023).

Hence, zeta (ζ) potential analysis allows predictions about AgNP stability within a colloidal suspension (Desai et al., 2023; Haj Bloukh et al., 2021). The zeta (ζ) potential of AgNPC and AgNPCA are −34.9 and −11.1 mV, respectively (Table 1). Their negative values point towards negatively charged AgNP surfaces (Bloukh et al., 2020; Desai et al., 2023; Haj Bloukh et al., 2021; Sukhanova et al., 2018). The negative charge of −34.9 mV indicates that AgNPC solution is stable, while AgNPCA appears to form agglomerates due

TABLE 1 DLS and Zeta Potential results for AgNPCA and AgNPC.

Sample	Zeta potential (mV)	Particle size mean (nm)	Z-Average (nm)	Polydispersity index (PDI)
AgNPC	−34.9	12.8 ± 11.2	65.6	0.458
AgNPCA	−11.1	36.0 ± 34.3	-	-

to its much bigger zeta potential of −11.1 mV. The negative charge of −34.9 mV indicates that AgNPC solution is stable, while AgNPCA appears to form agglomerates due to its much bigger zeta potential of −11.1 mV. However, apart from electrostatic stabilization, steric stabilization from clove biocompounds and clarithromycin molecules surrounding the nanoparticles could sustain stability, although the zeta potential approaches towards zero (Adil et al., 2023; Bloukh et al., 2020; Desai et al., 2023; Haj Bloukh et al., 2021; Pani and Chandrasekaran, 2024; Sukhanova et al., 2018). Possibly, higher cytotoxicity is expected in AgNPCA compared to AgNPC, because NP with ζ higher than ±30 mV are more stable and do not agglomerate in general (Desai et al., 2023; Sukhanova et al., 2018). The DLS results confirm a slight decrease in colloidal stability for AgNPCA, while steric stabilization by surrounding clarithromycin and clove biocompunds is achieved (Adil et al., 2023).

However, in comparison to Pani et al., clarithromycin addition into a suspension with polymers resulted in changes of the zeta-potential, size and PDI (Pani and Chandrasekaran, 2024). Clarithromycin is a large molecule with several electronegative oxygen atoms, nitrogen atoms and hydroxide groups in the periphery of the macrocyclic molecule. Once it is introduced into AgNPC, the zeta potential changes to a higher, but still negative number (−11.1 mV) compared to AgNPC with −34.9 mV. This change is also seen in the study of Pani et al., when clarithromycin was added into the nanoparticle suspension (Pani and Chandrasekaran, 2024). The zeta potential changed from −52.2 mV to −14.3 mV with clarithromycin (Pani and Chandrasekaran, 2024). Pereira et al. added chitosan to AgNP and observed similar increase in the zeta potential from −26.3 mV with the chitosan coating towards −15.9 mV (Pereira et al., 2024). The authors stated, that chitosan introduced a slight positive charge, increasing the zeta potential slightly (Pereira et al., 2024). Our results also confirm a slight decrease of negative charge towards higher zeta potential by adding clarithromycin (Table 1). Therefore, the zeta potential changes confirm changes on the AgNP surface and size of the resulting AgNPCA. In this regard, Pani et al. have seen a change in AgNP size from initially 545.7–1,289.8 nm, while our results show an increase from 12.8 towards 36 nm, when clarithromycin was introduced (Pani and Chandrasekaran, 2024). The reported PDI for Pani et al. was 0.286 initially and changed to 0.056 after adding clarithromycin (Pani and Chandrasekaran, 2024). In comparison, our DLS analysis shows a PDI of 0.458, while AgNPCA was not detected (Table 1). All the DLS results point towards aggregation induced by an increasing layer of organic molecules around the silver nanoparticles after adding clarithromycin into the formulation. This assumption is confirmed by a comparison between the particle size measurements of SEM and DLS analysis (Table 1, Supplementary Material S4). The SEM measurements provide 7.3 ± 0.3 nm for AgNPC and 7.7 ± 0.6 nm for AgNPCA, while Table 1 mentions hydrodynamic diameters of 12.8 and 36 nm, respectively (Supplementary Material S4). Accordingly, the difference between SEM and DLS analysis points towards 28.3 nm around AgNPCA and 5.5 nm around AgNPC. These measurements highlight the thickness of the organic layer around the nanoparticles.

In conclusion, AgNPC presents as a stable, homogenous bio-nano-compound, with small average particle size and high stability. The clove-based phenolic compounds with their -OH and -C=O groups surrounded the AgNP surface and prevented agglomeration through further secondary nucleation (Bloukh et al., 2020; Desai et al., 2023; Haj Bloukh et al., 2021, 2023; Singh et al., 2024). This monolayer of plant phenolic compounds is compromised by the addition of clarithromycin. The antibiotic possibly removes the layer of phenolic compounds and exposes AgNP to agglomeration, although steric stabilization is achieved, an increased size and changes in the antimicrobial activities are observed (Bloukh et al., 2020; Desai et al., 2023; Haj Bloukh et al., 2021, 2023; Singh et al., 2024).

3.3 X-ray diffraction (XRD) of AgNPC and AgNPCA

The XRD analysis of AgNPC and AgNPCA depict the composition and the crystalline nature of the two samples (Figure 2).

The XRD analysis reveals in both nano-compounds crystalline phases of pure AgNP (Figure 2). AgNPCA (red) shows sharp, very strong peaks with 2θ values around 32° while AgNPC (blue) has almost similar, but much weaker reflections with 2Theta values of 18.80° (001), 27.35° (001), 29.78° (003), 32.24° (001), 38.13° (111), 46.33° (200) and 62.61° (003) for AgNP (Figure 2; Table 2) (Al Aboody, 2019; Ankegowda et al., 2020; El-Kahky et al., 2021; Al-Otibi et al., 2021; Haj Bloukh et al., 2021; Samuggam et al., 2021; Suvandee et al., 2022).

A detailed analysis of AgNPCA reveals an AgNP-XRD pattern with diffraction peaks at 2Theta values of 38.28°, 46.24°, 67.44°, and 77.0° corresponding to (111), (200), (220), and (311). These Bragg reflections belong to the lattice planes of face-centered cubic (fcc) Ag crystals according to JCPDS 04–0783 (Lakhan et al., 2020; Murtaza et al., 2024; Singh et al., 2023; Suvandee et al., 2022). Additionally, crystallographic planes of Ag2O related to fcc (JCPDS 041–1,104) are available at 27.8° (110), 32.24° (111), 37.9° (200), 54.86° (220), 61.72° (331), and 72.9° (222) (Figure 2; Table 2). The weak peaks in AgNPCA at 30.40°, and 29.04° are due to AgCl in agreement with previous reports (Figure 2; Table 2) (Al Aboody, 2019; Haj Bloukh et al., 2021). These compounds form after the addition of the antibiotic clarithromycin as by-products as a result to changes on the AgNP surface. After its addition, clarithromycin starts to compete with the clove-based compounds acting as stabilizing and capping agents on the AgNP surface. The antibiotic settles

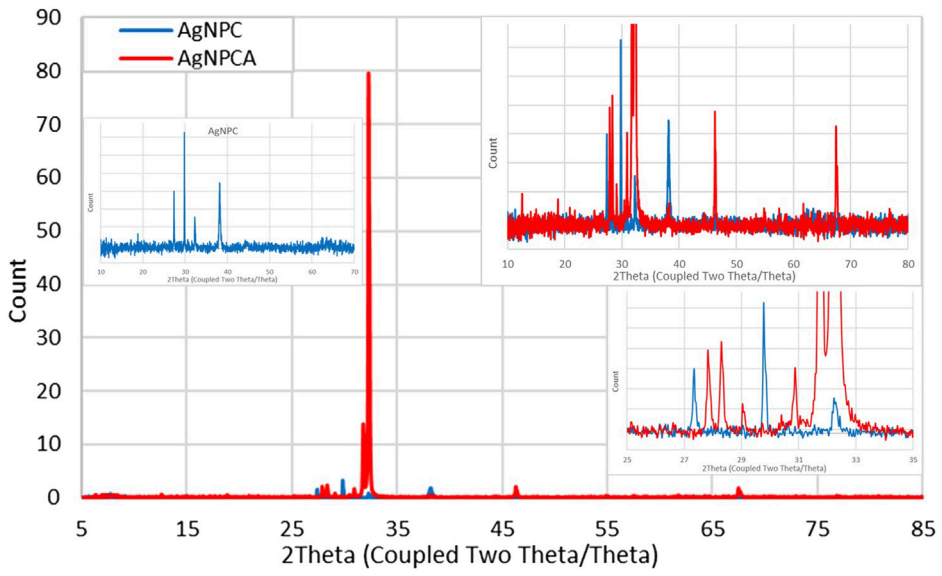

FIGURE 2
X-ray diffraction (XRD) study of AgNPCA (red) and AgNPC (blue).

TABLE 2 XRD study of AgNPCA, AgNPC, clarithromycin (Antibiotic) and other investigations with their calculated planes (2Theta°).

	AgNPCA	AgNPC	1	2	3	4	5	6	7	Planes
AgNP	18.08 w	18.80 w	19.02	-	-	-	-	-	-	(001)
	28.30 m	27.35 vw	28.35	-	-	-	-	-	-	(001)
	30.88 m	29.78 w	30.89	-	-	-	-	-	-	(003)
	31.73 m	32.24 vw	32.34	-	-	32	-	-	-	(001)
AgNP (JCPDS 04-0783)	38.28 w	38.13 w	38.08	38.4	38.61	-	38.25	38.08	-	(111)
	46.24 m	46.33 vw	-	44.5	46.43	47	44.43	44.21	-	(200)
	67.44 m	62.61 vw	-	64.8	65.52	68	64.67	64.42	-	(220)
	76.89 vw	75.99 vw	-	77.4	78.28	78	77.59	77.32	-	(311)
AgCl	29.04 w	-	-	-	-	-	-	-	-	
	30.40 w	-	-	-	-	-	-	-	-	
Ag_2O (JCPDS 041-1104)	27.83 m	-	-	26.7	-	-	28	-	-	(110)
	32.24 vs	-	-	32.7	-	-	32	-	-	(111)
	37.90 vw	-	-	37.9	-	-	46	-	-	(200)
	54.89 vw	-	-	54.9	-	-	-	-	-	(220)
	61.72 vw	-	-	65.5	-	-	-	-	-	(331)
	72.9 vw	-	-	69.0	-	-	-	-	-	(222)
Clarithromycin	-	-	-	-	-	-	-	-	11.41	
	12.52 w	-	-	-	-	-	-	-	13.69	
	-	-	-	-	-	-	-	-	15.11	
	-	-	-	-	-	-	-	-	17.23	
	20.87 vw	-	-	-	-	-	-	-	20.38	
	21.73 vw	-	-	-	-	-	-	-	23.08	

w, weak; v, very; s, strong; m, intermediate. 1, El-Kahky et al. (2021); 2, Singh et al. (2024); 3, Ankegowda et al. (2020); 4, Samuggam et al. (2021); 5, Murtaza et al. (2024); 6, Lakhan et al. (2020); 7, Khan et al. (2022).

partly on the AgNP surface by dipol-dipol bonds between silver and its abundant oxygen atoms and compromises the monolayer on the AgNP surface. Furthermore, silver ions are released through oxidation and exchange processes during the equilibrium (Al Aboody, 2019; Reda et al., 2019; Singh et al., 2023). As a result, AgCl forms due to the availability of chloride ions in the clove bud extract and as inactive ingredient in clarithromycin itself, while Ag_2O is formed increasingly through oxidation (Al Aboody, 2019; Reda et al., 2019; Singh et al., 2023).

The very weak bands around 5°–23.08° are due to semicrystalline, amorphous phases originating from clarithromycin and clove-based compounds within the sample (Figure 2; Table 2). Clarithromycin related weak to very weak peaks are seen in the red graph at 2Theta values of 12.52°, 20.87° and 21.73° in agreement with previous investigations (Figure 2; Table 2) (Khan et al., 2022).

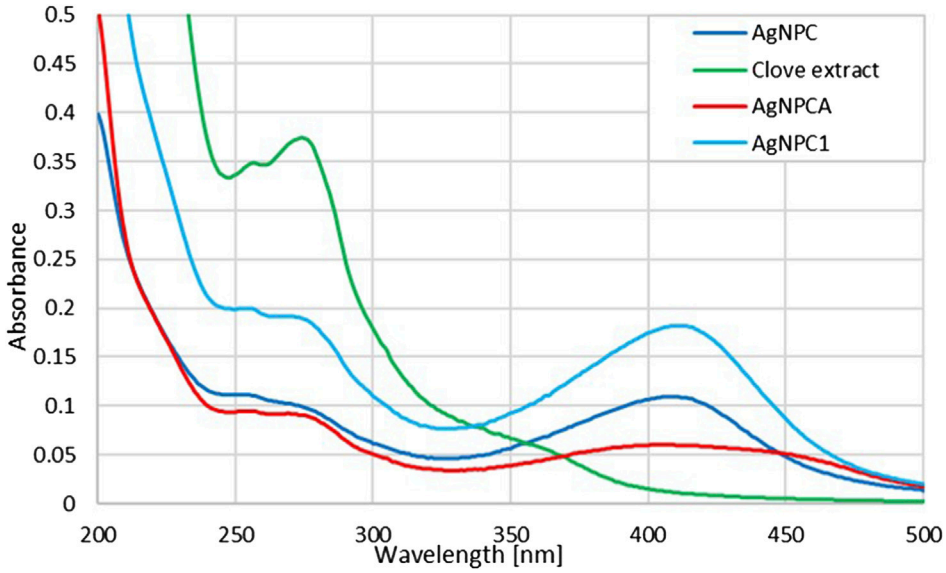

FIGURE 3
UV-vis analysis of AgNPCA, AgNPC, AgNPC1 and clove extract (200–500 nm). (AgNPCA: red; AgNPC: blue; AgNPC1: light blue; clove extract: green).

TABLE 3 UV-vis absorption signals in the samples clove extract, AgNPCA, AgNPC, AgNPC1, and further investigations [nm].

	Clove extract	AgNPCA	AgNPC	AgNPC1	1	2	3	4	5	6
	257 s 274 s 305 w, sh 364 w, sh	254 w, br 269 w, br 305 vw, sh 364[a]	251 w, br 269 w 305 vw, sh 364[a]	253 m, br 267 m, br 307 w, sh 364[a]	200 - 300 350	- - - -	206 - - -	- - 289 -	- 275 310 360	- - - -
AgNP	-	408 w, br	411 w, br	412 m, br	470–480	411	400–411	-	351	376

vw, very weak; br, broad; s, strong; m, intermediate; sh, shoulder; 1, Lakhan et al. (2020); 2, Mussin and Giusiano (2024); 3, Suvandee et al. (2022); 4, Murtaza et al. (2024); 5, Singh et al. (2024); 6, Ruban et al. (2023).
[a]Broad bands cause overlapping, therefore peak cannot be located precisely.

As a conclusion, the sharp peaks in the XRD study of AgNPCA and AgNPC point to mainly crystalline AgNP with very limited semicrystalline, amorphous phases due to clove extract biomolecules and clarithromycin (Figure 2; Table 2). The overall XRD investigation confirms the purity of the nano-biohybrid AgNPC. Meanwhile in AgNPCA, AgCl and Ag_2O emerge due to the addition of clarithromycin (Figure 2; Table 2).

3.4 UV-vis spectroscopy

The UV-vis spectral analysis of clove extract, AgNPC, AgNPC1 and AgNPCA are presented in Figure 3.

Figure 3 provides insight into the changes of the clove extract during the AgNP formation (AgNPC). Furthermore, it presents the developments after introducing the antibiotic clarithromycin (AgNPCA). The phenolic compounds in the clove extract reduce the silver ions to metallic silver. The UV-vis spectrum can be used to verify these biocompounds in all the four samples (Figure 3; Table 3).

The clove-based phenolic compounds appear in the region around 240–370 nm (Table 3). Therefore confirming availability of flavonoids, phenolic acids as hydroxybenzoic acids and hydroxycinnamic acids, as well as hydroxyphenyl propenes (Singh et al., 2023). The phenolic compounds are comprised of mainly eugenol, quercetin and kaempferol, ellagic acid, caffeic acid, as well as ferulic acid (Bloukh et al., 2020; Haj Bloukh et al., 2021; Singh et al., 2023). These compounds are verified in the green curve of clove extract by two main, strong absorption peaks at 257 and 274 nm, followed by a broad band at 364 nm and a weak shoulder at 305 nm (Figure 3; Table 3) (Bloukh et al., 2020; Haj Bloukh et al., 2021; Lakhan et al., 2020; Murtaza et al., 2024; Singh et al., 2023). The first three peaks at 257, 274 and possibly 305 nm can be attributed to flavonoids quercetin and kaempferol (flavonols), while the broad band at 364 nm indicates presence of phenolic acids (Bloukh et al., 2020; Haj Bloukh et al., 2021; Singh et al., 2023). The concerned phenolic compounds around 364 nm are related to eugenol, caffeic acid, ferulic acid and ellagic acid (Bloukh et al., 2020; Haj Bloukh et al., 2021; Lakhan et al., 2020; Murtaza et al., 2024; Singh et al., 2023) (Figure 3; Table 3).

The clove extract biocompounds absorption peaks at 257 and 274 nm are blue shifted towards shorter wavelengths in AgNPC (251 and 269 nm), AgNPC1 (253 and 267 nm), as well as in AgNPCA (254 and 269 nm) (Figure 3; Table 3). This

hypsochromic effect underlines removal of conjugation and chromophores, solvent effect, saturation of -C=O to -C-O and an overall decreased size of the newly formed compounds compared to the clove extract components. AgNPC1 and AgNPCA were prepared by adding 10 mL of 10% $AgNO_3$ into the clove extract, while AgNPC was based on 7.5 mL of a 10% $AgNO_3$ solution into the clove extract. However, the best inhibitory results were achieved by AgNPC and AgNPCA as explained in the upcoming section below. Therefore, a smaller AgNP concentration in AgNPC leads to smaller NP size and better antimicrobial properties (Table 1). In comparison, higher Ag concentration in AgNPCA reveals better antimicrobial properties at larger NP size (Table 1). A second look at the undergoing change after adding clarithromycin reveals a red shift from 251 nm (AgNPC) to 254 nm (AgNPCA). The red curve of AgNPCA reveals also a shoulder at around 281 nm corresponding to clarithromycin itself in accordance to Pani and Chandrasekaran (2024)).

The UV-vis study shows the AgNP plasmonic peak at λ-max at 408, 411 and 412 nm for AgNPCA (red), AgNPC (blue) and AgNPC1 (light blue), respectively (Figure 3; Table 3). The surface plasmon resonance (SPR) absorbance band of AgNP undergoes two different shifts in this scenario. Adding clarithromycin into the sample AgNPC blue shifts the SPR band from 411 nm towards a broad band with a maximum at 408 nm in AgNPCA with a small shoulder at 450 nm. The blue shift confirms the capping of AgNPC by clarithromycin with its functional groups leading to aggregation (Adil et al., 2023). The same was reported by Adil et al. in their investigation of cephalosporins capped plant-based AgNP describing the phenomenon as accumulation of chemical groups around AgNP (Adil et al., 2023). The weak shoulder at 450 nm could be due to the aggregation and coating of AgNPC by organic molecules (Adil et al., 2023).

Additionally, the UV-vis spectrum shows a reduction of the AgNP peak starting from AgNPC1 to AgNPC and finally AgNPCA. The reduction of the AgNP peak indicates an increased coating of the AgNP surface by the available organic compounds in the solution, while resulting in a reduction of free AgNP (Pereira et al., 2024; Zúñiga-Miranda et al., 2023). However, once AgNPCA is formed by the addition of clarithromycin, the antibiotic induces the removal of the monolayer on the AgNPC and allows secondary nucleation. Organic molecules within the solution start coating the AgNP surface and lead to bigger sized aggregates coupled with a red shift (Table 1). Clarithromycin induces the removal of the monolayer on the AgNPC and allows secondary nucleation. Organic molecules within the solution start coating the AgNP surface and lead to bigger size coupled with a red shift (Table 1) (Ormeño-Martínez et al., 2024; Pereira et al., 2024; Samari-Kermani et al., 2021; Ullah et al., 2023; Yang et al., 2017; Zúñiga-Miranda et al., 2023). This red shift verifies the DLS measurements and the XRD results by underscoring the increase in AgNP size (Tables 1, 2).

The SPR band is in accordance with previous investigations. Mussini et al. and Suvandee et al. had an AgNP SPR band around 411 nm, while other studies reported lower wavelengths between 350 and 400 nm (Lakhan et al., 2020; Mussin and Giusiano, 2024; Samuggam et al., 2021; Suvandee et al., 2022). Our previous investigations of plant-based synthesis of AgNP with *Cinnamomum zeylanicum* and *Lepidium sativum* resulted in SPR bands around 390-415 and 400 nm, respectively (Bloukh et al., 2020; Haj Bloukh et al., 2021). The pH levels in both studies were around 8.5, with a silver ion concentration of 10%, while in the synthesis of AgNPC, the best results were achieved with 30% silver ion concentration and a pH of 8.5 (Bloukh et al., 2020; Haj Bloukh et al., 2021). In general, the SPR band shape and values depend on the surrounding environment, stabilizing agents, method of synthesis, size morphology and further factors (Desai et al., 2023).

3.5 Fourier-transform infrared (FTIR) spectroscopy

The FTIR analysis of AgNPCA, AgNPC and pure clove extract reveals purity and similar structural features within the samples (Figure 4).

The FTIR analysis of the title compounds AgNPC (blue) and AgNPCA (red), together with the clove extract (green) in Figure 4 allow insight into the changes during nanoparticle formation and antibiotic addition. Both nanoparticle formulations have similar pattern in the FTIR spectrum and are in accordance with previous reports (Figure 4) (Bloukh et al., 2020; Haj Bloukh et al., 2021). In general, the FTIR study reveals highest absorption intensities for the clove extract (green), followed by AgNPC (blue) and lastly AgNPCA (red) (Figure 4). This pattern is exempted in the regions around 1,647 cm^{-1}, 1,100–1,000 cm^{-1} and 800–600 cm^{-1}, which belong to vibrational stretching bands of -C=O, -C-O, as well as twisting- and bending vibrations of $-CH_2$, -C-H and O-H groups (Figure 4; Table 4).

The mentioned exceptions in absorption intensity point towards developments triggered by AgNP synthesis and addition of clarithromycin (Figure 4). The concerned functional groups in AgNPC absorb more with high intensity, because they are less encapsulated/complexed by hydrogen bonding. Once clarithromycin is added, hydrogen bonding is enabled between the many functional groups of the antibiotic with the already existing clove extract phenolic compounds, flavonoids, the solvent and the AgNP surface. All together reduce the absorption intensity of AgNPCA. These affected structural parts of the AgNPCA molecules are vibrational stretching bands of -C=O at 1,647 cm^{-1}, as well as -C-O at 1,101, 1,070, 1,065, 1,055, 1,047 and 1,038 (Figure 4; Table 4). Additionally, vibrational twisting bands of $-CH_2$ at 883 and 878 cm^{-1}, as well as out-of-plane bending vibrations of -CH at 802 cm^{-1} and bending vibrations of -OH at 667 cm^{-1}. The three latter seem to undergo complexation or encapsulation processes throughout the molecules, seemingly decreasing their interatomic distances. Therefore, the twisting/out-of-plan/bending motions of the methylene-, -C-H, as well as the hydroxyl-groups are characterized by reduced flexibility and are not free enough to interact with the IR light.

The vibrational stretching band at 1,647 cm^{-1} related to -C=O bonds has the highest intensity for AgNPC, followed by AgNPCA and the clove extract. The increased absorbance of carbonyl stretching vibrations in AgNPC is the result of an increase in conjugation systems and chromophores after adding silver ions into the clove extract. The increase in intensity verifies the formation of Ag-O interactions between the metallic silver in AgNP and the surrounding biocomponents. The biocompounds

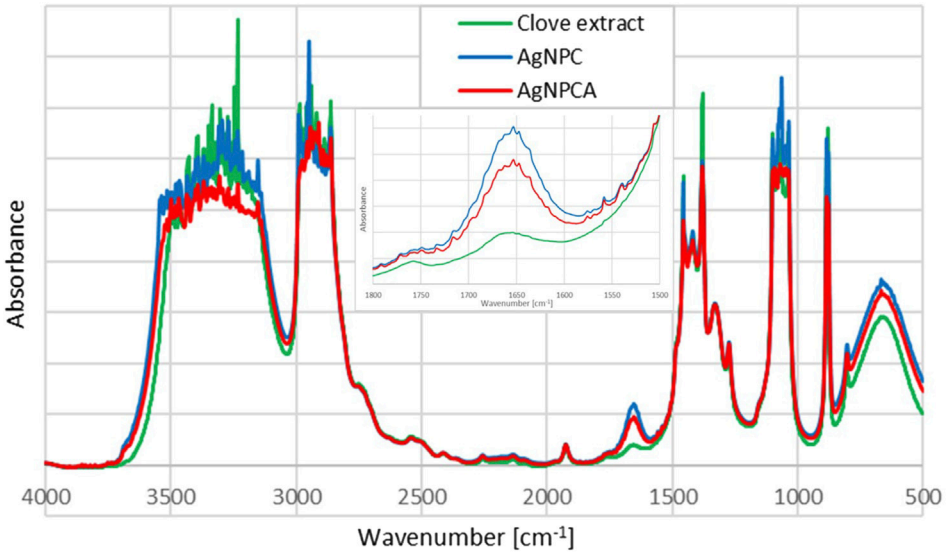

FIGURE 4
Fourier-Transform Infrared (FTIR) spectroscopic analysis of AgNPCA (red), AgNPC (blue) and pure clove extract (green).

TABLE 4 FTIR analysis of AgNPCA, AgNPC, and clove extract in solvent ethanol [cm^{-1}].

	$\nu_{1,2}$ (O–H)$_{s,a}$ ν (COOH)$_a$	ν (C–H)$_a$	ν (C-H)$_s$	ν (C=O)$_a$	δ (C-H)$_a$ δ (CH$_2$) δ (O-H)	ν (C-C)	ν (C-O)	ν (C-O) ν (C-N)
AgNPCA	3497 s 3466 s 3369 s 3305 vs 3232 s 3152 s	2988 sh 2982 s 2941 s	2909 s 2889 s 2862 s	1749 vw 1730 vw 1717 vw 1647 w,br 1570 w 1574 vw 1531 w 1506 m	1456 m δ(CH$_3$)$_{s,\ in\text{-}plane}$ 1417 m δ(CH$_3$)$_{a,\ in\text{-}plane}$ 883 s δ(CH$_2$)$_{twisting}$ 878 s δ(CH$_2$)$_{twisting}$ 802 m δ(C-H)$_{out\text{-}of\text{-}plane}$ 667 s δ(O-H)	1379 s 1321 m	1271 m	1154 w,sh ν (C-N) 1101 s ν (C-O) 1092 s ν (C-O) 1070 vs ν (C-O) 1065 s ν (C-O) 1055 s ν (C-O) 1051 s ν (C-O) 1047 s ν (C-O) 1042 s ν (C-O) 1038 s ν (C-O)
AgNPC	3497 s 3466 s 3368 s 3305 vs 3232 s 3152 s	2989 s 2982 s 2947 vs	2909 s 2889 s 2862 s	1749 vw 1730 vw 1717 vw 1647 w,br 1570 w 1574 vw 1531 w 1506 m	1456 s δ(CH$_3$)$_{s,\ in\text{-}plane}$ 1417 m δ(CH$_3$)$_{a,\ in\text{-}plane}$ 885 vs δ(CH$_2$)$_{twisting}$ 878 s δ(CH$_2$)$_{twisting}$ 802 m δ(C-H)$_{out\text{-}of\text{-}plane}$ 667 s δ(O-H)	1379 s 1321 m	1271 m	1154 w,sh ν (C-N) 1099 vs ν (C-O) 1092 s ν (C-O) 1072 vs ν (C-O) 1065 vs ν (C-O) 1055 s ν (C-O) 1051 s ν (C-O) 1043 s ν (C-O) 1042 s ν (C-O) 1036 vs ν (C-O)
Clove extract	3478 s 3399 s 3334 vs 3232 s	2986 vs 2978 s 2945 s	2909 s 2889 s 2862 vs	1647 vw,br	1456 s δ(CH$_3$)$_{s,\ in\text{-}plane}$ 1417 m δ(CH$_3$)$_{a,\ in\text{-}plane}$ 883 s δ(CH$_2$)$_{twisting}$ 878 s δ(CH$_2$)$_{twisting}$ 802 m δ(C-H)$_{out\text{-}of\text{-}plane}$ 667 s δ(O-H)	1379 vs 1321 m	1271 m	1154 w,sh ν (C-N) 1101 vs ν (C-O) 1070 vs ν (C-O) 1051 s ν (C-O) 1036 s ν (C-O)

ν, vibrational stretching; δ, deformation; s, symmetric; a, asymmetric; absorption intensity: vs, very strong; s, strong; m, medium, vw, very weak; sh, shoulder; red color, red shift from AgNPC to AgNPCA; blue color, blue shift from AgNPC to AgNPCA and yellow highlighting, not available in clove extract (C).

with -C-OH groups in the clove extract, including eugenol are oxidized to -C=O and reduce the silver ions to metallic silver nanoparticles. During this process, the phenolic compounds and flavonoids act as capping and stabilizing agent on the silver surface, forming a monolayer, preventing secondary nucleation. Furthermore, this action prevents agglomeration and keeps the size of AgNP in AgNPC small verifying the results in the DLS analysis. Once clarithromycin is added into the compound, AgNPCA is formed. AgNPCA has lower absorption intensities for carbonyl- (1,647 cm^{-1}) and -C-O (1,099–1,036 cm^{-1})

stretching vibrations in comparison to AgNPC. Here, the monolayer is compromised by clarithromycin, which competes and interacts with the other biocompounds on the Ag surface. Accordingly, there is a breach in the monolayer, which leads to release of silver-ions, formation of AgCl and Ag_2O (Al Aboody, 2019; Haj Bloukh et al., 2021; Singh et al., 2024). Additionally, secondary nucleation steps in leading to increase of AgNP size through agglomeration, which is also verified by DLS studies and UV-vis analysis. Similar processes influence the twisting- and bending vibrations of methylene, -CH and hydroxyl groups around 800–600 cm^{-1} (Figure 4; Table 4). The absorption bands for these groups also show lower intensities in AgNPCA due to the increased hydrogen bonding between clarithromycin and AgNPC.

AgNPC and AgNPCA absorption bands between 3,500 and 3,100 cm^{-1} are related to -COOH and -OH groups. Both spectra show a slight broadening compared to the clove extract indicating more hydrogen bonding for these groups (Figure 4; Table 4). Both AgNP samples contain new, very strong vibrational bands at 3,305 and 3,125 cm^{-1}, which are lacking in the clove extract (Table 4, yellow highlighted). The region for asymmetric and symmetric vibrational -C-H stretching bands between 3,000 and 2,860 cm^{-1} contains interesting details. The FTIR spectra of AgNPC displays two very strong vibrational asymmetric stretching bands for -C-H bonds at 2,989 and 2,947 cm^{-1} (Figure 4; Table 4). These two are red shifted towards 2,988 and 2,941 cm^{-1} with lower absorption intensity in AgNPCA. Therefore, a weakening of asymmetric -C-H bonds due to the addition of clarithromycin is expected. The same happens to the very strong vibrational stretching bands of -C-O at 1,072 cm^{-1} in AgNPC, which are red shifted in AgNPCA to 1,070 cm^{-1} (Figure 4; Table 4). After adding clarithromycin, blue shifts as a marker for stronger bonds and encapsulation for the concerned -C-O stretching bands are present in AgNPC at 1,099, 1,043 and 1,036 cm^{-1} towards AgNPCA at 1,101, 1,047 and 1,038 cm^{-1}, respectively (Figure 4; Table 4).

Ullah et al. detected in the FTIR analysis alcohol O-H stretching bands at 3,744.1 cm^{-1}, carboxylic acid O-H stretching bands at 2,961.4 cm^{-1}, alkane C-H bending at 1,462.2, and bands related to alcohol C-O stretching at 1,012.1 cm^{-1} (Ullah et al., 2023). AgNPCA reveals in the FTIR spectrum similar related bands at 3,694.9, 2,943.4, 1,456.3 and 1,039.6 cm^{-1}, respectively (Figure 4). All these bands are in comparison to pure clarithromycin red shifted, except for the alcohol C-O stretching (Ullah et al., 2023). The red shifts indicate an increase in conjugation systems for the related groups, while the only small blue shift of the alcohol C-O stretching maybe due to solvent effect. As a result, the addition of clarithromycin leads to an increase in conjugation systems by oxidation of alcoholic groups on clarithromycin (Ullah et al., 2023).

The FTIR spectrum of pure clove extract contains eugenol as one of its main ingredients (Hameed et al., 2021). The bands at 3,369 cm^{-1} (-OH), 2,982 cm^{-1} (-C-H), 1,647 cm^{-1} (-C=O), 1,456 cm^{-1} ($-CH_3$), 1,154 cm^{-1} (-C-N), 1,051 cm^{-1} (-C-O) can be assigned to eugenol according to previous studies (Hameed et al., 2021; Mohammed at el., 2021; Murtaza et al., 2024).

In conclusion, the increase in absorption intensity of C=O groups at 1,647 cm^{-1} from clove extract to AgNPC verifies the synthesis of AgNP through oxidation of hydroxyl groups in the phenolic compounds and flavonoids. These biocompounds form Ag---O=C interactions and stabilize or cap the metallic Ag surface, establishing a monolayer and preventing agglomeration (Figure 5).

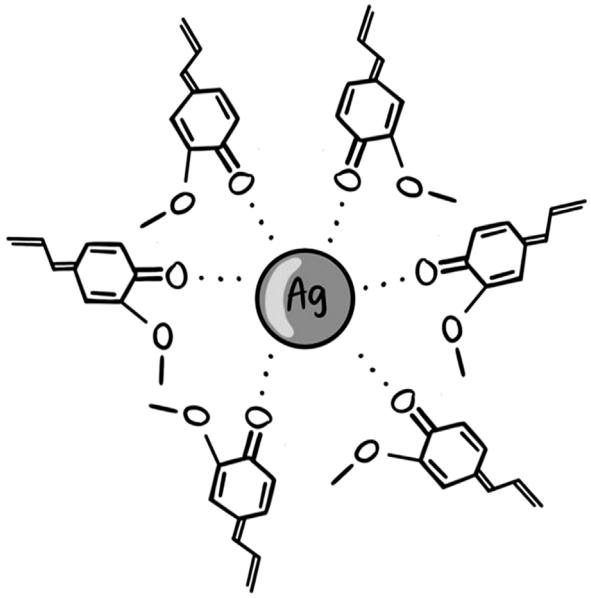

FIGURE 5
Proposed illustration for AgNPC stabilized by oxidized eugenol molecules.

Once clarithromycin is introduced into the system, the capping agents are degraded, destabilized, leading to a lower acetylation degree (Haj Bloukh et al., 2021).

3.6 Antimicrobial activities of AgNPC and AgNPCA

Disc diffusion assay (DD) was utilized in order to check the title compounds AgNPC and AgNPCA effect on ten reference strains. The selected panel consisted of Gram-positive bacteria *S. pneumoniae* ATCC 49619, *S. aureus* ATCC 25923, *S. pyogenes* ATCC 19615, *E. faecalis* ATCC 29212 and *B. subtilis* WDCM0003, as well as the Gram-negative *E. coli* WDCM 00013 Vitroids, *P. mirabilis ATCC 29906*, *P. aeruginosa* WDCM 00026 Vitroids and *K. pneumoniae* WDCM00097 Vitroids) and one fungus type (*C. albicans* WDCM 00054 Vitroids).

The antimicrobial testing results on positive control antibiotics (A), clove extract (1), AgNPC (0.81 μg/mL), AgNPC1 (1.08 μg/mL) (2), AgNPCA (1.08 μg/mL), AgNPCA1 (0.81 μg/mL) (4) and clarithromycin solution (1.34 μg/mL) (5) are presented in Table 5.

Table 5 signifies the vulnerability of 9 microorganism strains towards the two formulations AgNPC and AgNPCA. When the results of both formulations are compared, it is noted that AgNPC generally has better results, except in two strains (Gram-positive *B. subtilis* WDCM 00003 and Gram-negative *K. pneumoniae* WDCM 000097) (Table 5). The results show a lower reaction to *B. subtilis* WDCM 00003 (10 mm) and a complete resistance against *K. pneumoniae* WDCM 000097, which indicates that the formulation with the antibiotic clarithromycin worked better against those 2 strains (Table 5). The results were almost similar in both formulations against *S. aureus* ATCC 25923, *S. pyogenes* ATCC 19615, and *P. aeruginosa* WDCM 00026. *C. albicans* WDCM

TABLE 5 Antimicrobial testing of antibiotics (A), clove extract (1), AgNPC, AgNPC1 (2) AgNPCA (3), AgNPCA1 (4) and clarithromycin solution (5). ZOI (mm) against microbial strains by disk diffusion (DD) assay.

Strain	Antibiotic	A	1	AgNPC	2	AgNPCA	4	5
S. aureus ATCC 25923	G	28	7	25	12	25	25	25
E. faecalis ATCC 29212	G	25	R	20	17	15	R	16
S. pyogenes ATCC 19615	G	25	R	17	18	16	R	17
S. pneumoniae ATCC 49619	G	18	R	18	18	15	R	17
B. subtilis WDCM 00003	G	21	R	10	R	30	30	25
P. mirabilis ATCC 29906	G	30	R	20	R	R	R	R
E. coli WDCM 00013	G	30	R	15	7	11	12	R
P. aeruginosa WDCM 00026	G	23	R	8	10	7	11	R
K. pneumoniae WDCM 000097	G	30	R	R	12	12	13	R
C. albicans WDCM 00054	NY	16	R	R	R	R	R	R

Disc diffusion studies (6 mm disc impregnated with 2 mL of clove extract (5 μg/mL) (1), AgNPC (0.81 μg/mL), AgNPC1 (1.08 μg/mL) (2), AgNPCA (1.08 μg/mL), AgNPCA1 (0.81 μg/mL) (4) and clarithromycin (1.34 μg/mL) (5). A = Gentamicin (G, 30 μg/disc). Nystatin (NY, 100 IU). The grey shaded area represents Gram-negative bacteria. 0 = Resistant. No statistically significant differences ($p > 0.05$) between row-based values through Pearson correlation.

00054 shows resistance to all tests done except to the positive control antibiotic nystatin with a result of 16 mm (Table 5). Interestingly, when the antibiotic clarithromycin is present (AgNPCA) resistance is observed in *P. mirabilis* ATCC 29906, while in AgNPC the resistance is resolved and an inhibition zone of 20 mm is seen instead (Table 5). The opposite is detected for *K. pneumoniae* WDCM 000097, where the resistance was in AgNPC, and an inhibitory zone of 12 mm in AgNPCA (Table 5). Clove extract showed resistance to all strains except *S. aureus* ATCC 25923, where it had a result of 7 mm (Table 5). Similarly, clarithromycin diluted in ultradistilled water was resistant to all negative bacterial strains, but when added into the formulation showed good results. This implies that the addition of clove extract and silver nanoparticles helped overcome the resistance by working synergistically (Table 5; Figure 6).

AgNPC inhibits all gram-positive and Gram-negative strains except *K. pneumoniae* WDCM 000097 and the fungus *C. albicans* WDCM 00054 (Table 5; Figure 6). Comparatively, AgNPCA inhibited all Gram-positive bacteria and some Gram-negative excluding *P. mirabilis* ATCC 29906 and *C. albicans* WDCM 00054 (Table 5; Figure 6). Furthermore, the highest inhibition of strains occurs in the AgNPCA formulation against *B. subtilis* WDCM 00003 (30 mm), followed by *S. aureus* ATCC 25923 (25 mm) seen in both AgNPC and AgNPCA (Table 5; Figure 6).

Previous studies with plant biosynthesized AgNP display mixed results (Bloukh et al., 2020; Haj Bloukh et al., 2021). In comparison, our studies of *Lepidium Sativum* L. based AgNP (LS-AgNP-1.08 μg/mL) with the same set of 10 reference strains achieved ZOI of 20 mm for Gram-negative *P. aeruginosa* WDCM 00026, 15 mm for *E. coli* WDCM 00013 and *K. pneumoniae* WDCM 000097 (Haj Bloukh et al., 2021). However, Gram-positive *S. pneumoniae* (15 mm), *S. aureus* ATCC 25923 (14 mm), *S. pyogenes* ATCC 19615 (13 mm), and *E. faecalis* ATCC 29212 (13 mm) were less susceptible towards LS-AgNP (Haj Bloukh et al., 2021). In another study, we investigated AgNP through trans-cinnamic acid (TCA) and *Cinnamomum Zeylanicum* (Cinn) (Bloukh et al., 2020). Under the set of 10 reference strains, TCA-AgNP performed even better than LS-AgNP and Cinn-AgNP (Bloukh et al., 2020). At a concentrations of 50 μg/mL, TCA-AgNP exerted antifungal properties against *C. albicans* WDCM 00054 (Bloukh et al., 2020). Therefore, we reported, that the antifungal properties do not originate from AgNP, nor Cinn extract (Bloukh et al., 2020). Singh et al. investigated their Ag-Fe bimetallic nanoparticles based on clove bud extract (Singh et al., 2024). Their Agar-Well (AW) diffusion tests revealed ZOI = 11, 9.3 and 10 mm against *S. aureus*, *E. coli* and *P. aeruginosa* (Singh et al., 2024). AW studies usually achieve higher ZOI, because the sample is directly poured in a well inside the petri-dish. In our studies, we used DD methods, which first require dip-coating and then drying the disks at ambient temperature. Accordingly, DD studies may record smaller inhibitory zones. Further recent investigations used clove buds and clove powder extracts for the biosynthesis of AgNP and/or Ag-FeNP and reported similar results (Lakhan et al., 2020; Murtaza et al., 2024).

As a result, discs impregnated with the two formulations exhibit somewhat similar promising antibacterial activities with a few variations such as the resistance mentioned with *P. mirabilis* ATCC 29906 against AgNPCA and the resistance observed in *K. pneumoniae* WDCM 000097 against AgNPC. *C. albicans* WDCM 00054 was not susceptible to AgNPC and AgNPCA (Table 5; Figure 6).

Further interesting results were demonstrated by AgNPCA against *B. subtilis* WDCM 00003 (30 mm), followed by Gram-positive *S. aureus* ATCC 25923 (25 mm), *S. pyogenes* ATCC 19615 (16 mm), *E. faecalis* ATCC 29212 (15 mm) and *S. pneumoniae* ATCC 49619 (15 mm), Gram-negative *K. pneumoniae* WDCM 000097 (12 mm), *E. coli* WDCM 00013 (11 mm), *P. aeruginosa* WDCM 00026 (7 mm) (Table 5; Figure 6).

AgNPC showed the best results in *S. aureus* ATCC 25923, *E. faecalis* ATCC 29212 and *P. mirabilis* ATCC 29906, *S. pneumoniae* ATCC 49619, *S. pyogenes* ATCC 19615, *E. coli* WDCM 00013, *B. subtilis* WDCM 00003, and lastly *P. aeruginosa* WDCM 00026 (Table 5; Figure 6).

Additional *in vivo*, as well as toxicity studies are needed to confirm the potential use of AgNPC and AgNPCA as antibacterial agents.

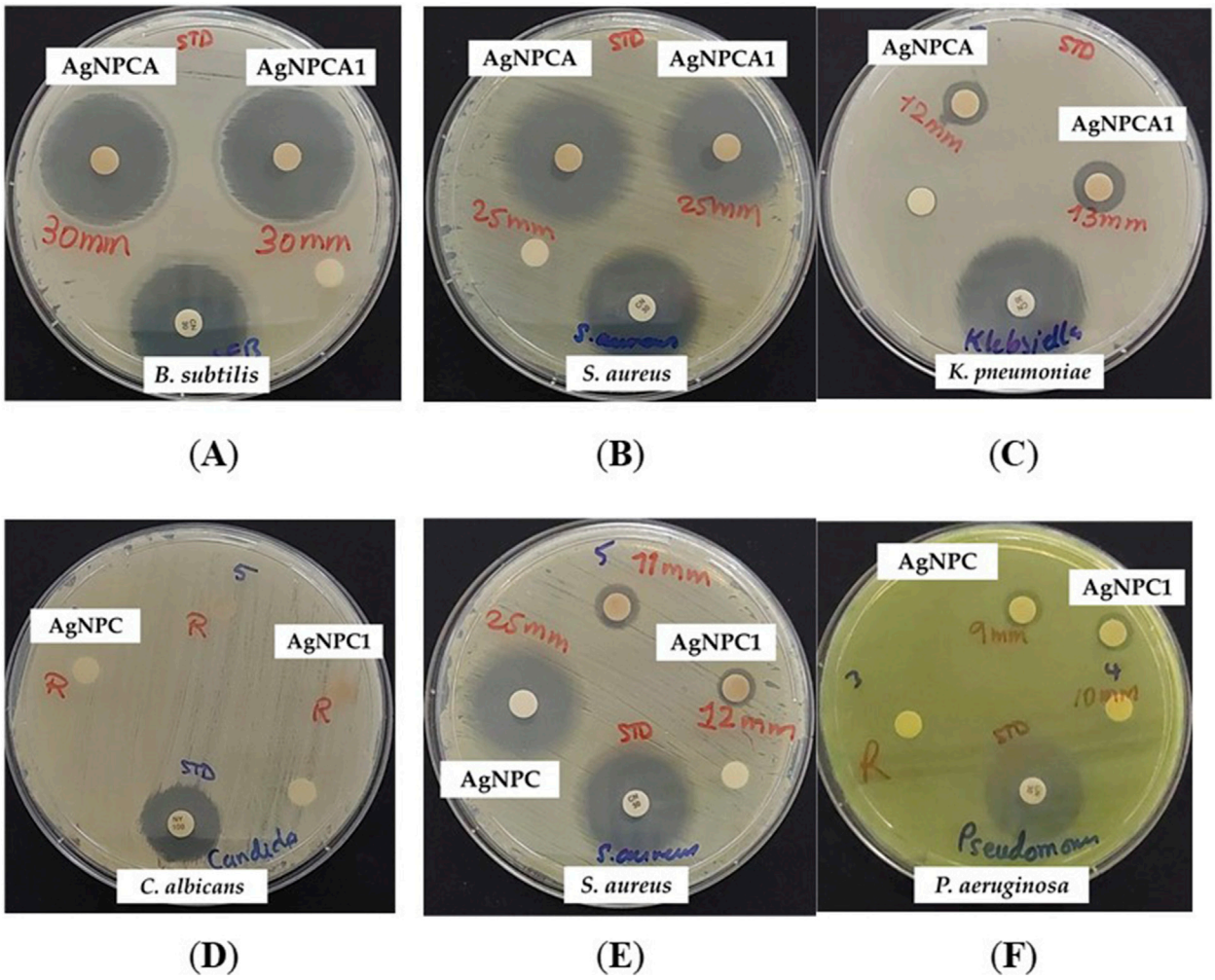

FIGURE 6
AgNPCA and AgNPC coated sterile discs (disc diffusion assay) with positive control antibiotic nystatin (100 IU) and gentamicin (30 μg/disc). From left to right: AgNPCA (1.08 μg/mL) against **(A)** *B. subtilis* WDCM 00003; **(B)** *S. aureus* ATCC 25932; **(C)** *K. pneumoniae* WDCM 00097; AgNPC (0.81 μg/mL) against **(D)** *C. albicans* WDCM 00054; **(E)** *S. aureus* ATCC 25932; **(F)** *P. aeruginosa* WDCM 00026.

4 Conclusion

Antimicrobial resistance is a fatal threat to human health, causing drastic changes in the medical field. Plant based alternatives have been proven by countless studies to contain components that have antimicrobial, antiviral, antioxidant and antifungal properties. The combination of plant-based AgNP with antibiotics, here clarithromycin, offers possible solutions to existing problems. Synergistic effects between these compounds could increase antimicrobial properties, reduce the needed dosage of antibiotic, mitigate toxicity and AMR. This study shed light to the potential of the title compounds AgNPC and AgNPCA as antibacterial agents.

AgNPCA revealed synergistic action between the antibiotic clarithromycin, AgNP and clove extract. In this regard, *B. subtilis* WDCM 00003 and *S. aureus* ATCC25923 were higly susceptible with 30 and 25 mm ZOI towards AgNPCA, respectively. As a result, the studied Gram-negative pathogens were susceptible towards AgNPCA. Clarithromycin alone does not inhibit any Gram-negative pathogen. However, the presence of clarithromycin in AgNPCA removed partly the stabilizing capping agents consisting of phenolic compounds and flavonoids from the clove extract.

The stability of AgNPC is confirmed by DLS analysis through a suitable nanoparticle size with negative zeta potential. However, adding clarithromycin, a relatively big, macrocyclic compound in AgNPCA increases size and zeta potentials. The electrostatic interactions between clarithromycin functional groups with the capping agents and the Ag surface in AgNPCA resulted in secondary nucleation, partly release of capping agents and silver ions. The EDS of AgNPCA confirmed the availability of AgCl and Ag_2O as a result of the release of silver ions. The DLS analysis reported increase of nanoparticle size and instability of the NP in the colloidal solution when clarithromycin was added resulting in AgNPCA. However, the impact of steric stabilization due to clarithromycin and clove biocompounds seem to counterbalance agglomeration. A comparison between SEM and DLS size measurements reveals the formation of a stabilizing organic layer around the nanoparticles.

AgNPC achieved the best disc diffusion results with ZOI = 20 mm against the Gram-positive strains *S. aureus* ATCC 25923 and *E. faecalis* ATCC 29212, as well as the Gram-negative, highly motile *P. mirabilis* ATCC 29906. *S. pneumoniae* ATCC 49619, a known resistant pathogen was susceptible towards the title compound AgNPC with 18 mm on the same level of gentamycin (positive control). AgNPC and AgNPCA have shown to have promising results at low concentrations but failed to overcome the resistance caused by *C. albicans* WDCM 00054. This pathogen is not susceptible to AgNP nor a low concentration of biocompounds from plant extracts.

As a conclusion, the clove extract-based biosynthesis of silver nanoparticles resulted in small sized, stable AgNPC with almost homogenous morphology and high purity. The increase in the nanoparticle size was not detrimental for inhibitory action of AgNPCA against Gram-negative pathogens in comparison to pure clarithromycin and AgNPC. Pathogens resistant against the heterocyclic antibiotic clarithromycin were inhibited by AgNPCA. Further *in vivo* and cytotoxicity studies are necessary to verify the use of AgNPC and AgNPCA as antibacterial agents.

Data availability statement

The original contributions presented in the study are included in the article/Supplementary Material, further inquiries can be directed to the corresponding author.

Author contributions

ZE: Conceptualization, Data curation, Funding acquisition, Investigation, Methodology, Project administration, Resources, Software, Supervision, Validation, Visualization, Writing–original draft, Writing–review and editing. SH: Writing–original draft, Writing–review and editing, Conceptualization, Data curation, Formal Analysis, Funding acquisition, Investigation, Methodology, Project administration, Resources, Supervision, Validation. AA: Writing–review and editing, Conceptualization, Funding acquisition, Methodology, Project administration, Resources, Supervision. MA-T: Writing–review and editing, Conceptualization, Funding acquisition, Project administration, Resources, Supervision, Validation. MS: Writing–review and editing, Conceptualization, Funding acquisition, Project administration, Resources, Supervision, Validation. HmA: Writing–review and editing, Conceptualization, Data curation, Formal Analysis, Investigation, Methodology, Resources, Software, Validation, Visualization. SB: Writing–review and editing, Funding acquisition, Methodology, Project administration, Resources, Supervision. SK: Writing–review and editing, Conceptualization, Data curation, Formal Analysis, Investigation, Methodology, Resources, Software, Validation. IbB: Writing–original draft, Writing–review and editing, Methodology, Software, Visualization. ME: Writing–original draft, Writing–review and editing, Data curation, Formal Analysis, Investigation, Methodology, Resources. SS: Writing–original draft, Writing–review and editing, Data curation, Formal Analysis, Investigation, Methodology, Resources. HnA: Writing–original draft, Writing–review and editing, Conceptualization, Data curation, Formal Analysis, Investigation, Methodology, Resources. ImB: Writing–original draft, Writing–review and editing, Conceptualization, Data curation, Software, Visualization. NH: Writing–review and editing, Conceptualization, Funding acquisition, Project administration, Resources, Supervision.

Funding

The author(s) declare that financial support was received for the research, authorship, and/or publication of this article. This work and the APC was kindly supported by Ajman University, Deanship of Research and Graduate Studies, Ajman, United Arab Emirates with the Internal Research Grant No. (Ref. No. # 2022-IRG-PH-3). The research findings presented in this article are solely the responsibility of the authors.

Acknowledgments

We are immensely thankful to Hussain Alawadhi, Mohammad Shameer, Muhammed Irshad and Fatima Mohammed Abla from Sharjah University for their kind support and efforts by providing us with high-quality SEM, XRD, Raman and EDS analysis. We are thankful to the artist "@art_by_amie_" (Iman Haj Bloukh, IHB, Ajman University) for preparing digital art images as graphical abstract, illustration and figures.

Conflict of interest

The authors declare that the research was conducted in the absence of any commercial or financial relationships that could be construed as a potential conflict of interest.

Generative AI statement

The author(s) declare that no Generative AI was used in the creation of this manuscript.

Publisher's note

Supplementary material

The Supplementary Material for this article can be found online at: https://www.frontiersin.org/articles/10.3389/fchem.2024.1513150/full#supplementary-material

References

Adamczak, A., Ożarowski, M., and Karpiński, T. M. (2020). Antibacterial activity of some flavonoids and organic acids widely distributed in plants. *J. Clin. Med.* 9, 109. doi:10.3390/jcm9010109

Adil, M., Alam, S., Amin, U., Ullah, I., Muhammad, M., Ullah, M., et al. (2023). Efficient green silver nanoparticles-antibiotic combinations against antibiotic-resistant bacteria. *Amb. Expr.* 13, 115. doi:10.1186/s13568-023-01619-7

Al Aboody, M. S. (2019). Silver/silver chloride (Ag/AgCl) nanoparticles synthesized from Azadirachta indica lalex and its antibiofilm activity against fluconazole resistant *Candida tropicalis*. *Art. Cells Nanomed. Biotech.* 47, 2107–2113. doi:10.1080/21691401.2019.1620257

Al-Otibi, F., Al-Ahaidib, R. A., Alharbi, R. I., Al-Otaibi, R. M., and Albasher, G. (2021). Antimicrobial potential of biosynthesized silver nanoparticles by *Aaronsohnia factorovskyi* extract. *Molecules* 26, 130. doi:10.3390/molecules26010130

Ankegowda, V. M., Kollur, S. P., Prasad, S. K., Pradeep, S., Dhramashekara, C., Jain, A. S., et al. (2020). Phyto-mediated synthesis of silver nanoparticles using *Terminalia chebula* fruit extract and evaluation of its cytotoxic and antimicrobial potential. *Molecules* 25, 5042. doi:10.3390/molecules25215042

Ashraf, M. V., Pant, S., Khan, M. A. H., Shah, A. A., Siddiqui, S., Jeridi, M., et al. (2023). Phytochemicals as antimicrobials: prospecting himalayan medicinal plants as source of alternate medicine to combat antimicrobial resistance. *Pharmaceuticals* 16, 881. doi:10.3390/ph16060881

Baran, A., Kwiatkowska, A., and Potocki, L. (2023). Antibiotics and bacterial resistance—a short story of an endless arms race. *Int. J. Mol. Sci.* 24, 5777. doi:10.3390/ijms24065777

Barik, B., Satapathy, B. S., Pattnaik, G., Bhavrao, D. V., and Shetty, K. P. (2024). Sustainable synthesis of silver nanoparticles from Azadirachta indica: antimicrobial, antioxidant and *in silico* analysis for periodontal treatment. *Front. Chem.* 12, 1489253. doi:10.3389/fchem.2024.1489253

Bauer, A. W., Perry, D. M., and Kirby, W. M. M. (1959). Single-disk antibiotic-sensitivity testing of staphylococci: an analysis of technique and results. *AMA Arch. Intern. Med.* 104, 208–216. doi:10.1001/archinte.1959.00270080034004

Bloukh, S. H., Edis, Z., Ibrahim, M. R., and Abu Sara, H. (2020). "Smart" antimicrobial nanocomplexes with potential to decrease surgical site infections (SSI). *Pharmaceutics* 12, 361. doi:10.3390/pharmaceutics12040361

Bruna, T., Maldonado-Bravo, F., Jara, P., and Caro, N. (2021). Silver nanoparticles and their antibacterial applications. *Int. J. Mol. Sci.* 22, 7202. doi:10.3390/ijms22137202

Chen, W., Li, Y., Liu, C., Kang, Y., Qin, D., Chen, S., et al. (2023). *In situ* engineering of tumor-associated macrophages via a nanodrug-delivering-drug (β-Elemene@Stanene) strategy for enhanced cancer chemo-immunotherapy. *Angew. Chem. Int. Ed.* 62 (41), e202308413. doi:10.1002/anie.202308413

Cheng, Z., Li, H., Chen, C., Lv, X., Zuo, E., Xie, X., et al. (2023). Application of serum SERS technology based on thermally annealed silver nanoparticle composite substrate in breast cancer. *Photodiagnosis Photodyn. Ther.* 41, 103284. doi:10.1016/j.pdpdt.2023.103284

CLSI (2019). *Performance standards for antimicrobial susceptibility testing*. 29th ed., 39. Wayne, PA, USA: Clinical and Laboratory Standards Institute.

Corciovă, A., Mircea, C., Fifere, A., Turin-Moleavin, I.-A., Roşca, I., Macovei, I., et al. (2024). Biogenic synthesis of silver nanoparticles mediated by *Aronia melanocarpa* and their biological evaluation. *Life* 14, 1211. doi:10.3390/life14091211

De Fazio, R., Oppedisano, F., Caioni, G., Tilocca, B., Piras, C., and Britti, D. (2024). Plants with antimicrobial activity against *Escherichia coli*, a meta-analysis for green veterinary pharmacology applications. *Microorganisms* 12, 1784. doi:10.3390/microorganisms12091784

Desai, A. S., Ashok, A., Edis, Z., Bloukh, S. H., Gaikwad, M., Patil, R., et al. (2023). Meta-analysis of cytotoxicity studies using machine learning models on physical properties of plant extract-derived silver nanoparticles. *Int. J. Mol. Sci.* 24, 4220. doi:10.3390/ijms24044220

Di Lorenzo, C., Colombo, F., Biella, S., Stockley, C., and Restani, P. (2021). Polyphenols and human health: the role of bioavailability. *Nutrients* 13, 273. doi:10.3390/nu13010273

Domanovich-Asor, T., Motro, Y., Khalfin, B., Craddock, H. A., Peretz, A., and Moran-Gilad, J. (2021). Genomic analysis of antimicrobial resistance genotype-to-phenotype agreement in *Helicobacter pylori*. *Microorganisms* 9, 2. doi:10.3390/microorganisms9010002

Dove, A. S., Dzurny, D. I., Dees, W. R., Qin, N., Nunez, R. C. C., Alt, L. A., et al. (2023). Silver nanoparticles enhance the efficacy of aminoglycosides against antibiotic-resistant bacteria. *Front. Microbiol.* 13, 1064095–302X. doi:10.3389/fmicb.2022.1064095

Edis, Z., and Bloukh, S. H. (2020). Facile synthesis of antimicrobial aloe Vera-"Smart" triiodide-PVP biomaterials. *Biomimetics* 5, 45. doi:10.3390/biomimetics5030045

Edis, Z., and Bloukh, S. H. (2021). Facile synthesis of bio-antimicrobials with "smart" triiodides. *Molecules* 26, 3553. doi:10.3390/molecules26123553

Edis, Z., and Bloukh, S. H. (2024). Thymol, a monoterpenoid within polymeric iodophor formulations and their antimicrobial activities. *Int. J. Mol. Sci.* 25, 4949. doi:10.3390/ijms25094949

Edis, Z., Bloukh, S. H., Sara, H. A., and Azelee, N. I. W. (2022). Antimicrobial biomaterial on sutures, bandages and face masks with potential for infection control. *Polymers* 14, 1932. doi:10.3390/polym14101932

Edis, Z., Bloukh, S. H., Sara, H. A., and Bloukh, I. H. (2024). Green synthesized polymeric iodophors with thyme as antimicrobial agents. *Int. J. Mol. Sci.* 25, 1133. doi:10.3390/ijms25021133

El-Kahky, D., Attia, M., Easa, S. M., Awad, N. M., and Helmy, E. A. (2021). Interactive effects of biosynthesized nanocomposites and their antimicrobial and cytotoxic potentials. *Nanomaterials* 11, 903. doi:10.3390/nano11040903

El-Sawy, E. R., Abdel-Aziz, M. S., Abdelmegeed, H., and Kirsch, G. (2024). Coumarins: *quorum* sensing and biofilm formation inhibition. *Molecules* 29, 4534. doi:10.3390/molecules29194534

Haj Bloukh, S., Edis, Z., Abu Sara, H., and Alhamaidah, M. A. (2021). Antimicrobial properties of *Lepidium sativum* L. Facilitated silver nanoparticles. *Pharmaceutics* 13, 1352. doi:10.3390/pharmaceutics13091352

Hameed, M., Rasul, A., Waqas, M. K., Saadullah, M., Aslam, N., Abbas, G., et al. (2021). Formulation and evaluation of a clove oil-encapsulated nanofiber formulation for effective wound-healing. *Molecules* 26, 2491. doi:10.3390/molecules26092491

Hasoon, B. A., Jawad, K. H., Mohammed, I. S., Hussein, N. N., Al-azawi, K. F., and Jabir, M. S. (2024). Silver nanoparticles conjugated amoxicillin: a promising nano-suspension for overcoming multidrug resistance bacteria and preservation of endotracheal tube. *Inorg. Chem. Comm.* 165, 112456. doi:10.1016/j.inoche.2024.112456

Hernández-Venegas, P. A., Martínez-Martínez, R. E., Zaragoza-Contreras, E. A., Domínguez-Pérez, R. A., Reyes-López, S. Y., Donohue-Cornejo, A., et al. (2023). Bactericidal activity of silver nanoparticles on oral biofilms related to patients with and without periodontal disease. *J. Funct. Biomater.* 14, 311. doi:10.3390/jfb14060311

Khan, I. U., Shoukat, M., Asif, M., Khalid, S. H., Asghar, S., Munir, M. U., et al. (2022). Assessing the synergistic activity of clarithromycin and therapeutic oils encapsulated in sodium alginate based floating microbeads. *Microorganisms* 10, 1171. doi:10.3390/microorganisms10061171

Lakhan, M. N., Chen, R., Shar, A. H., Chand, K., Shah, A. H., Ahmed, M., et al. (2020). Eco-friendly green synthesis of clove buds extract functionalized silver nanoparticles and evaluation of antibacterial and antidiatom activity. *J. Microbiol. Met.* 173, 105934. doi:10.1016/j.mimet.2020.105934

Lalević, D., Ilić, Z. S., Stanojević, L., Milenković, L., Šunić, L., Kovač, R., et al. (2023). Shade-induced effects on essential oil yield, chemical profiling, and biological activity in some *lamiaceae* plants cultivated in Serbia. *Horticulturae* 9, 84. doi:10.3390/horticulturae9010084

Lebel, M. (1993). Pharmacokinetic properties of clarithromycin: a comparison with erythromycin and azithromycin. *Can. J. Infect. Dis.* 4 (3), 148–152. doi:10.1155/1993/168061

Lou, J., Zhao, L., Huang, Z., Chen, X., Xu, J., Tai, W. C., et al. (2021). Ginkgetin derived from Ginkgo biloba leaves enhances the therapeutic effect of cisplatin via ferroptosis-mediated disruption of the Nrf2/HO-1 axis in EGFR wild-type non-small-cell lung cancer. *Phytomedicine* 80, 153370. doi:10.1016/j.phymed.2020.153370

Maggini, V., Semenzato, G., Gallo, E., Nunziata, A., Fani, R., and Firenzuoli, F. (2024). Antimicrobial activity of *Syzygium aromaticum* essential oil in human health treatment. *Molecules* 29, 999. doi:10.3390/molecules29050999

Mahoney, A. R., Safaee, M. M., Wuest, W. M., and Furst, A. L. (2021). The silent pandemic: emergent antibiotic resistances following the global response to SARS-CoV-2. *iScience* 24, 102304. doi:10.1016/j.isci.2021.102304

Mateo, E. M., and Jiménez, M. (2022). Silver nanoparticle-based therapy: can it Be useful to combat multi-drug resistant bacteria? *Antibiotics* 11, 1205. doi:10.3390/antibiotics11091205

Menichetti, A., Mavridi-Printezi, A., Mordini, D., and Montalti, M. (2023). Effect of size, shape and surface functionalization on the antibacterial activity of silver nanoparticles. *J. Funct. Biomater.* 14, 244. doi:10.3390/jfb14050244

Mohammed, H. B., Rayyif, S. M. I., Curutiu, C., Birca, A. C., Oprea, O.-C., Grumezescu, A. M., et al. (2021). Eugenol-Functionalized magnetite nanoparticles modulate virulence and persistence in *Pseudomonas aeruginosa* clinical strains. *Molecules* 26, 2189. doi:10.3390/molecules26082189

Murtaza, F., Akhter, N., Qamar, M. A., Yaqoob, A., Chaudhary, A. A., Patil, B. R., et al. (2024). *Syzygium aromaticum* bud extracted core–shell Ag–Fe bimetallic nanoparticles: phytotoxic, antioxidant, insecticidal, and antibacterial properties. *Crystals* 14, 510. doi:10.3390/cryst14060510

Mussin, J., and Giusiano, G. (2024). Synergistic antimicrobial activity of biogenic silver nanoparticles and *Acanthospermum australe* essential oil against skin infection pathogens. *Antibiotics* 13, 674. doi:10.3390/antibiotics13070674

Nguyen, N. P. U., Dang, N. T., Doan, L., and Nguyen, T. T. H. (2023). Synthesis of silver nanoparticles: from conventional to 'modern' methods—a review. *Processes* 11, 2617. doi:10.3390/pr11092617

Ormeño-Martínez, M., Guzmán, E., Fernández-Peña, L., Greaves, A. J., Bureau, L., Ortega, F., et al. (2024). Roles of polymer concentration and ionic strength in the deposition of chitosan of fungal origin onto negatively charged surfaces. *Biomimetics* 9, 534. doi:10.3390/biomimetics9090534

Pani, B. S. U. L., and Chandrasekaran, N. (2024). Adsorption of clarithromycin on polystyrene nanoplastics surface and its combined adverse effect on serum albumin. *Coll. Surf. B Biointerfaces* 234, 113673. doi:10.1016/j.colsurfb.2023.113673

Patanè, G. T., Calderaro, A., Putaggio, S., Ginestra, G., Mandalari, G., Cirmi, S., et al. (2024). Novel bioplastic based on PVA functionalized with anthocyanins: synthesis, biochemical properties and food applications. *Int. J. Mol. Sci.* 25, 9929. doi:10.3390/ijms25189929

Pereira, D., Ferreira, S., Ramírez-Rodríguez, G. B., Alves, N., Sousa, Â., and Valente, J. F. A. (2024). Silver and antimicrobial polymer nanocomplexes to enhance biocidal effects. *Int. J. Mol. Sci.* 25, 1256. doi:10.3390/ijms25021256

Reda, M., Ashames, A., Edis, Z., Bloukh, S., Bhandare, R., and Abu Sara, H. (2019). Green synthesis of potent antimicrobial silver nanoparticles using different plant extracts and their mixtures. *Processes* 7, 510. doi:10.3390/pr7080510

Riau, A. K., Aung, T. T., Setiawan, M., Yang, L. H. F., Yam, G., W. Beuerman, R., et al. (2019). Surface immobilization of nano-silver on polymeric medical devices to prevent bacterial biofilm formation. *Pathogens* 8, 93. doi:10.3390/pathogens8030093

Ricardo-Rodrigues, S., Rouxinol, M. I., Agulheiro-Santos, A. C., Potes, M. E., Laranjo, M., and Elias, M. (2024). The antioxidant and antibacterial potential of thyme and clove essential oils for meat preservation—an overview. *Appl. Biosci.* 3, 87–101. doi:10.3390/applbiosci3010006

Romanescu, M., Oprean, C., Lombrea, A., Badescu, B., Teodor, A., Constantin, G. D., et al. (2023). Current state of knowledge regarding WHO high priority pathogens—resistance mechanisms and proposed solutions through candidates such as essential oils: a systematic review. *Int. J. Mol. Sci.* 24, 9727. doi:10.3390/ijms24119727

Ruban, P., Reddy, S. J. L. J., Manickam, R., Rathinam, R., Ali, M. S., Rajkumar, S., et al. (2023). Green synthesis, characterizations, and antibacterial activity of silver nanoparticles from *Themeda quadrivalvis*, in conjugation with macrolide antibiotics against respiratory pathogens. *Rev. Adv. Mat. Sc.* 62 (1), 20220301. doi:10.1515/rams-2022-0301

Samari-Kermani, M., Jafari, S., Rahnama, M., and Raoof, A. (2021). Ionic strength and zeta potential effects on colloid transport and retention processes. *Col. Interface Sc. Comm.* 42, 100389. doi:10.1016/j.colcom.2021.100389

Samuggam, S., Chinni, S. V., Mutusamy, P., Gopinath, S. C. B., Anbu, P., Venugopal, V., et al. (2021). Green synthesis and characterization of silver nanoparticles using *Spondias mombin* extract and their antimicrobial activity against biofilm-producing bacteria. *Molecules* 26, 2681. doi:10.3390/molecules26092681

Shi, S., Li, K., Peng, J., Li, J., Luo, L., Liu, M., et al. (2022). Chemical characterization of extracts of leaves of Kadsua coccinea (Lem.) A.C. Sm. by UHPLC-Q-Exactive Orbitrap Mass spectrometry and assessment of their antioxidant and anti-inflammatory activities. *Biomed. and Pharmacother.* 149, 112828. doi:10.1016/j.biopha.2022.112828

Singh, D., Tiwari, A., Singh, R. P., and Singh, A. K. (2024). Clove bud extract mediated green synthesis of bimetallic Ag–Fe nanoparticles: antimicrobial, antioxidant and dye adsorption behavior and mechanistic insights of metal ion reduction. *Mat. Chem. Phys.* 311, 128529. doi:10.1016/j.matchemphys.2023.128529

Sukhanova, A., Bozrova, S., Sokolov, P., Berestovoy, M., Karaulov, A., and Nabiev, I. (2018). Dependence of nanoparticle toxicity on their physical and chemical properties. *Nanoscale Res. Lett.* 13, 44–21. doi:10.1186/s11671-018-2457-x

Suvandee, W., Teeranachaideekul, V., Jeenduang, N., Nooeaid, P., Makarasen, A., Chuenchom, L., et al. (2022). One-pot and green preparation of *Phyllanthus emblica* extract/silver nanoparticles/polyvinylpyrrolidone spray-on dressing. *Polymers* 14, 2205. doi:10.3390/polym14112205

Takemori, N., Ooi, H. K., Imai, G., Hoshino, K., and Saio, M. (2020). Possible mechanisms of action of clarithromycin and its clinical application as a repurposing drug for treating multiple myeloma. *Ecancer Med. Sc.* 14, 1088. doi:10.3332/ecancer.2020.1088

Tang, J., Li, J., Li, G., Zhang, H., Wang, L., Li, D., et al. (2017). Spermidine-mediated poly(lactic-co-glycolic acid) nanoparticles containing fluorofenidone for the treatment of idiopathic pulmonary fibrosis. *Int. J. Nanomedicine* 12, 6687–6704. doi:10.2147/IJN.S140569

Tang, K. W. K., Millar, B. C., and Moore, J. E. (2023). Antimicrobial resistance (AMR). *Br. J. Biomed. Sci.* 80, 11387. doi:10.3389/bjbs.2023.11387

Uddin, T. M., Chakraborty, A. J., Khusro, A., Zidan, B. R. M., Mitra, S., Bin Emran, T., et al. (2021). Antibiotic resistance in microbes: history, mechanisms, therapeutic strategies and future prospects. *J. Infect. Public Health* 14, 1750–1766. doi:10.1016/j.jiph.2021.10.020

Ullah, G., Nawaz, A., Latif, M. S., Shah, K. U., Ahmad, S., Javed, F., et al. (2023). Clarithromycin and pantoprazole gastro-retentive floating bilayer tablet for the treatment of Helicobacter pylori: formulation and characterization. *Gels* 9, 43. doi:10.3390/gels9010043

Wang, N., Zhang, Z., Zhang, Y., Xu, X., and Guan, Q. (2025). Fe-Mn oxide activating persufate for the *in-situ* chemical remediation of organic contaminated groundwater. *Sep. Purif. Technol.* 355, 129566. doi:10.1016/j.seppur.2024.129566

Wang, Y., Lyu, H., Du, Y., Cheng, Q., Liu, Y., Ma, J., et al. (2024). Unraveling how Fe-Mn modified biochar mitigates sulfamonomethoxine in soil water: the activated biodegradation and hydroxyl radicals formation. Journal of Hazardous *Materials. J. Hazard. Mater.* 465, 133490. doi:10.1016/j.jhazmat.2024.133490

Xu, Y., Chen, H., Zhang, L., and Xu, Y. (2023). Clove essential oil loaded chitosan nanocapsules on quality and shelf-life of blueberries. *Int. J. Biol. Macromol.* 249, 126091. doi:10.1016/j.ijbiomac.2023.126091

Yamamoto, K., Hosogaya, N., Sakamoto, N., Yoshida, H., Ishii, H., Yatera, K., et al. (2021). Efficacy of clarithromycin in patients with mild COVID-19 pneumonia not receiving oxygen administration: protocol for an exploratory, multicentre, open-label, randomised controlled trial CAME COVID-19 study. *BMJ Open* 11, e053325. doi:10.1136/bmjopen-2021-053325

Yang, F., Wu, W., Chen, S., and Gan, W. (2017). The ionic strength dependent zeta potential at the surface of hexadecane droplets in water and the corresponding interfacial adsorption of surfactants. *Soft Matter* 13, 638–646. doi:10.1039/C6SM02174C

Zeng, G., Wu, Z., Cao, W., Wang, Y., Deng, X., Zhou, Y., et al. (2020). Identification of anti-nociceptive constituents from the pollen of Typha angustifolia L. using effect-directed fractionation. *Nat. Prod. Res.* 34 (7), 1041–1045. doi:10.1080/14786419.2018.1539979

Zúñiga-Miranda, J., Guerra, J., Mueller, A., Mayorga-Ramos, A., Carrera-Pacheco, S. E., Barba-Ostria, C., et al. (2023). Iron oxide nanoparticles: green synthesis and their antimicrobial activity. *Nanomaterials* 13, 2919. doi:10.3390/nano13222919

frontiers | Frontiers in Chemistry

TYPE Original Research
PUBLISHED 16 January 2025
DOI 10.3389/fchem.2024.1521298

OPEN ACCESS

EDITED BY
Afzal Basha Shaik,
Jawaharlal Nehru Technological University,
Kakinada, India

REVIEWED BY
Bruno Tasso,
University of Genoa, Italy
Dilep Kumar Sigalapalli,
University of Washington, United States

*CORRESPONDENCE
Amany Belal,
a.belal@tu.edu.sa,
abilalmoh1@yahoo.com
Eun Joo Roh,
r8636@kist.re.kr

RECEIVED 01 November 2024
ACCEPTED 17 December 2024
PUBLISHED 16 January 2025

CITATION
Belal A, Abdou A, Miski SF, Ali MAM, Ghamry HI, Obaidullah AJ, Zaky MY, Hassan AHE, Roh EJ, Al-Karmalawy AA and Ibrahim MH (2025) Exploring the potential of some natural indoles as antiviral agents: quantum chemical analysis, inverse molecular docking, and affinity calculations.
Front. Chem. 12:1521298.
doi: 10.3389/fchem.2024.1521298

Exploring the potential of some natural indoles as antiviral agents: quantum chemical analysis, inverse molecular docking, and affinity calculations

Amany Belal[1]*, Aly Abdou[2], Samar F. Miski[3], Mohamed A. M. Ali[4], Heba I. Ghamry[5], Ahmad J. Obaidullah[6,7], Mohamed Y. Zaky[8], Ahmed H. E. Hassan[9,10], Eun Joo Roh[11,12]*, Ahmed A. Al-Karmalawy[13,14] and Mona H. Ibrahim[15]

[1]Department of Pharmaceutical Chemistry, College of Pharmacy, Taif University, Taif, Saudi Arabia, [2]Chemistry Department, Faculty of science, Sohag university, Sohag, Egypt, [3]Pharmacology and Toxicology Department, College of Pharmacy, Taibah University, Madinah, Saudi Arabia, [4]Department of Biology, College of Science, Imam Mohammad Ibn Saud Islamic University (IMSIU), Riyadh, Saudi Arabia, [5]Nutrition and Food Science, Department of Biology, College of Science, King Khalid University, Abha, Saudi Arabia, [6]Department of Pharmaceutical Chemistry, College of Pharmacy, King Saud University, Riyadh, Saudi Arabia, [7]Drug Exploration and Development Chair (DEDC), Department of Pharmaceutical Chemistry, College of Pharmacy, King Saudi University, Riyadh, Saudi Arabia, [8]Molecular Physiology Division, Zoology Department, Faculty of Science, Beni-Suef University, BeniSuef, Egypt, [9]Medicinal Chemistry Laboratory, Department of Pharmacy, College of Pharmacy, Kyung Hee University, Seoul, Republic of Korea, [10]Department of Medicinal Chemistry, Faculty of Pharmacy, Mansoura University, Mansoura, Egypt, [11]Chemical and Biological Integrative Research Center, Korea Institute of Science and Technology (KIST), Seoul, Republic of Korea, [12]Division of Bio-Medical Science & Technology, University of Science and Technology, Daejeon, Republic of Korea, [13]Department of Pharmaceutical Chemistry, College of Pharmacy, The University of Mashreq, Baghdad, Iraq, [14]Department of Pharmaceutical Chemistry, Faculty of Pharmacy, Horus University-Egypt, New Damietta, Egypt, [15]Department of Pharmaceutical Medicinal Chemistry and Drug Design, Faculty of Pharmacy (Girls), Al-Azhar University, Cairo, Egypt

Human immunodeficiency virus (HIV) and hepatitis C virus (HCV) infections represent critical global health challenges due to the high morbidity and mortality associated with co-infections. HIV, the causative agent of acquired immunodeficiency syndrome (AIDS), infects 4,000 people daily, potentially leading to 1.2 million new cases by 2025, while HCV chronically affects 58 million people, causing cirrhosis and hepatocellular carcinoma. Indole-based compounds play a crucial role in antiviral drug development due to their "privileged scaffold" structure. This study investigates the antiviral potential of natural indoles, gardflorine A–C, derived from *Gardneria multiflora* Makino, a plant traditionally used to treat various ailments. We employed molecular docking, ADMET analysis, and computational techniques [frontier molecular orbital (FMO), natural bond orbital (NBO), and density functional theory (DFT)] to evaluate these compounds" potential as multi-target antiviral agents against HIV and HCV proteins.

KEYWORDS

indole alkaloids, HCV, HIV, DFT, NBO analysis

1 Introduction

Human immunodeficiency virus (HIV) and hepatitis C virus (HCV) infections have emerged as pressing global public health concerns. Even more striking is the quick emergence of HIV–HCV co-infection as a leading cause of illness and mortality (Akhtar et al., 2022). Acquired immunodeficiency syndrome (AIDS) is caused by HIV, which infects 4,000 people daily. If current trends continue, 1.2 million people will be newly infected with HIV in 2025, which is three times the target of 370,000 new infections set for 2025 (2022-global-aids-update-summary_en, 2022). Currently, 58 million people have chronic hepatitis C virus infection, and yearly, there are approximately 1.5 million new cases. Cirrhosis and hepatocellular carcinoma were the primary causes of death associated with hepatitis C in 2019, as estimated by the World Health Organization (Parsons, 2022; Wang et al., 2024; Duan et al., 2024). HIV belongs to the *Lentivirus* genus within the Orthoretrovirinae subfamily of the Retroviridae family. HIV is divided into types 1 and 2 based on genetic traits and antigenic distinctions (HIV-1 and HIV-2) (Seitz, 2016). The HIV genome is composed of two identical single-stranded RNA molecules encased within the virus particle's nucleus. The HIV provirus genome, also known as proviral DNA, is produced via reverse transcription of the viral RNA genome into DNA, destruction of the RNA, and integration of double-stranded HIV DNA into the human genome (Seitz, 2016; Hu et al., 2022; Kang et al., 2018). The initial stages of cell infection are characterized by intricate protein–protein interactions (PPIs). The mature HIV particle's surface glycoprotein gp120 interacts with the specific receptors of the host organism (Sundquist and Kräusslich, 2012; Li et al., 2018; Wang et al., 2024). Afterward, the fusion of the cell membrane and viral envelope is accomplished. The fusion of the viral and cellular membranes causes the translocation of the viral capsid into the cytoplasm. The endosome absorbs the capsid, and a change in pH in the phagosome triggers the release of the capsid's contents into the cytoplasm (Seitz, 2016; Lou et al., 2023). The activation of reverse transcriptase (RT) occurs in the cytoplasm. HIV RT transfers the HIV genome from single-stranded RNA to complementary DNA. Parallel to DNA synthesis, RNase H degrades the RNA strand enzymatically. Then, the DNA-dependent DNA polymerase activity of RT converts single-stranded cDNA into double-stranded DNA (proviral DNA) (Isel et al., 2010). This DNA is transported into the cell nucleus by integrase (IN) and linear or circular proviral DNA via nucleopores. Integrase then randomly integrates the proviral genome into the genome of the human host cell. The incorporation of proviral DNA completes the HIV infection process within the cell, establishing a persistent infection (Di Santo, 2014). Yet, following the activation of infected cells, the LTR promoter of the proviral genome can serve as an attachment point for cellular DNA-dependent RNA polymerases and several transcription factors that initiate the synthesis of viral mRNA and genomic RNA (Rampersad and Tennant, 2018). The main target proteins in HIV/AIDS treatment are reverse transcriptase, protease, and integrase, which suppress viral replication below detectable levels (Arhel and Kirchhoff, 2010). HCV is associated with a high incidence of liver disorders and poses a significant hazard to public health. HCV encodes a single polyprotein; the HCV viral structure consists of envelope glycoproteins in a lipid bilayer containing the viral core protein and RNA (Li and Lo, 2015; Morozov and Lagaye, 2018). Viral RNA is translated by host machinery into a polyprotein, which is cleaved by host and viral-encoded proteases into 10 mature viral proteins, along with several nonstructural (NS) proteins, following cell entrance (Bonamassa et al., 2015). A complex of two viral proteases, NS3 and NS4A proteins, is involved in post-translational processing. NS3 is responsible for proteolytic activity, while NS4A, a membrane protein, acts as a cofactor (Lin). A highly structured replication complex composed of NS3, NS4A, NS4B, NS5A, and NS5B synthesizes new viral RNA. NS5B is an RNA-dependent RNA polymerase required for viral replication. NS5A has a putative involvement in the formation of the replication complex and in controlling replication (Romero-Brey and Lohmann, 2016). It also participates in the assembly of the viral particle discharged by the host cell. The NS3/4A protease, NS5A protein, and NS5B polymerase are inhibited by direct-acting antivirals (Salam and Akimitsu, 2013). Indole constitutes one of the most essential structural patterns in drug development and is considered a "privileged scaffold," a term coined by Evans et al. (1988) to describe scaffolds that can serve as ligands for a variety of receptors. Researchers are working diligently to enhance the antiviral potency of novel indole derivatives as indole belongs to a class of alluring pharmacological substances. Indole scaffolds have been discovered to possess antimicrobial properties, antimalarial activities, and anti-tumor activity. Antiviral medications containing indole are developed to treat viral infections (Dorababu, 2020). A large number of researchers work around the clock to uncover antiviral drugs. Figure 1 demonstrates several compounds with anti-HCV and anti-HIV activity. Among them, compound I showed potent anti-HIV activity (IC_{50} = 1.4 μM) (Dorababu, 2020). In addition, 5,6-dihydroxyindole carboxamide derivative II displayed strong anti-HIV-1 integrase activity (IC_{50} = 1.4 μM). The *in vitro* IC_{50} value of delavirdine for HIV-1 averages 0.26 μM (Dueweke et al., 1993). Furthermore, indole derivatives IV and V displayed high anti-HCV activity, with EC_{50} values of 1.16 μM and 0.6 μM, respectively (Dorababu, 2020).

Many species of plants, animals, and marine organisms contain indole derivatives. The indole core is present in many physiologically active natural compounds (Zhang et al., 2015). *Gardneria multiflora* leaves were found to contain the monoterpenoid indole alkaloids gardflorine A, gardflorine B, and gardflorine C (Figure 2) (Zhang et al., 2021; Zhong et al., 2014). *Gardneria multiflora Makino*, a member of the Loganiaceae family, is mostly found in the southwestern region of China, and its stems have been used to cure food poisoning, snake bites, blisters, macula, dermatitis, herpes, and musculoskeletal pain (Yang et al., 2018). Gardflorine A displayed significant vasorelaxant activity, whereas gardflorine B (2) and gardflorine C inhibited AChE activity (Zhang et al., 2021).

This paper compiles and evaluates the antiviral activity of natural indoles, gardflorine **A–C**, using multi-target molecular docking studies against HIV and HCV, constant inhibition

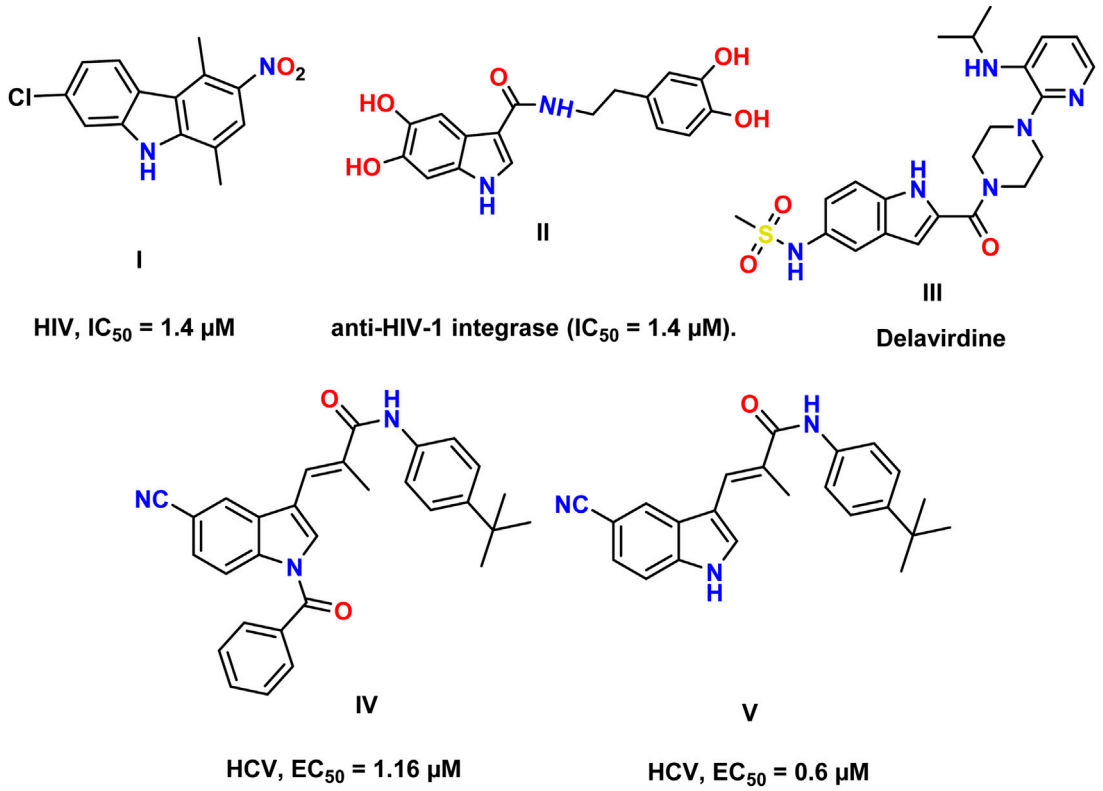

FIGURE 1
Reported indole compounds I, II, and III as anti-HIV and IV, and V as anti-HCV agents.

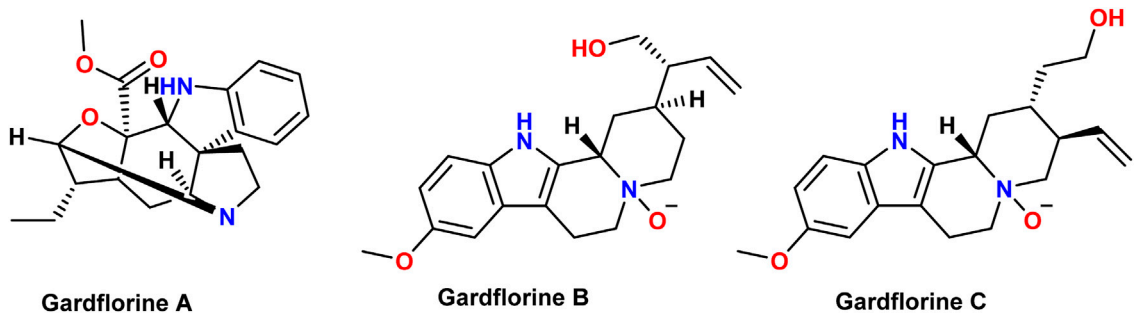

FIGURE 2
Structures of gardflorine **(A–C)**.

calculations (Ki), ADMET studies, frontier molecular orbital (FMO), natural bond orbital (NBO), and density functional theory (DFT) calculations.

2 Methodology

2.1 ADME studies

SwissADME was utilized to predict the ADME properties of each compound (last accessed on 20 February 2023, at http://www.swissadme.ch/index.php) (Daina et al., 2017).

2.2 Multiple target predictions

The LigTMap web server (https://github.com/ShirleyWISiu/LigTMap, last accessed 10 January 2023) (Shaikh et al., 2021) was used to perform multiple predictions for HCV and HIV targets with the tested compounds, gardflorine A–C, and the reference drugs.

2.2.1 Inverse molecular docking

The crystal structures of the target enzymes were obtained from the Protein Data Bank (PDB). For the docking activities, Autodock Vina was utilized, which requires both the receptor and ligands to be

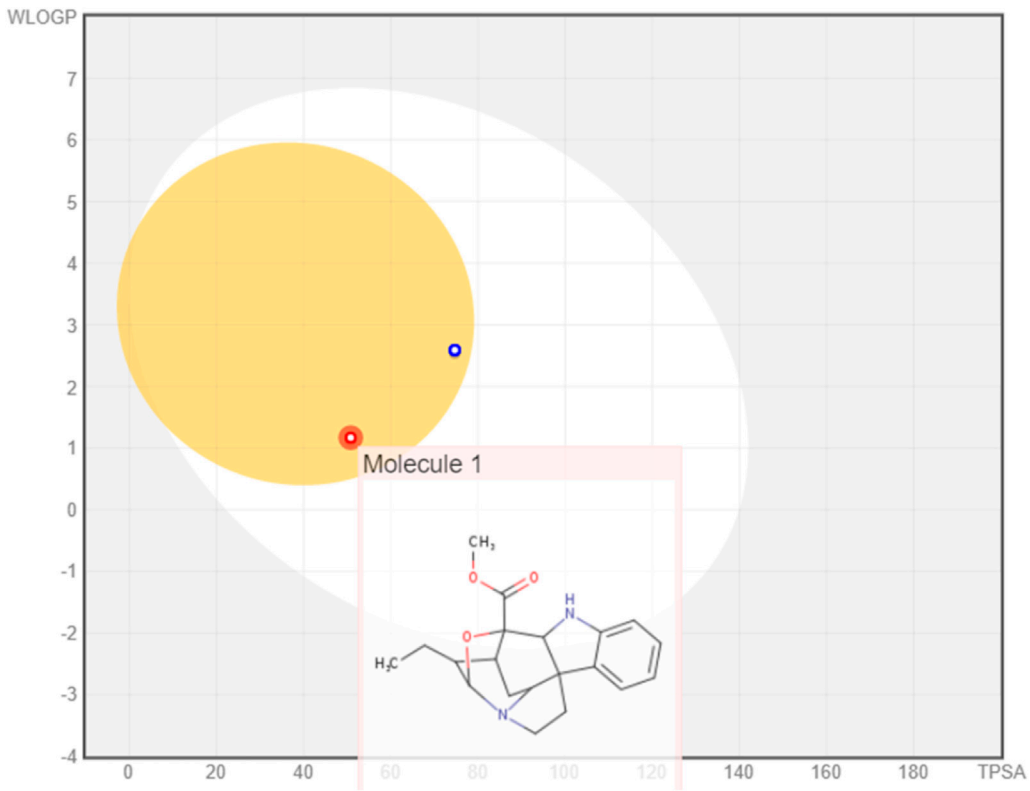

FIGURE 3
Boiled egg model of gardflorine A–C.

in pdbqt extension. Before docking, M.G.L instruments were necessary to prepare the two enzymes (Trott and Olson, 2009). The docking findings were visualized using the Discovery Studio 4.5 visualizer (Dassault Systemes, 2023).

2.3 Inhibition constant (Ki value)

The binding energy was used to calculate the inhibition constant (Ki value) using the equation (ki = $^{10\ [\text{Binding Energy}/1.366]}$) (Edwards et al., 2010).

2.4 Quantum chemical studies

The DFT calculations (Zhong et al., 2014) were done using ChemCompute Lab servers (Yang et al., 2018). The Becke, 3-parameter, Lee–Yang–Parr (B3LYP) level (Becke, 1993) with the 6–311++G (d,p) basis set (Papajak et al., 2011) has been utilized to optimize the molecular structure of the examined molecules, FMOs, and the molecular electrostatic potential (MEP). Various calculations were performed to determine the values of E_{HOMO}, E_{LUMO}, gap energy (ΔE_{gap}), ionization potential (I), electron affinity (A), electronegativity (χ), electronic chemical potential (μ), electrophilicity index (ω), global hardness (η), and global softness (S) calculated as outlined in the literature (Ismael et al., 2018) and then used to analyze the electronic features.

3 Results and discussions

3.1 ADMET

The boiled egg model revealed the ability of the three monoterpenoid indoles to penetrate the BBB; however, gardflorine A was shown to be a non-substrate to P-glycoprotein like B and C derivatives as shown in Figure 3 (Daina and Zoete, 2016; Şahin and Dege, 2021).

Bioavailability radar charts for the tested compounds showed their good potential for bioavailability, as shown in Figure 4.

Table 1 illustrates the pharmacokinetic profile of gardflorine A–C, all revealed the ability to penetrate the BBB, and all also showed a high opportunity to be absorbed from the GIT. Gardflorine A only showed to be a non-substrate for P-glycoprotein. All are lead-like molecules with no violation of the Lipinski rule of 5.

3.2 Multiple targets of gardflorine A–C against HCV and HIV

Figures 5, 6 show the target distribution; gardflorine A can target more than 50 targets in HIV and more than 20 targets in HCV. Gardflorine B and C showed more selectivity toward HCV proteins than HIV targets compared to gardflorine A.

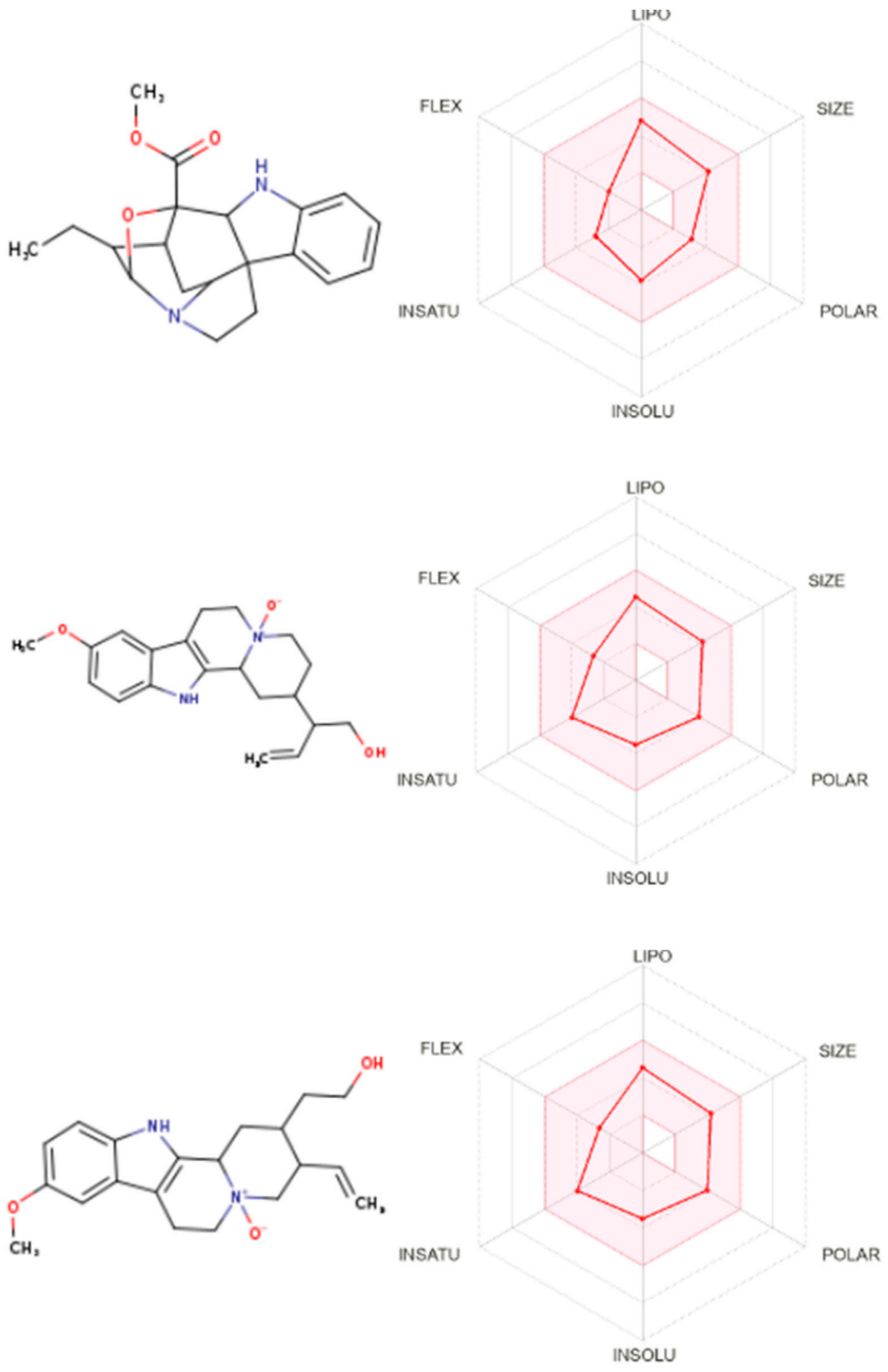

FIGURE 4
Bioavailability radar for gardflorine A–C.

TABLE 1 Pharmacokinetic profile for gardflorine A-C.

Item	Gardflorine-A	Gardflorine-B	Gardflorine-C
Formula	$C_{20}H_{24}N_2O_3$	$C_{20}H_{26}N_2O_3$	$C_{20}H_{26}N_2O_3$
Log $P_{o/w}$ (iLOGP)	3.26	1.94	1.81
GI absorption	High	High	High
BBB permeant	Yes	Yes	Yes
P-gp substrate	No	Yes	Yes
Lipinski	Yes; 0 violation	Yes; 0 violation	Yes; 0 violation
Leadlikeness	Yes	Yes	Yes

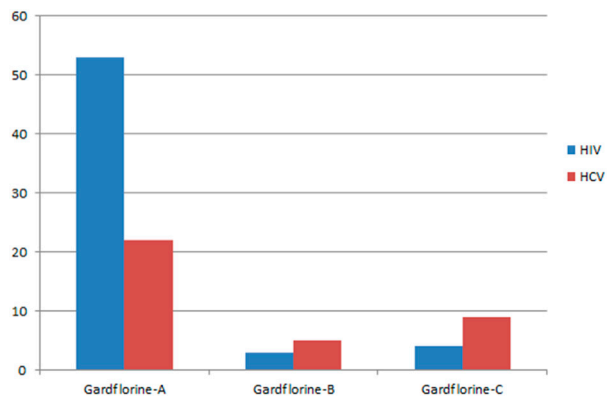

FIGURE 5
Bar chart illustrating a number of predicted targets of gardflorine A–C; Y-axis (no. Of targets), and *X*-axis (monoterpenoid indole).

3.3 Molecular docking and inhibition constant (Ki value)

Docking studies were performed for gardflorine A–C and delavirdine against protein targets in HIV and HCV. Delavirdine displayed the ability to target 29 HCV-affecting proteins and 14 HIV-affecting proteins. Gardflorine A revealed the ability to target 53 proteins (Figures 5, 6) that affect HIV and 21 proteins that affect HCV (Figures 5, 6). Gardflorine B and C revealed the ability to target three and four proteins that affect HIV, respectively, and five and nine proteins that affect HCV, respectively. All proteins are listed in Supplementary Tables 1–4 with their pdb ID codes, ligand names, similarity and docking scores, and inhibition constant (Ki value).

The docking methodology was rigorously validated through re-docking and superimposition of the native ligands originally co-crystallized within the active sites of target proteins (pdb ID: 2PK5,

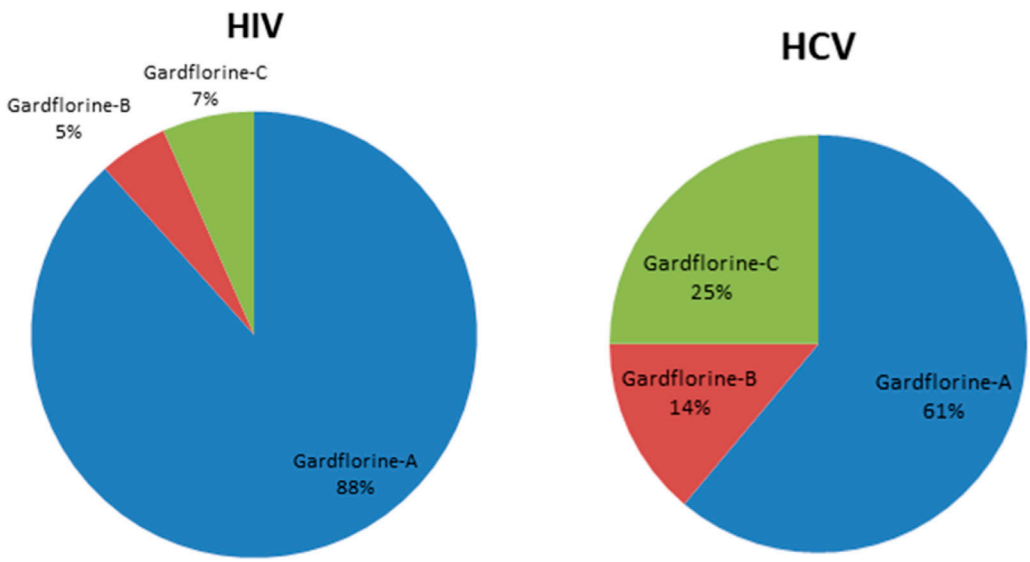

FIGURE 6
Pie chart illustrating percentage distribution of the predicted targets in HIV and HCV for gardflorine A–C.

2PK6, 3HKW, 3I0R, 3NF6, 3OK9, 3QO9, 3UPI, 3VQS, 4NWK, 4ZIP, 5EQQ, 5ETX, and 5KGW). During the validation, the binding pose of this co-crystallized ligand was accurately reproduced, ensuring that the docking protocol was reliable. The superimposition of the re-docked ligand with the native ligand demonstrated a high degree of alignment, confirming that the docking procedure could precisely mimic the original ligand's interactions within the active site. This successful validation, depicted in Fig. S. X (supplementary data), underscores the robustness and accuracy of the docking protocol, making it suitable for predicting the binding modes of other compounds in subsequent studies.

3.4 Molecular docking studies against HCV proteins

3.4.1 RNA-directed RNA polymerase

One of the primary focuses of medication research and development is a viral protein called HCV NS5B RNA polymerase, which plays a crucial role in the replication of the HCV gene (Shaw et al., 2009). Similar to other members of the Pol I family, the HCV NS5B crystal structure reveals an overall subdomain architecture with a deep active site cavity at the top of the "palm" subdomain, sealed at its base by a distinctive b-loop (Ikegashira et al., 2006). Moreover, an unexpected interaction was found between the tip of the "fingers" subdomain and the "thumb" subdomain, which serves to ring the hypothesized nucleoside triphosphate substrate entrance trajectory (Tedesco et al., 2006). Sequence variation analysis reveals that residues lining the active site cavity ("palm site") are more conserved than in locations such as the "thumb site (Figure 7). This renders the palm site an intriguing target for the inhibition of the viral polymerase, although not all residues surrounding this site are entirely conserved. Non-nucleoside inhibitors that bind to the palm, thumb, and finger-loop subdomains are effective in clinical trials (Velázquez et al., 2012). The X-ray structure of NS5B verifies that the ligand interacts with Cys366, Met414, Leu384, and Tyr415 in the "palm site" of the active site cavity of the apoprotein (Ando et al., 2012). Via its indole moiety, delavirdine displayed three Pi interactions with residues Try448, Phe193, and Cys366. In addition, it formed three hydrogen bonds with Leu547, Phe193, and Try452 residues, with two additional interactions involving Phe193 and Try452 (Figure 8; Supplementary Table 5). The natural indole compounds gardflorine A, gardflorine B, and gardflorine C with docking scores of −7.35, −7.64, and −7.56 kcal/mol (Table 2; Supplementary Table 5), respectively, are also docked to the same binding site of the RNA-polymerase enzyme as delavirdine. The three natural indole compounds showed pi-alkyl interactions with the crucial amino acid Cys366. Gardflorine A formed one hydrogen bond interaction with Asn316, in addition to four hydrophobic interactions. The indole moiety of gardflorine B and C shared more than four interactions with various amino acids in the active site cavity (palm site) (Figure 8; Supplementary Table 5). In the case of gardflorine B, it interacted with Cys366 and Phe415, and gardflorine C interacted with Cys 366, Tyr 448, and Met414. The inhibition constant (Ki) values of delavirdine and gardflorine A, B, and C were 1.85, 4.11, 2.52, and 2.92 μM, respectively.

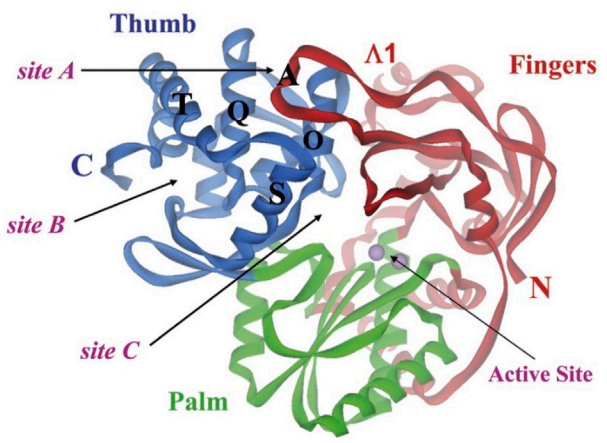

FIGURE 7
Binding sites on HCV NS5B polymerase. The three locations are confined inside the helices O, Q, S, and T. Each of the sites A and B is situated on the surface of the thumb domain. Site C is near the enzyme active site (Rydberg et al., 2009).

3.4.2 NS3/A4 protease

Four known locations along the virally encoded polyprotein are cleaved by the HCV NS3/4A protease, a chymotrypsin-like serine protease that is a prime therapeutic target (Lemke et al., 2011). Pharmaceutical companies have made substantial investments in the development of NS3/4A protease inhibitors (Ikegashira et al., 2006). Most inhibitors interact with the Arg155, Ala 157, and Ser159 residues of the protease backbone. Additionally, the catalytic amino acids serine 139 and His 57 are essential for proper binding (Scola et al., 2014). Delavirdine formed three hydrogen bonds with Ser159 and Ala157, and docking scores of −6.69 kcal/mol were obtained, along with hydrophobic interactions with His57 and Ala157 (Figure 9; Table 2; Supplementary Table 6). Gardflorine A and C bind to the catalytic His 57 residue and the essential Ala157 amino acid (Figure 9; Table 2; Supplementary Table 6). Gardflorine A displayed one H-bond with the catalytic residue His 57 (3.20 Å) and three alkyl bonds with Ala156, Ala157, and His57 with a docking score equal to −6.23 kcal/mol. In the case of gardflorine B, the catalytic amino acid serine 139 contributes two hydrogen bonds. Moreover, gardflorine B showed another two H-bonds with Leu 135 and Thr 42 and two pi–alkyl bonds with Lys136 and Ala157 with a docking score equal to −6.15 kcal/mol (Figure 9; Table 2; Supplementary Table 6). Gardflorine C interacts through five types of interactions and forms 14 bonds with essential residues, including Lys136, Thr42, Lys 136, His 57, Ala157, Ile132, Cys159, and Ala139 (Figure 9; Table 2; Supplementary Table 6). Moreover, gardflorine C had the lowest inhibition constant (Ki) of 7.13 μM.

3.5 Molecular docking studies against HIV proteins

3.5.1 Protease

As a dimer, HIV-1 protease (PR) is catalytically active, and the catalytic Asp25 residues from both subunits interact strongly at the

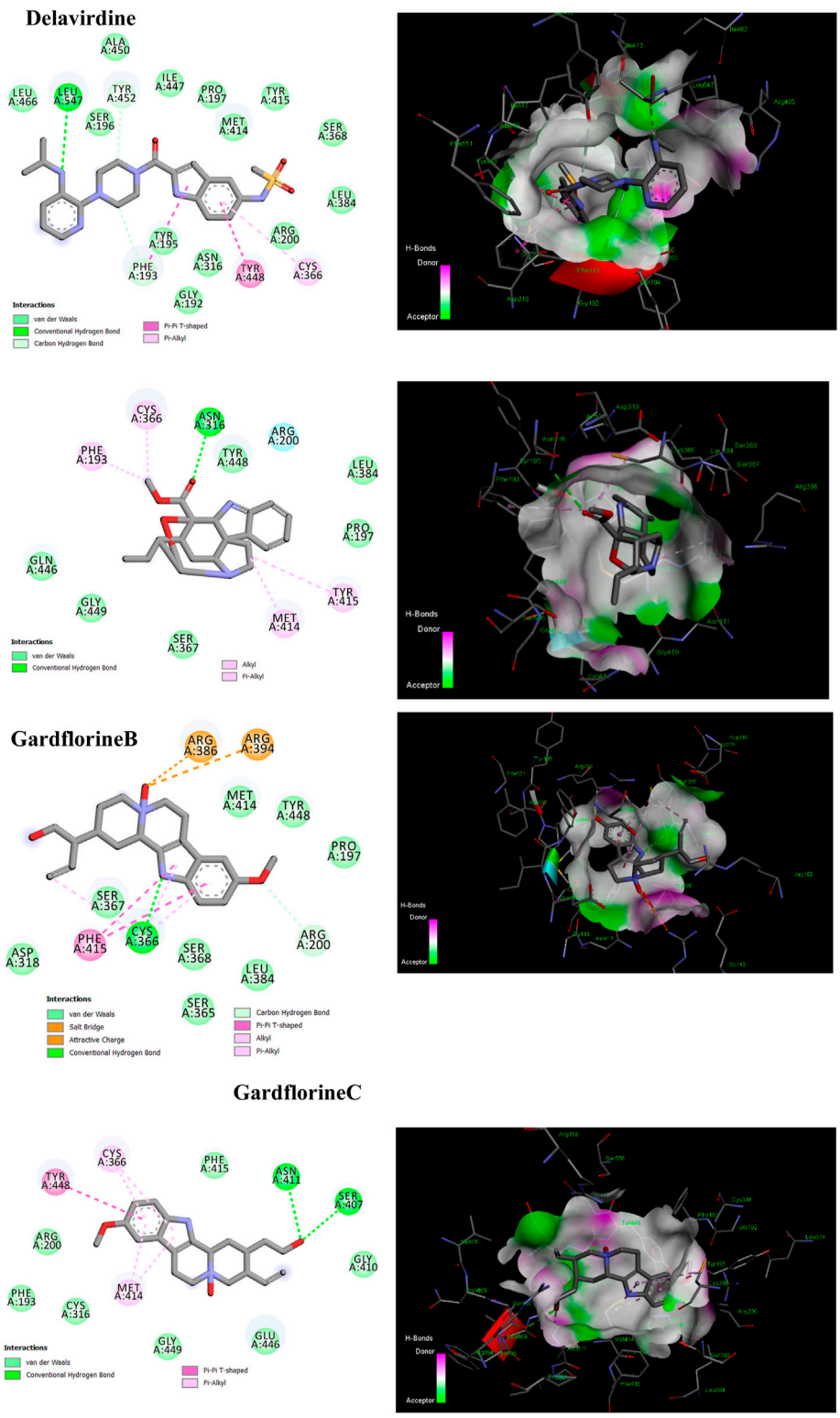

FIGURE 8
2D and 3D representation of the predicted binding mode for compounds delavirdine (PDB ID: 3vqs), gardflorine A (PDB ID: 3upi), gardflorine B (PDB ID: 3hkw), and gardflorine C (PDB ID: 3hkw) against HCV RNA-directed RNA polymerase.

subunit interface (Lafont et al., 2007). The binding site contains the residues Ala28, Asp29, Asp30, Met46, Val82, Val32, Ile47, and Ile84 (Tie et al., 2004). Some inhibitors bind via van der Waals forces with the protease residues Leu23, Gly49, Ile50, Pro81, Val82, and Ile84 from both subunits (Zhang et al., 2013). Delavirdine had fewer hydrogen bond interactions with the protease residues

TABLE 2 Protein targets with the highest docking score in HIV and HCV, Pdb IDs, ligand names, ligand similarity and docking scores of delavirdine, monoterpenoid indole gardflorine A, B, and C, and calculated inhibition constant values.

Compound	PDB	Target class	Target name	Ligand name	Ligand similarity score	PSO Vina2 docking score (kcal/mol) ▼	Predicted Ki (μmol)
Delavirdine	3vqs	HCV	RNA polymerase	JT1	0.442	−7.83	1.85
	5etx	HCV	NS3/ A4 protease	5RS	0.423	−6.691	12.64
	4zip	HIV	Protease	G64	0.406	−7.804	1.93
	3i0r	HIV	Reverse transcriptase	RT3	0.412	−8.157	1.06
Gardflorine A	3upi	HCV	RNA polymerase	0C2	0.405	−7.357	4.11
	5etx	HCV	NS3/ A4 protease	5RS	0.426	−6.231	27.44
	3ok9	HIV	Protease	G52	0.407	−9.722	0.076
	3qo9	HIV	Reverse transcriptase	QO9	0.409	−8.389	0.72
	3nf6	HIV	Integrase	IMV	0.401	−6.079	35.46
Gardflorine B	3hkw	HCV	RNA polymerase	IX6	0.408	−7.647	2.52
	4nwk	HCV	NS3/ A4 protease	2R8	0.401	−6.156	31.14
	2pk6	HIV	Protease	O33	0.401	−5.899	48.03
	5kgw	HIV	Integrase	7SK	0.404	−4.827	292.63
Gardflorine C	3hkw	HCV	RNA polymerase	IX6	0.419	−7.56	2.92
	5eqq	HCV	NS3 protease	5RS	0.402	−7.03	7.13
	2pk5	HIV	Protease	075	0.405	−7.447	3.53
	5kgw	HIV	Integrase	7SK	0.404	−4.598	430.4

Gly27 and Pro81, two pi–sigma bonds with Ala 28 and Ile47, and two alkyl bonds with Ala28 and Ile84; its docking score was −7.80 kcal/mol (Figure 10; Table 2 and Table S7). Gardflorine A–C anchored correctly in the binding site of the HIV-protease enzyme. Gardflorine A showed the highest docking score of −9.72 kcal/mol and a higher number of hydrogen bonds than gardflorine B and C (Figure 10; Table 2, and Supplementary Table 7). Gardflorine A revealed four hydrogen bonds with Gly49 and Ile47, along with nine alkyl interactions with Ala28, Pro81, Ile54, Val32, Ile47, and Val82. Gardflorine B exhibited the lowest docking score of – 5.89. Delavirdine and gardflorine A, B, and C exhibited respective inhibition constants (Ki) of 1.93, 0.076, 48.03, and 3.53 μM.

3.5.2 Reverse transcriptase

p66 (66 kDa) and p51 (51 kDa) subunits form a heterodimer to form HIV-1 RT. Three catalytic trio aspartate residues (Asp110, Asp185, and Asp186) are necessary for DNA polymerization (Parrish et al., 2013). Non-nucleoside reverse transcriptase inhibitors (NNRTIs) are essential components of HIV-1 infection-treating multidrug regimens known as HAART (highly active antiretroviral treatment). It was reported that the drug's interaction with Trp229 and Lys103 results in extraordinary effectiveness (Su et al., 2009; Das et al., 2011). According to our investigation, neither gardflorine B nor gardflorine C was an HIV-reverse transcriptase target. Gardflorine A docked in the same manner as delavirdine at the active site. In addition, gardflorine A showed higher docking scores than delavirdine, −8.38 *versus* −8.15 kcal/mol. Delavirdine displayed three hydrogen bonds and thirteen hydrophobic interactions. Gardflorine A exhibited hydrogen bond interactions with Try 318; a pi bond with Try229, Tyr 318, Try 181, Try 188, Trp 229, and Lys102; and a pi-stacking interaction with Try 181, Try 188, and Try 188. Moreover, three alkyl linkages occurred between gardflorine A and Leu100, Val 106, and Leu 234 (Figure 11; Table 2, and Supplementary Table 8). Delavirdine and gardflorine A have respective inhibition constants (Ki) of 1.06 and 0.72 μM.

3.5.3 Integrase

By facilitating the insertion of viral DNA into the host genome, HIV-1 integrase (IN) plays a vital role in viral replication. The entire process is mediated by the well-ordered formation of a stable synaptic complex (SSC) through the multimerization of HIV IN

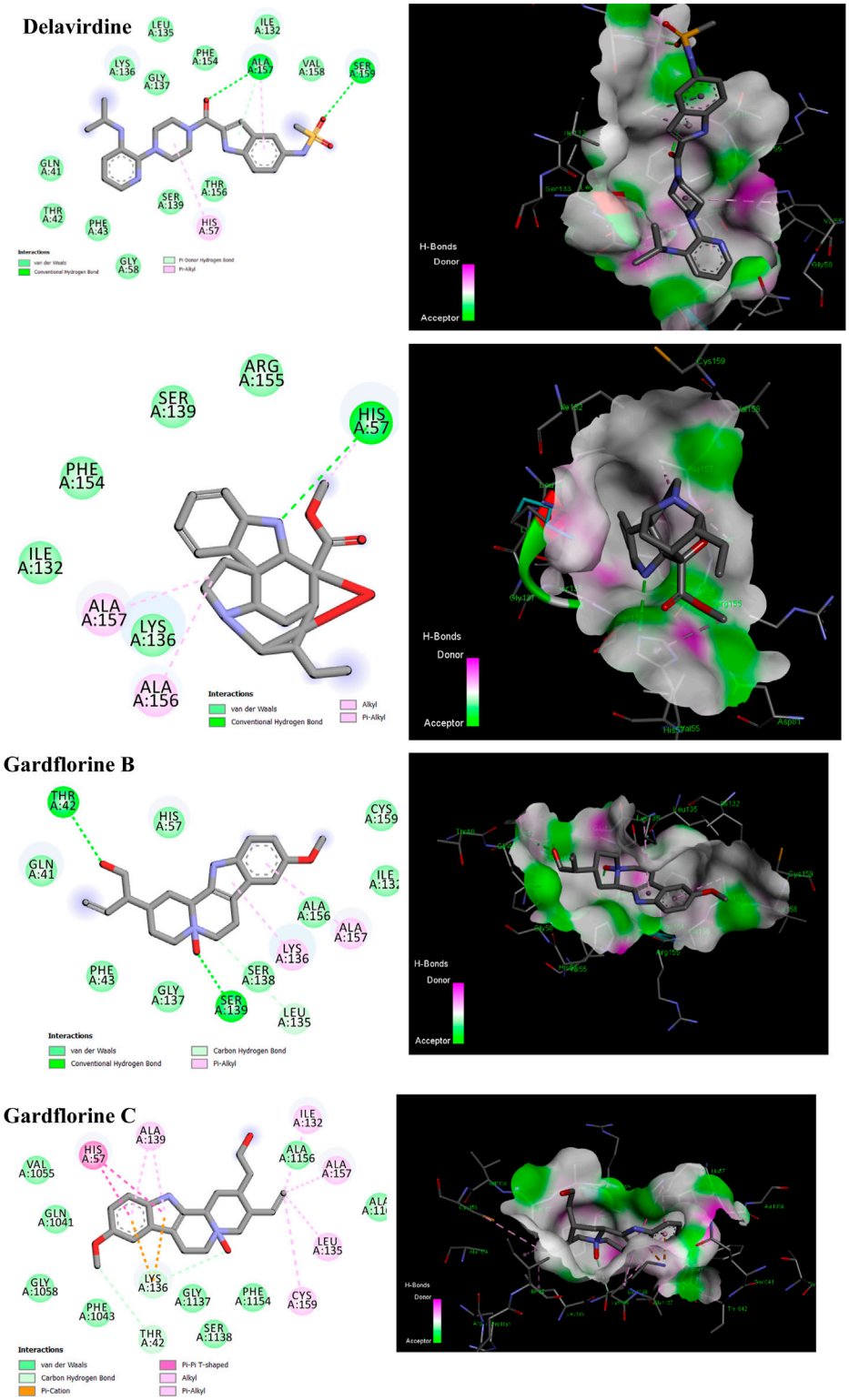

FIGURE 9
2D and 3D representation of predicted binding mode for compounds delavirdine (PDB ID: 5etx), gardflorine A (PDB ID: 5etx), gardflorine B (PDB ID: 4nwk), and gardflorine C (PDB ID: 5eqq) against HCV N53 protease.

into a tetramer on viral DNA. Given the significance of HIV-1 IN for viral infection, there has been considerable interest in the development of drugs capable of inhibiting IN activity (Rhodes et al., 2011). The enzymatic activity of integrase requires two magnesium ions to be coordinated by a DDE motif (Asp64, Asp116, and Glu152) at the active site of integrase, with the

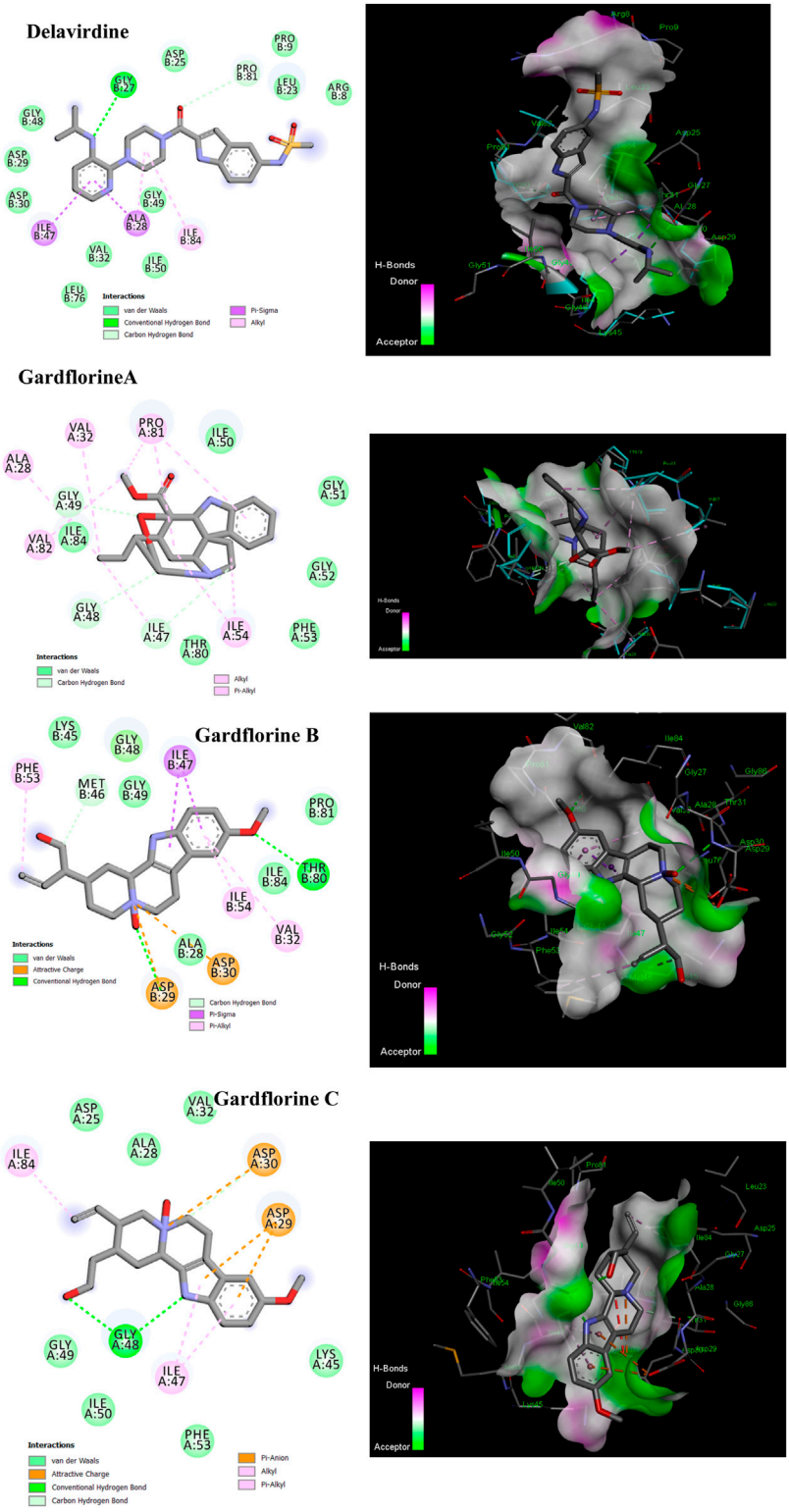

FIGURE 10
2D and 3D representations of the predicted binding mode for compounds delavirdine (PDB ID: 4zip), gardflorine A (PDB ID: 3ok9), gardflorine B (PDB ID: 2pk6), and gardflorine C (PDB ID: 2pk5) against HCV N53 protease.

position of Glu152 modified by the mobile loop (residues Gly140 to Gly149), suggesting that the loop plays a role in metal positioning (Gupta et al., 2014). Gardflorine A has the lowest binding energy, at −6.07 kcal/mol; it interacts with Tyr 83 and Glu85 by forming three H-bonds and alkyl bonds with Val180, Tyr 83, Phe 181, and His 185. Gardflorine B and C have docking scores

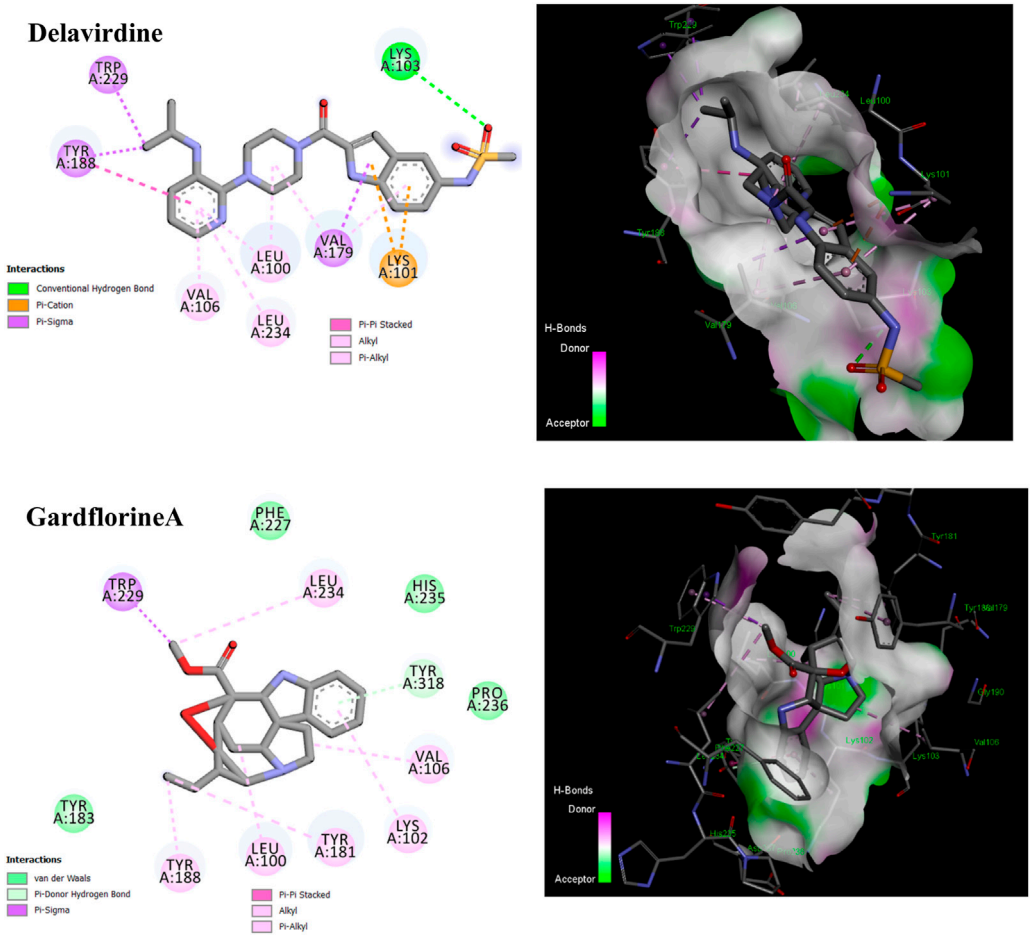

FIGURE 11
2D and 3D representations of the predicted binding mode for compounds delavirdine (PDB ID: 3i0r) and gardflorine A (PDB ID: 3qo9) against HCV RT.

of −4.82 and −4.59, respectively, and they interact with the complementary pocket residues Thr 174 Met 178. Gardflorine C exhibited six hydrogen bonds with Glu 170, His 171, Thr174, and Gln168, along with pi–sulfur and pi–alkyl bonds with Met 178 (Figure 12; Table 2; Supplementary Table 9). The inhibition constants (Ki) for gardflorine A, B, and C were 35.46, 292.63, and 430.4 μM, respectively.

4 Quantum chemical studies

4.1 FMO analysis and chemical reactivity

The optimized structures of the title compounds are shown in Figure 13. The most significant concept for researchers that provides data on chemical reactivities is the FMO (Ismael et al., 2021a). FMOs refer to the energies of a compound's lowest unoccupied molecular orbital (LUMO) and highest occupied molecular orbital (HOMO). These orbitals control how the molecule interacts with other species. HOMO stands for the ability to give an electron, whereas LUMO stands for the ability to take an electron.

For A, B, and C, respectively, the calculated HOMO energies were −5.52, −4.81, and −5.16 eV, while the corresponding LUMO energies were −0.81, −0.65, and −0.74 eV. The molecule's chemical stability is described by the gap energy (ΔE_{gap}) (Ismael et al., 2021b). The Egap values of A, B, and C were determined to be 4.71, 4.16, and 4.43 eV, respectively. Normally, when the ΔE_{gap} is small, the molecule is highly polarizable and is associated with low kinetic stability and high chemical reactivity, and it is referred to as a soft molecule. In conclusion, the title molecule structure's biological reactivity is demonstrated by the low value of ΔE_{gap} (Abdou et al., 2022).

The HOMO and LUMO map's incorporation in molecules A, B, and C are depicted in Figure 14. The molecular orbital wave function's negative and positive phases are represented, respectively, by the green and red color distributions. These images show that the lowest unoccupied molecular orbitals, or LUMOs, and the highest occupied molecular orbitals, or HOMOs, are mostly concentrated across the whole molecule structure, as shown in Figure 14.

Understanding the connection between structural stability and global chemical reactivity relies on the knowledge of global reactivity parameters. The calculated values of the HOMO and LUMO

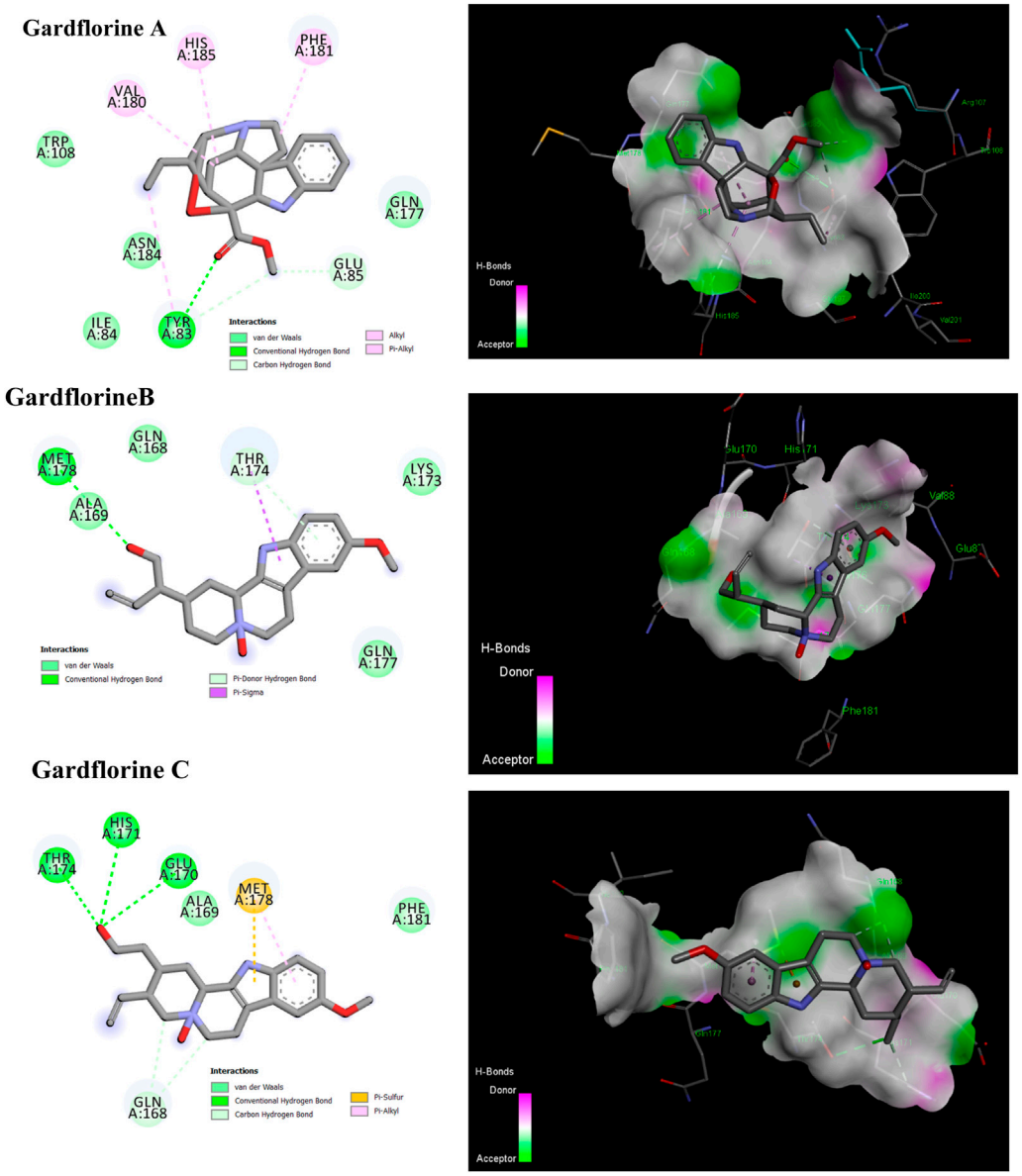

FIGURE 12
2D and 3D representations of the predicted binding mode for compounds gardflorine A (PDB ID: 3nf6) and gardflorine B and C (PDB ID: 5kgw) against HCV-Integrase.

energies, the gap energy (ΔE_{gap}), the ionization potential (I), the electron affinity (A), the total energy of the optimized molecular structure (E_{Total}), and some global reactivity properties like electronegativity (χ), the electronic chemical potential (μ), the electrophilicity index (ω), global hardness (η), and global softness (S) for the A, B, and C structures in the gas are tabulated in Table 3. The optimized geometries of the A, B, and C atoms have total energy values (E_{Total}) of −30256.87, −30287.96, and −30260.86 e.V., respectively, as shown in Table 3, indicating high stability.

As for the dipole moment (μ) value, it was discovered to be 1.31, 4.18, and 6.05 Debye, respectively, for the A, B, and C structures produced using the DFT technique in the gas phase. The ionization potential (I) values of the structures A, B, and C are lower than the average (5.52, 4.81, and 5.16 eV), which suggests that they have better electron donor properties. Additionally, it was determined that the values of A, B, and C's global chemical hardness (η) and softness (S) were (2.35, 2.08, and 2.21 eV) and (0.21, 0.24, and 0.23 eV), respectively. One interpretation of the values is as an indicator of intramolecular charge transfer. Additionally, the low and high chemical hardness (η) and softness (S) values obtained show that the studied structure is a soft molecule.

The electrophilic index (ω) of the A, B, and C structures was determined to be 2.13, 1.79, and 1.97 eV, respectively. According to Domingo *et al.*'s classification of organic compounds, the title molecule structurally falls into the category of "high electrophiles" (>1.50 eV). The ability of an atom or set of atoms to draw electrons is quantified by the electronegativity (χ) descriptor. According to calculations, A, B, and C's electronegativity and electronic chemical potential (CP) are, respectively, (3.17, 2.73, and 2.95) eV and (−3.17, −2.73, and −2.95) eV.

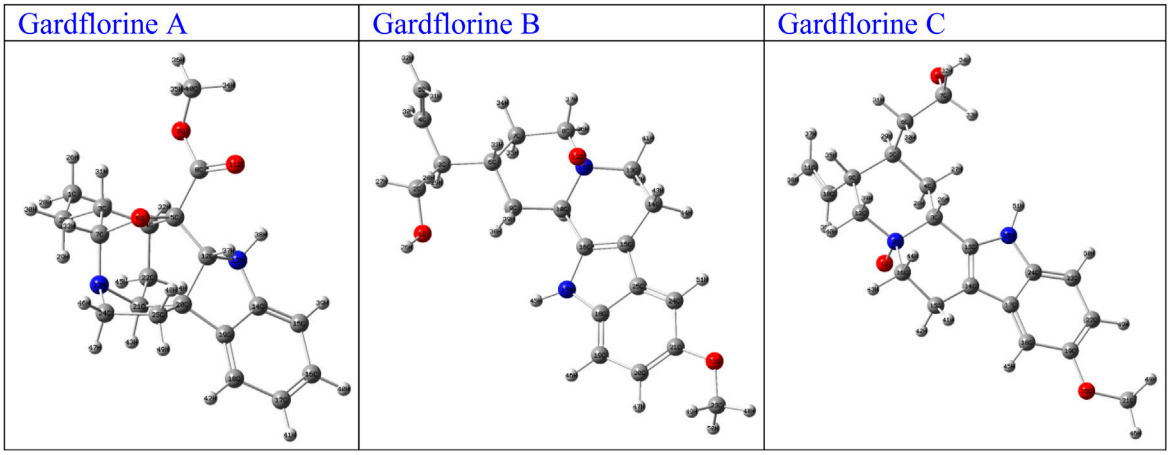

FIGURE 13
Optimized structures of gardflorine (A–C) with the scheme of atom numbering obtained by B3LYP/6–311++G (d,p) in the gas phase.

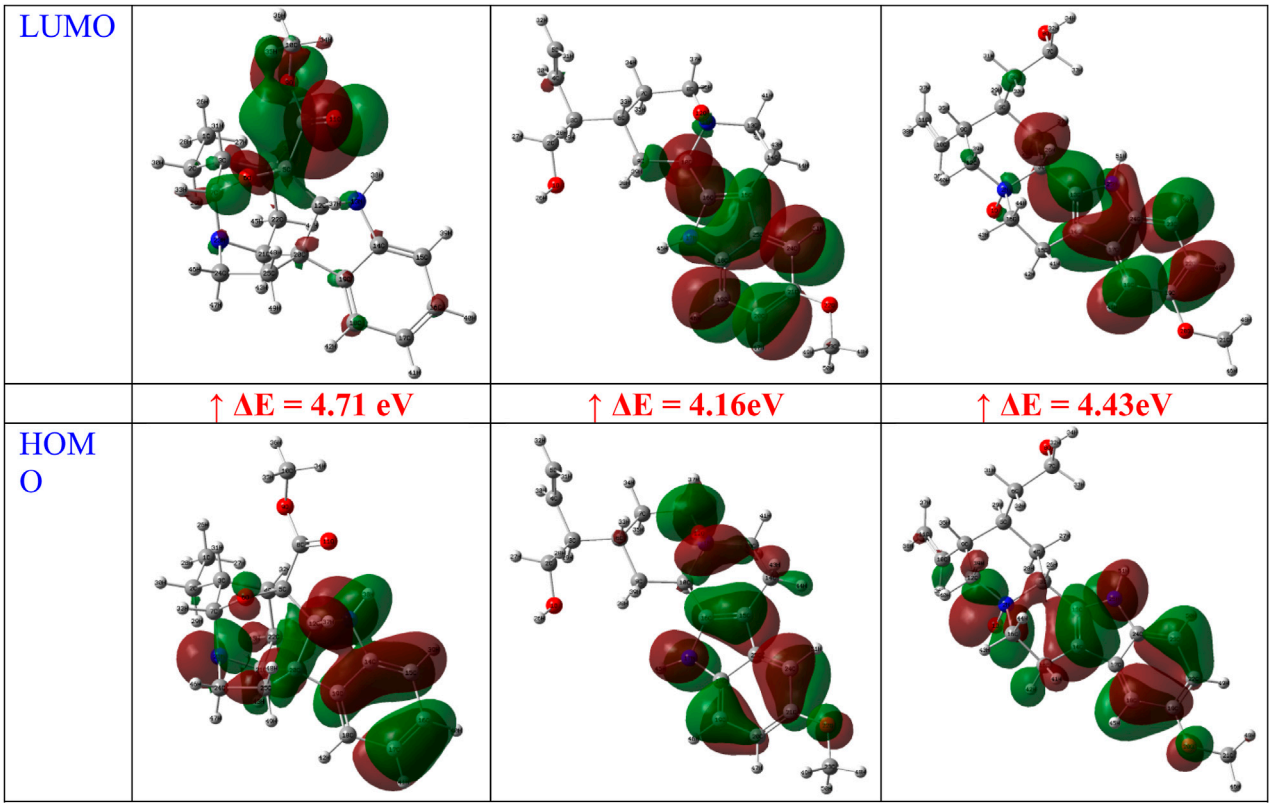

FIGURE 14
FMOs of gardflorine (A–C) at B3LYP/6–311++G (d,p) in the gas phase.

4.2 Molecular electrostatic potential

The MEP is a valuable tool for illustrating the electronic density in molecules, and it is used to identify places with surfaces that have both positive and negative electrostatic potentials by utilizing different colored dots (Domingo et al., 2002). On the other hand, the red, orange, or yellow negative sites (high electron density) represent the electrophilic assault, the green positive sites (low electron density) reflect the nucleophilic attack, and the blue positive sites (high electron density) represent the neutral regions. A, B, and C's MEP surfaces were calculated using the B3LYP/6–311++G (d,p) (Gas) level of theory (Figure 15).

The negative areas of the A, B, and C molecules were located around the oxygen atoms, as shown in Figure 15. Additionally, the

TABLE 3 Calculated chemical parameters.

	E_{Total}	μ	E_{HOMO}	E_{LUMO}	ΔE	I	A	χ	CP	η	S	ω
A	−30256.87	1.31	−5.52	−0.81	4.71	5.52	0.81	3.17	−3.17	2.35	0.21	2.13
B	−30287.96	4.18	−4.81	−0.65	4.16	4.81	0.65	2.73	−2.73	2.08	0.24	1.79
C	−30260.86	6.05	−5.16	−0.74	4.43	5.16	0.74	2.95	−2.95	2.21	0.23	1.97

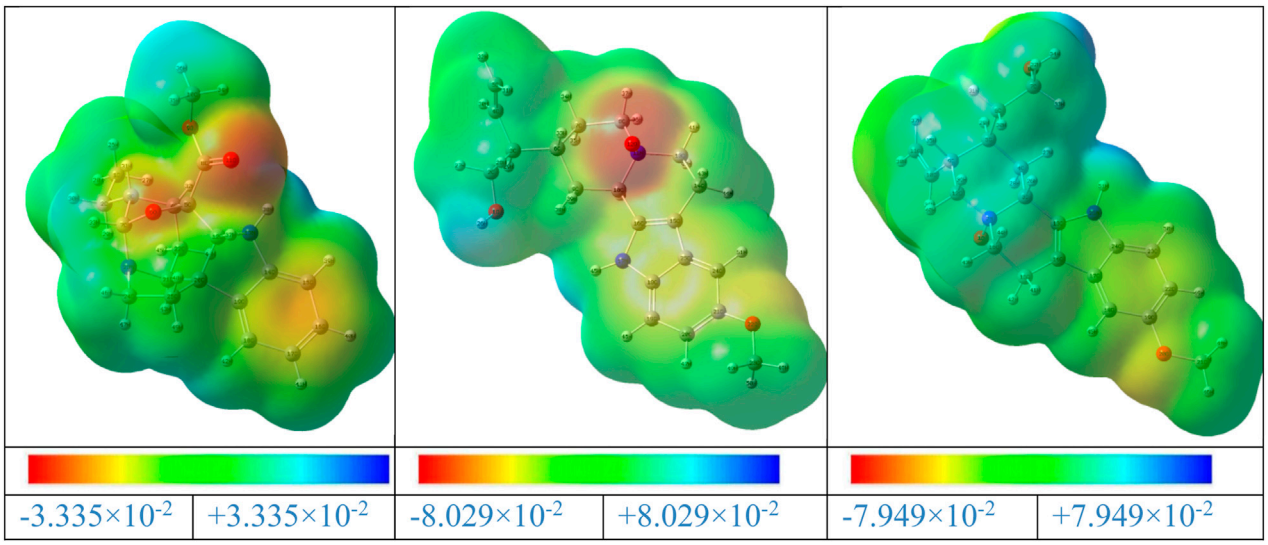

FIGURE 15
MEP maps of the gardflorine (A–C) molecules computed using the B3LYP/6–311++G (d,p) in the gas phase.

hydrogen atom linked to the nitrogen in the A, B, and C structures is the center of the positive areas, making it vulnerable to nucleophilic assault. Additionally, the areas with faint blue coloring represent weak interaction locations. Additionally, the places of the title compounds' structures that are colored green display neutral areas with no potential.

4.3 Natural charge analysis

Because they represent the physicochemical characteristics of a molecule (the electronic structure, vibrational spectra, dipole moment, polarizability, and other molecular properties), atomic charges play a significant role in molecules (Shahab et al., 2020). The atomic charges of A, B, and C molecules in the current investigation were calculated using NBO analysis at the B3LYP/6–311++G (d,p) level of theory in the gaseous phase. The findings are presented in Supplementary Table 11, and the atoms are numbered in accordance with Figure 16.

Understanding electronegativity equalization and charge transfer in the chemical reactivity of the title molecule is made easier with the use of NBO analysis. The NBO analysis of the molecule reveals that carbon atoms in A, B, and C contain both positive and negative charges. Positive carbons are observed for carbon atoms coupled with the electron-withdrawing oxygen and nitrogen atoms, as illustrated in Supplementary Table 11 and Figure 16, including (C14, C5, C7, and C8), (C2, C18, C16, and C21) and (C7, C24, C13, and C19) atoms in the tile A, B, and C molecules, respectively. Moreover, the other carbon atoms, including carbon atoms (C22, C25, C2, C15, C3, C4, C17, C18, C10, C16, C24, C20, and C19), (C14, C7, C9, C5, C20, C3, C24, C19, C6, C23, C4, C8, C13, C15, C25, and C10) and (C6, C4, C15, C11, C22, C9, C18, C23, C5, C21, C10, C12, C16, C14, C17, and C3), have a negative charge in the tiled A, B, and C molecules, respectively.

Additionally, C8 (0.85006e), C21 (0.31877e), and C19 (0.32007e) atoms in the A, B, and C molecules, respectively, have the largest positive charges due to their connection to withdrawing oxygen atoms (O11, O9), (O22), and (O20), as opposed to other carbon atoms. The most negatively charged atoms in compounds A, B, and C are (N13, O6, O11, and O9), (O12, O1, N17, and O22), and (O1, O8, N25, and O20), respectively. All hydrogen atoms in A, B, and C are positively charged, according to the findings. The fact that (N13), (O10 and N17), and (O8 and N25) atoms are electron-withdrawing means that the (H38), (H26 and H45), and (H34 and H51) hydrogen atoms in compounds A, B, and C have the largest positive charges in contrast to other hydrogen atoms.

4.4 Natural bond orbital analysis

The NBO technique is regarded as a quick method for comprehending the characteristics of the electronic structure. As

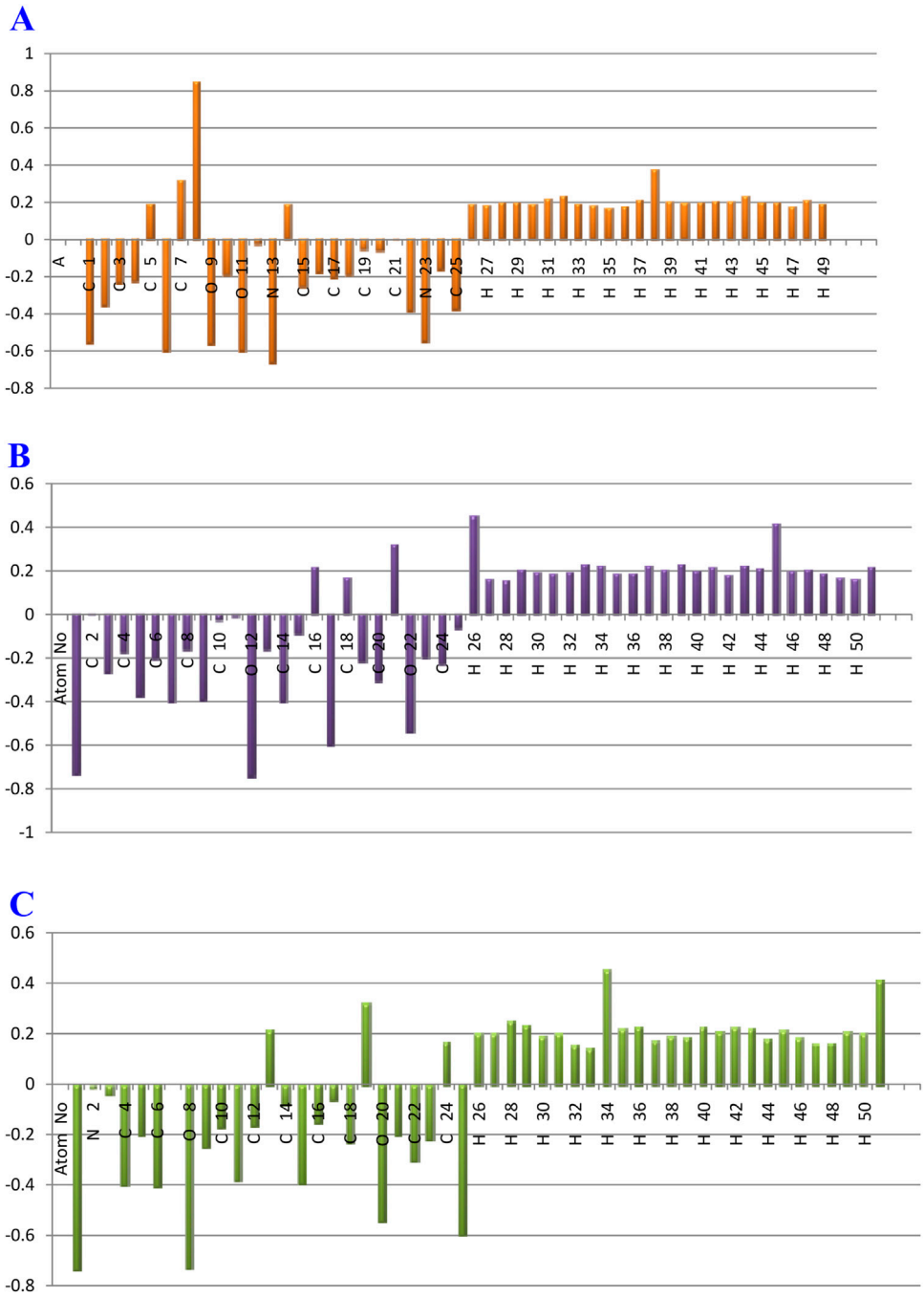

FIGURE 16
Plot of natural charge distribution of the gardflorine **(A–C)** molecules computed using the B3LYP/6−311++G (d,p) in the gas phase.

a straightforward framework for analyzing charge transfer, delocalization, and conjugative interactions in molecules, it is also a useful technique for assessing interactions between donors and acceptors (Weinhold and Landis, 2001).

The NBO analysis tool is a useful method for investigating both intra- and intermolecular bonding. It can effectively provide insights into charge transfer and hyper-conjugative interactions. In particular, NBO 5.0 software is utilized to compute electron density, rehybridization, and intramolecular charge delocalization within molecules. Furthermore, the NBO approach allows for quantitative analysis of bonding and anti-bonding interactions caused by second-order perturbation, expressed as perturbation energies E(2) by Refs. $E^{(2)} = \Delta E_{ij} = qi\ (F\ (i,j)^2/E_j - E_i)$, where Ei and Ej are the diagonal elements, qi is donor orbital occupancy, and Fi,j is the NBO off-diagonal matrix element.

For both compounds, the computed and listed interactions between the Lewis-type occupied NBO orbital (bonding) and non-Lewis unoccupied NBO orbital (anti-bonding) are shown in

Supplementary Table 11. There are only two types of donors, namely σ and π, and two types of acceptors, namely σ and π, according to the local inspection of the various donors and acceptors. According to observations of perturbation energy $E^{(2)}$ for various transitions between these donors and acceptors, the following transitions for A molecule are extremely likely to occur: C16-C17→C14-C15 (96.87 kj/mol, π→π*), C16-C17→C18-C19 (63.97 kj/mol, π→π*), O9→C8-O11 (29.54 kj/mol, LP→π*), O11→C8-O9 (29.44 kj/mol, LP→π*), and N13→C14-C15 (63.97 kj/mol, LP→π*); for B molecule: C20-C21→C18-C19 (119.04 kj/mol, π→π*), C20-C21→C24-C25 (84.09 kj/mol, π→π*), N17→C18-C19 (33.29 kj/mol, LP→π*), N17→C15-C16 (29.78 kj/mol, LP→π*), and O22→C20-C21 (25.43 kj/mol, LP→π*); and for C molecule: C19-C22→C23-C24 (122.59 kj/mol, π→π*), C19-C22→C17-C18 (84.86 kj/mol, π→π*), N25→C23-C24 (31.97 kj/mol, LP→π*), N25→C13-C14 (28.54 kj/mol, LP→π*), O20→C19-C22 (25.49 kj/mol, LP→π*). These are the most probable transitions.

These transitions show stronger electron density, with strong intramolecular hyperconjugative interactions contributing more. Strong intramolecular interactions between the lone pairs (O9 to π* C8-O11, O11 to π* C8-O9, and N13 to π* C14-C15), (N17 to π* C18-C19, N17 to π* C15-C16, and O22 to π* C20-C21), and (N25 to π* C23-C24 and O20 to π* C19-C22) were also revealed by the NBO analysis. These interactions result in intramolecular charge transfer (ICT), which stabilizes the system.

5 Conclusion

The DME study of the three tested compounds revealed their ability to penetrate the BBB, and all showed a high potential for absorption from the GIT. Gardflorine A was the compound identified as a non-substrate for P-glycoprotein. All are lead-like molecules with no violation of the Lipinski rule of 5. In addition, the multi-target prediction showed that delavirdine could target 29 HCV-affecting proteins and 14 HIV-affecting proteins, while gardflorine A could target 53 proteins affecting HIV and 21 proteins affecting HCV. Gardflorine B targeted five HCV-affecting proteins and three HIV HIV-affecting proteins, while gardflorine C targeted nine HCV-affecting proteins and four HIV-affecting proteins. The docking study of gardflorine A, gardflorine B, and gardflorine C, with docking scores of −7.35, −7.64, and −7.56 kcal/mol, respectively, showed that they are also docked to the same binding site of HCV RNA-polymerase enzyme as delavirdine. The three natural indole compounds showed pi–alkyl interactions with the crucial amino acid Cys366. All compounds demonstrated interactions at the conserved palm site, with delavirdine displaying the strongest binding affinity. However, the natural indole compounds, particularly Gardflorine B, showed promising binding properties and inhibition potential, making them valuable candidates for further optimization and therapeutic development. The docking study results of HCV NS3/4A protease revealed the potential of these compounds as effective NS3/4A protease inhibitors. Among the compounds, gardflorine A demonstrated the strongest binding affinity and inhibitory potential, making it a promising candidate for targeting HIV-1 protease, HIV-1 RT, and HIV-1 integrase. The FMO analysis and chemical reactivity showed that the molecular structures of the compounds fall into the category of "high electrophiles," with low values of ΔE_{gap}, indicating high chemical reactivity. The calculated atomic charges using NBO analysis revealed both positive and negative charges in carbon atoms. Furthermore, the NBO analysis also showed strong intramolecular interactions between the lone pairs resulting in intramolecular charge transfer (ICT), which stabilizes the system. This study's results provide new insights for developing drugs targeting HCV and HIV using molecular docking techniques and chemical reactivity analysis. Gardflorine B and C showed more selectivity toward HCV proteins than HIV targets compared to gardflorine A.

Data availability statement

All data are provided in the article and the supplementary files.

Author contributions

AB: Conceptualization, Methodology, Writing–original draft, Writing–review and editing. AA: Investigation, Methodology, Writing–review and editing. SM: Investigation, Validation, Writing–review and editing. MA: Data curation, Visualization, Writing–review and editing. HG: Validation, Visualization, Writing–review and editing. AO: Formal Analysis, Investigation, Writing–review and editing. MZ: Data curation, Validation, Writing–review and editing. AH: Formal Analysis, Investigation, Writing–review and editing. ER: Data curation, Visualization, Writing–review and editing. AA-K: Data curation, Visualization, Writing–review and editing. I: Methodology, Validation, Writing–original draft.

Funding

The author(s) declare that financial support was received for the research, authorship, and/or publication of this article. This research was funded by Taif University, Saudi Arabia, Project No. (TU-DSPP-2024-64). This research was also supported by the National Research Council of Science & Technology (NST) grant by the Korea government (MSIT) (No. CAP23011-100), KIST Institutional programs (2E33133) from Korea Institute of Science and Technology (KIST).

Acknowledgments

The authors extend their appreciation to Taif University, Saudi Arabia for supporting this work through the project number (TU-DSPP-2024-64). This research was also supported by the National Research Council of Science & Technology (NST) grant by the Korea government (MSIT) (No. CAP23011-100), KIST Institutional programs (2E33133) from Korea Institute of Science and Technology (KIST).

Conflict of interest

The authors declare that the research was conducted in the absence of any commercial or financial relationships that could be construed as a potential conflict of interest.

The author(s) declared that they were an editorial board member of Frontiers, at the time of submission. This had no impact on the peer review process and the final decision.

Generative AI statement

The authors declare that no Generative AI was used in the creation of this manuscript.

Publisher's note

All claims expressed in this article are solely those of the authors and do not necessarily represent those of their affiliated organizations, or those of the publisher, the editors, and the reviewers. Any product that may be evaluated in this article, or claim that may be made by its manufacturer, is not guaranteed or endorsed by the publisher.

Supplementary material

The Supplementary Material for this article can be found online at: https://www.frontiersin.org/articles/10.3389/fchem.2024.1521298/full#supplementary-material

References

2022-global-aids-update-summary_en (2022). *Global-aids-update-summary*.

Abdou, A., Omran, O. A., Nafady, A., and Antipin, I. S. (2022). Structural, spectroscopic, FMOs, and non-linear optical properties exploration of three thiacaix(4)arenes derivatives. *Arabian J. Chem.* 15, 103656. doi:10.1016/j.arabjc.2021.103656

Akhtar, A., Fatima, S., Saeed, H., Soo, C. T., and Khan, A. H. (2022). HIV-HCV coinfection: prevalence and treatment outcomes in Malaysia. *Intervirology* 65, 87–93. doi:10.1159/000518836

Ando, I., Adachi, T., Ogura, N., Toyonaga, Y., Sugimoto, K., Abe, H., et al. (2012). Preclinical characterization of JTK-853, a novel nonnucleoside inhibitor of the hepatitis C virus RNA-dependent RNA polymerase. *Antimicrob. Agents Chemother.* 56, 4250–4256. doi:10.1128/AAC.00312-12

Arhel, N., and Kirchhoff, F. (2010). Host proteins involved in HIV infection: new therapeutic targets. *Biochim. Biophys. Acta Mol. Basis Dis.* 1802, 313–321. doi:10.1016/j.bbadis.2009.12.003

Becke, A. D. (1993). Density-functional thermochemistry. III. The role of exact exchange. *J. Chem. Phys.* 98, 5648–5652. doi:10.1063/1.464913

Bonamassa, B., Ciccarese, F., Di Antonio, V., Contarini, A., Palù, G., and Alvisi, G. (2015). Hepatitis C virus and host cell nuclear transport machinery: a clandestine affair. *Front. Microbiol.* 6, 619. doi:10.3389/fmicb.2015.00619

Daina, A., Michielin, O., and Zoete, V. (2017). SwissADME: a free web tool to evaluate pharmacokinetics, drug-likeness and medicinal chemistry friendliness of small molecules. *Sci. Rep.* 7, 42717. doi:10.1038/srep42717

Daina, A., and Zoete, V. (2016). A BOILED-egg to predict gastrointestinal absorption and brain penetration of small molecules. *ChemMedChem* 11, 1117–1121. doi:10.1002/cmdc.201600182

Das, K., Bauman, J. D., Rim, A. S., Dharia, C., Clark, A. D., Camarasa, M. J., et al. (2011). Crystal structure of tert -butyldimethylsilyl-spiroaminooxathioledioxide-thymine (TSAO-T) in complex with HIV-1 reverse transcriptase (RT) redefines the elastic limits of the non-nucleoside inhibitor-binding pocket. *J. Med. Chem.* 54, 2727–2737. doi:10.1021/jm101536x

Dassault Systemes (2023). *Biovia Discovery Studio comprehensive modeling and simulations for life sciences*. Dassault Systemes. Available at: https://discover.3ds.com/discovery-studio-visualizer-download.

Di Santo, R. (2014). Inhibiting the HIV integration process: past, present, and the future. *J. Med. Chem.* 57, 539–566. doi:10.1021/jm400674a

Domingo, L. R., Aurell, M. J., Pérez, P., and Contreras, R. (2002). Quantitative characterization of the local electrophilicity of organic molecules. Understanding the regioselectivity on Diels-Alder reactions. *J. Phys. Chem. A* 106, 6871–6875. doi:10.1021/jp020715j

Dorababu, A. (2020). Indole-a promising pharmacophore in recent antiviral drug discovery. *RSC Med. Chem.* 11, 1335–1353. doi:10.1039/d0md00288g

Duan, J.-L., Wang, C.-C., Yuan, Y., Hui, Z., Zhang, H., Mao, N.-D., et al. (2024). Design, synthesis, and structure–activity relationship of novel pyridazinone-based PARP7/HDACs dual inhibitors for elucidating the relationship between antitumor immunity and HDACs inhibition. *J. Med. Chem.* 67, 4950–4976. doi:10.1021/acs.jmedchem.4c00090

Dueweke, T. J., Poppe, S. M., Romero, D. L., Swaney, S. M., So, A. G., Downey, K. M., et al. (1993). U-90152, a potent inhibitor of human immunodeficiency virus type 1 replication. *Antimicrob. Agents Chemother.* 37, 1127–1131. doi:10.1128/AAC.37.5.1127

Edwards, M. P., and Price, D. A. (2010). "Chapter 23 - role of physicochemical properties and ligand lipophilicity efficiency in addressing drug safety risks," in *Annu rep med chem*. Editor J. E. Macor (Academic Press), 380–391. doi:10.1016/S0065-7743(10)45023-X

Evans, B. E., Rittle, K. E., Bock, M. G., DiPardo, R. M., Freidinger, R. M., Whitter, W. L., et al. (1988). Methods for drug discovery: development of potent, selective, orally effective cholecystokinin antagonists. *J. Med. Chem.* 31, 2235–2246. doi:10.1021/jm00120a002

Gupta, K., Brady, T., Dyer, B. M., Malani, N., Hwang, Y., Male, F., et al. (2014). Allosteric inhibition of human immunodeficiency virus integrase: late block during viral replication and abnormal multimerization involving specific protein domains. *J. Biol. Chem.* 289, 20477–20488. doi:10.1074/jbc.M114.551119

Hu, S., Jiang, S., Qi, X., Bai, R., Ye, X. Y., and Xie, T. (2022). Races of small molecule clinical trials for the treatment of COVID-19: an up-to-date comprehensive review. *Drug Dev. Res.* 83, 16–54. doi:10.1002/ddr.21895

Ikegashira, K., Oka, T., Hirashima, S., Noji, S., Yamanaka, H., Hara, Y., et al. (2006). Discovery of conformationally constrained tetracyclic compounds as potent hepatitis C virus NS5B RNA polymerase inhibitors. *J. Med. Chem.* 49, 6950–6953. doi:10.1021/jm0610245

Isel, C., Ehresmann, C., and Marquet, R. (2010). Initiation of HIV reverse transcription. *Viruses* 2, 213–243. doi:10.3390/v2010213

Ismael, M., Abdel-Mawgoud, A. M. M., Rabia, M. K., and Abdou, A. (2021a). Synthesis, characterization, molecular modeling and preliminary biochemical evaluation of new copper (II) mixed-ligand complexes. *J. Mol. Struct.* 1227, 129695. doi:10.1016/j.molstruc.2020.129695

Ismael, M., Abdel-Mawgoud, A. M. M., Rabia, M. K., and Abdou, A. (2021b). Ni(II) mixed-ligand chelates based on 2-hydroxy-1-naphthaldehyde as antimicrobial agents: synthesis, characterization, and molecular modeling. *J. Mol. Liq.* 330, 115611. doi:10.1016/j.molliq.2021.115611

Ismael, M., Abdou, A., and Abdel-Mawgoud, A. M. (2018). Synthesis, characterization, modeling, and antimicrobial activity of FeIII, CoII, NiII, CuII, and ZnII complexes based on tri-substituted imidazole ligand. *Z Anorg. Allg. Chem.* 644, 1203–1214. doi:10.1002/zaac.201800230

Kang, L., Gao, X. H., Liu, H. R., Men, X., Wu, H. N., Cui, P. W., et al. (2018). Structure–activity relationship investigation of coumarin–chalcone hybrids with diverse side-chains as acetylcholinesterase and butyrylcholinesterase inhibitors. *Mol. Divers* 22, 893–906. doi:10.1007/s11030-018-9839-y

Lafont, V., Armstrong, A. A., Ohtaka, H., Kiso, Y., Mario Amzel, L., and Freire, E. (2007). Compensating enthalpic and entropic changes hinder binding affinity optimization. *Chem. Biol. Drug Des.* 69, 413–422. doi:10.1111/j.1747-0285.2007.00519.x

Lemke, C. T., Goudreau, N., Zhao, S., Hucke, O., Thibeault, D., Llinàs-Brunet, M., et al. (2011). Combined x-ray, NMR, and kinetic analyses reveal uncommon binding characteristics of the hepatitis C virus NS3-NS4A protease inhibitor BI 201335. *J. Biol. Chem.* 286, 11434–11443. doi:10.1074/jbc.M110.211417

Li, H., Jiang, Y., Wang, Y., Lv, H., Xie, H., Yang, G., et al. (2018). The effects of warfarin on the pharmacokinetics of senkyunolide I in a rat model of biliary drainage after administration of chuanxiong. *Front. Pharmacol.* 9, 1461. doi:10.3389/fphar.2018.01461

Li, H. C., and Lo, S. Y. (2015). Hepatitis C virus: virology, diagnosis and treatment. *World J. Hepatol.* 7, 1377–1389. doi:10.4254/wjh.v7.i10.1377

Lin, C. 2024. HCV NS3-4A serine protease.

Lou, Y., Song, F., Cheng, M., Hu, Y., Chai, Y., Hu, Q., et al. (2023). Effects of the CYP3A inhibitors, voriconazole, itraconazole, and fluconazole on the pharmacokinetics of osimertinib in rats. *PeerJ* 11, e15844. doi:10.7717/peerj.15844

Morozov, V. A., and Lagaye, S. (2018). Hepatitis C virus: morphogenesis, infection and therapy. *World J. Hepatol.* 10, 186–212. doi:10.4254/wjh.v10.i2.186

Papajak, E., Zheng, J., Xu, X., Leverentz, H. R., and Truhlar, D. G. (2011). Perspectives on basis sets beautiful: seasonal plantings of diffuse basis functions. *J. Chem. Theory Comput.* 7, 3027–3034. doi:10.1021/ct200106a

Parrish, J., Tong, L., Wang, M., Chen, X., Lansdon, E. B., Cannizzaro, C., et al. (2013). Synthesis and biological evaluation of phosphonate analogues of nevirapine. *Bioorg Med. Chem. Lett.* 23, 1493–1497. doi:10.1016/j.bmcl.2012.12.049

Parsons, G. (2022). Hepatitis C: epidemiology, transmission and presentation. *Prescriber* 33, 20–23. doi:10.1002/psb.1992

Rampersad, S., and Tennant, P. (2018). "Replication and expression strategies of viruses," in *Viruses: molecular biology, host interactions, and applications to biotechnology* (Elsevier), 55–82. doi:10.1016/B978-0-12-811257-1.00003-6

Rhodes, D. I., Peat, T. S., Vandegraaff, N., Jeevarajah, D., Le, G., Jones, E. D., et al. (2011). Structural basis for a new mechanism of inhibition of HIV-1 integrase identified by fragment screening and structure-based design. *Antivir. Chem. Chemother.* 21, 155–168. doi:10.3851/IMP1716

Romero-Brey, I., and Lohmann, V. (2016). "The HCV replicase complex and viral RNA synthesis," in *Hepatitis C virus I: cellular and molecular virology* (Springer Japan), 149–196. doi:10.1007/978-4-431-56098-2_8

Rydberg, E. H., Cellucci, A., Bartholomew, L., Mattu, M., Barbato, G., Ludmerer, S. W., et al. (2009). Structural basis for resistance of the genotype 2b hepatitis C virus NS5B polymerase to site A non-nucleoside inhibitors. *J. Mol. Biol.* 390, 1048–1059. doi:10.1016/j.jmb.2009.06.012

Şahin, S., and Dege, N. (2021). Synthesis, characterization, X-ray, HOMO-LUMO, MEP, FT-IR, NLO, Hirshfeld surface, ADMET, boiled-egg model properties and molecular docking studies with human cyclophilin D (CypD) of a Schiff base compound: (E)-1-(5-nitro-2-(piperidin-1-yl)phenyl)-N-(3-nitrophenyl)methanimine. *Polyhedron* 205, 115320. doi:10.1016/j.poly.2021.115320

Salam, K. A., and Akimitsu, N. (2013). Hepatitis C virus NS3 inhibitors: current and future perspectives. *Biomed. Res. Int.* 2013, 1–9. doi:10.1155/2013/467869

Scola, P. M., Wang, A. X., Good, A. C., Sun, L. Q., Combrink, K. D., Campbell, J. A., et al. (2014). Discovery and early clinical evaluation of BMS-605339, a potent and orally efficacious tripeptidic acylsulfonamide ns3 protease inhibitor for the treatment of hepatitis C virus infection. *J. Med. Chem.* 57, 1708–1729. doi:10.1021/jm401840s

Seitz, R. (2016). Human immunodeficiency virus (HIV). *Transfus. Med. Hemotherapy* 43, 203–222. doi:10.1159/000445852

Shahab, S., Sheikhi, M., Filippovich, L., Alnajjar, R., Ihnatovich, Z., Laznev, K., et al. (2020). Quantum-chemical modeling, spectroscopic (FT-IR, excited states, UV/Vis, polarization, and Dichroism) studies of two new benzo[d]oxazole derivatives. *J. Mol. Struct.* 1202, 127352. doi:10.1016/j.molstruc.2019.127352

Shaikh, F., Tai, H. K., Desai, N., and Siu, S. W. I. (2021). LigTMap: ligand and structure-based target identification and activity prediction for small molecular compounds. *J. Cheminform* 13, 44. doi:10.1186/s13321-021-00523-1

Shaw, A. N., Tedesco, R., Bambal, R., Chai, D., Concha, N. O., Darcy, M. G., et al. (2009). Substituted benzothiadizine inhibitors of Hepatitis C virus polymerase. *Bioorg Med. Chem. Lett.* 19, 4350–4353. doi:10.1016/j.bmcl.2009.05.091

Su, D. S., Lim, J. J., Tinney, E., Wan, B. L., Young, M. B., Anderson, K. D., et al. (2009). Substituted tetrahydroquinolines as potent allosteric inhibitors of reverse transcriptase and its key mutants. *Bioorg Med. Chem. Lett.* 19, 5119–5123. doi:10.1016/j.bmcl.2009.07.031

Sundquist, W. I., and Kräusslich, H. G. (2012). HIV-1 assembly, budding, and maturation. *Cold Spring Harb. Perspect. Med.* 2, a006924. doi:10.1101/cshperspect.a006924

Tedesco, R., Shaw, A. N., Bambal, R., Chai, D., Concha, N. O., Darcy, M. G., et al. (2006). 3-(1,1-dioxo-2H-(1,2,4)-benzothiadiazin-3-yl)-4-hydroxy-2(1H)-quinolinones, potent inhibitors of hepatitis C virus RNA-dependent RNA polymerase. *J. Med. Chem.* 49, 971–983. doi:10.1021/jm050855s

Tie, Y., Boross, P. I., Wang, Y. F., Gaddis, L., Hussain, A. K., Leshchenko, S., et al. (2004). High resolution crystal structures of HIV-1 protease with a potent non-peptide inhibitor (UIC-94017) active against multi-drug-resistant clinical strains. *J. Mol. Biol.* 338, 341–352. doi:10.1016/j.jmb.2004.02.052

Trott, O., and Olson, A. J. (2009). AutoDock Vina: improving the speed and accuracy of docking with a new scoring function, efficient optimization, and multithreading. *J. Comput. Chem.* 31, 455–461. NA-NA. doi:10.1002/jcc.21334

Velázquez, F., Venkatraman, S., Lesburg, C. A., Duca, J., Rosenblum, S. B., Kozlowski, J. A., et al. (2012). Synthesis of new 4,5-dihydrofuranoindoles and their evaluation as HCV NS5B polymerase inhibitors. *Org. Lett.* 14, 556–559. doi:10.1021/ol203177g

Wang, K., Yin, J., Chen, J., Ma, J., Si, H., and Xia, D. (2024b). Inhibition of inflammation by berberine: molecular mechanism and network pharmacology analysis. *Phytomedicine* 128, 155258. doi:10.1016/j.phymed.2023.155258

Wang, R., Wang, Z., Yuan, H., Li, C., and Zhu, N. (2024a). Mechanistic exploration of COVID-19 antiviral drug ritonavir on anaerobic digestion through experimental validation coupled with metagenomics analysis. *J. Hazard Mater* 479, 135603. doi:10.1016/j.jhazmat.2024.135603

Weinhold, F., and Landis, C. R. (2001). Natural bond orbitals and extensions of localized bonding concepts. *Chem. Educ. Res. Pract.* 2, 91–104. doi:10.1039/b1rp90011k

Yang, W. X., Chen, Y. F., Yang, J., Huang, T., Wu, L. L., Xiao, N., et al. (2018). Monoterpenoid indole alkaloids from Gardneria multiflora. *Fitoterapia* 124, 8–11. doi:10.1016/j.fitote.2017.09.017

Zhang, H., Wang, Y. F., Shen, C. H., Agniswamy, J., Rao, K. V., Xu, C. X., et al. (2013). Novel P2 tris-tetrahydrofuran group in antiviral compound 1 (GRL-0519) fills the S2 binding pocket of selected mutants of HIV-1 protease. *J. Med. Chem.* 56, 1074–1083. doi:10.1021/jm301519z

Zhang, M. Z., Chen, Q., and Yang, G. F. (2015). A review on recent developments of indole-containing antiviral agents. *Eur. J. Med. Chem.* 89, 421–441. doi:10.1016/j.ejmech.2014.10.065

Zhang, S. Y., Li, Z. W., Xu, J., Chen, Q. L., Song, M., and Zhang, Q. W. (2021). Discovery of three new monoterpenoid indole alkaloids from the leaves of gardneria multiflora and their vasorelaxant and ache inhibitory activities. *Molecules* 26, 7191. doi:10.3390/molecules26237191

Zhong, X. H., Xiao, L., Wang, Q., Zhang, B. J., Bao, M. F., Cai, X. H., et al. (2014). Cytotoxic 7S-oxindole alkaloids from Gardneria multiflora. *Phytochem. Lett.* 10, 55–59. doi:10.1016/j.phytol.2014.08.001

frontiers | Frontiers in Chemistry

TYPE Original Research
PUBLISHED 19 February 2025
DOI 10.3389/fchem.2025.1541250

OPEN ACCESS

EDITED BY
Mukhlesur Rahman,
University of East London, United Kingdom

REVIEWED BY
Kasireddy Sudarshan,
Purdue University, United States
Sevki Adem,
Cankiri Karatekin University, Türkiye
Bharat Kumar Reddy Sanapalli,
JSSAHER, India

*CORRESPONDENCE
Kevser Kübra Kırboğa,
kubra.kirboga@bilecik.edu.tr
Mithun Rudrapal,
rsmrpal@gmail.com
Johra Khan,
j.khan@mu.edu.sa

RECEIVED 07 December 2024
ACCEPTED 21 January 2025
PUBLISHED 19 February 2025

CITATION
Altın S, Işık M, Alp C, Dikici E, Köksal E, Kırboğa KK, Rudrapal M, Rakshit G, Beydemir Ş and Khan J (2025) Therapeutic potential of *Laurus nobilis* extract by experimental and computational approaches: phenolic content and bioactivities for antioxidant, antidiabetic, and anticholinergic properties. *Front. Chem.* 13:1541250. doi: 10.3389/fchem.2025.1541250

Therapeutic potential of *Laurus nobilis* extract by experimental and computational approaches: phenolic content and bioactivities for antioxidant, antidiabetic, and anticholinergic properties

Sevgi Altın[1], Mesut Işık[2], Cemalettin Alp[1], Emrah Dikici[3], Ekrem Köksal[1], Kevser Kübra Kırboğa[2]*, Mithun Rudrapal[4]*, Gourav Rakshit[5], Şükrü Beydemir[6] and Johra Khan[7,8]*

[1]Department of Chemistry, Erzincan Binali Yıldırım University, Faculty of Science and Art, Erzincan, Türkiye, [2]Department of Bioengineering, Faculty of Engineering, Bilecik Şeyh Edebali University, Bilecik, Türkiye, [3]Science and Technology Application and Research Center, Aksaray University, Aksaray, Türkiye, [4]Department of Pharmaceutical Sciences, School of Biotechnology and Pharmaceutical Sciences, Vignan's Foundation for Science, Technology and Research, Guntur, India, [5]Department of Pharmaceutical Sciences and Technology, Birla Institute of Technology, Ranchi, India, [6]Department of Biochemistry, Faculty of Pharmacy, Anadolu University, Eskişehir, Türkiye, [7]Department of Medical Laboratory Sciences, College of Applied Medical Laboratory Sciences, Majmaah University, Al Majma'ah, Saudi Arabia, [8]Health and Basic Science Research Center, Majmaah University, Al Majma'ah, Saudi Arabia

Introduction: *Laurus nobilis* (LN), has traditional medicinal uses, and this study investigates its therapeutic potential by focusing on its phenolic content and bioactivities such as antioxidant, antidiabetic, and anticholinergic properties. Phenolic compounds play key roles in reducing oxidative stress and modulating enzymatic activities, relevant to metabolic and neurodegenerative disorders.

Methods: LN leaf extracts were prepared via ethanol maceration, followed by filtration and concentration. Phenolic content was analyzed using LC-MS/MS. Antioxidant activity was assessed through ferric thiocyanate, DPPH, ABTS, and FRAP assays. Enzyme inhibition assays targeted AChE, BChE, and α-GLY, with IC50 values from dose-response curves. *In silico* analyses were conducted using molecular docking techniques to predict the binding mechanisms of identified phenolic compounds with the active sites of target enzymes, evaluating binding affinities and interaction profiles.

Results: Vanillic acid and catechin hydrate were the most abundant phenolics. LN extract showed strong lipid peroxidation inhibition (50.53%) compared to Trolox (28.33%) and α-tocopherol (37.79%). Moderate radical scavenging and metal reduction potentials were observed. IC50 values were 2.57 μg/L for AChE, 3.78 μg/L for BChE, and 4.65 μg/L for α-GLY, indicating notable bioactivity. *In silico* studies confirmed strong binding affinities of phenolics to target enzymes.

Discussion: LN extracts demonstrated promising antioxidant, antidiabetic, and anticholinergic activities, attributed to high phenolic content. Enzyme inhibition

results suggest potential in managing metabolic and neurodegenerative disorders. *In silico* findings support these bioactivities, highlighting LN's therapeutic potential.

KEYWORDS

Laurus nobilis **L., phenolic content, antioxidant, antidiabetic, molecular dynamics, molecular docking**

1 Introduction

Many medicinal plants containing aromatic compounds are used as natural therapeutic agents and attract attention due to their rich bioactive properties (Veeresham, 2012; Zeng et al., 2020; Shi et al., 2022). Knowing the medicinal properties of plants on earth is essential due to their contributions to human health and the countries' economies (Wangchuk and Tobgay, 2015; Sofowora et al., 2013). Studies reporting the biological activities of the plant extracts serve as a reference for discovering plants with therapeutic potential for many diseases (Altın et al., 2017; Balunas and Kinghorn, 2005; Tohma et al., 2019; Koksal, 2011). Plant extracts are the precursors of pure compounds responsible for their various biological activities, creating remarkable value for further research (Tonisi et al., 2020; Li et al., 2024). Traditionally used plants for therapeutic purposes can be analysed using modern techniques and may lead to obtaining novel promising compounds for treating some severe diseases (Dzobo, 2022).

Turkey has a rich flora and a long history of using plants for medicinal purposes. Turkey hosts many different plants because of their other geographical regions (Avci, 1996; Sargin and Büyükcengiz, 2019; Akan and Çakır, 2023). Turkey has over ten thousand plant taxa, and about four thousand are endemic (Avci, 1996; Sekercioglu et al., 2011). Some of these plants have been used for centuries by local people to treat various ailments, such as inflammation, infection, pain, diabetes, and neurological disorders. However, the scientific evidence for the efficacy and safety of these plants still needs to be improved. Therefore, there is a need for more comprehensive and systematic studies to evaluate the phytochemical and pharmacological properties of these plants and to identify their active constituents and mechanisms of action. *Lauraceae* is a plant family spreading in Turkey with a high economic and medicinal value. Only one species in Turkey represents *Lauraceae*, Laurus nobulis. *Laurus Nobilis* (LN) is a species native to the Mediterranean region, cultivated in many countries with temperate and subtropical climates. The commercial value of this species lies in its essential oils (Turgut et al., 2023). The leaves and fruit parts contain plenty of oil, and soap and skin cream are made using this oil. The leaves of the plant are dried and used as a spice. LN is a versatile and valuable plant with a long history of culinary and medicinal use.

LN has been reported to have various biological activities, such as antibacterial, antifungal, antiviral, antidiabetic, antispasmodic, anti-inflammatory, and antioxidant effects (Brinza et al., 2021). These activities are mainly attributed to the phenolic compounds present in the plant, especially flavonoids and phenolic acids. Phenolic compounds are secondary metabolites found naturally in the structure of plants and are delivered to humans and animals through the consumption of plant nutrients. These structures are an integral part of human and animal diets. Phenolic compounds form a significant group of natural antioxidants. For this reason, it is essential to determine which phenolic compounds are present in the structure of the plants whose antioxidant activity is investigated and what their amounts are. For this purpose, many chromatographic methods have been developed and used (Shi et al., 2022).

Phenolic compounds and flavonoids are secondary metabolites naturally found in plants, exhibiting a wide range of biological activities such as antioxidant, antimicrobial, neuroprotective, and anticancer effects (Sun and Shahrajabian, 2023). Flavonoid isomers such as Catechin, Myricetin, Naringenin, Luteolin, and Kaempferol also play crucial roles in modulating various biological pathways (Ysrafil et al., 2023). For instance, Catechin's significant free radical scavenging capacity makes it a key candidate in mitigating oxidative stress-related diseases (Sheng et al., 2023). Myricetin has demonstrated neuroprotective properties, improving synaptic plasticity and showing promise for managing neurodegenerative conditions such as Alzheimer's disease (Semwal et al., 2016; Ramezani et al., 2016; Wang et al., 2025; Tang et al., 2023). Similarly, Luteolin exhibits anti-inflammatory effects by inhibiting key enzymes like COX(Cyclooxygenase) and LOX (Chen et al., 2014; Dong et al., 2023), while Kaempferol (Kmp) has been shown to regulate apoptotic pathways, providing anticarcinogenic benefits (Qattan et al., 2022). Naringenin, with its antioxidant and antimicrobial properties, holds potential for addressing metabolic disorders (Cai et al., 2023). Among the isomers of these compounds, isocoumarins stand out for their potential to influence multiple biological processes, particularly in inflammation, cancer, and neurological disorders. Isocoumarins have been reported to inhibit key enzymes involved in inflammation, such as 5-lipoxygenase (5-LOX) and prostaglandin E2 (PGE2) synthase, thereby exerting anti-inflammatory effects. For instance, 3-aryl isocoumarin derivative 1c has been identified as a dual inhibitor effectively suppressing both 5-LOX and PGE2 production. This property suggests that isocoumarins may offer effects comparable to clinically utilized dual inhibitors like Licofelone (Ramanan et al., 2016). Moreover, isocoumarins demonstrate not only anti-inflammatory but also neuroprotective properties. A recent study revealed that an 8-hydroxy-3-aryl isocoumarin derivative exhibited neurotrophic effects by binding to the TrkB receptor and enhancing synaptic plasticity. This isocoumarin derivative increased dendritic arborization and microtubule-associated protein 2 (MAP2) expression in neuronal cells, shedding light on the mechanisms underlying its neuroprotective effects (Sudarshan et al., 2019). The TrkB receptor-mediated effects emphasize the therapeutic potential of isocoumarins in addressing central nervous system disorders such as Alzheimer's disease and major depression. In this context, a comprehensive evaluation of the biological activities of phenolic compounds and flavonoids is crucial for the development of

therapeutic approaches. Comparing derivatives like isocoumarins with traditional phenolic compounds offers a significant opportunity to deepen our understanding of their biological and pharmacological potentials. These studies aim to elucidate the interactions of phenolic compounds with therapeutically targetable enzymes and receptors, ultimately enhancing their applicability in biomedical fields.

Flavonoids are widely distributed throughout almost all parts of plants, including leaves, flowers, fruits, stems, and roots, and they represent the most abundant and structurally diverse subgroup of phenolic compounds (Panche et al., 2016; Roy et al., 2022). These secondary metabolites are particularly concentrated in the photosynthetic tissues of plants, such as leaves and flower petals, where they play critical roles in protecting plants against UV radiation and oxidative stress (Chen et al., 2022; Singh et al., 2023). Additionally, flavonoids contribute significantly to the vivid pigmentation of flowering plants, serving as essential natural colorants that attract pollinators and aid in reproductive processes (Elessawy et al., 2023). Their multifunctional presence underscores their importance in plant physiology and their potential therapeutic and industrial applications. Like many phenolic compounds, they cannot be synthesised by human and animal cells and must be obtained by consuming plant foods. Many studies have reported that plants' therapeutic potential is due to their phenolic compounds, especially flavonoids (Tungmunnithum et al., 2018; Sun and Shahrajabian, 2023). Nearly 10,000 phenolic compounds have been detected in different plant sources, and about half of them are formed by flavonoids.

In addition to their antioxidant activity, phenolic compounds have been shown to have anticholinergic and antidiabetic effects. Anticholinergic agents inhibit the action of the neurotransmitter acetylcholine in the central and peripheral nervous system. They treat various conditions, such as Parkinson's disease, Alzheimer's disease, motion sickness, and overactive bladder (Durmaz et al., 2022; Bingol et al., 2021). Antidiabetic agents are substances that lower blood glucose levels and improve glucose metabolism. They treat diabetes mellitus, a chronic metabolic disorder characterised by hyperglycemia and impaired insulin secretion or action (Chaudhury et al., 2017). Phenolic compounds can modulate the activity of enzymes involved in the synthesis and degradation of acetylcholine, such as acetylcholinesterase and choline acetyltransferase, thus affecting the cholinergic system (Colović et al., 2013). Phenolic compounds can also modulate the activity of enzymes involved in glucose metabolism, such as alpha-glucosidase, alpha-amylase, and glucose-6-phosphatase, thus affecting glycemic control (Sarkar et al., 2021).

This study investigated the phenolic content and antioxidant, anticholinergic and antidiabetic potential of LN leaves. The phenolic compounds were identified and quantified by liquid chromatography-tandem mass spectrometry (LC-MS/MS). The antioxidant activity was evaluated using different methods, such as lipid peroxidation inhibition, radical scavenging (DPPH and ABTS), and metal reduction potentials. The anticholinergic activity was assessed by measuring the inhibition of AChE and BChE enzymes. The antidiabetic activity was evaluated by measuring the inhibition of alpha-glucosidase enzymes. The study's results may support the traditional use of LN as a natural source of antioxidants and a potential remedy for neurological and metabolic disorders.

2 Materials and methods

2.1 Chemicals

2,2-diphenyl-1-picrylhydrazyl, gallic acid, Folin and Ciocalteu's phenol reagent, quercetin (Cheng et al., 2024), ethylenediaminetetraacetic acid (EDTA), trihydroxymethylaminomethane (Tris), sodium citrate, 5,5′-dithio-bis (2-nitrobenzoic acid) (DTNB) which used in the studies were obtained from Sigma Aldrich.

2.2 Plant materials

LN L. leaves were collected from the vicinity of Esenpınar village, 750 m, Erdemli district of Mersin, Türkiye, during the plant's flowering period in August 2021. Dr Ali Kandemir taxonomically defined the samples collected for analysis, and the herbarium samples were stored in Erzincan Binali Yıldırım University Herbarium with the code Kandemir 6,069.

2.3 Preparation of the extract

The collected plant material was dried at room temperature, in a place without ventilation problems and away from sunlight, and then crushed with liquid nitrogen to powder. The resulting sample was mixed with ethanol (1:10 ratio). Extraction was carried out in a shaker for 24 h. The solid was filtered through filter paper (Whatman No. 1) and evaporated. The dry extract was stored at +4°C until used in analysis studies.

2.4 LC-MS/MS analysis

The phenolic content of L. nobilis leaves was determined using LC–MS/MS, an analytical chemistry technique combining high-pressure liquid chromatography (UHPLC) and mass spectrometry (MS). This technique physically separates the compounds in the mixture by liquid chromatography, while mass spectrometry provides the structural identity and quantification of individual compounds with high sensitivity and specificity. A verification method was developed for 20 phenolic substances. Determining the phenolic compound in LN was done using the technique developed by Yilmaz (2020). In this method, the C18 Inertsil ODS-4 (3.0 mm × 100 mm, 2 μM) analytical column was used for chromatographic separation of analytes. This column is designed for reverse-phase chromatography and separates non-polar compounds. The column temperature was fixed at 40°C. This temperature is optimised to shorten the passage time of analytes through the column and increase solubility. The liquid chromatography system consists of components such as a SIL-30AC automatic sampling device, LC-30AD double pumps, CTO-10ASVP column oven and DGU-20A3R degasser. The

elution gradient was established using mobile phase A (water and 0.1% formic acid) and mobile phase B (methanol and 0.1% formic acid). Formic acid was added to increase the ionisation of analytes and prevent corrosion in the ion source. The ratio of mobile phases was varied to improve the analytes' escape times and peak shapes from the column. The sample injection volume was set as 4 μL, and the flow rate was kept at 0.5 mL min^{-1}. Calculations were made with Lab Solutions software (Shimadzu, Kyoto, Japan) (Division shimadzu corporation, 2024). Analyses were measured using multiple reaction monitoring (MRM) mode. In this mode, the mass spectrometer records only the signals of the targeted compounds by selecting the analytes' molecular ions and their fragmentation products (Yilmaz, 2020; Al-Khayri et al., 2022; Güven et al., 2023). In this way, background noise is reduced, and specificity is increased. In the study, three applications were made to determine each compound's quantitative amount, and the results were averaged.

2.5 Antioxidant activity

2.5.1 Inhibition of linoleic acid peroxidation

The assessment of the inhibitory effect of the LN ethanol extract on linoleic acid peroxidation was conducted using the ferric thiocyanate method, as outlined in the reference (Kavaz et al., 2021; Mitsuda et al., 1966). This methodology is based on quantifying the hydroperoxide generated during linoleic acid oxidation via spectrophotometric analysis at a wavelength of 500 nm. Elevated absorbance values indicate an excessive accumulation of peroxides resulting from the peroxidation process. These hydroperoxides subsequently catalyse the conversion of Fe2+ to Fe3+. Later, Fe3+ forms a coordination complex with the introduced thiocyanate reagent, which exhibits a peak absorbance at 500 nm.

2.5.2 Radical scavenging activity

In this method, 2,2-diphenyl-1-picrylhydrazyl (DPPH•) scavenging activity of the plant extract was performed according to the method reported by Blois with slight modifications (Blois, 1958). Briefly, 0.26 mM solution of DPPH in 1 mL methanol was added to 3 mL of the sample solution in various concentrations. After mixing by vortex, the mixture was incubated for 30 min in the dark and at room temperature. The absorbance of the mixture was measured at 517 nm. Oxidants oxidise ABTS to the intensely coloured radical cation ABTS.+, and the antioxidant potential is determined as the ability of the test compounds to reduce colour by reacting directly with the ABTS radical (Re et al., 1999). ABTS (2 mmol L−1) solution was mixed with 2.45 mmol L−1 potassium persulfate (K2S2O8) solution. The new solution was incubated in the dark for 14 h at 25 °C. Firstly, ABTS.+ radical solution was diluted with sodium phosphate buffer (0.1 mol L−1, pH 7.4) until an absorbance of 0.750 ± 0.025 at 734 nm was obtained. The absorbance was measured using a spectrophotometer at 734 nm. The results were reported as per cent of radical scavenging activity.

2.5.3 Iron (III) ion reducing capacity (FRAP)

The iron-reducing power capacity of the plant extract was determined according to the method reported by Oyaizu with slight modifications (Güder and Korkmaz, 2012). Accordingly, the stock solutions (1 mg/mL) of the extracts and standards were prepared in the test tubes containing 1.25 mL phosphate buffer (0.2 M, pH 6.6). Then, 1.25 mL of potassium ferric cyanide [K3Fe(CN)6] (1%) was added to the mixture and incubated at 50°C for 20 min. After 1.25 mL of 10% trichloroacetic acid (TCA) and 0.25 mL of 0.1% FeCl3 solution were added, the absorbances of the final mixture were measured spectrophotometrically at 700 nm. The results were expressed as mg TE/g extract.

2.5.4 Cupric ions (Cu2+) (II) reducing capacity (CUPRAC)

This method was first discovered by Apak et al. (2006) and is a widely used effective method for determining antioxidant activity (Apak et al., 2013). It is based on reducing Cu2+ to Cu+ in the presence of neocuproine (2,9-dimethyl-1,10-phenanthroline). Cu + - neocuproine complex yields maximum absorbance at 450 nm. 1 mL of CuCl2 (0.01 M), 1 mL of neocuprin, and 1 mL of ammonium acetate (NH4Ac) as buffer solution were added to the test tube and mixed. Then, the different amounts of extract (10, 20, 40 μg mL−1) were added, and the total volume was adjusted to 4 mL with pure water. The absorbance was measured at 450 nm. The results were compared to standard antioxidants.

2.5.5 Determination of total phenolic content

The extract's total phenolic content was determined by the Folin-Ciocalteu method (Öztürk et al., 2022). Briefly, 100 μL of the stock solutions of the samples (1 mg/mL) were taken into test tubes containing 4.5 mL of distilled water. Then, 100 μL of Folin-Ciocalteu reagent and 300 μL of 2% Na2CO3 solution were added to the mixture. The mixture was vortexed and incubated for 120 min at room temperature. The absorbance of the mix was measured spectrophotometrically at 760 nm. A calibration curve was created with different concentrations of gallic acid used as a standard, and the phenolic content of the extracts was stated as mg gallic acid equivalent/g extract.

2.5.6 Determination of total flavonoid content

The total flavonoid content of the plant extract was determined using the Aluminium chloride colourimetric method (Shraim et al., 2021). Accordingly, 100 μL of the extracts and standard stock solutions (1 mg/mL) was taken, and the volume was completed to 4.8 mL with methanol. Then, 100 μL of 1 M NH4CH3COO solution and 100 μL of 10% AlCl3 solution were added to the test tubes, and the mixture was incubated for 45 min at room temperature. After incubation, the absorbance of the mixture was measured spectrophotometerically at 415 nm. A calibration curve was created with different concentrations of quercetin used as a standard, and the flavonoid content of the extracts was given as mg quercetin equivalent/g extract.

2.5.7 Cholinesterase inhibition assay

The inhibitory effect of the plant ethanol extract on cholinesterase (AChE and BChE) enzymes was determined using the Ellman spectrophotometric method described in reference (Ellman et al., 1961; Türkeş et al., 2022). A reaction solution containing 50 μL of 5,5′-dithio-bis(2-nitrobenzoic) acid (DTNB),

100 μL of Tris-HCl buffer (1 M, pH 8.0), and 50 μL of cholinesterase (5.32×10^{-3} U) was incubated at 30°C and mixed for 15 min. Subsequently, the reaction was initiated by adding 50 μL of acetylthiocholine iodide for AChE and butyrylthiocholine iodide for BChE as substrates. The enzymatic hydrolysis of the substrates was detected by spectrophotometry at 412 nm. The impact of the ethanol extract on cholinesterases was assessed across different concentration ranges. The IC50 values for the extract were calculated from activity (%)-[Inhibitor] graphs.

2.5.8 α-GLY inhibition assay

The inhibitory potential of plant ethanol extract on α-GLY was assessed by employing p-nitrophenyl-D-glycopyranoside (p-NPG) as the substrate, following the established protocols in prior research endeavours (Türkeş et al., 2022; Tao et al., 2013). The absorbance values were quantified through spectrophotometric measurements at a wavelength of 405 nm. The impact of the ethanol extract on cholinesterases was assessed across different concentration ranges. The IC50 values for the extract were calculated from activity (%)-[Inhibitor] graphs.

2.6 In-silico studies

2.6.1 Hardware and software utilised

Molecular docking studies were performed on a workstation with the following specifications: Operating System - Ubuntu 22.04 (LTS), 64-bit; Processor - Intel® Core™ i5-12400 CPU @ 2.30 GHz; RAM - 16 GB; Graphics - 8 GB Nvidia GeForce RTX 3050 GPU. The protein structures in complexes with ligands were sourced from the Protein Data Bank (PDB) (Bernstein et al., 1978). Glide modules of Schrödinger software v2021.4 (Institute license: BIT Mesra) were employed for molecular docking studies (Friesner et al., 2006).

2.6.2 Protein and ligand structure preparation for molecular docking

This study utilized three proteins, Recombinant Human Acetylcholinesterase in Complex with Donepezil (PDB ID:4EY7, 2.35 Å) (Cheung et al., 2012; Kang et al., 2018), Human Butyrylcholinesterase in Complex with 3F9 (PDB ID:4TPK, 2.70 Å) (Brus et al., 2014; Gao et al., 2019; Lu et al., 2020), and Human Lysosomal Acid-Alpha-Glucosidase, GAA, in Complex with acarbose (PDB ID:5NN8,2.45 Å) (Roig-Zamboni et al., 2017). The X-ray crystal structures of these proteins, each bound to an inhibitor, were obtained from the Protein Data Bank (PDB). The PDB structures utilized in this study were carefully selected based on multiple criteria to ensure their suitability for the docking studies (Figure 1). First, the chosen proteins are directly relevant to the study's therapeutic focus, targeting acetylcholinesterase, butyrylcholinesterase, and lysosomal acid-alpha-glucosidase, all of which play crucial roles in the pathophysiology of neurodegenerative and metabolic disorders. Second, these structures (Table 1) were specifically selected because they are available in complex with known inhibitors, providing validated binding poses that serve as benchmarks for evaluating the binding potential of the tested compounds. This pre-complexed state ensures that the selected conformations are biologically relevant and optimized for inhibitor interactions. Third, the resolutions of the selected structures—2.35 Å (4EY7), 2.70 Å (4TPK), and 2.45 Å (5NN8)—were key factors in their selection. These high-resolution structures provide detailed atomic information, enabling precise modeling of protein-ligand interactions and minimizing inaccuracies in docking predictions.

Protein preparation was conducted using the protein preparation wizard module of Schrödinger software. This process included the addition of missing polar hydrogens, removal of water molecules beyond 5Å from hetero groups, ionization, generation of tautomeric states at pH 7.0 ± 2.0, optimization of hydrogen bonds, and energy minimization. The triple inhibitory potential of twenty phytochemicals or inhibitors was evaluated against these three proteins. Ligand preparation involved sketching the structures in ChemDraw, verifying their correctness with the structure checker module, generating 3D structures using the Chem3D module, and optimizing them with the LigPrep module using the OPLS force field X (Schrödinger Release 2021-3). During this process, compound tautomers were generated, maintaining the desired chirality for each compound.

2.6.3 Validation of the docking program

Validation of a docking program is a critical step in assessing its reliability and accuracy in predicting ligand-protein interactions and evaluating the program's ability to reposition native ligands into their crystallographically observed binding sites correctly. Successful redocking indicates that the program can reproduce known binding modes (Rakshit and Jayaprakash,

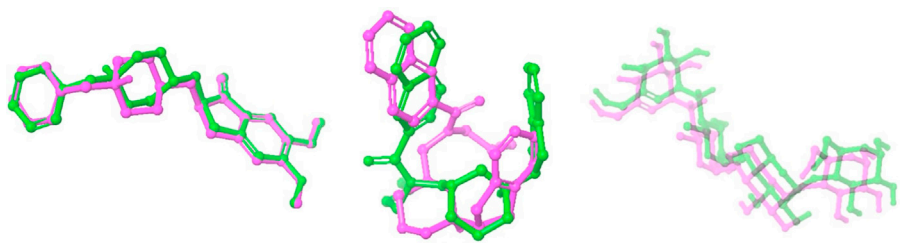

FIGURE 1
Overlay of docked ligand and crystallized conformation. This figure presents a superimposed view of the docked internal ligand (displayed in green) against its crystallised conformation (shown in pink), derived from the co-crystallized complex. The overlay provides a visual comparison of the ligand positions within the binding site, emphasising the accuracy of the docking process in replicating the actual ligand orientation observed in the crystal structure.

TABLE 1 Bioactive ligands utilised in this study, along with their code, structure, and details.

Code	Compound	Structure	Details
MG1	Quercetin	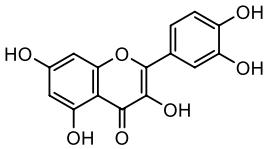	IUPAC Benzene carboxylic acid Chemical Formula: C7H6O2 Molecular Weight: 122.123 g/mol
MG2	Acetohydroxamic Acid	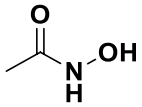	IUPAC N-Hydroxyacetamide Chemical Formula: C2H5NO2 Molecular Weight: 75.067 g/mol
MG3	Catechin hydrate	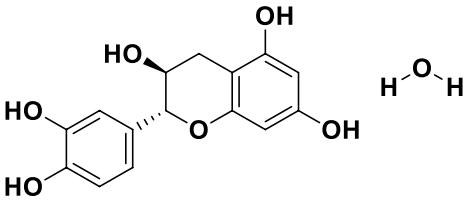	IUPAC: (2R,3S)-2-(3,4-dihydroxyphenyl)-3,4-dihydro-2H-chromene-3,5,7-triol; hydrate Chemical Formula: C15H16O7 Molecular Weight: 308.28 g/mol
MG4	Vanillic Acid	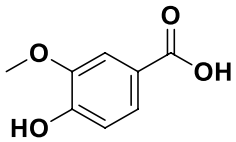	IUPAC 4-Hydroxy-3-methoxybenzoic acid Chemical Formula: C8H8O4 Molecular Weight: 168.148 g/mol
MG5	Resveratrol	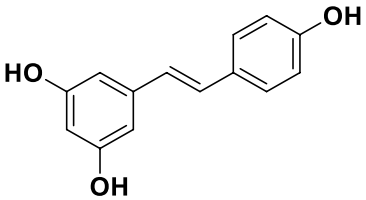	IUPAC 5-[(E)-2-(4-Hydroxyphenyl)ethen-1-yl]benzene-1,3-diol Chemical Formula: C14H12O3 Molecular Weight: 228.247 g/mol
MG6	Fumaric Acid	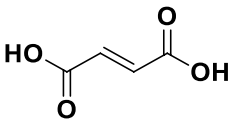	IUPAC: (2E)-But-2-enedioic acid Chemical Formula: C4H4O4 Molecular Weight: 116.072 g/mol
MG7	Gallic acid	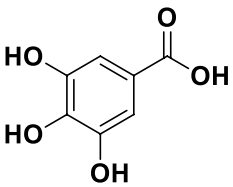	IUPAC 3,4,5-Trihydroxybenzoic acid Chemical Formula: C7H6O5 Molecular Weight: 170.12 g/mol
MG8	Caffeic Acid	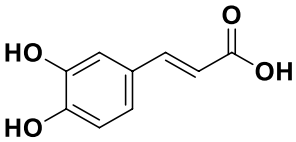	IUPAC 3-(3,4-Dihydroxyphenyl)-2-propenoic acid Chemical Formula: C9H8O4 Molecular Weight: 180.16 g/mol
MG9	Phloridzin dihydrate	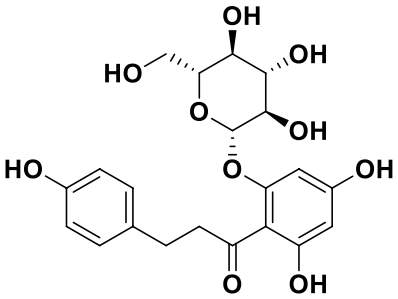	IUPAC: (2E)-But-2-enedioic acid Chemical Formula: C21H24O10 Molecular Weight: 436.413 g/mol

(Continued on following page)

TABLE 1 (*Continued*) Bioactive ligands utilised in this study, along with their code, structure, and details.

Code	Compound	Structure	Details
MG10	Oleuropein	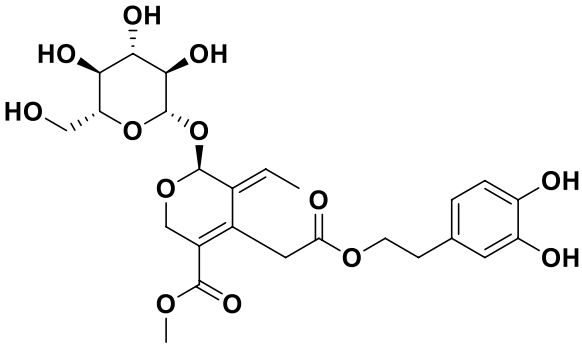	IUPAC: methyl (4S,5E,6S)-4-[2-[2-(3,4-dihydroxyphenyl) ethoxy]-2-oxoethyl]-5-ethylidene-6-[(2S,3R,4S,5S,6R)-3,4,5-trihydroxy-6-(hydroxymethyl)oxan-2-yl]oxy-4H-pyran-3-carboxylate Chemical Formula: C25H32O13 Molecular Weight: 540.5 g/mol
MG11	Ellagic Acid	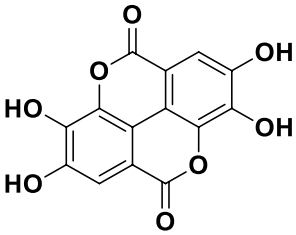	IUPAC 2,3,7,8-Tetrahydroxy[1]benzopyrano[5,4,3-cde][1] benzopyran-5,10-dione Chemical Formula: C14H6O8 Molecular Weight: 302.197 g/mol
MG12	Myricetin	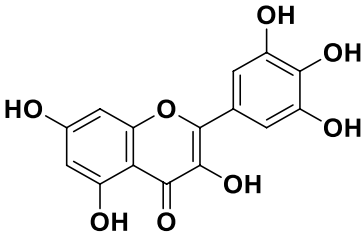	IUPAC 3,3′,4′,5,5′,7-Hexahydroxyflavone Chemical Formula: C15H10O8 Molecular Weight: 318.237 g/mol
MG13	Protocatechuic acid	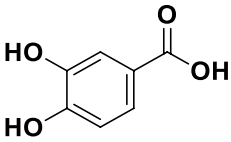	IUPAC 3,4-Dihydroxybenzoic acid Chemical Formula: C7H6O4 Molecular Weight: 154.12 g/mol
MG14	Butein	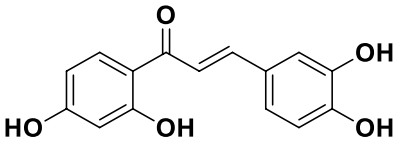	IUPAC 2′,3,4,4′-Tetrahydroxychalcone Chemical Formula: C15H12O5 Molecular Weight: 272.25 g/mol
MG15	Naringenin	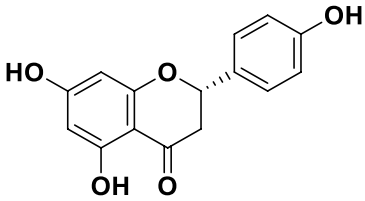	IUPAC: (2S)-4′,5,7-Trihydroxyflavan-4-one Chemical Formula: $C_{15}H_{12}O_5$ Molecular Weight: 272.256 g/mol
MG16	Luteolin	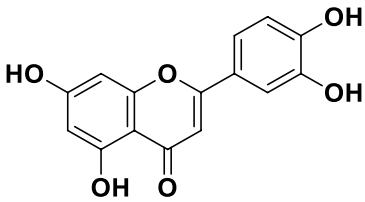	IUPAC 3′,4′,5,7-Tetrahydroxyflavone Chemical Formula: $C_{15}H_{10}O_6$ Molecular Weight: 286.239 g/mol

(Continued on following page)

TABLE 1 (*Continued*) Bioactive ligands utilised in this study, along with their code, structure, and details.

Code	Compound	Structure	Details
MG17	Kaempferol	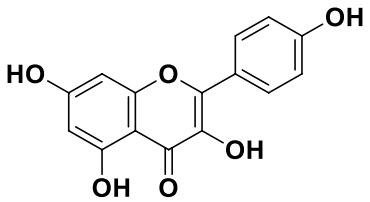	IUPAC 3,4′,5,7-Tetrahydroxyflavone Chemical Formula: $C_{15}H_{10}O_6$ Molecular Weight: 286.23 g/mol
MG18	Alizarin	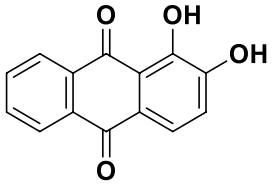	IUPAC 1,2-Dihydroxyanthracene-9,10-dione Chemical Formula: $C_{14}H_8O_4$ Molecular Weight: 240.214 g/mol
MG19	4-Hydroxybenzoic Acid	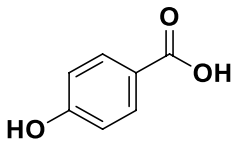	IUPAC: (1E,6E)-1,7-bis(4-hydroxy-3-methoxyphenyl) hepta-1,6-diene-3,5-dione Chemical Formula: $C_{21}H_{20}O_6$ Molecular Weight: 368.39
MG20	Salicylic acid	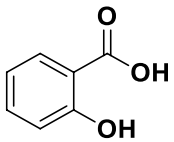	IUPAC 2-Hydroxybenzoic acid Chemical Formula: $C_7H_6O_3$ Molecular Weight: 138.122 g/mol

2023; Yele et al., 2022). This was performed for all three co-crystallized protein-ligand complexes.

2.6.4 Protein-ligand docking

All molecular docking simulation studies were conducted using the ligand docking program within the Maestro 2021.4 module of Schrödinger (Friesner et al., 2006; Hu et al., 2024; Gao et al., 2023). Before initiating the docking process, the active site coordinates on the target proteins were generated using the Receptor Grid Generation module. The van der Waals radii scaling factor and partial charge cutoff were set at 1.0 and 0.25, respectively, while the remaining parameters were kept as default. The Extra Precision (XP) mode was employed to carry out molecular docking of the three phytocompounds in the active site of their respective proteins (Friesner et al., 2006; Sanapalli et al., 2022). Subsequently, the binding affinities and molecular interactions were analysed, and the data were recorded. Finally, the interactions within the protein-ligand complexes were visualised in 2D/3D using the ligand interaction module, and high-quality images were saved for representation.

2.6.5 ADME and toxicity prediction

ADME (absorption, distribution, metabolism, and excretion) plays a pivotal role in predicting the pharmacodynamics of the molecule under study, potentially serving as a lead candidate for future drug development. The online web server SWISSADME, developed and maintained by the Swiss Institute of Bioinformatics (SIB) (https://www.swissadme.ch), was utilised for ADME evaluation based on molecular docking and dynamics results (Daina et al., 2017). The identified potential hit molecules were individually uploaded in SMILES format to the Marvin JS input panel on the website http://swissadme.ch/index.php. The server then performed *in silico* ADME predictions. In addition to ADME considerations, predicting toxicity is vital for assessing the safety profile of a drug. Using graph-based signatures, the pkCSM web server was employed to predict small-molecule pharmacokinetic properties (Pires et al., 2015). The web server database details toxicity, including AMES toxicity, maximum tolerated dose, hepatotoxicity, skin sensitisation, and hERG I and II inhibition. Toxicity assessments were conducted in prediction mode.

3 Results and discussion

3.1 The phenolic content of the LN

In this study, the phenolic content of the bay laurel plant was analysed using the LC-MS/MS method. Phenolic compounds are bioactive molecules that are essential to plants and human health. Human health has biological activities such as antioxidant, anti-inflammatory, anticancer, antidiabetic, antimicrobial, antiviral, antiallergic, antithrombotic and neuroprotective (Shahidi and Yeo, 2018; Rahman et al., 2021). The LC-MS/MS method is an effective method for identifying and quantifying these components. Thanks to this method, quality control of herbal products and supplements obtained from the bay plant can be made. Additionally, the potential health benefits of the phenolic components of the bay plant can be better understood. The LC-MS/MS method also provides information about the biosynthesis pathways and metabolic regulation of phenolic components of the

bay plant (Mateos et al., 2020). This information is useful for understanding how environmental factors and genetic manipulation affect the bay plant's production of bioactive compounds. Therefore, analysis of the phenolic content of the bay laurel plant by LC-MS/MS method is essential to advance the health effects of plant-based foods and drugs. Chromatographic and spectrometric parameters and the linear regression equations of standard phenolics and phenolic compounds in the LN samples are presented in Table 2, Supplementary Table S1 and Supplementary Figure S1. The phenolic content of the bay laurel plant was found by comparing it with standards. The most abundant compound was determined to be vanillic acid (4,599.00 μg/L). Vanillic acid was followed by catechin hydrate (3,351.53 μg/L). Therefore, these two compounds can be defined as the main compounds found in the structure of the LN. Luteolin (5.81 μg/L) and ellagic acid (5.47 μg/L) compounds were determined as the least common minor compounds in the structure of the LN. Vanillic acid has been identified as an essential secondary metabolite in many plant extracts whose biological activities have been investigated and isolated from many plants. Vanillic acid is a phenolic compound found in various dietary sources and herbs. In addition to being obtained from these biological sources, it is also synthesised chemically. It is used as a flavouring in different food products. It has been reported to have anticancer, antiobesity, antidiabetic, antibacterial, anti-inflammatory and antioxidant effects. In this study, it was reported for the first time that it was found to be the main compound in the bay laurel plant.

In 2021, Dobroslavić et al. (2021) evaluated the phenolic profile and antioxidant capacity of extracts obtained from bay leaves by green extraction techniques such as microwave-assisted extraction (MAE) and ultrasound-assisted extraction (UAE) with UPLC-MS/MS and ORAC methods. They detected 29 phenolic compounds in the extracts and found that kaempferol and quercetin glycosides were the most dominant among them. The extracts' total phenolic content, flavonoid content, and antioxidant capacity were also determined. Green extraction techniques have advantages such as higher efficiency, shorter time, and less solvent and energy consumption than conventional extraction techniques. This study showed that bay leaves are a rich source of phenolic compounds, and green extraction techniques are suitable for obtaining these compounds. Dobroslavić et al., 29 phenolic compounds were detected in extracts obtained from LN L. Among these compounds, there are also compounds such as vanillic acid,

TABLE 2 Quantitative amounts of phenolic compounds in ethanol extracts of *Laurus nobilis*.

Standard compounds	[a]MRM	[b]LOD/LOQ (μg/L)	Recovery (%)	[c]RT	[d]R^2	Concentration (μg/L)
Quercetin (MG1)	301.1 > 151	22.5/25.7	1.001	0.389	0.999	190,18
Acetohydroxamic Acid (MG2)	76.10 > 58.10	2.8/8.2	1.000	0.398	0.999	58,38
Catechin hydrate (MG3)	291.10 > 139.00	8.2/11.4	0.994	2,722	0.999	3351,53
Vanillic Acid (MG4)	168.80 > 93.00	125.5/142.2	1.001	2,885	0.998	4599,00
Resveratrol (MG5)	229.10 > 135.00	9.0/13.6	0.998	4,314	0.998	284,89
Fumaric Acid (MG6)	115.20 > 71.00	25.2/31.3	0.997	0.507	0.999	167,96
Gallic acid (MG7)	169.20 > 125.00	0.90/1.6	1.000	1.442	0.999	N.D.
Caffeic Acid (MG8)	179.20 > 135.00	6.3/10.7	1.009	2,778	0.996	17,25
Phloridzin dihydrate (MG9)	435.00 > 273.10	61.0/207.0	1.000	3,462	0.999	59,54
Oleuropein (MG10)	539.10 > 377.20	0.05/1.0	0.997	3.567	0.999	N.D.
Ellagic Acid (MG11)	300.90 > 145.10	0.101/0.333	1.002	3,900	1.000	5,47
Myricetin (MG12)	317.10 > 150.90	55.4/59.6	0.999	5.017	0.999	N.D.
Protocatechuic acid (MG13)	181.20 > 108.00	30.3/35.4	1.011	3.556	0.994	N.D.
Butein (MG14)	271.10 > 135.00	22.7/28.6	0.096	3,853	0.999	62,84
Naringenin (MG15)	271.10 > 150.90	5.4/6.4	0.998	3,879	0.996	N.D.
Luteolin (MG16)	285.20 > 132.90	0.5/2.5	1.007	4,124	0.998	5,81
Kaempferol (MG17)	285.10 > 116.90	206.6/214.3	0.999	4,115	0.999	68,46
Alizarin (MG18)	239.20 > 210.90	65.2/77.5	0.966	4.594	0.998	N.D.
4-Hydroxybenzoic Acid (MG19)	137.20 > 93.00	30.5/40.25	0.996	3.531	0.999	21,20
Salicylic acid (MG20)	137.20 > 93.00	4.2/7.6	1.009	3.534	0.999	27,44

[a]MRM, multiple reaction monitoring.
[b]LOD/LOQ (μg/L): limit of detection/limit of quantitation.
[c]T, retention time.
[d]R^2: determination coefficient. N.D: not detected.

catechin hydrate, luteolin and ellagic acid, which were also found in our study. This indicates that these compounds are essential among the phenolic components of the LN. According to Rúa et al. (2017), vanillic acid is a phenolic acid that has antioxidant, anti-inflammatory, antimicrobial, and anticancer activities. It is found in various plant sources, such as fruits, vegetables, herbs, spices, and tea. Catechin hydrate is a flavonoid with antioxidant, anti-inflammatory, antidiabetic, neuroprotective, and cardioprotective effects. It is widely distributed in many plant foods, especially tea, cocoa, grapes, and berries (Veiko et al., 2021). Luteolin is a flavone with antioxidant, anti-inflammatory, anticancer, antiallergic, and neuroprotective properties. It is present in many plant species, particularly in leaves, barks, clover blossoms, and herbs. Some dietary sources of luteolin include celery, broccoli, artichoke, parsley, thyme, and mint (Petkova et al., 2019). Ellagic acid is a polyphenol with antioxidant, anti-inflammatory, antimutagenic, and antitumor activities (Deepika and Maurya, 2022). It is produced in plants mainly by hydrolysis of ellagitannins, abundant in fruits, nuts, and bark. Some foods rich in ellagic acid include pomegranate, raspberry, strawberry, blackberry, walnut, and oak. These references show that these compounds are essential among the phenolic components of the *Laurus Nobilis*, as they have various biological activities and are widely distributed in plants. The LC-MS/MS method was used in both studies. This method is an effective method for the identification and quantification of phenolic compounds. However, the performance of the LC-MS/MS method depends on the chromatographic conditions, sample preparation methods, and standard compounds used. Therefore, the differences in these parameters used in both studies should be considered. In our analysis, the phenolic content of the bay laurel plant was found by comparing it with standards. The amounts of 6 of the 20 compounds used as standards could not be determined. This may mean these compounds are absent in the LN or below detectable levels. However, a more sensitive method or a more significant number of standard compounds may need to be used to determine whether these compounds are present in Bay Laurel. In addition, it would be useful to create a more comprehensive phenolic profile to detect other phenolic compounds in bay laurel.

Irakli et al. (2021) analysed the phenolic content of extracts obtained from solid wastes of plants belonging to the Lamiaceae family (thyme, sage, mint, basil, laurel) by LC-MS method. They detected 16 phenolic compounds in the extracts and reported that the Lamiaceae family also found rosmarinic acid, caffeic acid, chlorogenic acid, luteolin, and apigenin. In this study, evaluating solid wastes in terms of phenolic compounds is considered an environmentally and economically critical issue. In this study, it has been shown that the solid waste of the Lamiaceae family plant is a rich source of phenolic compounds and is a potential material for investigating the effects of these compounds on health. Our study analysed the phenolic content of extracts obtained from plant solid wastes using 100% ethanol solvent. This solvent was chosen to increase the solubility of phenolic compounds and reduce the effect of other compounds in the plant material. Our study shows that 100% ethanol solvent is similar to that of Irakli et al. (2021) and provides higher phenolic content, flavonoid content and antioxidant capacity than the 0.1% formic acid and acetonitrile mixture used by Irakli et al. (2021). These results reveal that the choice of solvent is an essential factor in the analysis of phenolic compounds and that ethanol is a suitable solvent for evaluating plant solid wastes.

LN has been extensively studied for its phenolic content and biological activities; however, comparisons with similar plants can significantly contribute to contextualizing the findings in such studies. In our research on LN, major phenolic compounds such as vanillic acid (4,599 μg/L) and catechin hydrate (3,351 μg/L) demonstrated superior lipid peroxidation inhibition compared to standard antioxidants such as Trolox (28.33%) and α-tocopherol (37.79%) with an inhibition rate of 50.53%. Similarly, studies on *Rosmarinus officinalis* (rosemary) have reported that phenolic compounds like rosmarinic acid and carnosic acid exhibit strong antioxidant activities when extracted using eco-friendly methods (Irakli et al., 2023). Likewise, species such as *Salvia ekimiana*, with phenolic profiles rich in vanillic acid, highlight the importance of this compound in antioxidant activities and its neurological effects (Orhan et al., 2012). Furthermore, *Origanum vulgare* (oregano), a rich source of vanillic acid, has demonstrated potent antioxidant effects, outperforming ascorbic acid and Trolox in reactive oxygen species (ROS) inhibition in H2O2-treated cells. Additionally, its antimelanogenic effects reveal a significant potential for biological activities (Chou et al., 2010).

The phenolic profile of LN is unique not only for its antioxidant activities but also for its DNA damage prevention properties. For instance, studies on the water extract of *Primula vulgaris* (WEP) have reported that phenolics such as p-coumaric acid and rutin are dominant, with a FRAP value of 82.63 ± 0.31 μM Trolox/g. Additionally, WEP has been shown to reduce H2O2-induced DNA damage in fibroblast cells in a concentration-dependent manner (Tugce Ozkan et al., 2017). When compared within this broader biological context, LN's high vanillic acid content further underscores its distinctive potential. Finally, it has been reported that the co-processing of *Argania spinosa* oil and *Origanum vulgare* leaves enhances phenolic content and oxidative stability, demonstrating a synergistic approach that improves product quality and shelf life (Oubannin et al., 2024). While LN exhibits antidiabetic and anticholinergic effects that extend beyond its antioxidant capacity, comparative analyses with similar plants in terms of phenolic content and biological activities will contribute to the contextualization and standardization of these findings.

3.2 Antioxidant activity

The antioxidant activity of plants may vary depending on factors such as plant species, growing conditions, harvesting methods and extraction techniques (Tungmunnithum et al., 2018). Therefore, determining plants' antioxidant activity is essential to understanding and evaluating their potential health and environmental benefits. In this study, we aimed to determine the antioxidant activity of LN L. leaves, which are widely consumed in the kitchen in many countries. In Table 3, the phenolic content of the plant extract was found to be 22.72 μg GAE/mg extract, and the flavonoid content was 57.36 μg QE/mg extract. These values indicate that the plant extract contains high amounts of phenolic and flavonoid compounds. DPPH and ABTS radical scavenging tests measure the plant extract's ability to neutralise free radicals. In these tests, the radical scavenging activity of the plant extract was compared to the standard antioxidants BHA,

TABLE 3 Radical removal and metal reduction activity *Laurus nobilis*.

Antioxidants	Total phenolic/ flavonoid content (µg GAE/QE mg^{-1} extract)	DPPH[a] (0.3 mg mL^{-1})	ABTS[a] (0.3 mg mL^{-1})	FRAP assay[b] (0.2 mg mL^{-1})	CUPRAC assay[b] (0.2 mg mL^{-1})
Laurus nobilis	22.72/57.36	43.47 ± 0.20	48.75 ± 1.20	0.249 ± 0.17	0.415 ± 0.03
BHA		71.64 ± 6.17	82.95 ± 6.37	0.43 ± 0.06	0.61 ± 0.04
BHT		46.67 ± 3.41	48.79 ± 3.20	0.65 ± 0.08	0.66 ± 0.05
Trolox		82.63 ± 6.37	79.68 ± 5.31	0.28 ± 0.01	0.52 ± 0.04

Standard antioxidants (BHA, butylated hydroxyanisole; BHT, butylated hydroxytoluene, trolox). GAE/QE: gallic acid equivalents/quercetin equivalent.
[a]Values are expressed as per cent radical scavenging activity.
[b]Values are expressed as absorbance. High absorbance indicates high metal reduction capacity.

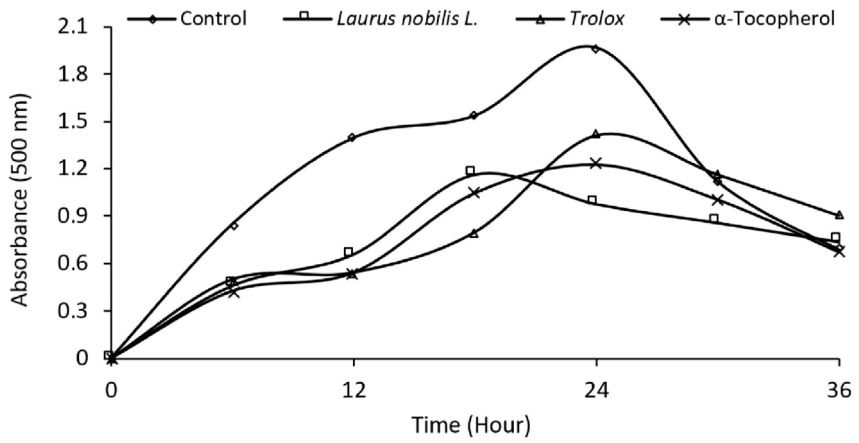

FIGURE 2
Comparative Inhibition of Linoleic Acid Peroxidation. This figure illustrates the inhibitory effects of standard antioxidants and ethanol extracts of *Laurus nobilis* L (20 µg/mL) on linoleic acid peroxidation. The data represent the extent of inhibition, highlighting the potential antioxidative properties of the extracts in comparison to established standards.

BHT and Trolox. According to Table 3, the DPPH radical scavenging activity of the plant extract was found to be 43.47% and 48.75% for ABTS. These values indicate that the radical scavenging activity of the plant extract is lower than standard antioxidants (71.64%–82.95%).

FRAP and CUPRAC metal reduction tests measure the ability of the plant extract to reduce metal ions. Metal ions can cause cell damage by increasing oxidative stress. Plant extract can reduce oxidative stress by reducing metal ions. In these tests, the metal-reducing activity of the plant extract was compared to the standard antioxidants BHA, BHT and Trolox. According to Table 3, the metal reduction activity of the plant extract in the FRAP test was 0.249, and the metal reduction activity in the CUPRAC test was 0.415. These values indicate that the metal-reducing activity of the plant extract is lower than the metal-reducing activity of standard antioxidants (0.43–0.66). In this way, determining the antioxidant activity of LN leaves is essential to reducing oxidative stress, revealing antifungal, antidiabetic, and anticholinergic effects, and evaluating the plant extract for different applications. Dhifi et al. (2018) DPPH, ABTS, FRAP and CUPRAC tests were used to measure the antioxidant activity of ethanol extract obtained from LN leaves. The IC50 values of ethanol extract were 0.3, 0.3, 0.2 and 0.2 mg/mL in DPPH, ABTS, FRAP and CUPRAC tests, respectively. This indicates that the ethanol extract poorly scavenges or reduces free radicals and metal ions. We can see that the antioxidant activity of LN in other regions and our region varies depending on the plant part, extraction solvent and method used. Essential oil from LN flowers appears to have the highest antioxidant activity in studies. Ethanol extract obtained from LN leaves has the lowest antioxidant activity. Table 3 shows that the radical scavenging and metal reduction activity of LN leaves is lower than that of standard antioxidants such as BHA, BHT, and Trolox. Therefore, the antioxidant activity of LN needs to be standardised, considering regional and methodological differences, to improve the quality and effectiveness of the plant extract and to determine the suitability of the plant extract for different applications. Figure 2 shows the effect of standard antioxidants and LN L. ethanol extracts (20 µg mL^{-1}). Linoleic acid peroxidation is a measure of lipid oxidation. Lipid oxidation is a process that causes oxidative damage to cell membranes, proteins and DNA by producing free radicals (Ayala et al., 2014). Plant extracts can prevent lipid oxidation and reduce oxidative stress by inhibiting linoleic acid peroxidation (Dhifi et al.,

2018; Awada et al., 2023). This may indicate the potential benefits of plant extracts to prevent or treat oxidative stress-related diseases. According to Figure 2, the extract inhibited lipid peroxidation by 50.53% after 24 h, compared to 28.33% and 37.79% by Trolox and α-tocopherol, respectively. The study suggests that LN L. ethanol extract inhibits linoleic acid peroxidation more effectively. The results indicate that LN L. ethanol extract may be a potential source of antioxidants to prevent lipid oxidation and reduce oxidative stress.

3.3 Antidiabetic and anticholinergic potential

In the community, the incidence of Type 2 diabetes has significantly increased, primarily attributed to ageing and overweight conditions. Inhibiting the activities of α-amylase and α-glucosidase enzymes can suppress carbohydrate digestion, delay glucose absorption, and reduce blood sugar levels. Slowing down glucose absorption provides additional time for insulin secretion by β-cells, ultimately enhancing the pharmacotherapeutic control of Type 2 diabetes. Therefore, exploring novel α-amylase and α-glucosidase inhibitors capable of decelerating or halting carbohydrate metabolism is critical in managing Type 2 diabetes (Atmaca, 2012). In this context, the ethanol extracts have shown promising results. The IC_{50} values of these extracts, indicating their inhibition effects on AChE and BChE as anticholinergic potential, were found to be 2.58 μg/L and 3.79 μg/L, respectively. Moreover, as an antidiabetic, the inhibition effect on α-GLY was found to be 4.65 μg/L (Table 4; Supplementary Figure S2). These findings suggest that these ethanol extracts could effectively inhibit α-amylase and α-glucosidase, thereby contributing to managing Type 2 diabetes. In individuals with diabetes, dietary therapy aims to reduce early postprandial hyperglycemia and control late postprandial hyperglycemia. Hence, medications that transiently inhibit the activities of enzymes in the gastrointestinal system are expected to mitigate postprandial glucose spikes effectively. Blocking α-amylase and α-glucosidase activities delays carbohydrate absorption, thereby preventing postprandial glucose elevation (Butterworth et al., 2011). Dirir et al. (2022) evaluated the α-amylase and α-glucosidase inhibition activities of 12 plant extracts. The results showed that plant extracts inhibited α-amylase activity by 10%–60% but inhibited α-glucosidase activity by 80%–100%. This study suggested that plant extracts may play a potential role in controlling postprandial hyperglycemia through α-glucosidase inhibition. Poovitha and Parani (2016) investigated the α-amylase and α-glucosidase inhibition activities and antioxidant capacities of 10 plant extracts. The results showed that plant extracts inhibited α-amylase activity by 20%–90% and α-glucosidase activity by 30%–100%. This study found a positive correlation between α-amylase and α-glucosidase inhibition and antioxidant capacity of plant extracts. Compared with our study, these studies show that the α-amylase and α-glucosidase inhibition activities of plant extracts vary depending on the plant, solvent, concentration and analysis method. Furthermore, these studies reveal that the α-glucosidase inhibition activity of plant extracts is higher than the α-amylase inhibition activity. This suggests that plant extracts inhibit the α-glucosidase enzyme more effectively to slow carbohydrate metabolism and prevent postprandial glucose elevation. It also shows that ethanol extracts may effectively inhibit Type 2 diabetes. Mssillou et al. (2020) investigated the chemical composition, antioxidant and antifungal effects of the essential oil obtained from LN flowers grown in Morocco. They showed that *L. nobilis* essential oil has a strong total antioxidant capacity (TAC) with the ability to scavenge free radical DPPH. This study shows that the essential oil obtained from L. nobilis flowers has significant antifungal and antioxidant activities due to its high level of 1,8-cineole.

3.4 Molecular docking analysis

The present study employs molecular docking and ADME analyses to predict the interactions and pharmacokinetic properties of the compounds under investigation. While these computational methods provide valuable insights and are widely recognized as essential tools in drug discovery and development, it is important to acknowledge their inherent limitations. Computational predictions, although robust, may not always fully replicate the complexity of biological systems. Therefore, future studies should aim to incorporate experimental validation, such as *in vitro* and *in vivo* assays, to confirm the computational findings. This integration of experimental approaches would not only enhance the reliability of the results but also provide a more comprehensive understanding of the real-world interactions and therapeutic potentials of the compounds. Such a combined methodology would further strengthen the translational relevance of the findings and contribute to the development of more effective therapeutic agents.

3.4.1 Validation of the docking program

The validation model of proteins with PDB ID: 4EY7, 4TPK, and 5NN8 revealed predicted binding energy of −16.9623, −13.6368, and −10.2322 kcal and reference RMSD of 0.815, 0.514, and 0.462 Å. The overlay confirmation of the internal ligands with their co-crystallized conformations has been shown in Figure 2.

TABLE 4 Inhibition effect of *Laurus nobilis* ethanol extract on AChE, BChE and α-glucosidase.

Inhibitors	AChE IC_{50} (μg/mL)	R^2	BChE IC_{50} (μg/mL)	R^2	α-glucosidase IC_{50} (μg/mL)	R^2
Laurus nobilis	2.58	0.9911	3.79	0.994	4.65	0.9757
Tacrine	3.19	0.9896	2.54	0.9878		
Acarbose					3.15	0.9961

10.3389/fchem.2025.1541250

TABLE 5 Results of molecular docking study of 20 natural product analogues against PDB ID: 4EY7, 4TPK, and 5NN8.

Ligand code	Binding affinity/Docking score of ligands (kcal/mol)					
	Protein ID: 4EY7		Protein ID: 4TPK		Protein ID: 5NN8	
	Glide score	Glide energy	Glide score	Glide energy	Glide score	Glide energy
MG1	−104.728	−445.388	−857.568	−470.811	−632.384	−354.436
MG2	−404.947	−206.707	−342.002	−171.309	−258.114	−177.402
MG3	−116.426	−411.835	−788.135	−432.203	−555.464	−343.572
MG4	−503.073	−227.416	−482.051	−225.903	−329.187	−175.679
MG5	−813.859	−349.491	−641.676	−391.736	−418.447	−334.843
MG6	−175.516	−135.348	−158.337	−106.483	−177.372	−620.704
MG7	−652.698	−248.471	−516.443	−228.568	−52.501	−139.267
MG8	−594.813	−236.833	−506.936	−21.822	−442.585	−225.287
MG9	−994.026	−554.522	−113.674	−575.109	−610.376	−475.614
MG10	−132.312	−647.063	−113.349	−65.368	−762.853	−472.404
MG11	−12.042	−431.189	−804.857	−403.251	−587.159	−35.096
MG12	−112.578	−465.925	−933.071	−38.201	−661.733	−376.156
MG13	−621.367	−217.483	−563.581	−174.145	−432.082	−195.925
MG14	−135.282	−471.769	−841.473	−406.698	−613.093	−327.361
MG15	−918.431	−416.205	−730.281	−433.583	−578.454	−322.395
MG16	−101.879	−458.971	−817.514	−466.215	−608.195	−333.539
MG17	−99.949	−397.095	−778.845	−432.854	−529.828	−33.405
MG18	−10.713	−389.422	−738.376	−368.297	−444.138	−334.634
MG19	−532.888	−195.572	−445.109	−189.536	−342.589	−145.945
MG20	−556.356	−19.779	−528.975	−18.397	−394.646	−153.281

TABLE 6 Tabular representation of the top 25% ligands obtained through docking-based screening against all three proteins.

Binding affinity/Docking score of ligands (kcal/mol)								
Ligand Code	Protein ID: 4EY7		Ligand	Protein ID: 4TPK		Ligand	Protein ID: 5NN8	
	Glide score	Glide energy	Code	Glide score	Glide energy	Code	Glide score	Glide energy
MG14	−135.282	−471.769	MG9	−113.674	−575.109	MG10	−762.853	−472.404
MG10	−132.312	−647.063	MG10	−113.349	−65.368	MG12	−661.733	−376.156
MG11	−12.042	−431.189	MG12	−933.071	−38.201	MG1	−632.384	−354.436
MG3	−116.426	−116.426	MG1	−857.568	−470.811	MG14	−613.093	−327.361
MG12	−112.578	−465.925	MG14	−841.473	−406.698	MG9	−610.376	−475.614

3.4.2 Docking

The docking analysis of all ligands with the three proteins indicated favourable binding energies and inhibition constants. Notably, it was observed that nearly all ligands exhibited a superior binding affinity compared to the reference internal ligand. This observation underscores the practical accommodation of the ligands within the sub-pockets of all three proteins. The binding energies, docking scores, and inhibition constants for all molecules are provided in Table 5.

Upon observation, it was noted that the top 25% of compounds identified exhibited the most negative binding energies. Specifically, Oleuropein and Myricetin were found to interact with all three proteins, demonstrating substantial binding potential. Table 6 shows the top 25% of ligands obtained through docking-based screening

TABLE 7 Tabular representation of the top 25% ligands obtained through docking-based screening against protein with PDB ID: 4EY7.

Sl. No.	Code	Docking interactions with active site amino acid residues	H-bond distance (Å)
1	MG14	H-bond- Tyr337, Asp74, Arg296, and Phe295 Hydrophobic- Phe338, His447, Trp86, Phe297, Tyr124, Val294, Ser293, Leu289, and Trp286 π-π stacking- Tyr341	1.33, 1.12, 1.21, and 2.81
2	MG10	H-bond- Tyr341, Thr75, Arg296, and Phe295 Hydrophobic- Ser203, Glu202, Trp86, Gly121, Gly122, Tyr124, Phe297, Val294, Ser293, Leu289, Trp286, Tyr72, Asp74, Leu76, Gly342, and Phe338 π-π stacking- Tyr337 and His447	2.87, 2.81, 2.33 and 2.23
3	MG11	H-bond- Ser293 and Phe295 Hydrophobic- Leu289, Phe338, Val294, Arg296, Phe297, Asp74 and Tyr72 π-π stacking- Tyr341, Trp286, and Tyr124	3.21 and 2.95
4	MG3	H-bond- Phe295 Hydrophobic- Ser293, Val394, Arg296, Phe297, His447, Tyr124, Gly121, Tyr337 and Tyr72 π-π stacking- Tyr341, Phe338, and Trp286	2.96
5	MG12	H-bond- Arg296, Ser293 and Asp74 Hydrophobic- Trp286, Leu289, Val294, Phe395, Phe297, Tyr72, Tyr124, Phe338 and Tyr337 π-π stacking- Tyr341	2.80, 3.08 and 3.20

against all three proteins. These two molecules, Oleuropein and Myricetin, demonstrated strong binding with all three proteins. They effectively accommodated within the active site and interacted with the residues, forming hydrogen bonds, various hydrophobic interactions, and other molecular interactions. The effective binding energies can be attributed to numerous hydroxy functional groups in these ligands. These groups facilitate hydrogen bonding with various amino acid residues in the active site, contributing to the overall stability of the ligand-protein interactions.

3.4.3 Interaction analysis

We chose the top 5 ligands (25%) that exhibited strong binding with all three proteins. Upon critical observation, it was noted that the top-scoring compounds showed favourable docking scores, indicating that they retained all the structural requirements to be considered suitable ligands. Additionally, these compounds displayed promising pharmacophores. Among these top 5 hit molecules, Oleuropein and Myricetin demonstrated promising inhibitory results against all three selected proteins. Oleuropein and Myricetin displayed H-bonding with Tyr341, Thr75, Arg296, Phe295, Ser293 and Asp74 residues. Individually, Tyr341 (Tyrosine 341) acts as a key component in substrate binding and stabilisation, contributing to the formation of the acetylcholine binding pocket (Figure 2), Thr75 (Threonine 75) plays a role in stabilising the ligand through hydrogen bonding and contributes to the overall architecture of the active site, Arg296 (Arginine 296) functions in substrate recognition and binding, facilitating interactions with acetylcholine and other ligands, Phe295 (Phenylalanine 295) plays a role in forming hydrophobic interactions within the active site, contributing to substrate recognition and stabilisation, Ser293 (Serine 293) partakes in the hydrogen bonding network within the active site, influencing the stability of ligand binding, Asp74 (Aspartic acid 74) plays a crucial role in the catalytic mechanism of acetylcholinesterase, serving as a key residue involved in substrate hydrolysis. The interaction with Tyr337 is critical for inhibiting this human enzyme (Ashani et al., 1994). Hydrophobic residues, such as Phe297 and Phe338, form hydrophobic pockets within the active site. These interactions are crucial for stabilising ligands and substrates through nonpolar forces. They also aid in substrate specificity and are often involved in conformational changes of proteins. Hydrophobic residues may undergo dynamic rearrangements in the active site to accommodate different ligands or substrates. Aromatic residues, such as phenylalanine (Phe338) in acetylcholinesterase, can engage in π-π stacking with aromatic rings of ligands, suggesting a role in substrate recognition. These interactions also contribute to the overall stability of protein structures and can influence the catalytic mechanism of enzymes. However, the variations in the binding patterns of these flexible ligands, spanning the active site gorge across related species of acetylcholinesterase, are evident. The probable cause for such distinctions lies in the subtle alterations observed in the shape of the gorge during our analysis. It is anticipated that these differences in gorge shape may significantly impact the binding affinity of elongated inhibitors with conformational variability. This is particularly pertinent for dual acetylcholinesterase (AChE) inhibitors, characterised by moieties separated by a tether that simultaneously binds to both the peripheral and catalytic sites. The ligand interactions are detailed in Table 7 and Supplementary Figure S3.

3.4.4 Ligand interaction with human butyrylcholinesterase (PDB ID: 4TPK)

Oleuropein and Myricetin displayed H-bonding with His438, Glu197, Gly115 and Ala328 residues. Individually, His438 (Histidine 438) has two roles; firstly, it is involved in the catalytic mechanism of butyrylcholinesterase, acting as a general base or acid during substrate hydrolysis. Secondly, it plays a crucial role in stabilizing the transition state of the enzymatic reaction, facilitating the efficient breakdown of substrates. Glu197 (Glutamic Acid 197) is crucial for butyrylcholinesterase's catalytic activity. It may act as a general base or acid, aiding the hydrolysis of substrates and active site configuration. Glu197 contributes to shaping the active site and assisting in substrate recognition

TABLE 8 Tabular representation of the top 25% ligands obtained through docking-based screening against protein with PDB ID: 4TPK.

Sl. No.	Code	Docking interactions with active site amino acid residues	H-bond distance (Å)
1	MG9	H-bond- Ala328, Pro285, Ser287, His438 and Tyr128 Hydrophobic- Leu286, Val288, Gly117, Gly116, Gly115, Tyr114, Thr120, Phe398, Trp231, Gly121, Thr122, Gly122, Gly439, Ala199, Leu125, Ser198, Glu197, Trp82, Phe329 π-π stacking- Tyr332	1.58, 2.20, 2.83, 3.20, 2.21
2	MG10	H-bond- His438, Glu197 and Gly115 Hydrophobic- Trp231, Phe398, Gly121, Thr120, Gln119, Asp70, Gly439, Tyr440, Ile442, Ser198, Ala199, Gly117, Gly116, Tyr114, Tyr128, Trp82, Ser79, Tyr332, Pro285, Leu286, Ser287, Val288 and Ala328 π-π stacking-Phe329	3.82, 3.96, 1.55
3	MG12	H-bond- Glu197, Gly115 and Ala328 Hydrophobic- Thr120, Gly121, Gly116, Tyr114, Tyr128, Ile442, Ser198, Tyr440, Gly439, His438, Met437, Trp430, Gly78, Met434, Phe329, Val331, Tyr332 and Asp70 π-π stacking- Trp82	1.82, 1.56 and 1.23, 1.35
4	MG1	H-bond- Glu197 and Leu286 Hydrophobic- Pro285, Ser287, Val288, Phe398, Trp82, Gly439, Ile442, Tyr128, Ser198, Gly115, Gly116 and Gly117 π-π stacking- His438, Phe329 and Trp231	2.25, 3.02 and 2.85
5	MG14	H-bond- His438, Glu197 and Leu286 Hydrophobic- Ser287, Val288, Phe398, Ser198, Glu197, Tyr128, Ile442, Tyr440, Gly439, Trp82, Gly117, Gly116 and Gly115 π-π stacking- His438, Phe329 and Trp231	2.23, 1.85, 2.86 and 2.94

TABLE 9 Tabular representation of the top 25% ligands obtained through docking-based screening against protein with PDB ID: 5NN8.

Sl. No.	Code	Docking interactions with active site amino acid residues	H-bond distance (Å)
1	MG10	H-bond- Asp616, Arg600 and Asp282 Hydrophobic- Leu678, Leu677, Ser676, His674, Gly615, Trp613, Phe649, Leu650, Trp481, Arg672, Asp645, Trp516, Asp518, Met519, Asp404, Leu405, Ile441, Trp376, Ser523, Phe525, Ala555, Arg281, Leu283 and Ala284	2.80, 2.86, 2.83 and 3.20
2	MG12	H-bond- Ser676, Asp404 and Asp518 Hydrophobic- Asp616, Arg600, Trp613, Trp516, Ile441, Trp481, Trp376, Leu405, Leu650, Leu678 and Leu677 π-π stacking- Phe649	2.24, 2.35, 2.84
3	MG1	H-bond- Ser676 and Asp518 Hydrophobic- Met519, Asp616, Arg600, Trp481, Ile441, Leu405, Asp404, Trp376, Leu650, Gly651, Leu677 and Leu678 π-π stacking- Phe649	1.82, 1.56 and 1.23
4	MG14	H-bond- Ser676, Leu677, Asp518, Arg600 and Asp616 Hydrophobic- Trp618, Tyr292, Asp282, Met519, Trp481, Ile441, Leu650, Gly651, Ser679, Trp376 and Leu678 π-π stacking- Phe649	2.25, 2.50, 2.12, 2.35 and 2.45
5	MG9	H-bond- Arg411, Asp518, Asp404 and Asp616 Hydrophobic- Leu678, Leu677, Ser676, His674, Trp516, Ile441, Arg672, Arg600, Leu405, Trp613, Trp376, Gly615, Leu650, Tyr292 and Asp282 π-π stacking- Trp481 and Phe649	2.25, 2.40, 2.55 and 3.02

through its interactions with ligands. Gly115 (Glycine 115), a flexible structural element, introduces flexibility to the active site, which is essential for accommodating various ligands and substrates with different sizes and conformations. Gly115 may undergo conformational changes during substrate binding, contributing to the induced-fit mechanism of butyrylcholinesterase, Ala328 (Alanine 328), being an alanine residue, contributes to the hydrophobic environment within the active site. This is crucial for stabilising hydrophobic portions of substrates or inhibitors, helps maintain the structural integrity of the active site, and may participate in forming hydrophobic interactions with ligands. The hydrophobic residues collectively contribute to a protein's structure, stability, and function by forming a hydrophobic core within the protein. Their interactions drive the formation of secondary and tertiary structures, determining the overall three-dimensional conformation of the protein. Hydrophobic residues can contribute to ligand recognition by forming interactions with hydrophobic regions of ligands. They may play a role in the conformational dynamics of proteins. Herein, the π-π stacking interactions majorly contribute to the adaptability of the active site to different ligands. The ligand interactions are detailed in Table 8 and Supplementary Figure S4.

3.4.5 Ligand interaction with human lysosomal acid-alpha-glucosidase (PDB ID: 5NN8)

The narrow substrate-binding pocket of this protein is located near the C-terminal ends of β-strands of the catalytic (β/α) domain and is shaped by a loop from the N-terminal β-sheet domain and both inserts I and II. Oleuropein and Myricetin displayed H-bonding with Asp616, Arg600, Asp282, Ser676, Asp404, and Asp518 residues. Hydrogen

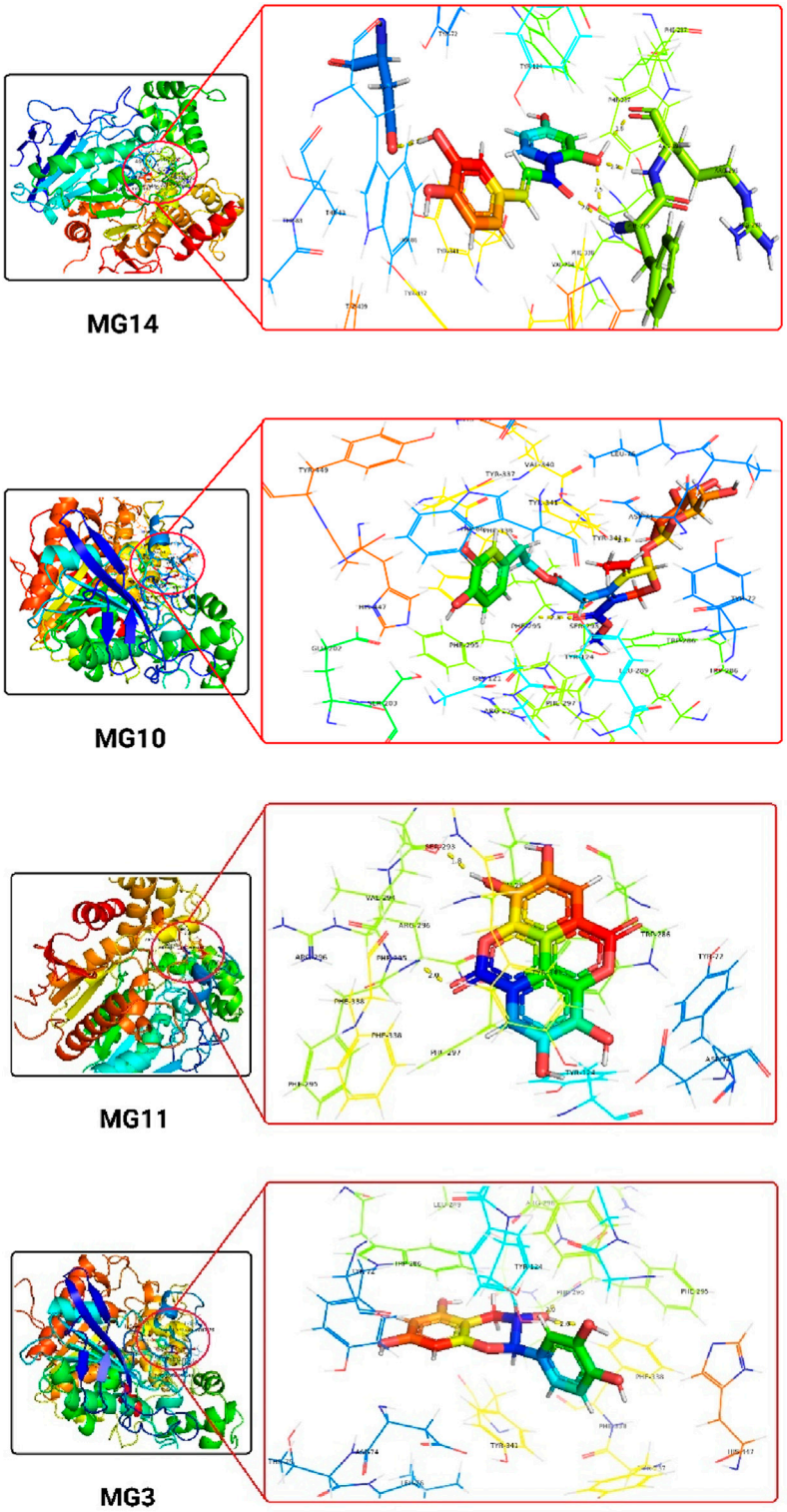

FIGURE 3
(Continued).

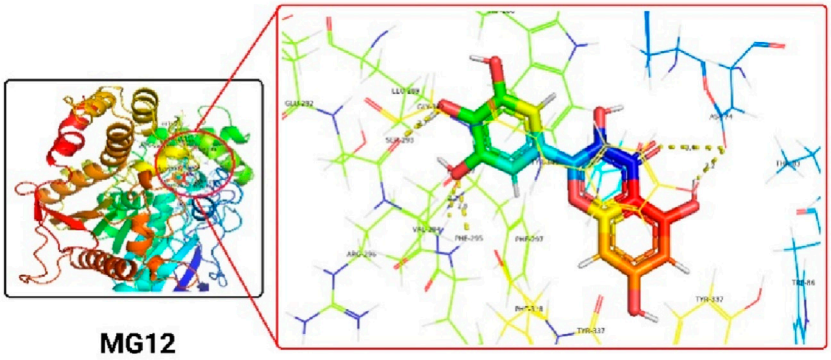

FIGURE 3
(Continued). The detailed 3D atomic interactions of the top 5 ligands at the active site of recombinant human acetylcholinesterase (PDB ID: 4EY7) .

bonding with Asp616 may play a role in the enzyme's catalytic mechanism, potentially stabilising intermediates during substrate hydrolysis. It also contributes to the architecture of the active site, influencing substrate binding and catalysis, Arg600 are likely involved in substrate recognition, contributing to the enzyme's specificity for certain substrates. These interactions may help stabilise the substrate within the active site, facilitating the enzymatic reaction. Hydrogen bonds with Asp282 may be essential for the enzyme's catalytic activity, potentially participating in proton transfer during substrate hydrolysis and contributing to maintaining the structural integrity of the active site. Ser676 likely contributes to the enzyme's overall stability and conformational integrity and may play a role in the dynamic behaviour of the active site, influencing conformational changes during catalysis. Hydrogen bonds with Asp404 may be involved in the catalytic mechanism, potentially assisting in substrate binding and positioning for hydrolysis, shaping the active site and influencing the enzyme's catalytic properties. Hydrogen bonds with Asp518 are likely crucial for substrate recognition and binding and contribute to the specific configuration of the active site, influencing the enzyme's catalytic efficiency. The hydrophobic residues are likely key players in substrate recognition, catalysis, and the overall stability of the enzyme, making them potential targets for therapeutic interventions or modifications for specific functionalities. The ligand interactions are detailed in Table 9 and Supplementary Figure S5.

The 3D docking images of the best top scored compounds against 4EY7, 4TPK and 5NN8 are displayed in Figures 3–5, respectively.

3.4.6 ADME analysis

The ADMET profiles of the two primary ligands investigated were assessed using online web servers, specifically SwissADME (http://www.swissadme.ch/). A comprehensive presentation of the acquired ADME properties is provided in Table 10. The fate of a compound within the human body is frequently assessed through its ADME properties, which encompass absorption, distribution, metabolism, and elimination. This evaluation sheds light on the molecule's behaviour and interactions within the human physiological system (Guan et al., 2019; Ferreira and Andricopulo, 2019; Norinder and Bergström, 2006). The findings revealed that the molar refractivity, reflecting the overall polarity of the molecules, was 104.70 for Oleuropein and 92.42 for Myricetin. These values fell within the typical range (30–140) (Ertlet al., 2000). The topological polar surface area (TPSA) for Oleuropein and Myricetin was measured at 88.60 and 59.66 $Å^2$, respectively. TPSA reflects a molecule's potential for cell permeation, with values greater than 140 $Å^2$ indicating poor permeability. Generally, a TPSA less than 90 $Å^2$ is preferred for molecules to traverse the blood-brain barrier (BBB) and exert an effect on the central nervous system (CNS) (Ertl et al., 2000). This implies that both compounds can cross the blood-brain barrier (BBB). Regarding drug properties influencing ADMET, the "solubility class lipophilicity" pertains to a molecule's capacity to dissolve in a lipophilic medium (Arnott and Planey, 2012). These properties encompass permeability, absorption, distribution, metabolism, excretion, solubility, plasma protein binding, and toxicity. Results of iLOGP (Daina, et al., 2014) and SILICOS-IT suggested that the iLOGP values of all the molecules were in the acceptable range (3. 72 and 3.51), while SILICOS-IT values for all the identified leads were in the most favourable range (−4.40 and −4.01). Water solubility is crucial in influencing a drug's distribution and absorption. Log S calculations provide insight into the molecule's solubility in water at 25 °C. According to the ESOL model, calculated log S values should not exceed six for optimal solubility (Delaney, 2004). Oleuropein and Myricetin exhibited log S values of −3. 92 and −3.50, indicating a favourable solubility profile. Based on these results, all lead compounds demonstrated a harmonious balance between permeability and solubility, suggesting potential acceptable bioavailability upon oral administration. Additionally, all molecules showed highly predicted gastrointestinal (GI) absorption (Daina and Zoete, 2016). Understanding the results of ADMET and cell-based bioassays is aided by permeability predictions (Potts and Guy, 1992). Results indicated that the permeability over human skin was −6.25 and −5.82 cm/s for Oleuropein and Myricetin. These predicted values were acceptable (Potts and Guy, 1992). Drug interactions resulting from metabolism can sometimes diminish a drug's bioavailability. Drug-metabolizing enzymes can only interact with the drug in its unbound state. Cytochrome P450 enzymes (CYPs), the most significant class of metabolizing enzymes, must be investigated to comprehend the metabolic behaviour of our molecules. The inhibitory activity of all lead compounds on cytochrome P450 enzymes, specifically those in human liver microsomes (HLM), was assessed (Cortes and Vapnik, 1995). A molecule's drug-likeness indicates its potential to be developed into

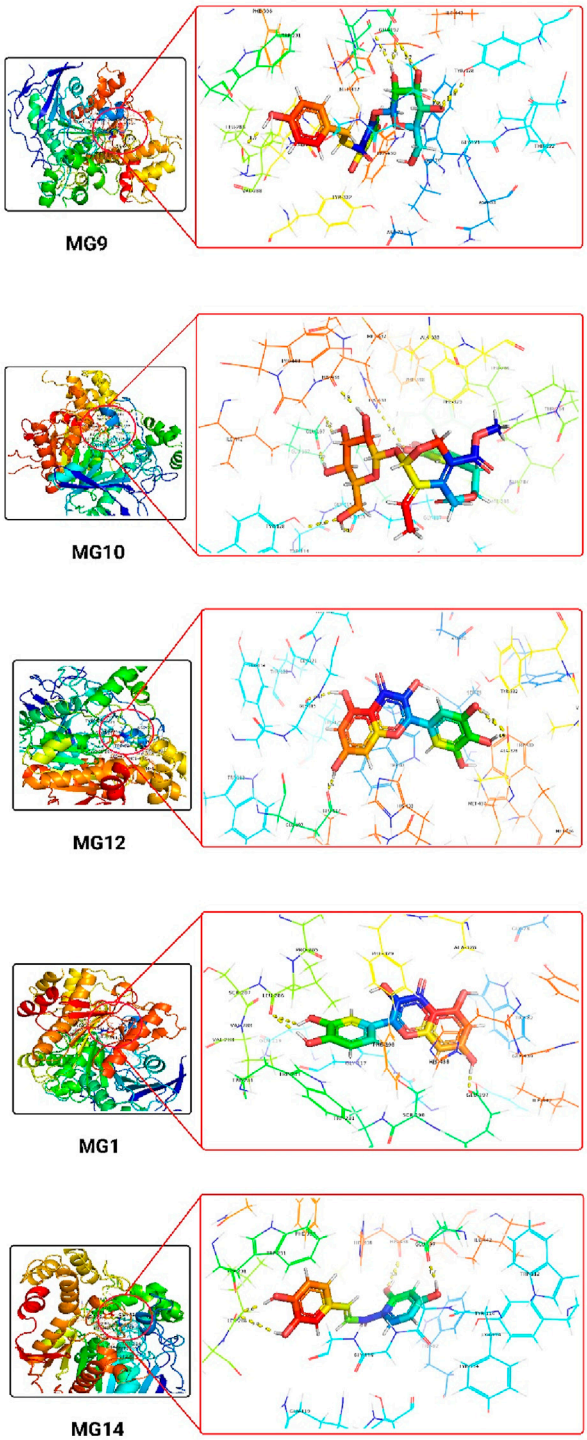

FIGURE 4
The detailed 3D atomic interactions of the top 5 ligands at the active site of recombinant human butyrylcholinesterase (PDB ID: 4TPK).

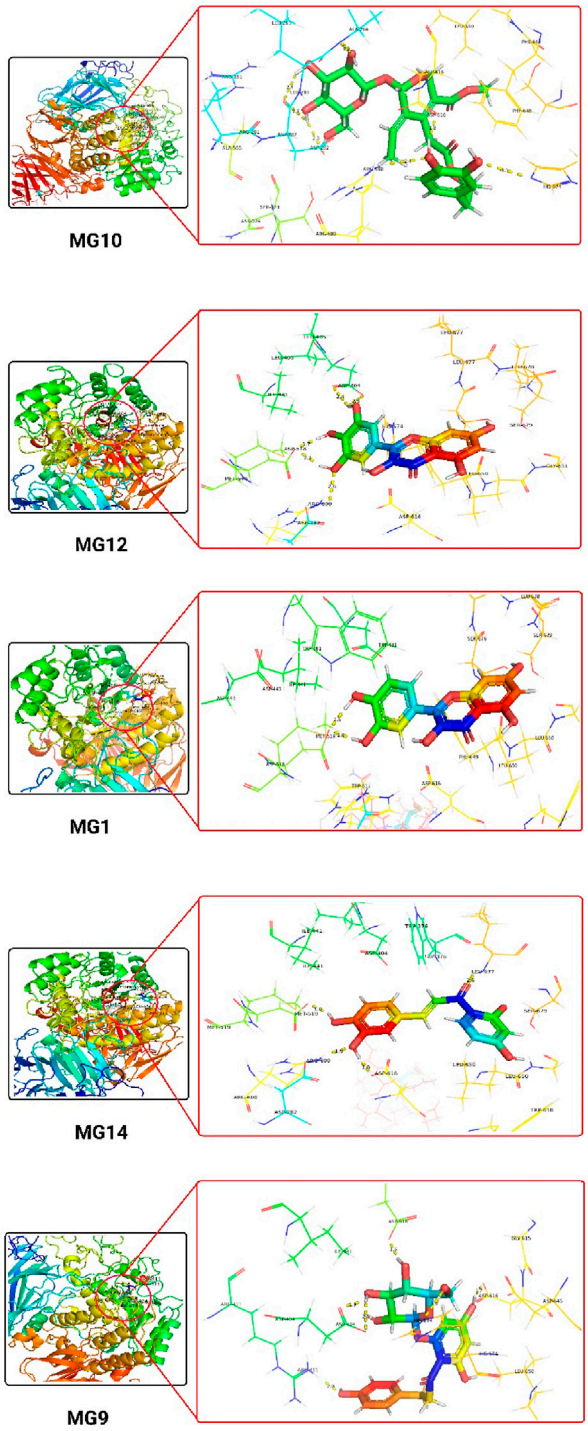

FIGURE 5
The detailed 3D atomic interactions of the top 5 ligands at the active site of Human lysosomal acid-α-GLY (PDB ID: 5NN8).

an oral medication. In our study, drug-likeness was evaluated using five different filters. All molecules passed without violating drug-likeness rules and achieved a bioavailability score of 55% (indicating good bioavailability). The Abbott Bioavailability score, determined by feasibility scores of 11%, 17%, 56%, or 85%, predicts the fate of a chemical for an experiment, including quantifiable Caco-2 cell line permeability or 10% oral bioavailability (in rats) (Martin, 2005). PAINS and Brenk techniques were employed to uncover potential ambiguous regions that might lead to false-positive biological results (Brenk et al., 2008; Baell and Nissink, 2018). All molecules were found to comply with PAINS and Brenk rules. Additionally, the synthetic accessibility for all molecules was estimated (Ertl and

TABLE 10 Description of *in silico* ADME parameters of all three ligands under study.

	Compounds code		MG10	MG12
ADME PROFILE	Physiochemical parameters	Formula	$C_{25}H_{32}O_8$	$C_{15}H_{10}O_8$
		Molecular weight	540.518 g/mol	318.197 g/mol
		Mol. Refractivity	104.70	92.42
		TPSA	88.60 Å^2	59.66 Å^2
	Lipophilicity	ILOGP	3.72	3.51
		SILICOS-IT	−4.40	−4.01
	Water Solubility	Log S (ESOL), Class	−3.92 Soluble	−3.50 Soluble
	Pharmacokinetics	GI absorption	High	High
		Plasma Protein Binding (human)	70.35	79.22
		BBB permeant	No	Yes
		Log K_p(skin perm.)	−6.25 cm/s	−5.82 cm/s
		CYP1A2	No	Yes
		CYP2D6	No	Yes
	Drug-likeness Rules	Lipinski (Pfizer)	Yes	Yes
		Ghose (Amgen)	Yes	Yes
		Veber (GSK)	Yes	Yes
		Egan (Pharmacia)	Yes	Yes
		Muege (Bayer)	Yes	Yes
		Bioavailability Score	0.55	0.55
	Medicinal Chemistry	PAINS	0 alert	0 alert
		Brenk	0 alert	0 alert
		Synthetic accessibility	2.92	2.37

Schuffenhauer, 2009). According to the criteria, all compounds exhibited a moderate level of hardness on a scale ranging from 1 (easy) to 10 (very tough). Consequently, based on the provided data, it is evident that the predicted ADME data for both molecules fall within the recommended values.

3.4.7 Toxicity

The toxicity profiles of the top two molecules (Oleuropein and Myricetin) were assessed using the online web server pkCSM (https://biosig.lab.uq.edu.au/pkcsm/prediction). The AMES test, which utilises microorganisms to predict the mutagenic potential of a chemical compound, yielded positive results for all molecules, indicating no AMES toxicity. The maximally tolerated dose (MTD), representing the highest dose most patients can take, was technically calculated. For Oleuropein and Myricetin, the maximum tolerated doses (human) were 0.486 and 0.722 Log mg/kg/day, respectively, indicating a moderate dosage level according to established protocols, with both being the most potent. hERG I and II (human Ether-a-go-go-Related gene) codes for proteins regulating ion channels crucial for the cardiac electrical action potential of the heart. Therefore, during drug development, drugs need to avoid inhibiting these channels. Only Myricetin showed no hERG I and II inhibition, minimising the likelihood of ventricular arrhythmias. The Oral Rat Acute Toxicity (LD50) values were 3.721 and 2.484 mol/kg, respectively, while the Oral Rat Chronic Toxicity (LOAEL) values were 4.484 and 3.307, respectively, indicating a favourable safety profile. All molecules were predicted to be non-hepatotoxic and demonstrated no skin sensitisation. The toxicity levels for T. Pyriformis and Minnow were within acceptable ranges. Furthermore, Myricetin's non-inhibition of hERG I and II highlights its potential for enhanced cardiac safety, an important consideration during drug development. While these computational predictions provide promising insights, the importance of experimental validation is recognised. Future studies will aim to experimentally verify these predictions, including key parameters such as AMES test outcomes and hERG channel interactions, to strengthen the translational relevance of these findings. A detailed presentation of the expected toxicity results for all molecules under study is provided in Table 11.

The stability of bioactive compounds is a critical parameter for their pharmaceutical application. Although this study primarily focuses on the biological activities of the identified compounds, future research could incorporate a detailed stability assessment. Such studies could include evaluations under various conditions such as temperature, pH, and light exposure to determine the long-term viability of these compounds. Stability testing not only provides

TABLE 11 Tabular representation data of predicted toxicity identified leads.

Model name	Units	Compounds name	
		MG10	MG12
AMES toxicity	Yes/No	No	No
Max. Tolerated dose (human)	Log mg/kg/day	0.468	0.722
hERG I inhibitor	Yes/No	No	No
hERG II inhibitor	Yes/No	Yes	No
Oral Rat Acute Toxicity (LD50)	Mol/kg	3.721	2.484
Oral Rat Chronic Toxicity (LOAEL)	Log mg/kg_bw/day	4.484	3.307
Hepatotoxicity	Yes/No	No	No
Skin Sensitisation	Yes/No	No	No
T. Pyriformis toxicity	Log ug/L	0.285	0.285
Minnow toxicity	Log mM	4.093	1.402

insights into the shelf-life of the compounds but also their feasibility for formulation into pharmaceutical products. Exploring stabilization strategies, such as encapsulation or the use of stabilizing agents, may further enhance the applicability of these compounds. This consideration would complement the current findings and expand their relevance in practical applications.

4 Conclusion

The LC-MS/MS analysis revealed the presence of various phenolic compounds in the LN, with the significant levels being vanillic acid and catechin hydrate. These compounds are known for their antioxidant properties and may contribute to the observed biological activities of the LN. In conclusion, this study sheds light on the antioxidant and anticholinergic potential of LN leaves and provides valuable information about the phenolic content in the LN. These findings may pave the way for further research into the therapeutic applications of this plant, especially in the context of neurodegenerative diseases such as Alzheimer's. Moreover, observations show that the ligands, especially Oleuropein and Myricetin, exhibit strong binding affinities with effective interactions at the active site. The findings from this study add valuable information to the development of receptor-targeted ligand therapies (triple inhibitors). The study also highlights the importance of ADME assessment in predicting the pharmacokinetics of our best results. The use of tools such as SWISSADME and the pkCSM web server contributes to a comprehensive understanding of the drug-likeness and toxicity profiles of identified hit molecules. Further experimental validation and optimisation of these two hit molecules identified *in silico* are warranted for future drug development efforts.

Data availability statement

The original contributions presented in the study are included in the article/Supplementary Material, further inquiries can be directed to the corresponding authors.

Author contributions

SA: Conceptualization, Data curation, Project administration, Writing–original draft. MI: Data curation, Formal Analysis, Methodology, Writing–original draft, Writing–review and editing. CA: Data curation, Project administration, Writing–original draft. ED: Investigation, Methodology, Writing–original draft. EK: Data curation, Project administration, Writing–original draft. KK: Writing–original draft, Writing–review and editing. MR: Funding acquisition, Resources, Software, Writing–original draft. GR: Resources, Software, Writing–original draft, Writing–review and editing. SB: Supervision, Writing–original draft. JK: Funding acquisition, Supervision, Writing–review and editing.

Funding

The author(s) declare that financial support was received for the research, authorship, and/or publication of this article. This work is funded by the Deanship of Postgraduate Studies and Scientific Research at Majmaah University, Saudi Arabia through the project number (R-2025-1541).

Acknowledgments

The authors thank the Deanship of Postgraduate Studies and Scientific Research at Majmaah University, Saudi Arabia for supporting this research work under the project number (R-2025-1541).

Conflict of interest

The authors declare that the research was conducted in the absence of any commercial or financial relationships that could be construed as a potential conflict of interest.

Generative AI statement

The author(s) declare that no Generative AI was used in the creation of this manuscript.

Publisher's note

All claims expressed in this article are solely those of the authors and do not necessarily represent those of their affiliated organizations, or those of the publisher, the editors and the reviewers. Any product that may be evaluated in this article, or claim that may be made by its manufacturer, is not guaranteed or endorsed by the publisher.

Supplementary material

The Supplementary Material for this article can be found online at: https://www.frontiersin.org/articles/10.3389/fchem.2025.1541250/full#supplementary-material

References

Akan, H., and Çakır, D. (2023). A review on medicinal plants used for women's diseases and health in anatolia (Turkey). *Int. J. Nat. Life Sci.* 7 (2), 36–54. doi:10.47947/ijnls.1329378

Al-Khayri, J. M., Yüksel, A. K., Yüksel, M., Işık, M., and Dikici, E. (2022). Phenolic profile and antioxidant, anticholinergic, and antibacterial properties of corn tassel. *Plants (Basel)* 11 (15), 1899. doi:10.3390/plants11151899

Altın, S., Tohma, H., Gülçin, İ., and Köksal, E. (2017). Purification, characterization, and inhibition sensitivity of peroxidase from wheat (*Triticum aestivum* ssp. vulgare). *Int. J. Food Prop.* 20 (9), 1949–1959. doi:10.1080/10942912.2016.1225308

Apak, R., Özyürek, M., Karademir Çelik, S., and Güçlü, K. (2013). Methods of measurement and evaluation of natural antioxidant capacity/activity (IUPAC Technical Report). *Pure Appl. Chem.* 85 (5), 957–998. doi:10.1351/PAC-REP-12-07-15

Apak, R., Güçlü, K., Ozyürek, M., Esin Karademir, S., and Erçağ, E. (2006). The cupric ion reducing antioxidant capacity and polyphenolic content of some herbal teas. *Int. J. Food Sci. Nutr.* 57 (5-6), 292–304. doi:10.1080/09637480600798132

Arnott, J. A., and Planey, S. L. (2012). The influence of lipophilicity in drug discovery and design. *Expert Opin. Drug Discov.* 7 (10), 863–875. doi:10.1517/17460441.2012.714363

Ashani, Y., Grunwald, J., Kronman, C., Velan, B., and Shafferman, A. (1994). Role of tyrosine 337 in the binding of huperzine A to the active site of human acetylcholinesterase. *Mol. Pharmacol.* 45 (3), 555–560.

Atmaca, M. H. (2012). Oral antidiyabetik ajanlar. *J. Exp. Clin. Med.* 29 (s1), s23–s29. doi:10.5835/jecm.omu.29.s1.006

Avci, M. (1996). The floristic regions of Turkey and a geographical approach for Anatolian Diagonal. *Rev. Dep. Geogr. Univ. İstanbul* 3, 59–91.

Awada, F., Hamade, K., Kassir, M., Hammoud, Z., Mesnard, F., Rammal, H., et al. (2023). Laurus nobilis leaves and fruits: a review of metabolite composition and interest in human health. *Appl. Sci.* 13 (7), 4606. doi:10.3390/app13074606

Ayala, A., Muñoz, M. F., and Argüelles, S. (2014). Lipid peroxidation: production, metabolism, and signaling mechanisms of malondialdehyde and 4-hydroxy-2-nonenal. *Oxid. Med. Cell. Longev.* 2014, 1–31. doi:10.1155/2014/360438

Baell, J. B., and Nissink, J. W. M. (2018). Seven year itch: pan-assay interference compounds (PAINS) in 2017—utility and limitations. *ACS Chem. Biol.* 13 (1), 36–44. doi:10.1021/acschembio.7b00903

Balunas, M. J., and Kinghorn, A. D. (2005). Drug discovery from medicinal plants. *Life Sci.* 78 (5), 431–441. doi:10.1016/j.lfs.2005.09.012

Bernstein, F. C., Koetzle, T. F., Williams, G. J., Meyer, E. F., Jr., Brice, M. D., Rodgers, J. R., et al. (1978). The Protein Data Bank: a computer-based archival file for macromolecular structures. *Arch. Biochem. Biophys.* 185 (2), 584–591. doi:10.1016/0003-9861(78)90204-7

Bingol, Z., Kızıltaş, H., Gören, A. C., Kose, L. P., Topal, M., Durmaz, L., et al. (2021). Antidiabetic, anticholinergic and antioxidant activities of aerial parts of shaggy bindweed (Convulvulus betonicifolia Miller subsp.) - profiling of phenolic compounds by LC-HRMS. *Heliyon* 7 (5), e06986. doi:10.1016/j.heliyon.2021.e06986

Blois, M. S. (1958). Antioxidant determinations by the use of a stable free radical. *Nature* 181 (4617), 1199–1200. doi:10.1038/1811199a0

Brenk, R., Schipani, A., James, D., Krasowski, A., Gilbert, I. H., Frearson, J., et al. (2008). Lessons learnt from assembling screening libraries for drug discovery for neglected diseases. *ChemMedChem* 3 (3), 435–444. doi:10.1002/cmdc.200700139

Brinza, I., Boiangiu, R. S., Hancianu, M., Cioanca, O., Erdogan Orhan, I., and Hritcu, L. (2021). Bay leaf (Laurus nobilis L.) incense improved scopolamine-induced amnesic rats by restoring cholinergic dysfunction and brain antioxidant status. *Antioxidants (Basel)* 10 (2), 259. doi:10.3390/antiox10020259

Brus, B., Košak, U., Turk, S., Pišlar, A., Coquelle, N., Kos, J., et al. (2014). Discovery, biological evaluation, and crystal structure of a novel nanomolar selective butyrylcholinesterase inhibitor. *J. Med. Chem.* 57 (19), 8167–8179. doi:10.1021/jm501195e

Butterworth, P. J., Warren, F. J., and Ellis, P. R. (2011). Human α-amylase and starch digestion: an interesting marriage. *Starch - Stärke* 63 (7): 395–405. doi:10.1002/star.201000150

Cai, Ji, Wen, H., Zhou, He, Zhang, D., Lan, D., Liu, S., et al. (2023). Naringenin: a flavanone with anti-inflammatory and anti-infective properties. *Biomed. and Pharmacother.* 164, 114990. doi:10.1016/j.biopha.2023.114990

Chaudhury, A., Duvoor, C., Reddy Dendi, V. S., Kraleti, S., Chada, A., Ravilla, R., et al. (2017). Clinical review of antidiabetic drugs: implications for type 2 diabetes mellitus management. *Front. Endocrinol. (Lausanne)* 8, 6. doi:10.3389/fendo.2017.00006

Chen, D., Bi, A., Dong, X., Jiang, Y., Rui, B., Liu, J., et al. (2014). Luteolin exhibits anti-inflammatory effects by blocking the activity of heat shock protein 90 in macrophages. *Biochem. Biophys. Res. Commun.* 443 (1), 326–332. doi:10.1016/j.bbrc.2013.11.122

Chen, D., Mubeen, B., Hasnain, A., Rizwan, M., Adrees, M., Naqvi, S. A. H., et al. (2022). Role of promising secondary metabolites to confer resistance against environmental stresses in crop plants: current scenario and future perspectives. *Front. Plant Sci.* 13, 881032. doi:10.3389/fpls.2022.881032

Cheng, X., Huang, J., Li, H., Zhao, D., Liu, Z., Zhu, L., et al. (2024). Quercetin: a promising therapy for diabetic encephalopathy through inhibition of hippocampal ferroptosis. *Phytomedicine* 126, 154887. doi:10.1016/j.phymed.2023.154887

Cheung, J., Rudolph, M. J., Burshteyn, F., Cassidy, M. S., Gary, E. N., Love, J., et al. (2012). Structures of human acetylcholinesterase in complex with pharmacologically important ligands. *J. Med. Chem.* 55 (22), 10282–10286. doi:10.1021/jm300871x

Chou, T. H., Ding, H. Y., Hung, W. J., and Liang, C. H. (2010). Antioxidative characteristics and inhibition of α-melanocyte-stimulating hormone-stimulated melanogenesis of vanillin and vanillic acid from *Origanum vulgare*. *Exp. Dermatol* 19 (8), 742–750. doi:10.1111/j.1600-0625.2010.01091.x

Colović, M. B., Krstić, D. Z., Lazarević-Pašti, T. D., Bondžić, A. M., and Vasić, V. M. (2013). Acetylcholinesterase inhibitors: pharmacology and toxicology. *Curr. Neuropharmacol.* 11 (3), 315–335. doi:10.2174/1570159x11311030006

Cortes, C., and Vapnik, V. (1995). Support-vector networks. *Mach. Learn.* 20 (3), 273–297. doi:10.1007/BF00994018

Daina, A., Michielin, O., and Zoete, V. (2017). SwissADME: a free web tool to evaluate pharmacokinetics, drug-likeness and medicinal chemistry friendliness of small molecules. *Sci. Rep.* 7 (1): 42717. doi:10.1038/srep42717

Daina, A., Michielin, O., and Zoete, V. (2014). iLOGP: a simple, robust, and efficient description of n-octanol/water partition coefficient for drug design using the GB/SA approach. *J. Chem. Inf. Model.* 54 (12), 3284–3301. doi:10.1021/ci500467k

Daina, A., and Zoete, V. (2016). A BOILED-egg to predict gastrointestinal absorption and brain penetration of small molecules. *ChemMedChem* 11 (11): 1117–1121. doi:10.1002/cmdc.201600182

Deepika, P., and Maurya, K. (2022). Ellagic acid: insight into its protective effects in age-associated disorders. *3 Biotech.* 12 (12), 340. doi:10.1007/s13205-022-03409-7

Delaney, J. S. (2004). ESOL: estimating aqueous solubility directly from molecular structure. *J. Chem. Inf. Comput. Sci.* 44 (3), 1000–1005. doi:10.1021/ci034243x

Dhifi, W., Bellili, S., Jazi, S., Nasr, S., El Beyrouthy, M., and Mnif, W. (2018). Phytochemical composition and antioxidant activity of Tunisian Laurus nobilis. *Pak. J. Pharm. Sci.* 31, 2397–2402.

Dirir, A. M., Daou, M., Yousef, A. F., and Yousef, L. F. (2022). A review of alpha-glucosidase inhibitors from plants as potential candidates for the treatment of type-2 diabetes. *Phytochem. Rev.* 21 (4), 1049–1079. doi:10.1007/s11101-021-09773-1

Division shimadzu corporation6 (2024). International marketing. *Shimadzu*. Available at: http://www.shimadzu.com.

Dobroslavić, E., Garofulić, I. E., Zorić, Z., Pedisić, S., and Dragović-Uzelac, V. (2021). Polyphenolic characterization and antioxidant capacity of Laurus nobilis L. Leaf extracts

obtained by green and conventional extraction techniques. *Processes* 9 (10), 1840. doi:10.3390/pr9101840

Dong, M., Luo, Y., Lan, Y., He, Q., Xu, L., and Pei, Z. (2023). Luteolin reduces cardiac damage caused by hyperlipidemia in Sprague-Dawley rats. *Heliyon* 9 (6), e17613. doi:10.1016/j.heliyon.2023.e17613

Durmaz, L., Erturk, A., Akyüz, M., Polat Kose, L., Uc, E. M., Bingol, Z., et al. (2022). Screening of carbonic anhydrase, acetylcholinesterase, butyrylcholinesterase, and α-glycosidase enzyme inhibition effects and antioxidant activity of coumestrol. *Molecules* 27 (10), 3091. doi:10.3390/molecules27103091

Dzobo, K. (2022). The role of natural products as sources of therapeutic agents for innovative drug discovery. *Compr. Pharmacol.*, 408–422. doi:10.1016/B978-0-12-820472-6.00041-4

Elessawy, F. E., Hughes, J., Khazaei, H., Vandenberg, A., El-Aneed, A., and Purves, R. (2023). A comparative metabolomics investigation of flavonoid variation in faba bean flowers. *Metabolomics* 19, 52. doi:10.1007/s11306-023-02014-w

Ellman, G. L., Courtney, K. D., Andres, V., Jr., and Feather-Stone, R. M. (1961). A new and rapid colorimetric determination of acetylcholinesterase activity. *Biochem. Pharmacol.* 7, 88–95. doi:10.1016/0006-2952(61)90145-9

Ertl, P., Rohde, B., and Paul, S. (2000). Fast calculation of molecular polar surface area as a sum of fragment-based contributions and its application to the prediction of drug transport properties. *J. Med. Chem.* 43 (20): 3714–3717. doi:10.1021/jm000942e

Ertl, P., and Schuffenhauer, A. (2009). Estimation of synthetic accessibility score of drug-like molecules based on molecular complexity and fragment contributions. *J. Cheminformatics* 1 (1), 8. doi:10.1186/1758-2946-1-8

Ferreira, L. L. G., and Andricopulo, A. D. (2019). ADMET modeling approaches in drug discovery. *Drug Discov. Today* 24 (5), 1157–1165. doi:10.1016/j.drudis.2019.03.015

Friesner, R. A., Murphy, R. B., Repasky, M. P., Frye, L. L., Greenwood, J. R., Halgren, T. A., et al. (2006). Extra precision glide: docking and scoring incorporating a model of hydrophobic enclosure for Protein–Ligand complexes. *J. Med. Chem.* 49 (21), 6177–6196. doi:10.1021/jm051256o

Gao, X.-H., Tang, J. J., Liu, H.-R., Liu, L. B., and Liu, Y. Z. (2019). Structure–activity study of fluorine or chlorine-substituted cinnamic acid derivatives with tertiary amine side chain in acetylcholinesterase and butyrylcholinesterase inhibition. *Drug Dev. Res.* 80 (4): 438–445. doi:10.1002/ddr.21515

Gao, Y., Duan, J., Dang, X., Yuan, Y., Wang, Y., He, X., et al. (2023). Design, synthesis and biological evaluation of novel histone deacetylase (HDAC) inhibitors derived from *β* -elemene scaffold. *J. Enzyme Inhibition Med. Chem.* 38 (1), 2195991. doi:10.1080/14756366.2023.2195991

Guan, L., Yang, H., Cai, Y., Sun, L., Di, P., Li, W., et al. (2019). ADMET-score - a comprehensive scoring function for evaluation of chemical drug-likeness. *Medchemcomm* 10 (1), 148–157. doi:10.1039/c8md00472b

Güder, A., and Korkmaz, H. (2012). Evaluation of *in-vitro* antioxidant properties of hydroalcoholic solution extracts urtica dioica L., malva neglecta wallr. And their mixture. *Iran. J. Pharm. Res.* 11 (3), 913–923.

Güven, L., Erturk, A., Miloğlu, F. D., Alwasel, S., and Gulcin, İ. (2023). Screening of antiglaucoma, antidiabetic, anti-alzheimer, and antioxidant activities of Astragalus alopecurus pall-analysis of phenolics profiles by LC-MS/MS. *Pharm. (Basel)* 16 (5), 659. doi:10.3390/ph16050659

Hu, Y., Zhang, Q., Bai, X., Men, L., Ma, J., Li, D., et al. (2024). Screening and modification of (+)-germacrene A synthase for the production of the anti-tumor drug (−)-β-elemene in engineered *Saccharomyces cerevisiae*. *Int. J. Biol. Macromol.* 279: 135455. doi:10.1016/j.ijbiomac.2024.135455

Irakli, M., Skendi, A., Bouloumpasi, E., Chatzopoulou, P., and Biliaderis, C. G. (2021). LC-MS identification and quantification of phenolic compounds in solid residues from the essential oil industry. *Antioxidants* 10 (12), 2016. doi:10.3390/antiox10122016

Irakli, M., Skendi, A., Bouloumpasi, E., Christaki, S., Biliaderis, C. G., and Chatzopoulou, P. (2023). Sustainable recovery of phenolic compounds from distilled rosemary by-product using green extraction methods: optimization, comparison, and antioxidant activity. *Molecules* 28 (18), 6669. doi:10.3390/molecules28186669

Kang, Lu, Gao, X.-H., Liu, H.-R., Men, X., Wu, H.-N., Cui, P.-Wu, et al. (2018). Structure–activity relationship investigation of coumarin–chalcone hybrids with diverse side-chains as acetylcholinesterase and butyrylcholinesterase inhibitors. *Mol. Divers.* 22 (4), 893–906. doi:10.1007/s11030-018-9839-y

Kavaz, A., Dikici, E., Yüksel, M., Işık, M., Tozoğlu, F., and Koksal, E. (2021). Phytochemical, phenolic profle, antioxidant, anticholinergic and antibacterial properties of Epilobium angustifolium (Onagraceae). *J. Food Meas. Charact.* 15. doi:10.1007/s11694-021-01050-1

Koksal, E. (2011). Peroxidase from leaves of spinach (spinacia oleracea): partial purification and some biochemical properties. *Int. J. Pharmacol.* 7, 135–139. doi:10.3923/ijp.2011.135.139

Li, W., Xiang, L., Liu, Z., Xing, Q., Liu, R., Wu, Q., et al. (2024). The signaling pathways of selected traditional Chinese medicine prescriptions and their metabolites in the treatment of diabetic cardiomyopathy: a review. *Front. Pharmacol.* 15, 1416403. doi:10.3389/fphar.2024.1416403

Lu, Q.-Q., Chen, Y. M., Liu, H. R., Yan, J. Y, Cui, P. W, Zhang, Q. F., et al. (2020). Nitrogen-containing flavonoid and their analogs with diverse B-ring in acetylcholinesterase and butyrylcholinesterase inhibition. *Drug Dev. Res.* 81 (8): 1037–1047. doi:10.1002/ddr.21726

Martin, Y. C. (2005). A bioavailability score. *J. Med. Chem.* 48 (9), 3164–3170. doi:10.1021/jm0492002

Mateos, R., Pérez-Correa, J. R., and Domínguez, H. (2020). Bioactive properties of marine phenolics. *Mar. Drugs* 18 (10), 501. doi:10.3390/md18100501

Mitsuda, H., Yasumoto, K., and Iwami, K. (1966). Antioxidative action of indole compounds during the autoxidation of linoleic acid. *Eiyo To Shokuryo* 19 (3), 210–214. doi:10.4327/jsnfs1949.19.210

Mssillou, I., Agour, A., El Ghouizi, A., Hamamouch, N., Lyoussi, B., and Derwich, E. (2020). Chemical composition, antioxidant activity, and antifungal effects of essential oil from *Laurus nobilis* L. Flowers growing in Morocco. *J. Food Qual.* 2020: 8819311. 8. doi:10.1155/2020/8819311

Norinder, U., and Bergström, C. A. (2006). Prediction of ADMET properties. *ChemMedChem* 1 (9), 920–937. doi:10.1002/cmdc.200600155

Orhan, I. E., Senol, F. S., Ozturk, N., Akaydin, G., and Sener, B. (2012). "Profiling of *in vitro* neurobiological effects and phenolic acids of selected endemic Salvia species." *Food Chem.* 132 (3): 1360–1367. doi:10.1016/j.foodchem.2011.11.119

Oubannin, S., Asbbane, A., Hallouch, O., Giuffrè, A. M., Sakar, El H., and Said, G. (2024). Synergistic potential of co-millinged edible argan oil (Argania spinosa L.) and oregano leaves (Origanum vulgare L.) in food applications. *Future Foods* 10: 100430. doi:10.1016/j.fufo.2024.100430

Öztürk, Ş., Hazer, Y., Kaşkatepe, B., and Ören, M. (2022). Determination of total phenol contents, antibacterial and antioxidant activity of some mosses species. *Karaelmas Sci. Eng. J.* 12 (1): 86–92. doi:10.7212/karaelmasfen.1009713

Panche, A. N., Diwan, A. D., and Chandra, S. R. (2016). Flavonoids: an overview. *J. Nutr. Sci.* 5, e47. doi:10.1017/jns.2016.41

Petkova, Z., Stefanova, G., Girova, T., Antova, G., Stoyanova, M., Damianova, S., et al. (2019). Phytochemical investigations of laurel fruits (Laurus nobilis). *Nat. Product. Commun.* 14 (8), 1934578X19868876. doi:10.1177/1934578x19868876

Pires, D. E. V., Blundell, T. L., and Ascher, D. B. (2015). pkCSM: predicting small-molecule pharmacokinetic and toxicity properties using graph-based signatures. *J. Med. Chem.* 58 (9), 4066–4072. doi:10.1021/acs.jmedchem.5b00104

Poovitha, S., and Parani, M. (2016). *In vitro* and *in vivo* α-amylase and α-glucosidase inhibiting activities of the protein extracts from two varieties of bitter gourd (Momordica charantia L.). *BMC Complementary Altern. Med.* 16 (1), 185. doi:10.1186/s12906-016-1085-1

Potts, R. O., and Guy, R. H. (1992). Predicting skin permeability. *Pharm. Res.* 9 (5), 663–669. doi:10.1023/a:1015810312465

Qattan, M. Y., Khan, M. I., Alharbi, S. H., Verma, A. K., Al-Saeed, F. A., Abduallah, A. M., et al. (2022). Therapeutic importance of kaempferol in the treatment of cancer through the modulation of cell signalling pathways. *Molecules* 27 (24), 8864. doi:10.3390/molecules27248864

Rahman, M. M., Rahaman, M. S., Islam, M. R., Rahman, F., Mithi, F. M., Alqahtani, T., et al. (2021). Role of phenolic compounds in human disease: current knowledge and future prospects. *Molecules* 27 (1), 233. doi:10.3390/molecules27010233

Rakshit, G., and Jayaprakash, V. (2023). Tuberculosis and HIV responses threatened by nCOVID-19: a situation prompting an *in silico* investigation of reported MbtA inhibitors for combined inhibition of SARS-CoV-2 and HIV-TB co-infection. *Struct. Chem.* 34 (2), 655–679. doi:10.1007/s11224-022-02013-y

Ramanan, M., Sinha, S., Sudarshan, K., Singh Aidhen, I., and Doble, M. (2016). Inhibition of the enzymes in the leukotriene and prostaglandin pathways in inflammation by 3-aryl isocoumarins. *Eur. J. Med. Chem.* 124: 428–434. doi:10.1016/j.ejmech.2016.08.066

Ramezani, M., Darbandi, N., Khodagholi, F., and Hashemi, A. (2016). Myricetin protects hippocampal CA3 pyramidal neurons and improves learning and memory impairments in rats with Alzheimer's disease. *Neural Regen. Res.* 11 (12), 1976–1980. doi:10.4103/1673-5374.197141

Re, R., Pellegrini, N., Proteggente, A., Pannala, A., Yang, M., and Rice-Evans, C. (1999). Antioxidant activity applying an improved ABTS radical cation decolorization assay. *Free Radic. Biol. Med.* 26 (9-10), 1231–1237. doi:10.1016/s0891-5849(98)00315-3

Roig-Zamboni, V., Cobucci-Ponzano, B., Iacono, R., Ferrara, M. C., Germany, S., Bourne, Y., et al. (2017). Structure of human lysosomal acid α-glucosidase-a guide for the treatment of Pompe disease. *Nat. Commun.* 8 (1), 1111. doi:10.1038/s41467-017-01263-3

Roy, A., Khan, A., Ahmad, I., Alghamdi, S., Rajab, B. S., Babalghith, A. O., et al. (2022). Flavonoids a bioactive compound from medicinal plants and its therapeutic applications. *Biomed. Res. Int.* 2022, 5445291. doi:10.1155/2022/5445291

Rúa, J., de Arriaga, D., García-Armesto, M. R., Busto, F., and Valle, P. d. (2017). Binary combinations of natural phenolic compounds with gallic acid or with its alkyl esters: an approach to understand the antioxidant interactions. *Eur. Food Res. Technol.* 243 (7), 1211–1217. doi:10.1007/s00217-016-2838-2

Sanapalli, B. K. R., Yele, V., Baldaniya, L., and Veera Venkata Satyanarayana Reddy Karri (2022). Identification of novel protein kinase C-βII inhibitors: virtual screening,

molecular docking and molecular dynamics simulation studies. *J. Mol. Model.* 28 (5), 117. doi:10.1007/s00894-022-05104-z

Sargin, S. A., and Büyükcengiz, M. (2019). Plants used in ethnomedicinal practices in Gulnar district of Mersin, Turkey. *J. Herb. Med.* 15: 100224. doi:10.1016/j.hermed.2018.06.003

Sarkar, D., Christopher, A., and Shetty, K. (2021). Phenolic bioactives from plant-based foods for glycemic control. *Front. Endocrinol. (Lausanne)* 12, 727503. doi:10.3389/fendo.2021.727503

Schrödinger. Release (2021). LigPrep, schrödinger. Available at: https://www.scirp.org/reference/referencespapers?referenceid=3115697.

Sekercioglu, C., Anderson, S., Akcay, E., Bilgin, R., Can, O., Semiz, G., et al. (2011). Turkey's globally important biodiversity in crisis. *Biol. Conserv.* 144, 2752–2769. doi:10.1016/j.biocon.2011.06.025

Semwal, D. K., Semwal, R. B., Combrinck, S., and Viljoen, A. (2016). Myricetin: a dietary molecule with diverse biological activities. *Nutrients* 8 (2), 90. doi:10.3390/nu8020090

Shahidi, F., and Yeo, J. (2018). Bioactivities of phenolics by focusing on suppression of chronic diseases: a review. *Int. J. Mol. Sci.* 19 (6), 1573. doi:10.3390/ijms19061573

Sheng, Y., Sun, Y., Tang, Y., Yu, Y., Wang, J., Zheng, F., et al. (2023). Catechins: protective mechanism of antioxidant stress in atherosclerosis. *Front. Pharmacol.* 14, 1144878. doi:10.3389/fphar.2023.1144878

Shi, L., Zhao, W., Yang, Z., Subbiah, V., and Suleria, H. A. R. (2022). Extraction and characterization of phenolic compounds and their potential antioxidant activities. *Environ. Sci. Pollut. Res. Int.* 29 (54), 81112–81129. doi:10.1007/s11356-022-23337-6

Shi, S., Li, K., Peng, J., Li, J., Luo, L., Liu, M., et al. (2022). Chemical characterization of extracts of leaves of Kadsua coccinea (Lem.) A.C. Sm. by UHPLC-Q-Exactive Orbitrap Mass spectrometry and assessment of their antioxidant and anti-inflammatory activities. *Biomed. and Pharmacother.* 149: 112828. doi:10.1016/j.biopha.2022.112828

Shraim, A. M., Ahmed, T. A., Rahman, Md M., and Hijji, Y. M. (2021). Determination of total flavonoid content by aluminum chloride assay: a critical evaluation. *LWT* 150: 111932. doi:10.1016/j.lwt.2021.111932

Singh, P., Singh, A., and Choudhary, K. K. (2023). Revisiting the role of phenylpropanoids in plant defense against UV-B stress. *Plant Stress* 7: 100143. doi:10.1016/j.stress.2023.100143

Sofowora, A., Ogunbodede, E., and Onayade, A. (2013). The role and place of medicinal plants in the strategies for disease prevention. *Afr. J. Tradit. Complement. Altern. Med.* 10 (5), 210–229. doi:10.4314/ajtcam.v10i5.2

Sudarshan, K., kumar Boda, A., Dogra, S., Bose, I., Yadav, P. N., and Aidhen, I. S. (2019). Discovery of an isocoumarin analogue that modulates neuronal functions via neurotrophin receptor TrkB. *Bioorg. and Med. Chem. Lett.* 29 (4): 585–590. doi:10.1016/j.bmcl.2018.12.057

Sun, W., and Shahrajabian, M. H. (2023). Therapeutic potential of phenolic compounds in medicinal plants-natural health products for human health. *Molecules* 28 (4), 1845. doi:10.3390/molecules28041845

Tang, L., Wang, Y., Gong, X., Xiang, Ju, Zhang, Y., Xiang, Q., et al. (2023). Integrated transcriptome and metabolome analysis to investigate the mechanism of intranasal insulin treatment in a rat model of vascular dementia. *Front. Pharmacol.* 14, 1182803. doi:10.3389/fphar.2023.1182803

Tao, Y., Zhang, Y., Cheng, Y., and Wang, Y. (2013). Rapid screening and identification of α-glucosidase inhibitors from mulberry leaves using enzyme-immobilized magnetic beads coupled with HPLC/MS and NMR. *Biomed. Chromatogr.* 27 (2), 148–155. doi:10.1002/bmc.2761

Tohma, H., Altay, A., Köksal, E., Gören, A. C., and Gülçin, İ. (2019). Measurement of anticancer, antidiabetic and anticholinergic properties of sumac (Rhus coriaria): analysis of its phenolic compounds by LC–MS/MS. *J. Food Meas. Charact.* 13 (2), 1607–1619. doi:10.1007/s11694-019-00077-9

Tonisi, S., Okaiyeto, K., Mabinya, L. V., and Okoh, A. I. (2020). Evaluation of bioactive compounds, free radical scavenging and anticancer activities of bulb extracts of Boophone disticha from Eastern Cape Province, South Africa. *Saudi J. Biol. Sci.* 27 (12), 3559–3569. doi:10.1016/j.sjbs.2020.07.028

Tugce Ozkan, M., Aliyazicioglu, R., Demir, S., Misir, S., Turan, I., Yildirmis, S., et al. (2017). Phenolic characterisation and antioxidant activity of Primula vulgaris and its antigenotoxic effect on fibroblast cells. *Jundishapur J. Nat. Pharm. Prod.* 12 (1), e40073. doi:10.5812/jjnpp.40073

Tungmunnithum, D., Thongboonyou, A., Pholboon, A., and Yangsabai, A. (2018). Flavonoids and other phenolic compounds from medicinal plants for pharmaceutical and medical aspects: an overview. *Med. (Basel)* 5 (3), 93. doi:10.3390/medicines5030093

Turgut, K., Baydar, H., and Telci, İ. (2023). "Cultivation and breeding of medicinal and aromatic plants in Turkey," in *Medicinal and aromatic plants of Turkey*. Editors Á. Máthé, and K. Turgut (Cham: Springer International Publishing), 131–167.

Türkeş, C., Akocak, S., Işık, M., Lolak, N., Taslimi, P., Durgun, M., et al. (2022). Novel inhibitors with sulfamethazine backbone: synthesis and biological study of multi-target cholinesterases and α-glucosidase inhibitors. *J. Biomol. Struct. Dyn.* 40 (19), 8752–8764. doi:10.1080/07391102.2021.1916599

Veeresham, C. (2012). Natural products derived from plants as a source of drugs. *J. Adv. Pharm. Technol. Res.* 3 (4), 200–201. doi:10.4103/2231-4040.104709

Veiko, A. G., Lapshina, E. A., and Zavodnik, I. B. (2021). Comparative analysis of molecular properties and reactions with oxidants for quercetin, catechin, and naringenin. *Mol. Cell. Biochem.* 476 (12), 4287–4299. doi:10.1007/s11010-021-04243-w

Wang, H., Yan, Z., Yang, W., Liu, R., Fan, G., Gu, Z., et al. (2025). "A strategy of monitoring acetylcholinesterase and screening of natural inhibitors from Uncaria for Alzheimer's disease therapy based on near-infrared fluorescence probe." *Sensors Actuators B Chem.* 424: 136895. doi:10.1016/j.snb.2024.136895

Wangchuk, P., and Tobgay, T. (2015). Contributions of medicinal plants to the gross national happiness and biodiscovery in Bhutan. *J. Ethnobiol. Ethnomed* 11, 48. doi:10.1186/s13002-015-0035-1

Yele, V., Sanapalli, B. K. R., and Mohammed, A. A. (2022). Imidazoles and benzimidazoles as putative inhibitors of SARS-CoV-2 B.1.1.7 (Alpha) and P.1 (Gamma) variant spike glycoproteins: a computational approach. *Chem. Zvesti* 76 (2), 1107–1117. doi:10.1007/s11696-021-01900-8

Yilmaz, M. A. (2020). Simultaneous quantitative screening of 53 phytochemicals in 33 species of medicinal and aromatic plants: a detailed, robust and comprehensive LC–MS/MS method validation. *Industrial Crops Prod.* 149, 112347. doi:10.1016/j.indcrop.2020.112347

Ysrafil, Y., Sapiun, Z., Slamet, N. S., Mohamad, F., Hartati, H., Damiti, S. A., et al. (2023). Anti-inflammatory activities of flavonoid derivates. *Admet dmpk* 11 (3), 331–359. doi:10.5599/admet.1918

Zeng, G., Wu, Z., Cao, W., Wang, Y., Deng, Xu, and Zhou, Y. (2020). Identification of anti-nociceptive constituents from the pollen of Typha angustifolia L. using effect-directed fractionation. *Nat. Prod. Res.* 34 (7), 1041–1045. doi:10.1080/14786419.2018.1539979

frontiers | Frontiers in Chemistry

TYPE Original Research
PUBLISHED 27 February 2025
DOI 10.3389/fchem.2025.1543075

OPEN ACCESS

EDITED BY
Afzal Basha Shaik,
Jawaharlal Nehru Technological University,
Kakinada, India

REVIEWED BY
Vidyasrilekha Sanapalli,
SVKM'S NMIMS University, India
Bhaskara Rao Karri,
University of Minnesota Twin Cities,
United States

*CORRESPONDENCE
Sanmati Kumar Jain,
sanmatijain72@yahoo.co.in

RECEIVED 10 December 2024
ACCEPTED 04 February 2025
PUBLISHED 27 February 2025

CITATION
Thakur GS, Gupta AK, Pal D, Vaishnav Y, Kumar N, Annadurai S and Jain SK (2025) Designing novel cabozantinib analogues as p-glycoprotein inhibitors to target cancer cell resistance using molecular docking study, ADMET screening, bioisosteric approach, and molecular dynamics simulations.
Front. Chem. 13:1543075.
doi: 10.3389/fchem.2025.1543075

Designing novel cabozantinib analogues as p-glycoprotein inhibitors to target cancer cell resistance using molecular docking study, ADMET screening, bioisosteric approach, and molecular dynamics simulations

Gajendra Singh Thakur[1], Ajay Kumar Gupta[1], Dipti Pal[1], Yogesh Vaishnav[1], Neeraj Kumar[2], Sivakumar Annadurai[3] and Sanmati Kumar Jain [1]*

[1]Drug Discovery and Research Laboratory, Department of Pharmacy, Guru Ghasidas Vishwavidyalaya (A Central University), Bilaspur, Chhattisgarh, India, [2]Department of Pharmaceutical Chemistry, Bhupal Nobles' College of Pharmacy, Udaipur, Rajasthan, India, [3]Department of Pharmacognosy, College of Pharmacy, King Khalid University, Abha, Saudi Arabia

Introduction: One of the foremost contributors to mortality worldwide is cancer. Chemotherapy remains the principal strategy for cancer treatment. A significant factor leading to the failure of cancer chemotherapy is the phenomenon of multidrug resistance (MDR) in cancer cells. The primary instigator of MDR is the over expression of P-glycoprotein (P-gp), a protein that imparts resistance and facilitates the ATP-dependent efflux of various anticancer agents. Numerous efforts have been made to inhibit P-gp function with the aim of restoring the effectiveness of chemotherapy due to its broad specificity. The main objective has been to create compounds that either serve as direct P-gp inhibitors or interact with cancer therapies to modulate transport. Despite substantial in vitro achievements, there are currently no approved drugs available that can effectively "block" P-gp mediated resistance. Cabozantinib (CBZ), a multi-kinase inhibitor, is utilized in the treatment of various carcinomas. CBZ has been shown to inhibit P-gp efflux activity, thereby reversing P-gp mediated MDR. Consequently, P-gp has emerged as a critical target for research in anti-cancer therapies.

Methods: The purpose of this study was to computationally identify new andsafer analogues of CBZ using bioisosteric approach, focusing on improved pharmacokinetic properties andreduced toxicity. The physicochemical, medicinal, and ADMET profiles of generated analogues were computed using the ADMETLab 3.0 server. We also predicted the drug likeness (DL) and drug score (DS) of analogues. The molecular docking studies of screened analogues against the protein (PDB ID: 3G5U) were conducted using AutoDock Vina flowing by BIOVIA Discovery Studio for visualizing interactions.Molecular dynamics (MD) simulation of docked ligands was done using Schrödinger suite.

Results and Discussion: The docking scores for the ligands CBZ01, CBZ06, CBZ11, CBZ13, CBZ25, CBZ34, and CBZ38 ranged from −8.0 to −6.4 kcal/mol

against the protein (PDB ID: 3G5U). A molecular dynamics (MD) simulation of CBZ01, CBZ13, and CBZ38 was conducted using the Schrödinger suite, revealing that these complexesmaintained stability throughout the 100 ns simulation.

Conclusion: An integrated computational approach combining bioisosteric approach, molecular docking, drug likeness calculations, and MD simulations highlights the promise of ligands CBZ01 and CBZ13 as candidates for the development of potential anticancer agents for the treatment of various cancers.

KEYWORDS

anti-cancer agent, newer analogues, bioisosteric approach, cabozantinib, molecular docking, MD simulation

1 Introduction

Cancer continues to be a primary cause of worldwide mortality. The International Agency for Research on Cancer (IARC), a division of the World Health Organization (WHO), which is dedicated to cancer studies, has published its recent estimates regarding the global cancer burden. An estimated 20 million new cancer cases and over 9.7 million cancer-related deaths occurred in 2022. Around 53.5 million people survived for at least 5 years after their diagnosis. Lung cancer has emerged as the most prevalent cancer globally, with 2.5 million new cases, representing 12.4% of all new diagnoses. Following lung cancer, female breast cancer ranked second in prevalence at 11.6%, succeeded by colorectal cancer (9.6%), prostate cancer (7.3%), and stomach cancer (4.9%). Forecasts show that the number of new cancer cases could escalate to 35 million by 2050, which marks an increase of 77% compared to the figures recorded in 2022. This significant rise in the global cancer burden is largely attributed to an aging population, overall population growth, and shifts in exposure to various risk factors, many of which are linked to socioeconomic development. Key contributors to the rising incidence of cancer include tobacco use, alcohol consumption, and obesity, while air pollution remains a significant environmental risk factor (Ferlay et al., 2024; Sung et al., 2021).

The treatment of cancer is recognized as a particularly challenging endeavour, encompassing methods such as chemotherapy, radiotherapy, and surgical interventions (Cao et al., 2024; Bray et al., 2024; Liu B. et al., 2024). A significant obstacle in contemporary cancer research is the emergence of drug resistance and the recurrence of cancer, which often undermine the effectiveness of even the most potent anti-cancer therapies (Anand et al., 2023; Khan et al., 2024). In the context of chemotherapy, one of the primary reasons for treatment failure is the phenomenon of multidrug resistance (MDR) observed in cancer cells. The over expression of P-glycoprotein (P-gp), an ATP-binding cassette transporter, is a key factor contributing to MDR, as it enhances the efflux of various anti-cancer agents from the cells. P-gp was the first protein identified to be linked to drug resistance (Bukowski et al., 2020; Lin et al., 2016a; Lin et al., 2016b; Goebel et al., 2021; Zhang et al., 2022; Garrigues et al., 2002). P-gp, identified in 1976, is a membrane glycoprotein with an estimated molecular weight of 170 kDa, found in drug-resistant Chinese hamster ovary cells. It consists of two transmembrane domains (TMDs) and two nucleotide-binding domains (NBDs) (Kim and Chen, 2018; Tian et al., 2023; Sun et al., 2023). The NBDs, located in the cytoplasm, facilitate the movement of substrates by transferring energy across cellular membranes, while the TMDs, composed of six transmembrane helices, provide substrate selectivity (Vasiliou et al., 2009; Johnson and Chen, 2018).

P-gp is recognized as a significant MDR transporter, particularly in relation to its role in conferring resistance to cancer chemotherapy. Its expression has been found to be elevated in various tumor types, such as osteosarcoma, kidney cancer, liver cancer, breast cancer, gastric cancer, lung cancer, and colorectal cancer, which contributes to the development of chemotherapy resistance (Karthika et al., 2022; Heming et al., 2022; Sharom, 2011). Cabozantinib (CBZ), a small-molecule, multitargeted tyrosine kinase inhibitor, is utilized in the treatment of several cancers, including metastatic medullary thyroid cancer, RCC, and HCC. Patients undergoing CBZ therapy may experience a range of toxicities, including hepatotoxicity and renal impairment, which can be severe or potentially life-threatening (Srigadha et al., 2023; Markowitz and Fancher, 2018; Choueiri et al., 2015). According to LiverTox, the hepatotoxicity likelihood score of cabozantinib is E*, unproven but probably rare cause of clinically apparent liver damage (National Center for Biotechnology Information, 2025). According to DrugBank, cabozantinib has extensive plasma protein binding (≥99.7%) (National Center for Biotechnology Information, 2025). The toxicities of cabozantinib may affect the patient's quality of life. The most common adverse events (AEs) are diarrhea, fatigue, hypertension, hand-foot syndrome, weight loss, nausea, stomatitis, gastrointestinal perforation, hypothyroidism and myelotoxicity (Schmidinger and Danesi, 2018). Adverse reactions were recorded from clinic reports and the most common were hypertension, mucositis/hand-foot skin reaction (HFSR), or gastrointestinal toxicity (Martini et al., 2022). Cabozantinib has a higher risk of hepatotoxicity (Wang K. et al., 2024). Krens et al. (2022) reported that cabozantinib is registered at a fixed dose of 60 mg. However, 46%–62% of patients in pivotal studies required dose reduction due to toxicity. Consequently, it is crucial to modify the structure of the CBZ molecule to develop analogues that are less toxic and safer. Adverse effects associated with CBZ treatment include diarrhea, hypertension, hand-foot syndrome, weight loss, reduced appetite, stomatitis, and nausea (Schwartz et al., 2020; Rimassa et al., 2019; Zuo et al., 2015). Numerous reports have documented hepatotoxicity and a variety of dose-dependent side effects linked to CBZ (Barnhill et al., 2020; Andrade et al., 2019; Chiruvella et al., 2020). Due to these toxicities, it is imperative to modify the structure of the CBZ molecule to create safer and less toxic analogues.

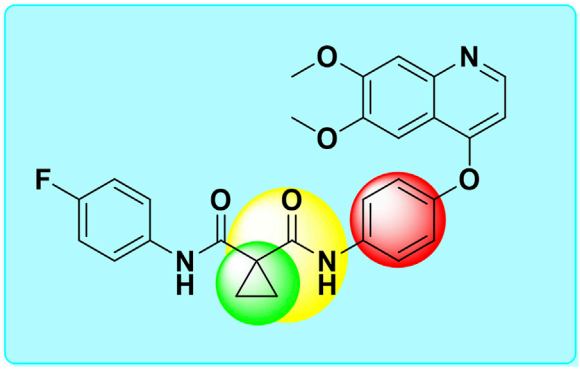

FIGURE 1
Structure of cabozantinib and its bioisosterically modified groups [Cyclopropyl (green circle), amide cyclopropyl (yellow circle), and phenyl (red circle)].

The development of a lead chemical into a pharmaceutical agent presents significant challenges and often incurs high costs. Most candidates fail primarily due to pharmacokinetic and metabolic complications rather than a lack of efficacy. Even when a lead molecule exhibits the desired pharmacological effect, it may still present adverse side effects, characteristics that hinder its bioavailability, or chemical structures that impede its metabolism and elimination from the body. To address these issues, researchers employ the strategy of bioisosterism, which involves the selective modification of lead compounds to create safer and more effective medications. Bioisosterism is often perceived as a qualitative and intuitive concept. The common physicochemical properties of a set of bioisosteres are believed to contribute to their capacity to elicit similar biological responses. By leveraging an understanding of pharmacophores and physicochemical features, researchers are increasingly substituting bioisosteres for functional groups, thereby enhancing the potential for the development of innovative therapeutic agents. The foundational work of Langmuir in 1919 laid the groundwork for the bioisosterism approach to modifying lead compounds. Through the bioisosteric method, chemists can adjust various characteristics of the lead compound, including its size, shape, electrical distribution, polarizability, dipole moment, polarity, lipophilicity, and pKa, while ensuring effective binding to the target. Consequently, the strategic application of the bioisosteric method allows for the modification of lead compounds to yield more favorable therapeutic drugs with enhanced potency, selectivity, improved physical and metabolic properties, and minimized side effects (Giordano et al., 2022; Das et al., 2022; Jayashree et al., 2022).

Structure-based drug design represents a highly effective and powerful approach within the broader context of drug discovery. The drug development process, which encompasses combinatorial chemistry, various screening methodologies, and the assessment of parameters such as absorption, distribution, metabolism, excretion, and toxicity (ADMET), can be significantly accelerated through the use of computational resources (Anderson, 2003; Jiang et al., 2018; Nie et al., 2020; Ejalonibu et al., 2021; Gao et al., 2023; Li et al., 2024). Recently, molecular docking has become an essential element of *in silico* drug discovery. This technique focuses on predicting the atomic-level interactions between proteins and small molecules. The accessibility of free software for conducting docking simulations of protein-ligand systems has facilitated a growing number of studies utilizing this approach, with tools like AutoDock, ArgusLab, and GOLD providing docking estimates for a variety of receptor-ligand interactions. The docking interactions suggest the most favorable docked conformers based on the overall energy of the system. Additionally, it assists in identifying the specific amino acids of the protein that interact with the test molecules, thereby helping to evaluate the affinity of the tested molecule for the target protein (Bhagat et al., 2021; Du et al., 2016; Ferreira et al., 2015; Duan et al., 2024; Kang et al., 2018). To elucidate the molecular basis of protein function, molecular dynamics (MD) simulation is the predominant computational method employed to investigate the structure and dynamic behavior of proteins. Based on the docking scores and interactions, we selected three complexes of CBZ analogues for MD simulations (Salo-Ahen et al., 2020; Gao et al., 2019; Naresh and Guruprasad, 2020; Ajmal et al., 2016). The primary objective of this study is to modify various groups within the CBZ molecule, specifically phenyl, amide cyclopropyl, and cyclopropyl groups (Figure 1). The goal is to create CBZ analogues that are both safer and more effective. Additionally, we conducted ADMET predictions, molecular docking analyses, and MD simulations on the chosen CBZ analogues. The overall workflow of the present study is shown in Figure 2.

2 Materials and methods

2.1 Designing of CBZ Bioisosteres

The smile notation for CBZ analogues was acquired from DrugBank, a prominent chemical information platform. The bioisosteres of CBZ were created utilizing the MolOpt software, an online tool that produces bioisosteres through data mining, similarity assessments, and AI generative models (Shan and Ji, 2020; Subbaiah and Meanwell, 2021).

2.2 Pharmacokinetic and toxicological (ADMET) Profile Predictions

The pharmacokinetic and toxicological profile were forecasted utilizing the ADMETLab 3.0 online software. This comprises 119 quantitative and qualitative predictable endpoints, which effectively and thoroughly assess ADMET characteristics for novel ligands that exhibit ADMET properties similar to those observed in mammals (Dulsat et al., 2023; Gupta et al., 2024; Lou et al., 2023; Liu M. et al., 2024).

2.3 Drug likeness (DL) and drug score (DS) prediction

The primary variables leading to the failure of drug candidates in clinical trials are often intolerable toxicity levels or unfavourable pharmacokinetic characteristics. Therefore, it is crucial to conduct

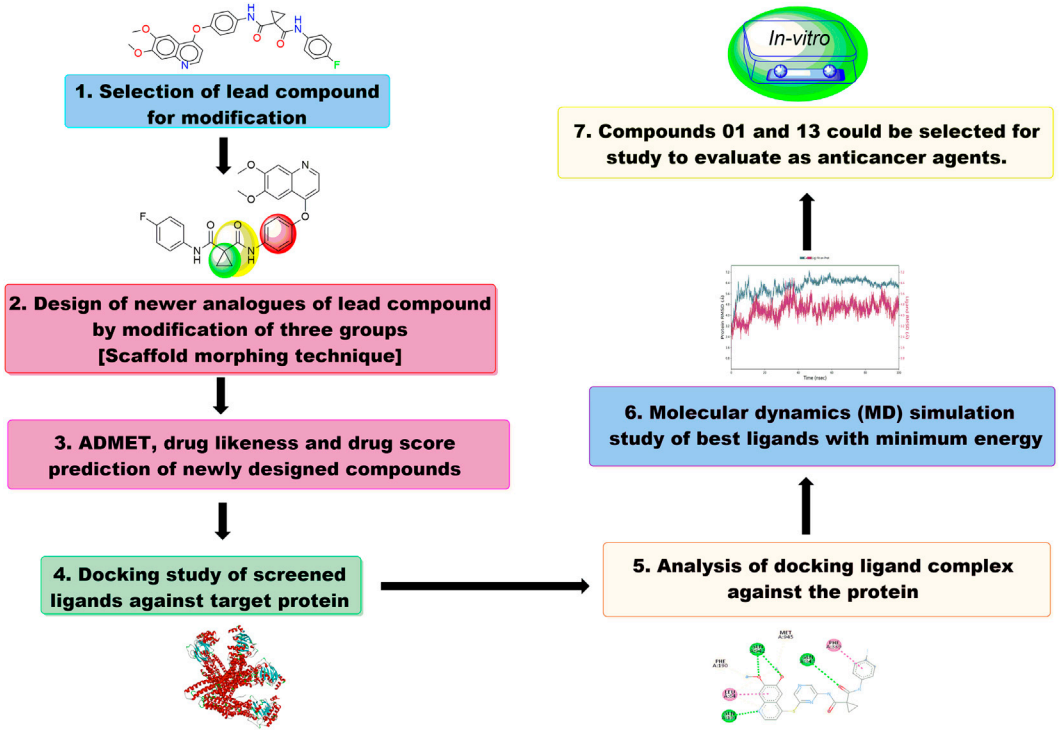

FIGURE 2
The overall work flow of the present study.

evaluations of DL and DS in the early stages of the drug development process. The calculations for drug score and drug likeness were performed utilizing the Osiris property explorer (Sun et al., 2022).

2.4 Molecular docking studies

Molecular docking is essential in drug discovery and structural molecular biology for predicting the main binding mode(s) of a ligand with a protein of known 3D structure. In this context, commonly used docking-related terminology (such as Apo protein, positive control, native ligand, and co-crystal inhibitors) is employed to elucidate the core principles of molecular docking, which encompass binding affinity, binding orientation, and ligand interactions. The docking analysis was conducted using AutoDock Vina (ADV) as the primary tool, and the interactions were evaluated with Discovery studio software (De Ruyck et al., 2016; Trott and Olson, 2010; Wang Z. et al., 2024; Ikwu et al., 2020). P-gp is integral to the process of cellular detoxification, as it facilitates the removal of a wide range of chemically diverse toxins. However, it is also linked to the phenomenon of multidrug resistance (MDR) in cancer treatments. Among the various transporters associated with MDR, P-gp is the most significant member of the ATP-binding cassette (ABC). P-gp demonstrates remarkable poly-specificity, enabling it to recognize a broad spectrum of compounds with molecular weights ranging from 330 Da to 4,000 Da. The X-ray crystallographic analysis of apo-P-gp with a resolution of 3.8 Å shows an internal cavity that is approximately 6,000 $Å^3$, with a separation of 30 Å between the two nucleotide binding domains (NBD). In addition, two additional P-gp structures, which complex with cyclic peptide inhibitors, illustrate different drug binding sites within the inner cavity that have a stereoselectivity influenced by hydrophobic and aromatic interactions. Therefore, the P-gp protein, which has the ability to absorb a variety of substrates, is a defining feature of its function and makes a structural understanding of the poly-specific drug binding necessary for the rational development of anticancer agents and MDR inhibitors (PDB ID: 3G5U), chosen for the present study.

2.4.1 Protein preparation

The crystal structure of the P-gp (PDB ID: 3G5U) was acquired from the Protein Data Bank (Aller et al., 2009). To prepare the protein for docking studies, we initially introduced hydrogen atoms, applied Kollman charges, and eliminated water molecules. Subsequently, we saved the modified structure in PDBQT format after addressing the missing atoms (Sastry et al., 2013).

2.4.2 Ligand preparation

The ligands 2D chemical structures were created utilizing ChemDraw. Subsequently, the 2D representations of CBZ and their corresponding analogues were converted into 3D structures through Chem3D software. The newly developed CBZ bioisosteres underwent energy minimization in Chem3D and were subsequently saved in SDF format. Using OpenBabel, the ligands were transformed into MOL2 format (Zielesny, 2005). These ligands were then incorporated into ADV tool and saved in pdbqt format to facilitate the docking process. Additionally, protein was

also dragged into the ADV tool, and a grid box was prepared that defines the boundary for the docking process.

2.4.3 Protein–ligand interactions using ADV

Utilizing the ADV software, we conducted docking study involving the ligands and the protein. The entire active site of the protein was encompassed within a grid box with the size of dimensions at X = 84, Y = 84 and Z = 84. The center of the grid was positioned at X = 28, Y = 86, and Z = 40. The default configurations for other docking parameters, such as ADV settings, crossover rates, and gene mutation rates, were maintained. The interaction between ligand and amino acid residue of protein were studied using Discovery Studio to produce 2D and 3D pose of interactions. The binding site of the target protein includes LEU64, PHE724, GLN942, MET945, PHE974 and VAL978, which are used to determine potential binding sites of the target protein with respect to the designed ligands (Xiang et al., 2015).

2.5 Molecular dynamics (MD) simulation

The MD simulation aims to explore the dynamic behavior and stability of protein-ligand complexes. We selected three complexes based on their interaction profiles and docking scores. The simulations were executed on an Acer workstation operating with Ubuntu 22.04. The Desmond program, part of the Schrödinger suite, was utilized to perform the MD simulations and to assess the docking of molecules, evaluating the efficacy of the predicted ligands (Elekofehinti et al., 2021). The protein-ligand complexes were constructed using the 'System Builder' tool. Following a reduction in volume, we opted for the SPC water model configured in an orthorhombic arrangement. The periodic boundary conditions for the X, Y, and Z-axes of the protein-ligand complex were established at 10 × 10 × 10 Å. Additionally, the crystal structure of the P-gp (PDB ID: 3G5U) served as a reference, illustrating its ability to accommodate 50.447 mM sodium and 53.855 mM chloride ions. Ions and salts within a 20 Å radius were omitted from the neutralization simulation. Before commencing the MD simulations, we applied the OPLS 2005 force field to minimize the energy of the complex, facilitating its transition to an equilibrium state. The OPLS 2005 force field, known as Optimized Potentials for Liquid Simulations, is a well-known force field in molecular mechanics designed to effectively simulate molecular interactions, particularly in the context of small organic molecules and biomolecular systems. This version represents an advance over the original OPLS force field and provides greater precision for simulations (González, 2011; Banks et al., 2005). To refine the complexes, we employed a minimization approach based on the steepest descent method. The complexes were subsequently heated to 300 K, achieving equilibrium after 1000 steps, with a time step of 100 ns. The final production run for the complexes was carried out over a period of 100 ns.

2.5.1 Binding free energy calculations

The binding affinity of ligand-protein complexes, represented by binding free energy, was assessed through the binding energies protocol available in the Desmond program. The complexes CBZ01-3G5U and CBZ13-3G5U, which were produced following molecular dynamics (MD) simulations, underwent analysis for binding energy estimation. Both Poisson-Boltzmann and generalized Born models, in conjunction with surface area continuum solvation methods (MM-PBSA and MM-GBSA), were utilized for solvation analysis. Furthermore, binding energy calculations were performed without considering solvation effects. The free energy derived from the MM-PBSA method was computed using the gmx_MMPBSA tool, which necessitates the input of ".top" and ".trr" files. To generate these files, the Desmond Composite Model System files (.cms) were initially converted using the InterMol software (https://github.com/shirtsgroup/InterMol), leading to the creation of ".gro" and ".top" files. Subsequently, the Desmond trajectory was imported into VMD and saved in the ".trr" format. After preparing all required input files, MM-GBSA calculations were carried out using the gmx_MMPBSA tool. The MM-GBSA approach integrates molecular dynamics simulations with thermodynamic principles, enabling the calculation of the total binding free energy between a ligand and a protein, as illustrated in Equation 1 (Wang et al., 2019; Bouricha and Hakmi, 2024; Matore et al., 2023).

$$\Delta G_{binding} = \Delta G_{MM} + \Delta G_{sol} - T\Delta G \quad (1)$$

3 Results and discussion

3.1 Bioisosteres of cabozantinib

Bioisosterism represents a strategy in medicinal chemistry that employs a lead compound as a primary method for molecular modification, aimed at the rational development of new pharmaceuticals (Karmacharya et al., 2021). We have applied the bioisosterism to improve ADMET profile and reduce undesirable toxic effects. MolOpt produced 592 analogues of CBZ, targeting various groups including phenyl, amide cyclopropyl, and cyclopropyl within the CBZ drug framework. The compounds that were screened are detailed in Supplementary Table S1.

3.2 Physicochemical properties prediction

The aim of molecular property prediction is to ascertain the physicochemical, bioactive, toxicological, and other characteristics of a target compound based on its molecular structure. Supplementary Table S1 presents the predicted molecular properties for CBZ bioisosteres. All analogues complies with Lipinski's rule of five, suggesting that these drug candidates possess favorable absorption and bioavailability. Furthermore, all analogues demonstrated a commendable topological polar surface area (TPSA) score, highlighting their capability to permeate cell membranes and reach target sites in the body.

3.3 Medicinal properties prediction

In the initial stages of drug development, the selection of molecules based on their drug-likeness is of paramount importance. This concept encompasses eight characteristics that

10.3389/fchem.2025.1543075

TABLE 1 Medicinal, drug likeness (DL) and drug score (DS) properties of CBZ analogues.

Compound no.	QED	Synth	MCE-18	Lipinski	Pfizer	GSK	GT	DL	DS
CBZ01	0.45	2.97	70	0	0	1	1	4.56	0.59
CBZ02	0.45	2.82	71	0	0	1	1	4.45	0.49
CBZ03	0.30	3.80	99	0	0	1	1	2.40	0.51
CBZ04	0.36	3.20	82	0	0	1	1	−3.09	0.22
CBZ05	0.46	3.28	99	0	0	1	0	3.68	0.52
CBZ06	0.36	2.91	64	0	0	1	0	4.14	0.21
CBZ07	0.35	3.02	66	1	0	1	1	3.44	0.24
CBZ08	0.31	3.04	66	1	0	1	1	3.45	0.23
CBZ09	0.35	2.98	66	0	0	1	1	3.52	0.19
CBZ10	0.34	2.85	66	0	0	1	1	2.83	0.41
CBZ11	0.26	3.12	57	0	0	1	1	0.85	0.44
CBZ12	0.32	3.23	96	0	0	1	0	2.53	0.46
CBZ13	0.43	3.66	102	0	0	1	1	3.76	0.45
CBZ14	0.33	3.33	82	0	0	1	0	3.85	0.53
CBZ15	0.35	2.83	57	0	0	1	0	2.73	0.56
CBZ16	0.22	3.40	83	0	0	1	0	0.89	0.29
CBZ17	0.34	2.90	61	0	0	1	1	−21.00	0.22
CBZ18	0.28	3.35	89	0	0	1	1	0.31	0.41
CBZ19	0.28	3.02	56	0	0	1	1	3.06	0.20
CBZ 20	0.33	2.89	65	0	0	1	1	2.70	0.37
CBZ21	0.36	2.91	54	0	0	1	1	−0.34	0.30
CBZ22	0.32	2.92	65	0	0	1	1	4.86	0.43
CBZ23	0.41	3.67	101	0	0	1	1	3.48	0.50
CBZ24	0.41	3.31	99	0	0	1	1	2.23	0.45
CBZ25	0.31	3.16	79	0	0	1	0	−0.37	0.41
CBZ26	0.33	2.98	64	1	0	1	1	1.11	0.15
CBZ27	0.35	3.14	79	0	0	1	0	−108.00	0.37
CBZ28	0.28	3.31	79	0	0	1	0	2.33	0.47
CBZ29	0.38	3.03	79	0	0	1	0	2.16	0.49
CBZ30	0.35	2.90	64	0	0	1	1	1.12	0.35
CBZ31	0.39	3.11	79	0	0	1	0	2.49	0.59
CBZ32	0.14	2.72	68	0	0	1	1	0.00	0.29
CBZ33	0.21	3.15	95	0	0	1	1	1.70	0.39
CBZ34	0.21	3.05	56	0	0	1	1	−2.47	0.13
CBZ35	0.24	2.85	54	0	0	1	0	3.19	0.54
CBZ36	0.31	2.58	55	0	0	1	0	−51.00	0.19
CBZ37	0.31	3.41	88	0	0	1	1	1.88	0.41
CBZ38	0.23	2.86	65	0	0	1	1	2.05	0.24

(Continued on following page)

TABLE 1 (*Continued*) Medicinal, drug likeness (DL) and drug score (DS) properties of CBZ analogues.

Compound no.	QED	Synth	MCE-18	Lipinski	Pfizer	GSK	GT	DL	DS
CBZ39	0.21	3.16	95	0	0	1	1	2.18	0.39
CBZ40	0.25	2.87	63	0	0	1	1	1.33	0.33
CBZ41	0.30	2.51	63	0	0	1	1	2.31	0.35
CBZ42	0.31	2.62	63	0	0	1	1	1.67	0.37
CBZ43	0.32	3.01	67	0	0	1	1	2.55	0.32
CBZ44	0.27	2.66	65	0	0	1	1	1.53	0.34
CBZ45	0.24	3.25	65	1	0	1	1	4.13	0.41
CBZ46	0.30	2.90	67	0	0	1	1	3.72	0.37
CBZ47	0.24	3.26	64	1	0	1	1	−2.47	0.06
CBZ48	0.33	3.10	83	0	0	1	1	0.19	0.45
CBZ49	0.19	3.44	89	0	0	1	1	−6.42	0.22
CBZ50	0.37	3.37	85	0	0	1	1	2.57	0.46
CBZ 51	0.16	3.09	57	0	0	1	1	2.61	0.39
CBZ52	0.32	2.70	48	0	0	1	0	1.88	0.35
CBZ53	0.26	2.94	48	0	0	1	0	3.10	0.37
CBZ54	0.32	2.84	48	0	0	1	0	1.40	0.41
CBZ55	0.33	2.56	26	0	0	1	1	2.11	0.21
CBZ56	0.30	2.33	27	0	0	1	1	6.20	0.42
CBZ57	0.33	3.11	95	0	0	1	1	5.23	0.33
CBZ58	0.33	2.94	90	0	0	1	1	4.57	0.29
CBZ59	0.38	2.43	24	0	0	1	0	2.66	0.21
CBZ60	0.22	3.13	107	0	0	1	1	4.64	0.23
CBZ61	0.34	2.64	26	0	0	1	1	0.76	0.19
CBZ62	0.27	2.99	91	0	0	1	1	1.85	0.09
CBZ63	0.27	2.99	91	0	0	1	1	−3.64	0.03
CBZ64	0.18	2.62	26	1	0	1	1	−4.51	0.05
CBZ65	0.19	3.02	52	1	0	1	1	−4.51	0.05
CBZ66	0.19	3.02	52	1	0	1	1	1.89	0.05
CBZ67	0.30	2.60	63	0	0	1	1	4.89	0.41
CBZ68	0.28	3.06	52	0	0	1	1	-	-
CBZ69	0.27	3.35	52	0	0	1	1	−5.82	0.10
CBZ70	0.22	2.80	48	0	0	1	1	1.40	0.41
CBZ71	0.32	2.84	48	0	0	1	1	3.10	0.37
CBZ72	0.26	2.94	48	0	0	1	1	3.64	0.42
CBZ73	0.11	3.12	48	0	0	1	1	−1.18	0.15
CBZ74	0.33	2.86	48	0	0	1	1	2.94	0.42
CBZ75	0.29	2.86	48	0	0	1	1	3.39	0.30
CBZ76	0.31	2.48	24	0	0	1	1	4.36	0.44

(Continued on following page)

TABLE 1 (*Continued*) Medicinal, drug likeness (DL) and drug score (DS) properties of CBZ analogues.

Compound no.	QED	Synth	MCE-18	Lipinski	Pfizer	GSK	GT	DL	DS
CBZ77	0.29	2.86	48	0	0	1	1	2.97	0.09
CBZ78	0.22	2.87	48	0	0	1	1	3.34	0.41
CBZ79	0.27	3.17	52	0	0	1	1	−32.00	0.14
CBZ80	0.17	3.14	54	1	0	1	1	3.53	0.03
CBZ81	0.28	3.07	54	0	0	1	1	2.21	0.20
CBZ	0.31	2.42	63	0	0	1	1	2.08	0.34

QED, a measure of drug-likeness based on the concept of desirability; Synth, synthetic accessibility score; Fsp3, number of sp3 hybridized carbons/total carbon count; MCE-18, medicinal chemistry evolution in 2018; GT, golden triangle; DL, drug likeness; DS, drug score.

are indicative of drug-related properties. The quantitative estimation of drug-likeness (QED) scores for the designed analogues, including CBZ01-02, CBZ05, and CBZ23-CBZ24, fall below the desirable QED score threshold (>0.67) but exceed the score of a standard drug (0.31). In the realm of drug design, predicting synthetic accessibility is a vital task that entails evaluating the ease of laboratory synthesis for a specific molecule. The synthetic accessibility scores for all designed analogues were determined to be within an acceptable range (<6). A research team from the Medicinal Chemistry Department of *in silico* Medicine has introduced the original descriptor MCE-18, which outlines the essential features of "next-generation" molecules and examines the evolution of medicinal chemistry over time (Ivanenkov et al., 2019). We utilized MCE-2018 to evaluate the efficacy of newly designed molecules such as CBZ03-04, CBZ05, CBZ12-14, CBZ16, CBZ18, CBZ23-25, CBZ27-29, CBZ31, CBZ33, CBZ37, CBZ39, CBZ48, CBZ49-50, CBZ57, and CBZ63, which yielded scores exceeding 63. Consequently, these analogues require visual inspection to determine their drug-likeness and target profiles. With the exception of CBZ07, CBZ08, CBZ26, CBZ45, CBZ47, CBZ64-66 and CBZ80, all designed analogues met the acceptance criteria of Lipinski's rule of five (Karami et al., 2022). Additionally, Pfizer's rule was satisfied by all analogues, indicating favorable physicochemical properties with potential for cellular permeability. The GT rule found accepted for anlogues such as CBZ05-06, CBZ12, CBZ14-16, CBZ25, CBZ27-29, CBZ31, CBZ35-36, CBZ52-54, and CBZ59. The medicinal properties of CBZ analogues are presented in Table 1.

3.4 Prediction of DS and DL score

DL and DS are qualitative metrics utilized in drug design to assess the "drug-like" characteristics of a molecule, particularly in relation to factors such as bioavailability. These metrics are extensively integrated into the early stages of lead and drug discovery (Bickerton et al., 2012). During the initial phases of drug development, it is essential to screen compounds based on their drug-likeness and DS. Accurately predicting a compound's drug-likeness is vital, as it offers valuable insights that can enhance the likelihood of transforming lead compounds into viable drugs, necessitating various drug-like attributes (Lagu et al., 2022). The DL score of compounds can indicate their potential effectiveness and safety. The DS serves as a comprehensive metric that consolidates factors such as toxicity concerns, cLogP, logs, molecular weight, and drug-likeness into a singular value. Among the analogues, CBZ56-57 and CBZ69 exhibit higher DL scores, while CBZ01-02, CBZ22, CBZ45, CBZ67, and CBZ76 demonstrate scores ranging from 4 to 4.5, surpassing the standard drug CBZ, which has a score of 2.08. The DL and DS scores of analogues are tabulated in Table 1.

3.5 Pharmacokinetic profile

Pharmacokinetics plays a crucial role in the drug discovery process by guiding the optimization of a compound's absorption, distribution, metabolism, and excretion (ADME) properties. The primary objective is to ensure that a lead compound achieves a concentration-time profile within the body that supports the desired efficacy and safety outcomes. By incorporating ADMET data into the drug design framework, researchers can improve a compound's solubility, permeability, and stability, ultimately developing clinical drug candidates capable of maintaining therapeutic concentrations for the required duration while minimizing potential risks. The predictable Caco-2 permeability scores offer valuable insights into the ability of substances to traverse intestinal cell membranes, which is a critical aspect of oral drug absorption. The Caco-2 scores for compounds CBZ01, CBZ04, CBZ06-15, CBZ17, CBZ19-21, CBZ24-31, CBZ33, CBZ34, CBZ37-47, CBZ49-51, CBZ55, CBZ64-66, CBZ77, and CBZ80 ≤ -5.15 log cm/s, indicating effective transport across intestinal membranes and favorable permeability. Conversely, the Caco-2 scores for compounds CBZ02, CBZ03, CBZ05, CBZ16, CBZ18, CBZ22, CBZ23, CBZ32, CBZ35, CBZ36, CBZ48, CBZ52-54, CBZ56-63, CBZ67-76, CBZ78, and CBZ79 fall ≥ -5.15, suggesting potentially poor permeability. Madin-Darby Canine Kidney (MDCK) cells are acknowledged as a reliable *in vitro* model for evaluating permeability, providing critical insights into the absorption efficiency of chemical substances within the body. The MDCK permeability scores for all evaluated compounds exceed 2×10^{-6} cm/s, indicating excellent MDCK permeability. This finding suggests that these compounds are likely to exhibit favorable permeability characteristics, making them promising candidates for effective systemic absorption.

The results show that all compounds reach a praising human intestinal absorption score (HIA) between 0 and 0.3, which indicates the significant potential for effective absorption in the human gastrointestinal tract. This favorable absorption profile implies that these compounds are likely to have high oral bioavailability, which is essential for the maintenance of the therapeutic drug level

TABLE 2 ADME properties of CBZ analogues.

Compound no.	Caco-2 (log cm/s)	MDCK	HIA	BBB	PPB (%)	VD (L/kg)	Fu (%)	CYP3A4	CL (mL/min/kg)	$T_{1/2}$
CBZ01	−5.02	Ex	Ex	0.07	91.41	0.24	7.63	+	3.38	1.31
CBZ02	−5.37	Ex	Ex	0.07	88.71	0.55	9.96	+	3.04	1.16
CBZ03	−5.37	Ex	Ex	0.06	80.73	0.59	17.74	+	2.39	1.83
CBZ04	−4.89	Ex	Ex	0.06	97.25	0.00	2.34	+	2.77	1.10
CBZ05	−5.24	Ex	Ex	0.02	88.73	0.54	10.07	+	2.89	1.21
CBZ06	−4.54	Ex	Ex	0.09	92.98	0.35	5.95	+	3.23	0.97
CBZ07	−4.83	Ex	Ex	0.07	91.47	0.36	6.92	+	2.04	1.31
CBZ08	−5.03	Ex	Ex	0.02	89.34	0.26	9.31	+	2.44	1.33
CBZ09	−4.69	Ex	Ex	0.16	93.15	0.52	5.41	+	1.76	1.24
CBZ10	−4.65	Ex	Ex	0.16	93.13	0.46	6.15	+	1.42	1.36
CBZ11	−4.59	Ex	Ex	0.00	93.90	0.18	4.97	+	2.46	1.16
CBZ12	−4.67	Ex	Ex	0.02	96.21	0.29	3.23	+	4.44	0.79
CBZ13	−4.91	Ex	Ex	0.03	90.99	0.70	6.71	+	3.13	1.01
CBZ14	−4.91	Ex	Ex	0.24	89.50	0.39	8.44	+	5.65	0.73
CBZ15	−5.05	Ex	Ex	0.06	84.21	0.18	17.03	+	3.45	0.80
CBZ16	−5.31	Ex	Ex	0.37	72.70	0.50	27.61	+	4.98	0.82
CBZ17	−4.69	Ex	Ex	0.00	93.73	0.07	5.58	+	2.32	1.08
CBZ18	−5.33	Ex	Ex	0.02	85.00	0.75	12.27	-	4.04	1.02
CBZ19	−4.71	Ex	Ex	0.43	95.71	0.22	3.60	+	4.67	0.58
CBZ 20	−4.64	Ex	Ex	0.35	91.97	0.49	7.16	+	2.91	0.93
CBZ21	−4.74	Ex	Ex	0.02	95.72	0.37	3.53	+	4.36	0.73
CBZ22	−5.17	Ex	Ex	0.01	96.48	0.01	3.09	+	3.51	1.04
CBZ23	−5.17	Ex	Ex	0.17	88.35	0.26	10.31	+	3.57	1.12
CBZ24	−5.02	Ex	Ex	0.40	91.97	0.40	6.55	+	5.13	0.69
CBZ25	−4.74	Ex	Ex	0.07	91.33	0.16	8.21	+	5.83	0.73
CBZ26	−4.92	Ex	Ex	0.03	87.00	−0.16	11.49	+	3.33	0.94
CBZ27	−5.06	Ex	Ex	0.02	76.44	0.17	22.43	+	5.97	0.85
CBZ28	−5.13	Ex	Ex	0.14	80.25	0.41	17.90	+	5.73	0.80
CBZ29	−4.77	Ex	Ex	0.03	93.92	0.15	4.63	+	5.67	0.71
CBZ30	−4.65	Ex	Ex	0.15	94.84	0.56	4.40	+	4.74	0.77
CBZ31	−4.66	Ex	Ex	0.11	91.72	0.11	7.59	+	5.63	1.00
CBZ32	−5.26	Ex	Ex	0.06	94.53	0.36	5.27	+	1.01	1.79
CBZ33	−4.80	Ex	Ex	0.07	92.09	0.57	6.40	+	1.84	1.14
CBZ34	−4.62	Ex	Ex	0.20	97.56	0.21	2.17	+	4.14	0.71
CBZ35	−5.20	Ex	Ex	0.12	86.91	0.37	12.34	+	5.93	0.69
CBZ36	−5.39	Ex	Ex	0.00	85.12	0.26	13.80	+	4.61	0.73
CBZ37	−5.04	Ex	Ex	0.04	91.72	0.17	7.03	+	2.86	1.10
CBZ38	−4.68	Ex	Ex	0.65	94.52	0.58	4.56	+	2.61	0.97

(Continued on following page)

TABLE 2 (*Continued*) ADME properties of CBZ analogues.

Compound no.	Caco-2 (log cm/s)	MDCK	HIA	BBB	PPB (%)	VD (L/kg)	Fu (%)	CYP3A4	CL (mL/min/kg)	$T_{1/2}$
CBZ39	−4.94	Ex	Ex	0.10	92.41	0.67	6.03	+	1.59	1.28
CBZ40	−4.62	Ex	Ex	0.04	95.30	−0.05	4.07	+	2.42	1.22
CBZ41	−4.93	Ex	Ex	0.08	97.88	0.00	1.92	+	4.24	0.76
CBZ42	−4.81	Ex	Ex	0.05	96.65	−0.06	3.03	+	3.24	1.01
CBZ43	−4.89	Ex	Ex	0.77	93.39	0.67	5.12	+	3.28	0.82
CBZ44	−5.04	Ex	Ex	0.19	92.78	0.04	6.05	+	3.48	0.95
CBZ45	−5.14	Ex	Ex	0.02	96.76	−0.02	3.11	+	4.48	1.06
CBZ46	−4.82	Ex	Ex	0.73	92.38	0.37	5.75	+	2.87	0.99
CBZ47	−4.74	Ex	Ex	0.70	93.98	−0.08	5.19	+	3.19	1.09
CBZ48	−5.58	Ex	Ex	0.00	85.52	−0.30	10.21	+	2.57	1.26
CBZ49	−4.92	Ex	Ex	0.01	97.26	0.39	2.34	+	2.35	1.38
CBZ50	−4.98	Ex	Ex	0.07	92.26	0.34	5.86	+	5.70	0.63
CBZ 51	−4.91	Ex	Ex	0.00	89.72	−0.61	7.26	+	0.85	1.68
CBZ52	−5.48	Ex	Ex	0.03	98.52	0.74	1.08	+	3.57	0.24
CBZ53	−5.36	Ex	Ex	0.11	98.17	0.66	1.46	+	3.14	0.20
CBZ54	−5.39	Ex	Ex	0.18	97.06	0.60	1.83	+	7.36	0.46
CBZ55	−5.03	Ex	Ex	0.01	99.24	0.33	0.52	+	3.93	0.21
CBZ56	−5.20	Ex	Ex	0.08	98.47	0.89	1.25	+	7.39	0.10
CBZ57	−5.34	Ex	Ex	0.02	97.99	0.48	1.31	+	2.36	0.16
CBZ58	−5.21	Ex	Ex	0.03	98.00	0.38	1.22	+	5.79	0.10
CBZ59	−5.30	Ex	Ex	0.04	97.88	0.48	2.58	+	3.08	0.20
CBZ60	−5.75	Ex	Ex	0.02	98.79	0.57	1.40	+	4.40	0.09
CBZ61	−5.33	Ex	Ex	0.01	98.83	0.28	1.10	+	2.56	0.16
CBZ62	−5.38	Ex	Ex	0.04	98.00	0.67	1.30	+	7.22	0.22
CBZ63	−5.33	Ex	Ex	0.11	98.96	0.53	2.54	+	1.93	0.12
CBZ64	−5.04	Ex	Ex	0.03	99.44	0.52	1.02	+	7.83	0.12
CBZ65	−5.04	Ex	Ex	0.03	99.44	0.52	1.02	+	7.83	0.12
CBZ66	−4.83	Ex	Ex	0.03	99.74	0.54	0.67	+	6.91	0.17
CBZ67	−5.42	Ex	Ex	0.44	95.38	2.31	2.29	+	10.00	0.27
CBZ68	−5.52	Ex	Ex	0.08	98.91	2.16	1.90	+	5.30	0.86
CBZ69	−5.44	Ex	Ex	0.03	98.83	0.63	1.12	+	2.94	0.17
CBZ70	−5.39	Ex	Ex	0.18	97.06	0.60	1.83	+	7.36	0.46
CBZ71	−5.36	Ex	Ex	0.11	98.17	0.66	1.46	+	3.14	0.20
CBZ72	−5.26	Ex	Ex	0.04	99.15	0.63	1.10	+	2.00	0.28
CBZ73	−5.35	Ex	Ex	0.05	98.04	0.46	1.65	+	4.85	0.22
CBZ74	−5.53	Ex	Ex	0.20	96.01	1.25	2.22	+	4.35	0.35
CBZ75	−5.31	Ex	Ex	0.02	98.65	0.49	0.99	+	7.00	0.18
CBZ76	−5.53	Ex	Ex	0.56	96.10	1.64	2.39	+	4.74	0.31

(Continued on following page)

TABLE 2 (*Continued*) ADME properties of CBZ analogues.

Compound no.	Caco-2 (log cm/s)	MDCK	HIA	BBB	PPB (%)	VD (L/kg)	Fu (%)	CYP3A4	CL (mL/min/kg)	$T_{1/2}$
CBZ77	−5.12	Ex	Ex	0.03	99.18	0.54	0.91	+	3.94	0.28
CBZ78	−5.42	Ex	Ex	0.04	98.41	0.51	1.37	+	4.10	0.27
CBZ79	−5.43	Ex	Ex	0.01	98.53	0.59	1.25	+	10.15	0.24
CBZ80	−4.69	Ex	Ex	0.04	99.20	0.59	0.70	+	7.33	0.14
CBZ81	−5.49	Ex	Ex	0.03	98.72	0.52	1.21	+	10.97	0.24
CBZ	−5.26	EX	Ex	0.04	97.74	1.00	1.20	+	3.51	0.18

Caco-2: the human colon adenocarcinoma cell lines; MDCK: madin-darby canine kidney cells; HIA: human intestinal absorption; PPB: plasma protein binding; BBB: blood–brain barrier; VD: volume distribution; Fu: the fraction unbound in plasms; Ex: excellent; (−): indicates inhibitor; (+): indicates substrate of human cytochrome P450 (five isozymes-1A2, 3A4, 2C9, 2C19 and 2D6); CL: the clearance of a drug; $T_{1/2}$: the half-life of a drug.

in systemic circulation. In addition, none of the compounds are classified as poorly absorbed (HIA+ with a value of more than 0.7), which reduces the likelihood of bioavailability problems associated with inadequate intestinal absorption. In addition, the results show that all compounds from 0 to 1 have values, which reflects the different probabilities of penetrating the blood-brain barrier (BBB). The findings further indicate that all compounds demonstrate the varying probabilities of traversing the blood-brain barrier (BBB). Plasma protein binding (PPB) is crucial in influencing the absorption, distribution, and pharmacodynamics of pharmaceuticals. The degree to which drugs associate with plasma proteins affects the concentration of the unbound drug that is available for therapeutic action. Compounds such as CBZ02, CBZ03, CBZ05, CBZ08, CBZ14-16, CBZ18, CBZ23, CBZ26, CBZ27, CBZ28, CBZ35, CBZ36, CBZ48, and CBZ51 demonstrate PPB values of 90% or less, indicating strong binding properties that promote an optimal equilibrium between the concentration of free drug and its therapeutic efficacy. In addition, compounds like CBZ34, CBZ41, CBZ52, CBZ53, CBZ55-66, CBZ68, CBZ69, CBZ71-73, CBZ75, and CBZ77-81 exhibit PPB values exceeding 90%, similar to CBZ, which has a PPB of 97.74%. The volume of distribution at steady state (VDss) serves as a pharmacokinetic indicator of how extensively a drug is distributed in the body relative to its plasma concentration. The expected VDss is measured in L/kg, with an optimal range of 0.04–20 L/kg indicated. All compounds show a projected VDSS score that falls in the range from 0.04 to 20 L/kg, which indicates superior distribution properties, with the exception of CBZ04, CBZ26, CBZ40-42, CBZ47, CBZ48 and CBZ51.

The unbound fraction (Fu) in plasma is a significant pharmacokinetic parameter that influences a drug's efficacy and distribution. It represents the proportion of a drug that remains unbound to serum proteins, enabling it to traverse cellular membranes and exert its pharmacological effects. The Fu values for compounds CBZ01-03, CBZ05-10, CBZ13-18, CBZ20, CBZ23-28, CBZ31-33, CBZ35-37, CBZ39, CBZ43, CBZ44, CBZ46-48, CBZ50, and CBZ51 are greater than 5%. These compounds exhibit favorable unbound drug fractions, suggesting their potential to effectively penetrate cellular membranes and reach their designated targets, thereby indicating their promise for further drug development. In contrast, other compounds, including CBZ, present Fu values below 5%. The results show that all compounds serve as substrates for CYP3A4, a key and prevailing enzyme within the CYP450 family, which is essential for the metabolism of phase I. CYP3A4 is crucial for the oxidative metabolism of numerous medicines and endogenous compounds that occur mainly in the liver and intestine.

Plasma clearance (CL) is an indicator of the body's ability to eliminate a drug from the plasma. This parameter directly affects the overall drug exposure and is crucial for determining the appropriate dosage required to maintain a stable plasma concentration. The compounds CBZ01-13, CBZ15-23, CBZ26, CBZ30, CBZ32-34, CBZ36-49, CBZ51-53, CBZ55, CBZ57, CBZ59-61, CBZ63, CBZ69, CBZ71-74, and CBZ76-78 exhibit CL scores ranging from 0 to 5 mL/min/kg, indicating excellent clearance profiles. Their elimination rates are effectively regulated, ensuring consistent drug exposure and optimal dosing. The half-life ($T_{1/2}$) serves as a measure of the interplay between clearance and volume of distribution. A precise evaluation of these two parameters provides comprehensive insight into the pharmacokinetics of drugs within the body. The T1/2 values for the compounds CBZ01-11, CBZ13, CBZ17, CBZ18, CBZ20, CBZ22, CBZ23, CBZ26, CBZ31-33, CBZ37-40, CBZ42, CBZ44-49, and CBZ51 exceed 0.903, indicating that these compounds are suitable for dosing that maintains therapeutic drug levels. In contrast, the remaining compounds exhibit $T_{1/2}$ values below 0.903, similar to that of CBZ, which implies the need for multiple dosing strategies. The pharmacokinetic (ADME) profile of CBZ analogues is mentioned in Table 2.

3.6 Prediction of toxicity characteristics

In the initial stages of drug development, it is essential to precisely predict the ADMET properties to identify molecules that exhibit optimal pharmacokinetics while minimizing toxicity. The results indicated that all analogues exhibited lower human hepatotoxicity (H-HT) and drug-induced liver injury (DILI), compared to the reference drug (CBZ), suggesting a reduced risk of toxicity. The hERG (cardiotoxicity) score of all compounds, such as CBZ07, CBZ09, CBZ10, CBZ14, CBZ15, CBZ17, CBZ19, CBZ25-27, CBZ29, CBZ34, CBZ36, CBZ40, CBZ43, CBZ45-48, CBZ50, CBZ51, CBZ57, CBZ63-65, CBZ69 and CBZ72 show less than 0.3, indicating a lower risk of cardiotoxicity compared to the standard drug (0.604). Researchers have advocated for the use of mutagenicity

TABLE 3 Toxicity profile of CBZ analogues.

Compound no.	H-HT	DILI	hERG	Ames	ROA	Carc	NR-AR	NR-AR-LBD
CBZ01	0.64	0.61	0.376	0.77	0.86	0.72	0.12	0.00
CBZ02	0.75	0.34	0.587	0.58	0.90	0.52	0.18	0.01
CBZ03	0.66	0.86	0.421	0.96	0.93	0.43	0.00	0.00
CBZ04	0.72	0.71	0.336	0.59	0.80	0.39	0.02	0.00
CBZ05	0.71	0.45	0.557	0.67	0.86	0.44	0.15	0.00
CBZ06	0.76	0.87	0.376	0.81	0.75	0.60	0.02	0.00
CBZ07	0.70	0.88	0.128	0.83	0.70	0.78	0.03	0.00
CBZ08	0.74	0.88	0.657	0.84	0.71	0.78	0.02	0.00
CBZ09	0.78	0.86	0.215	0.83	0.72	0.76	0.05	0.00
CBZ10	0.80	0.90	0.196	0.77	0.72	0.72	0.09	0.00
CBZ11	0.69	0.82	0.499	0.86	0.81	0.62	0.00	0.00
CBZ12	0.79	0.67	0.428	0.65	0.73	0.51	0.15	0.01
CBZ13	0.74	0.51	0.355	0.58	0.79	0.44	0.14	0.00
CBZ14	0.70	0.60	0.288	0.68	0.83	0.43	0.01	0.00
CBZ15	0.60	0.73	0.134	0.82	0.79	0.55	0.01	0.00
CBZ16	0.79	0.47	0.316	0.84	0.86	0.63	0.00	0.00
CBZ17	0.68	0.73	0.134	0.83	0.85	0.64	0.02	0.00
CBZ18	0.74	0.60	0.316	0.59	0.72	0.50	0.09	0.01
CBZ19	0.68	0.71	0.208	0.74	0.81	0.55	0.05	0.00
CBZ 20	0.81	0.88	0.343	0.85	0.79	0.72	0.07	0.00
CBZ21	0.68	0.75	0.393	0.65	0.72	0.62	0.10	0.00
CBZ22	0.76	0.83	0.357	0.83	0.82	0.72	0.00	0.00
CBZ23	0.73	0.55	0.458	0.66	0.79	0.64	0.06	0.00
CBZ24	0.69	0.30	0.555	0.66	0.87	0.53	0.02	0.00
CBZ25	0.67	0.42	0.260	0.81	0.75	0.59	0.06	0.01
CBZ26	0.77	0.82	0.240	0.80	0.83	0.60	0.00	0.00
CBZ27	0.78	0.47	0.223	0.83	0.61	0.65	0.11	0.01
CBZ28	0.73	0.64	0.345	0.69	0.81	0.42	0.01	0.00
CBZ29	0.71	0.33	0.271	0.75	0.71	0.57	0.04	0.01
CBZ30	0.65	0.61	0.421	0.47	0.71	0.79	0.03	0.00
CBZ31	0.70	0.63	0.327	0.77	0.71	0.63	0.04	0.00
CBZ32	0.73	0.89	0.312	0.76	0.80	0.47	0.11	0.00
CBZ33	0.70	0.74	0.475	0.74	0.71	0.51	0.11	0.00
CBZ34	0.70	0.61	0.299	0.57	0.80	0.42	0.11	0.00
CBZ35	0.65	0.37	0.335	0.82	0.78	0.65	0.01	0.00
CBZ36	0.51	0.61	0.141	0.94	0.94	0.60	0.03	0.00
CBZ37	0.80	0.80	0.303	0.66	0.71	0.58	0.01	0.00
CBZ38	0.69	0.87	0.357	0.79	0.73	0.58	0.03	0.00

(Continued on following page)

TABLE 3 (*Continued*) Toxicity profile of CBZ analogues.

Compound no.	H-HT	DILI	hERG	Ames	ROA	Carc	NR-AR	NR-AR-LBD
CBZ39	0.71	0.68	0.367	0.72	0.69	0.53	0.17	0.00
CBZ40	0.65	0.82	0.263	0.87	0.86	0.63	0.01	0.00
CBZ41	0.79	0.89	0.672	0.87	0.67	0.72	0.02	0.00
CBZ42	0.79	0.90	0.382	0.77	0.83	0.49	0.01	0.00
CBZ43	0.81	0.83	0.272	0.79	0.82	0.72	0.11	0.00
CBZ44	0.76	0.84	0.359	0.84	0.79	0.54	0.03	0.00
CBZ45	0.70	0.78	0.233	0.80	0.75	0.79	0.00	0.00
CBZ46	0.78	0.84	0.264	0.84	0.78	0.71	0.02	0.00
CBZ47	0.72	0.66	0.243	0.80	0.78	0.68	0.00	0.00
CBZ48	0.73	0.87	0.165	0.53	0.73	0.39	0.00	0.00
CBZ49	0.80	0.79	0.329	0.64	0.68	0.39	0.01	0.00
CBZ50	0.73	0.23	0.250	0.82	0.98	0.67	0.02	0.01
CBZ 51	0.70	0.87	0.169	0.76	0.80	0.68	0.20	0.03
CBZ52	0.92	0.96	0.609	0.88	0.46	0.57	0.69	0.06
CBZ53	0.95	0.96	0.421	0.93	0.27	0.12	0.23	0.10
CBZ54	0.80	0.94	0.691	0.87	0.68	0.48	0.52	0.06
CBZ55	0.89	1.00	0.482	0.01	0.13	0.22	0.55	0.06
CBZ56	0.91	0.98	0.867	0.26	0.19	0.76	0.33	0.05
CBZ57	0.84	0.98	0.277	0.11	0.27	0.74	0.04	0.01
CBZ58	0.84	0.94	0.796	0.89	0.25	0.42	0.70	0.14
CBZ59	0.94	0.98	0.430	0.62	0.40	0.88	0.69	0.13
CBZ60	0.92	0.98	0.742	0.34	0.29	0.86	0.55	0.47
CBZ61	0.89	0.98	0.525	0.40	0.75	0.74	0.45	0.15
CBZ62	0.91	0.96	0.530	0.90	0.67	0.89	0.44	0.12
CBZ63	0.30	0.97	0.007	0.68	0.75	0.27	0.33	0.18
CBZ64	0.32	0.96	0.182	0.86	0.43	0.40	0.24	0.18
CBZ65	0.32	0.96	0.182	0.86	0.43	0.40	0.24	0.18
CBZ66	0.52	0.96	0.326	0.92	0.60	0.56	0.62	0.15
CBZ67	0.93	0.81	0.798	0.87	0.64	0.43	0.01	0.00
CBZ68	0.80	0.93	0.337	0.81	0.48	0.06	0.01	0.00
CBZ69	0.78	0.96	0.106	0.76	0.31	0.35	0.43	0.07
CBZ70	0.80	0.94	0.691	0.87	0.68	0.48	0.52	0.06
CBZ71	0.95	0.96	0.421	0.93	0.27	0.12	0.23	0.10
CBZ72	0.93	0.96	0.245	0.93	0.22	0.67	0.04	0.05
CBZ73	0.91	0.97	0.457	0.93	0.45	0.06	0.23	0.07
CBZ74	0.84	0.94	0.730	0.91	0.70	0.27	0.58	0.03
CBZ75	0.76	0.98	0.608	0.85	0.25	0.57	0.72	0.03
CBZ76	0.97	0.93	0.836	0.87	0.61	0.07	0.04	0.01

(Continued on following page)

TABLE 3 (*Continued*) Toxicity profile of CBZ analogues.

Compound no.	H-HT	DILI	hERG	Ames	ROA	Carc	NR-AR	NR-AR-LBD
CBZ77	0.93	0.95	0.561	0.86	0.56	0.66	0.67	0.06
CBZ78	0.86	0.95	0.641	0.80	0.39	0.21	0.64	0.08
CBZ79	0.82	0.94	0.436	0.60	0.48	0.73	0.66	0.39
CBZ80	0.93	0.89	0.421	0.57	0.54	0.78	0.63	0.13
CBZ81	0.90	0.97	0.305	0.21	0.53	0.85	0.70	0.14
CBZ	0.81	0.91	0.604	0.82	0.81	0.90	0.48	0.30

H-HT: human hepatotoxicity; DILI: drug induced liver injury; hERG: cardiotoxicity; Ames: mutagenicity; ROA: rat oral acute toxicity; Carc.: carcinogenicity; NR-AR: nuclear receptor-androgen receptor; NR-AR-LBD: nuclear receptor-androgen receptor-ligand binding domain.

TABLE 4 Docking score and interaction of the selected CBZ analogues.

Compound no.	Docking score (kcal/mol)	Interactions with distance	
		Hydrogen bonding	Other interactions
CBZ01	−8.0	GLN942 (1.97Å), GLN128 (2.57Å), PHE938 (2.91Å), THR937 (2.96Å)	PHE934 (3.47Å)
CBZ06	−7.8	GLN942 (2.47Å and 2.7Å)	PHE938 (5.53Å), TRP132 (7.31Å)
CBZ11	−7.7	GLN942 (2.57Å), THR937 (2.78Å)	PHE938 (4.72Å), PHE934 (3.42Å)
CBZ13	−8.4	GLN942 (2.13Å), ASN347 (2.46Å)	GLU871 (3.64Å), GLY187 (3.54Å), PHE938 (3.55Å), VAL129 (4.40Å)
CBZ25	−6.4	GLN942 (2.48Å), PHE938 (3Å), THR937 (2.71Å)	PHE934 (3.65Å)
CBZ34	−7.2	GLN942 (2.25Å)	GLY187 (3.57Å), GLU871 (3.16Å), PHE938 (4.42Å)
CBZ38	−8.0	GLN942 (2.71Å and 2.80Å)	TRP132 (4.83Å), PHE190 (5.43Å)
CBZ	−7.5	GLN942 (1.86Å)	GLU871 (3.60Å), LEU875 (3.70Å), THR941 (3.97Å), PHE938 (5.12Å)

data as a relatively quick and cost-effective method to assess long-term human health risks, including cancer in somatic cells and heritable mutations in germ cells. Given the strong correlation between mutagenicity and carcinogenicity, this assay is frequently employed in evaluating the mutagenic potential of compounds. The mutagenicity scores for certain analogues, including CBZ02, CBZ05, CBZ12-14, CBZ18, CBZ21, CBZ23-24, CBZ28, CBZ30, CBZ34, CBZ48, CBZ49, CBZ56-57, CBZ59-61, CBZ63, and CBZ79-CBZ81, fall within a safer range (from 0 to 0.3), indicating their suitability for non-mutagenic effects. Assessing acute toxicity in mammals, such as rats or mice, is a critical component of the safety evaluation for drug candidates, with toxicity testing conducted to identify potential adverse reactions. The ROA scores (ranging from 0 to 0.3) for certain analogues, including CBZ53, CBZ55-58, CBZ60, CBZ72, and CBZ75, also indicate a safer profile. Carcinogenicity represents one of the numerous toxicological endpoints associated with chemicals, which raises considerable concern due to its harmful effects on human health. As the landscape of chemical exposure and cancer epidemiology evolves, it is imperative that the assessment of carcinogenicity adapts accordingly. The carcinogenicity scores (ranging from 0 to 0.3) for certain analogues, including CBZ53, CBZ55, CBZ63, CBZ68, CBZ71, CBZ73, CBZ74, and CBZ78, indicate a safer profile, making them appropriate for minimizing carcinogenic risks. The NR-AR and NR-AR-LBD scores of analogues found within the range of 0–0.3. The toxicity parameter scores are presented in Table 3.

3.7 Molecular docking analysis

Before the ligand's docking study begins, we ensured the validity of the docking procedure by downloading a co-crystalized ligand receptor complex from the protein database (PDB ID: 3G5U). The structure of the co-crystallized ligand and the associated protein was prepared and saved in pdbqt format. Then we carried out a redocking experiment with the native ligand, under which Autodock Vina was used to transform the original ligand into the active site of the protein. We then evaluated the docked pose against the crystallographic pose by calculating the Root Mean Square Deviation (RMSD). The results showed that the RMSD value of the optimal pose (0.48 Å) is within the acceptable threshold of 2 Å.

The interaction of designed ligands (Supplementary Table S1) and their docking score is being shown in Table 4, CBZ01 serves as a bioisostere of CBZ, characterized by the substitution of the phenyl group with a piperazine ring. The overall structure of CBZ01 closely resembles that of CBZ. Notably, the ligand CBZ01 exhibited the

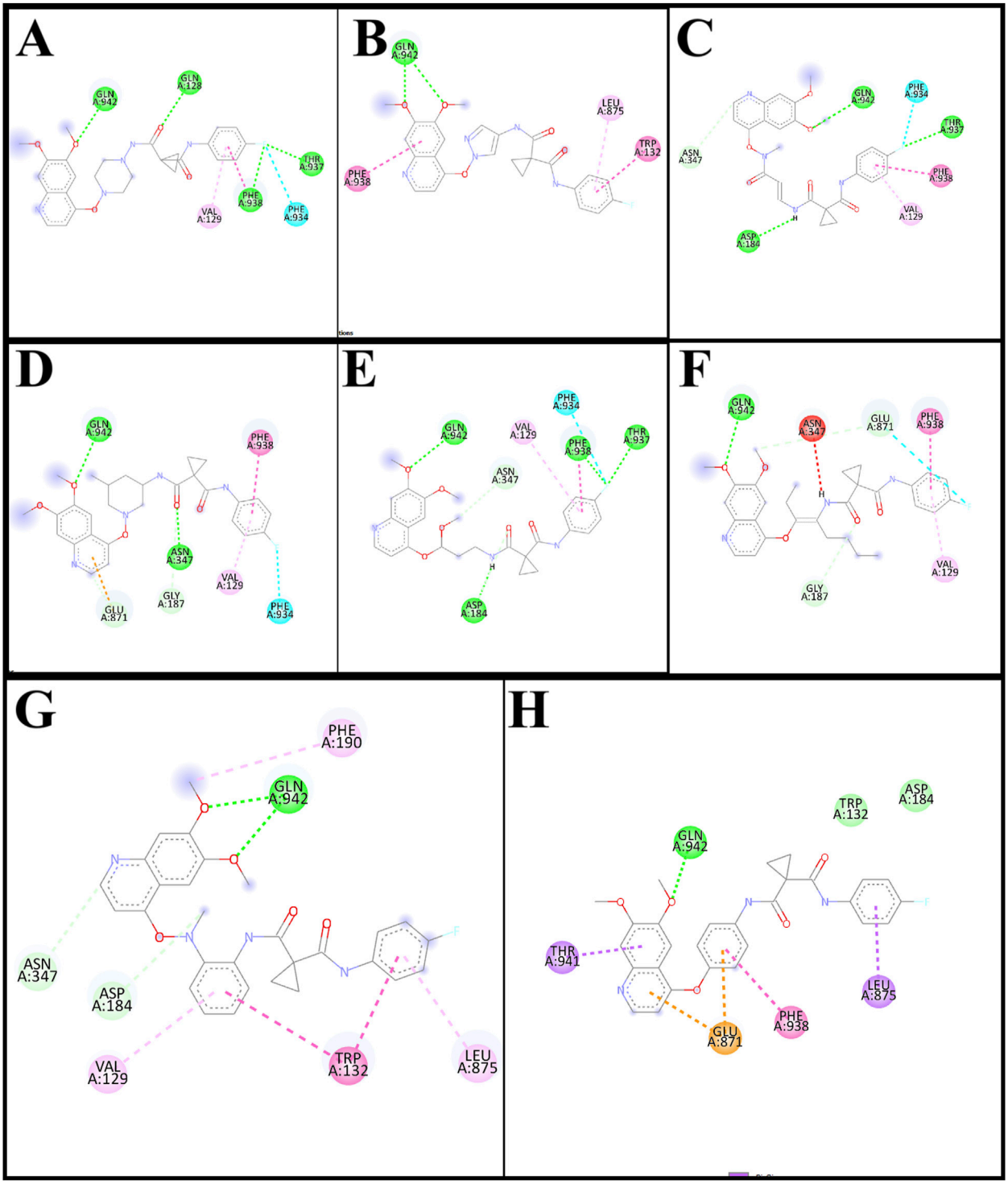

FIGURE 3
2D pose of ligands CBZ01 **(A)**, CBZ06 **(B)**, CBZ11 **(C)**, CBZ13 **(D)**, CBZ25 **(E)**, CBZ34 **(F)**, CBZ38 **(G)** and Cabozantinib **(H)**.

most favorable binding score of −8.0 kcal/mol. In the docked ADV complex, the residue GLN942 of the target protein forms hydrogen bonds with the oxygen of the methoxy group present in the quinoline ring of the ligand, with a distance of 1.9722 Å. The hydrogen bonds involving GLN942 are similar to those observed in CBZ. Additionally, residues GLN128 (2.5708 Å), PHE938 (2.9146 Å), and THR (2.9649 Å) demonstrated other hydrogen bond interactions with the carbonyl, phenyl, and fluorine atoms of the analogue. Furthermore, PHE934 established a halogenic bond with the fluorine atom of the fluorophenyl group of the ligand at a distance of 3.4667 Å. Figures 3A, 4A depict the 2D and 3D pose of the CBZ01, respectively.

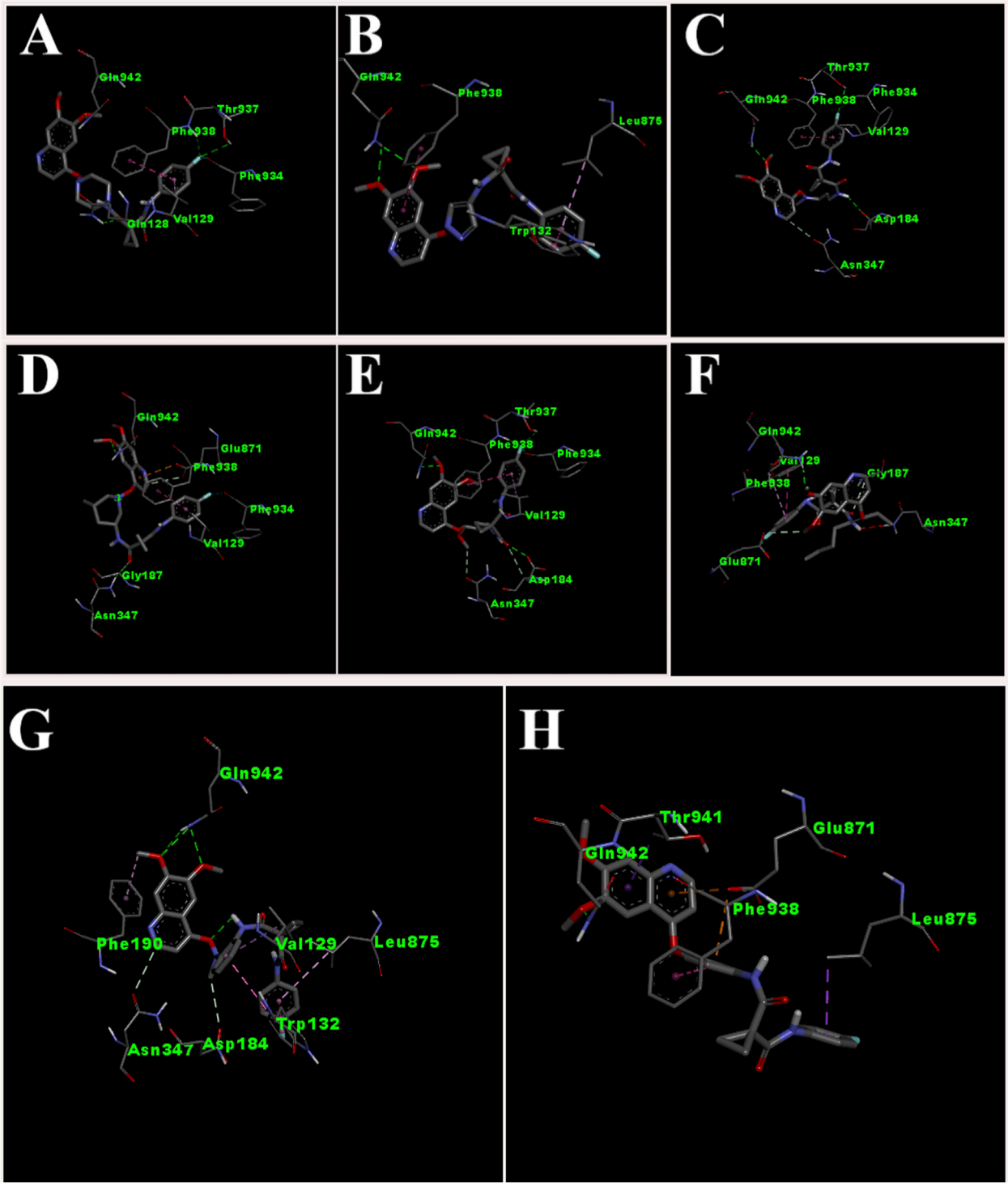

FIGURE 4
3D pose of ligands CBZ01 **(A)**, CBZ06 **(B)**, CBZ11 **(C)**, CBZ13 **(D)**, CBZ25 **(E)**, CBZ34 **(F)**, CBZ38 **(G)** and Cabozantinib **(H)**.

CBZ06 serves as a bioisostere of CBZ, characterized by the substitution of the phenyl group with a pyrazole ring. The overall structure of CBZ06 closely resembles that of CBZ. Notably, the ligand CBZ06 exhibited the most advantageous binding score of −7.8 kcal/mol. In the docked ADV complex, the residue GLN942 of the target protein establishes hydrogen bonds with the oxygen atoms of the methoxy groups present in the quinoline ring, at distances of 2.4658 Å and 2.7057 Å. The hydrogen bonding interactions involving GLN942 are similar to those observed with CBZ. Additionally, residues PHE938 (5.5257 Å) and TRP132 (7.031 Å) demonstrate π-π stacking interactions with the quinoline and phenyl rings of CBZ, respectively. Figures 3B, 4B

depict the 2D and 3D interactions of the ligand CBZ06, respectively.

CBZ11 serves as a bioisostere of CBZ, characterized by the substitution of the phenyl ring with a methyl amino-3-oxoprop-1-en-1-yl group. The overall structure of CBZ11 closely resembles that of CBZ. Notably, the ligand CBZ11 exhibited the most favorable binding score of −7.7 kcal/mol. In the docked ADV complex, the residue GLN942 of the target protein forms hydrogen bonds with the oxygen atoms of the methoxy groups present in the quinoline ring of the ligands, maintaining a distance of 2.5741 Å. The hydrogen bonds formed with GLN942 which was similar observed in the standard (CBZ). Additionally, residue THR937 demonstrates another hydrogen bond interaction with the amino and fluorine atoms of the analogue at a distance of 2.7844 Å. Furthermore, PHE934 forms a halogenic bond with the fluorine atom of the fluorophenyl group of the ligand, measured at a distance of 3.4229 Å PHE938 also engages in a π-π stacked interaction with the phenyl ring of the fluorophenyl group of the ligand, at a distance of 4.7230 Å. Figures 3C, 4C depict the 2D and 3D pose of the CBZ11, respectively.

CBZ13 serves as a bioisostere of CBZ, characterized by the substitution of the phenyl ring with a methylpiperidin-3-yl group. The overall structure of CBZ13 closely resembles that of CBZ. Notably, the ligand CBZ13 exhibited the most advantageous binding score of −8.4 kcal/mol. In the docked ADV complex, the residue GLN942 of the target protein engages in hydrogen bonding with the oxygen atoms of the methoxy groups located on the quinoline ring of the ligands, maintaining a distance of 2.1263 Å. Additionally, residue ASN347, at a distance of 2.4628 Å, displays another hydrogen bond interaction with the carbonyl group of the analogues. Residues GLU871 (3.6375 Å) and GLY187 (3.5368 Å) exhibit C-H bonding interactions with the quinoline ring and the carbonyl group, respectively. Furthermore, PHE938 and VAL129 establish π-π stacking and π-alkyl interactions with the fluorophenyl group of the ligand, at distances of 3.5515 Å and 4.3974 Å, respectively. Figures 3D, 4D depict the 2D and 3D pose of the CBZ13, respectively.

CBZ25 serves as a bioisostere of CBZ, characterized by the substitution of the phenyl ring with a methoxy propyl group. The overall structure of CBZ25 closely resembles that of CBZ. Notably, the ligand CBZ25 exhibited the most favorable binding score of −6.4 kcal/mol. In the docked ADV complex, the residue GLN942 of the target protein forms hydrogen bonds with the oxygen atoms of the methoxy groups present in the quinoline ring of the ligand, with a distance of 2.4776 Å. Additionally, residue PHE938 (2.9955 Å) and THR937 (2.7086 Å) demonstrate other hydrogen bond interactions with the fluorine atom of the CBZ analogue. Furthermore, PHE934 establishes a halogen bond with the fluorine atom of the fluorophenyl group of the ligand at a distance of 3.6510 Å. Figures 3E, 4E depict the 2D and 3D pose of the ligand CBZ25, respectively.

CBZ34 serves as a bioisostere of CBZ, characterized by the substitution of the phenyl ring with an oct-3-en-4-yl group. The overall structure of CBZ34 closely resembles that of CBZ. Notably, the ligand CBZ34 exhibited the most favorable binding score of −7.2 kcal/mol. In the docked ADV complex, the residue GLN942 of the target protein forms hydrogen bonds with the oxygen atoms of the methoxy groups located on the quinoline ring of the ligands, with a distance of 2.2471 Å. Additionally, residue GLY187 demonstrated a C-H bond with the carbonyl group of the analogues at a distance of 3.5685 Å. Furthermore, GLU871 established a halogen bond with the fluorine atom of the fluorophenyl group of the ligand, at a distance of 3.1584 Å. Lastly, residue PHE938 exhibited a π-π interaction with the phenyl ring of CBZ34 at a distance of 4.4169 Å. Figures 3F, 4F depict the 2D and 3D pose of the CBZ34, respectively.

CBZ38 serves as a bioisostere of CBZ, characterized by the substitution of the phenyl ring with a methyl amino phenyl group. The overall structure of CBZ38 closely resembles that of CBZ. The ligand CBZ38 exhibited the most favorable binding score of −8.0 kcal/mol. In the docked ADV complex, the residue GLN942 of the target protein forms hydrogen bonds with the oxygen atoms of the methoxy groups present in the quinoline ring of the ligand, at distances of 2.7084 Å and 2.7971 Å. Additionally, residue TRP132 demonstrates a π-π interaction at a distance of 4.8259 Å, while PHE190 forms a π-alkyl bond with the methoxy group of the quinoline in the ligand at a distance of 5.4208 Å. Figures 3G, 4G depict the 2D and 3D poseof the CBZ38, respectively.

The docking interaction of the standard drug (CBZ) exhibited a favorable binding score of −7.5 kcal/mol. The residue GLN942 of the target protein engages in hydrogen bonding with the oxygen atom of the methoxy group present in the quinoline ring, with a distance of 1.861 Å. The hydrogen bonds involving GLN942 are consistent across all ligands. Additionally, the residue GLU871 demonstrates a π-anionic interaction at a distance of 3.60 Å. The residue PHE190 forms a π-π interaction with the phenyl ring of quinoline in CBZ at a distance of 5.12 Å, while LEU875 shows a π-σ interaction. Figures 3H, 4H illustrate the 2D and 3D pose of the standard drug CBZ, respectively.

The comprehensive docking analysis showed that the designed ligands of CBZ, especially CBZ01 and CBZ13, had multiple interactions compared to CBZ itself. In the case of CBZ01, four hydrogen bonds were identified with residues GLN942, GLN128, PHE938, and THR937 of the target protein with distances of 1.97, 2.57, 2.91, and 2.96 Å, respectively. Furthermore, CBZ13 exhibited two hydrogen bonds with the target protein residues GLN942 and ASN347 of the target protein with distances of 2.13 and 2.46 Å, respectively. In contrast, CBZ showed a single interaction with residue GLN942 at a distance of 1.86 Å through hydrogen bonding. This could be the result of a change in the docking score between the parent compound cabozantinib (−7.5) and its analogues CBZ1 (−8.0) and CBZ13 (−8.4). The common amino acid residue GLN942 matches the key residue reported by Xiang et al. (2015). The authors suggested that residue GLN942 may play a crucial role in the reversal of P-gp-mediated MDR by CBZ analogues, which is achieved by inhibiting P-gp transporter function. Further validation of the docking study of these two ligands was carried out using a molecular dynamics (MD) simulation study. Examination of the MD simulation study revealed that the analogues CBZ01 and CBZ13 were found to be stable over the period of 100 ns.

3.8 Molecular dynamics (MD) simulation

MD simulations represent a computational approach that effectively models the physical behaviour of atoms and molecules,

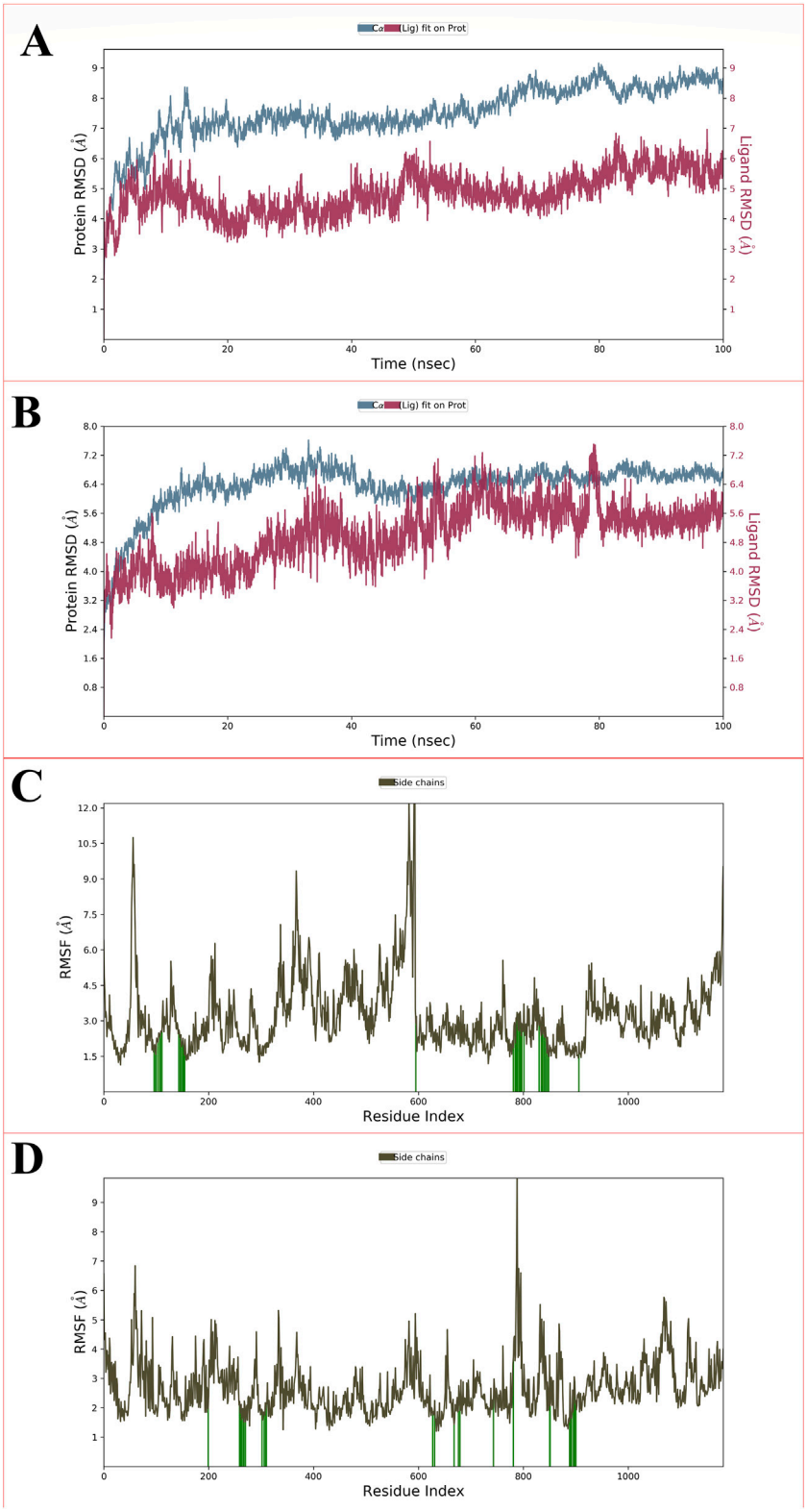

FIGURE 5
Showing the RMSD for P-glycoprotein with ligand CBZ01 **(A)** and ligand CBZ13 **(B)**; The protein-RMSF plot of P-glycoprotein concerning the CBZ01 **(C)** and ligand CBZ13 **(D)** throughout the 100 ns run.

thereby facilitating advancements in drug discovery. The dynamic properties of molecular atoms were investigated through MD simulations. This approach encompasses a series of algorithms aimed at assessing and predicting the stability of protein-ligand complexes. It is acknowledged as a powerful independent method for precisely detecting alterations at both molecular and atomic levels. To comprehend the stability of protein-ligand complexes, it is crucial to investigate the interactions between ligand molecules and proteins. The assessment of a ligand's stability and dynamic behaviour in relation to the protein relies heavily on MD simulations. We examined the MD simulation at 100 ns SPC water model-based simulation utilizing the simulation interaction diagram (SID). This examination yielded valuable insights into the deviations, fluctuations, and intermolecular interactions that transpired during the simulation. MD simulation was performed for the CBZ01, CBZ13, and CBZ38. Among these, the MD simulations for ligands CBZ01 and CBZ13 demonstrated stable complexes with the target protein, whereas the MD simulations for compound CBZ38 did not remain within the chosen parameters.

3.8.1 RMSD and RMSF

The root mean square deviation (RMSD) quantifies the deviation of an atom's molecule from its original structure or target over time. It is employed to evaluate the fluctuations in the protein's backbone (C and N) during the 100 nsrun. Throughout the MD simulation, only minor variations in RMSD values related to the protein backbone were detected. For the protein complexed with the CBZ01, the ligand displayed a fluctuation of 2.5 Å, while the backbone RMSD initially ranged from 0 to 4.2 Å at the 0.50 ns? In contrast, when the protein was associated with the ligand CBZ13, the initial RMSD deviations for the ligand and protein were recorded at 2.8 Å and 2.9 Å, respectively. The P-gp complexed with CBZ01 showed an average RMSD of 1.57 Å, whereas the ligand exhibited an RMSD of 2.03 Å at the 100 ns? Conversely, the P-gp in complex with CBZ13 demonstrated an average RMSD of 1.61 Å, with the ligand showing an RMSD of 0.75 Å at the same time point. Initially, a lower deviation was observed from 0 to 25 ns, with slight fluctuations noted for two frames. Stable complexes (CBZ01) were identified from 25 to 50 ns, followed by a consistent deviation value with minimal changes from 50 to 100 ns? In the case of complex CBZ13, a lower deviation was also noted from 0 to 25 ns, with slight fluctuations observed for three frames. Stable complexes (CBZ01) were again identified from 25 to 50 ns and from 50 to 80 ns, followed by a consistent deviation value with minor changes from 80 to 100 ns? Overall, a stable RMSD value with slight deviations was observed from 80 to 100 ns, indicating that both complexes-maintained stability throughout the 100 ns simulation. The RMSD values for ligands CBZ01 and CBZ13 are illustrated in Figures 5A, B, respectively.

The root mean square fluctuation (RMSF) serves to measure the fluctuation of individual residues from their average fluctuation over a specified time period. The peaks identified in the protein-RMSF graph indicate the residues that display the most significant fluctuations throughout the simulation. Secondary structural components, such as alpha helices and beta strands, tend to exhibit less fluctuation than loop regions, owing to their enhanced rigidity relative to the unstructured portions of the protein. The green vertical bars on the graph denote protein residues that interact with the ligand. The variability among the other amino acid residues is considerably lower, reflecting a diminished level of fluctuation. During the 100 ns simulation, the ligands CBZ01 and CBZ13 showed minimal alterations in their interactions with each other, likely attributable to their effective engagement with various amino acid residues. The overall fluctuation observed is relatively low, providing valuable insights for future studies involving proteins with both ligands, CBZ01 and CBZ13. Additionally, the rigidity of the protein is reinforced by hydrogen bonds, pi-pi stacking, and the presence of secondary structural elements. In both scenarios illustrated in Figures 5C,D (CBZ01 and CBZ13), the fluctuations remain below 2 Å, indicating promising results.

3.8.2 Intermolecular interactions

MD simulations facilitate the examination of intermolecular interactions, which are defined as the attractive or repulsive forces that exist between molecules. Over the course of a 100 ns simulation, we explored various binding interactions between the ligand and the protein. Numerous intramolecular interactions were identified in both complexes, encompassing hydrophobic, polar, water-mediated, and pi-pi stacking interactions. The presence of N, O, and NH atoms led to the formation of hydrophilic, hydrophobic, and cationic interactions across different percentiles. No direct interactions with carbon molecules were observed. Furthermore, the direction of the arrows indicates both donors and acceptors. The residue TRP132 engaged with the phenyl group through hydrophobic interactions. The carbonyl group of the amide was linked to LEU875 and LYS930 via a water bridge, exhibiting both hydrophobic and cationic characteristics. LYS930 also established a cationic interaction with the carbonyl group of the amide. The amino acid residue ASN179 interacted with the methoxy group of the ligands through polar interactions facilitated by a water bridge. Additionally, the nitrogen atom of the quinoline ring formed an anionic interaction with GLU887 through a water bridge. Figure 6A depicts the intramolecular interaction between the CBZ01 complex and the target protein.

The carbonyl group of the amide interacted with the GLN343 and ALA981 residues through polar and hydrophobic interactions, respectively. Moreover, the PHE979 and TYR303 residues formed hydrophobic interactions with the phenyl group and the carbonyl of the amide group, respectively. The NH of the amide and the phenyl group of the quinoline ring displayed hydrophobic interactions with the VAL292 and PHE766 residues, respectively. Additionally, the nitrogen atom of the quinoline ring established a hydrogen bond with the PHE766 residue, mediated by a water bridge. The intramolecular interactions of the CBZ13 complex with the target protein are depicted in Figure 6B. Figure 6C, D provide the histogram for ligands CBZ01 and CBZ13. The interactions between the protein and ligand are classified into four categories: ionic, hydrophobic, hydrogen bonding, and water bridges. The histogram illustrates that the stacked bar charts are standardized over the trajectory. The findings from the MD simulation indicate that both complexes, CBZ01 and CBZ13, demonstrated stability, characterized by lower RMDS and RMSF values, along with favorable interactions.

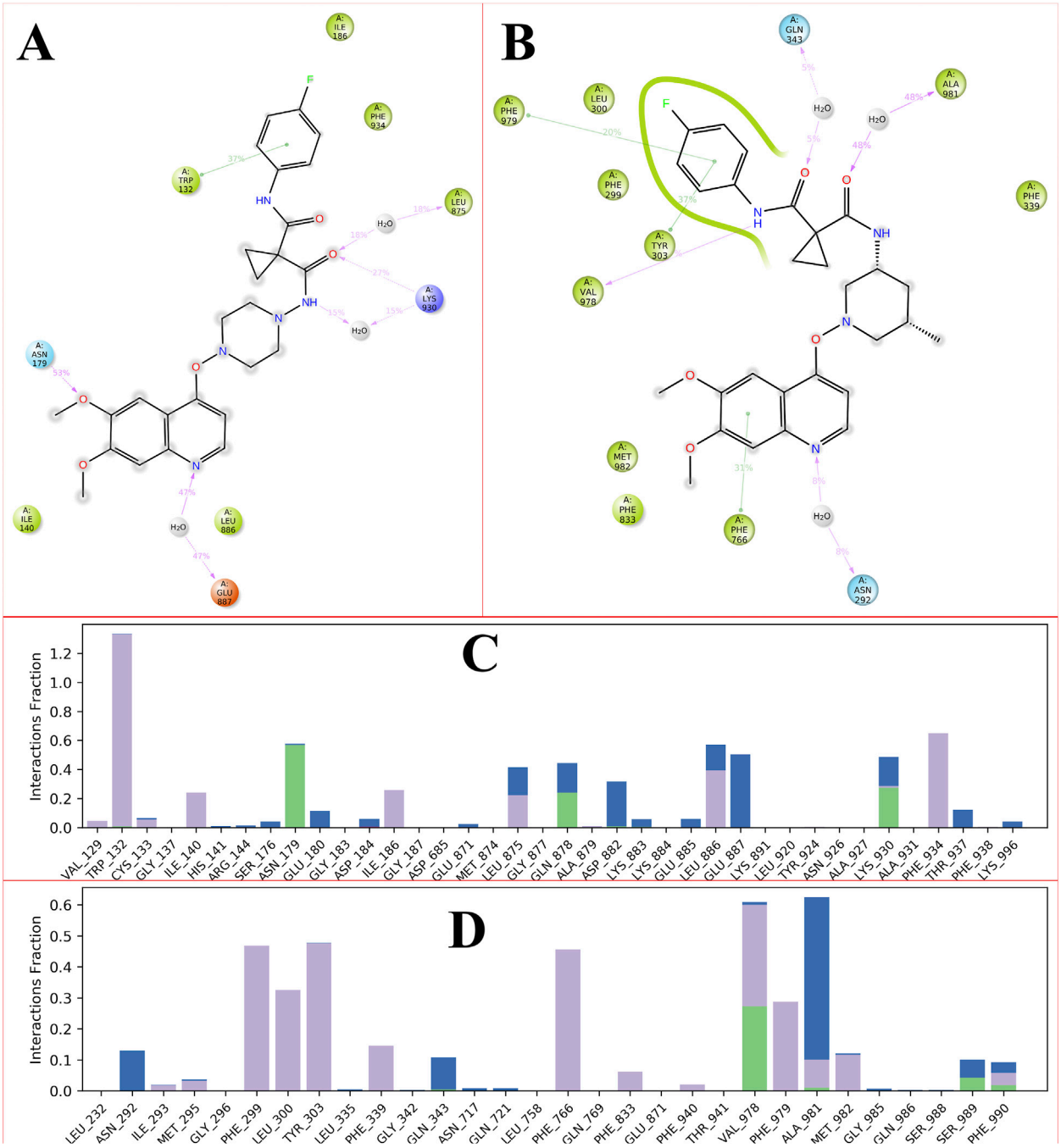

FIGURE 6
Showing the 2D-Summary of interacting atoms of P-glycoprotein with CBZ01 **(A)** and ligand CBZ13 **(B)**; The count of interactions in histogram form for P-glycoprotein with CBZ01 **(C)** and ligand CBZ13 **(D)** throughout the 100 ns run.

3.8.3 Binding free energy calculations and residue decomposition

Numerous methods are available to assess the binding free energy of protein-ligand complexes. MM-PBSA and MM-GBSA are currently the leading techniques due to their effectiveness in predicting the interactions between small molecules and biological entities (Genheden and Ryde, 2015). Energies associated with the protein (PDB ID: 3G5U), along with those of the CBZ01-3G5U and CBZ13-3G5U complexes, as well as the entropy derived from these methodologies, were documented. An MM-GBSA analysis was carried out to determine whether variations in binding mode can be differentiated in the predicted binding-free energy between the two systems.

The study demonstrated that the total energetic component breakdown for the CBZ01-3G5U and CBZ13-3G5U complexes was −40 kcal/mol and −50 kcal/mol, respectively, as illustrated in Figures 7A, B. For the ligand CBZ01, an extensive analysis of the free-energy components revealed that ΔG_{gas} (−65 kcal/mol) was

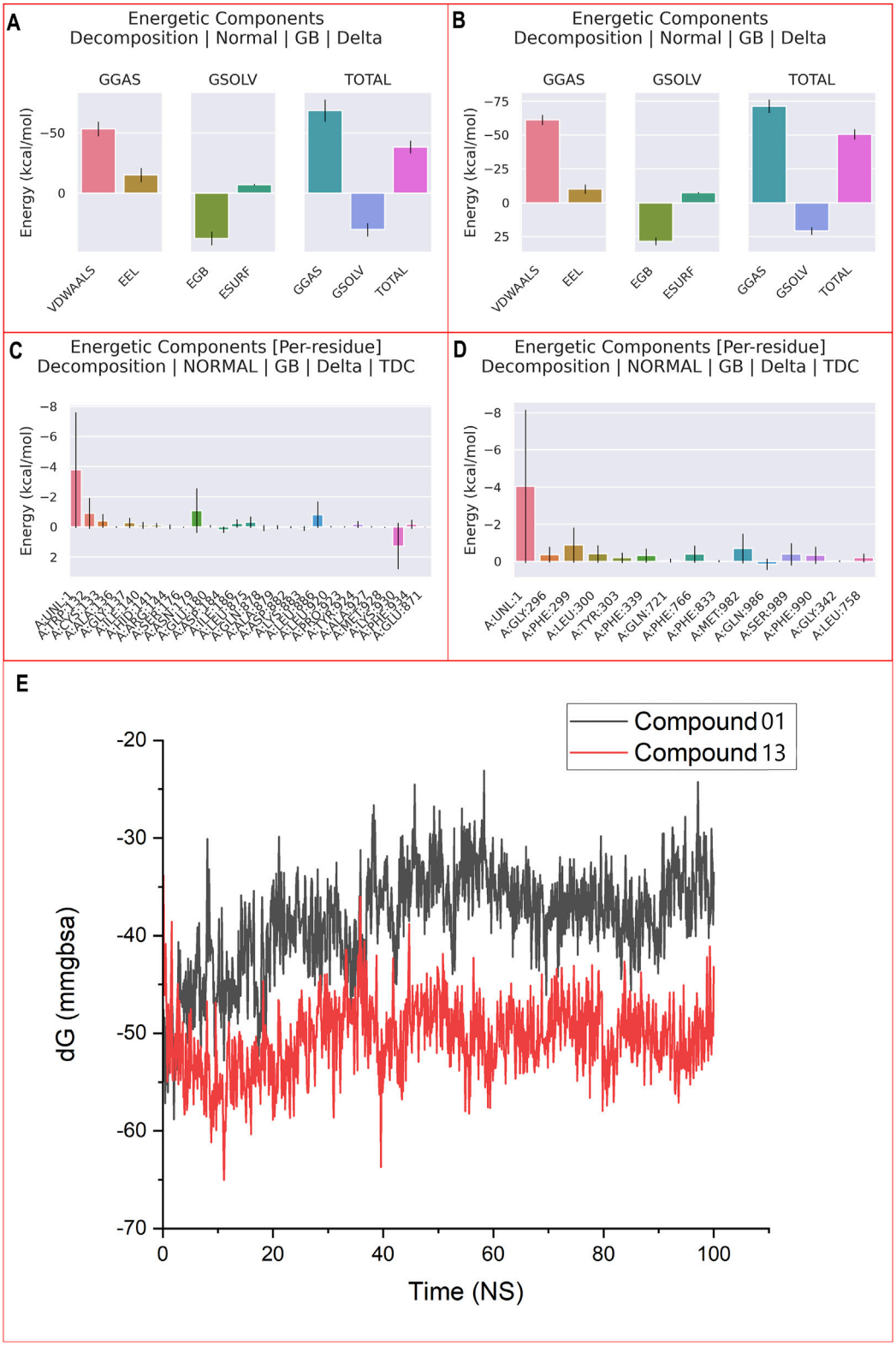

FIGURE 7
MM-PBSA binding free energy for ligand CBZ01-3G5U **(A)** and CBZ13-3G5U complexes **(B)**; per residue free energy decomposition for ligand CBZ01-3G5U **(C)** and CBZ13-3G5U complexes **(D)**; and MM-GBSA plot for CBZ01-3G5U and CBZ13-3G5U complexes **(E)**.

predominantly influenced within the protein environment. A minor decrease in $\Delta E_{vdwalls}$ (−55 kcal/mol) and a significant reduction in ΔE_{EEl} (−15 kcal/mol) contributed to the overall decline in ΔG_{gas} (−40 kcal/mol). In the case of ligand CBZ13, a thorough examination of the free-energy components indicated that ΔG_{gas} (−70 kcal/mol) was primarily affected within the protein. There was a slight decrease in $\Delta E_{vdwalls}$ (−60 kcal/mol) and a notable reduction in ΔE_{EEl} (−15 kcal/mol), leading to an overall decrease in ΔG_{gas} (−50 kcal/mol).

A detailed per-residue free energy decomposition analysis was performed on the CBZ01-3G5U and CBZ13-3G5U complexes to assess the contributions of various amino acid residues surrounding the binding site to the overall binding free energy (Figures 7C,D). The addition of 3G5U in the context of CBZ01 led to a reduction in energy contributions from several critical residues, particularly 136, 140, 141, 144, 176, 184, 186, 878, 879, 882, 883, 920, 923, 924, 927, 928, and 871. Similarly, the incorporation of 3G5U with respect to CBZ13 resulted in decreased energy contributions from key residues, namely, 296, 303, 721, 833, 342, and 758. The free energies of the CBZ01-3G5U and CBZ13-3G5U complexes were determined to be −38.40 and −50.56 kcal/mol, respectively, through the application of the GBSA solvation method (Figure 7E). We have computed the binding free energy for each five-frame interval over the course of the 100 ns simulation, totalling 5,000 frames (Supplementary Table S2). These results suggest that the CBZ13-3G5U complex shows considerable stability and a strong affinity for the P-gp receptor and thus effectively acts as an anti-cancer agent.

4 Conclusion

Certain cancers demonstrate varying degrees of resistance to medications, which significantly undermines the efficacy of chemotherapy in achieving favorable treatment outcomes. The cell membranes are characterized by the presence of P-gp, a crucial protein that expels several foreign substances from cells and may contribute to resistance to chemotherapeutic agents. The CBZ, a tyrosine kinase inhibitor, is utilized in the treatment of various types of cancer. P-gp plays a role in mediating multidrug resistance (MDR), a challenge that can be addressed by CBZ through the direct inhibition of its export mechanism. Consequently, P-gp represents a vital target for the development of anti-cancer therapeutics. Patients undergoing treatment with CBZ may experience a range of side effects, including liver dysfunction, hypertension, hand-foot syndrome, reduced appetite, and general malaise. To address these issues, modifications to the scaffold of the CBZ molecule are necessary to create safer, less toxic, and more effective agents against MDR. In this research, we developed novel CBZ analogues employing a bioisosteric approach. We assessed the pharmacokinetic and toxicological profiles of the newly designed CBZ bioisosteres using ADMETlab 3.0. Following the screening process, the selected ligands were docked against the target protein (PDB ID: 3G5U) utilizing ADV, and their interactions were examined using Discovery studio. The docking scores for the ligands ranged from −6.4 to −8.4 kcal/mol. The ligands CBZ01, CBZ06, CBZ11, CBZ13, CBZ25, CBZ34, and CBZ38 demonstrated favorable interactions with the target protein. The amino acid residue GLN942 was identified as a critical residue in the binding process, potentially contributing to the inhibitory activity of P-gp. We selected the top three ligands, CBZ01, CBZ13, and CBZ38, for a 100 ns MD simulation using the Schrödinger suite, based on their docking scores and interactions. The trajectory analysis indicated that CBZ01 and CBZ13 maintained stability when complexed with the target protein. This combined computational approach suggests that CBZ01 and CBZ13 may be promising candidates for further development of potential anticancer agents.

Further experimental studies are currently underway to substantiate the anti-cancer properties of the designed CBZ analogues.

Data availability statement

The original contributions presented in the study are included in the article/Supplementary Material, further inquiries can be directed to the corresponding author.

Author contributions

GT: Writing–review and editing, Data curation, Investigation, Methodology, Writing–original draft. AG: Data curation, Investigation, Methodology, Writing–original draft, Writing–review and editing. DP: Data curation, Writing–review and editing. YV: Writing–review and editing, Formal Analysis, Validation. NK: Writing–review and editing, Data curation, Investigation, Methodology. SA: Writing–review and editing, Formal Analysis, Funding acquisition, Validation. SJ: Formal Analysis, Conceptualization, Supervision, Writing–review and editing.

Funding

The author(s) declare that financial support was received for the research, authorship, and/or publication of this article. The author SA would like to extend his appreciation to the Deanship of Research and Graduate Studies at King Khalid University for funding this work through small group research under grant number RGP1/161/45.

Acknowledgments

The authors would like to thank Head, Department of Pharmacy, Guru Ghasidas Vishwavidyalaya, Koni, Bilaspur (Chhattisgarh), India for proving all necessary facilities.

Conflict of interest

The authors declare that the research was conducted in the absence of any commercial or financial relationships that could be construed as a potential conflict of interest.

Generative AI statement

The authors declare that no Generative AI was used in the creation of this manuscript.

Publisher's note

Supplementary material

The Supplementary Material for this article can be found online at: https://www.frontiersin.org/articles/10.3389/fchem.2025.1543075/full#supplementary-material

References

Ajmal, M. R., Abdelhameed, A. S., Alam, P., and Khan, R. H. (2016). Interaction of new kinase inhibitors cabozantinib and tofacitinib with human serum alpha-1 acid glycoprotein. A comprehensive spectroscopic and molecular docking approach. *Spectrochim. Acta A Mol. Biomol. Spectrosc.* 159, 199–208. doi:10.1016/j.saa.2016.01.049

Aller, S. G., Yu, J., Ward, A., Weng, Y., Chittaboina, S., Zhuo, R., et al. (2009). Structure of P-glycoprotein reveals a molecular basis for poly-specific drug binding. *Science* 323, 1718–1722. doi:10.1126/science.1168750

Anand, U., Dey, A., Chandel, A. K. S., Sanyal, R., Mishra, A., Pandey, D. K., et al. (2023). Cancer chemotherapy and beyond: current status, drug candidates, associated risks and progress in targeted therapeutics. *Genes Dis.* 10, 1367–1401. doi:10.1016/j.gendis.2022.02.007

Anderson, A. C. (2003). The process of structure-based drug design. *Chem. Biol.* 10, 787–797. doi:10.1016/j.chembiol.2003.09.002

Andrade, R. J., Chalasani, N., Björnsson, E. S., Suzuki, A., Kullak-Ublick, G. A., Watkins, P. B., et al. (2019). Drug-induced liver injury. *Nat. Rev. Dis. Prim.* 5, 58. doi:10.1038/s41572-019-0105-0

Banks, J. L., Beard, H. S., Cao, Y., Cho, A. E., Damm, W., Farid, R., et al. (2005). Integrated modeling program, applied chemical theory (IMPACT). *J. Comp. Chem.* 26, 1752–1780. doi:10.1002/jcc.20292

Barnhill, M. S., Steinberg, J. M., Jennings, J. J., and Lewis, J. H. (2020). Hepatotoxicty of agents used in the management of inflammatory bowel disease: a 2020 update. *Curr. Gastroenterol. Rep.* 22, 47–12. doi:10.1007/s11894-020-00781-3

Bhagat, R. T., Butle, S. R., Khobragade, D. S., Wankhede, S. B., Prasad, C. C., Mahure, D. S., et al. (2021). Molecular docking in drug discovery. *J. Pharm. Res. Int.* 33, 46–58. doi:10.9734/JPRI/2021/v33i30B31639

Bickerton, G. R., Paolini, G. V., Besnard, J., Muresan, S., and Hopkins, A. L. (2012). Quantifying the chemical beauty of drugs. *Nat. Chem.* 4, 90–98. doi:10.1038/nchem.1243

Bouricha, E. M., and Hakmi, M. (2024). Investigating lasofoxifene efficacy against the Y537S + F404V double-mutant estrogen receptor alpha using molecular dynamics simulations. *Bioinform. Biol. Insights* 18, 11779322241288703. doi:10.1177/11779322241288703

Bray, F., Laversanne, M., Sung, H., Ferlay, J., Siegel, R. L., Soerjomataram, I., et al. (2024). Global cancer statistics 2022: GLOBOCAN estimates of incidence and mortality worldwide for 36 cancers in 185 countries. *CA Cancer J. Clin.* 74, 229–263. doi:10.3322/caac.21834

Bukowski, K., Kciuk, M., and Kontek, R. (2020). Mechanisms of multidrug resistance in cancer chemotherapy. *Int. J. Mol. Sci.* 21, 3233. doi:10.3390/ijms21093233

Cao, W., Qin, K., Li, F., and Chen, W. (2024). Comparative study of cancer profiles between 2020 and 2022 using global cancer statistics (GLOBOCAN). *J. Natl. Cancer Cent.* 4, 128–134. doi:10.1016/j.jncc.2024.05.001

Chiruvella, V., Annamaraju, P., and Guddati, A. K. (2020). Management of nephrotoxicity of chemotherapy and targeted agents: 2020. *Am. J. Cancer Res.* 10, 4151–4164.

Choueiri, T. K., Escudier, B., Powles, T., Mainwaring, P. N., Rini, B. I., Donskov, F., et al. (2015). Cabozantinib versus everolimus in advanced renal-cell carcinoma. *N. Engl. J. Med.* 373, 1814–1823. doi:10.1056/NEJMoa1510016

Das, B., Baidya, A. T., Mathew, A. T., Yadav, A. K., and Kumar, R. (2022). Structural modification aimed for improving solubility of lead compounds in early phase drug discovery. *Bioorg. Med. Chem. Lett.* 56, 116614. doi:10.1016/j.bmc.2022.116614

De Ruyck, J., Brysbaert, G., Blossey, R., and Lensink, M. F. (2016). Molecular docking as a popular tool in drug design, an *in-silico* travel. *Adv. Appl. Bioinform.* 9, 1–11. doi:10.2147/AABC.S105289

Du, X., Li, Y., Xia, Y. L., Ai, S. M., Liang, J., Sang, P., et al. (2016). Insights into protein–ligand interactions: mechanisms, models, and methods. *Int. J. Mol. Sci.* 17, 144. doi:10.3390/ijms17020144

Duan, J. L., Wang, C. C., Yuan, Y., Hui, Z., Zhang, H., Mao, N. D., et al. (2024). Design, synthesis, and structure–activity relationship of novel pyridazinone-based PARP7/HDACs dual inhibitors for elucidating the relationship between antitumor immunity and HDACs inhibition. *J. Med. Chem.* 67, 4950–4976. doi:10.1021/acs.jmedchem.4c00090

Dulsat, J., López-Nieto, B., Estrada-Tejedor, R., and Borrell, J. I. (2023). Evaluation of free online ADMET tools for academic or small biotech environments. *Molecules* 28, 776. doi:10.3390/molecules28020776

Ejalonibu, M. A., Ogundare, S. A., Elrashedy, A. A., Ejalonibu, M. A., Lawal, M. M., Mhlongo, N. N., et al. (2021). Drug discovery for *Mycobacterium tuberculosis* using structure-based computer-aided drug design approach. *Int. J. Mol. Sci.* 22, 13259. doi:10.3390/ijms222413259

Elekofehinti, O. O., Iwaloye, O., Josiah, S. S., Lawal, A. O., Akinjiyan, M. O., and Ariyo, E. O. (2021). Molecular docking studies, molecular dynamics and ADME/tox reveal therapeutic potentials of STOCK1N-69160 against papain-like protease of SARS-CoV-2. *Mol. Divers.* 25, 1761–1773. doi:10.1007/s11030-020-10151-w

Ferlay, J., Ervik, M., Lam, F., Laversanne, M., Colombet, M., Mery, L., et al. (2024). *Global cancer observatory: cancer today*. Lyon, France: International Agency for Research on Cancer. Available at: https://gco.iarc.who.int/today (Accessed January 22, 2025).

Ferreira, L. G., Dos Santos, R. N., Oliva, G., and Andricopulo, A. D. (2015). Molecular docking and structure-based drug design strategies. *Molecules* 20, 13384–13421. doi:10.3390/molecules200713384

Gao, X., Tang, J., Liu, H., Liu, L., and Liu, Y. (2019). Structure–activity study of fluorine or chlorine-substituted cinnamic acid derivatives with tertiary amine side chain in acetylcholinesterase and butyrylcholinesterase inhibition. *Drug Dev. Res.* 80, 438–445. doi:10.1002/ddr.21515

Gao, Y., Duan, J., Dang, X., Yuan, Y., Wang, Y., He, X., et al. (2023). Design, synthesis and biological evaluation of novel histone deacetylase (HDAC) inhibitors derived from β -elemene scaffold. *J. Enzyme Inhib. Med. Chem.* 38, 2195991. doi:10.1080/14756366.2023.2195991

Garrigues, A., Escargueil, A. E., and Orlowski, S. (2002). The multidrug transporter, P-glycoprotein, actively mediates cholesterol redistribution in the cell membrane. *Proc. Natl. Acad. Sci.* 99, 10347–10352. doi:10.1073/pnas.162366399

Genheden, S., and Ryde, U. (2015). The MM/PBSA and MM/GBSA methods to estimate ligand-binding affinities. *Expert Opin. Drug Discov.* 10, 449–461. doi:10.1517/17460441.2015.1032936

Giordano, D., Biancaniello, C., Argenio, M. A., and Facchiano, A. (2022). Drug design by pharmacophore and virtual screening approach. *Pharmaceutical* 15, 646. doi:10.3390/ph15050646

Goebel, J., Chmielewski, J., and Hrycyna, C. A. (2021). The roles of the human ATP-binding cassette transporters P-glycoprotein and ABCG2 in multidrug resistance in cancer and at endogenous sites: future opportunities for structure-based drug design of inhibitors. *Cancer Drug Resist* 4, 784–804. doi:10.20517/cdr.2021.19

Gonzalez, M. A. (2011). Force fields and molecular dynamics simulations. *Collect. SFN* 12, 169–200. doi:10.1051/sfn/201112009

Gupta, A. K., Vaishnav, Y., Jain, S. K., Annadurai, S., and Kumar, N. (2024). Exploring novel Apalutamide analogues as potential therapeutics for prostate cancer: design, molecular docking investigations and molecular dynamics simulation. *Fron. Chem.* 12, 1418975. doi:10.3389/fchem.2024.1418975

Heming, C. P., Muriithi, W., Macharia, L. W., Niemeyer Filho, P., Moura-Neto, V., and Aran, V. (2022). P-glycoprotein and cancer: what do we currently know? *Heliyon* 8, e11171. doi:10.1016/j.heliyon.2022.e11171

Ikwu, F. A., Shallangwa, G. A., and Mamza, P. A. (2020). QSAR, QSTR, and molecular docking studies of the anti-proliferative activity of phenylpiperazine derivatives against DU145 prostate cancer cell lines. *Beni-Suef. Univ. J. Basic Appl. Sci.* 9, 35. doi:10.1186/s43088-020-00054-y

Ivanenkov, Y. A., Zagribelnyy, B. A., and Aladinskiy, V. A. (2019). Are we opening the door to a new era of medicinal chemistry or being collapsed to a chemical singularity? *J. Med. Chem.* 62, 10026–10043. doi:10.1021/acs.jmedchem.9b00004

Jayashree, B. S., Nikhil, P. S., and Paul, S. (2022). Bioisosterism in drug discovery and development-an overview. *Med. Chem.* 18, 915–925. doi:10.2174/1573406418666220127124228

Jiang, C., Sun, T., Xiang, D., Wei, S., and Li, W. (2018). Anticancer activity and mechanism of xanthohumol: a prenylated flavonoid from hops (Humulus lupulus L.). *Front. Pharmacol.* 9, 530. doi:10.3389/fphar.2018.00530

Johnson, Z. L., and Chen, J. (2018). ATP binding enables substrate release from multidrug resistance protein 1. *Cell* 172, 81–89.e10. doi:10.1016/j.cell.2017.12.005

Kang, L., Gao, X., Liu, H., Men, X., Wu, H., Cui, P., et al. (2018). Structure–activity relationship investigation of coumarin–chalcone hybrids with diverse side-chains as acetylcholinesterase and butyrylcholinesterase inhibitors. *Mol. Divers.* 22, 893–906. doi:10.1007/s11030-018-9839-y

Karami, T. K., Hailu, S., Feng, S., Graham, R., and Gukasyan, H. J. (2022). Eyes on lipinski's rule of five: a new "rule of thumb" for physicochemical design space of ophthalmic drugs. *J. Ocul. Pharmacol. Ther.* 38, 43–55. doi:10.1089/jop.2021.0069

Karmacharya, U., Guragain, D., Chaudhary, P., Jee, J. G., Kim, J. A., and Jeong, B. S. (2021). Novel pyridine bioisostere of cabozantinib as a potent c-met kinase inhibitor: synthesis and anti-tumor activity against hepatocellular carcinoma. *Int. J. Mol. Sci.* 22, 9685. doi:10.3390/ijms22189685

Karthika, C., Sureshkumar, R., Zehravi, M., Akter, R., Ali, F., Ramproshad, S., et al. (2022). Multidrug resistance of cancer cells and the vital role of P-glycoprotein. *Life* 12, 897. doi:10.3390/life12060897

Khan, S. U., Fatima, K., Aisha, S., and Malik, F. (2024). Unveiling the mechanisms and challenges of cancer drug resistance. *Cell Commun. Signal.* 22, 109. doi:10.1186/s12964-023-01302-1

Kim, Y., and Chen, J. (2018). Molecular structure of human P-glycoprotein in the ATP-bound, outward-facing conformation. *Science.* 359, 915–919. doi:10.1126/science.aar7389

Krens, S. D., van Boxtel, W., Uijen, M. J. M., Jansman, F. G. A., Desar, I. M. E., Mulder, S. F., et al. (2022). Exposure-toxicity relationship of cabozantinib in patients with renal cell cancer and salivary gland cancer. *Int. J. Cancer.* 150, 308–316. doi:10.1002/ijc.33797

Lagu, S. B., Yejella, R. P., Nissankararao, S., Bhandare, R. R., Golla, V. S., Lokesh, B. V., et al. (2022). Antitubercular activity assessment of fluorinated chalcones, 2-aminopyridine-3-carbonitrile and 2-amino-4H-Pyran-3-Carbonitrile derivatives: *in vitro*, molecular docking and in-silico drug likeliness studies. *PLoS One* 17, e0265068. doi:10.1371/journal.pone.0265068

Li, Y., Zhou, L., Qian, F., Fang, Q., Yu, Z., Cui, T., et al. (2024). ScImmOmics: a manually curated resource of single-cell multi-omics immune data. *Nucleic Acids Res.* 53, D1162–D1172. doi:10.1093/nar/gkae985

Lin, X., Liao, Y., Chen, X., Long, D., Yu, T., and Shen, F. (2016a). Regulation of oncoprotein 18/stathmin signaling by ERK concerns the resistance to taxol in nonsmall cell lung cancer cells. *Cancer biother. Radiopharm.* 31, 37–43. doi:10.1089/cbr.2015.1921

Lin, X., Yu, T., Zhang, L., Chen, S., Chen, X., Liao, Y., et al. (2016b). Silencing op18/stathmin by RNA interference promotes the sensitivity of nasopharyngeal carcinoma cells to taxol and high-grade differentiation of xenografted tumours in nude mice. *Basic Clin. Pharmacol. Toxicol.* 119, 611–620. doi:10.1111/bcpt.12633

Liu, B., Zhou, H., Tan, L., Siu, K. T. H., and Guan, X. Y. (2024). Exploring treatment options in cancer: tumor treatment strategies. *Signal Transduct. Target Ther.* 9, 175. doi:10.1038/s41392-024-01856-7

Liu, M., An, R., Wu, Z., Dai, L., Zeng, Q., and Chen, W. (2024). The trajectory of oral mucositis in Head and neck cancer patients undergoing radiotherapy and its influencing factors. *Ear Nose Throat J.*, 1455613241228211. doi:10.1177/01455613241228211

Lou, Y., Song, F., Cheng, M., Hu, Y., Chai, Y., Hu, Q., et al. (2023). Effects of the CYP3A inhibitors, voriconazole, itraconazole, and fluconazole on the pharmacokinetics of osimertinib in rats. *PeerJ* 11, e15844. doi:10.7717/peerj.15844

Lounnas, V., Ritschel, T., Kelder, J., McGuire, R., Bywater, R. P., and Foloppe, N. (2013). Current progress in structure-based rational drug design marks a new mindset in drug discovery. *Comput. Struct. Biotechnol. J.* 5, e201302011. doi:10.5936/csbj.201302011

Markowitz, J. N., and Fancher, K. M. (2018). Cabozantinib: a multitargeted oral tyrosine kinase inhibitor. *Pharmacotherapy* 38, 357–369. doi:10.1002/phar.2076

Martini, D. J., Evans, S. T., Liu, Y., Shabto, J. M., Uner, O. E., Olsen, T. A., et al. (2022). Analysis of toxicity and clinical outcomes in full versus reduced starting dose cabozantinib in metastatic renal cell carcinoma patients. *Clin. Genitourin. Cancer.* 20, 53–59. doi:10.1016/j.clgc.2021.11.004

Matore, B. W., Roy, P. P., and Singh, J. (2023). Discovery of novel VEGFR2-TK inhibitors by phthalimide pharmacophore based virtual screening, molecular docking, MD simulation and DFT. *J. Biomol. Struct. Dyn.* 41, 13056–13077. doi:10.1080/07391102.2023.2178510

Naresh, G. K. R. S., and Guruprasad, L. (2020). Structural dynamics of cabozantinib bound TAM receptor tyrosine kinases. *J. Biomol. Struct. Dyn.* 39, 1–20. doi:10.1080/07391102.2020.1730968

National Center for Biotechnology Information (2025). PubChem compound summary for CID 25102847. *Cabozantinib*. Available at: https://pubchem.ncbi.nlm.nih.gov/compound/Cabozantinib (Accessed January 1, 2025).

Nie, Y., Li, D., Peng, Y., Wang, S., Hu, S., Liu, M., et al. (2020). Metal organic framework coated MnO2 nanosheets delivering doxorubicin and self-activated DNAzyme for chemo-gene combinatorial treatment of cancer. *Int. J. Pharm.* 585, 119513. doi:10.1016/j.ijpharm.2020.119513

Rimassa, L., Danesi, R., Pressiani, T., and Merle, P. (2019). Management of adverse events associated with tyrosine kinase inhibitors: improving outcomes for patients with hepatocellular carcinoma. *Cancer Treat. Rev.* 77, 20–28. doi:10.1016/j.ctrv.2019.05.004

Salo-Ahen, O. M., Alanko, I., Bhadane, R., Bonvin, A. M., Honorato, R. V., Hossain, S., et al. (2020). Molecular dynamics simulations in drug discovery and pharmaceutical development. *Processes* 9, 71. doi:10.3390/pr9010071

Sastry, G. M., Adzhigirey, M., Day, T., Annabhimoju, R., and Sherman, W. (2013). Protein and ligand preparation: parameters, protocols, and influence on virtual screening enrichments. *J. Comput. Aided Mol. Des.* 27, 221–234. doi:10.1007/s10822-013-9644-8

Schmidinger, M., and Danesi, R. (2018). Management of adverse events associated with cabozantinib therapy in renal cell carcinoma. *Oncologist* 23, 306–315. doi:10.1634/theoncologist.2017-0335

Schwartz, G., Darling, J. O., Mindo, M., and Damicis, L. (2020). Management of adverse events associated with cabozantinib treatment in patients with advanced hepatocellular carcinoma. *Target Onco* 15, 549–565. doi:10.1007/s11523-020-00736-8

Shan, J., and Ji, C. (2020). MolOpt: a web server for drug design using bioisosteric transformation. *Curr. Comput-Aided Drug Des.* 16, 460–466. doi:10.2174/1573409915666190704093400

Sharom, F. J. (2011). The P-glycoprotein multidrug transporter. *Essays Biochem.* 50, 161–178. doi:10.1042/bse0500161

Shivakumar, D., Williams, J., Wu, Y., Damm, W., Shelley, J., and Sherman, W. (2010). Prediction of absolute solvation free energies using molecular dynamics free energy perturbation and the OPLS force field. *J. Chem. Theory Comp.* 6, 1509–1519. doi:10.1021/ct900587b

Srigadha, V. K., Prabhash, K., Noronha, V., Joshi, A., Patil, V. M., Menon, N., et al. (2023). Cabozantinib: a narrative drug review. *Cancer Res. Stat. Treat.* 6, 74–87. doi:10.4103/crst.crst_9_23

Subbaiah, M. A. M., and Meanwell, N. A. (2021). Bioisosteres of the phenyl ring: recent strategic applications in lead optimization and drug design. *J. Med. Chem.* 64, 14046–14128. doi:10.1021/acs.jmedchem.1c01215

Sun, D., Gao, W., Hu, H., and Zhou, S. (2022). Why 90% of clinical drug development fails and how to improve it? *Acta Pharm. Sin. B* 12, 3049–3062. doi:10.1016/j.apsb.2022.02.002

Sun, D., Li, X., Nie, S., Liu, J., and Wang, S. (2023). Disorders of cancer metabolism: the therapeutic potential of cannabinoids. *Biomed. Pharmacother.* 157, 113993. doi:10.1016/j.biopha.2022.113993

Sung, H., Ferlay, J., Siegel, R. L., Laversanne, M., Soerjomataram, I., Jemal, A., et al. (2021). Global cancer statistics 2020: GLOBOCAN estimates of incidence and mortality worldwide for 36 cancers in 185 countries. *CA Cancer J. Clin.* 71, 209–249. doi:10.3322/caac.21660

Tian, Y., Lei, Y., Wang, Y., Lai, J., Wang, J., and Xia, F. (2023). Mechanism of multidrug resistance to chemotherapy mediated by P-glycoprotein. *Int. J. Oncol.* 63, 1–19. doi:10.3892/ijo.2023.5567

Trott, O., and Olson, A. J. (2010). AutoDock Vina: improving the speed and accuracy of docking with a new scoring function, efficient optimization, and multithreading. *J. Comput. Chem.* 31, 455–461. doi:10.1002/jcc.21334

Vasiliou, V., Vasiliou, K., and Nebert, D. W. (2009). Human ATP-binding cassette (ABC) transporter family. *Hum. Genomics.* 3, 281–310. doi:10.1186/1479-7364-3-3-281

Wang, E., Sun, H., Wang, J., Wang, Z., Liu, H., Zhang, J. Z. H., et al. (2019). End-point binding free energy calculation with MM/PBSA and MM/GBSA: strategies and applications in drug design. *Chem. Rev.* 119, 9478–9508. doi:10.1021/acs.chemrev.9b00055

Wang, K., Yin, J., Chen, J., Ma, J., Si, H., and Xia, D. (2024). Inhibition of inflammation by berberine: molecular mechanism and network pharmacology analysis. *Phytomedicine* 128, 155258. doi:10.1016/j.phymed.2023.155258

Wang, Z., Jiang, L., Lv, X., Yin, H., Wang, Z., Li, W., et al. (2024). Higher risk of hepatotoxicity associated with cabozantinib in cancer patients. *Crit. Rev. Oncol.Hematol.* 196, 104298. doi:10.1016/j.critrevonc.2024.104298

Xiang, Q. F., Zhang, D. M., Wang, J. N., Zhang, H. W., Zheng, Z. Y., Yu, D. C., et al. (2015). Cabozantinib reverses multidrug resistance of human hepatoma HepG2/adr cells by modulating the function of P-glycoprotein. *Liver Int.* 35, 1010–1023. doi:10.1111/liv.12524

Xiong, G., Wu, Z., Yi, J., Fu, L., Yang, Z., Hsieh, C., et al. (2021). ADMETlab 2.0: an integrated online platform for accurate and comprehensive predictions of ADMET properties. *Nucleic. Acids Res.* 49, W5–W14. doi:10.1093/nar/gkab255

Zhang, L., Shi, H., Tan, X., Jiang, Z., Wang, P., and Qin, J. (2022). Ten-gram-scale mechanochemical synthesis of ternary lanthanum coordination polymers for antibacterial and antitumor activities. *Front. Chem.* 10, 898324. doi:10.3389/fchem.2022.898324

Zielesny, A. (2005). Chemistry software package Chem office ultra 2005. *J. Chem. Inf. Model.* 45, 1474–1477. doi:10.1021/ci050273j

Zuo, R. C., Apolo, A. B., DiGiovanna, J. J., Parnes, H. L., Keen, C. M., Nanda, S., et al. (2015). Cutaneous adverse effects associated with the tyrosine-kinase inhibitor cabozantinib. *JAMA dermatol.* 151, 170–177. doi:10.1001/jamadermatol.2014.2734

frontiers | Frontiers in Chemistry

TYPE Original Research
PUBLISHED 24 March 2025
DOI 10.3389/fchem.2025.1524384

OPEN ACCESS

EDITED BY
Marko Jukic,
University of Maribor, Slovenia

REVIEWED BY
Pradeep Kumar Jaiswal,
Texas A&M University College Station,
United States
Sayed K. Ramadan,
Ain Sham University, Egypt

*CORRESPONDENCE
Youssouf Ali Younous,
scientifcresearcher@gmail.com

RECEIVED 07 November 2024
ACCEPTED 07 February 2025
PUBLISHED 24 March 2025

CITATION
Al Mashud MA, Kumer A, Jahan I, Somrat MMH, Talukder MEK, Rahman MM, Uddin AFMS, Harun-Or-Rashid M, Rahman MM, Harun-Ur-Rashid M, Shazly GA and Ali Younous Y (2025) Chemoinformatics analysis of *Mangifera indica* leaves extracted phytochemicals as potential EGFR kinase modulators.
Front. Chem. 13:1524384.
doi: 10.3389/fchem.2025.1524384

Chemoinformatics analysis of *Mangifera indica* leaves extracted phytochemicals as potential EGFR kinase modulators

Md. Abdullah Al Mashud[1,2], Ajoy Kumer[3,4], Ismat Jahan[1], Md. Mehedi Hasan Somrat[1,2], Md. Enamul Kabir Talukder[5], Md. Mashiar Rahman[5], A. F. M. Shahab Uddin[6], Md. Harun-Or-Rashid[7,8], Md. Mizanur Rahman[9], Mohammad Harun-Ur-Rashid[4], Gamal A. Shazly[10] and Youssouf Ali Younous[11]*

[1]Biophysics and Biomedicine Research Lab, Department of Electrical and Electronic Engineering, Islamic University, Kushtia, Bangladesh, [2]Computational Bio-Info Lab, Research and Development Center for Sustainability, Scientific Foundation for Cancer Research, Kushtia, Bangladesh, [3]Center for Global Health Research, Saveetha Medical College and Hospitals, Saveetha Institute of Medical and Technical Sciences, Chennai, Tamil Nadu, India, [4]Department of Chemistry, College of Arts and Sciences, IUBAT-International University of Business Agriculture and Technology, Dhaka, Bangladesh, [5]Molecular and Cellular Biology Laboratory, Department of Genetic Engineering and Biotechnology, Jashore University of Science and Technology, Jashore, Bangladesh, [6]Department of Computer Science and Engineering, Jashore University of Science and Technology, Jashore, Bangladesh, [7]School of Engineering, Macquarie University Sydney, Sydney, NSW, Australia, [8]Computational Biology Research Laboratory, Department of Pharmacy, Faculty of Health and Life Sciences, Daffodil International University, Dhaka, Bangladesh, [9]Department of Mathematics, Islamic University, Kushtia, Bangladesh, [10]Department of Pharmaceutics, College of Pharmacy, King Saud University, Riyadh, Saudi Arabia, [11]Evangelical College BP 1200, N'Djamena, Chad

Breast cancer, being among the most frequent and fatal cancers in women, is an enormous issue globally. The critical requirement for novel treatment methods is underscored by its high mortality rate and relentless advancement. Even though breast cancer is one of the world's most common causes of death, the therapeutic avenue is still limited. The aim of this work is to investigate the potential inhibitory effects of specific compounds present in leaf extract from *Mangifera indica* on the growth of drug-resistant breast cancer protease PDB ID 3w32. The chemical compounds present in *Mangifera indica* leaves were used to analyze using molecular modeling techniques, such as molecular docking, molecular dynamics (MD) simulations, quantum mechanics (QM) calculations,

Abbreviations: ADME, Absorption, Distribution, Metabolism, and Excretion; ADMET, Absorption, Distribution, Metabolism, Excretion, and Toxicity; CADD, Computer-Aided Drug Design; DFT, Density Functional Theory; HOMO, Highest Occupied Molecular Orbital; LUMO, Lowest Unoccupied Molecular Orbital; C.B, Breast Cancer; CRT, Chemo-Radiation; RMSD, Root Mean Square Deviation; RMSF, Root Mean Square Fluctuation; MD, Molecular Dynamics; MEP, Molecular Electrostatic Potential; NMR, Nuclear Magnetic Resonance; PASS, Prediction of Activity Spectra for Substances; PK, Pharmacokinetics; QM, Quantum Mechanics; RT, Radiation Therapy; SID, Simulation Interaction Diagram; SASA, Solvent Accessible Surface Area; DMPK, Drug Metabolism and Pharmacokinetics; BBB, Blood-Brain Barrier; CYP 2D6, Cytochrome P450 2D6 (a liver enzyme involved in drug metabolism); OCT2, Organic Cation Transporter 2; LD50, Lethal Dose, 50% (the dose required to kill half the members of a tested population); bw, Body Weight; 3w32, PDB ID of the protein structure used in the study; PDB, Protein Data Bank; AMES, Ames Test (a test used to assess mutagenicity); T. Pyriformis, *Tetrahymena* Pyriformis (a ciliate protozoan used in toxicity testing).

and the Absorption, Distribution, Metabolism, Excretion, and Toxicity (ADMET) method, in order to examine three key chemical constituents: quercetin (08), catechin (09), and elagic acid (10). The ligands undergo extensive testing to figure out how effective they are against the 3w32-overexpressing breast cancer protein. Quantum calculations retaining HOMO-LUMO analysis might identify important characteristics of molecules, such as chemical potential, electronegativity, hardness, softness, and orbital energy gaps. According to the molecular docking inquiry, ligands 08, 09, and 10 are strong candidates with strong binding affinity for the breast cancer protein that overexpresses 3w32. The protein binding site stability of the chosen natural ligands was verified by MD simulation. These three ligands not only surpass the efficacy of the FDA-approved treatment, but also fulfill the requirements for a possible new inhibitor of breast cancer.

KEYWORDS

breast cancer, ADMET, frontier molecular orbitals, DFT, molecular dynamic simulation, 3w32 protein. −5.668

Introduction

Breast cancer is a life-threatening problem around the world particularly women. It is common and ranks as the second-most deadly cancer among all cancers (Sun et al., 2017; Kolak et al., 2017) as well as widely viewed as a disease that affects older women and is thought to be relatively uncommon in younger women (Azim and Partridge, 2014). The risk factors of Breast cancer include sex, age, family history, reproductive variables (late menopause, early menarche, low parity, first pregnancy at a late age, nursing, abortion, number of live births, and so on), estrogen, and lifestyle (Rojas and Stuckey, 2016). Benign breast tumors began as ductal hyperproliferation and were later transformed into malignant or metastatic breast tumors using mutagens. Some genes, such as BRCA1, BRCA2, HER2, Epidermal Growth Factor Receptor (EGFR), c-Myc, Ras, and others, are also linked to breast cancer (Sun et al., 2017).

Treatment for breast cancer is determined by its stage, biomarkers, and histology. Chemotherapy, radiation therapy, surgery, endocrine therapy, and neoadjuvant or adjuvant chemotherapy are some of the treatments available (Hortobagyi, 1998; Fisusi and Akala, 2019). Some medicines, such as capecitabine, gemcitabine, vinorelbine, taxane, anthracycline, methotrexate, mitomycin C, docetaxel, and cisplatin, are used in various combinations to treat breast cancer and are administered by nanoparticles due to their diverse properties as drug delivery vehicles (Fisusi and Akala, 2019; Tran et al., 2020). However, these treatments are costly, can lead to further post-treatment problems, and cancer recurrence is common. Keeping these dangers in mind, researchers are currently working to produce novel medications from natural sources that will cure breast cancer more effectively while also assuring patient safety.

Mangifera indica is a popular fruit plant in the Anacardiaceae family, and extensive research has been conducted on its leaves due to its numerous health advantages. *Mangifera indica L.* leaves contain a variety of phytochemicals, including gallic acid, protocatechuic acid, shikimic acid, mangiferin, homomangiferin, and quercetin. These leaves are also high in proteins, vitamins, and minerals, and they have antimicrobial, antioxidant, anti-diabetic, anti-cancer, lipid-lowering, hepatoprotective, anti-obesity, and anti-diarrheal effects (Kumar et al., 2021; Mirza et al., 2021). It is already being researched as a potential treatment for breast cancer. Researchers discovered that the phytochemicals in this plant extract can effectively suppress breast cancer cell growth, proliferation, invasion, and migration while also initiating cell cycle arrest and death (Rasul et al., 2021; Yap et al., 2021a).

We applied Computer-aided drug design (CADD) to investigate the anticancer properties of the phytochemical presents in this plant. This *in silico* approaches provide dynamics in overall drug design and development by reducing costs, time, and laboratory equipment (Macalino et al., 2015; Yu and MacKerell, 2017). The major goal of this work is to identify prospective therapeutic candidates from phytochemicals found in *Mangifera indica L.* leaves against particularly sensitive breast cancer proteins.

Materials and methods

Ligand's profiling and optimization

Only ligands that meet particular criteria, such as being in the correct tautomer and ionization states and having the correct bond ordering, can be used in virtual screening (Madhavi Sastry et al., 2013). The Gaussian version 09 approach and realistic density functional theory (DFT) methodologies were employed to accomplish substantial atomic enlargement (Hosen et al., 2021). We employed a modified version of the Gaussian code with modifications to its polarization capability premise set (DNP), B3LYP, and Gaussian version 09 capabilities to obtain the highest achievable accuracy (Mohapatra et al., 2021). The files that represent electron negativity, electron partiality, energy gap, synthetic potential, hardness, delicate quality, and electrophilicity were solved using the criteria listed in the order (Equations 1–8). Subatomic limit orbital charts (HOMO and LUMO) were then calculate using mathematical procedures of given equations. The modified particle was then stored in a PDB file.

$$E_{gap} = (E_{LUMO} - E_{HOMO}) \quad (1)$$

$$I = -E_{LUMO} \quad (2)$$

$$A = -E_{HOMO} \quad (3)$$

$$(\chi) = \frac{I + A}{2} \quad (4)$$

$$(\omega) = \frac{\mu^2}{2\eta} \quad (5)$$

$$(\mu) = -\frac{I + A}{2} \quad (6)$$

$$(\eta) = \frac{I - A}{2} \quad (7)$$

$$(S) = \frac{1}{\eta} \quad (8)$$

Prediction of activity spectra (PASS) assessment

The PASS Online resource is freely available on the internet (http://www.way2drug.com/passonline). This tool seeks to predict the biological activity spectra of organic compounds for over 4000 different types of biological activity using their structural formulae (Poroikov et al., 2019). Over 95% of the time, it properly predicts the outcome. Researchers examined the structure-activity relationships in the training set to create the forecast. This set contains information on the structures and biological functions of approximately 300,000 chemical molecules. We examine the advantages and disadvantages of this strategy. There is information available on how to interpret the forecast's findings (Druzhilovskiy et al., 2016). The PASS Online website has real-world applications that prioritize chemical synthesis and biological testing based on prediction findings. New pharmacological medications are being created, and PASS Online is expected to play a growing role as a multidisciplinary academic research center in this area (Siddikey et al., 2022).

Pharmacokinetics properties assessment

Pharmacokinetics refers to the mathematical study of the ADME characteristics of a drug in relation to its dose and duration. The computational drug design and development process helps optimize a molecular candidate into a viable treatment by assessing pharmacokinetic features early on (Zhou et al., 2016). Therefore, the pharmacokinetic parameters of the selected drugs were determined using the Swiss-ADME server (http://www.swissadme.ch/index.php) (Daina et al., 2017). By utilizing the server, one can observe and anticipate the drug's various pharmacokinetic and pharmacodynamics features.

Protein retrieved and preparation

A number of different proteins contribute to the development of breast cancer in females. Proteins with PDB IDs 3W32 were chosen as breast cancer susceptibility proteins after careful consideration of literature, methodologies, resolution, and organisms utilized for protein isolation. The choosing factors of the protein PBD ID 3w32 is depicted in the Supplementary Table S1. Crystal structures of these proteins were sourced from the Protein Data Bank (PDB) maintained by the RCSB (https://www.rcsb.org) (Burley et al., 2023). In order to remove water molecules and protein ligands, proteins were purified using the PYMOL software (version 2.4.1) before protein production. The website CASTp (http://sts.bioe.uic.edu/castp/index.html?2was) was utilized to gather the active site residues of the target proteins. Information on the proteins that were produced is shown in Table 1.

Binding site identification and receptor grid generation

In protein-ligand interactions, binding sites can be found by looking for well-known pockets. The protein's binding site was examined using BIOVIA Discovery Studio Visualizer v19.1 (BIOVIA) following a PDB search for the known and experimentally verified protein structure in complex with the ligand (PDB ID: 3w32). As shown in Figure 1, the binding site obtained from the complex structure was used in the receptor grid construction during the molecular docking using the PyRx virtual screening tool.

Molecular docking simulation

To find the best hit candidates against the needed protein, a molecular docking simulation was performed using the PyRx program (Dallakyan and Olson, 2015). PyRx is a free, free and open-source virtual screening implementation that also includes the docking wizards AutoDock 4 and Vina. It may search a big database of molecules for a specific macromolecule with a medical application. We used the AutoDock Vina wizard with Pyrex's default settings to simulate molecular docking. To begin, we used Pyrex's conjugate gradient approach to reduce the energy of the chosen ligands in the Merc molecular force field (mmff94 force field). The final phase of docking was to convert these energy to PDBQT format. Autodocking was performed with grid box dimensions of 58.5633 X, 53.9165 Y, and 66.1292 Z, with center X, Y, and Z values of 18.8128, 25.7483, and 14.2748, respectively. All of the ligands and proteins had their surfaces covered with a grid box.

Quantum mechanics (QM) calculation

The conformation of the ligand to the protein binding site is the most important factor in determining a potential active conformation, binding affinity, and strain discipline related to the binding mechanism. Structure optimization and least energy conformation methods based on the solution phase and the same gas-phase energy can be used to accomplish this kind of binding. Because of the metal ions, the ligand-protein combination does not conform to the expectations of classical molecular mechanics (MM) (Bronowska, 2011). The development of scoring functions that may describe electronic structure, electronic transitions, and system-specific charges in a molecular system reaction has recently been greatly aided by QM-based calculations. Eighty to ninety percent of modern quantum mechanics (QM) calculations employ DFT. For

TABLE 1 Information of protein's selected for breast cancer.

Properties	3W32
Method	X-ray diffraction
Resolution	1.80 Å
Organism	*Homo sapiens*
Active Site Residues	LEU718, GLY719, SER720, GLY721, ALA722, PHE723, GLY724, VAL726, ALA743, LYS745, MET766, VAL769, ASP770, ASN771, VAL774, CYS775, ARG776, LEU777, LEU778, THR790, GLN791, LEU792, MET793, GLY796, CYS797, LEU799, ASP800, ASP837, ARG841, ASN842, LEU844, LYS852, THR854, ASP855, PHE856, LEU858, PRO877, PHE997, LEU1001, ALA1013, ASP1014, LEU1017

this study, DFT quantum mechanical computations on a subset of molecules were required. We started by finding compounds with the best possible bond lengths, angles, and dihedral angles. The DFT of the compounds was then calculated using Gaussian version 09 (Abdelrhman et al., 2021). The B3LYP functional set was utilized by.

DFT. The DFT needed the 6311G basis set to describe the molecule's electronic wave functions.

Molecular dynamics simulation

The degree of stability of the chosen candidate compounds when bound to the active site cavity of the target protein was assessed by applying molecular dynamics (MD) simulations on the complex structure for a duration of 100 nanoseconds. This technique was done in order to assess whether the binding was secure. A molecular dynamics (MD) simulation of the complicated structure was performed in the Schrodinger research edition using the 'Desmond v3.6 Program' (Bharadwaj et al., 2021). The Linux operating system was used to conduct this simulation. This process has to be followed in order to ascertain whether thermodynamic stability is present in the receptor-ligand pair. Using a pre-set TIP3P water model and making sure the volume didn't change during the procedure solved the issue. By positioning an orthorhombic periodic box shape at a distance of 10 s on either side of the border, this was possible. It was found that the right ions, such as Na+ and Cl-, were selected and then randomly distributed throughout the solvated system in order to electrically neutralize it. The concentration of salt was 0.15 M. The Desmond module defined a procedure for reducing and relaxing the ligand and protein after they had come together to form the solvated system. The characteristics of the OPLS-2005 force field were used in this technique. The NPT ensemble was kept at a temperature of 300 K and an atmospheric pressure of one (1.01325 bar) by using the Nose-Hoover temperature coupling and isotropic scaling technique after fifty PS recording intervals with an energy of 1.2 were completed. The goal of doing this was to provide precise temperature coupling.

Simulation trajectory analysis

Schrodinger's Maestro interface version 9.5 was utilized in order to render each and every image that was captured during the computational modelling simulation. The MD simulation was deemed to be of sufficient quality, and the Simulation Interaction Diagram (SID), which is a component of the Desmond module of the Schrodinger package, was utilized in order to conduct an analysis of the simulation event. According to this evaluation, the MD simulation is capable of meeting the requirements that are considered acceptable. On the basis of the trajectory output, the root mean square deviation (RMSD), root-mean-square fluctuation (RMSF), protein-ligand contacts (P-L contacts), and hydrogen-bond

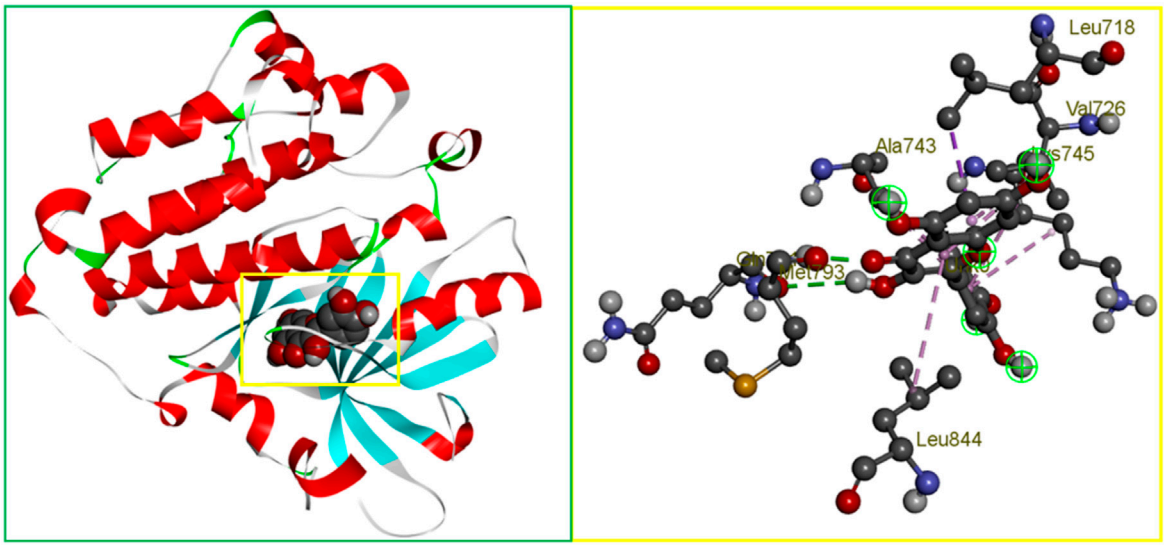

FIGURE 1
The binding site position of breast cancer identified from the protein–ligand complex (PDB ID: 3w32) structure. Ball shape 3D representation of the binding site with the grid box shown on the left side in the figure, where 2D binding site position has also been represented on the right side of the figure.

interactions were utilized in order to assess the stability of the complex structure. This investigation was conducted with the purpose of determining whether or not the intricate construction was capable of withstanding a variety of stresses without deteriorating in its shape.

Root mean square deviation (RMSD) *analysis*

The RMSD is a statistic used in molecular dynamics (MD) modelling to calculate the average distance an atom moves in comparison to a standard over a given time period (Fukutani et al., 2021). Distance is relative when compared to a starting point in time. Following the alignment of the relative mean square deviation (RMSD) of the protein-fit ligand atoms from each time frame, a comparison to the reference time, in this case 100 nanoseconds is performed. This comparison is based on the RMSD of the protein's structural atoms, which include the Ca, backbone, sidechain, and heavy atoms. It would be evident whether or not the alignment was satisfactory as soon as the reference time arrived. The RMSD required for an MD simulation of length x time steps can be determined using the equation shown below (Equation 9).

$$RMSD_x = \sqrt{\frac{1}{N}\sum_{i=1}^{N}\left(r_i^{'}\left(t_x\right)\right) - r_i\left(t_{ref}\right)\Big)^2} \tag{9}$$

here, N specifies the total number of selected atoms, t_{ref} denotes the reference time, and r' denotes the position of the selected ref atom in frame x. After superimposing the reference frame, Tx defines the recording intervals.

Root mean square fluctuation *(RMSF) analysis*

In order to characterize and keep track of the local conformational shift that takes place within a protein structure, the RMSF is primarily applied (Ding and Peng, 2019). An MD simulation of a protein can be constructed by using the equation (Equation 10), which asks for the number of residues and the RMSF value.

$$RMSF_i = \sqrt{\frac{1}{T}\sum_{t=1}^{T} < \left(r_i^{'}\left(t\right)\right) - r_i\left(t_{ref}\right)\Big)^2 >} \tag{10}$$

In this case, T mainly denotes the trajectory time, r' denotes the chosen atoms' position in the reference frame as overlaid on frame i, t_{ref} denotes the reference or given time, and (<>) denotes the average of the square distance over residue b.

Toxicity assessment

The amount of toxicity of a chemical substance can be measured by determining the extent to which it poses a risk to humans or animals, or by determining if it has the power to destroy an organ. Toxicity evaluation refers to both of these procedures. Prior to the initiation of a drug study, an investigation of the potential detrimental effects of chemical substances must be conducted. The conduct of a toxicity test is commonly recognized as one of the most important and critical components of the pharmaceutical production process. As a result, the web-based pkCSM server (Pires et al., 2015) was used to successfully complete the evaluation of the toxicity of the compounds chosen.

Results and analysis

Chemistry of extracted phytochemicals

The diversity of natural phytochemicals, along with their intriguing biological roles, sets them apart from synthetic phytochemicals. It is difficult to draw clear functional and structure-activity relationships regarding the effects of phytochemicals on biological systems' activity (Efferth and Koch, 2011). This is mostly due to the complex interactions that take place inside physiological systems as well as the high concentration of phytochemicals that have structural similarities. In addition, a significantly larger number of phytochemicals likely exist in nature, given the vast number already discovered. Technological advancements in synthesis, along with the development of more effective methods for isolation and analysis, have increased and help to identify the novel phytochemicals as lead compounds for the treatments of various diseases (Avidon et al., 1982). Figure 2 was generated with ChemDraw Ultra 12.0 and shows the chemical formulas and two-dimensional structures of top two ligands or phytochemicals and one FDA-approved medication (D1: Abemaciclib). The supplemental ST-2 contains an abundance of ligand-related information, and the 2D chemical structures of the selected ligands is depicted in Supplementary Figure S1.

Geometry optimized structures of ligands

In the discipline of computational chemistry, it is common practice to employ quantum mechanical methods to determine the thermodynamic, molecular orbital, and electrostatic properties of molecules. Each calculated derivative was strengthened and geometrically changed using the Gaussian 09 program to produce better results. Using DFT, we were able to boost the molecular orbital and thermal properties, allowing us to make predictions. This theory is compatible with both the hybrid model of B3LYP (Becke, 3-parameter, Lee-Yang-Parr) and the Gaussian version 09 polarization function basis set 6-311G (split-valence basis set) (Singh and Singh, 2017). Each chemical compound's electrical energy, dipole moment, enthalpy, and free energy were calculated. Figure 3 depicts the optimal geometry and structure of the top most phytochemicals, and the all-optimized structure are shown in Supplementary Figure S2.

Optimized chemical structures of ligands are crucial in drug discovery, molecular docking, and computational chemistry, as they represent the most stable, energy-minimized conformations. By optimizing ligand structures, researchers ensure accurate interaction predictions with target biomolecules, enhancing binding affinity and specificity. This process helps in rational drug design, reducing experimental costs and time. Furthermore,

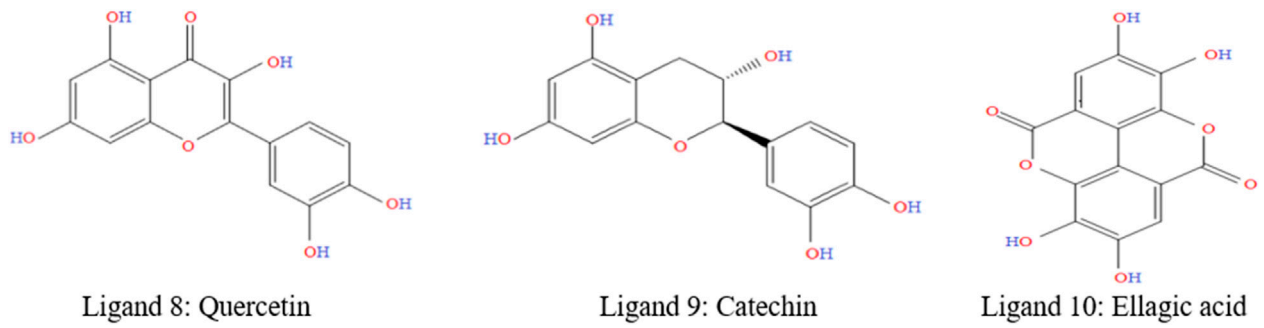

FIGURE 2
2D chemical structure of top selected ligands.

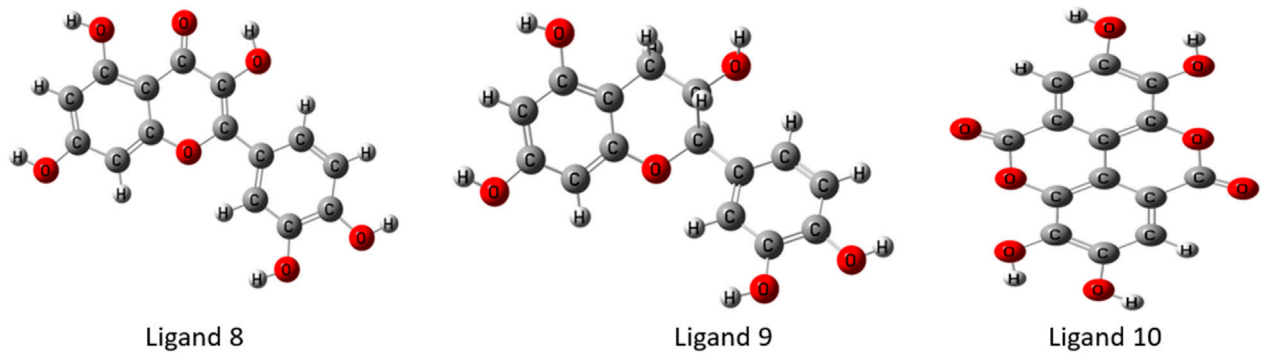

FIGURE 3
Geometry optimized chemical structures of top ligands.

optimized ligands improve the accuracy of pharmacokinetic and pharmacodynamic modeling, leading to more effective and safer therapeutic agents.

Frontier molecular orbitals (FMOs) evaluations

Chemical descriptors (HOMO and LUMO) and FMOs control the kinetic stability and chemical reactivity of molecules, respectively. Molecular orbitals that are least occupied are called LUMOs, and those that are most populated are called HOMOs. The electronic absorption of molecules releases one electron, which is caused by the HOMO state. The LUMO state accepts the electron simultaneously, and an energy gap forms as a result. These properties—kinetic stability, chemical reactivity, and atomic electrical transmission—are built upon this energy gap. The larger the energy difference, the more stable the molecule is when its HOMO and LUMO are far apart. The reason behind this is that the DFT method is used to calculate the energy gap. However, chemical stability is negatively affected by a small energy gap when the distance between a molecule's HOMO and LUMO is small (Ahamed et al., 2023) (Kobir et al., 2023) (Yu et al., 2022). The small energy gap is the root cause of the chemical instability. In Figure 4, the color radish brown is used to represent the molecules' positive node in both HOMO and LUMO situations, whereas the color deep green is used to represent the molecules' negative node.

Quantum mechanics (QM) and chemical reactivity analysis

The table below covers several medications and phytochemicals, as well as information regarding their reactivity and frontier molecular orbitals (HOMO-LUMO). The sign A denotes HOMO energy, the letter I denotes LUMO energy, the letter μ represents chemical potential, the letter η denotes hardness, the letter σ denotes softness, the letter X denotes electronegativity, and the letter ω denotes electrophilicity. When we examine the energy gap between each of the fifteen molecules, we can find that Ligand No. 07 has the highest chemical stability at 11.3746 eV and the lowest at 7.49021 eV. This information can be found in Table 2. The Supplemental ST-3 has an extremely comprehensive computation.

The HOMO energy varies between −10.4799 eV (Ligand 7) and −8.54465 eV (Ligand 8), while the LUMO energy ranges from 0.89471 eV (Ligand 7) to −1.92793 eV (Ligand 10). The energy gap (E_gap) spans from 7.49021 eV (Ligand 10) to 11.3746 eV (Ligand 7), indicating significant variations in electronic stability and reactivity among the ligands. The chemical potential (μ) ranges

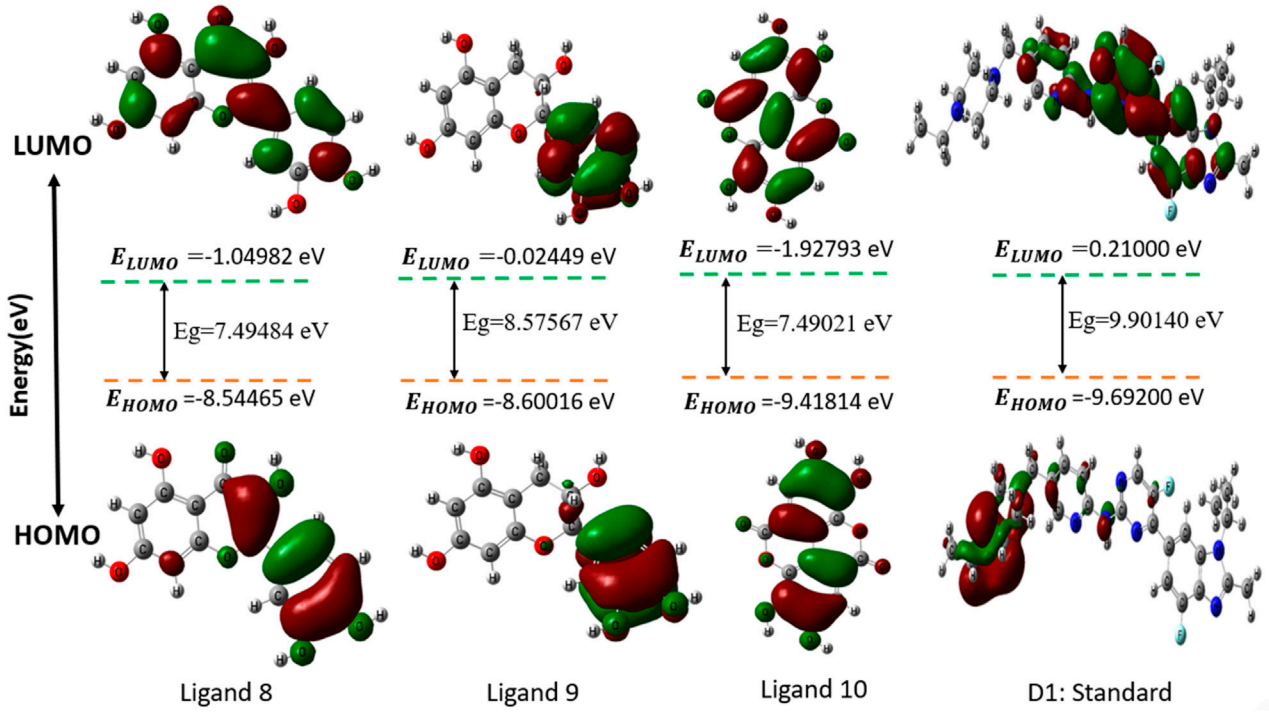

FIGURE 4
Diagram of HOMO-LUMO for selected compounds.

TABLE 2 Frontier molecular orbitals and reactivity descriptor analysis.

Ligand no.	A = HOMO (eV)	I = LUMO(eV)	E gap = (I-A)eV	Chemical potential (μ) = - (I + A)/2	Hardness (η) = (I-A)/2	Softness (σ) = 1/μ	Electronegativity (X) = (I + A)/2	Electrophilicity (ω) = μ2/2η
1	−9.14657	−1.08410	8.06247	5.11534	4.03123	0.19549	−5.11534	3.24549
2	−10.4680	−1.08927	9.37868	5.77861	4.68934	0.17305	−5.77861	3.56045
3	−9.20290	−0.93226	8.27063	5.06758	4.13532	0.19733	−5.06758	3.10501
4	−9.76780	0.378240	10.1460	4.69478	5.07302	0.21300	−4.69478	2.17237
5	−8.92997	−0.85934	8.07063	4.89465	4.03531	0.20430	−4.89465	2.96849
6	−9.05350	−0.93036	8.12315	4.99193	4.06157	0.20032	−4.99193	3.06770
7	−10.4799	0.89471	11.3746	4.79261	5.68732	0.20865	−4.79261	2.01933
8	−8.54465	−1.04982	7.49484	4.79723	3.74742	0.20845	−4.79723	3.07057
9	−8.60016	−0.02449	8.57567	4.31233	4.28784	0.23189	−4.31233	2.16848
10	−9.41814	−1.92793	7.49021	5.67303	3.74510	0.17627	−5.67303	4.29672
11	−8.86466	−1.11757	7.74709	4.99111	3.87354	0.20036	−4.99111	3.21556
12	−9.22358	−1.27132	7.95226	5.24745	3.97613	0.19057	−5.24745	3.46263
13	−9.14793	−1.18669	7.96124	5.16731	3.98062	0.19352	−5.16731	3.35388
14	−8.88371	−1.14995	7.73375	5.01683	3.86688	0.19933	−5.01683	3.25438
15	−9.27120	−1.36084	7.91035	5.31602	3.95518	0.18811	−5.31602	3.57254
D-1	−9.69200	0.21000	9.90140	4.74100	4.95100	0.21100	−4.74100	2.27000

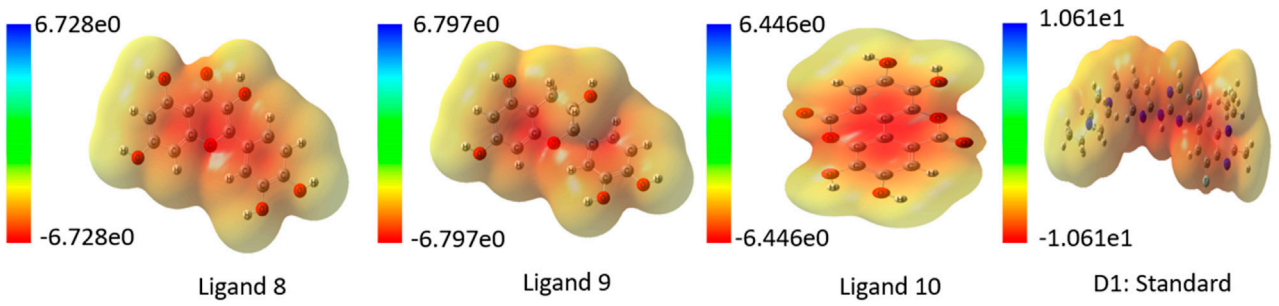

FIGURE 5
Charge distribution in Molecular Electrostatic Potential (MEP) for top ligands.

from −5.77861 eV (Ligand 2) to −4.31233 eV (Ligand 9), with electronegativity (X) following the same trend. Hardness (η) varies from 3.74510 eV (Ligand 10) to 5.68732 eV (Ligand 7), while softness (σ) exhibits an inverse trend, emphasizing the ligands' adaptability to electronic perturbations. Electrophilicity index (ω) values range from 2.01933 eV (Ligand 7) to 4.29672 eV (Ligand 10), indicating differences in their propensity to accept electrons. Notably, D-1 exhibits moderate values across all parameters, serving as a reference for comparative evaluation. These quantum chemical descriptors provide insights into the ligands' stability, reactivity, and potential applications in coordination chemistry, catalysis, and molecular design.

Analysis of molecular electrostatic potential (MEP)

An essential part of computer-aided drug design is determining the ligands' molecular electrostatic potential (MEP), which yields a charge distribution map based on electron availability and scarcity. Additionally, it shows where the protein and ligand bind and how the charges are distributed in three-dimensional ligand structures. When applied to ligand surface analysis, MEP analysis can further help pinpoint where ligands are vulnerable to attack from electrophiles and nucleophiles (Lakshminarayanan et al., 2021; Guerrab et al., 2022). Utilizing quantum chemistry techniques, the MEP map was generated, and Gaussian functions were assessed with the use of Gaussian fundamental sets. In this study, blue represents positive charge, red negative charge, and green neutral charge. A lower negative charge than a larger positive charge is observed in all of the discovered ligands, as shown in the MEP map of top ligands in Figure 5. In Supplementary Figure S3 contains MEP map for all ligands.

Analysis of PASS prediction data

The PASS prediction assessment displays the details of the antiviral, antibacterial, antifungal, antiparasitic, anticarcinogenic, anticancer (breast cancer), and inhibitory effects of drugs and ligands on breast cancer-resistant proteins. It is used to assess the potential biological activity against the targeted disease. According to our investigation, the Ligand No. 07 has low to moderate antiviral activity (Pa > 0.454), Ligand No. 11 and 14 have moderate to high antibacterial activity (Pa> 0.599), and Ligand No. 15 has low to significantly high antifungal activity (Pa > 0.678). To top it all off, most ligands have excellent anti-carcinogenic activity, meaning they won't cause cancer when taken orally. Ligands 05 (Pa > 0.649), 08 (Pa > 0.577), 11, and 14 (Pa > 0.502), as well as No (Pa> 0.526), exhibit strong anticancer properties, according to additional research. After reviewing the PASS prediction data for breast cancer-resistant protein has been selected, and we found that Ligand No. 05 has a very good Pa value (Pa > 0.516) as illustrate in Supplementary Table S4.

Evaluation of ligands' drug likeliness and pharmacokinetics properties

Pharmacokinetics (PK), an important parameter in medicine design, explains the time it takes for the body to absorb, distribute, metabolize, excrete, and contaminate a drug or foreign chemical after administration. This word is commonly used by pharmacists. As a result, PK promotes effective drug design (Lavé et al., 2016). Table 4 displays information for certain ligands and the medicine on drug likelihood, pharmacokinetics, Lipinski's rule of five, and other topics. A ligand must meet ADME standards before it may be evaluated for drug candidate certification. The five Lipinski rules must be followed: a molecular weight ranging from 150 to 500 g/mol, a limited number of hydrogen bond donors, a number of rotatable bonds, a high bioavailability score, and a topological surface area value ranging from 20 $Å^2$ to 130 $Å^2$ (Singh et al., 2022; Al Hasib et al., 2022).

The Table 3 reveals that, with the exception of Ligands 11, 12, 13, 14, and 15, all of the ligands follow Lipinski's rule of five. In terms of molecular weight, all of the ligands have the necessary molecular weights (150–500 g/mol), with the exception of drug D-1 (506.59 g/mol) and Ligand No. 15 (594.52 g/mol). As a result, with the exception of Ligands 04, 11, 14, and 15 (which have six rotatable bonds) and Ligand D-1 (17 rotatable bonds), no ligand can have more than three rotatable bonds. Except for Ligands 11 (12) and 12, the hydrogen bond acceptor can only receive a maximum of 10 hydrogen bonds from any of the ligands. Ligands are the numbers 12, 15, and N0 13. Except for ligands 7, 8, 9, 11, 12, 13, 14, and 15, no other ligand contributes more than five hydrogen bonds. Ligands 8, 10, 11, 12, 13, 14, and 15 do not match the drug development criteria since their topological surface areas exceed the range of 202 $Å^2$ to 130 $Å^2$. Apart from Ligands 11, 12, 13, 14, and 15,

TABLE 3 Data of ligands' drug likeliness, pharmacokinetics properties, and Lipinski's rule.

Ligand no.	Molecular weight (g/mol)	Number of rotatable bonds	Hydrogen bond acceptor	Hydrogen bond donor	Topological polar surface area (Å^2)	Lipinski's rule		Bioavailability score
						Results	Violation	
01	170.12	1	5	4	97.99	Yes	00	0.56
02	174.15	1	5	4	97.99	Yes	00	0.56
03	154.12	1	4	3	77.76	Yes	00	0.56
04	213.23	4	5	3	86.63	Yes	00	0.56
05	260.20	0	6	4	111.13	Yes	00	0.55
06	184.15	2	5	3	86.99	Yes	00	0.55
07	180.16	1	6	5	110.38	Yes	00	0.55
08	302.24	1	7	5	131.36	Yes	00	0.55
09	290.27	1	6	5	110.38	Yes	00	0.55
10	302.19	0	8	4	141.34	Yes	00	0.55
11	464.38	4	12	8	210.51	No	02	0.17
12	422.34	2	11	8	201.28	No	02	0.17
13	436.37	3	11	7	190.28	No	02	0.17
14	464.38	4	12	8	210.51	No	02	0.17
15	594.52	6	15	9	249.20	No	03	0.17
D-1	235.07	4	8	6	180.93	Yes	1	0.55

TABLE 4 Data of binding energy and name of interacted ligand for breast cancer protease (3W32).

Ligand No.	Binding affinity (kcal/mol)	No. of H bond	No. of hydrophobic bond	No. of van der waal bond	Total bonds
1	−6.1	05	02	Absent	07
2	−6.4	03	00	Absent	03
3	−6.3	03	04	Absent	07
4	−5.8	02	05	Absent	07
5	−7.6	02	05	Absent	07
6	−5.9	03	03	Absent	06
7	−5.7	03	00	Absent	03
8	−8.5	02	08	Absent	10
9	−8.4	04	05	Absent	09
10	−8.8	01	10	Absent	11
11	−8.6	01	03	Absent	04
12	−8.7	02	07	Absent	09
13	−8.5	04	04	Absent	08
14	−6.1	04	03	Absent	07
15	−6.4	04	08	Absent	12
D-1	−7.8	04	00	Absent	04

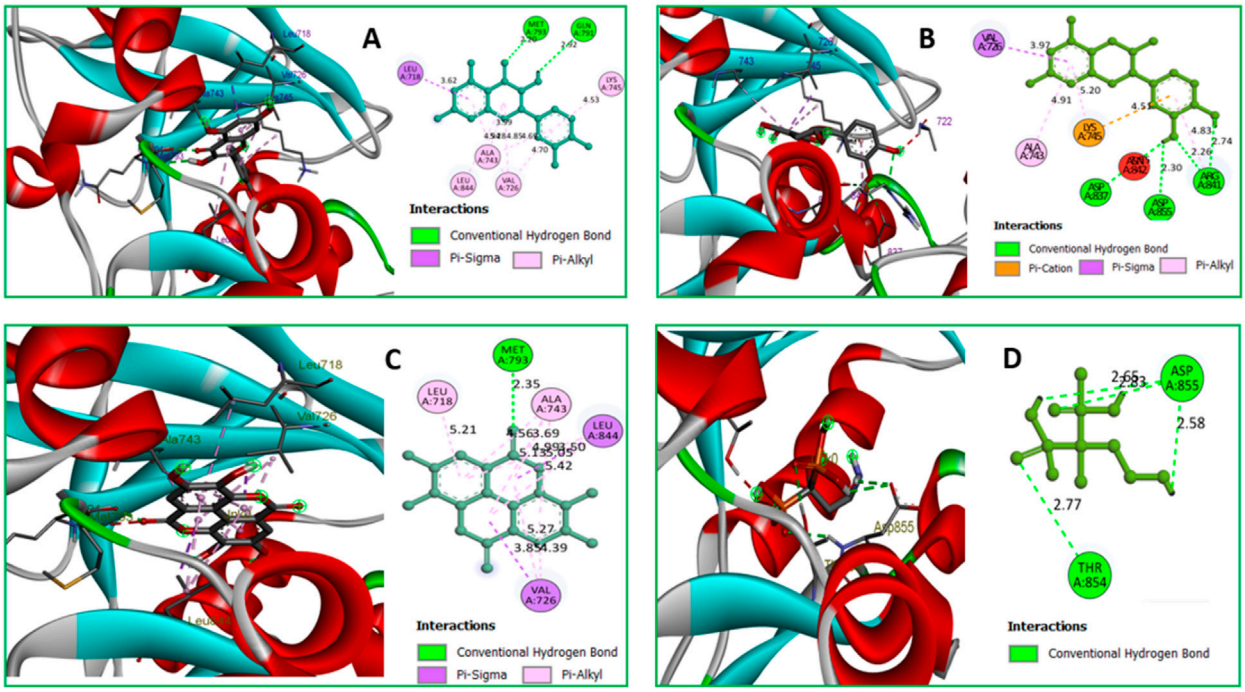

FIGURE 6
(A) The interaction between the 3w32 protein and Ligand 08 compounds. The 3D interaction has represented left side of the figure, where 2D interaction has depicted in right side of the figure accordingly. **(B)** The interaction between the3w32 protein and Ligand 09 compounds. The 3D interaction has represented left side of the figure, where 2D interaction has depicted in right side of the figure accordingly. **(C)** The interaction between the 3w32 protein and Ligand 10 compounds. The 3D interaction has represented left side of the figure, where 2D interaction has been depicted in the right side of the figure accordingly, and **(D)** The interaction between the 3w32 protein and Standard D1 compounds. The 3D interaction has represented left side of the figure, where 2D interaction has been depicted in the right side of the figure accordingly.

all of the other ligands had acceptable bioavailability values. After evaluating the facts offered previously, a conclusion can be reached. Several ligands have been removed from consideration as prospective pharmaceutical candidates; nevertheless, ligands 01, 02, 03, 05, and 06 remain on the list.

Molecular docking analysis of selected proteins and ligands

To identify possible breast cancer medication candidates, auto-docking was carried out with selected proteins susceptible to breast cancer (PDB ID: 3W32). Table 4 displays the molecular docking simulation data with binding affinities. In molecular docking, three chosen proteins have the highest binding affinities when interacting with Ligands Nos. 10, 11, and 12. However, Ligands 11 and 12 do not match the ADME criteria listed in Table 4. Ligands No. 08, 09, and 10 meet all drug property criteria in this study, having binding affinities of −8.5 kcal/mol, −8.4 kcal/mol, and −8.8 kcal/mol, respectively.

Protein-ligand interactions diagram

Protein-ligand interactions (PLIs) and protein-protein interactions (PPIs) play critical roles in identifying possible drug candidates for a target protein in structure-based drug design and drug discovery (Zhao and Bourne, 2022; Fu et al., 2018). This is why it is referred to as a critical component of the process. On the other hand, this part of the therapeutic goal is very important in and of itself. Because of the unique structural properties of protein interactions with ligands, it is today regarded as one of the most difficult areas of drug development. Bond distance research on the principal protease of breast cancer proteins have been conducted, with the primary focus of the studies being on the interaction of medicinal medicines with 3w32. Figure 6 depicts the key interactions that proteins and ligands have with amino acid residues.

Interacted amino acids with bond distance

Data on hydrogen bonds, hydrophobic bonds, and bond distances between amino acids are shown in Table 5. One of the most important factors in selecting a potential drug candidate is the bond distance, with a value between 3.1 Å to 3.55 Å indicating a weak link and a value between 2.5 Å to 3.1 Å indicating a strong binding, according to previous studies (da Cunha Xavier et al., 2024). Since the ADME screening and molecular docking did not include any other Ligands, we looked at how proteins with PDB ID 3W32 interacted with Ligands No. 01, to 15, and standard D1. From the, it shows that ligand 08 forms GLN791 (2.92 Å) and MET793 (2.20 Å) two strong hydrogen bonds, LEU718 (3.62 Å), VAL726 (4.70Å), VAL726 (3.99 Å), VAL726 (4.95 Å), LEU844 (4.69Å), ALA743 (4.28 Å), ALA743 (4.85 Å), LYS745 (4.53 Å) other bonds with

TABLE 5 Protein-ligand interactions and interacting bonds.

Protein PDB ID: 3W32									
No.	Hydrogen bond		Hydrophobic bond		No.	Hydrogen bond		Hydrophobic bond	
	Interacting residue of Amino acid	Distance A°	Interacting residue of Amino acid	Distance A°		Interacting residue of Amino acid	Distance A°	Interacting residue of Amino acid	Distance A°
01	MET 766 THR 790 THR 854 ASP 855 PHE 856	2.94 3.00 2.57 3.24 1.99	MET 766 LEU 777	5.17 4.66	09	ASP 837 ASP 855 ARG 841 ARG 841	2.55 3.30 2.26 2.74	VAL 726 ARG 841 ALA 743 LYS 745 LYS 745	3.97 4.83 4.91 5.20 4.51
02	MET 766 LEU 777 THR 790	2.73 2.65 2.70	Absent		10	MET 793	2.35	LEU 718 VAL 726 VAL 726 ALA 743 ALA 743 ALA 743 ALA 743 LEU 844 VAL 726 LEU 844	5.21 5.27 4.39 4.56 5.13 3.69 4.99 5.05 3.85 3.50
03	MET 766 LEU 777 ASP 855	2.79 2.51 2.64	MET 766 LEU 777 LEU 788 PHE 856	5.08 3.62 5.47 5.48	11	ASN 842	2.88	VAL 726 ALA 743 LYS 745	4.33 4.79 4.63
04	MET 793 MET 793	1.93 1.94	VAL726 ALA743 ALA 743 LEU 844 LYS745	4.05 3.79 4.43 4.94 4.53	12	LYS 745 ASP 855	2.49 3.65	VAL 726 ALA 743 ALA 743 LYS 745 LYS 745 LEU 844 VAL 726	4.44 4.73 4.90 5.30 4.59 5.24 3.83
05	MET 793 ASP 855	2.22 2.59	LEU 718 VAL 726 VAL 726 LEU 844 LEU 844	5.42 4.55 4.91 4.69 5.73	13	LYS 745 ASP 800 ARG 841 ASN 842	4.11 3.01 2.49 3.54	VAL 726 LYS 845 LYS 845 VAL 726	4.77 4.80 4.74 3.88
06	MET 766 ASP 855 ASP 855	2.73 3.51 3.19	LEU 777 MET 766 PHE 856	4.75 5.29 5.33	14	MET 793 ASN 842 ASP 855 GLY 721	2.70 2.69 2.20 3.23	VAL 726 ALA 743 LYS 745	4.31 4.80 4.62
07	ASN 771 VAL 774 LYS 852	2.11 2.21 2.08	Absent		15	LEU 718 LYS 745 ASP 800 ASP 855	2.93 2.69 2.14 2.47	VAL 726 VAL 726 ALA 743 ALA 743 LEU 844 LEU 844 ARG 841 LYS 745	4.63 4.60 5.35 5.25 5.00 4.93 4.11 4.95
08	GLN 791 MET 793	2.92 2.20	LEU 718 VAL726 VAL726 VAL726 LEU 844 ALA743 ALA 743 LYS745	3.62 4.70 3.99 4.95 4.69 4.28 4.85 4.53	D-1	ASP855 ASP 855 ASP 855 THR854	2.65 2.83 2.58 2.77	Absent	

protein 3W32. The ligand 09 forms ASP837 (2.55 Å), ASP855 (3.30 Å), AR841 (2.26 Å), and ARG841 (2.74 Å) strong bonds, and VAL726 (3.97 Å), ARG841 (4.83 Å), ALA743 (4.91 Å), LYS745 (5.20 Å), and LYS745 (4.51 Å) other bonds. On the other hand, ligand 10 forms MET793 (2.35Å) strong bond, and LEU718 (5.21Å), VAL726 (5.27Å), VAL726 (4.39Å), ALA743 (4.56Å), ALA743 (5.13Å), ALA743 (3.69 Å), ALA743 (4.99 Å), LEU844 (5.05 Å), VAL726 (3.85 Å), and LEU844 (3.50 Å) other bonds. Besides the standard D1 form ASP855 (2.65 Å), ASP855 (2.83 Å), ASP855 (2.58 Å), and THR854 (2.77 Å) strong bond

with protein. For more details on the various bond classifications and types, see supplementary SF-4 and Supplementary Table S5.

Molecular dynamic simulation

MD simulation modelling, which is employed in computer-aided drug discovery, may study the protein-ligand complex's stability and intermolecular interactions in real time. In a controlled situation, it can also detect conformational changes in complicated systems. A 100 ns molecular dynamics simulation was used to investigate the protein's structural changes during its interaction with the chosen ligand. Multimolecular activity was measured on final images acquired from the appropriate 100 ns trajectories. It was examined the findings of a molecular dynamics (MD) simulation, and this comprised solvent accessible surface area (SASA), radius of gyration (Rg), root mean square fluctuation (RMSF), and root mean square deviation.

Analysis of protein's RMSD

The average dislocation change of a chosen group of atoms over a certain period of time in relation to a reference time can be found using an RMSD value. A protein-ligand complex's optimal RMSD shift falls between 1 Å and 3 Å, or 0.1 and 0.3 ns. When the RMSD value exceeds the permitted limit, the protein's structure has undergone a significant alteration. To determine the RMSD value of the essential protein in association with the selected molecule and ligands 08, 09, and 10, we performed a 100 ns MD simulation. Figure 7 displays the RMSDs, or relative standard deviations, of several complexes. The following protein-ligand complexes are displayed: Apo-protein (red), protein-3w32 and ligand-08 (purple), protein-3w32 and ligand-10 (green), and protein-3w32 and ligand-D1 (standard) (blue). In Figure 7D, you can see all of these complexes unified. Prior to making comparisons, the red Apo protein Apo's RMSD is shown. Figure 7A shows that the average RMSD value ranges from 1.5 Å to 2.6 Å when comparing the protein-ligand combination 3w32_08 (purple color) to Apo (red color). Figure 7B shows that between 1.7 Å and 2.8 Å, the protein-ligand combination 3w32_09 (green) compared to Apo (red). Comparing the protein-ligand combination 3w32_10 (orange color) with Apo (red color), Figure 7C shows the RMSD variation within 1.4 Å to 2.3 Å. The four compounds (3w32_D1 in blue, Apo in red, 3w33_08 in purple, 3w32_09 in green, and 3w32_10 in orange) had an average RMSD value between 1.5 Å to 2.6 Å. This means that the compound's value fluctuation falls within the target range, as stated in references (Timofeev et al., 2023; Akash et al., 2023).

Ligand RMSD analysis

We analyzed the tested drugs and controls with respect to their RMSDs to find out which one was more stable. See Figure 8 for the RMSD values for Ligand No. 08 (purple), Ligand No. 09 (green), Ligand No. 10 (orange), and conventional D1 (blue). The compounds' RMSD was determined after aligning the docking complex with the Apo standard protein backbone. To find the optimal RMSD for each chemical, complex observation was utilized in this situation. The green RMSD of Ligand No. 09 fluctuates, although it stays within the permissible range of 0.5–1.4 Å (Liu et al., 2017; Sherman et al., 2006). Because of minute differences, Ligands No. 08 (purple) and No. 10 (orange) are rather inflexible. There isn't a whole lot of movement in the blue control D1 here. After looking at the RMSD values, this study revealed that all of the ligands were stable, but that Ligand No. 09 (green) was the most stable.

Protein Cα RMSF analysis

The root mean square fluctuation, or RMSF, can be used to identify and define the local modifications that occur along the protein chain when drugs interact with certain residues. So, to see how the shape of proteins changes when certain ligands attach to a specific remaining site, we calculated and displayed the RMSF value of the initial protein-ligand complexes in Figure 9. The variations of different chemical complexes with the targeted protein 3w32 are compared in this study. Figure 9A compares the 3w32_08 (purple) complex protein to the Apo (red), revealing that only PRO753, HIS870, ARG889, and SER921 were more fluctuating. That is, 98.73% of the residues were stable. Figure 9B compares 3w32_09 (green) complex protein to Apo (red) protein and reveals that THR751, GLU868, GLY873, and SER921 residues are more volatile, implying that 98.73% of residues are stable. Figure 9C compares 3w32_10 (orange) complex proteins to Apo (red), revealing that ALA702, PRO753, and GLY874 residues were more variable, indicating that 99.05% of the residues were stable. The conventional 3w32_D1 complex was compared to Apo (red) protein in Figure 9D, and it was discovered that GLN701, ALA722, GLY873, SER921, and GLY983 residues were more fluctuating, implying that 98.41% of the residues were stable. Protein stiffness is indicated by the substantially smaller variability of residues in the complex structure compared to the native structural components (Apo). Because the N- and C-terminal domains are located at the beginning and end of the protein, the majority of the changes are found there. As a result, ligands 08, 09, and 10 are suitable candidates for a molecule in which the possibility of a specific atom being displaced in a real-world environment is low.

Protein-ligand contacts evaluations

The interactions between the four selected ligands (Ligand 08, Ligand 09, Ligand 10, and Standard D1) and the breast cancer proteins 3w32 were monitored throughout the SID. Drug selectivity, metabolization, and adsorption seem to be significantly influenced by hydrogen-bonding properties in drug design, as demonstrated by the MD simulation's identification of hydrogen bonds, hydrophobic, ionic, and water bridge interactions. The simulation amply demonstrated the hydrogen bonding connection stated for both compounds up to the very last AA residue. In all structures, the protein residue and the ligand form a variety of interactions, including as hydrogen bonds, hydrophobic interactions, ionic interactions, and water

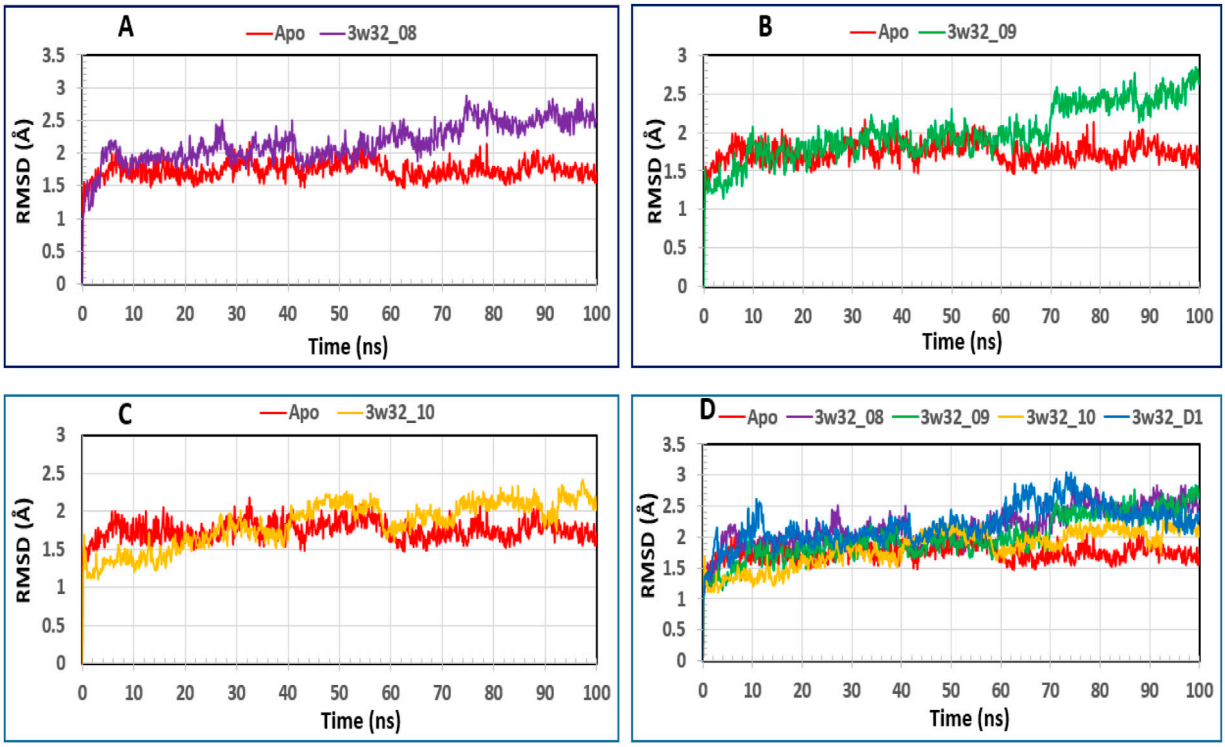

FIGURE 7
The RMSD measurements of the Cα atoms in the four compounds selected to form a complex with the breast cancer protein are illustrated: Herein, showing the RMSD of breast cancer protein 3w32 as Apo (Red) in complex with the compounds **(A)** 3w32_08 (purple), **(B)** 3w32_09 (Green), and **(C)** 3w32_10 (Orange), where **(D)** 3w32_D1 standard (Blue) representing all the compounds and protein RMSD together.

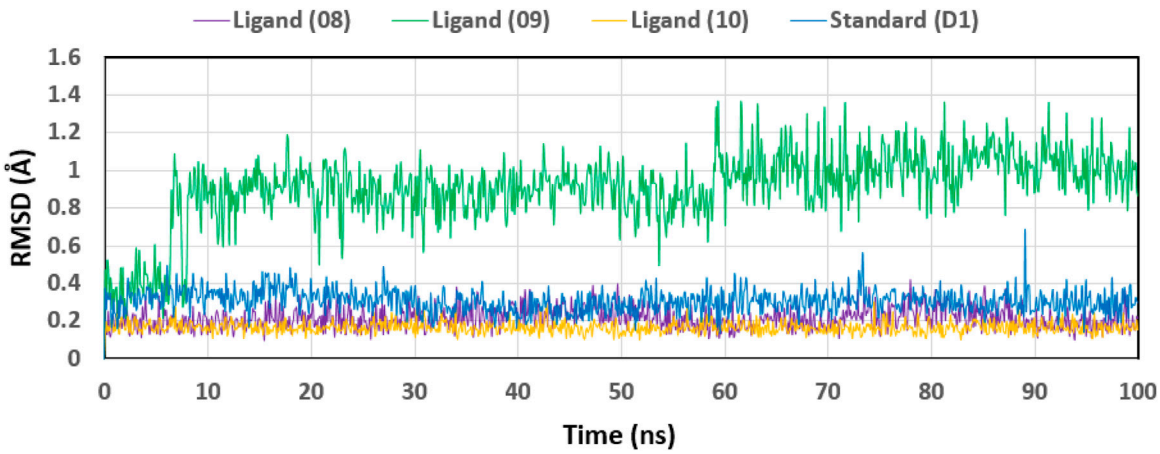

FIGURE 8
Displaying the RMSD values of the four compounds that were chosen and isolated from the complex system's Ca atoms. The four compounds—Lagend Nos. 08, 09, 10, and D1—were shown as purple, green, orange, and blue, respectively.

bridges, as Figure 10 shows. The complex 3w32_08 for ligand 08 produced multiple (more than two) interactions at the residues of ASP855, MET793, GLN790, ALA743, ASP800, ASG841, CYS797, LEU844, LEU718, LYS745, PRO794, and ASN842 with an interaction fraction (IF) value of 1.85, 1.25, 1.00, 0.85, 0.55, 0.50, 0.48, 0.45, 0.25, 0.20, and 0.20, respectively. This means that for 155%, 125%, 100%, 85%, 55%, 50%, 48%, 48%, 45%, 20%, and 20% of the simulation time, the specific interaction is maintained by the multiple contacts of the same subtype with the ligand as indicated in Figure 10A. Multiple interactions of the 3w32_09 complex have been observed in the case of ligand 09 at the positions of ASP800 (1.6), MET793 (1.4),

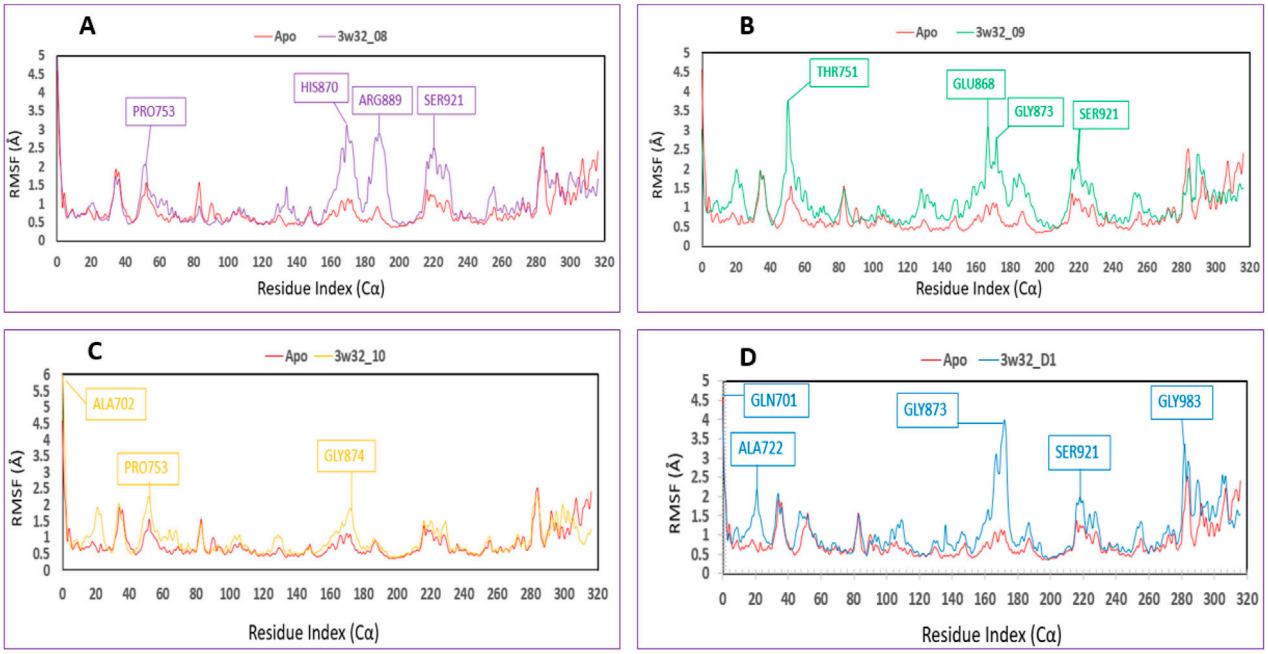

FIGURE 9
Showing the RMSF values that were taken out of the Cα atoms of the four compounds and were chosen to be in complex with the 3w32 protein. Herein, comparison of the RMSF of 3w32 Apo (Red) in complex with the compounds **(A)** 3w32_08 (purple), **(B)** 3w32_09 (Green), and **(C)** 3w32_10 (Orange), where **(D)** 3w32_D1 standard (Blue).

ARG841 (1.0), GLN791 (0.98), CYS797 (0.98), THR790 (0.7), SER720 (0.6), ALA743 (0.5), LYS745 (0.45), LEU844 (0.4), LEU718 (0.19), VAL726 (0.13), THR854 (0.10), and ASP855 (0.10) residues maintained by 160%, 140%, 100%, 98%, 98%, 70%, 60%, 50%, 45%, 40%, 19%, 13%, 10%, and 10% of the simulation time the in particular interaction indicated in Figure 10B. For ligand 10, it has been found that multiple interactions of the 3w32_10 complex are maintained by 200%, 198%, 100%, 60%, 50%, 50%, 45%, 30%, 30%, 25%, 15%, and 10% of the simulation time in the specific interaction shown in Figure 10C. These interactions are at the positions of ASP800 (2.00), ASP855 (1.98), MET793 (1.00), ARG841 (0.60), GLN791 (0.50), ASN842 (0.50), LEU844 (0.45), LEU718 (0.30), LYS745 (0.30), THR790 (0.25), THR854 (0.25), and SER720 (0.10) residues. Additionally, it has been discovered that, in the case of the standard D1, multiple interactions of the 3w32_D1 complex are maintained by 285%, 250%, 230%, 210%, 100%, 70%, 100%, and 5% of the simulation time in the specific interaction shown in Figure 10D. These interactions occur at the positions of ASP855 (2.85), PHE856 (2.50), THR854 (2.3), LYS745 (2.1), THR790 (1.00), GLN791 (1.00), ARG776 (0.70), LEU858 (0.10), and CYS775 (0.05) residues.

Ligand properties analysis

We assessed the stability of the four compounds (ligand 08, ligand 09, ligand 10, and standard D1) in the MD simulation using ligand characteristics. We employed the Radius of Gyration (rGyr), Intramolecular Hydrogen Bonds (intraHB), Molecular Surface Area (MolSA), Solvent Accessible Surface Area (SASA), and Polar Surface Area (PSA) to examine the characteristics of the ligands. In this analysis the molar surface area (MolSA) as depicted in SF-5 and the Polar Surface Area (PSA) as shown in SF-6, were used to analyze the ligand properties, all of which were found to be favorable for the ligands.

Radius of gyration (Rg)

One approach to think about the radius of gyration (Rg) of a protein-ligand complex system is in terms of atomic distribution along its axis. Rg is a useful tool and an important measure of the structural function of a macromolecule that can be used to predict changes in complex stiffness. Thus, we also investigated the stability of four ligands in their interaction with the target protein via Rg throughout the 100 ns simulation time depicted in Figure 11: ligand No. 08 (purple color), ligand No. 09 (green color), ligand No. 10 (orange color), and standard D1 (blue color). The compounds Ligand No. 08, Ligand No. 09, Ligand No. 10, and standard D1 were found to have average Rg values of 3.75, 3.76, 3.25, and 2.4, respectively. This implies that, upon binding the chosen compounds, the protein's active site did not experience any appreciable conformational changes (Mendichi et al., 2003).

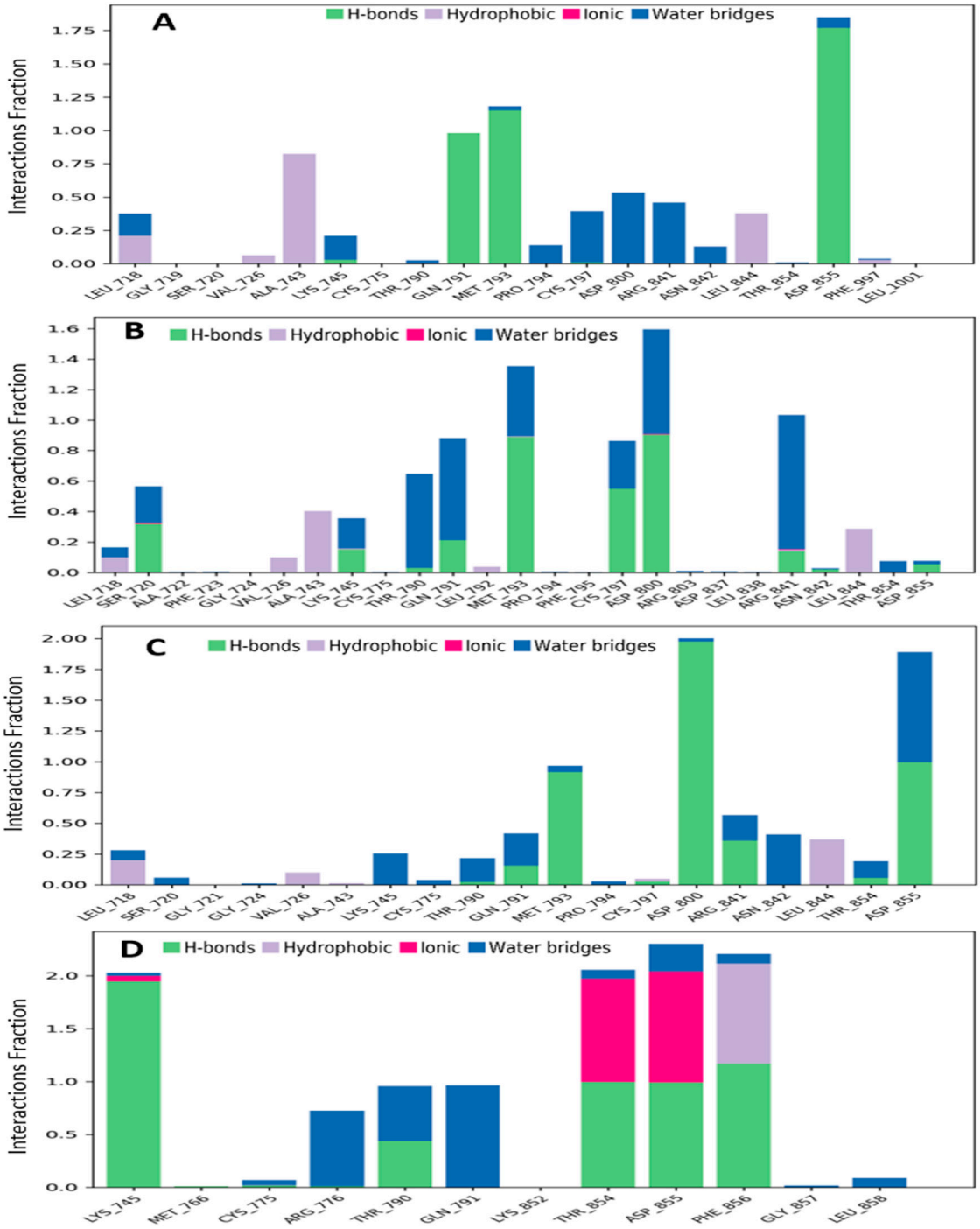

FIGURE 10
Graphs exhibiting the information about the protein–ligand interaction by 100 ns time of MD simulation. Herein, representing the compounds **(A)** ligand 08, **(B)** ligand 09, **(C)** ligand 10 and **(D)** standard D1 with the interactions of protein ID 3w32.

Solvent accessible surface area (SASA)

Biological macromolecules' Solvent-Accessible Surface Area (SASA) affects both their structure and functionality. The residues of amino acids on the surface of proteins are usually hydrophobic or hydrophilic molecules that interact with other molecules and ligands to generate active sites and/or provide information about the behavior of molecules and protein-ligand complexes in various solvents. Thus, Figure 12 displays the SASA value of the protein upon interaction with Ligand Nos. 08, 09, 10, and D1. The complex system's SASA value, which was found to be a mean between 05 and 165 $Å^2$, demonstrated a high level of interaction between an amino acid residue and the selected molecule (Bogatyreva and Ivankov, 2008).

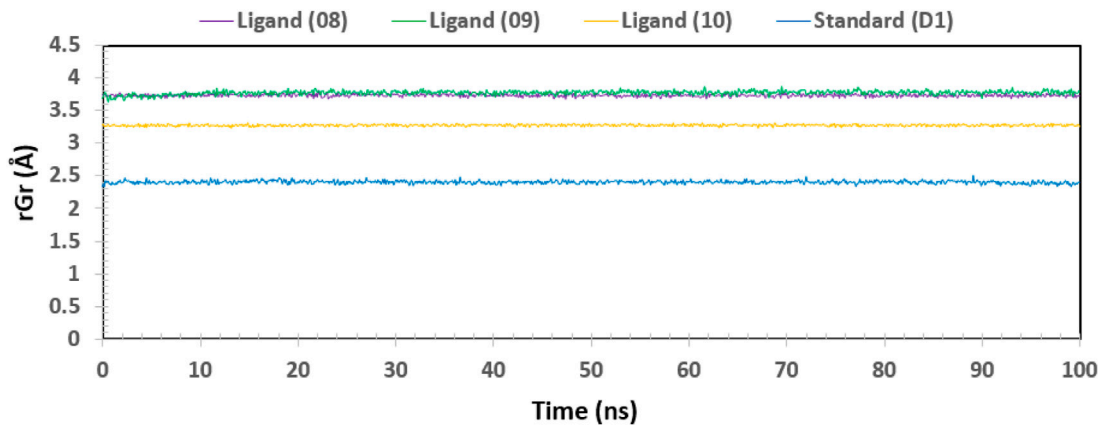

FIGURE 11
The radius of gyration (Rg) of the protein–ligand complex was calculated from the 100 ns simulation. The Rg value of the selected four compounds ligand (08), ligand (09) ligand (10) and standard (D1) in complex with the protein ID 3w32 represented by a purple, green, orange, and blue color, respectively.

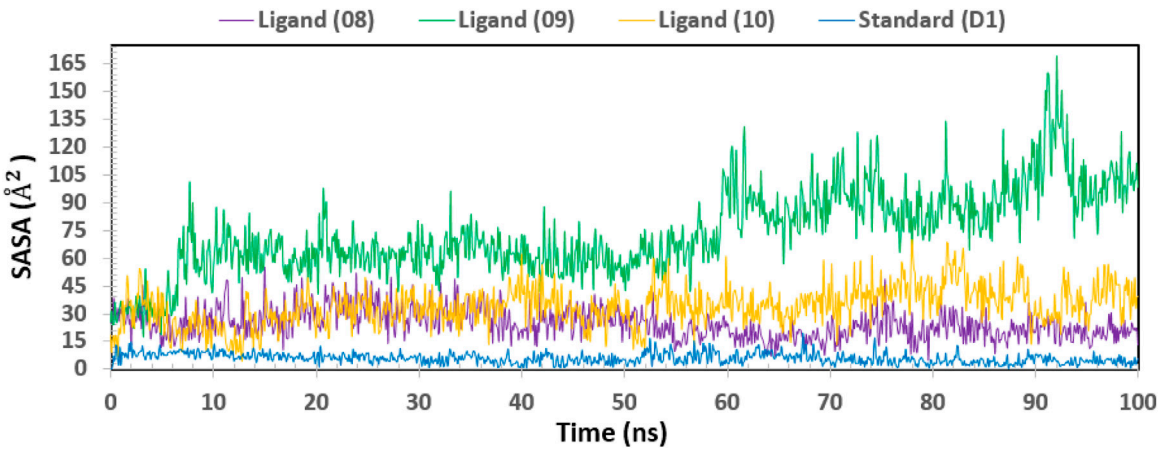

FIGURE 12
Showing the graph of solvent accessible surface area (SASA) of the protein–ligand complex for 100 ns simulation. The SASA value of the selected four compounds ligand (08), ligand (09) ligand (10) and standard (D1) in complex with the breast cancer represented by a purple, green, orange, and blue color, respectively.

Ligand-protein contacts evaluations

One of the most crucial and significant discoveries made during the SID monitoring for the 100 ns MD simulation is the evaluation of the ligand and protein contract. Following simulations, the four selected ligands (Ligand 08, Ligand 09, Ligand 10, and Standard D1) and the 3w32 proteins identified in breast cancer are shown in their interaction diagrams in Figure 13. At the active sides of ASP855, MET793, GLN791, ASP800, and CYS797, the ligand 08 interacts with protein 3w32 to form numerous (more than two) interactions with simulation times of 99%, 99%, 98%, 45%, and 34% of specific interactions sustained by the multiple contacts illustrated in Figure 13A. When ligand 09 and protein 3w32 are coupled, as Figure 13B illustrates, they interact with the active sides of MET793, GLN791, THR790, ASP800, CYS797, and ARG841 with 88%, 67%, 58%, 42%, 39%, and 35%, respectively. The active sides of ASP800, ASP855, MET793, ASN842, and ARG841 interact at 99%, 99%, 92%, 40%, and 35% when ligand 10 contracts with protein 3w32 in Figure 13C. The active sides LYS745, THR854, ASP855, PHE856, GLN791, ARG776, and THR790 interact at 99%, 99%, 99%, 94%, 57%, 67%, and 49% when the standard D1 contracts with protein 3w32, as shown in Figure 13D.

Evaluation of ADME properties

The development of new medications relies heavily on DMPK analysis. The acronym ADME stands for "absorption, distribution, metabolism, and elimination," which describes the steps taken by the body to digest and eliminate a medicine (Pellegatti, 2012). Research like this is useful for gauging the possible effectiveness of a drug (Li, 2001). The first is distribution, which describes the

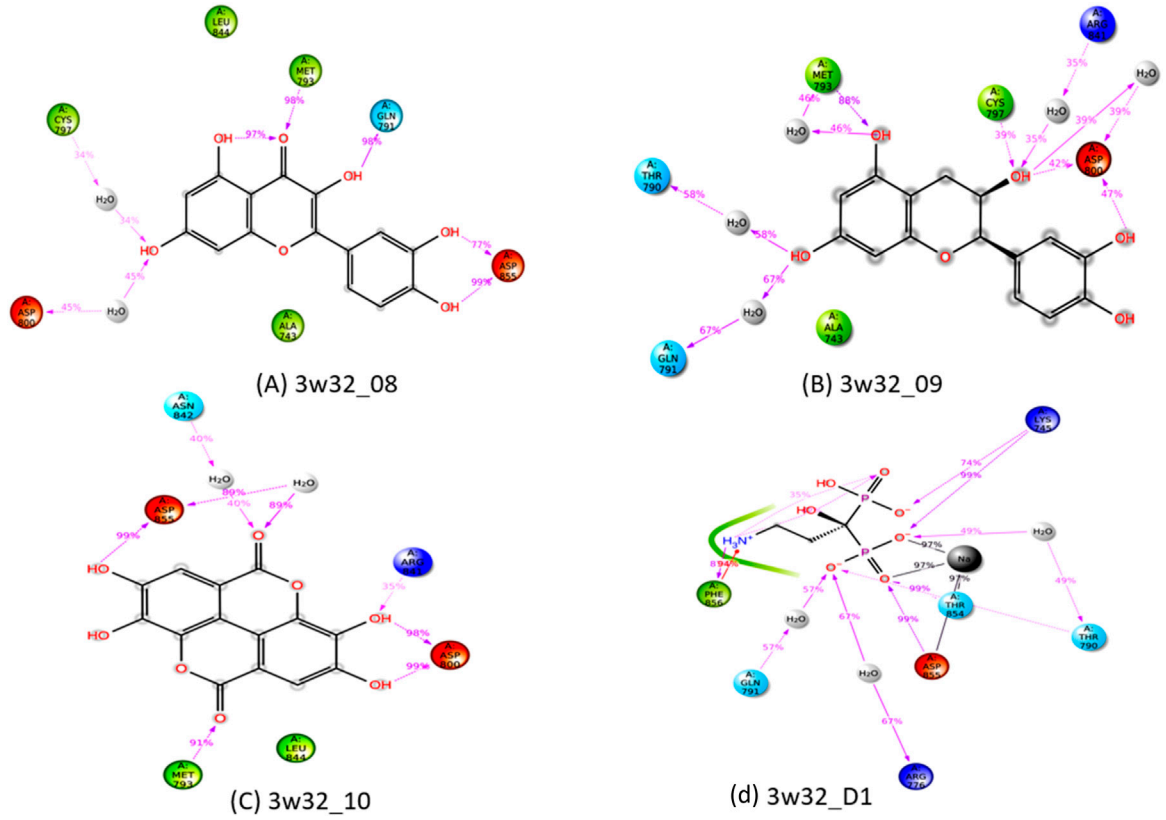

FIGURE 13
Ligand-Protein interactions diagram after simulations of 100ns: **(A)** complex of ligand 08 and protein 3w32, **(B)** complex of ligand 09and protein 3w32, **(C)** complex of ligand 10 and protein3w32, and **(D)** complex of standard D1 and protein 3w32.

speed and extent of medication delivery to various parts of the body following administration. The second component is absorption, which defines the rate and amount of medication absorption into the bloodstream following administration (Yang et al., 2017). The term "elimination" describes how quickly and efficiently a medicine is absorbed into the bloodstream. Metabolic rate (Zhang and Tang, 2018), action mechanism (Currie, 2018), metabolite structure (Guengerich, 2011), and therapeutic efficacy or safety (Smith, 2011) are all aspects of a medicine's metabolism. The negative and side effects of drugs are commonly referred to as "toxicology". Table 6 displays the methodology used to acquire data on the medicine's ADME profile from a computational forecasting internet resource. All possible therapeutic choices are quickly absorbed by humans due to their intestinal absorption rate of about 85%. For therapeutic chemicals to cross the blood-brain barrier, all of them have been found to be subcellularly localized in mitochondria. With values ranging from −1.381 to −6.773, all of the ligands were quite soluble in water; however, ligand 08 had the lowest aqua solubility value and ligand 09 had the highest. Neither a substrate nor an inhibitor for CYP 2D6 could be located.

Toxicity analysis

The possible negative effects of a substance that resembles a drug on living things are referred to as "toxicity" (Smith, 2011). The toxicity of the chosen ligands in Table 7 has been assessed in both aquatic and non-aquatic environments. Furthermore, none of the chemicals have any negative effects on the environment and are safe for ingestion by humans. The industrial compounds' acute oral toxicity varied greatly, from 1.156 kg/mol to 2.541 kg/mol. With the exception of ligands 05 and 06, all examined ligands have been confirmed to be carcinogen-free, indicating that the chemical described here does not pose a danger of cancer to living things. But it has also been shown that the ligands mentioned are non-toxic, which means that there is no risk to the environment or human health from them. Due to their lack of skin effects, the necessary ligands can be handled freely in the pharmaceutical business.

Discussion

Specifically, breast cancer refers to a malignant tumour that develops from cells within the breast. Among female-identifying cancers, it ranks first globally. Several factors, including heredity, lifestyle choices, and environmental exposure, increase the likelihood of breast cancer developing. Nevertheless, investigations into the underlying cellular and molecular processes of breast cancer's initiation, development, and metastasis are continuing. However, there are currently no viable alternatives to antiviral drugs that can combat the virus responsible for breast cancer. The proteins linked to breast cancer (PDB ID

TABLE 6 Data of ADME properties.

S/N	Absorption			Distribution		Metabolism		Excretion	
	Water solubility (Log mol/L)	Human Intestinal Absorption (%)	Caco-2 Permeability +/−	VDss (human) (log L/kg)	BBB Permeability (log BB)	CYP 2D6 Inhibitor	CYP 2D6 Substrate	Total Clearance (mL/min/kg)	Renal OCT2 substrate
01	−5.668	96.351	1.223	−0.048	0.705	No	No	0.151	No
02	−7.498	93.119	1.203	0.660	0.683	No	No	0.403	No
03	−3.181	86.684	0.335	0.375	−1.272	No	No	0.537	No
04	−3.040	74.29	0.032	1.274	−0.939	No	No	0.477	No
05	−1.381	13.831	−0.395	−0.998	−0.788	No	No	0.810	No
06	−0.660	71.748	0.603	−1.013	−0.163	No	No	0.722	No
07	−6.092	85.891	1.101	−0.016	1.222	No	No	2.188	No
08	−1.423	0.000	−0.240	−0.418	−1.017	No	No	0.895	No
09	−6.773	94.464	1.201	0.193	0.781	No	No	0.628	No
10	−6.267	95.124	1.231	0.192	0.689	No	No	−0.050	No
11	−2.504	95.277	1.184	0.034	−0.299	No	No	0.730	No
12	−3.444	95.824	1.251	−0.956	0.095	No	No	0.584	No
13	−1.377	21.510	−0.249	0.148	−0.943	No	No	0.626	No
14	−2.925	47.999	0.242	1.846	−1.688	No	No	0.394	No
15	−2.891	0.000	−1.668	0.310	−2.707	No	No	−0.418	No
D1	−3.258	100.000	0.521	1.163	−1.531	No	No	−0.411	No

3w32) play a crucial role in the advancement of the disease, according to recent discoveries. The goal of this study is to find a new and effective antiviral medication that can target the 3W32 proteins that are found in breast cancer. The experimental protein structure of 3w32 in the presence of many inhibitory drugs was initially sought after by searching the protein database. The fifteen compounds were selected from the leaf extract of Mangifera indica during the *in silico* investigation.

The assessment of the anti-viral and anti-cancer capacities, among other PASS predictive features, is shown in Supplementary Table S4. Activities against viruses and tumours were found in ligands 08, 09, and 10 (Yap et al., 2021b). We evaluated the pharmacokinetics of the four compounds using Lipinski's rules five (RO5) for molecules, and we found that they all had the desired ADME properties. Table 4 shows that all three of the selected ligands maintained RO5 levels and had excellent pharmacokinetic properties. Additional evaluation of the chemical's harmful effects on humans and animals has been conducted using the toxicity features of the molecule with good ADME properties. None or very little toxicity was seen with the three ligands selected for the study (Aljahdali et al., 2021a).

A computational DFT-based quantum mechanical simulation was used to investigate and optimize the ligand form. The DFT-optimized geometry was recovered. The FMO-based HOMO-LUMO energy gap was computed for a more thorough evaluation of the ligands' chemical activity. All of the ligands had HOMO-LUMO gap energies that were higher than 3.50 eV. Their low reactivity is consistent with their bioactivity, as seen in (Bouback et al., 2021). Molecular docking simulations were used to perform additional testing on the sixteen compounds that were selected, including standard (D1) and ligands 01–15. The docking scores produced by ligand 08, ligand 09, ligand 10, and standard (D1) against protein 3w32 were −8.5 kcal/mol, −8.4 kcal/mol, −8.5 kcal/mol, and −6.3 kcal/mol, respectively, as shown in Table 5. Not only does this docking score surpass the norm (>-6.0 kcal/mol) (Kodical et al., 2020), but we also found that the scores of the three selected ligands were greater than the standard (D1).

A molecular dynamics simulation is used to confirm the stability of a protein when it is bound to a ligand. Not only that, it can measure the stability and rigidity of protein-ligand complexes in a specific synthetic setting, like the human body (Alam et al., 2021) (Aljahdali et al., 2021b). By comparing the RMSD values of different complex systems, we can see which compounds are the most stable, and by comparing the RMSF values of different protein-ligand complexes, we can see how compact they are (Krupanidhi et al., 2021). Using the Ca atoms of the protein-ligand complexes, the RMSD of the system was calculated, validating the small protein changes. By calculating the protein's fluctuation using the RMSF value, we can see that the chemicals are stable for the target protein and that the complex system has low variation. With a smaller Rg value indicating tremendous compactness and a bigger value showing the disassociation of the ligands from the protein, all of the ligands display a greater Rg value (Elebeedy et al., 2021). A smaller SASA value indicates a less stable structure, which is indicative of a more compressed complex of water molecules and amino acid residues

TABLE 7 Aquatic and non-aquatic toxicity of selected ligands.

Ligand No	AMES toxicity	Hepatotoxicity	Oral rat Chronic Toxicity (mg/kg.bw/day)	Oral rat acute toxicity (LD50) (mol/kg)	Max. Tolerated dose (mg/kg/day)	T. Pyriformis toxicity (log ug/L)	Skin sensitisation
01	No	No	3.060	2.218	0.700	0.285	No
02	No	No	2.963	1.156	0.994	0.263	No
03	No	No	2.021	2.423	0.814	0.273	No
04	No	No	2.494	1.513	0.567	0.285	No
05	Yes	No	2.461	2.164	0.496	0.367	No
06	Yes	No	2.432	1.898	−0.296	0.195	No
07	No	No	3.897	1.214	1.896	0.285	No
08	No	No	2.612	2.471	0.499	0.288	No
09	No	No	2.500	2.428	0.438	0.347	No
10	No	No	2.698	2.399	0.476	0.295	No
11	No	No	4.417	2.541	0.569	0.285	No
12	No	No	4.277	2.396	0.58	0.285	No
13	No	No	3.977	2.373	0.613	0.285	No
14	No	No	4.417	2.541	0.569	0.285	No
15	No	No	5.113	2.481	0.4	0.285	No
D1	No	No	4.417	2.541	0.569	0.285	No

(Mahmud et al., 2021; Mahmoud et al., 2021). Results showed that the three selected ligands all had optimal Rg and SASA values. Following the evaluation of the three ligands chosen based on different qualities, which yielded a range of outcomes, the chemical has been chosen for additional research utilizing a number of wet lab-based experimental approaches.

To expedite the process of discovering new medication candidates, computational drug design enables scientists to foretell the interactions between chemicals and biological targets. Efficiently screening large chemical libraries, optimizing molecular structures, and lowering experimental costs are all made possible by this. It boosts the chances of success in subsequent experimental phases and speeds up the discovery process by simulating interactions.

Conclusion

An increasingly important, effective, and external method for finding inhibitory molecules against a particular target protein is computer-aided drug design. This work reports on the rapid and effective identification of novel natural inhibitors of cancer proteins through the application of CADD. Ligands 10, 8, and 12 emerge as the top-performing candidates due to their superior binding affinities and high numbers of interactions, with hydrophobic interactions playing a key role in enhancing their binding efficiency. Ligands 9 and 13 also show promise, although they are slightly less effective than the top performers. In contrast, ligands with fewer total bonds and weaker binding affinities, such as ligands 2, 7, and 11, are less favourable for further consideration. In addition, these compounds (Ligands 10, 8, and 12) have the potential to inhibit the activity of breast cancer cells and prevent the replication of ASP855, MET793, GLN791, ASP800, and CYS797 residues by ligand 08, MET793, GLN791, THR790, ASP800, CYS797, and ARG841 residues by ligand 09, and ASP800, ASP855, MET793, ASN842, and ARG841 residues by ligand 10 of 3w32 protease into the human host cell. Next, Ligands 1, 2, 9, 10, 12, and D1 are top candidates due to excellent absorption, balanced distribution, and moderate clearance. Ligands 8 and 15 are poor performers with zero absorption and low distribution. Ligand 7 shows potential for CNS-targeted therapies with high BBB permeability but may require adjustments due to rapid clearance. Further optimization is needed for ligands with extreme values like 5, 6, 8, and 15. However, Ligands 10, 8, and 12 emerge as the top-performing candidates for breast cancer due to investigation of their superior binding affinities, quantum descriptors and strong interactions, making them promising options for further development and investigation.

Data availability statement

The original contributions presented in the study are included in the article/Supplementary Material, further inquiries can be directed to the corresponding author.

Author contributions

MA: Methodology, Writing–original draft. AK: Data curation, Formal Analysis, Writing–original draft. IJ: Data curation, Methodology, Writing–original draft. MS: Writing–original draft, Writing–review and editing. MT: Investigation, Validation, Writing–original draft. MaR: Resources, Visualization, Writing–review and editing. AU: Resources, Software, Writing–review and editing. MH-O-R: Data curation, Methodology, Formal analysis, Investigation, Writing–review and editing. MiR: Data curation, Project administration, Writing–original draft. MH-U-R: Funding acquisition, Supervision, Writing–original draft. GS: Funding acquisition, Supervision, Writing–original draft. YA: Resources, Supervision, Writing–original draft.

Funding

The author(s) declare that financial support was received for the research, authorship, and/or publication of this article. The research was financially supported through Researchers Supporting Project Number (RSPD2025R1118), King Saud University, Riyadh, Saudi Arabia.

Acknowledgments

The authors extend their appreciation to the Researchers Supporting Project number (RSPD2025R1118) King Saud University, Riyadh, Saud Arabia.

Conflict of interest

The authors declare that the research was conducted in the absence of any commercial or financial relationships that could be construed as a potential conflict of interest.

Generative AI statement

The author(s) declare that no Generative AI was used in the creation of this manuscript.

Publisher's note

All claims expressed in this article are solely those of the authors and do not necessarily represent those of their affiliated organizations, or those of the publisher, the editors and the reviewers. Any product that may be evaluated in this article, or claim that may be made by its manufacturer, is not guaranteed or endorsed by the publisher.

Supplementary material

The Supplementary Material for this article can be found online at: https://www.frontiersin.org/articles/10.3389/fchem.2025.1524384/full#supplementary-material

References

Abdelrhman, E. M., El-Shetary, B. A., Shebl, M., and Adly, O. M. I. (2021). Coordinating behavior of hydrazone ligand bearing chromone moiety towards Cu (II) ions: synthesis, spectral, density functional theory (DFT) calculations, antitumor, and docking studies. *Appl. Organomet. Chem.* 35 (5), e6183. doi:10.1002/aoc.6183

Ahamed, F. M. M., Chinnam, S., Challa, M., Kariyanna, G., Kumer, A., Jadoun, S., et al. (2023). Molecular dynamics simulation, QSAR, DFT, molecular docking, ADMET, and synthesis of ethyl 3-((5-Bromopyridin-2-yl) imino) butanoate analogues as potential inhibitors of SARS-CoV-2. *Polycycl. Aromat. Compd.* 44, 294–312. doi:10.1080/10406638.2023.2173618

Akash, S., Abdelkrim, G., Bayil, I., Hosen, M. E., Mukerjee, N., Shater, A. F., et al. (2023). Antimalarial drug discovery against malaria parasites through haplopine modification: an advanced computational approach. *J. Cell. Mol. Med.* 27 (20), 3168–3188. doi:10.1111/jcmm.17940

Alam, R., Imon, R. R., Kabir Talukder, M. E., Akhter, S., Hossain, M. A., Ahammad, F., et al. (2021). GC-MS analysis of phytoconstituents from Ruellia prostrata and Senna tora and identification of potential anti-viral activity against SARS-CoV-2. *Rsc Adv.* 11 (63), 40120–40135. doi:10.1039/d1ra06842c

Al Hasib, R., Ali, M. C., Rahman, M. S., Rahman, M. M., Ahmed, F. F., Mashud, M. A. A., et al. (2022). A computational biology approach for the identification of potential SARS-CoV-2 main protease inhibitors from natural essential oil compounds. *F1000Res* 10, 1313. doi:10.12688/f1000research.73999.2

Aljahdali, M. O., Molla, M. H. R., and Ahammad, F. (2021a). Compounds identified from marine mangrove plant (*Avicennia alba*) as potential antiviral drug candidates against WDSV, an in-silico approach. *Mar. Drugs* 19 (5), 253. doi:10.3390/md19050253

Aljahdali, M. O., Molla, M. H. R., and Ahammad, F. (2021b). Compounds identified from marine mangrove plant (*Avicennia alba*) as potential antiviral drug candidates against WDSV, an in-silico approach. *Mar. Drugs* 19 (5), 253. doi:10.3390/md19050253

Azim, H. A., and Partridge, A. H. (2014). Biology of breast cancer in young women. *Breast cancer Res.* 16 (4), 427–429. doi:10.1186/s13058-014-0427-5

Bharadwaj, S., Dubey, A., Yadava, U., Mishra, S. K., Kang, S. G., and Dwivedi, V. D. (2021). Exploration of natural compounds with anti-SARS-CoV-2 activity via inhibition of SARS-CoV-2 Mpro. *Brief. Bioinform* 22 (2), 1361–1377. doi:10.1093/bib/bbaa382

Bogatyreva, N. S., and Ivankov, D. N. (2008). The relationship between the solvent-accessible surface area of a protein and the number of native contacts in its structure. *Mol. Biol.* 42, 932–938. doi:10.1134/s0026893308060150

Bouback, T. A., Pokhrel, S., Albeshri, A., Aljohani, A. M., Samad, A., Alam, R., et al. (2021). Pharmacophore-based virtual screening, quantum mechanics calculations, and molecular dynamics simulation approaches identified potential natural antiviral drug candidates against MERS-CoV S1-NTD. *Molecules* 26 (16), 4961. doi:10.3390/molecules26164961

Bronowska, A. K. (2011). "Thermodynamics of ligand-protein interactions: implications for molecular design," in *Thermodynamics-interaction studies-solids, liquids and gases* (IntechOpen).

Burley, S. K., Bhikadiya, C., Bi, C., Bittrich, S., Chao, H., Chen, L., et al. (2023). RCSB Protein Data Bank (RCSB. org): delivery of experimentally-determined PDB structures alongside one million computed structure models of proteins from artificial intelligence/machine learning. *Nucleic Acids Res.* 51 (D1), D488–D508. doi:10.1093/nar/gkac1077

Currie, G. M. (2018). Pharmacology, part 2: introduction to pharmacokinetics. *J. Nucl. Med. Technol.* 46 (3), 221–230. doi:10.2967/jnmt.117.199638

da Cunha Xavier, J., dos Santos, H. S., Machado Marinho, M., Nunes da Rocha, M., Rodrigues Teixeira, A. M., Coutinho, H. D. M., et al. (2024). Chalcones as potent agents against *Staphylococcus aureus*: a computational approach. *Lett. Drug Des. Discov.* 21 (4), 684–700. doi:10.2174/1570180820666230120145921

Daina, A., Michielin, O., and Zoete, V. (2017). SwissADME: a free web tool to evaluate pharmacokinetics, drug-likeness and medicinal chemistry friendliness of small molecules. *Sci. Rep.* 7, 42717. doi:10.1038/srep42717

Dallakyan, S., and Olson, A. J. (2015). Small-molecule library screening by docking with PyRx. *Chem. Biol. methods Protoc.* 1263, 243–250. doi:10.1007/978-1-4939-2269-7_19

Ding, F., and Peng, W. (2019). Probing the local conformational flexibility in receptor recognition: mechanistic insight from an atomic-scale investigation. *RSC Adv.* 9 (25), 13968–13980. doi:10.1039/c9ra01906e

Druzhilovskiy, D. S., V Rudik, A., Filimonov, D. A., Lagunin, A. A., Gloriozova, T. A., and V Poroikov, V. (2016). Online resources for the prediction of biological activity of organic compounds. *Russ. Chem. Bull.* 65, 384–393. doi:10.1007/s11172-016-1310-6

Efferth, T., and Koch, E. (2011). Complex interactions between phytochemicals. The multi-target therapeutic concept of phytotherapy. *Curr. Drug Targets* 12 (1), 122–132. doi:10.2174/138945011793591626

Elebeedy, D., Elkhatib, W. F., Kandeil, A., Ghanem, A., Kutkat, O., Alnajjar, R., et al. (2021). Anti-SARS-CoV-2 activities of tanshinone IIA, carnosic acid, rosmarinic acid, salvianolic acid, baicalein, and glycyrrhetinic acid between computational and *in vitro* insights. *RSC Adv.* 11 (47), 29267–29286. doi:10.1039/d1ra05268c

Fisusi, F. A., and Akala, E. O. (2019). Drug combinations in breast cancer therapy. *Pharm. Nanotechnol.* 7 (1), 3–23. doi:10.2174/2211738507666190122111224

Fu, Y., Zhao, J., and Chen, Z. (2018). Insights into the molecular mechanisms of protein-ligand interactions by molecular docking and molecular dynamics simulation: a case of oligopeptide binding protein. *Comput. Math. Methods Med.* 2018, 1–12. doi:10.1155/2018/3502514

Fukutani, T., Miyazawa, K., Iwata, S., and Satoh, H. (2021). G-RMSD: root mean square deviation based method for three-dimensional molecular similarity determination. *Bull. Chem. Soc. Jpn.* 94 (2), 655–665. doi:10.1246/bcsj.20200258

Guengerich, F. P. (2011). Mechanisms of drug toxicity and relevance to pharmaceutical development. *Drug Metab. Pharmacokinet.* 26 (1), 3–14. doi:10.2133/dmpk.dmpk-10-rv-062

Guerrab, W., El Jemli, M., Akachar, J., Demirtaş, G., Mague, J. T., Taoufik, J., et al. (2022). Design, synthesis, structural and molecular characterization, toxicity, psychotropic activity and molecular docking evaluation of a novel phenytoin derivative: 3-decyl-5, 5-diphenylimidazolidine-2, 4-dione. *J. Biomol. Struct. Dyn.* 40 (19), 8765–8782. doi:10.1080/07391102.2021.1922096

Hortobagyi, G. N. (1998). Treatment of breast cancer. *N. Engl. J. Med.* 339 (14), 974–984. doi:10.1056/nejm199810013391407

Hosen, M. A., Alam, A., Islam, M., Fujii, Y., Ozeki, Y., and Kawsar, S. M. A. (2021). Geometrical optimization, PASS prediction, molecular docking, and *in silico* ADMET studies of thymidine derivatives against FimH adhesin of *Escherichia coli*. *Bulg. Chem. Commun.* 53 (3), 327–342.

Kobir, M. E., Ahmed, A., Roni, M. A. H., Chakma, U., Amin, M. R., Chandro, A., et al. (2023). Anti-lung cancer drug discovery approaches by polysaccharides: an *in silico* study, quantum calculation and molecular dynamics study. *J. Biomol. Struct. Dyn.* 41 (14), 6616–6632. doi:10.1080/07391102.2022.2110156

Kodical, D. D., James, J. P., Deepthi, K., Kumar, P., Cyriac, C., and V Gopika, K. (2020). ADMET, Molecular docking studies and binding energy calculations of Pyrimidine-2-Thiol Derivatives as Cox Inhibitors. *Res. J. Pharm. Technol.* 13 (9), 4200–4206. doi:10.5958/0974-360x.2020.00742.8

Kolak, A., Kamińska, M., Sygit, K., Budny, A., Surdyka, D., Kukiełka-Budny, B., et al. (2017). Primary and secondary prevention of breast cancer. *Ann. Agric. Environ. Med.* 24 (4), 549–553. doi:10.26444/aaem/75943

Krupanidhi, S., Abraham Peele, K., Venkateswarulu, T. C., Ayyagari, V. S., Nazneen Bobby, M., John Babu, D., et al. (2021). Screening of phytochemical compounds of Tinospora cordifolia for their inhibitory activity on SARS-CoV-2: an *in silico* study. *J. Biomol. Struct. Dyn.* 39 (15), 5799–5803. doi:10.1080/07391102.2020.1787226

Kumar, M., Saurabh, V., Tomar, M., Hasan, M., Changan, S., Sasi, M., et al. (2021). Mango (Mangifera indica L.) leaves: nutritional composition, phytochemical profile, and health-promoting bioactivities. *Antioxidants* 10 (2), 299. doi:10.3390/antiox10020299

Lakshminarayanan, S., Jeyasingh, V., Murugesan, K., Selvapalam, N., and Dass, G. (2021). Molecular electrostatic potential (MEP) surface analysis of chemo sensors: an extra supporting hand for strength, selectivity and non-traditional interactions. *J. Photochem Photobiol.* 6, 100022. doi:10.1016/j.jpap.2021.100022

Lavé, T., Caruso, A., Parrott, N., and Walz, A. (2016). Translational PK/PD modeling to increase probability of success in drug discovery and early development. *Drug Discov. Today Technol.* 21, 27–34. doi:10.1016/j.ddtec.2016.11.005

Li, A. P. (2001). Screening for human ADME/Tox drug properties in drug discovery. *Drug Discov. Today* 6 (7), 357–366. doi:10.1016/s1359-6446(01)01712-3

Liu, K., Watanabe, E., and Kokubo, H. (2017). Exploring the stability of ligand binding modes to proteins by molecular dynamics simulations. *J. Comput. Aided Mol. Des.* 31, 201–211. doi:10.1007/s10822-016-0005-2

Macalino, S. J. Y., Gosu, V., Hong, S., and Choi, S. (2015). Role of computer-aided drug design in modern drug discovery. *Arch. Pharm. Res.* 38, 1686–1701. doi:10.1007/s12272-015-0640-5

Madhavi Sastry, G., Adzhigirey, M., Day, T., Annabhimoju, R., and Sherman, W. (2013). Protein and ligand preparation: parameters, protocols, and influence on virtual screening enrichments. *J. Comput. Aided Mol. Des.* 27 (3), 221–234. doi:10.1007/s10822-013-9644-8

Mahmoud, A., Mostafa, A., Al-Karmalawy, A. A., Zidan, A., Abulkhair, H. S., Mahmoud, S. H., et al. (2021). Telaprevir is a potential drug for repurposing against SARS-CoV-2: computational and *in vitro* studies. *Heliyon* 7 (9), e07962. doi:10.1016/j.heliyon.2021.e07962

Mahmud, S., Rahman, E., Nain, Z., Billah, M., Karmakar, S., Mohanto, S. C., et al. (2021). Computational discovery of plant-based inhibitors against human carbonic anhydrase IX and molecular dynamics simulation. *J. Biomol. Struct. Dyn.* 39 (8), 2754–2770. doi:10.1080/07391102.2020.1753579

Mendichi, R., Šoltés, L., and Giacometti Schieroni, A. (2003). Evaluation of radius of gyration and intrinsic viscosity molar mass dependence and stiffness of hyaluronan. *Biomacromolecules* 4 (6), 1805–1810. doi:10.1021/bm0342178

Mirza, B., Croley, C. R., Ahmad, M., Pumarol, J., Das, N., Sethi, G., et al. (2021). Mango (Mangifera indica L.): a magnificent plant with cancer preventive and anticancer therapeutic potential. *Crit. Rev. Food Sci. Nutr.* 61 (13), 2125–2151. doi:10.1080/10408398.2020.1771678

Mohapatra, R. K., El-ajaily, M. M., Alassbaly, F. S., Sarangi, A. K., Das, D., Maihub, A. A., et al. (2021). DFT, anticancer, antioxidant and molecular docking investigations of some ternary Ni (II) complexes with 2-[(E)-[4-(dimethylamino) phenyl] methyleneamino] phenol. *Chem. Pap.* 75, 1005–1019. doi:10.1007/s11696-020-01342-8

Pellegatti, M. (2012). Preclinical *in vivo* ADME studies in drug development: a critical review. *Expert Opin. Drug Metab. Toxicol.* 8 (2), 161–172. doi:10.1517/17425255.2012.652084

Poroikov, V. V., Filimonov, D. A., Gloriozova, T. A., Lagunin, A. A., Druzhilovskiy, D. S., Rudik, A. V., et al. (2019). Computer-aided prediction of biological activity spectra for organic compounds: the possibilities and limitations. *Russ. Chem. Bull.* 68, 2143–2154. doi:10.1007/s11172-019-2683-0

Rasul, A., Riaz, A., Wei, W., Sarfraz, I., Hassan, M., Li, J., et al. (2021). [Retracted] Mangifera indica extracts as novel PKM2 inhibitors for treatment of triple negative breast cancer. *Biomed. Res. Int.* 2021, 1–11. doi:10.1155/2021/5514669

Rojas, K., and Stuckey, A. (2016). Breast cancer epidemiology and risk factors. *Clin. Obstet. Gynecol.* 59 (4), 651–672. doi:10.1097/grf.0000000000000239

Sherman, W., Day, T., Jacobson, M. P., Friesner, R. A., and Farid, R. (2006). Novel procedure for modeling ligand/receptor induced fit effects. *J. Med. Chem.* 49 (2), 534–553. doi:10.1021/jm050540c

Siddikey, F., Roni, M., Kumer, A., Chakma, U., and Matin, M. (2022). Computational investigation of Betalain derivatives as natural inhibitor against food borne bacteria. *Curr. Chem. Lett.* 11 (3), 309–320. doi:10.5267/j.ccl.2022.3.003

Singh, R., Bhardwaj, V. K., and Purohit, R. (2022). Inhibition of nonstructural protein 15 of SARS-CoV-2 by golden spice: a computational insight. *Cell. Biochem. Funct.* 40 (8), 926–934. doi:10.1002/cbf.3753

Singh, R. K., and Singh, A. K. (2017). DFT calculations on molecular structure, spectral analysis, multiple interactions, reactivity, NLO property and molecular docking study of flavanol-2, 4-dinitrophenylhydrazone. *J. Mol. Struct.* 1129, 128–141. doi:10.1016/j.molstruc.2016.09.072

Smith, G. F. (2011). "Designing drugs to avoid toxicity," in *Prog. Med. Chem.*, vol. 50. 1–47. doi:10.1016/b978-0-12-381290-2.00001-x

Sun, Y.-S., Zhao, Z., Yang, Z. N., Xu, F., Lu, H. J., Zhu, Z. Y., et al. (2017). Risk factors and preventions of breast cancer. *Int. J. Biol. Sci.* 13 (11), 1387–1397. doi:10.7150/ijbs.21635

Timofeev, V. I., Gaponov, Y., Petrenko, D., Peters, G., Agapova, Y., Nikolaeva, A., et al. (2023). How the hinge region affects interactions between the catalytic and β-propeller domains in oligopeptidase B. *Cryst. (Basel)* 13 (12), 1642. doi:10.3390/cryst13121642

Tran, P., Lee, S.-E., Kim, D.-H., Pyo, Y.-C., and Park, J.-S. (2020). Recent advances of nanotechnology for the delivery of anticancer drugs for breast cancer treatment. *J. Pharm. Investig.* 50, 261–270. doi:10.1007/s40005-019-00459-7

Avidon, V., Pomerantsev, I. A., Golender, V. E., and Rozenblit, A. B. (1982). Structure-activity relationship oriented languages for chemical structure representation. *J. Chem. Inf. Comput. Sci.* 22 (4), 207–214. doi:10.1021/ci00036a006

Pires, D. E., Blundell, T. L., and Ascher, D. B. (2015). pkCSM: predicting small-molecule pharmacokinetic and toxicity properties using graph-based signatures. *J. Med. Chem.* 58 (9), 4066–4072. doi:10.1021/acs.jmedchem.5b00104

Yang, Y., Zhao, Y., Yu, A., Sun, D., and Yu, L. X. (2017). "Oral drug absorption: evaluation and prediction," in *Developing solid oral dosage forms* (Elsevier), 331–354.

Yap, K. M., Sekar, M., Seow, L. J., Gan, S. H., Bonam, S. R., Mat Rani, N. N. I., et al. (2021a). Mangifera indica (Mango): a promising medicinal plant for breast cancer therapy and understanding its potential mechanisms of action. *Breast Cancer Targets Ther.* Vol. 13, 471–503. doi:10.2147/bctt.s316667

Yap, K. M., Sekar, M., Seow, L. J., Gan, S. H., Bonam, S. R., Mat Rani, N. N. I., et al. (2021b). Mangifera indica (Mango): a promising medicinal plant for breast cancer therapy and understanding its potential mechanisms of action. *Breast Cancer Targets Ther.* Vol. 13, 471–503. doi:10.2147/bctt.s316667

Yu, J., Su, N. Q., and Yang, W. (2022). Describing chemical reactivity with frontier molecular orbitalets. *JACS Au* 2 (6), 1383–1394. doi:10.1021/jacsau.2c00085

Yu, W., and MacKerell, A. D. (2017). "Computer-aided drug design methods," in *Antibiotics: methods and protocols*, 85–106.

Zhang, Z., and Tang, W. (2018). Drug metabolism in drug discovery and development. *Acta Pharm. Sin. B* 8 (5), 721–732. doi:10.1016/j.apsb.2018.04.003

Zhao, Z., and Bourne, P. E. (2022). Harnessing systematic protein–ligand interaction fingerprints for drug discovery. *Drug Discov. Today* 27, 103319. doi:10.1016/j.drudis.2022.07.004

Zhou, W., Wang, Y., Lu, A., and Zhang, G. (2016). Systems pharmacology in small molecular drug discovery. *Int. J. Mol. Sci.* 17, 246. doi:10.3390/ijms17020246

Frontiers in Chemistry

Explores all fields of chemical science across the periodic table

Advances our understanding of how atoms, ions, and molecules come together and come apart. It explores the role of chemistry in our everyday lives - from electronic devices to health and wellbeing.

Discover the latest Research Topics

See more →

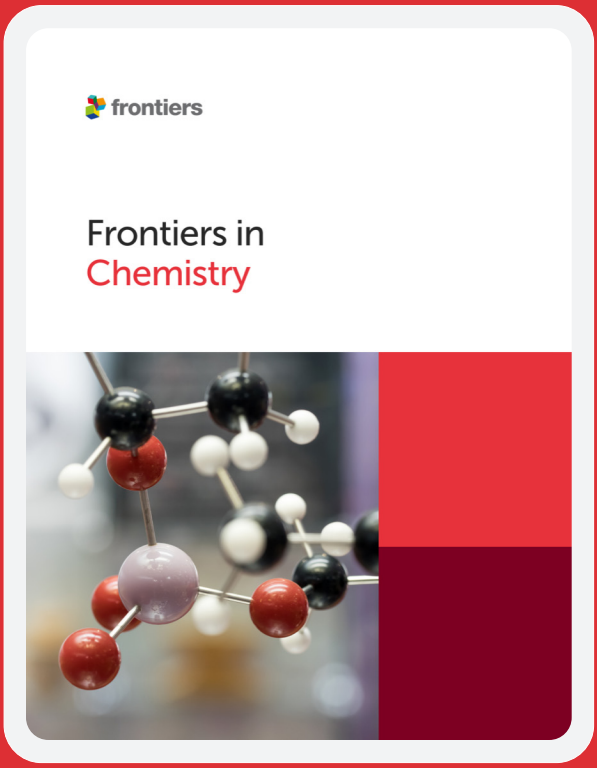

Frontiers

Avenue du Tribunal-Fédéral 34
1005 Lausanne, Switzerland
frontiersin.org

Contact us

+41 (0)21 510 17 00
frontiersin.org/about/contact